Abstracts of the 20th International Symposium on Advanced Technology (ISAT-20)

Advanced Technologies for SDG

November 23-24, 2021

Kogakuin University of Technology and Engineering, Japan

A Virtual Conference organized by the

Kogakuin University of Technology and Engineering

Co-Sponsored by

Southern Taiwan University of Science and Technology

The University of Danang - Danang University of Science and Technology

University of the Philippines

University of the Philippines Los Banos

Edited by the

20th International Symposium on Advanced Technology

Published by the

Kogakuin University of Technology & Engineering, Japan

ISSN 2434-4273

The 20th International Symposium on Advanced Technology (ISAT-20)

November 23-24, 2021

Kogakuin University of Technology and Engineering, Japan

Table of Contents

Message from Kogakuin University of Technology and Engineering

Greetings from Tokyo, Japan!

Kogakuin University of Technology and Engineering (KUTE-Tokyo) is proud and happy to welcome you all to the virtual iteration of the ISAT-20, the 20th International Symposium on Advanced Technology.

This symposium had first held at KUTE-Tokyo in 2002 and is being held annually in turn between partner universities to share the scientific research excellences and to foster the scientific cooperation between the member universities. And it is the 20th anniversary symposium this year. For this year, our main theme, “Advanced Technologies for SDGs” is highly relevant as we face current global issues.

The terrible infection of the COVID-19 is spread in the world and interferes with the person-to-person direct contact over past 2 years. On the other hand, this important symposium ISAT aims to develop the sustainable society by promoting “close relationship construction.” Under any circumstances, ISAT is convinced of a great opportunity to gather wisdom regarding "science and technology" and continuously contribute to the development of sustainable society.

We thank all participants. The numbers and various fields of the submitted papers helps us predict a fantastic symposium.
I would like to express my sincere thanks to the committee members and my appreciation to the partner universities. And we do hope to have opportunity to share the time on site in near future.

Shinichiro Ito
President, Kogakuin University of Technology and Engineering

Southern Taiwan University of Science and Technology

Message for ISAT from STUST

The ISAT (International Symposium on Advanced Technology) conference has been held by Kogakuin University in 2002 and has entered the 20th anniversary this year. The main purpose of ISAT is to promote academic communication between scholars from east Asian countries. At present, scholars from Japan, Taiwan, Vietnam, and the Philippines have participated, and the number of papers and the scale of conferences are gradually expanding. Thanks to the efforts from the scholars from all countries, this conference has shown its excellent results in enhancing the academic exchange goals of East Asia.

STUST is Taiwan's leading university of science and technology. The educational mission of this school is to combine academic research and technological development to cultivate high-quality scientific and technological talents for Taiwan. In the past two years, countries have faced great pressure due to the impact of the COVID-19 pandemic. Therefore, this year's conference was held online. Fortunately, the impact of the epidemic has gradually diminished. I believe that the day when outstanding scholars from all over the world gather again to discuss academic issues together is not far away.

I would like to thank again the host Professor Ito and Sato, principles of Kogakuin University for their continuous efforts to promote ISAT, and I also express my best regard to all the participants.

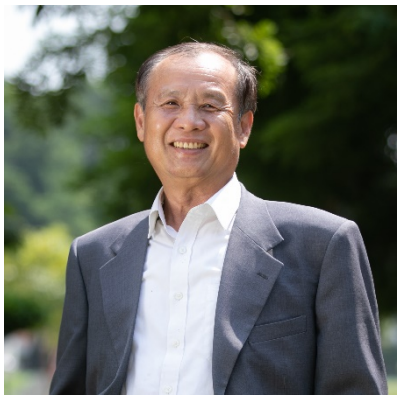

Deng-Maw Lu

Prof. Lu, Deng-Maw

President, Southern Taiwan University of Science and Technology

Message from DUT

The University of Danang – University of Science and Technology (UD-DUT) has since its establishment in 1975 predicated its leading position in the system of higher education in Vietnam and in Southeastern Asia. Not only is UD-DUT a center for training highly-qualified human resources in various industrial fields, but also a hub for scientific research, innovation and technology transfer for Central Vietnam and for the whole country. In that spirit, UD-DUT is very proud to be one of four sponsors for the International Symposium on Advanced Technology (ISAT). This annual symposium is a valuable forum aiming to promote scientific and technologic exchange between leading scientists, researchers for the purpose of resolving pressing national and social issues.

Due to the Covid-19 pandemic, the 20th ISAT, which will be organized online from 23 to 24 November 2021, is hosted by Kogakuin University of Technology and Engineering (Japan), which is also the founding member of this symposium. The main theme of ISAT-20 is "Advanced Technologies for SDGs" in which many specific topics will be covered, including "Biochemistry and Food Science", "Synthetic Chemistry and Medicinal Chemistry", "Information and Communications Technology", "Energy and Transportation", "Architecture and Civil Engineering". I truly believe that the technical program, with a broad range of specific discussion topics and with participants' positive contributions, will make ISAT-20 most productive and fruitful. I also truly believe that successful outcomes from ISAT-20 will certainly contribute in response to the achievement of 17 Sustainable Development Goals which were addressed by the United Nations in 2015.

I would like to express my sincere thanks to the organizing committee members and wish you a pleasurable and rewarding ISAT-20.

Sincerely Yours,

Prof. DOAN Quang Vinh

Rector, The University of Danang – University of Science and Technology

University of the Philippines
LOS BAÑOS

OFFICE OF THE CHANCELLOR

MESSAGE

On behalf of the University of the Philippines Los Baños (UPLB), I warmly welcome all the speakers, presenters, participants, and partners of the **20th International Symposium on Advanced Technology (ISAT-20)**.

With the theme "Advanced Technologies for Sustainable Development Goals (SDGs)," ISAT-20 provides an avenue for relevant and timely conversations, as well as exchanges of knowledge, about current and emerging advanced technologies that can help bring us closer to achieving our goals for our country and planet.

I am confident that the wide thematic scope of ISAT-20 Conference will foster further collaboration and participation among attending scholars to come up with more exciting, inclusive, and sustainable technologies that could help us achieve our collective goals.

I congratulate the UPLB College of Engineering and Agro-Industrial Technology, Kogakuin University of Technology and Engineering, Southern Taiwan University of the Science and Technology, University of Danang, and Danang University of Science and Technology (DUST) for their collaborative effort in staging ISAT-20.

I wish everyone an insightful and inspiring conference.

JOSE V. CAMACHO, JR.
Chancellor

(+63) 49 536 2567 | (+63) 49 536 2894 (+63) 49 536 3673 oc.uplb@up.edu.ph www.uplb.edu.ph
College, Los Baños, Laguna, Philippines 4031

General Information of ISAT-20

1. Main theme of ISAT-20: Advanced Technologies for SDGs

Topics of ISAT-20 include, but not limited to:

1. Biochemistry and Food Science
2. Synthetic Chemistry and Medicinal Chemistry
3. Information and Communications Technology (ICT)
4. Energy and Transportation
5. Advanced Functional Materials
6. Architectural and Civil Engineering
7. Intelligent and Secure Systems
8. Education and Human Studies
9. Environmental Chemistry and Chemical Engineering
10. Simulation Science, Measurement Science, Computational Science
11. Electric Engineering and Electronic Engineering
12. Mechanical Engineering

The symposium program will consist of key-note lectures, oral presentations, and lightning talk sessions.

Language: English will be the official language during the conference.
Conference Venue: The conference will be held by online
Conference website: https://www.kogakuin.ac.jp/isat/

2. Presentation Guidelines

Presentation Type	Presentation Time
Keynote Sessions	35 minutes (LIVE)
Oral Sessions	15 minutes (LIVE)
Lightning Talk Sessions	5 minutes (pre-recorded)

Live Keynote and Oral Presentations Sessions:

The time allocated to each presentation will be:

Key-note: 35 minutes talk and 5 minutes for discussion
Oral Session: 15 minutes talk and 5 minutes for discussion.

Lightning Talk Sessions:

5 minutes pre-recorded presentation will be open to the conference website.
The presenters are required to communicate with attendees via online.

Organization

Advisory and Committee members

Organizing committee

Chairperson:

Prof. Shinichiro Ito	President, Kogakuin University of Technology and Engineering (KUTE), Japan

Co-chairperson:

Prof. Deng-Maw Lu	President, Southern Taiwan University of Science and Technology (STUST), Taiwan
Prof. DOAN Quang Vinh	Rector, The University of Danang - University of Science and Technology (UD-DUT), Vietnam
Dr. Jose V. Camacho, Jr.	Chancellor, University of the Philippines Los Baños (UPLB), Philippines

Vice-chairperson:

Prof. Yasushi Nozawa	Vice President, School of Architecture, Kogakuin University of Technology and Engineering (KUTE), Japan
Prof. Miyuki Kamachi	Vice President, Faculty of Informatics, Kogakuin University of Technology and Engineering (KUTE), Japan
Prof. Ming-Shyan Wang	Department of Electrical Engineering, Southern Taiwan University of Science and Technology (STUST), Taiwan
Prof. Sheng-Chang Wang	Department of Mechanical Engineering, Southern Taiwan University of Science and Technology (STUST), Taiwan
Prof. Zong-Xian Yin	Department of Computer Science and Information, Southern Taiwan University of Science and Technology (STUST), Taiwan
Prof. LE Thi Kim Oanh	Vice Rector, The University of Danang - University of Science and Technology (UD-DUT), Vietnam
Prof. Rossana Marie C. Amongo	Dean, College of Engineering and Agro-industrial Technology University of the Philippines Los Baños (UPLB), Philippines

Advisory Board

Board of directors:

Prof. Osamu Goto	Chair, Board of Trustees, KUTE

Members:

Prof. Masayuki Tamagawa	Managing Executive Director, KUTE
Mr. Hiroshi Mieno	Managing Executive Director, KUTE
Prof. Yasutada Imamura	Executive Director, KUTE
Mr. Akira Sugihara	Executive Director, KUTE
Mr. Hideki Kuji	Full-time Auditor

Executive committee

Chairperson:

Prof. Kazuhito Nishimura	Chair, International Committee, KUTE

Members:

Prof. Fumitaka Oyama	Dean, School of Advanced Engineering, KUTE
Prof. Ichiro Takano	Dean, Faculty of Engineering, KUTE
Prof. Atsuo Kakehi	Dean, School of Architecture, KUTE
Prof. Yoshio Miki	Dean, Faculty of Informatics, KUTE
Prof. Tetsuo Shindo	Dean, Center for Promotion of Higher Education, KUTE

Technical Program committee

Chairperson:

Prof. Masaki Tamura	Department of Architecture, School of Architecture, KUTE

Members:

Dr. Nobuhiro Aburai	Department of Chemistry and Life Science, School of Advanced Engineering, KUTE
Dr. Hideki Hashimoto	Department of Applied Chemistry, School of Advanced Engineering, KUTE
Dr. Hiroki Nagai	Department of Applied Physics, School of Advanced Engineering, KUTE
Dr. Koji Hasegawa	Department of Mechanical Engineering, Faculty of Engineering, KUTE
Dr. Masakazu Mukai	Department of Electrical and Electronic Engineering, Faculty of Engineering, KUTE
Prof. Yusuke Nakajima	Department of Urban Design and Planning, School of Architecture, KUTE
Dr. Yukihiro Kudoh	Department of Information and Communications Engineering, Faculty of Informatics, KUTE
Dr. Kanta Tachibana	Department of Information System and Applied Mathematics, Faculty of Informatics, KUTE
Prof. Morio Yoshida	Division of Global and Carrier Education, Center for Promotion of Higher Education, KUTE
Prof. Hong-Ru Lin	Department of Chemical and Materials Engineering, STUST, Taiwan
Prof. Po-Ting Chen	Department of Biotechnology and Food Technology, STUST, Taiwan
Prof. Jeng-Han Li	Department of Electrical Engineering, STUST, Taiwan
Prof. Nai-Shang Liou	Department of Mechanical Engineering, STUST, Taiwan
Dr. TAO Quang Bang	Head of the Department of Science, Technology, and International Cooperation The University of Danang – University of Science and Technology (UD-DUT), Vietnam
Dr. NGUYEN Thanh Binh	Deputy Head of the Department of Science, Technology, and International Cooperation The University of Danang - University of Science and Technology (UD-DUT), Vietnam
Dr. Kevin F. Yaptenco	University of the Philippines Los Baños (UPLB), Philippines
Dr. Roger A. Luyun, Jr	University of the Philippines Los Baños (UPLB), Philippines
Dr. Monet Concepcion M. Detras	University of the Philippines Los Baños (UPLB), Philippines
Dr. Butch G. Bataller	University of the Philippines Los Baños (UPLB), Philippines
Dr. Marion Lux Y. Castro	University of the Philippines Los Baños (UPLB), Philippines

General Schedule

◆November 23rd

Japan (JST)	Taiwan, Philippines (TST/PTS)	Vietnam (ICT)						
11:45	10:45	9:45	LOG-IN AND ROLL CALL https://zoom.us/j/92411282908 Passcode: isat					
12:00	11:00	10:00	OPENING CEREMONY **Prof. Shinichiro Ito** President, Kogakuin University of Technology and Engineering **Prof. Lu, Deng-Maw** President, Southern Taiwan University of Science and Technology **Prof. Doan Quang Vinh** Rector, The University of Danang - University of Science and Technology **Prof. Jose D. Camacho, Jr.** Chancellor, University of the Philippines Los Baños Master of Ceremony: Dr. Kanta Tachibana, KUTE-Tokyo					
12:30	11:30	10:30	KEYNOTE PRESENTATION 1 Why do animals have their shape? - Movement and shape - **Prof. Shinichiro Ito** **Department of Mechanical Engineering, Faculty of Engineering** **President, Kogakuin University of Technology and Engineering, Japan** Chair Person: Prof. Yi-Chu Hsu, Department of Mechanical Engineering STUST					
13:15	12:15	11:15	KEYNOTE PRESENTATION 2 Case study of using artificial intelligence technology to construct a smart hospital **Prof. Chang, Wan-Jung,** **Department of Electronic Engineering, Director of Medical and Intelligence Technology Research Center (MIT Center)** **Southern Taiwan University of Science and Technology, Taiwan** Chair Person: Dr Ngo Minh Tri, Dean of the department Electronics and Telecommunication, DUT					
14:00	13:00	12:00	BREAK, LOG-IN AND ROLL CALL					
			ORAL PRESENTATION, PARAREL SESSHON https://zoom.us/j/91076792471 Passcode: isat					
			Breakout Room	**1**	**2**	**3**	**4**	**5**
14:10	13:10	12:10	**ORAL1**	BFS1	EEE1	ECC1	SSM1	ME1
14:30	13:30	12:30	**ORAL2**	BFS2	EEE2	ECC2	SSM2	ME2
14:50	13:50	12:50	**ORAL3**	BFS3	EEE3	ECC3	SSM3	ME3
15:10	14:10	13:10	**ORAL4**	SC1	EEE4	ECC4	SSM4	ME4
15:30	14:30	13:30	BREAK, LOG-IN AND ROLL CALL					
			LIGHTNING TALK SESSION, PARAREL SESSHON https://zoom.us/j/91076792471 Passcode: isat					
			Breakout Room	**1**	**2**	**3**	**4**	**5**
15:45	14:45	13:45	**LIGHTNING1**	AFML 1-5	EEEL 1-5	ICTL 1-5	SSML 1-4	MEL 1-4
16:15	15:15	14:15	**LIGHTNING2**	AFML 6-9	EEEL 6-10	ICTL 6,8,9,11,12	SSML 5-8	MEL 5-7
16:45	15:45	14:45	BREAK					
			Breakout Room	**1**	**2**	**3**	**4**	**5**
17:00	16:00	15:00	**LIGHTNING3**	BFSL 1-4	EEEL 11-15	ICTL 7,10,13,14	EHSL 1-3	ACEL 1-6
17:30	16:30	15:30	**LIGHTNING4**	BFSL 5-8	EEEL 16-19	ICTL 15-18 ISSL 1	ETL 1-3	ECCL 1-4

◆November 24th

Japan (JST)	Taiwan, Philippines (TST/PTS)	Vietnam (ICT)						
11:45	10:45	9:45	LOG-IN AND ROLL CALL https://zoom.us/j/92411282908 Passcode: isat					
12:00	11:00	10:00	KEYNOTE PRESENTATION 3 Development of BK-Anticovid Robot **Dr. VO Nhu Thanh and Dr. LE Hoai Nam** **Mechatronic Division, Faculty of Mechanical Engineering,** **University of Science and Technology, The University of Da Nang, Viet Nam** Chair Person: Assistant Professor Erwin P. Quilloy Agri-biosystems Machinery and Power Engineering Division, Institute of Agricultural and Biosystems Engineering College of Engineering and Agro-industrial Technology, UPLB						
12:45	11:45	10:45	KEYNOTE PRESENTATION 4 **Honorable Danilo L. Concepcion** **President, University of the Philippines** Chair Person: Prof. Yasushi Nozawa, School of Architecture Vice President, Kogakuin University of Technology and Engineering					
13:30	12:30	11:30	BREAK, LOG-IN AND ROLL CALL					
			ORAL PRESENTATION, PARAREL SESSHON https://zoom.us/j/91076792471 Pass Cord: isat					
			Breakout Room	**1**	**2**	**3**	**4**	**5**
13:40	12:40	11:40	**ORAL5**	AFM1	ACE1	ICT1	EHS1	ME5
14:00	13:00	12:00	**ORAL6**	AFM2	ACE2	ICT2	EHS2	ME6
14:20	13:20	12:20	**ORAL7**	AFM3	ACE3	ICT3	EHS3	ME7
14:40	13:40	12:40	**ORAL8**	AFM4	ACE4	ICT4	EHS4	ME8
15:00	14:00	13:00	BREAK					
15:20	14:20	13:20	**ORAL9**	AFM5	ACE5	ICT5	EHS5	ME9
15:40	14:40	13:40	**ORAL10**	AFM6	ACE6	ICT6	EHS6	ME10
16:00	15:00	14:00	**ORAL11**	ET1	ACE7	ICT7	EHS7	ME11
16:20	15:20	14:20	**ORAL12**			ISS1	EHS8	ME12
16:45	15:45	14:45	BREAK, LOG-IN AND ROLL CALL https://zoom.us/j/92411282908 Passcode: isat					
17:00	16:00	15:00	AWARDING CEREMONY ・Honorary Membership to Prof. Oanh, DUT and Prof. Sato, KUTE Awarding from Prof. Lu, Deng-Maw President, Southern Taiwan University of Science and Technology ・Presentation Award Awarding from Prof. Miyuki Kamachi Vice President, Kogakuin University of Technology and Engineering Master of Ceremony: Dr. Koji Hasegawa, KUTE-Tokyo					
17:30	16:30	15:30	CLOSING CEREMONY CLOSING REMARKS ・**Prof. Miyuki Kamachi** Vice President, Kogakuin University of Technology and Engineering ・**Next Host：Prof. Doan Quang Vinh** Rector, The University of Danang - University of Science and Technology Master of Ceremony: Dr. Koji Hasegawa, KUTE-Tokyo					

Keynote Presentation 1 (November 23rd from 12:30 to 13:15 (JST))

Presentation No.	Presentation Information	Page
KY1.	**Why do animals have their shape? - Movement and shape -** **Prof. Shinichiro Ito** Department of Mechanical Engineering, Faculty of Engineering President, Kogakuin University of Technology and Engineering, Japan Chair Person: Prof. Yi-Chu Hsu, Department of Mechanical Engineering STUST	27

Keynote Presentation 2 (November 23rd from 13:15 to 14:00 (JST))

Presentation No.	Presentation Information	Page
KY2.	**Case study of using artificial intelligence technology to construct a smart hospital** **Prof. Chang, Wan-Jung,** Department of Electronic Engineering, Director of Medical and Intelligence Technology Research Center (MIT Center) Southern Taiwan University of Science and Technology, Taiwan Chair Person: Dr Ngo Minh Tri, Dean of the department Electronics and Telecommunication, DUT	28

Keynote Presentation 3 (November 24th from 12:00 to 12:45 (JST))

Presentation No.	Presentation Information	Page
KY3.	**Development of BK-Anticovid Robot** **Dr. VO Nhu Thanh and Dr. LE Hoai Nam** Mechatronic Division, Faculty of Mechanical Engineering, University of Science and Technology, The University of Da Nang, Viet Nam Chair Person: Assistant Professor Erwin P. Quilloy Agri-biosystems Machinery and Power Engineering Division, Institute of Agricultural and Biosystems Engineering College of Engineering and Agro-industrial Technology, UPLB	29

Keynote Presentation 4 (November 24th from 12:45 to 13:30 (JST))

Presentation No.	Presentation Information	Page
KY4.	**Honorable Danilo L. Concepcion** President, University of the Philippines Chair Person: Prof. Yasushi Nozawa, School of Architecture Vice President, Kogakuin University of Technology and Engineering	31

Oral Presentation (November 23rd from 14:10 to 15:30 (JST))

Breakout Room #1

Biochemistry and Food Science & Synthetic Chemistry and Medicinal Chemistry

Chair Person: Prof. Masayoshi Sakaguchi, KUTE

Presentation No.	Title	Author	Page
BFS1.	Crab-eating monkey acidic chitinase: strong chitinolytic activity under the various conditions	Maiko Uehara, E. Tabata and F. Oyama	33
BFS2.	Performance of Aerobic Rice Under Different Levels of N-Fertilizer Using Surface Irrigation and Drip Fertigation	Abigail R Barredo	34
BFS3.	The Use of Machine Vision for Postharvest Processing of Achacha Fruits	Nai-Shang Liou, Ngo Minh Tri Nguyen, Quoc Thien Pham, Hoang Huy Nguyen	36
SC1.	Surface Functionalization of Chitosan Hydrogel Using Atmospheric Pressure	Kathrina Lois M Taaca, Mark Jeffry De Leon, Hideki Nakajima, Kanjana Thumanu, Eloise Prieto, and Magdaleno Vasquez Jr.	37

Breakout Room #2

Electric Engineering and Electronic Engineering

Chair Person: Prof. Shinya Aikawa, KUTE

Presentation No.	Title	Author	Page
EEE1.	Examination of Improvement of Supply Stability by Introducing Wind Power Generation in Disaster-robust Zero Energy Vehicle(D-ZEV)	Bian Ning, Yasuhiro Noro	39
EEE2.	ElderFit: A Physical Fitness Motion Detection System for Older Adults Based on Deep Learning Technology	Wan-Jung Chang, Jian-Ping Su	43
EEE3.	Investigation of the Relationship between Muscle Strength and the Power of Electromyograph Signal	Chun-Ju Hou, Yen-Ting Chen, Ji-Jer Huang, and Mycel Capilayan	44
EEE4.	Optimization for elevation-plane beam configuration in 3D beamforming technology	Yuji Omura, Hiroyuki Otsuka	46

Breakout Room #3

Environmental Chemistry and Chemical Engineering

Chair Person: Prof. Kazuki Akamatsu, KUTE

Presentation No.	Title	Author	Page
ECC1.	Development of low-fouling microfiltration membranes with high permeability by blending PVDF with poly (2-methoxyethyl acrylate)	Seiya Ohno, Shin-ichi Nakao, Xiao-lin Wang, Kazuki Akamatsu	48
ECC2.	Application of wastewater treatment by microalgae cultivation technology for aquatic products processing facilities	Xuan Thanh Nguyen Thi, Nguyen Quốc Vương, Nguyen Hoang Minh	49
ECC3.	Investigation and optimization of harvesting microalgae using Electro-coagulation and flotation (ECF) method	Nguyen Nhat Cuong, Nguyen Thi Thanh Xuan	50
ECC4.	Separation mechanism of carbon dioxide through CHA membrane under high pressure	Fumiya Hirosawa, Masaya Miyagawa, and Hiromitsu Takaba	51

Oral Presentation (November 23rd from 14:10 to 15:30 (JST))

Breakout Room #4

Simulation Science, Measurement Science, Computational Science

Chair Person: Prof. Junji Yamato, KUTE

Presentation No.	Title	Author	Page
SSM1.	Effect of femur and tibia marker positions on measuring ankle joint angles in optical motion analysis	Natsuki Nakamura, Satoru Kizawa, and Ayuko Saito	53
SSM2.	Effect of actuator on muscle force estimation using a musculoskeletal model	Takuto Hosoya, Tomoaki Ichikawa, Shinichiro Morichi, Yoshikazu Kobayashi, Satoru Kizawa, and Ayuko Saito	56
SSM3.	Study on design of a noise covariance in pose estimation using 9-axis motion sensor	Hayato Sato, Kentaro Goto, Satoru Kizawa, and Ayuko Saito	58
SSM4.	A study on effect of geomagnetic sensor correction for pose estimation	Kentaro Goto, Hayato Sato, Satoru Kizawa, and Ayuko Saito	61

Breakout Room #5

Mechanical Engineering

Chair Person: Prof. Masaki Hiratsuka, KUTE

Presentation No.	Title	Author	Page
ME1.	Flow Characteristics of an Excited Jet with a Time-varying Velocity Distribution	Chisato Ichihara, K. Nishibe, and K. Sato	65
ME2.	Influence of secondary synthetic jet on vortex arrangement in combined jet	Yu Tamanoi, Koichi Nishibe, and Kotaro Sato	67
ME3.	Fundamental study on jet vectoring by circulation control wing	Shoichi Fukui, Shoichi Fukui, Qiang Zhang, Kotaro Sato	69
ME4.	Performance Evaluation of Soccer Balls with Different Panel Shapes	Kaito Tada, Shinichiro Ito, and Masaki Hiratsuka	71

Oral Presentation (November 24th from 13:40 to 16:45 (JST))

Breakout Room #1

Advanced Functional Materials & Energy and Transportation

Chair Person: Prof. Hideki Hashimoto, KUTE and Prof. Tomohiro Yamaguchi, KUTE

Presentation No.	Title	Author	Page
AFM1.	Facile hydrothermal synthesis of interlayer-expanded MoS_2/rGO	Kien Nguyen-Ba, Huy Le-Quoc, Trang Nguyen-Thi-Thu, and Khan Dinh-Thanh	86
AFM2.	Fabrication of Anodic Aluminum Oxide Templates	Lance Tristan Oliver Roncal Pengson, M. Vasquez Jr	89
AFM3.	Carrier gas type dependence of Ga_2O_3 thin film grown by mist Chemical Vapor Deposition	Rie Yamada, S. Takahashi, A. Sekiguchi, T. Onuma, T. Honda, and T. Yamaguchi	91
AFM4.	A Study on Smart Fluid Technology and its Applications in Haptics	Aaron Raymond See, Kohila Chandramohan	93
AFM5.	Growth of GaInN multi quantum well on strain-controlled layer by RF-MBE toward realization of light emitting diodes operating in red spectral region	Masaki Matsuda, R. Yoshida, K. Tahara, T. Yamaguchi, T. Onuma, and T. Honda	98
AFM6.	Fluorescent immune-biosensor on the glass biochip used for albumin detection	Ying-Nien,Chou, Lien-Chiang,Hung	100
ET1.	Home Energy Management System Considering Stationary Storage and Electrical Vehicle	Jeeng-Min Ling, Firoj Ismail Mulani	102

Breakout Room #2

Architectural and Civil Engineering

Chair Person: Prof. Yoshiaki Hisada, KUTE and Prof. Masaki Tamura, KUTE

Presentation No.	Title	Author	Page
ACE1.	Study on Optimum Room Temperature in Offices with Thermal Controllable Chairs	Shintaro Hanazono, Tatsuo Nobe	106
ACE2.	Optimized artificial neural network model to classify tasks in construction and project management field	Trang Thi Phuong Pham	107
ACE3.	Application of Biological Process for Enhancing Carbonation of MgO Cement	Huyen Thanh Do, Tung Hoang	112
ACE4.	Detachment diagnosis based on frequency characteristics using a tile specimen with a pseudo-dissociation part	Tatsuya Yamada, Masaki Tamura, Nobuyuki Sanjoba	114
ACE5.	Pineapple Core Sugar Extract as Set Retarder in Cement Paste	Rondel Arganza Dela Cruz	117
ACE6.	Non-Ergodic Probabilistic Seismic Hazard Analysis using Physics-Based Ground Motion Prediction: A Case of L'Aquila, Italy	Jedidiah Joel Carlos Aguirre, Bruno Rubino, Maurizio Vasallo, Guiseppe di Guilio, Francesco Visini	118
ACE7.	A mathematical model of two-dimensional vertical flow based on the dual approach	The-Hung NGUYEN	121

Oral Presentation (November 24th from 13:40 to 16:45 (JST))

Breakout Room #3

Information and Communications Technology (ICT) & Intelligent and Secure Systems

Chair Person: Prof. Hiroyuki Otsuka, KUTE and Prof. Qiu Chen, KUTE

Presentation No.	Title	Author	Page
ICT1.	Beautification Algorithm for Handwritten Characters Based on Deep Learning	Ko-Ting Wu, Qiu Chen	125
ICT2.	An approach for ceramic tile defects classification based on genetic algorithm and CNN	Nhat-To Huynh	128
ICT3.	Creating Strong AIWolf Agents using Systematic Tactical Evaluation	Shunsuke Hatta, Keisuke Takahashi, Kazunari Furukawa, Junji Yamato	129
ICT4.	A Study on Optical Burst Transfer Method in Torus Type Data Center Network	Yuya Ogino, Ken-ichi Baba	133
ICT5.	Effect of cell range expansion of picocells with a wide bandwidth in multiband HetNets	Ayumi Yoneyama, Hiroyuki Otsuka	135
ICT6.	Impact of phase noise for OFDM-based 1024-QAM transmission	Daisuke Kosuge, Hiroyuki Otsuka	136
ICT7.	A Study of QUIC and Application Development	Jiun-Yu Tu, Pei-Ying Tsai, Ya-Ting Zhuang	137
ISS1.	Verification of Dentition Shape Extraction Method	Yutaro Iso, Kazuhiro Suga	141

Breakout Room #4

Education and Human Studies

Chair Person: Prof. Nguyen Hoang Mai, DUT

Presentation No.	Title	Author	Page
EHS1.	Evaluation of internal rotation gait and normal gait based on the interarticular coordination	Natsuki Sai, Tatsuro Sato, Shinichiro Morichi, Satoru Kizawa, and Ayuko Saito	143
EHS2.	A study on coordination between a line of sight and motion of body during hitting a ball with a racket	Toshikazu Yagi, Satoru Kizawa, and Ayuko Saito	146
EHS3.	Study on the movement during walking beautifully and the perception of beauty	Yura Honda, Shogo Takeuchi, Jun Muramatsu, Satoru Kizawa, Masaki Tamura, and Ayuko Saito	150
EHS4.	Research on recognition of movement using an optical motion capture system	Shun Shiotani, Satoru Kizawa, Masaki Tamura, and Ayuko Saito	153

Chair Person: Prof. Morio Yoshida, KUTE

Presentation No.	Title	Author	Page
EHS5.	A New Perspective on English Education for Engineering Majors −Optimizing English Education at Kogakuin University–	Tomoko Wada	157
EHS6.	A Practical Report on English Education at Kogakuin University: A Lesson from Basic English I/II	Takayuki Akimoto	159
EHS7.	English Education in the Age of SDGs: A Survey on English Learning among Kogakuin University Students	Tomomi Yamada, Kazunori Suzuki	160
EHS8.	An Application of CNN in Answer Analyzing and Estimation Education Advanced Technology	Nguyen Hoang Mai	163

Oral Presentation (November 24th from 13:40 to 16:45 (JST))

Breakout Room #5

Mechanical Engineering

Chair Person: Prof. Koji Hasegawa, KUTE

Lightning Talk Session (November 23rd from 15:45 to 18:00 (JST))

Breakout Room #1

Advanced Functional Materials

Chair Person: Prof. Hideki Hashimoto, KUTE

Presentation No.	Title	Author	Page
AFML1.	Effect of visible light for photocatalytic property of TiO_2/Cu_2O thin films	Katsuyuki Takeda, Ichiro Takano	170
AFML2.	Dependence on Ar incident angles of PTFE surface treated by plasma	Yoshitaka Nakayama, Ichiro Takano	171
AFML3.	Analysis of High Thermal Conductivity Mechanism of Naphthyl Benzoate-Twin Mesogenic Epoxy Polymers with Alkyl Chain Length 2 Having 2,7-Naphthyl Benzoate as the Mesogenic Skeleton	Yuu Miyama, T. Kawai, and Y. Itoh	172
AFML4.	Hardness of alumina film formed on aluminum by anodic oxidation with oxalic acid and alcohol	Takuma Sano, Hidetaka Asoh	174
AFML5.	Study on high thermal conductivity mechanism of phenyl benzoate twin-mesogen epoxy polymers by vibrational spectroscopy	Takeru Ishizawa, T. Kawai, and Y. Itoh	177
AFML6.	Influence of a CuO layer for conversion efficiency of CuO/TiO_2 thin films	Masaki. Yanagisawa, Ichiro. Takano	179
AFML7.	Theoretical calculation of infrared absorption spectra of hydrogen in various polymers under high-pressure hydrogen	Masayoshi Tsuji, T. Kawai and Y. Itoh	180
AFML8.	Improvement of Electrical Property of α-In_2O_3 Films Grown by Mist Chemical Vapor Deposition Using In_2O_3 Powder as Source Precursor	Akito Taguchi, T. Onuma, T. Honda, and T. Yamaguchi	181
AFML9.	Study on thermal conductivities of poly(methacrylic acid ester) having azobenzene as a mesogen with different spacer carbon numbers and the end group carbon numbers	Nanako Sakai, Tadatomo Kawai, and Yuzo Itoh	183

Biochemistry and Food Science

Chair Person: Prof. Osamu Ohno, KUTE

Presentation No.	Title	Author	Page
BFSL1.	Investigation of extraction method for antimicrobial substances accumulated in aerial microalgae	Toshihiro Sekizawa, Nobuhiro Aburai, and Katsuhiko Fujii	185
BFSL2.	Isolation of lichen photobionts by a density gradient centrifugation	Kotomi Hirose, Nobuhiro Aburai, and Katsuhiko Fujii	186
BFSL3.	Development of microflora which produces hydrogen from digested sludge	Yuhei Hayakawa, Nobuhiro Aburai, and Katsuhiko Fujii	187
BFSL4.	The ability of wild Bacillus sp. to produce polyglutamic acid	Suzuka Sato, Nobuhiro Aburai, and Katsuhiko Fujii	188
BFSL5.	Screening of carotenoid-rich aerial microalgae	Yuta Hiki, Nobuhiro Aburai, and Katsuhiko Fujii	189
BFSL6.	Functional Properties of Chitin Deacetylase from *Aspergillus fumigatus*	Hidetoshi Suzuki, Masashi Ohkura, Kazuaki Okawa and Fumitaka Oyama	190
BFSL7.	Mechanistic insights of inactivation of YKL-40, a chitinase-like protein	Keita Suzuki, Kazuaki Okawa, and Fumitaka Oyama	191
BFSL8.	Component imaging of spheroids by using an FIB-TOF-SIMS	Tomoki Goto, Hyogo Takeuchi, Mizuki Shu, Reiko Saito, Kazuya Matsushima, Makoto Saito, Sanshiro Hanada, Nobuhiko Kojima, Masato Morita, and Tetsuo Sakamoto	192

Lightning Talk Session (November 23rd from 15:45 to 18:00 (JST))

Breakout Room #2

Electric Engineering and Electronic Engineering

Chair Person: Prof. Masakazu Mukai, KUTE and Prof. Tomohiro Yamaguchi, KUTE

Presentation No.	Title	Author	Page
EEEL1.	UV-irradiated fabrication of SWCNT/SiO_2 Composite thin film at room temperature via Molecular Precursor Method	Naoki Ogawa, Hiroki Nagai, and Mitsunobu Sato	196
EEEL2.	Fabrication of visible-light responsive WO_3 Thin Film *via* Molecular Precursor Method	Taichi Murayama, H. Nagai, and M. Sato	197
EEEL3.	Remarkable mechanical flexibility of intentionally strain-induced amorphous B-doped In_2O_3 transparent conductive film	Shun Mori, Yukiya Ichinoseki, Kotaro Watanabe, Kaito Murano, Kaito Oe and Shinya Aikawa	198
EEEL4.	Understanding the switching mechanism of stacked ZrO_2-based ReRAM by insertion of SiO_x thin layer at the electrode interfaces	Keito Toyama, Ryusuke Akiyama, Kento Yuki and Shinya Aikawa	200
EEEL5.	Residual strain in GaN nanocolumns grown on Si(111)	Naoki Goto, Y. Hosoya, T. Onuma, T. Yamaguchi, and T. Honda	202
EEEL6.	Identification of Killer Defects in β-Ga_2O_3 Schottky Barrier Diodes by Raman Mapping Measurements	Masahiko Nakanishi, K. Shoji, S. Masuya, M. Kasu, T. Yamaguchi, T. Honda, K. Sasaki, A. Kuramata, and T. Onuma	204
EEEL7.	p-type behavior of lattice-expanded SnO_x by post-deposition N2 annealing	Kotaro Watanabe, Takuma Kawaguchi, and Shinya Aikawa	206
EEEL8.	Relationship between resistivity of NiO thin films and oxygen plasma condition at different deposition pressures	Mamoru Murayama, A. Ishikawa, T. Yamaguchi, T. Honda, K. Sasaki, A. Kuramata, and T. Onuma	208
EEEL9.	Measurement of Flexoelectric Coefficient (e_{11}-e_{33}) Using HAN Cells with Concentric-shaped Interdigitated Array Electrodes	Hiroki Shimoda, Yukihiro Kudoh, and Taiju Takahashi	210
EEEL10.	Well width dependence on residual strain in high In composition GaInN/GaInN MQW by RF-MBE	Kaigo Tahara, J. Yamada, T. Yamaguchi, Y. Nanishi, T. Onuma, T. Honda, and K. Kishino	212
EEEL11.	Micro scale analysis of LFP cathode of all solid state battery by FIB TOF SIMS	Akihiro Kawasugi, Naoki Gomyo, Linchun He, Masato Morita, and Tetsuo Sakamoto	215
EEEL12.	Development of resonance ionization mass spectrometry imaging method for radioactive Sr isotopes analysis	Takeru Yoshida, Takumi Umedate, Masato Morita, Tetsuo Sakamoto, Yue Zhao, Vollker Sonnenschein, Hideki Tomita, Toshihide Kawai, Takeo Okumura, Yukihiko Sato, Masabumi Miyabe and Ikuo Wakaida	216
EEEL13.	Trade-off relation of F concentration in CaF_2 co-sputtered In_2O_3-based transparent conductive film	Kaito Oe, Shun Mori, Kotaro Watanabe and Shinya Aikawa	217
EEEL14.	Emission Properties of Rocksalt-structured MgZnO Microcrystals for VUV Light Emitter	Wataru Kosaka, S. Hoshi, K. Kanta, K. Kaneko, T. Yamaguchi, T. Honda, S. Fujita, and T. Onuma	219
EEEL15.	Analysis of aerosol in urban city air using FIB-TOF-SIMS	Kentaro Sakai, Shokei Tsuchida, Noa Kato, Masato Morita, and Tetsuo Sakamoto	222

Lightning Talk Session (November 23rd from 15:45 to 18:00 (JST))

Breakout Room #3

Information and Communications Technology (ICT) & Intelligent and Secure Systems

Chair Person: Prof. Osamu Mizuno, KUTE and Prof. Akihiro Fujii, KUTE

Presentation No.	Title	Author	Page
ICTL1.	Design Thinking-based Requirements Elicitation Method using Role-Based Prototyping and its Evaluation	Senju Nakajima, Takayuki Kitagawa, Tadahisa Kondo, and Mari Inoki	230
ICTL2.	The bottleneck of MTD System Operation	Shintaro Kawamura, Osamu Mizuno	233
ICTL3.	A Study on Access Control Methods in IoT Data Distribution using Fog Computing	Masaki Yoshii, Ryohei Banno, and Osamu Mizuno	234
ICTL4.	Non-functional Requirements Summarization Method Using Convolutional Neural Network and Domain Ontology	Yuta Saikawa, Takeshi Nagaoka, Takayuki Kitagawa, and Mari Inoki	235
ICTL5.	Determination of intermittent defects by a method that focuses on the rows before and after the defective shot	Yusuke Takada, Yoshio Miki	239
ICTL6.	Transmission Control in DTN Considering Data Amount	Hiyu Suzuki, Osamu Mizuno	240
ICTL7.	Fast Adjacent Communication with RDMA and Double Buffering	Kota Yoshimoto, Akihiro Fujii, and Teruo Tanaka	242
ICTL8.	Preliminary Experiments for the Realization of ICN based Wireless Sensor Networks	Eishin Nagaoka, Masaki Yoshii, Ryohei Banno and Osamu Mizuno	245
ICTL9.	Personalization of Service Controller for Home Network Devices	Taich Kimura, Osamu Mizuno	247
ICTL10.	Parallelization of Automatic Tuning using Multiple Jobs for Machine Learning Programs	Sorataro Fujika, Teruo Tanaka, Akihiro Fujii, Yuka Kato, Satoshi Ohshima, andTakahiro Katagiri	248
ICTL11.	A Method for Detecting Anomalies in IoT Devices Using LSTM	Yutaro Nakamura, Osamu Mizuno	252
ICTL12.	A Study of Applying Plumtree Algorithm for Blockchain Networks	Yusuke Kitagawa, Kazuyuki Shudo, Osamu Mizuno, Ryohei Banno	253
ICTL13.	PAPR Reduction Effect by Applying Clipping in Spectrum Suppressed Transmission	Teppei Kanke, Takatoshi Sugiyama	254
ICTL14.	Performance Analyses of Efficient Belief Propagation Bit-flip Decoding Schemes for Polar Codes with Permutated Factor Graphs	Hidetoshi Saito, Naoya Takahashi	255
ICTL15.	Interleaving Depth Optimization for Concatenated FEC in 2.4GHz Ingenu System	Kentaro Yamamoto, Takatoshi Sugiyama	259
ICTL16.	Calculated Distance Error Performances by Relay Type GPS in Shinjuku Area	Kouhei Yoshida, Takatoshi Sugiyama	261
ICTL17.	The Child's Residual Limb Model Reconstruction by using Point Cloud Data	Ding-Horng Chen, Qiao-Ting Shen	263
ICTL18.	An Image Segmentation Method based on Unsupervised Learning Algorithms	Zong-Xian Yin	266
ISSL1.	Wired cable proposal on the feasibility of a stratospheric platform -Background and wired connections and strategies for orbital elevators-	Koichiro Murata	267

Lightning Talk Session (November 23rd from 15:45 to 18:00 (JST))

Breakout Room #4

Simulation Science, Measurement Science, Computational Science

Chair Person: Prof. Chandrasiri Naiwala Pathirannehelage, KUTE

Presentation No.	Title	Author	Page
SSML1.	Theoretical study on interfacial interaction of zig-zag carbon nanotubes/epoxy resin nanocomposite	Yurika Serizawa, Tomoe Yayama, and Fumiko Akagi	269
SSML2.	Predicting of Pedestrian Trajectory Using Sequence to Sequence Learning with Neural Networks	Tomoya Ono, Takashi Kanamaru	270
SSML3.	Separation Control around NACA0015 Airfoil using Vortex Generator Type Plasma Actuator over Low Reynolds Number Conditions	Shota Mayahara, Makoto Sato	271
SSML4.	GPS Positioning Error Improvements by Number of Reflections and Incident Angle Estimations	Koichi Saito, Takatoshi Sugiyama	272
SSML5.	Extraction of useful products from specialty stores using clumpiness	Taro Numase, Yoshio Miki	275
SSML6.	Examination of Measures to Encourage Unplanned Purchasing Using Social Norms at Specialty Stores	Ryou Miyokawa, Yoshio Miki	277
SSML7.	Non-Invasive Concentration Variation Measurements of Chemical Solutions by Using a Birefringent Sensing Head in a Heterodyne Interferometer	Ruey-Ching Twu, Yi-Ren Sun	279
SSML8.	A Computational Framework for Predicting the Surface Morphology of Laser Powder Bed Fusion Parts after Laser Polishing	Dac - Phuc Pham, Hong - Chuong Tran	280

Education and Human Studies

Chair Person: Prof. Ayuko Saito, KUTE

Presentation No.	Title	Author	Page
EHSL1.	Effects of Skin and Water Conditions on Water Surface Perception	Kohei Kawamata, Miyuki G.Kamachi	287
EHSL2.	Influence of eating Meals on facial expressions	Mao Maekawa, Miyuki G. Kamachi	292
EHSL3.	A study of facilitation evaluation methods in group discussions for students	Takuya Hirayanagi, Daigo Misaki	296
ETL1.	Optimization of Service Frequency based on Short-term Passenger Forecasting on Scheduled Bus -Case Study on the Route for Kogakuin University-	Yuya Nagai, Yoshio Miki	297
ETL2.	Study on Driving Skill Analysis in Curve Sections using Adaboost Algorithm with Driving Simulator	Eisho Kanno, Masakazu Mukai	302
ETL3.	Development of *Operando* Raman Analysis at the Reaction Cross-Section of All-Solid-State Batteries	Takaaki Ono, Koji Hiraoka, Hibiki Miyauchi, Takeshi Kobayashi and Shiro Seki	304

Lightning Talk Session (November 23rd from 15:45 to 18:00 (JST))

Breakout Room #5

Mechanical Engineering

Chair Person: Prof. Koji Hasegawa, KUTE

Presentation No.	Title	Author	Page
MEL1.	Research on Motion Analysis of Pedestrians Using OpenPose	Genki Bamba, Kazuki Weerakoon Miyakawa,Takashi Kato, and Daigo Misaki	306
MEL2.	Audio glasses for confining acoustic field in near field	Shuzo Terauchi, Tsutomu Kaizuka	307
MEL3.	Jet formation after droplet impact into water pool	Futa Minami, K. Hasegawa	308
MEL4.	Visualization of vibration behavior of multiple samples levitated in an acoustic field	Manami Murata, K. Hasegawa	309
MEL5.	Study on the presentation method of the automated driving experience simulator by wizard of oz prototyping	Kazuki Miyakawa Weerakoon, Genki Bamba, Takashi Kato, and Daigo Misaki	310
MEL6.	Development of a robot to assist in optimal parts supply at cell production sites	Shutaro Ito, Daigo Misaki	311
MEL7.	Development of Self-Lubricating Slide Bearings with Sintered Porous Metals	Taiga Itoi, S. Kawajiri, Y. Sasaki, E. Takami, Y. Fujita, and M. Shiomi	312

Architectural and Civil Engineering

Chair Person: Prof. Sumie Suzuki, KUTE and Prof. Masaki Tamura, KUTE

Presentation No.	Title	Author	Page
ACEL1.	Evaluation of Plaster Layer of Wood lath and Plaster Ceiling in Non-Destructive Testing	Sakura Yoshida, Kentaro Oka, Masaki Tamura	314
ACEL2.	Quantitative evaluation of the deterioration state of the modified wood shingle exposed outdoors and construction of an index to judge the deterioration	Hideto Takeuchi, Masaki Tamura	316
ACEL3.	Examination of resin repair method for wood damaged by termites	Yusuke Harada, Masaki Tamura	318
ACEL4.	Study on transportation power in DHC area for the AEM	Ryuhei Tanaka, Yusuke Nakajima	322
ACEL5.	History and development of wood lath and plaster techniques in Japan	Kentaro Oka, Masaki Tamura	326
ACEL6.	GIS-Based Assessment of Emergency Referral Systems and Ideal Locations for Ambulance Stations in the Province of Cavite, Philippines	Kathleen Ann E. Villapol, Jedidiah Joel C. Aguirre, Judie Ann A. Ramos, and Harvey S. Maunahan	329

Environmental Chemistry and Chemical Engineering

Chair Person: Prof. Hideki Hashimoto, KUTE

Keynote Presentation 1 (November 23rd from 12:30 to 13:15 (JST))

Presentation No.	Presentation Information	
KY1.	**Why do animals have their shape? - Movement and shape -** **Prof. Shinichiro Ito** Department of Mechanical Engineering, Faculty of Engineering President, Kogakuin University of Technology and Engineering, Japan Chair Person: Prof. Yi-Chu Hsu, Department of Mechanical Engineering STUST	27

Keynote Presentation 2 (November 23rd from 13:15 to 14:00 (JST))

Presentation No.	Presentation Information	
KY2.	**Case study of using artificial intelligence technology to construct a smart hospital** **Prof. Chang, Wan-Jung,** Department of Electronic Engineering, Director of Medical and Intelligence Technology Research Center (MIT Center) Southern Taiwan University of Science and Technology, Taiwan Chair Person: Dr Ngo Minh Tri, Dean of the department Electronics and Telecommunication, DUT	28

Keynote Presentation 3 (November 24th from 12:00 to 12:45 (JST))

Presentation No.	Presentation Information	
KY3.	**Development of BK-Anticovid Robot** **Dr. VO Nhu Thanh and Dr. LE Hoai Nam** Mechatronic Division, Faculty of Mechanical Engineering, University of Science and Technology, The University of Da Nang, Viet Nam Chair Person: Assistant Professor Erwin P. Quilloy Agri-biosystems Machinery and Power Engineering Division, Institute of Agricultural and Biosystems Engineering College of Engineering and Agro-industrial Technology, UPLB	29

Keynote Presentation 4 (November 24th from 12:45 to 13:30 (JST))

Presentation No.	Presentation Information	
KY4.	**Honorable Danilo L. Concepcion** President, University of the Philippines Chair Person: Prof. Yasushi Nozawa, School of Architecture Vice President, Kogakuin University of Technology and Engineering	31

Why do animals have their shape?

Shinichiro Ito

President, Kogakuin University, Tokyo, Japan
E-mail: president@sc.kogakuin.ac.jp

Abstract

The shapes of aquatic creatures/animals have been changing by their life form and their living environments. Their movement changes the bodies of their propulsive mechanism. Therefore, the propulsive mechanism or technology can be developed by learning their motion and their shapes. Roughly speaking, The propulsive lift motion is suitable for continuous movement, and the drag propulsive motion is fit for rapid transfer motion. This study summarizes the shape and the action of aquatic creatures/animals.

The movement of creatures/animals changes with the lifestyle, and the movement pattern changes. The propulsion method also varies depending on the form of action. By learning their movement form and propulsion technology, it will be possible to develop new propulsion organisms.

Propulsion is required for the movement of living things, and they can be roughly divided into drag propulsion and lift propulsion.

Lift is the force that acts at right angles to an object placed in the flow. For example, as the airplane moves in the direction of travel, lift acts on the wings at right angles to the direction of travel. A well-designed airfoil efficiently generates lift force from the flow. Therefore, the shape of the organ that promotes lift is "streamlined" without disturbing the flow. It can be a bird's wing or a fish's tail fin. The lift propulsion mechanism is due to the reciprocating motion of the creatures, such as flapping their wings.

The propulsion method by drag is based on the law of action and reaction, and it is an easy-to-understand mechanism that the same force as the pushing force becomes the propulsion force. It is jet propulsion motion like a squid. A mixture propulsion mechanism of lift and drag force can be seen in many aquatic organisms. Creatures change their shape by making good use of lift and drag. Their shape changes according to the living environment.

The exercise mode is determined so that the energy related to life is optimized by natural selection, centering on the lifestyle of living things. In general, the movement of the drag propulsion system is mostly the instantaneous force system in the normally inactive activity, and the lift propulsion is mostly the daily activity system.

For this reason, the muscles are also composed of instantaneous and endurance muscles. Since pufferfish, which is usually still, is required to have a quick force, its body is composed of fast muscles or white muscle. On the other hand, tuna composed of slow muscles of endurance system has a red muscle. Therefore, it is interesting to infer the living environment and exercise mode from the color of the meat.

References: Akira Azuma, The Biokinetics of Flying And Swimming (AIAA Ed. Series) (2006).

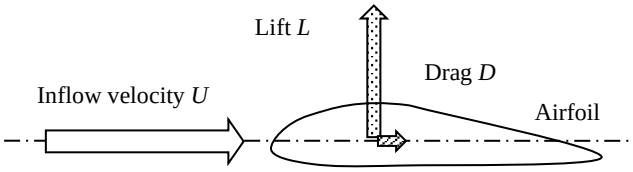

Fig.1(a) Lift propulsion mechanism acting perpendicularly on the advancing direction

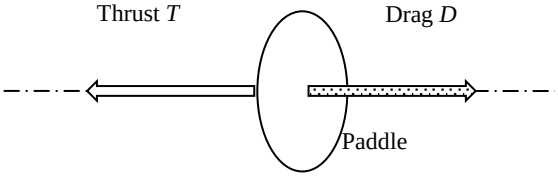

Fig.1(b) Reaction (drag) propulsion mechanism acting directly to the advancing direction

Figs.1 Difference in propulsion mechanism: Lift propulsion and reaction (drag) propulsion

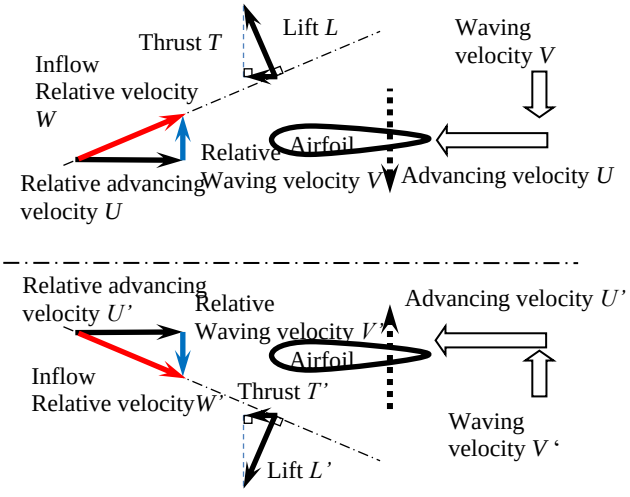

Fig.2 The mechanism that produces driving force on a flap wing: Driving force occurs thrust force *T* consistently to the advancing direction. Furthermore, the generating force grows big because of twisting wing.

Keynote

Prof. Chang, Wan-Jung,

Title: Case study of using artificial intelligence technology to construct a smart hospital

Department and Faculty: Department of Electronic Engineering, Director of Medical and Intelligence Technology Research Center (MIT Center)

Nowadays, the hardware and software systems of smart hospitals are developing at a rapid rate. Both major manufacturers and startups are actively negotiating with medical institutions to find out unmet medical procedures and industrial ecological needs, and then provide appropriate help. According to the data from the Taiwan Patient-safety Reporting(TPR) system, medication and fall are accounted for about 55% of hospitals' incidents, ranking among the top two reported in Taiwan. Accordingly, In this talk, we will focus on how to use 5G+AIoT technology to reduce the probability of falls and medication errors in hospitals to improve patient hospitalization and medication safety.

Development of BK-Anticovid Robot

Vo Nhu Thanh*, Le Hoai Nam

Mechatronic Division, Faculty of Mechanical Engineering, University of Science and Technology, The University of Da Nang, Viet Nam
E-mail: vnthanh@dut.udn.vn, lehoainam@dut.udn.vn

Abstract
This manuscript introduces the development of the BK-Anticovid robot that was designed and built within one week to serve at the quarantine area of a hospital. The robot was developed based on the specific requirement of the hospital staff that it could move slowly and easily to turn and control by a staff. The BK-Anticovid robot had multifunction that can serve for food or medicine delivery, and bacteria sterilizing by chemical spraying and UV sterilizing.

Introduction

Due to Covid 19 crisis, there was a need to rapidly apply technology to give a helping hand in the fight against it. The project of designing and manufacturing Bk-Anticovid Robot with three integrated functions including transporting essentials to the quarantine area, spraying disinfectant, and sterilizing with UV rays. This robot is currently being used at Da Nang Maternity and Children's Hospital.

Robot configuration

The robot has one main part for delivering the essentials for patients and a separated module for spraying disinfectant and sterilizing with UV rays. The specification for the main part of the robot was 650x500x250mm in size and 80 Kg in weight. The robot has its main part as a mobile robot driven by two 24V-250W-120 rpm DC motors attached to the two wheels of the robot by a 17mm diameter shaft. driven by a customized controller board using PIC 18F887A Microcontroller and the velocity is feedback via a 600 pulse encoder. This main part of the robot was also equipped with a camera for observation. The algorithm for control the stable speed is a discrete PID controller for both wheels of the robot. Fig.1 showed the design and prototype of this robot.

Fig. 1. Design and prototype of the robot

The module for spraying disinfectant with 6LPM pressure pump was designed to be remotely attached to the main body if needed. The spray head was pointed backward so that the spraying chemical would not get into the robot when the motor was moving forward. The UV sterilizing consisted of 4 high-power UV light bulbs controlled by a 12V-1000W inverter, suitable for extirpating bacterial within 1 meter radius within 1 minute. The picture of the modules is showed in Fig.2

Fig. 2. UV module and spraying module.

The whole system's power was supplied by a 12V 40ah battery, which helped the robot operate around 5 hours when fully charged.

Conclusion and application

We handed the robot to hospital staff for serving at the hospital and got very good feedback. The robot was easy to operate, and the multifunction was very useful when preparing rooms for new patients.

The use of the robot saves a lot of costs on protective medical equipment (each protective suit is worn only once and costs about 40 to 50USD a day) since the robot is serving from March 23, 2020, to the present time, the amount of cost savings is quite large. Applying robots to transport disinfection and sterilization reduces the risk of cross-infection and creates more peace of mind for doctors and nurses on the front lines against the epidemic.

Acknowledgment

This work was support by Francophone University Community Foundation (AUF). Code: DRAP-5457/Project 2320.

References

[1] V.N. Thanh, et al., *Restaurant Serving Robot with Double Line Sensors Following Approach,* IEEE International Conference on Mechatronics and Automation (ICMA), 235-239 (2019).

[2] V.N.Thanh, et al., *Reinforcement Q-learning PID Controller for a Restaurant Mobile Robot with Double Line-Sensors*,—=Conference on

Machine Learning and Soft Computing ICMLSC, 164-167 (2020).

KY4

Keynote Speech for the 20th International Symposium on Advanced Technology

Danilo L. Concepcion

President, University of the Philippines
E-mail:

Abstract

Oral Presentation

Biochemistry and Food Science & Synthetic Chemistry and Medicinal Chemistry

November 23rd

Presentation No.	Title	Author	
BFS1.	Crab-eating monkey acidic chitinase: strong chitinolytic activity under the various conditions	Maiko Uehara, E. Tabata and F. Oyama	33
BFS2.	Performance of Aerobic Rice Under Different Levels of N-Fertilizer Using Surface Irrigation and Drip Fertigation	Abigail R Barredo	34
BFS3.	The Use of Machine Vision for Postharvest Processing of Achacha Fruits	Nai-Shang Liou, Ngo Minh Tri Nguyen, Quoc Thien Pham, Hoang Huy Nguyen	36
SC1.	Surface Functionalization of Chitosan Hydrogel Using Atmospheric Pressure	Kathrina Lois M Taaca, Mark Jeffry De Leon, Hideki Nakajima, Kanjana Thumanu, Eloise Prieto, and Magdaleno Vasquez Jr.	37

Crab-eating monkey acidic chitinase: strong chitinolytic activity under the various conditions

M. Uehara, E. Tabata and F. Oyama

Department of Chemistry and Life Science, School of Advanced Engineering, Kogakuin University, Tokyo, Japan
E-mail: bd19001@ns.kogakuin.ac.jp

Abstract

We analyzed the enzymatic properties of crab-eating monkey CHIA (monkey CHIA) under different pH conditions. When we compared with mouse Chia, monkey CHIA exhibits stronger chitinolytic activity at broad pH (1.0-7.0) and temperature (30-70℃) range. Thus, monkey CHIA maintained high chitinolytic activity under broad range of pH and temperature conditions.

Introduction

Chitin, a polymer of *N*-acetyl-D-glucosamine (GlcNAc), is the second most abundant polysaccharide in nature. Although mammals do not produce endogenous chitin, they express two active mammalian chitinases, acidic chitinase (CHIA) and chitotriosidase (CHIT1). In particular, CHIA plays an essential role in pathophysiological conditions. It was shown that mouse, chicken and pig Chia are major protease-resistant glycosidases in the respective digestive systems [1-3].

The crab-eating monkey is one of the important nonhuman primate animal models in basic and applied biomedical researches. We have previously performed gene expression analysis and found that the monkey expresses a high level of CHIA mRNA in the stomach [4]. Here, we investigated the enzymatic properties of the monkey CHIA.

Method

We expressed recombinant monkey CHIA and mouse Chia proteins in *E. coli*. The chitinolytic activities were measured using 4-nitrophenyl *N,N'*-diacetyl-β-D-chitobioside [4-NP-$(GlcNAc)_2$] at different pH [0.1 M Gly-HCl buffer (pH 1.0-3.0) or McIlvaine's buffer (pH 2.0-8.0)] and temperature (30-80℃) for 60 min. The absorbance of the released 4-nitrophenol (4-NP) was measured at 405 nm.

Result and Discussion

First, we analyzed the pH dependence of monkey CHIA. Monkey CHIA showed the peak activity at pH 5.0. The activity retained high levels between pH 1.0-7.0 (Fig. 1). The optimal pH of monkey CHIA showed unique properties.

When compared to mouse Chia, monkey CHIA had higher activity at each condition. There was a threefold difference in their peak activities monkey CHIA at pH 5.0 and mouse Chia at pH 2.0. Monkey CHIA was also 2x, 16x, and 10x more active at pH 2.0, 5.0, and 7.0, respectively, than mouse Chia.

Next, we analyzed the temperature of pH dependence. Under the optimal pH condition (pH 5.0), the reaction rate increased with the temperature and reached the maximum level at 65℃. Monkey CHIA maintained its high activity even at 70℃. In addition, monkey CHIA was stable under acid and high-temperature conditions.

Our results show that unique features of monkey CHIA including its thermostability warrant the nomination of this enzyme for potential agricultural and biomedical applications.

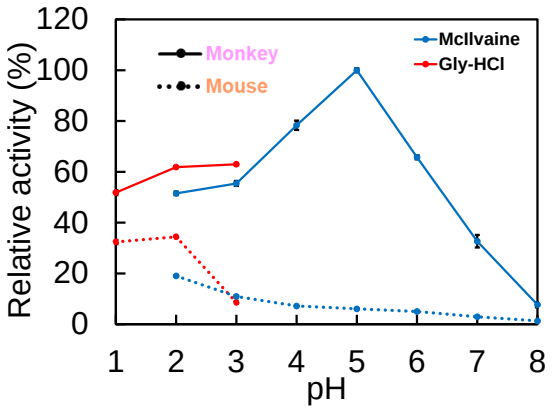

Fig. 1. Optimal pH of monkey CHIA and comparison with mouse Chia.

References:

[1] M. Ohno, M, Kimura, H. Miyazaki, K. Okawa, R. Onuki, C. Nemoto, E. Tabata, S. Wakita, A. Kashimura, M. Sakaguchi, Y. Sugahara, N. Nukina, PO. Bauer and F. Oyama. *Sci. Rep.* **6,** 37756 (2016).

[2] E. Tabata, A. Kashimura, S. Wakita, M. Ohno, M. Sakaguchi, Y. Sugahara, Y. Kino, V. Matoska, PO. Bauer and F. Oyama. *Sci. Rep.* **7,** 6662 (2017).

[3] E. Tabata, A. Kashimura, S. Wakita, M. Ohno, M. Sakaguchi, Y. Sugahara, Y. Imamura, S. Seki, H. Ueda, V. Matoska, PO. Bauer and F. Oyama. *Sci. Rep.* **7,** 12963 (2017).

[4] M. Uehara, E. Tabata, K. Ishii, A. Sawa, M. Ohno, M. Sakaguchi, V. Matoska, PO. Bauer and F. Oyama. *Genes* **9,** 9050244 (2018).

ABSTRACT

BARREDO, ABIGAIL R., University of the Philippines Los Baños, August 2021. **Performance of Aerobic Rice Under Different Levels of N-Fertilizer Using Surface Irrigation and Drip Fertigation.**

Major Professor: Dr. Rubenito M. Lampayan

Aerobic rice system is a remarkable development to combat water crises in rice agriculture. Although this technology shows great promise, further studies are still required to potentially adapt drip fertigation to it. Therefore, this study aims to evaluate the effects of different Nitrogen (N) fertilizer levels to the NSIC Rc222 aerobic rice variety via surface irrigation and drip fertigation. The field experiment was laid in a split plot design with irrigation methods as the main plot and the four levels of N-fertilizer (0%, 50%, 75% and 100%) was the subplot. Results have showed that the crop growth and final grain yield of NSIC Rc222 were unaffected by the irrigation method but are significantly affected by the N-fertilizer level. The interaction between the irrigation method and N-fertilizer level were significant for water productivity but not with both crop growth and final grain yield. The aerobic rice yield obtained ranged from 3, 020.43 to 4, 872.03 kg/ha. Grain yield as at N-fertilizer level, treatments of N100% and N75% were not significantly different, just as there were no significant difference between N75% and N50% treatments. Among the yield components, the number of tillers per m^2, number of panicles per m^2, and percent filled spikelets were mainly influenced by the different levels of nitrogen fertilizer applied. In contrast, number of spikelets per number of panicles and 1000 grain weight were influenced by the drip fertigation and surface irrigation systems. Harvest index values ranged

from 0.47 to 0.57. A total of 398.33 mm or 34% of water input can be saved using drip fertigation (783.50 mm) compared to surface irrigation (1181.83 mm). Water productivity was mainly influenced by the interaction of water regimes and applied N-fertilizer. The highest water productivity observed was 0.62 kg/m^3 under the treatment combination N75% using drip fertigation. In terms of nitrogen use efficiency, highest partial factor productivity (PFP) was observed at N50% recommended dose of fertilizer (RDNF) under surface irrigation (73.74 kg grain per kg N applied), and highest AE was obtained at N50% RDNF under drip fertigation (23.30 kg of grain per kg N applied). Growing aerobic rice under drip fertigation requires much less water without reducing yields. In the study, N-fertilizer for optimal crop growth and yield performance was 90 kg N/ha in either irrigation method.

The Use of Machine Vision for Postharvest Processing of Achacha Fruits

Ngo Minh Tri Nguyen[1], Quoc Thien Pham[2], Hoang Huy Nguyen[1] and Nai-Shang Liou[1]*

[1]Southern Taiwan University of Science and Technology, Tainan, Taiwan, R.O.C
[2]Ho Chi Minh City University of Technology, Ho Chi Minh City, Vietnam
E-mail: nliou@stust.edu.tw

Abstract

This study aimed to develop machine vision methods for the postharvest processing of achacha fruits. The hyperspectral data of achacha fruits along with the partial least square regression were used to evaluating the ripeness stage of achacha fruits. The RGB images and a Mask RCNN model were used for classification of achacha fruits with normal or defective surfaces. The accuracies for ripeness stage prediction and defect classification are 63% and 97% respectively.

The achacha (Garcinia humilis) is a tropical fruit native to South America and becomes novel fruit of Taiwan currently. In Taiwan, sorting and grading are two important postharvest processes of achacha fruits. Grading of achacha fruits, based on the weight of fruit, can be dealt with by weight sorter automatically. However, sorting of achacha fruits, removing under/over-ripe fruits or fruits with irregular shapes, colors, surface defects, is performed manually. The machine vision systems were widely used to identify external quality characteristics, such as color, texture, size, shape, and certain apparent defects of agriculture products. The objective of this study was to develop the machine vision-based methods and systems (Fig. 1) for ripeness stage evaluation and surface defect detection of achacha fruits.

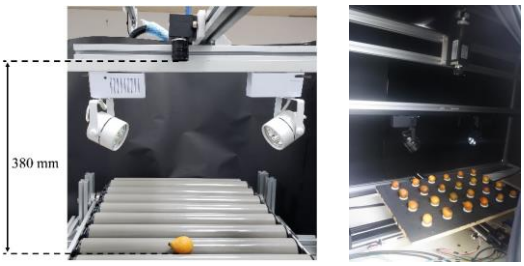

Fig. 1. The experimental setups of machine vision-based systems for postharvest processing of achacha fruits.

The hyperspectral data of achacha fruits and the partial least square regression (PLSR) [1] were used to evaluating the ripeness stage of achacha fruits. The fruit specimens without surface defect were divided to 7 ripeness stages and scanned by a push-broom hyperspectral imaging system. And then, the raw hyperspectral data of each sample was calibrated with the use of black and white references. The pseudo RGB image was created by concatenating three images at suitable wavelengths to create masks for spectral feature extraction. The spectral data extracted from the masks were used to train PLSR model with the optimal number of components. The methods based on statics (i.e. Mean, Median and Mode) were used to determine the ripeness level of samples base on PLS result of all pixels within their masks. 400 specimens were used to evaluate the PLSR model.

The RGB images and a Mask RCNN model were used for classification of achacha fruits with normal or defective surfaces. A total of 400 images of specimens with normal or defective surfaces were collected and used for training and validating of the Mask RCNN model.

The accuracies for ripeness stage prediction and defect classification are 63% (Fig. 2) and 97% (Table 1) respectively.

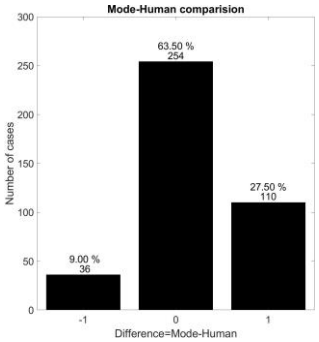

Fig. 2. The differences of ripeness stages predicted by PLSR model and evaluated by human expert.

Table 1. Confusion matrix of Mask RCNN model.

Actual	**Classified as**	
	Normal	Defect
Normal	51 TN	1 FP
Defect	2 FN	46 TP

References:

1. Wang, H., et al., *Integration of Partial Least Squares Regression and Hyperspectral Data Processing for the Nondestructive Detection of the Scaling Rate of Carp (Cyprinus carpio).* Foods, 2020. 9(4).

Surface Functionalization of Chitosan Hydrogel Using Atmospheric Pressure

Kathrina Lois Taaca[1,2,] *, Mark Jeffry De Leon[1], Hideki Nakajima[3], Kanjana Thumanu[3], Eloise Prieto[4] and Magdaleno Vasquez Jr.[1]

[1] Department of Mining, Metallurgical and Materials Engineering, University of the Philippines-Diliman, Philippines
[2] Materials Science and Engineering Program, University of the Philippines-Diliman, Philippines
[3]Synchrotron Light Research Institute, Nakhon Ratchasima, Thailand
[4]National Institute of Molecular Biology and Biotechnology, University of the Philippines-Diliman Philippines
E-mail: kmtaaca@up.edu.ph

1. Introduction

Active involvement of wound dressing was initiated in the 1960s [1]. This results to the development of functional active dressings that can create and maintain a moist environment for wound healing [1]. Hyrdogel-based wound dressings are considered to have the greatest potential among other dressings available in the market. In this study, chitosan (Cs), a linear cationic biopolymer containing two (2) polysaccharide units β-(1-4) linked 2-acetamide-2-deoxy-D-glucose, and 2-amino-2-deoxy-D-glucose, was formed into a hydrogel using covalent crosslinking with acrylic acid (AA) as the gelling agent. Atmospheric pressure plasma (APP) system was utilized to functionalize the surface properties of the synthesized hydrogel.

2. Methodology

Chitosan hydrogel was fabricated by mixing 2 wt% Cs and 7 % (v/v) AA in 2% acetic acid (HAc) solution at 40°C for 2 hours. About 0.1 g of ammonium persulfate (APS) was added to the solution, prior to APP treatment. The Cs-AA mixture was then exposed to APP treatment with air as treatment gas for 2 minutes. The samples were then dried at 60°C for 4 hours.

The Cs-AA samples were then post-treated with an acetone-methanol mixture for 5 minutes and stored after air drying, prior to characterizations.

3. Results and Discussion

Spectroscopic characterizations were employed to investigate the chemical features of the synthesized Cs-based hydrogels. Figure 1 shows the FTIR spectra of pure Cs, Cs-AA, and APP-treated Cs-AA hydrogels. Characteristic peaks of Cs are observed at peaks centered at 3300 cm-1, 1400 cm-1 and 1100 cm-1. Characteristic peaks of AA are observed at the range 1700-1100 cm-1. Change in the peak at 2900 cm-1 may indicate possible crosslinking of Cs and AA.

Near-edge x-ray absorption fine structure spectroscopy was utilized to determine the changes in the local electronic structure of the hydrogels. The TFY and TEY C K edge of the APP-treated hydrogel, shown in Figure 2, illustrates the distinct characteristic features of Cs. However, the TFY and TEY yields of APP-treated hydrogel showed decrease in the intensity in the 1s-3p/σ* C-C and 1s-π* C=O transitions, implying a difference in the bulk and surface structure of the hydrogel after APP treatment.

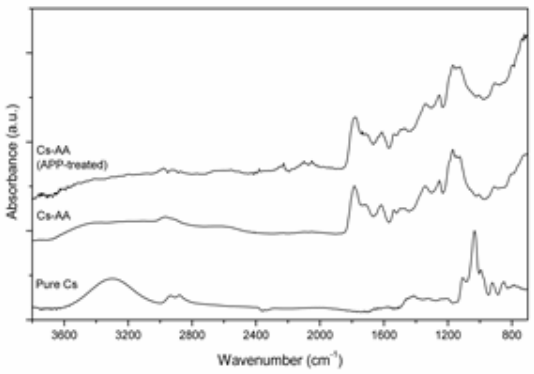

Fig. 1. FTIR Spectra of Cs-based hydrogels.

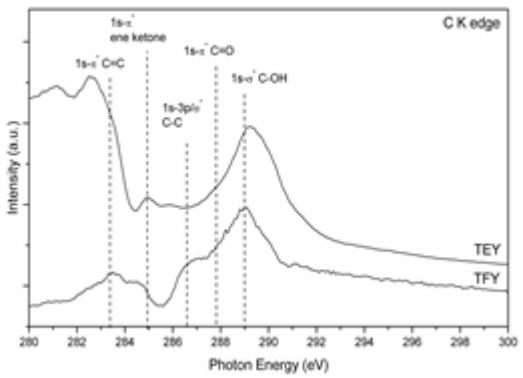

Fig. 2. NEXAFS TFY and TEY C K edge spectra of Cs-AA hydrogel with APP treatment

4. Acknowledgments

K.L.M. Taaca would like to acknowledge the 2017 DARETO Cycle 2 Program of the Commission on Higher Education (CHED) Philippines.

References:

[1] H. Liu, et al. *RSC Adv.*, **8**, 7533 (2018).

Oral Presentation

Electric Engineering and Electronic Engineering

November 23rd

Presentation No.	Title	Author	
EEE1.	Examination of Improvement of Supply Stability by Introducing Wind Power Generation in Disaster-robust Zero Energy Vehicle(D-ZEV)	Bian Ning, Yasuhiro Noro	39
EEE2.	ElderFit: A Physical Fitness Motion Detection System for Older Adults Based on Deep Learning Technology	Wan-Jung Chang, Jian-Ping Su	43
EEE3.	Investigation of the Relationship between Muscle Strength and the Power of Electromyograph Signal	Chun-Ju Hou, Yen-Ting Chen, Ji-Jer Huang, and Mycel Capilayan	44
EEE4.	Optimization for elevation-plane beam configuration in 3D beamforming technology	Yuji Omura, Hiroyuki Otsuka	46

Examination of Improvement of Supply Stability by Introducing Wind Power Generation in Disaster-robust Zero Energy Vehicle(D-ZEV)

Bian Ning, Yasuhiro Noro

Department of Electrical and Electronic Engineering, Kogakuin University, Tokyo, Japan
E-mail: cm20047@ ns.kogakuin.ac.jp

Abstract

In this paper, simulation experiments of a new D-ZEV retrofitted small wind power generation are conducted and analyzed on MATLAB by improving the conventional MPPT algorithm and optimizing the design of the energy storage system.

1. Background:

This paper is based on the self-sustaining power supply system D-ZEV [1], and the new D-ZEV was simulated and the results were analyzed.The original D-ZEV uses photovoltaic generation as a power source to supply power to shelters and facilities needed for rescue in the event of a disaster. In this paper, the original D-ZEV is optimized with wind power generation equipment, solar power generation and energy storage to meet the long and stable power supply under severe weather conditions, such as continuous rainy weather, when sufficient sunlight is not available.

2. Object System:

By using MATLAB software, the model of the new D-ZEV is constructed and the MPPT control part of solar power generation and the energy storage structure part are analyzed with emphasis. The whole system was simulated after the addition of the wind turbine and the results were analyzed. The structure diagram of the new D-ZEV is shown as follows:

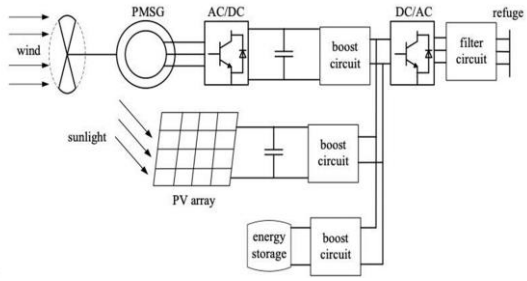

Fig.1.The structure diagram of the new D-ZEV

3. The use of MPPT control methods and optimization of energy storage system:

3.1 Improvement of MPPT of PV power generation system

In order to get more solar power, we need to use MPPT to ensure that the PV system works around the Maximum Power Point (MPP) as much as possible [2]. If we can get the voltage U at the MPP and adjust the PV cell output voltage close to the U, then we can get the MPPT control effect we need. Since the environment is complex and variable, the P-U curve changes accordingly, so it is necessary to find its optimal operating voltage to track the maximum power point. The tracking of the maximum power point is generally done by the MPPT algorithm. Among all MPPT algorithms, the perturbation observation method is in the mainstream.It is shown in Figure2:

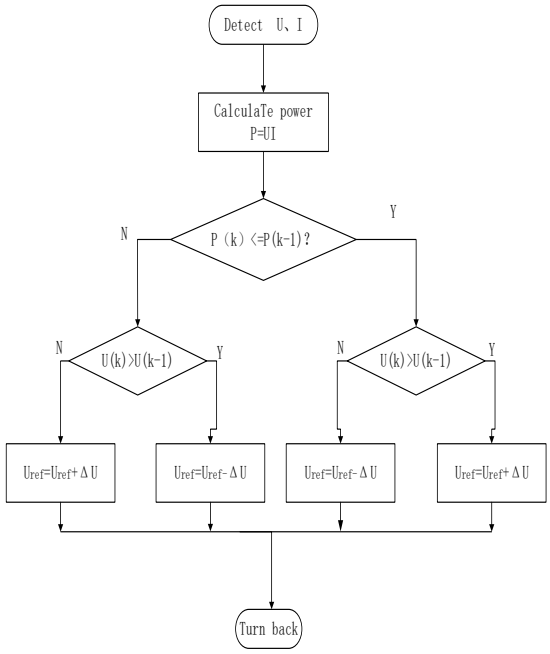

Fig.2.Perturbation observation method flow chart

The basic principle of the perturbation observation method is relatively simple, but if the maximum power point changes frequently, it will be difficult to achieve accurate tracking in this case, and it should be improved. The tracking accuracy is to some extent opposed to the tracking speed, and it is not possible to set the step size exactly. To optimize for this problem, it is assumed that if the maximum power point and the working point are far away, then a large step size must be used for tracking. The workflow is as follows: there is a "coarse tuning mode" and a "fine tuning mode". If it is "coarse tuning mode", there is a relatively long disturbance step, and the tracking speed is very fast; if it is "fine tuning mode", there is a relatively small disturbance step, and the tracking accuracy can be very high. The specific control flow chart is shown in Figure 3:

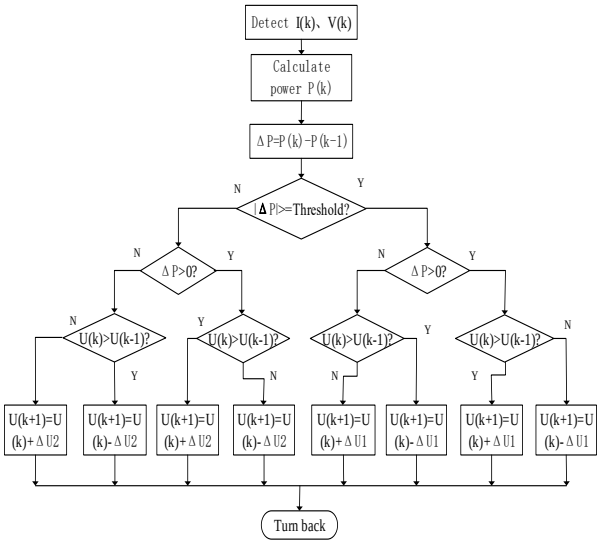

Fig. 3. Flow chart of improved perturbation observation method

When analyze the flow chart of the modified perturbation observation method, we can see that firstly, a threshold value is set and then two voltage change steps are set, ΔU1 and ΔU2 (ΔU1>ΔU2). When the power difference measured at adjacent moments is larger than the threshold value, then the PV cell has a higher output power change and is tracked with the help of ΔU1; when the PV cell has a lower output power change, then it is tracked with the help of ΔU2. This method is used in this paper because of its practicality.

3.2 Optimization of energy storage structure

For the D-ZEV power supply system of the target research, the storage needs to be charged when the power supply is available, and in the event of a power failure, the battery must also have a discharge function to maintain the normal operation of the load equipment. In this proposed design in the D-ZEV system coordination control, the battery using constant voltage charging (discharge) control strategy. The constant voltage charging of the battery is to keep the charging voltage constant, using voltage and current double closed loop control. The current control loop includes a limiting link to prevent over-current charging during the charging process, which may cause damage to the battery components. he constant voltage discharge is controlled by a double closed-loop voltage and current control, with the outer loop controlling the DC side voltage and the inner loop controlling the discharge current. In the outer loop, the collected DC bus voltage is compared with the given reference value, and the difference is sent to the PI regulator, which is used as the inner loop current reference value after a current limiting link and compared with the actual battery current, and the obtained signal is used as the control signal for the switching tubes of the discharge circuit through the PWM waveform generated by the modulator after the PI regulator.

In order to obtain better control performance, the paper takes advantage of the advantages of Active Disturbance Rejection Control (ADRC) [3] and considers the actual situation of the energy storage system, the existence of charging and discharging operating processes, and designs a control block diagram for double closed-loop ADRC as shown in Figure 4.

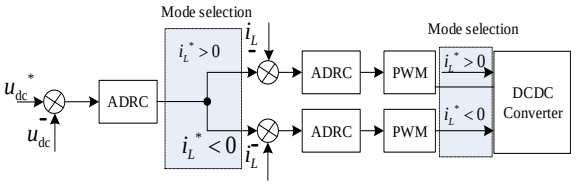

Fig. 4. Block diagram of Active Disturbance Rejection Control of bidirectional DCDC converter

According to the mathematical expression of the bidirectional DC/DC converter, combined with the basic principle of second-order ADRC, the controller consists of three parts: tracking differentiator (TD), expanded state observer (ESO), and nonlinear feedback controller (NLSEF). The specific control block diagram is shown in Figure 5[4].

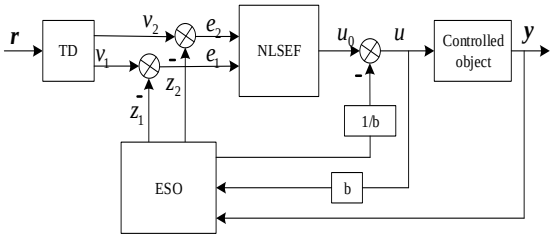

Fig. 5. Control block diagram of second-order self-tampering controller

The role of TD is to track the reference (U_{dc}* and i_L*) signals in order to resolve the contradiction between the presence of overshoot and rapidity in the control system, as expressed by:

$$\begin{cases} \dot{v}_1 = v_2 \\ \dot{v}_2 = f_{han}(x_1, x_2, r, h_0) \\ x_1 = v_1 - v_0 \\ x_2 = v_2 \end{cases} \quad (1)$$

where v_0 is the reference signal, v_1 is the tracking signal of v_0, and v_2 is the differential signal of v_1; r is the velocity tracking factor; f_{han} () is the maximum velocity control function, which is a controller parameter that can be taken as a value appropriately larger than the step size h_0.

The main function of ESO is to accurately track the actual voltage and current of the control loops, and to estimate the amount of internal and external disturbances in the system, as expressed by:

$$\begin{cases} e = z_1 - y \\ \dot{z}_1 = z_2 - \beta_{01} e \\ \dot{z}_2 = z_3 - \beta_{02} f_{al}\left(e, \frac{1}{2}, \delta\right) \\ \dot{z}_3 = -\beta_{03} f_{al}\left(e, \frac{1}{4}, \delta\right) + bu \end{cases} \quad (2)$$

where z_1 and z_2 are the tracking and differential signals of the actual voltage U_{dc} and current i_L, respectively, z_3 is the observed signal of the total disturbance, and $\beta_{01} = \beta_{02} = \beta_{03}$ is generally taken as the parameter of the state observer, and the f_{al} function shape is as follows:

$$f_{al}(x, a, \delta) = \begin{cases} |x|^a sign(x), |x| > \delta, \delta > 0 \\ \frac{x}{\delta^{(1-a)}}, |x| \le \delta \end{cases} \quad (3)$$

The main function of NLSEF is to obtain the error and differential signal between the target value and the feedback value of the system according to the output of TD and ESO, and to obtain the feedback control rate of the system by combining the linear and nonlinear error signals, so as to achieve the effect of no static difference without the "integration link", which is expressed as follows:

$$\begin{cases} e_1 = v_1 - z_1 \\ e_2 = v_2 - z_2 \\ fe_1 = f_{al}(e_1, \alpha_1, \delta_1) \\ fe_2 = f_{al}(e_2, \alpha_2, \delta_2) \\ u_0 = \beta_1 fe_1 + \beta_2 fe_2 \\ u = u_0 - \frac{z_3}{b_0} \end{cases} \quad (4)$$

where e_1 is the error signal, e_2 is the differential error signal, α_1, α_2 are the nonlinear factors; δ_1, δ_2 is the filtering factor; and u is the compensation control amount.

3.3 Control of wind power generation part

The structure of a small wind power generation system that uses a permanent magnet synchronous generator as a generator and a boost converter as a power adjustment circuit can achieve maximum power point tracking. This simulation uses the traditional hill-climbing legal step perturbation MPPT strategy, as shown in Figure 6.

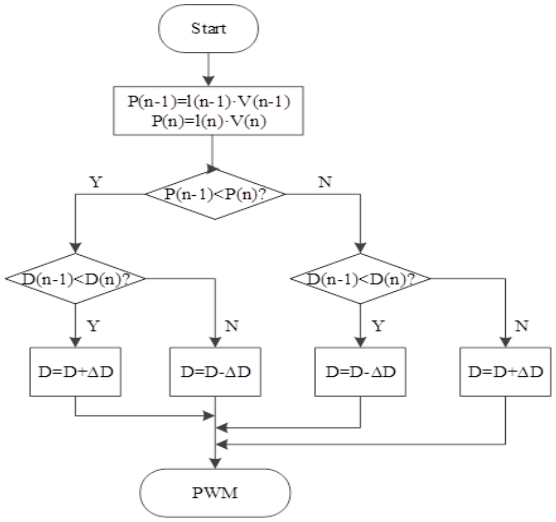

Fig. 6. Control principle diagram of hill climbing method

3.4 Simulation results of the simulated D-ZEV system

The parameters in the simulation are set as follows: the reference value of DC bus voltage is 400 V, the reference voltage of inverter is set to voltage amplitude 311 V (RMS 220 V), frequency 50 Hz. The initial value of solar intensity is 800 W/m^2, abruptly changes to 1000 W/m2 at t=2 s, abruptly changes to 600 W/m^2 at t=3 s; the initial value of wind speed is 5 m/s, abruptly changes to 3 m/s at t= 2.5 s, abruptly changes to 5 m/s at t=4 s; the initial value of the load power is 3 kW, and the load power becomes 7 kW with a sudden increase of 4 kW at t=1.5 s, and the overall simulation time is 4 s.

The simulation results are shown in Figure 7. As can be seen from Figure 7, when the external environment changes, PV Ppv and wind power system Pwind can quickly track to near the maximum power point and output stable power.

When t=0-1.5 s, the sum of PV output power Ppv and wind output power Pwind is greater than the load power Pload, when the excess energy charges the battery, the SOC of the battery gradually rises.

In the period from 1.5 s to 2 s, the load power increases, but the sum of Ppv and Pwind is less than the Pload, at this time the missing energy is discharged by the battery, the SOC of the battery gradually decreases.

In the period from 2 s to 2.5 s, the PV power increases, but the sum of Ppv and wind Pwind is less than the Pload, at this time the missing energy is discharged by the battery, the SOC of the battery is still gradually decreasing.

In the period from 2.5 s to 3 s, the wind power decreases, but the sum of Ppv and Pwind is less than the Pload, at this time the missing energy is discharged by the battery, the SOC of the battery is still gradually decreasing.

In the period from 3 s to 4 s, the wind power increases, but the sum of Ppv and Pwind is less than the Pload, at this time the missing energy is discharged by the battery, the SOC of the battery is still gradually

decreasing.

As can be seen from the figure, when the load output power changes, the external environment changes, the DC bus voltage will have a slight fluctuation outside, basically stable in a straight line, that is, the bus voltage always fluctuates in a small range above and below 400V, and the fluctuation range gradually decreases and gradually converges to a constant value of 400 V.

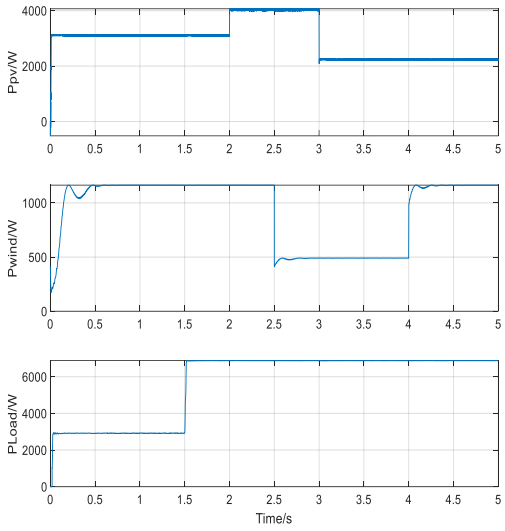

(a) Photovoltaic, wind power, battery and load power

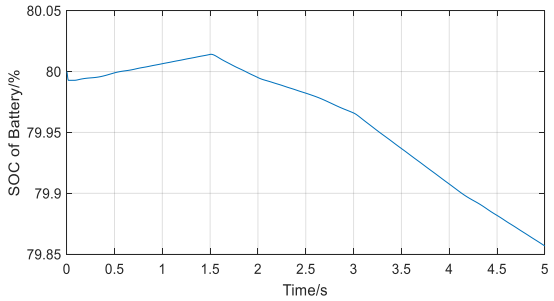

(b) SOC of the battery

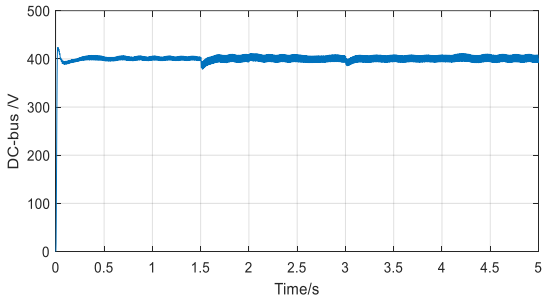

(c) DC bus voltage

Fig.7.Simulation Results

4. Conclusion:

This study adds a small wind power generation system to the original D-ZEV with photovoltaic power generation , and improves the MPPT control algorithm of the photovoltaic system to improve the accuracy of maximum power point tracking. The study also designed the energy storage structure, which is applicable to the automatic charging and discharging of the energy storage system of the new D-ZEV. Through the analysis and simulation experimental results of this paper, the new MPPT control algorithm has good tracking and control effect, and ADRC has good control effect for battery charging and discharging. Based on this paper, the construction of D-ZEV through MATLAB, the D-ZEV structure will be practically optimized in the future, with the aim that the new system will be able to provide sustainable and stable power supply to disaster response facilities such as shelters under more severe weather conditions.

References:

[1] Yohei Kubo, Yasuhiro Noro. Study of power supply system for Disaster-robust Zero Energy Vehicle, International Workshop on Power Engineering in Remote Islands (IWPI 2018) October 31,2018, PE-18-193:35-40

[2] Boutabba Tarek, Sahraoui Hamza. A Comparative Study of MPPT Techniques for Standalone Hybrid PV-Wind with Power Management[C]. 4th International Conference on Electrical Engineering and Control Applications, ICEECA 2019, December 17, 2019.

[3] Han,Jingqing. Auto Disturances Rejection Control Technique, Frontier Science Quarterly,2007-1, Issue 1:24-31

[4] Hu, Junxiang, Ge, Yuan, Zhou Xu. Research on the course control of USV based on improved ADRC[J].Systems Science and Control Engineering, 2021,9(1): 44-51.

ElderFit: A Physical Fitness Motion Detection System for Older Adults Based on Deep Learning Technology

Wan-Jung Chang* and Jian-Ping Su

Department of Electronic Engineering, Southern Taiwan University of Science and Technology, Tainan, Taiwan
E-mail: allenchang@stust.edu.tw

Abstract

The statistics pointed out that the population over 60 years old will reach 21% of the total population by 2050. As the population is aging, the problem of disability of the elderly caused by sarcopenia is also increased [1]. To reduce the incidence of sarcopenia, the elderly need to maintain good exercise habits. Recently, many researchers have proposed exercise monitor systems to encourage elderly people to maintain good exercise habits. In order to reduce the incidence of sarcopenia, Jones and Rikli [2] proposed seven physical fitness exercises (see Table 1) and demonstrated that sarcopenia can be greatly reduced if the elderly regularly practice these physical fitness exercises in life. Nowadays, since the elderly who do these seven physical fitness exercises need rehabilitations to teach and observe their exercise status as the evaluation index listed in Table 1, these physical fitness exercises cannot be extensive and comprehensively promoted to the community and family.

To address this issue, this paper proposes a deep learning-based physical fitness motion system, named ElderFit. Fig. 1 shows the system architecture of the proposed ElderFit system consisting of a camera, an AI edge module, and a fitness management platform. The camera captures physical human fitness images of one elderly located at the test zone (Z) and then wirelessly forwards the human images to the AI edge module operated with the deep learning-based OpenPose algorithm [3]. The OpenPose is used to perform the skeleton of the human images by recognizing a total of 18 joint points K_i (i={0, 1,…, 17}). Each joint is given a coordinate (X_i, Y_i). Through the use of coordinates of joint points, this paper proposes a fitness recognition algorithm implemented on the AI edge module to identify the evaluation index (I) of the fitness exercises(S) in Table 1. It is noted that due to the length limitation, this paper only focus on the recognition manner for fitness exercises with the evaluation index of times (i.e., fitness exercises S1, S2, and S4 in Table 1).

As shown in Fig. 2, the ElderFit system is established in the Zuozhen community in Tainan, Taiwan. In Zuozhen community, a total of four elderly people are selected to actually do fitness exercises S_1, S_2, and S_4, 30 times for each to verify the effectiveness of ElderFit system. In Table 2, it can be seen that ElderFit can achieve a high recognition accuracy of fitness exercises S_1, S_2, and S_4.

Table 1: The list of 7 physical fitness exercises.

No.	Fitness Exercises (*S*)	Evaluation Index (*I*)
1.	30-Second Chair stand	times
2.	30-Second Arm Curl	times
3.	6-Min Walk	moving distance
4.	2-Min Step	times
5.	Chair Sit-&-Reach	moving distance
6.	Back Scratch	moving distance
7.	8-Foot Up-and-Go	period of time

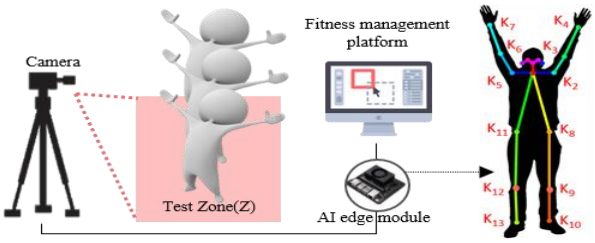

Fig. 1. System architecture of the proposed ElderFit system.

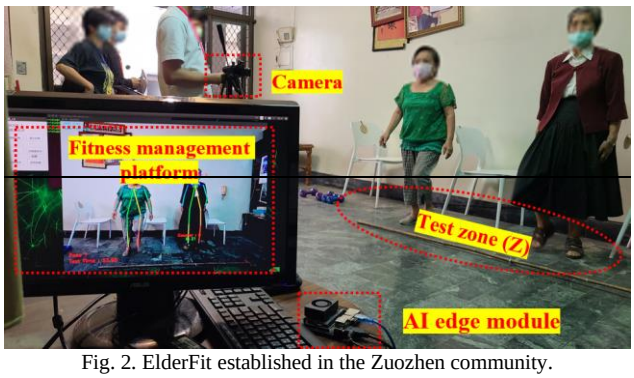

Fig. 2. ElderFit established in the Zuozhen community.

Table 2: Performance evaluation of ElderFit.

No.	Sex	Fitness Exercises	Index(*I*) (times)	Accuracy
1	female	S1	27	90.0%
		S2	29	96.6%
		S4	29	96.6%
2	female	S1	28	93.3%
		S2	30	100%
		S4	29	96.6%
3	male	S1	30	100%
		S2	29	96.6%
		S4	30	100%
4	male	S1	28	93.3%
		S2	30	100%
		S4	27	90.0%

References:

[1] M. Bogliolo, et al., "A robot instructor for the prevention and treatment of Sarcopenia in the aging population: A pilot study," in *Proc. 2020 29th IEEE RO-MAN*, pp. 1075-1080, 2020.
[2] C. J. Jones and R. E. Rikli "Measuring functional fitness of older adults," *The Journal on active aging*, vol. 43 pp. 25-30, 2002.
[3] Z. Cao, *et al*., "OpenPose: Realtime Multi-Person 2D Pose Estimation using Part Affinity Fields," *IEEE Transactions on Pattern Analysis and Machine Intelligence*, vol. 43, pp. 172-186, 2021.

Investigation of the Relationship between Muscle Strength and the Power of Electromyograph Signal

Chun-Ju Hou, Yen-Ting Chen*, Ji-Jer Huang and Mycel Capilayan

Department of Electrical Engineering, Southern Taiwan University of Science and Technology, Tainan, Taiwan
E-mail: ytchen@stust.edu.tw

Abstract

The purpose of this paper is to investigate the relationship between a person's muscle strength and the power from the electromyograph (EMG) signal. The results show that when the weight bearing was raised, the subject had to use more effort and muscle contraction to maintain the posture in subjects with low body mass index (BMI) and low skeletal muscle mass (SMM). The root-mean square value of EMG is relative to the muscle strength.

The ageing of Taiwan's population is continuously progressing. As of March 2018, the proportion of Taiwan's elderly population has exceeded 14%, and it has officially reached the internationally defined Aged Society [1]. It is estimated that the estimated proportion will reach 20% in 2026, becoming a super-aged society. As people get older, the organ function can also decline. Among them, the muscle mass related to the activity function will also be significantly reduced. In addition to the decrease in muscle mass, it is accompanied by the decline of muscle strength and muscle function. This condition is called sarcopenia [2]. Sarcopenia can cause health problems, such as being unable to walk for long, unable to stand up, and muscle weakness, which can easily cause falls, fracture, and disability. It will affect the health and safety of the elderly, so sarcopenia should not be underestimated. The handgrip strength is a common testing method for the assessment of muscle strength. Based on the Asian Working Group for Sarcopenia (AWGS) recommendations, low muscle strength is defined as the handgrip strength of less than 28 kg for men, and 18 kg for woman [3]. This experiment aimed to explore the relationship between the muscle strength and the root-mean square (RMS) value of EMG's amplitude.

A total of 24 college students (10 males and 14 females) participated in this experiment. The subjects' ages ranged between 20 and 24 years old. The males were divided into 3 groups (G_{m1}: BMI 17.7±0.3, SMM 21.8±0.3, Fat 8.1±0.8; G_{m2}: BMI 22.6±2.2, SMM 19.3±3.7, Fat 17.4±2.8; G_{m3}: BMI 30.6±4.1, SMM 27.4±4.8, Fat 32.3±9.9), and females were divided into 4 groups (G_{f1}: BMI 19.0±1.8, SMM 13.9±1.7, Fat 13.0±3.5; G_{f2}: BMI 22.3±1.8, SMM 16.8±0.6, Fat 17.1±2.2; G_{f3}: BMI 25.8±1.0, SMM 18.8±0.8, Fat 25.5±2.1; G_{f4}: BMI 27.1±3.2, SMM 18.1±1.8, Fat 30.8±4.9). The BIOPAC MP150 equipment was used for collecting EMG signal with the sampling rate of 1 kHz. The EMG was processed and analyzed using MATLAB 2017b software. The dumbbells consisted of seven weights, 1.48 kg, 1.91 kg, 2.33 kg, 3.47 kg, 4.26 kg, 4.56 kg, and 5.41 kg. The subject used their dominant hand to lift the dumbbell and hold for 30 seconds. Before the EMG measurement, the skin surface of the arm was wiped with an alcohol swab. The positive and negative electrodes were attached on the biceps brachii muscle, and the reference electrode was attached to the wrist, as shown in Fig. 1. The subject's elbow joint maintained a flexion posture. The weight-bearing EMG signal was recorded, and then the subject put the dumbbell down for the rest of 30 seconds. This process was repeated for dumbbells of different weights.

Fig. 1. Position of electrodes on the subject's arm.

The RMS value of the EMG's amplitude, M_{rms}, is calculated, and the formula is represented as follows.

$$M_{rms} = \sqrt{\frac{1}{N}\sum_{n=0}^{N-1}(x[n])^2}$$

where $x[n]$ is the EMG sequence, and N is the length of the sequence. The relationship between the RMS value of the EMG and weights was analyzed using a simple linear regression method.

In male subjects, the results show that the slope of RMS value vs dumbbell weights has no significant differences among 3 groups when the weight is less than 2.33kg, and the slope in G_{m1} is higher than that of G_{m2} and G_{m3} when the weight is greater than 2.33kg (Fig. 2). In G_{m1}, when the weight bearing was raised, the subject had to use more effort and muscle contraction to maintain the posture. In G_{m2} and G_{m3}, when the weight bearing was raised, the subject could hold the dumbbell stably.

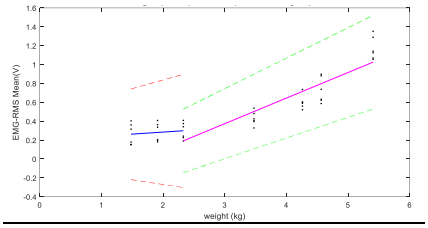

(a) G_{m1}

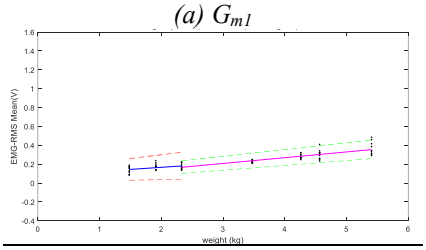

(b) G_{m2}

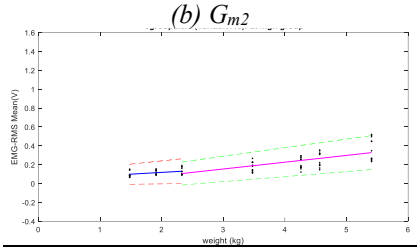

(c) G_{m3}

Fig. 2. Relationship between the weight-bearing and EMG's RMS value of 3 groups in male subjects

In female subjects, the results show that the slop3 in G_{f1} is greater than that in G_{f2}, G_{f3}, and G_{f4} (Fig. 3). The body type of subjects in G_{f1} is a low SMM and a low fat. They were unable to lift the heaviest dumbbell due to a low muscle strength and had to use more muscle fibers to produce muscle power. The muscle strength of female subjects is lower than that of male subjects.

Based on the experimental and statistical results, it was found that EMG is related to muscle strength. The heavier the dumbbell, the more power the muscles have to exert. In future studies, this setup can be set and matched with wearable devices. The signals can be displayed to the user as reference in real time. This can help us understand the human body better and how to prevent sarcopenia, especially among the elderly population.

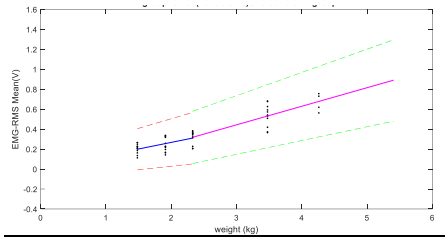

(a) G_{f1}

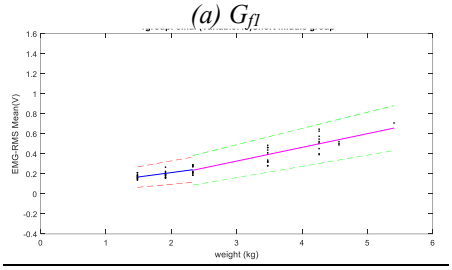

(b) G_{f2}

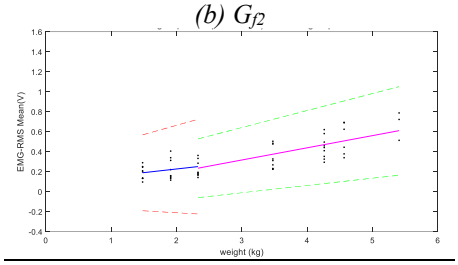

(c) G_{f3}

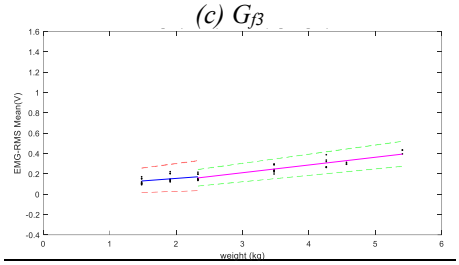

(d) G_{f4}

Fig.3. Relationship between the weight-bearing and EMG's RMS value of 4 groups in female subjects

References:

[1] (Web) Taiwan National Development Commission Population Estimation System, https://pop-proj.ndc.gov.tw/index.aspx, Visit: November 2020.

[2] C-W. Chang, H-. Tang, J-H. Syu, The diagnosis and assessment of sarcopenia in the elderly, *Culture and Sports Journal*, **24**, (2017).

[3] Liang-Kung Chen, Asian Working Group for Sarcopenia: 2019 Consensus Update on Sarcopenia Diagnosis and Treatment, *J Am Med Dir Assoc*, 21(3):300-307, 2020.

Optimization for elevation-plane beam configuration in 3D beamforming technology

Yuji Omura and Hiroyuki Otsuka

Graduate School of Engineering, Kogakuin University, Tokyo, Japan
E-mail: cm20012@ns.kogakuin.ac.jp

Abstract

Three-dimensional beamforming (3D-BF) can improve data rates and/or extend cell coverage in fifth-generation mobile systems (5G). In this paper, we discuss the optimization of downlink 3D-BF comparing with the transmission performance for two types of elevation-plane beam configuration using system-level computer simulations.

Figure 1 shows the side view of eNB with three elevation-plane beams for two types of beam configuration, i.e., types A and B. The number of azimuth-plane beams is fixed to eight, and its beamwidth is 8.8 degree. The number of elevation-plane beams is three and its beamwidth is 3.3 degree listed in Table 1[1, 2]. The primary simulation parameters are listed in Table 2. In Type A, two beams among three beams radiate upper direction than the antenna downtilt angle. In Type B, the peak power direction of center beam is the same as the antenna downtilt angle.

Table 1. Beam Parameters used in 3D-BF

Number of beams per sector	Non BF	24
Max. Tx antenna gain (dBi)	14	27.8
Azimuth 3 dB beamwidth (deg.)	70	8.8
Elevation 3dB beamwidth (deg.)	10	3.3

Table 2. Primary Simulation Parameters

Parameter	Assumption
Cell layout	Hexagonal grid, 19 cell sites, 3 sectors per site
Cell radius	289 m (ISD = 500 m)
Carrier frequency	2.0 GHz
System bandwidth	10 MHz
eNB Tx power	46 dBm
eNB Tx antenna downtilt	15 deg.
eNB antenna height	32 m
UE distribution	Uniform distribution, 30 UEs per sector
UE Rx antenna height	1.5 m
Link adaptation	25MCS (QPSK to 1024-QAM)

Figure 2 shows the average and 5-percentile user throughput of the mobile network using 3D-BF defined by Table II. Type A can improve the average and 5-percentile user throughput by approximately 2.2 and 1.8 times compared with the non-BF, respectively. On the other hand, Type B can improve the average and 5-percentile user throughput by approximately 1.8 and 1.0 times compared with the non-BF, respectively.

In summary, we clarified the user throughput performance for two types of elevation-plane beam configuration in downlink 3D-BF. It was shown that the user throughput of Type A is better than that of Type B.

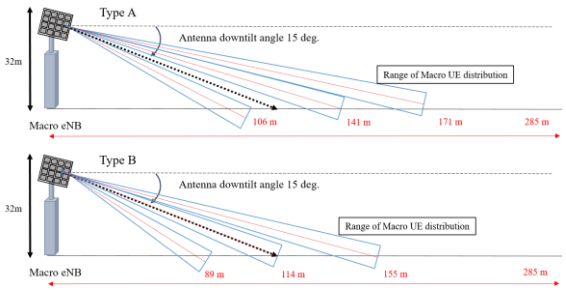

Fig. 1. Side view of eNB with three elevation-plane beams.

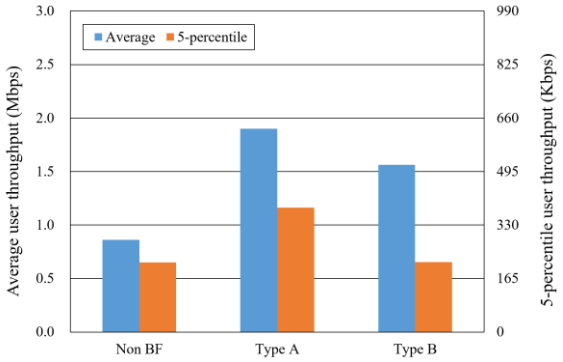

Fig. 2. Average and 5-percentile user throughput.

References:

[1] Y. Omura, F. Kemmochi, K. Fujisawa and H. Otsuka, "Implementation of MCS Incorporating 1024-QAM and Beam-Based Transmission in 3D-BF," in Proc. VTC2020-Spring, 1D-2, May 2020.

[2] Y. Omura, H. Otsuka, "User Throughput Improvement by Three-dimensional Beamforming in Mobile Systems,", ISAT-19, Information and Communications Technology, January 2021.

Oral Presentation

Environmental Chemistry and Chemical Engineering

November 23rd

Presentation No.	Title	Author	
ECC1.	Development of low-fouling microfiltration membranes with high permeability by blending PVDF with poly (2-methoxyethyl acrylate)	Seiya Ohno, Shin-ichi Nakao, Xiao-lin Wang, Kazuki Akamatsu	48
ECC2.	Application of wastewater treatment by microalgae cultivation technology for aquatic products processing facilities	Xuan Thanh Nguyen Thi, Nguyen Quốc Vương, Nguyen Hoang Minh	49
ECC3.	Investigation and optimization of harvesting microalgae using Electro-coagulation and flotation (ECF) method	Nguyen Nhat Cuong, Nguyen Thi Thanh Xuan	50
ECC4.	Separation mechanism of carbon dioxide through CHA membrane under high pressure	Fumiya Hirosawa, Masaya Miyagawa, and Hiromitsu Takaba	51

Development of low-fouling microfiltration membranes with high permeability by blending PVDF with poly(2-methoxyethyl acrylate)

Seiya Ohno[1,*], Shin-ichi Nakao[1], Xiao-lin Wang[1,2], Kazuki Akamatsu[1]
[1] Department of Environmental Chemistry and Chemical Engineering, School of Advanced Engineering, Kogakuin University, Tokyo, Japan
[2] Department of Chemical Engineering, Tsinghua University, Beijing, People's Republic of China
E-mail: bm20009@ns.kogakuin.ac.jp

Abstract

To remove organic matters from water in water purification and wastewater treatment processes, the use of membrane separation and filtration technologies is indispensable in terms of separation efficiency, energy consumption, and space requirements. Among the various membrane materials, poly(vinylidene fluoride) (PVDF) is one of the most commercially available materials in microfiltration membranes. However, fouling caused by adsorption of proteins and polysaccharides reduces membrane performance. Numerous researchers have developed low-fouling PVDF membranes modified with low-fouling polymers on the surface and pore walls of membrane substances. The immobilization methods are mainly classified into the chemical immobilization method and the physical immobilization method. Our earlier study developed low-fouling membranes using plasma graft polymerization which chemically immobilized poly(2-methoxyethyl acrylate) (PMEA) as a low-fouling polymer to polyethylene membranes [1]. PMEA has unique features that it suppresses protein adsorption, and is insoluble in water. The physical immobilization methods which physically deposit the low-fouling polymers onto membrane surfaces easily donate low-fouling properties to the membranes [2]. Even though these immobilization methods are effective for preventing fouling, the polymers used for the modification become additional filtration resistance, which also reduces membrane performance relative to unmodified membranes.

In this study, we developed low-fouling membranes in another approach. In the novel procedure, we first blended PVDF with PMEA before fabricating membranes via non-solvent induced phase separation (NIPS). NIPS is practically used for fabricating PVDF-based membranes. The membranes were prepared from five dope solutions containing 15 wt% PVDF and 0, 1, 3, 5, or 7 wt% PMEA synthesized by free-radical polymerization in *N*-methyl-2-pyrrolidone as a solvent. Each dope solution was cast onto a glass plate in the form of thin film. The glass plate was then immersed in a pure water coagulation bath to proceed membrane formation by phase separation. The low-fouling properties of the prepared membranes were evaluated in bovine serum albumin (BSA) filtration tests in a closed-loop cross-flow system.

Fig. 1 shows the time courses of the flux in the BSA filtration tests under constant pressure operation. Just after the addition of a 1000 ppm BSA aqueous solution after supplying pure water for 30 min, the flux in the pristine PVDF membrane drastically decreased to less than 1×10^{-6} m^3 m^{-2} s^{-1} from the initial flux, indicating that a severe BSA fouling occurred. Although the flux in the PVDF membrane blended with 1 wt% PMEA also decreased sharply due to insufficient PMEA blending, the fluxes for the membranes with higher blending ratios maintained high fluxes. As a result, the low-fouling properties increased with PMEA blending ratio, and the membrane blended with 7 wt% PMEA demonstrated the highest low-fouling property in the prepared membranes [3].

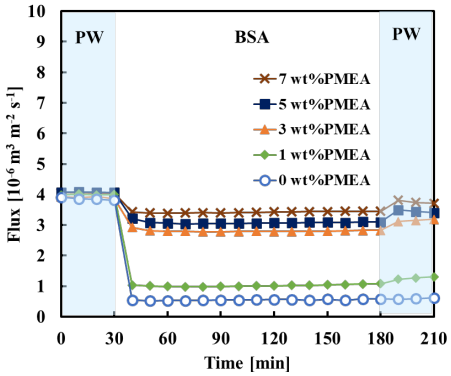

Fig. 1. Effect of PMEA concentration on the flux in a 1000 ppm BSA filtration test.

References:

[1] K. Akamatsu, T. Furue, F. Han, S. Nakao, *Sep. Purif. Technol.*, **102**, 157-162 (2013).
[2] C. Cheng, S. Li, W. Zhao, Q. Wei, S. Nie, S. Sun, C. Zhao, *J. Membr. Sci.*, **417-418**, 228-236 (2012).
[3] S. Ohno, I. Ibuki, R. Nagumo, K. Akamatsu, X. Wang, S. Nakao, *Sep. Purif. Technol.*, **276**, 119331 (2021).

Application of wastewater treatment by microalgae cultivation technology for aquatic products processing facilities

Nguyen Thi Thanh Xuan*, Nguyen Quốc Vương, Nguyen Hoang Minh,

Faculty of Chemical Engineering, University of Science and Technology, The University of Danang, Da Nang, Vietnam
E-mail: *nttxuan@dut.udn.vn

Abstract

It is now a given that global warming is happening and becomes one of the most urgent problems of our time. More than 90% of scientists are certain that it is primarily caused by the increase of greenhouse gases caused by human activities such as the burning of fossil fuels and deforestation. Currently, the cultivation of microalgae to treat aquatic wastewater and capture biomass for biofuel production or animal feed is being very interested and focused. The cost of producing biofuel from microalgae is very high, so the price of the product is also higher than that of petroleum fuel. The biofuel production combined with wastewater treatment and treatment of a large amount of CO_2 emitted from plants will help reduce this cost. In addition, the utilization of CO_2 emissions and high nutrient content in the wastewater environment to grow *C. Vulgaris* is an effective way not only to reduce environmental pollution but also contribute to creating a source of multi-application algae biomass. In this work, we investigated essential factors influencing on growth of C. vulgaris using untreated seafood wastewater as optimal culture medium. The results indicated that the *C. vulgaris* could grow very well in the untreated wastewater of its COD at value of 4000 – 5000 mg/l. The highest amount of chlorophyll-a of *C. vulgaris* (~5.3 g/l) was obtained at algae/ wastewater ratio of 10% (v/v) in condition of natural illumination (light intensity > 8000 lux) and medium aeration rate of 2 l/min. After algae recovery by electro-coagulation-flocculation (ECF) process, 95 % of total suspended solids as well as COD were removed from wastewater; the total nitrogenous has been reduced 87% and total phosphorous lowered up to 65% in treated effluent.

Investigation and optimization of harvesting microalgae using Electro-coagulation and flotation (ECF) method

Nguyen Nhat Cuong, Nguyen Thi Thanh Xuan

Faculty of Chemical Engineering, University of Science and Technology, The University of Danang, Da Nang, Vietnam
E-mail: nhatcuongnguyen2203@gmail.com, nttxuan@dut.udn.vn

Abstract

Microalgae is an organism that has a great photosysthesis ability thank to its microsize, high chlorophyll content. The use of microalgae in wastewater treatment and collecting biomass have limited success. However, microsize of microalgae makes it hard to collect them from cultivating medium. There are a lot of harvesting methods with their limits. Electro-coagulation and flotation has been proving its advantages in harvesting microalgae including: simple operation, ease maintenance, low operating cost and low bio-slugde contamination. This article focus on investigating electrolytic elements affecting ECF process such as electrode material, voltage, initiate pH, current density and electrolysis duration. Beside that, this work also provide evaluation of key operation parameters (current density, electrolysis duration) of ECF process for optimization of electrolysis efficiency, bio-slugde contamination and energy consumption. The result shown ECF process is able to collect 90.17% of biomass with 2.4 %weight bio-slugde contamination at 1.58 kWh/kg energy consumption.

1. Introduction

Microalgal biomass is considered as a renewable feedstock for production of fuel, feed, nutraceutical and pharmaceutical products. However, this resolution is not popular in reality due to its operating cost and biomass recover efficiency. The recovery of biomass could be done by several processes such as: coagulation, sedimentation, centrifugation, flotation,… with their limits. Electro-coagulation and flotation has been proving its advantages in harvesting biomass especially microalgal biomass. Currently, many other studies have also evaluated the ECF as a method with lower energy costs than centrifugation, less biomass contamination than chemical flocculation, simple operation, less loss, and very quick harvest time [1]. The aim of this article is to investigate affects of electrolytic elements contributed to ECF process to figure out key parameter of ECF process and choose optimize these parameter.

2. Result and discussion

The result show the ECF process for harvesting micoralgal biomass have the best performance (high electrolysis efficiency, low bio-slugde contamination and low enery consumption) when using inox cathode and Al anode with current density of 13.3 mA/cm^2 in 30 mins of electrolysis duration.

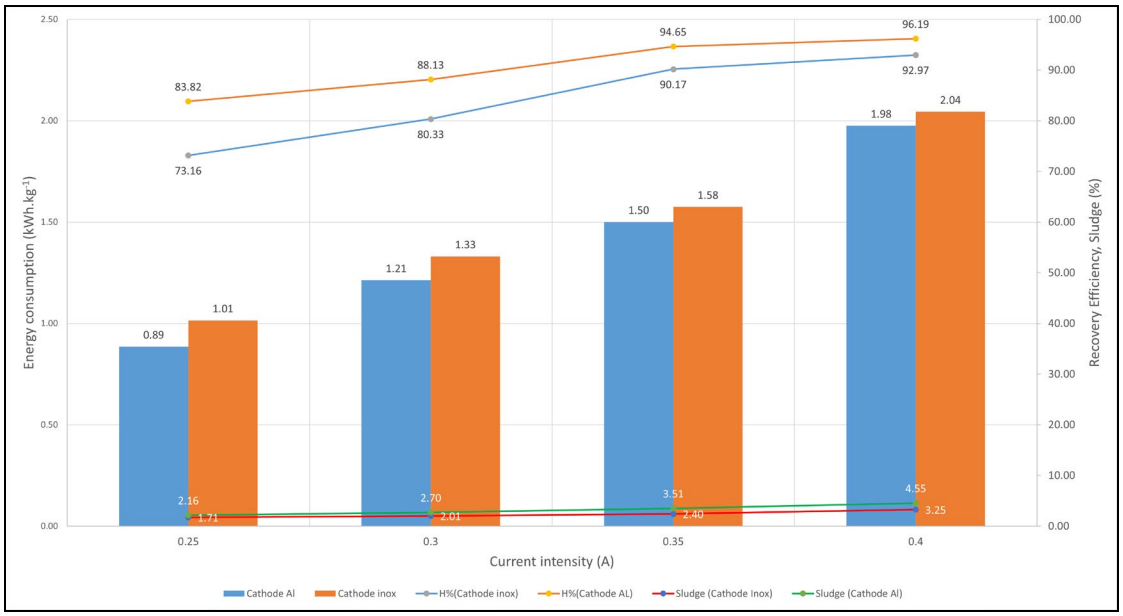

Figure 1. Electrolysis performance in 30 mins

Separation mechanism of carbon dioxide through CHA membrane under high pressure

Fumiya Hirosawa, Masaya Miyagawa, and Hiromitsu Takaba*

Department of Environmental Chemistry and Chemical Engineering,School of Advanced Engineering, Kogakuin University, Tokyo, Japan, E-mail: takaba@cc.kogakuin.ac.jp

Introduction

CHA zeolite membrane is known to show high CO_2 selectivity in the CO_2/CH_4 mixtures. However, there is concerned about decrease of separation performance under high pressure[1]. This can be attributed to the concentration polarization of the gas on the feed side and the presence of grain boundaries in the zeolite membrane, but the detailed mechanism is not yet understood due to the complexity of the membrane structure. The non-equilibrium molecular dynamics (NEMD) method is reported as an effective theoretical method for prediction of separation characteristics using a zeolite membrane[2]. In this study, we evaluated the CO_2 separation characteristics in the CO_2/CH_4 mixture by CHA membranes using the NEMD method and attempted to elucidate the mechanism of the decrease in CO_2 selectivity at high pressure at the molecular level.

Calculation method

In this study, the separation characteristics of the defect-free CHA membrane model were evaluated using the NEMD method for CO_2/CH_4 mixture and single gas in the pressure range from 0.5 to 8.0 MPa. In order to model the gas permeation under the condition of constant pressure difference between the feed and permeation regions, CO_2 and CH_4 molecules were generated from the top of the calculation cell toward the membrane model. Gas molecules that returned to the top of the feed region after molecular collisions in the gas region and gas molecules that permeated through the membrane region were removed from the system.

Results and discussions

Fig.1. shows snapshots of the unit cell from the NEMD simulations using single gas and CO_2/CH_4 mixture. In the case of the single gas, the pores of the zeolite membrane were occupied by CO_2 molecules in all pressure ranges.The zeolite pores are occupied with CO_2 molecules in the mixed gas systaem at 1.0 MPa, similar to the single gas results. However, the CO_2 molecules in the membrane become more sparse as the pressure increased. Fig.2. shows the permeability and separation factor at the NEMD results. The CO_2 permeability decreased with increasing pressure, whereas that of CH_4 remained almost constant. This indicate that the permeation of CO_2 is inhibited by CH_4. The diffusivity of CO_2 molecules in the membrane with respect to the permeation direction tended to decrease with increasing pressure in the mixture system. CO_2 molcules permeate through the zeolite pores in “single-file” at the high pressure, which is thought to be a factor that decrease the diffusivity of CO_2. At high pressures, the collision frequency of gas molecules with the membrane increases, and the number of CH_4 molecules increases as they diffuse into the membrane. On the other hand, the permeation of CO_2 molecules is suppressed by the slow intrapore diffusion of CH_4 molecules. As a result, the permeation decreases with increasing pressure. In other words, the decrease in the CO_2 permeability of the CHA membrane at high pressures is thought to be due to the larger contribution of diffusion than adsorption.

References:

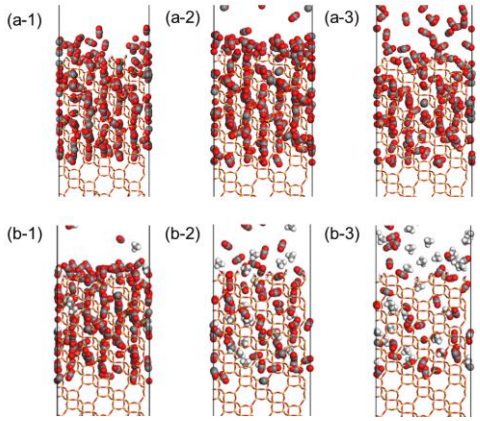

Fig. 1. Snapshots of NEMD results, (a) single gas, (b) Mixture, (1)1 MPa, (2) 4MPa, (3) 8MPa

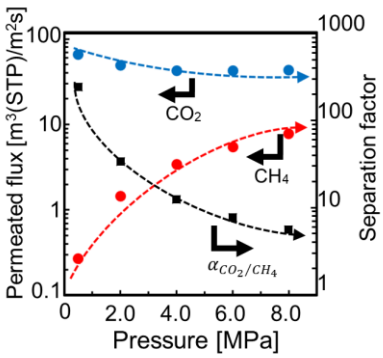

Fig. 2. Calculated permeability and separation factor at the different pressure.

[1] K. Kida *et al.*, *Sep. Purif. Tech.*, **197**,116 (2018).
[2] F. Hirosawa *et al.*, *J. Mem. Sci.*, **632**, 119348 (2021).

Oral Presentation

Simulation Science, Measurement Science, Computational Science

November 23rd

Presentation No.	Title	Author	
SSM1.	Effect of femur and tibia marker positions on measuring ankle joint angles in optical motion analysis	Natsuki Nakamura, Satoru Kizawa, and Ayuko Saito	53
SSM2.	Effect of actuator on muscle force estimation using a musculoskeletal model	Takuto Hosoya, Tomoaki Ichikawa, Shinichiro Morichi, Yoshikazu Kobayashi, Satoru Kizawa, and Ayuko Saito	56
SSM3.	Study on design of a noise covariance in pose estimation using 9-axis motion sensor	Hayato Sato, Kentaro Goto, Satoru Kizawa, and Ayuko Saito	58
SSM4.	A study on effect of geomagnetic sensor correction for pose estimation	Kentaro Goto, Hayato Sato, Satoru Kizawa, and Ayuko Saito	61

Effect of femur and tibia marker positions on measuring ankle joint angles in optical motion analysis

Natsuki Nakamura, Satoru Kizawa, and Ayuko Saito

Department of Mechanical Science and Engineering, Graduate School of Engineering, Kogakuin University, Tokyo, Japan
E-mail: s519036@ns.kogakuin.ac.jp

Abstract

The positions of the thigh and tibial markers in gait analysis are not strictly defined even in the most widely used Plugin-Gait. This study verified the measurement error of the ankle joint angle by focusing on the thigh and tibial marker positions using the Plug-in Gait model.

Gait analysis plays an important role in the diagnosis of bone and joint diseases that affect gait, clinical decision making for treatment and rehabilitation [1]. Optical motion capture systems, force plates, and inertial sensors have been mainly used for gait analysis. An optical motion capture system consists of multiple cameras which capture the reflective markers attached to the subject. Obtaining the coordinates of reflective markers enables the calculation of kinematic parameters. Gait analysis models such as Plug-in Gait and CAST have been proposed [2]. Each model has an original marker set. The use of marker coordinates enables the calculation of kinematic parameters easily. However, measurement errors may occur due to factors such as incorrect marker placement [3]. One of the factors causing measurement errors is that the joint center position can change due to differences in the position of the markers by only a few millimeters. The positions of the thigh and tibial markers are not strictly defined even in the most widely used Plugin-Gait. The positions of the markers are occasionally different from one measurement to another, which makes it difficult to obtain accurate joint angles. In the previous study, we verified the accuracy by shifting the thigh marker position anterior [4]. The results showed that the knee flexion and internal rotation results differed greatly when the position of the thigh marker was moved anteriorly by 45 degrees. In addition to the thigh marker, verifying the effect of the tibial marker position on measurement is required because the tibial marker position affects the definition of the ankle joint center. Therefore, this study verified the measurement error of the ankle joint angle by focusing on the thigh and tibial marker positions using the Plug-in Gait model.

A healthy male (1.78 m, 55 kg) was examined during the experiment. Following an explanation of the purpose and requirements of the study, the participants gave their written informed consent to participate in the study. Study approval was obtained from the Research Ethics Board, Kogakuin University, and National Institute of Technology, Akita College.

During the experiment, an optical motion capture system (Bonita 10; Vicon Motion Systems Ltd.) and a floor reaction force gauge (9286; Kistler Japan Co. Ltd.) measured the gait. The sampling frequency of both the optical 3D motion analyzer and the floor reaction force meter was 100 Hz.

16 reflective markers were attached to the subject's lower limbs by referring to the Plug-in Gait Lower body marker set (Figure 1). In addition, the additional thigh marker was attached to the anterior left thigh and the additional tibial marker was attached to the anterior left lower leg. Placements of LTHI1 and LTHI2 markers are shown in Figure 2. In figure 2 LTHI1 is the standard thigh marker attached to the outermost distal 1/3 of the thigh segment; LTHI2 is the additional thigh marker attached to anteriorly 1/8th of the thigh circumference R at the same height as the standard thigh marker. Similarly, LTIB1 is the standard tibial marker attached to the outermost distal 1/3 of the lower leg segment; LTIB2 is the additional tibial marker attached to anteriorly 1/8th of the lower leg circumference R at the same height as the standard tibial marker.

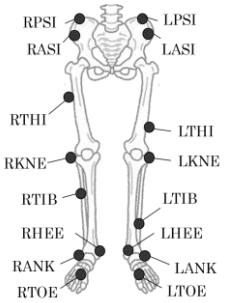

Fig.1 Marker set for lower limbs.

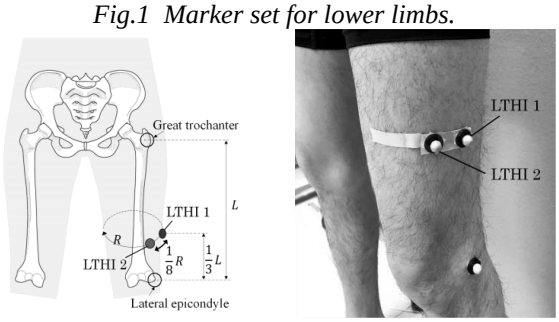

(a) Marker position. (b) Markers attached to subject.
Fig.2 Placements of LTHI1 and LTHI2 markers.

The analysis time was from the stance phase to the end of the swing phase of the left leg. After the experiment, the measurement data were copied into four files. The markers were labeled using analysis software (Nexus2, Vicon). In the first data, the standard thigh marker (LTHI1) was labeled with the LTHI label, and the standard tibial marker (LTIB1) was labeled with the LTIB label. In the second data, the standard thigh marker (LTHI1) was labeled with the LTHI label, and the additional tibial marker (LTIB2) was labeled with the LTIB label. In the third data, the additional thigh marker (LTHI2) was labeled with the LTHI label, and the standard tibial marker (LTIB1) was labeled with the LTIB label. In the fourth data, the additional thigh marker (LTHI2) was labeled with the LTHI label, and the additional tibial marker (LTIB2) was labeled with the LTIB label. The ankle joint angles were obtained by the Plug-in Gait Dynamic pipeline, respectively.

The hip joint center is determined using four markers (LASI, RASI, LPSI, RPSI) which are attached to the pelvis. Figure 3 shows the definition of the left knee and ankle joint centers (LKJC and LAJC). Figure 4 shows the definition of the left femoral and tibial segment coordinate system. LANK indicates the left ankle marker, LAJC indicates the left ankle joint center, and LTOE indicates the left second metatarsal head marker. In the left foot segment coordinate system, the axis from LTOE to LAJC is the Z-axis and the axis from LAJC to LANK is the Y-axis; the X-axis is determined perpendicular to the Z-axis and Y-axis according to the definition of the right-hand coordinate system.

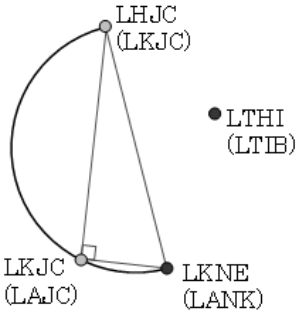

Fig.3 Definition of knee and ankle joint centers.

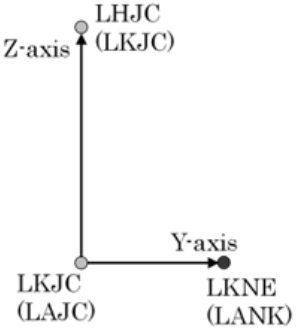

Fig.4 Definition of femoral and tibia segment coordinates.

Figure 5 shows the results of the left ankle joint angles obtained by the four types of marker set using the LTHI1 and LTHI2 markers and the LTIB1 and LTIB2 markers. The results using LTHI1 and LTIB1 markers as LTHI and LTIB markers are represented as Standard – Standard. The results using LTHI1 and LTIB2 markers are represented as Standard – 45. The results using LTHI2 and LTIB1 markers are represented as 45 – Standard. The results using LTHI2 and LTIB2 markers are represented as 45 - 45.

The results of Standard - Standard and Standard - 45 in Fig.5 show the same tendencies as the ankle angle during normal gait of a healthy person. Figure 5(b) shows that the internal/external rotation of the Standard - Standard and 45 - Standard is maintained at 0 degrees, indicating the normal gait of a healthy person, while the Standard - 45 and 45 - 45 maintain a large internal rotation throughout the entire gait cycle. Figure 5(c) shows that the 45-45 maintains 0 degrees throughout the entire gait cycle, however, the other three results show repeated internal and external rotation during the swing phase. The results suggest that the Standard - Standard is the most appropriate position for measuring the ankle joint angle using the Plug-in Gait marker set.

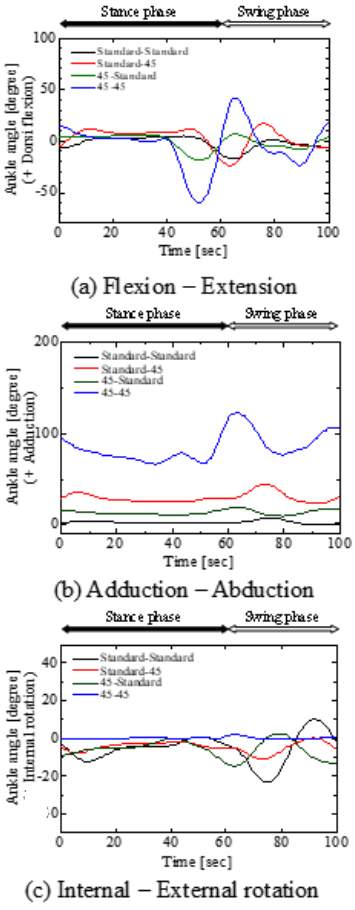

Fig.5 The sagittal ankle angle results.

References:

[1] Kay R. M., et al., The Effect of Preoperative Gait Analysis on Orthopaedic Decision Making, *Clinical orthopaedics and related research*, **372**, 217-222 (2000).

[2] Kadaba M. P., et al., Measurement of Lower Extremity Kinematics During Level Walking, *Journal of Orthopaedic Research*, **8-3**, 383-392 (1990).

[3] Cockcroft J., et al., Proximal placement of lateral thigh skin markers reduces soft tissue artefact during normal gait using the Conventional Gait Model, *Computer Methods in Biomechanics and Biomedical Engineering*, **19-14**, 1497-1504 (2016).

[4] Saito A., et al., Effect of anterior thigh marker on measuring knee joint angles during walking, *The Japan Society for Welfare Engineering*, **23-1**, 18-25 (2021).

Effect of actuator on muscle force estimation using a musculoskeletal model

Takuto Hosoya, Tomoaki Ichikawa, Shinichiro Morichi, Yoshikazu Kobayashi, Satoru Kizawa, and Ayuko Saito

Department of Mechanical Science and Engineering, School of Advanced Engineering, Kogakuin University, Tokyo, Japan
E-mail: s519044@ ns.kogakuin.ac.jp

Abstract

In this study, the musculoskeletal software OpenSim was used to estimate muscle force by applying the two actuators. The analysis time and muscle force obtained from two types of actuators were compared to examine the selection of suitable actuators for the musculoskeletal analysis of walking.

Musculoskeletal software is software that can calculate joint moment and muscle force by performing inverse kinematics and optimization calculations using the results of body movement measurements. Analysis using a musculoskeletal model, which is based on optical motion capture, is a non-invasive motion analysis. Thus, musculoskeletal analysis enables motion analysis in a wide range of fields.

There are several types of musculoskeletal software available. In addition, SIMM [1], ARMO [2], and AnyBody [3], which are commercially available, OpenSim [4], which is published by Stanford University, is widely used. OpenSim, which is free to use, is capable of analyzing loads on a muscle like other musculoskeletal software. All these software estimate muscle force using optimization calculations. An optimization calculation is performed to estimate muscle force that minimizes muscle fatigue. Since the level of muscle activation depends on the actuator which is used during the optimization calculation, the analysis time and results depend on the actuator.

Therefore, in this study, the musculoskeletal software OpenSim was used to estimate muscle force by applying the two actuators. The analysis time and muscle force obtained from two types of actuators were compared to examine the selection of suitable actuators for the musculoskeletal analysis of walking.

The experiment was conducted at National Institute of Technology, Akita College. Study approval was obtained from the Research Ethics Board, Kogakuin University, and National Institute of Technology, Akita College. The participant gave his written informed consent to participate after understanding the purpose and requirements of the study. Kinematic and kinetic data were collected using an optical motion capture (Bonita 10; Vicon Motion Systems, Ltd.) and two force plates (9286; Kistler Japan Co., Ltd.). The size of the force plate was 600 mm × 400 mm × 35 mm, and its length is 3600 mm. The force plates were placed on the walking path (Fig. 1). The sampling frequencies of the optical motion capture and the force plates were 100 Hz.

16 reflective markers were attached to the participant's lower limbs by referring to the Plug- in Gait Lower body marker set (Fig. 2). The participants were instructed to walk using a natural stride in time with a metronome (110 bpm). They performed the task with a gait with folded arms (folded-arms gait; see Fig. 3). The analysis period was defined as one gait cycle from the beginning of the stance phase of the left leg (on the first force plate) until the end of the swing phase.

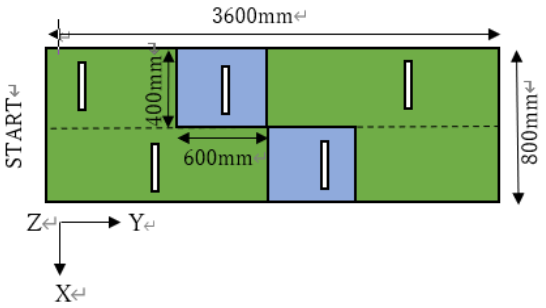

Fig. 1 Walking path

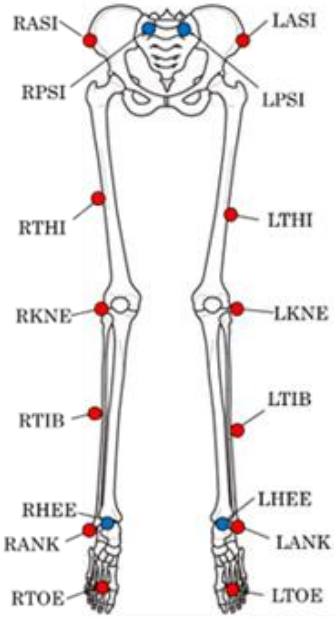

Fig. 2. Marker positions

Fig. 3. Pose with folded arms

The CMC actuator and the gait10of18musc_Strong actuator were used in this study. The force to complement the flexion-extension muscles of the lower limb was set to 1 N for the CMC actuator, and 100 N for the gait10dof18musc_Strong actuator.

The Gait 2392 model in OpenSim 3.3 was used for analysis. The model was scaled with respect to the subject's height. The joint angles were obtained from inverse kinematics using the reflective marker coordinates. The joint moments were obtained from inverse dynamics using the joint angles and floor reaction force data. Finally, the muscle force was estimated by performing the optimization calculation shown in Eq.(1) with the two actuators.

$$\text{minimize}=\Sigma_i^m \left(\frac{f_i}{PCSA_i}\right)^2 \quad (1)$$

where f_i is the muscle force of muscle i, $PCSA_i$ is the physiological cross-sectional area of muscle i and m is the number of muscles.

The results of the muscle force obtained by the optimization calculation of OpenSim using the two actuators are shown in Figure 4. Figure 4(a)~(i) shows the nine muscles of normal walking. The computation time for each actuator is shown in Table 1.

Comparing the results of the two actuators, dof resulted in too much muscle force in all muscles. Also, it's noisy.

In most of the muscles, the firing tendency during the stance phase was similar to previous studies in the results of the CMC actuator than in the gait10dof18musc_Strong actuator. Table 1 also shows that the computation time of the CMC actuator is about 1/6 of that of the gait10dof18musc_Strong actuator. Therefore, the use of the CMC actuator is more appropriate than the gait10dof18musc_Strong actuator for gait measurement.

The result for the rectus femoris muscle which was obtained by the optimization calculation of OpenSim, as an example, using the two actuators is shown in Fig. 4. The horizontal axis shows the normalized time, where one stance phase is 100%, and the vertical axis is the result of the muscle force calculated by OpenSim. Red solid curve presents result obtained using the CMC actuator, and blue solid curve presents result obtained using the gait10dof18musc_Strong actuator. The computation time for each actuator is shown in Table 1.

Comparing the two actuators' results, the gait10dof18musc_Strong actuator resulted in much larger muscle force than the CMC actuator. The muscle activity during the stance phase which was obtained by the CMC actuator was similar to those in previous studies. Table 1 shows that the computation time of the CMC actuator is about 1/6 of that of the gait10dof18musc_Strong actuator. Therefore, the results indicate that the use of the CMC actuator is more appropriate than the gait10dof18musc_Strong actuator for gait analysis.

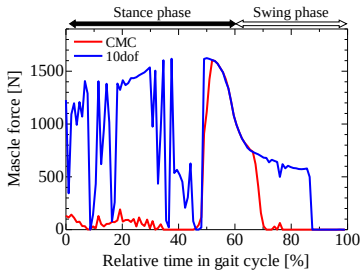

Fig. 4. Rectus femoris

Table 1 Actuator and analysis time

Actuator type	Analysis time
10dof	6 m 51 s
CMC	1 m 11 s

References:

[1] SIMM, nac Image Technology Inc. (online), available from <https://www.nacinc.jp/analysis/software/simm>, (accessed on 18 October, 2021).

[2] ARMO, gsport Inc. (online), available from < https://www.gsport.co.jp/p_l_armo.html>, (accessed on 18 October, 2021).

[3] AnyBody, Terrabyte Co.,Ltd. (online), available from < https://www.terrabyte.co.jp/AnyBody/>, (accessed on 18 October, 2021).

[4] F. C. Anderson and M. G. Pandy, “Dynamic Optimization of Human Walking”, Journal of Biomechanical Engineering, 123, 5, 381-390 (2001).

Study on design of a noise covariance in pose estimation using 9-axis motion sensor

Hayato Sato, Kentaro Goto, Satoru Kizawa, and Ayuko Saito

Department of Mechanical Science and Engineering, Graduate School of Engineering, Kogakuin University, Tokyo, Japan
E-mail: s519025@ns.kogakuin.ac.jp

Abstract

This paper presents an extended Kalman filter for pose estimation using noise covariance matrices based on sensor output. We designed three algorithms to accurately estimate the knee joint angle during walking. We verified the effectiveness of the algorithm by comparing them.

A Kalman filter has been mainly used in sensor fusion techniques for pose estimation. The Kalman filter is a sequential estimation and has the advantage that the calculation load is small. However, the estimation accuracy of pose estimation using the Kalman filter is greatly affected by the design of process and observation noise covariance. Therefore, in this study, we verified the accuracy of knee joint angle estimation during walking by using the process and observation noise covariance matrices of the extended Kalman filter based on the sensor output proposed in the previous study. The three types of algorism were designed in this study. The first algorism was designed which in only a process noise covariance matrix was based on the sensor output. The second algorism was designed in which only an observation noise covariance matrix was based on the sensor output. The third algorism was designed in which two noise covariance matrices were based on the sensor output. The effect of noise covariance matrices on estimation accuracy was considered by comparing the estimation results obtained from those algorisms.

The posture of the nine-axis motion sensor is represented by the roll angle (φ) around the X-axis, the pitch angle (θ) around the Y-axis, the yaw angle (ψ) around the Z-axis. The reference coordinate system is a right-handed system with a vertical Z-axis. The counterclockwise was rotation defined as positive. Euler definition and the reference coordinate system are represented in Fig.1. The nine-axis motion sensor is attached to the subject thing and lower leg. The local coordinate system of the sensor is converted system for the left knee angle estimation. [1]

The initial angles of roll and pitch can't be obtained from the output of the gyro sensor. The initial roll and pitch are expressed by equations (1) and (2) using the gravitational acceleration obtained from the acceleration sensor at rest.

$$\Phi_A = tan^{-1}\frac{A_y}{A_z} \quad (-\pi < \varphi_A < \pi) \tag{1}$$

$$\theta_A = tan^{-1}\frac{-A_x}{\sqrt{{A_y}^2+{A_z}^2}} \tag{2}$$

where A_x, A_y and A_z are the accelerometer outputs.

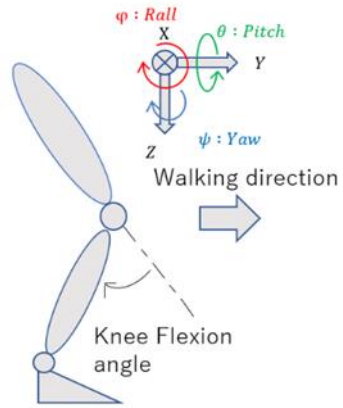

Fig.1. Reference coordinate system and the definition of knee joint angle

The initial Yaw is expressed by equation (3) after correcting the magnetic field disturbance and tilt error.

$$\Psi_m = tan^{-1}\frac{-{c_m}_y}{{c_m}_x} \tag{3}$$

The differential Euler angles are calculated by applying the gyro sensor output in equation (4).

$$\begin{bmatrix}\dot{\Psi}_t\\ \dot{\theta}_t\\ \dot{\varphi}_t\end{bmatrix} = \begin{bmatrix}0 & sin\varphi_t sec\theta_t & cos\varphi_t sec\theta_t\\ 0 & cos\varphi_t & -sin\varphi_t\\ 1 & sin\varphi_t tan\theta_t & cos\varphi_t tan\theta_t\end{bmatrix}\begin{bmatrix}\omega_t\\ \omega_t\\ \omega_t\end{bmatrix} \tag{4}$$

where $\dot{\varphi}_t, \dot{\theta}_t, \dot{\psi}_t$ are the differential Euler angles. Φ_t and θ_t are the roll and pitch angle at time t. ω_x, ω_y and ω_z the outputs the gyro sensor. Euler angles are obtained by applying equation (4) to equation (5).

$$\begin{bmatrix}\Psi_{t+1}\\ \theta_{t+1}\\ \varphi_{t+1}\end{bmatrix} = \int\begin{bmatrix}\dot{\psi}_t\\ \dot{\theta}_t\\ \dot{\varphi}_t\end{bmatrix}dt + \begin{bmatrix}\psi_t\\ \theta_t\\ \varphi_t\end{bmatrix} \tag{5}$$

where φ_{t+1}, θ_{t+1}, and ψ_{t+1} are the Euler angle.

The roll, pitch, and yaw angles of each sensor placed on the lower limb are estimated by the sensor fusion using the extended Kalman filter. The nonlinear state equation and nonlinear observation equation are shown in equations (6) and (7), respectively.

$$X_{t+1} = F(x_t) + w_t \quad (6)$$

$$x_t = \begin{bmatrix} \psi_{i,t} \\ \theta_{i,t} \\ \phi_{i,t} \end{bmatrix}, F(x_t) = \begin{bmatrix} \psi_{i,t} + sin\phi_{i,t} sec\theta_{i,t} \omega_{y_i,t} \cdot T_s + cos\phi_{i,t} sec\theta_{i,t} \omega_{z_i,t} \cdot T_s \\ \theta_{i,t} + cos\phi_{i,t} \omega_{y_t,t} \cdot T_s - sin\phi_{i,t} \omega_{z_i,t} \cdot T_s \\ \phi_{i,t} + \omega_{x_i,t} \cdot T_s + sin\phi_{i,t} tan\theta_{i,t} \omega_{y_i,t} \cdot T_s + cos\phi_{i,t} tan\phi_{i,t} \omega_{z_i,t} \cdot T_s \end{bmatrix}$$

$$y_t = H(x_t) + \nu_t \quad (7)$$

$$y_t = \begin{matrix} \psi_{m_i,t} \\ A_{x,s_i} \\ A_{y,s_i} \\ \lfloor A_{z,s_i} \rfloor \end{matrix}, H(x_t) = \begin{bmatrix} \psi_{i,t} \\ ({}^0R_i)_t^T \begin{bmatrix} 0 \\ 0 \\ g \end{bmatrix} \end{bmatrix}$$

In those equations, $\phi_{i,t}$, $\theta_{i,t}$, and $\psi_{i,t}$ respectively denote Euler angles of the sensor placed on each lower limb segment, as estimated using the extended Kalman filter. T_s is sampling time. In addition, $\omega_{x,t}$, $\omega_{y,t}$, and $\omega_{z,t}$ respectively denote the gyroscope outputs for the X, Y, and Z axes. Also, A_{S_x}, A_{S_y}, and A_{S_z} respectively express the accelerometer output for the X, Y, and Z axes. ${}^0R_i$ is the rotation matrix from the reference coordinate system to the sensor *i* coordinate system, g is the gravitational acceleration, and w_t and ν_t are the white noise. [2]

The partial derivatives of $F(x_t)$ and $H(x_t)$ are shown below:

$$f(x_t) = \frac{\partial F(x_t)}{\partial (x_t)} \quad (8)$$

$$h(x_t) = \frac{\partial H(x_t)}{\partial (x_t)} \quad (9)$$

Then, the prediction step [Eqs. (10) and (11)] and the filtering step [Eqs. (12)-(14)] are calculated using the nonlinear discrete-time system represented by Eqs. (8) and (9):

$$x_{\bar{t}+1} = F(x_t) \quad (10)$$

$$P_{\bar{t}+1} = f_t P_t f_t^T + Q \quad (11)$$

$$K_{t+1} = P_{\bar{t}+1} h_{t+1}^T (h_{t+1} P_{\bar{t}+1} h_{t+1}^T + R)^{-1} \quad (12)$$

$$x_{t+1} = x_{\bar{t}+1} + K_{t+1}(y_{t+1} - H(x_{\bar{t}+1})) \quad (13)$$

$$P_{t+1} = (I - K_{t+1} h_{t+1}) P_{\bar{t}+1} \quad (14)$$

Where P is the error covariance matrix, K is the Kalman gain, Q is the covariance matrix of the process noise w_t in the nonlinear state equation, and R is the covariance matrix of the observation noise ν_t in the nonlinear observation equations. $x_{\bar{t}+1}$, $P_{\bar{t}+1}$ are the state variables and error covariance matrix at time *t+1* estimated using the information up time to t. x_{t+1}, P_{t+1} are the state variables and error covariance matrix at time *t+1* estimated using the information up to time *t+1*. [3]

The process and observation noise covariance matrices in the extended Kalman filter were determined based on the state-space model dynamics and the sensor noise. The postural change appears in the gyroscope output because the rotational motion of the joints produces human movement. Consequently, the process noise covariance matrix was determined based on the gyroscope output as presented below:

$$Q_t = \begin{bmatrix} \Omega_{\omega,t} & 0 & 0 \\ 0 & \Omega_{\omega,t} & 0 \\ 0 & 0 & \Omega_{\omega,t} \end{bmatrix} \quad (15)$$

$$\Omega_{\omega,t} = a\sqrt{\omega^2{}_{x,t} + \omega^2{}_{y,t} + \omega^2{}_{z,t}}$$

$\omega_{x,t}$, $\omega_{y,t}$ and $\omega_{z,t}$ are gyro-sensor outputs for each axis, and *a*, *b* are the adjustment parameters. In this study, we set *a* = 1 and *b* = 0.

In the observation equations, the yaw angle calculated using the geomagnetic sensor output and the acceleration sensor output are used as observation values, so the covariance matrix of the process noise is adjusted based on the time series data of the geomagnetic sensor output and the acceleration sensor output. The constructed covariance matrix of the observation noise is shown in equation (16).

$$R_t = \begin{matrix} \Omega_{m,t} & 0 & 0 & 0 \\ 0 & \Omega_{a,t} & 0 & 0 \\ 0 & 0 & \Omega_{a,t} & 0 \\ \lfloor 0 & 0 & 0 & \Omega_{a,t} \rfloor \end{matrix} \quad (16)$$

$$\Omega_{m,t} = c\left(\sqrt{m_{x,t}^2 + m_{y,t}^2 + m_{z,t}^2} - \bar{m}\right) + d$$

$$\Omega_{a,t} = e\left(\sqrt{a_{x,t}^2 + a_{y,t}^2 + (a_{z,t} - g)^2}\right) + f$$

where $m_{x,t}$, $m_{y,t}$ and $m_{z,t}$ are the magnetometer outputs in each axis after tilt correction, $\bar{m}$ is the average of the sum of the magnetometer outputs over the entire measurement time, $a_{x,t}$, $a_{y,t}$ and $a_{z,t}$ are the accelerometer outputs in each axis, and *c*, *d*, *e* and *f* are paraments for adjustment. We set *c* = 0.1, *d* = 0, *e* = 0.00001 and *f* = 100.

The knee joint angle is calculated by Eq. (17) as shown below:

$$ {}^{i-1}R_i = ({}^{0}R_{i-1})^T \cdot ({}^{0}R_i) \quad (17) $$

$$ {}^{0}R_i = \begin{bmatrix} cos\ {}^{i}\psi & -sin\ {}^{i}\psi & 0 \\ sin\ {}^{i}\psi & cos\ {}^{i}\psi & 0 \\ 0 & 0 & 1 \end{bmatrix} \begin{bmatrix} cos\ {}^{i}\theta & 0 & sin\ {}^{i}\theta \\ 0 & 1 & 0 \\ -sin\ {}^{i}\theta & 0 & cos\ {}^{i}\theta \end{bmatrix} $$

Sensor *i* and sensor *i*-1 indicate sensor attached to the thigh and lower leg, respectively.

A nine-axis motion sensor and an optical motion capture system were used during the experiment. A healthy male (height 1.76m, weight 58kg) participated in the experiment. The nine-axis motion sensor was attached to the left thigh and left lower leg. The sensor positions and the reference coordinate system are shown in Fig.2. The participant was instructed to walk using a natural stride in time with a metronome (70 bpm). The sampling frequency of both the nine-axis motion sensor and the three-dimensional motion analyzer was 100Hz.

Figure 3 shows the estimated left knee joint angles (flexion-extension) using the extended Kalman filter and the results obtained from the three-dimensional motion measurement analysis device. The horizontal axis is 100% for one gait cycle, and one gait cycle including one stance phase and one walking phase as 100%. Black solid curves represent results obtained from the optical 3D motion analysis system. Red solid curves represent results obtained from the extended Kalman filter using the noise covariance matrices based on sensor output, hereinafter designated as Oo and Op. Green solid curves represent results obtained from Oo and Op, which used gyroscope output for the process noise covariance matrix and which used a constant value for the observation noise covariance matrix, hereinafter designated as Op. Blue solid curves represent results obtained from Oo and Op, which used the constant value for the process noise covariance matrix and which used accelerometer and magnetometer output for the observation noise covariance matrix, hereinafter designated as Oo. The constant noise covariance matrix was adjusted to match the results of the three-dimensional motion analyzer, with Ω_ω = 0.0005 for the process noise covariance matrix and $\Omega_m = \Omega_a$ = 1500 for the observation noise covariance matrix.

Fig. 3 shows that the proposed method Oo and Op is generally consistent with the result of the optical 3D motion analysis system. The proposed method was evaluated by using the root mean square error (RMSE) against the results of the optical 3D motion analysis system. The root mean square error is represented in Eq. (18).

$$ RMSE = \sqrt{\frac{1}{n}\sum_{k=1}^{n}(f_i - y_i)^2} \quad (18) $$

The results of the RMSE were Oo = 6.49 [degree], Op = 7.32[degree], and Oo and Op = 6.33[degree].

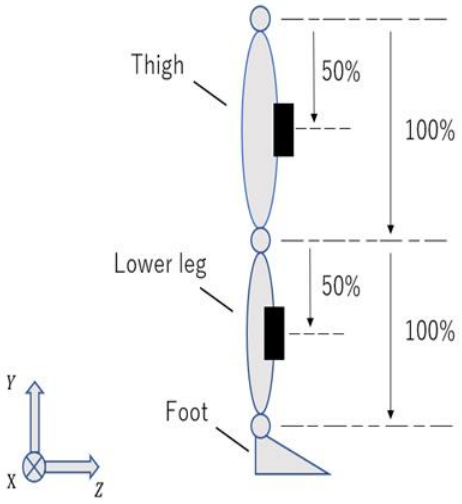

Fig.2. Sensor position and coordinate system

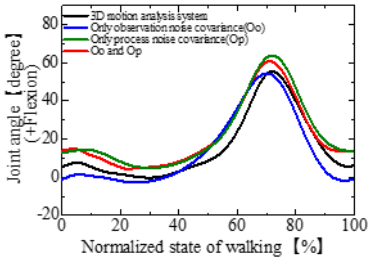

Fig.3. Knee joint angle during walking

As a result, we determined that Oo and Op are the suitable method for the pose estimation during walking.

In this study, we confirmed that the knee joint angle during walking can be estimated more accurately by adjusting the two noise covariance matrices based on the sensor output. However, the algorithm designed with the process noise covariance based on the sensor output and the observation noise covariance as a constant had lower estimation accuracy. In future work, we will build algorithms to minimize the environmental impact.

References:

[1] Saito, A., Kizawa, S., Kobayashi, Y. and Miyawaki, K., Pose estimation by extended Kalman filter using noise covariance matrices based on sensor output, ROBOMECH Journal, Vol.7, No. 36 (2020), DOI: 10.1186/s40648-020-00185-y.

[2] Hirose K, Doki H, Koda S, Nagasaku K (2011) Studies of the dynamic analysis and motion measurement of skiing turn using extended Kalman flter. Trans Jpn Soc Mech Eng, Series C 77(774):470–480 ((in Japanese))

[3] Rigatos, G. G., Extended Kalman and Particle Filtering for sensor fusion in motion control of mobile robots, Mathematics and Computers in Simulation, Vol.81, No. 3 (2010), pp.590–607.

A study on effect of geomagnetic sensor correction for pose estimation

Kentaro Goto, Hayato Sato, Satoru Kizawa, and Ayuko Saito

Department of Mechanical Science and Engineering, School of Advanced Engineering, Kogakuin University, Tokyo, Japan
E-mail: s519021@ns.kogakuin.ac.jp

Abstract

In the research, we propose a method that corrects the geomagnetic sensor output even in high-rise buildings and underground without complicated procedures. We confirmed that the geomagnetic correction parameters can be estimated more easily and appropriately using the proposed method than the method of the previous research.

In recent years, technological development has led to the use of many sensors in everyday life. MEMS sensors have come to be used for various functions of smartphones and automatic driving system. The 9-axis motion sensor, which is one of the sensor modules, is equipped with a three-axis gyro sensor, a three-axis acceleration sensor, and a three-axis geomagnetic sensor. The sensors are becoming smaller and lighter due to technological development. Therefore, the 9-axis motion sensor is used for various purposes such as motion measurement. Although human pose estimation can be performed using only the gyro sensor. estimation accuracy decreases due to drift error. The sensor fusion using a 9-axis motion sensor equipped with an acceleration sensor and a geomagnetic sensor enables high-precision pose estimation [1]. The geomagnetic sensor output is utilized to measure the yaw angle, which is the angle around the Z axis. However, correcting the geomagnetic sensor output is important because there are various environments in which the magnetic field is liable to fluctuate. Several sensor fusion techniques which avoided the influence of magnetic field fluctuations have been proposed [2][3]. In addition, the authors have proposed the method that corrected the geomagnetic sensor output with long-team motion measurement in a varying magnetic field [4]. Furthermore, since the previous experiment was conducted outdoors, verifying the effectiveness of the method even in high-rise buildings and underground is required. In the research, we propose a method that corrects the geomagnetic sensor output even in high-rise buildings and underground without complicated procedures.

In an external measurement environment where the magnetic field fluctuates for accurate estimation, applying the geomagnetic sensor correction method using the angular velocity obtained from the gyro sensor [3], estimate the optimum geomagnetic parameters (sensitivity / offset). The relation between the geomagnetic sensor output and magnetic field is represented by Eq. (1);

$$M_t = Gm_t + B \quad (1)$$

Where:

$$\mathrm{M_t} = \begin{bmatrix} \mathrm{M_{xt}} \\ \mathrm{M_{yt}} \\ \mathrm{M_{zt}} \end{bmatrix}, \begin{bmatrix} \mathrm{m_{xt}} \\ \mathrm{m_{yt}} \\ \mathrm{m_{zt}} \end{bmatrix}, \begin{bmatrix} \mathrm{G_x} & 0 & 0 \\ 0 & \mathrm{G_y} & 0 \\ 0 & 0 & \mathrm{G_z} \end{bmatrix}, \mathrm{B} = \begin{bmatrix} \mathrm{B_x} \\ \mathrm{B_y} \\ \mathrm{B_z} \end{bmatrix}$$

M_t is the geomagnetic sensor output, m_t is the corrected magnetic field, G is the sensitivity, and B is the offset.

Since the sensitivity and offset also fluctuate as the magnetic field fluctuates, estimating the geomagnetic parameters corresponding to the environment is required. Assuming that the total amount of magnetic field is constant, we constructed an algorithm to estimate the parameters. Eq. (2) represents the sum of the magnetic fields, and Eq. (3) represents the relation between the magnetic field in the i-link coordinates and those in the reference coordinates.

$$\sqrt{m_{xt}^2 + m_{yt}^2 + m_{zt}^2} = const \quad (2)$$

$$0R_{i,t}m_t = {}^0R_{i,t-1}m_{t-1} = {}^0m = const \quad (3)$$

Then, ${}^0R_{i,t}$ is the rotation matrix from the i-link coordinates to the reference coordinates. Equation (4) shows the differential of Eq. (3), and Eq. (5) shows the differential of the rotation matrix using angular velocity.

$$\frac{d}{dt}\left({}^0R_{i,t-1}m_{t-1}\right) = {}^0\dot{R}_{i,t-1}m_{t-1} + {}^0R_{i,t-1}\dot{m}_{t-1} = 0 \quad (4)$$

$${}^0\dot{R}_{i,t-1} = {}^0R_{i,t-1}[\omega_t \times] \quad (5)$$

Here, ω_t is the gyro sensor output and $[\omega_t \times]$ is the cross product. Equation (6) is obtained by substituting Eq. (5) into Eq. (4) and discretized by the finite difference method. Equation (7) which represents the relation between the magnetic field and the angular velocity is obtained by eliminating the rotation matrix from both sides of Eq. (6).

$${}^0R_{i,t-1}m_t = {}^0R_{i,t-1}(m_{t-1} - T_s[\omega_t \times]m_{t-1}) \quad (6)$$

$$m_t = m_{t-1} - T_s[\omega_t \times]m_{t-1} \quad (7)$$

Here, Ts is the sampling period. The geomagnetic sensor output is corrected by estimating the geomagnetic parameters that satisfy Eq. (7). A nonlinear discrete-time system is developed to construct an extended Kalman filter for parameter estimation. The nonlinear state equation is constructed

using Eq (7), which expresses the relation between the magnetic field and the angular velocity. The nonlinear observation equation is constructed using Eqs. (1) and (2). The nonlinear state equations and nonlinear observation equations are shown in Eqs. (8) and (9).

$$x_{t+1} = F(x_t) + w_t \quad (8)$$
$$y_t = H(x_t) + v_t \quad (9)$$

Where:

$$x_t = \begin{bmatrix} m_{xt} \\ m_{yt} \\ m_{zt} \\ G_x \\ G_y \\ G_z \\ B_x \\ B_y \\ B_Z \end{bmatrix}, \; F(x_t) = \begin{bmatrix} m_{xt} \\ m_{yt} \\ m_{zt} \\ G_x \\ G_y \\ G_z \\ B_x \\ B_y \\ B_Z \end{bmatrix} - Ts \begin{bmatrix} \omega_{yt} m_{zt} - \omega_{zt} m_{yt} \\ \omega_{zt} m_{xt} - \omega_{xt} m_{zt} \\ \omega_{xt} m_{yt} - \omega_{yt} m_{xt} \\ 0 \\ 0 \\ 0 \\ 0 \\ 0 \\ 0 \end{bmatrix}$$

$$y_t = \begin{bmatrix} M_{xt} \\ M_{yt} \\ M_{zt} \\ 1 \end{bmatrix}, H(x_t) = \begin{bmatrix} G_x m_{xt} + G_x m_{yt} + G_x m_{zt} \\ G_y m_{xt} + G_y m_{yt} + G_y m_{zt} \\ G_z m_{xt} + G_z m_{yt} + G_z m_{zt} \\ m_{xt}^2 + m_{yt}^2 + m_{zt}^2 \end{bmatrix} + \begin{bmatrix} B_x \\ B_y \\ B_z \\ 0 \end{bmatrix}$$

w_t, v_t is white noise. The extended Kalman filter is solved using the nonlinear state-space model. In the previous research, as the initial state values, m_{xt},m_{yt},m_{zt}, were determined using the geomagnetic measurement data. The initial state values G_x,G_y,G_z,B_x,B_y, and B_z were determined using the parameters obtained in advance. Therefore, the measurement procedure was complicated. In this study, constant values are inserted into the initial state value x_t The parameters for geomagnetic sensor correction are obtained only using the motion measurement data.

The magnetic field was measured using a 9-axis motion sensor (Sports Sensing, SS-WS1792) during the experiment. The 38 × 53 × 11 mm sensor weighs 30 g. The 9-axis motion sensor was fixed on the device shown in Figs. 1 and 2. The device was rotated around the x, y, and z axes of the sensor. The experiment was conducted on the first basement floor of Kogakuin University and Shinjuku Central Park. Figures 3 and 4 respectively show the X-axis results at Shinjuku Central Park and Kogakuin University, which were corrected using Eq. (1). Figures 3(a) and 4(a) are the magnetic fields corrected by adjusting parameters G and b manually using Eq. (1). Figures 3(b)and 4(b) are the magnetic fields corrected by the previous method. The previous method obtained the parameters by the Kalman filter algorithm (Eq. (8) and (9)) inserting the parameters G and b which were obtained manually using Eq.(1) as the initial state value. Figures 3(c)and 4(c) are the magnetic fields corrected by the proposed method in this study. The proposed method obtained the parameters by the Kalman filter algorithm (Eq. (8) and (9)) inserting arbitrary constants as the initial state value. The initial arbitrary constants used in this study were $m_{xt} = m_{yt} = m_{zt} = 0.01$, $G_x = G_y = G_z = 200$, $B_x = B_y = B_Z = 0$.

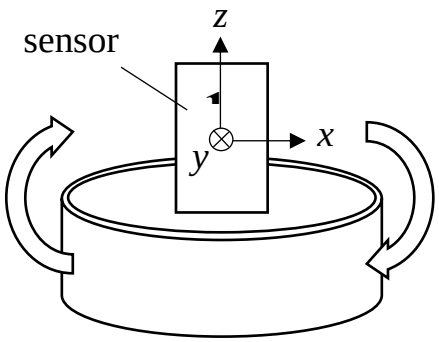

Fig.1. Frontal schematic view of the device

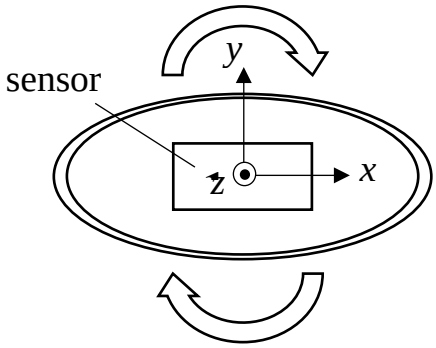

Fig.2. Plane schematic view of the device

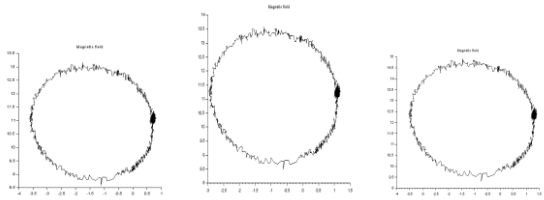

(a)Manual adjustment (b) Previous method (c) Proposed method
Fig.3. The corrected magnetic field around the X-axis (Shinjuku Central Park.)

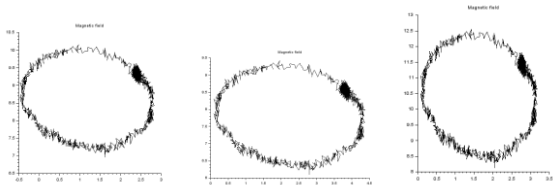

(a)Manual adjustment (b) Previous method (c) Proposed method
Fig.4. The corrected magnetic field around the X-axis (the first basement floor of Kogakuin University)

Figure 3 represents the results obtained in Shinjuku Central Park, and Fig.4 represents the results obtained in the first basement floor of Kogakuin University. These results are the corrected magnetic field around X-axis. The results in Shinjuku Central Park indicate that the almost perfect circles with all the correction methods were obtained. On the other hand, the results in the first basement floor of Kogakuin University indicate that the almost perfect circles only with the proposed methods were obtained.

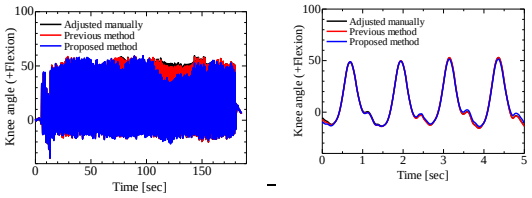

(a) *(b)*

Fig.5. Estimated result of knee joint angle in sagittal plane (Shinjuku Central Park.)

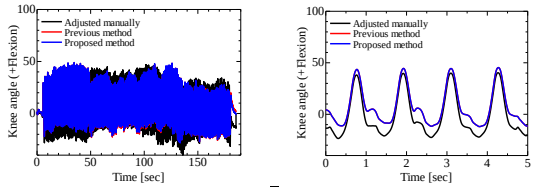

(a) *(b)*

Fig.6. Estimated result of knee joint angle in sagittal plane (the first basement floor of Kogakuin University).

Figure 5 represents the estimated knee joint angles during walking obtained by using the corrected magnetic field in Shinjuku Central Park, and Fig.4 represents the estimated knee joint angles during walking obtained in the first basement floor of Kogakuin University. Black curves are the results by using the magnetic parameters which were adjusted manually using Eq.(1). Red curves are the results by using the magnetic parameters which were adjusted by the previous method. Blue curves are the results by using the magnetic parameters which were adjusted by the proposed method. Panel(a)s show the results over the entire measurement time of 3 minutes. Panel(b)s show the results between 20 and 25 s after the start of measurement.

The same tendencies as the flexion and extension of the knee angles during normal walking of a healthy person can be confirmed in Fig.5. However, the result which was adjusted manually in Fig.6 is different compared to Fig.5. It could not be estimated properly using the method which was adjusted manually. We confirmed that the geomagnetic correction parameters can be estimated more easily and appropriately using the proposed method than the method of the previous research.

References:

[1] Jurman, D., Jankovec, M., Kamnik, R. and Topič, M., Calibration and data fusion solution for the miniature attitude and heading reference system, *Sensors and Actuators, A: Physical*, **138-2**, 411–420 (2007).

[2] Včelák, J., Ripka, P., Kubik, J., Platil, A. and Kašpar, P., AMR navigation systems and methods of their calibration, *Sensors and Actuators A: Physical*, **123-124**, 122-128 (2005).

[3] Kondo, A., Doki, H. and Hirose, K., A Study on calibration method of magnetic field sensor for body motion measurement using inertial sensor, *Proceedings of the Sports Engineering and Human Dynamics*, DOI: 10.1299/jsmeshd.2013._212-1_(2013).

[4] Saito, A., Nara, Y. and Miyawaki, K., A study on estimating knee joint angle using motion sensors under conditions of magnetic field variation, *Transactions of the JSME*, **85-873**, DOI:10.1299/transjsme.19-00061 (2019).

Oral Presentation

Mechanical Engineering

November 23rd

Presentation No.	Title	Author	
ME1.	Flow Characteristics of an Excited Jet with a Time-varying Velocity Distribution	Chisato Ichihara, K. Nishibe, and K. Sato	65
ME2.	Influence of secondary synthetic jet on vortex arrangement in combined jet	Yu Tamanoi, Koichi Nishibe, and Kotaro Sato	67
ME3.	Fundamental study on jet vectoring by circulation control wing	Shoichi Fukui, Shoichi Fukui, Qiang Zhang, Kotaro Sato	69
ME4.	Performance Evaluation of Soccer Balls with Different Panel Shapes	Kaito Tada, Shinichiro Ito, and Masaki Hiratsuka	71

November 24th

Presentation No.	Title	Author	
ME5.	FLOW CHARACTERISTICS AROUND A DOUBLE-SLOTTED CIRCULATION CONTROL WING	Daiki Yaguchi, T. Nakayama, and K. Sato	74
ME6.	VORTEX ARRANGEMENT OF SYNTHETIC JETS GENERATED BY ASYMMETRIC SLOTS	Takumi Ito, Kotaro Sato	76
ME7.	INFLUENCE OF SECONDARY FLOW INDUCED ON COANDA SURFACE ON JET DEFLECTION CHARACTERISTICS	Minoru Nakagawa, K. Sato	77
ME8.	Interaction between Continuous Jet and Synthetic Jet under the Same Momentum Ratio Conditions	Masaharu Mori, J. Matsuzaki, N. Ajino, K. Nisibe, and K. Sato	79
ME9.	INFLUENCE OF SECONDARY SUCTION/BLOWING FLOWS ON PRIMARY JET	Akio Yamada, K. SATO and D. KANG	81
ME11.	Development of a finite element model for mechanical analysis on colonic stent – organs interface	Minori Kunii, Kazuhiro Suga	83
ME12.	Measurement and Compensation of the 3D Printing using 2.5D Characterization	Yu-Sheng Lin	84

Flow Characteristics of an Excited Jet with a Time-varying Velocity Distribution

C. Ichihara, K. Nishibe, and K. Sato

Department of Mechanical Engineering, Graduate School of Engineering, Kogakuin University, Tokyo, Japan
E-mail: am20009@ns.kogakuin.ac.jp

Abstract

By combining two types of flows with different characteristics, a jet with a time-varying velocity distribution at the slot exit was generated. Here, the flow characteristics of the excited jet with asymmetric velocity distribution were investigated through numerical calculations. The fluctuating component of the jet was assumed to be a sinusoidal velocity component, and the velocity distribution was realized by combining two flows with a phase difference. The relationship between the unsteady characteristics and the jet structure that determine the vortex array was also investigated.

Jets are used in various situations; hence, controlling their structure is important from an engineering point of view. In the past, jet flow control was attempted by applying a device near the slot exit. Recently, excited jets, such as synthetic ones, have been widely used for flow control [1],[2]. However, owing to the complexity of the phenomenon, the relationship between the vibration characteristics and the jet structure is still not well understood. In this study, a numerical simulation was performed for a jet with time-varying velocity distribution at the slot exit, using a sinusoidal jet fluctuation component. The effect of the phase difference, between the two nozzle flows, on the flow field was investigated, and the relationship between the jet structure and the vortex array was discussed.

The main symbols used in this article are as follows.

a_{vs}	:	Pitch of the vortex [m]
b_0	:	Slot width (= 5.0×10^{-3} m)
b_{vs}	:	Width of the vortex column [m]
f	:	Frequency [Hz]
f^*	:	Dimensionless frequency (= fb_0/U_{p0}[-])
Re	:	Reynolds number (= $U_{p0}\, b_0/\nu$[-])
t	:	Time [s]
T	:	Period [s]
$u_0(t)$	:	Velocity in the x-direction [m/s]
u	:	Velocity at the slot exit [m⁄s]
U_{c0}	:	Time-averaged continuous jet flow velocity [m/s]
U_{p0}	:	Flow velocity at the slot exit [m/s]
U_{pa}	:	Velocity oscillation amplitude at the slot exit [m/s]
U_{pa}^*	:	Dimensionless velocity amplitude (=U_{pa}/U_{c0}[-])
ν	:	Kinematic viscosity coefficient [m²⁄s]
ω	:	Vorticity [1/s]
ω^*	:	Dimensionless vorticity (=$\omega b_0/U_{p0}$[-])
φ	:	Oscillating velocity phase difference between the upper and the lower part of the nozzle

For the numerical analysis, a two-dimensional incompressible viscous fluid was assumed, and ANSYS CFX (ANSYS, Inc.), a general-purpose thermo-fluid analysis software, using fluid unstructured meshes, was used. For our purposes, the standard k-ε model, which is a turbulent flow model, was used, and the mesh number was approximately 200,000. Fig. 1 shows the boundary conditions of the analytical model. The analysis domain was 400 b_0 in the x-direction and 200 b_0 in the y-direction. The slot inlets were divided into two groups, each of width $5b_0$. In this study, the velocity boundary condition was set by adding a synthetic jet to the continuous one. The slot outlet velocity $u_0(t)$ of the excited jet, which periodically changes the slot exit velocity, is defined by (1).

$$u_0(t) = U_{pa}\sin(2\pi ft) + U_{c0} \tag{1}$$

Static pressure was applied at the outlet of the jet, and the total pressure was applied at the upper and the lower boundaries. The wall surface was assumed to be no-slip, and 10 boundary layers were discretized in the region where the velocity gradient on the wall surface was large. U_{pa} was specified such that U_{c0}>U_{pa} for a time-averaged flow velocity of U_{c0} = 6 m/s. An excited jet without a suction process was considered. The flow velocity U_{p0} at the slot exit is given by (2).

$$U_{p0} = \frac{1}{T}\int_0^T u_0(t)dt = 6.0\ \mathrm{m/s} \tag{2}$$

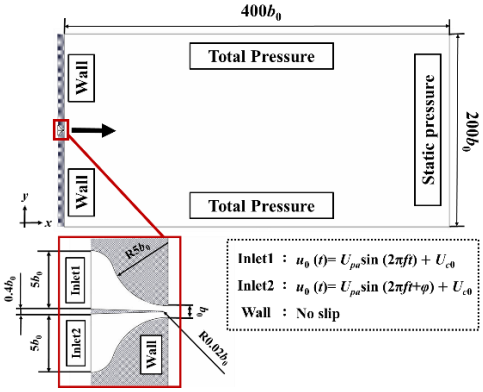

Fig. 1. Boundary conditions

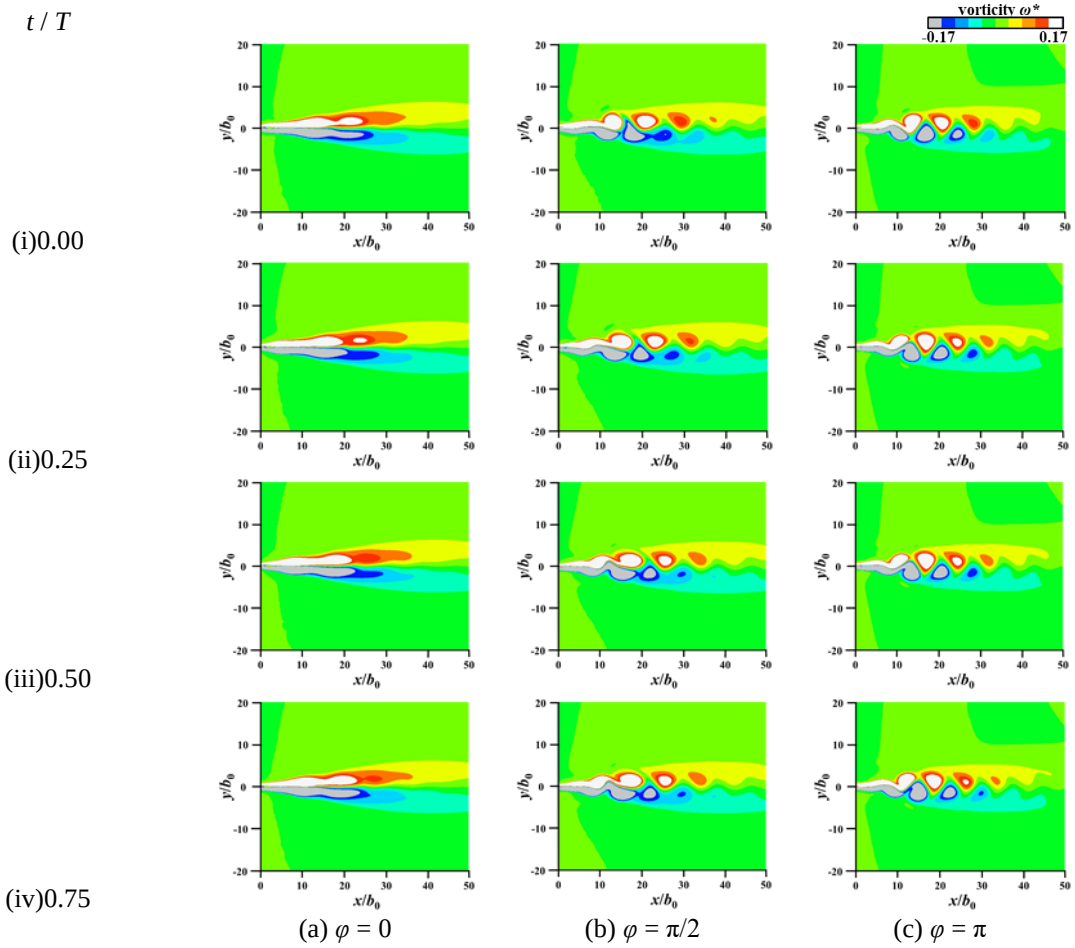

Fig. 2. Flow pattern
(U_{c0}= 6.0 m/s , U_{pa}= 1.0 m/s, U_{pa} = 0.17 , f* = 4.17× 10^{-2} , f = 50 , Re = 2050)*

Fig. 2 shows the flow pattern when the phase difference of the velocity at the slot exit is (a) $\varphi = 0$, (b) $\varphi = \pi/2$, and (c) $\varphi = \pi$, respectively for U_{c0} = 6.0 m/s, U_{pa} = 1.0 m/s, U_{pa}* = 0.17, Re = 2050, and f* = 4.17 × 10^{-2}. respectively. The vorticity distributions were obtained by numerical analysis for t/T values of 0.00, 0.25, 0.50, and 0.75, as shown in (i), (ii), (iii), and (iv), respectively. The dimensionless vorticity scales range from -0.17 to 0.17, with positive and negative over-scales shown in white and gray, respectively. In all conditions, it can be seen that the vortices are generated by the upwelling of the jet, and are propelled by the induced velocity of the jet. In the case of (a) $\varphi = 0$, the vortices are difficult to identify because of the phase equality. The overall flow looks similar to that of a steady jet; however, the existence of vortex pairs can be locally inferred, and the characteristics of a synthetic jet can be observed [1],[3]. In this condition, there is almost no spatial velocity distribution in the slots, and the flow field is vertically symmetric in the figure. By contrast, for (c) $\varphi = \pi$, the velocity distribution is reversed vertically. In this case, the flow rate at the slot exit does not vary with time. Under these conditions, the vortex trains formed in the flow field are arranged in staggered. In the case of (b) $\varphi = \pi/2$, there is no symmetry in the velocity distribution at the slot exit, and the upper and lower vortices have different winding positions in the x-direction. From the stability theory of the vortex train, it is known that the train is arranged in a neutral stable state [4]. The stability condition is that the ratio of the vortex width b_{vs} to the vortex pitch a_{vs} is b_{vs} / a_{vs} = 0.28. Therefore, it is suggested that the structure of the vortex array can be intentionally changed by adding a phase difference to the slot outlet velocity.

References:

[1] N. Nishibe, Y. Fujita, K. Sato, K. Yokota, and T. Koso, “Experimental and Numerical Study on the Flow Characteristics of Synthetic Jets,” J. Fluid Sci. Tech., 6, 425-436 (2011).

[2] Smith, B. L., and Glezer, A., “Vectoring of Adjacent Synthetic Jet,” AIAA J., 43(10), 2117-2124(2005).

[3] R. Kobayashi, K. Nishibe, Y. Watabe, K. Sato, K. Yokota, “Vector control of synthetic jets using an asymmetric slot,” ASME Journal of Fluids Engineering, 140(5):051102-051102-11 [DOI: 10.1115/1.4038660](2018)

[4] M. Hino, *Fluid Dynamics*, Asakura Publishing Co., Ltd.,Tokyo,Japan(1992)

Influence of secondary synthetic jet on vortex arrangement in combined jet

Yu Tamanoi*, Koichi Nishibe, and Kotaro Sato

Mechanical Engineering Program in the Graduate School of Engineering, Kogakuin University
1-24-2 Nishi-Shinjuku, Shinjuku-ku, Tokyo 163-8677, Japan
E-mail: am20042@ns.kogakuin.ac.jp
Department of Mechanical Engineering, Tokyo City University
1-28-1 Tamatsuzumi, Setagaya-ku, Tokyo 158-8557, Japan
E-mail: knishibe@tcu.ac.jp
Department of Mechanical System Engineering, Kogakuin University
1-24-2 Nishi-Shinjuku, Shinjuku-ku, Tokyo 163-8677, Japan
E-mail: at12164@ns.kogakuin.ac.jp

Abstract

Fluidic thrust vectoring has been attracting attention as a method that does not change the shape of the machine. The use of synthetic jets in secondary flow provides a wider control range than that of steady flow. However, there are still many unexplained characteristics of oscillating jet flow. In this study, the vortex array of a jet caused by oscillatory flow is discussed.

In recent years, fluidic thrust vectoring has been actively studied with the objective of improving the performance of aircraft and air-conditioning systems. This technology can control thrust without changing the geometric shape. Therefore, it has the potential of improving the performance of next-generation aircraft. It is also expected to be applied to turbomachinery as it can be used as a substitute technology for rudders and louvers.

Jets are controlled by using a Coanda surface, a secondary flow with steady injection and suction, and a synthetic jet. Jet control using steady secondary flow can be classified into three regions: dead zone, control region, and hypothetical saturation region [1]. Deflection control using the Coanda effect and synthetic jets has advanced, but the details of the mechanism are insufficient [2]. Fluidic thrust vectoring depends on several parameters. In particular, when the secondary flow is a synthetic jet, the number of parameters increases owing to the need to consider the oscillatory characteristics.

In this study, synthetic jets were used from a secondary flow slot located near the wall of a cylindrical cylinder. The slot geometry did not change, and the results were compared with visualization experiments and numerical simulations.

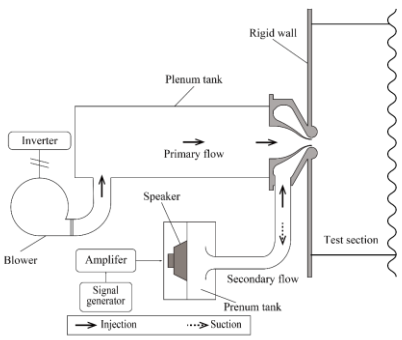

Fig. 1. Schematic of experimental apparatus [2].

Fig. 1 shows a schematic of the experiment. The primary flow was supplied to the flow field from a blower, and the secondary flow was a jet generated using a speaker. A camera was used for visualization was a Sony Corporation ZV-1 at 960 fps. The typical velocity of the secondary flow, U_2, is determined by adjusting the amplitude U_A, which is given by Eq. 1.

$$U_2 = \sqrt{\frac{1}{T}\int_0^T U_A^2 \sin^2 \frac{2\pi}{T} t dt} \qquad (1)$$

Fig. 2 shows the results of the visualization experiment and CFD under the same momentum ratio and dimensionless frequency conditions. t/T = 0.5 is the moment when the synthetic jet changes from the injection process to the suction process. The main result is that a staggered vortex array is observed, thereby forming an inverse Kalman vortex. The visualization and numerical simulation results show that the jet structure is generally consistent. The vortex pitch of the jet is determined by the dimensionless frequency.

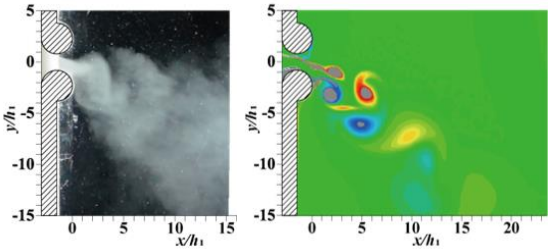

(a) Visualized flow fields (b) CFD [3]
Fig. 2. Typical flow patterns shown.
ξ = 0.1, f^* = 7.9 × 10^{-2}, t/T = 0.5.
(U_1 = 12 m/s, U_A = 12 m/s, f = 95.1 Hz,
h_1 = 10.0 × 10^{-3} m, h_2 = 2.0 × 10^{-3} m)

Nomenclature
h : slot width [m]
R : Radius of the Coanda surface (1.5×10^{-2}) [m]
U : Velocity of flow at slot exit [m/s]
M : Momentum of flow at slot exit ($\rho U^2 h$) [N]
ξ : Momentum ratio between the primary jet and secondary flow at the slot exit (M_2/M_1)
f^* : Dimensionless frequency of synthetic jet (fh_1/U_1)
t : Time [s]
T : Period of velocity oscillation at slot exit ($1/f$) [s]

Subscripts
1 : primary
2 : secondary

References:

[1] M.S. Mason., W.J. Crowther, Fluidic thrust vectoring of low observable aircraft, *CEAS Aerospace Aerodynamic Research Conference*, (June 10–12, 2002), Cambridge, UK.
[2] R. Kobayashi, Y. Watanabe, Y. Tamanoi, K. Nishibe, D. Kang and K. Sato, *Bulletin of the JSME, Mechanical Engineering Journal*, **7**, 5, (2020).
[3] Y. Tamanoi, K. Sato, D. Kang, K. Nishibe, *Mechanical Engineering Congress, 2021 Japan (MECJ-21)*, 1073–1076 (2021).

FUNDAMENTAL STUDY ON JET VECTORING BY CIRCULATION CONTROL WING

Shoichi Fukui, Qiang Zhang, Kotaro Sato

Department of Mechanical Engineering, Graduate School of Engineering, Kogakuin University, Tokyo, Japan
E-mail: am20058@ns.kogakuin.ac.jp

Abstract

In order to control the jet direction, the relationship between the deflection characteristics and non-dimensional parameters such as the momentum coefficient and relative coordinates of the primary jet and jet sheet is experimentally investigated using a tangential blowing cylinder as an alternative to the circulation control wing. The optimum conditions for the directional control of the jet flow are discussed, by considering the unsteady characteristics and structure of the jet flow, and the range of application of the circulation control wing is attempted to be clarified.

In recent years, a fluid control device called Circulation Control Wing (CCW) has been attracting attention from the viewpoints of obtaining high lift, not involving geometrical shape changes, and facilitating structural simplification. As an alternative to the CCW, various experiments have been conducted using a tangential blowing cylinder, such changing in the slot angle of the cylinder, and investigating the relationship between the jet width and the size of the tangential blowing cylinder. In these experiments, the positional relationship between the nozzle and tangential blowing cylinder is always the same. In other words, no studies have investigated the effect of the positional relationship between the nozzle and the tangential blowing cylinder on the jet. Therefore, in this study, we observe the change in the traveling direction of the primary flow due to the different positional relationships between the nozzle and the tangential blowing cylinder, and find the optimum conditions for controlling the traveling direction of the primary jet flow.

The nozzle width is 100 mm, and the area of experiment square platform is 1000 mm × 1000 mm. The nozzle outlet is located next to the center left of the platform. In addition, the diameter of the cylinder is 50 mm, and the slot width of the cylinder is 1 mm. To measure the pressure around the cylinder, a total of 37 static pressure holes with a diameter of 0.5 mm are spirally arranged on the surface of the cylinder. In this experiment, the angle of slot from front edge is 90°. A hot wire anemometer and a type I hot wire probe were used to measure the velocity distribution. The measurement range was 90° to 300° with a radius of 300 mm setting at the intersection between the vertical centerline of the cylinder and the horizontal centerline of nozzle as the measurement arc origin. The deflection angle θ_C, which is the angle from the front edge to the center line of the primary jet, and the primary jet center is defined as the centroid of the time-average jet velocity distribution obtained from the measurement arc at R = 300 mm. The Reynolds number is 2.7×10^4. Refer to Fig. 1 and Fig. 2 of Reference 3 for a schematic diagram of the experimental equipment, and Fig. 3 of Reference 3 for a schematic diagram of the cylinder, and Fig. 4 of Reference 3 for a diagram of the calculation method of deflection angle θ_C.

In this study, the cylinder was moved in the x-axis direction from 200 mm to 400 mm at 100 mm intervals. In addition, the center line of the primary was set to y

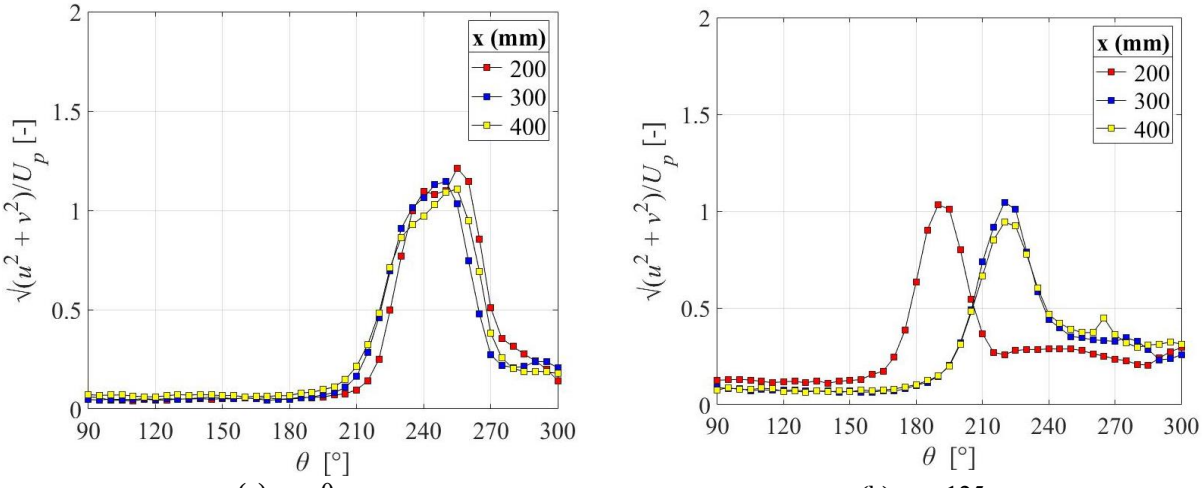

(a) y =0 (b) y=-125

Fig. 1. Dimensionless velocity distribution.

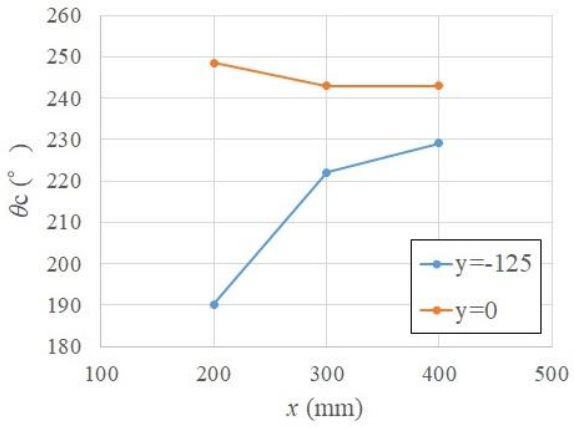

Fig. 2. Deflection angle θ_C distribution.

= 0, and the cylinder was moved in the y-axis direction from -125 mm to 125 mm at intervals of 25 mm.

The momentum coefficient C_{μ}, which is the momentum ratio between the primary jet and jet sheet, was fixed at 0.364. And when the circular cylinder was installed on the center-line of the nozzle (y = 0). Figure. 1 shows the dimensionless velocity distribution at different positions, and Figure. 2 shows the distribution of deflection angle θc under each condition. In these cases, the x was from 200 to 400 mm, and y was set at 0, -125. When y = -125, although there were some changes of deflection angle, the deflection angle θ_C was almost constant between 240° and 245°. On the other hand, when y = -125, θ_C is about 190° when the distance between the nozzle and the center of the cylinder is 200 mm and the deflection angle θ_C is 220° when it is 300 mm. The result was about 230° when x = 400 mm. Based on the experiment results, the flow direction of the primary jet depends on the amount of movement in the direction perpendicular to the primary jet of the cylinder. On the other hand, the deflection angle θc decreases as the cylinder moves away from the flow of the primary jet. This was obvious when the cylinder was installed at x = 200 mm and y = -125 mm. The θc at this condition is about 190°, 40 degrees smaller than other two conditions. This result due to the long distance between the cylinder and the main flow, which weakens the influence of the Coanda effect. But in the other two conditions, although the cylinder was also set at the far distance from the centerline of nozzle, due to the edge shear layer, the jet width and momentum of the main flow increase with the traveling distance which guaranteed the Coanda effect. Meanwhile, if the cylinder is on the extension of the center of the nozzle. Changes in the amount of movement in the x direction with respect to the primary jet of the cylinder do not affect the direction of the primary jet.

References:

[1] Y. Kamiya, T. Matsubara and K. Sato, Basic research for the development of circulation control Wing, The 64th General Assembly of the Kyushu Branch of the Japan Society of Mechanical Engineers, 89−90 (2011).

[2] A. Fujii, Direction control using a tangential blowing cylinder, Master's thesis, Graduate School of Engineering, Kogakuin University, (2019).

[3] Q. Zhang, F. Takahashi, K. Sato, W. Tsuru and K. Yokota, Jet Direction Control Using Circular Cylinder with Tangentional Blowing, 2020 The Japan Society for Aeronautical and Space Sciences, 181-188 (2020).

Performance Evaluation of Soccer Balls with Different Panel Shapes

Kaito Tada[1)], Shinichiro Ito[2)], and Masaki Hiratsuka[2)]

[1)]Department of Mechanical Engineering, Graduate School of Kogakuin University, Tokyo, Japan
E-mail: am21039@ns.kogakuin.ac.jp
[2)] Department of Mechanical Engineering, Kogakuin University, Tokyo, Japan
E-mail: ito@cc.kogakuin.ac.jp

Abstract

The design of soccer balls continues to change at every World Cup. The difference in panel shape has a great effect on the aerodynamic characteristics that affect the trajectory of the ball. In this study, the fluid force of 12 soccer balls with different panel patterns was measured by wind tunnel tests. The drag crises with different Reynolds numbers were confirmed depending on the panel shape. To understand this, the shapes of panel grooves were measured and the relationship between them was investigated. The flow separation point was also visualized by the oil film method and the particle image velocimetry (PIV) analysis. The separation points were confirmed to be different depending on the panel groove by the oil film method in a supercritical Reynolds region. The flow separation points were found to be almost the same position in the subcritical and supercritical state and to be partly different around the Reynolds number of drag crisis.

1 Introducton

The difference in panel shape will have a major influence on the aerodynamic characteristics that affect ball trajectory. The patterns of recent soccer balls are greatly different from that of the conventional soccer ball, with several changes being made to the shape and design of the surface of the ball. Various aerodynamic studies on soccer balls have been reported. Goff et al.[1] reported the aerodynamic difference of non-spinning several soccer balls by the different panel shapes. Hong et al. [2] showed that the separation point changed depending on the number of seams by a 2D-particle image velocimetry (PIV) method. In this study, the different aerodynamic characteristics of the different panels of soccer balls was investigated, and the relationship between the groove shape and drag crisis phenomenon was confirmed. The 2D-PIV analysis was also conducted on the different orientations of balls, and the reason for the different aspects of the drag crisis by the different panels was investigated.

2 Method

2.1 Fluid force experiment

Drag measurements were performed on 12 kinds of different soccer balls with a wind tunnel and a three-components load cell whose maximum load was 50.0 N on each component. The samplings were conducted at 1000 Hz for 9.0 seconds from a wind speed of 3 to 29 m/s in every 1 m/s under computer control, and the experimental values were averaged.

Fig.1 Wind tunnel test

2.2 Groove shape measurement

The cross-sectional area and the dimensions of the groove were taken with a one-shot 3D-shape instrument by VR-3000, KEYENCE. The groove length in the panel joint of each ball was measured by putting strings in all grooves. The total groove volume was calculated by multiplying and summing the groove length and the same cross-sectional area.

2.3 Oil film experiment

To confirm the flow separation on the panels of each ball, a mixture of oleic acid, liquid paraffin and tetra-tri-iron oxide as oil film was coated on the surface of the balls with the same system at a wind speed of 29.6 [m/s]. A representative panel-shaped four-ball type was used.

2.4 2D-PIV measurement

The 2D-PIV measurement in the section of flow circumferential direction was performed to visualize the separation point on a subcritical, critical, and supercritical *Re* number on the four types of balls.

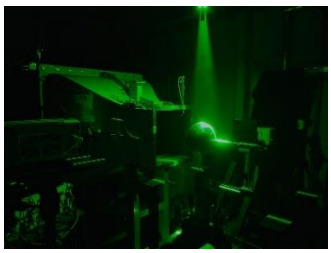

Fig.2 2D-PIV measurement

3 Result and Discussion

3.1 Fluid force experiment

Fig.3 shows the C_D diagram for each ball. Drag crisis is a phenomenon in which the drag coefficient drops off suddenly as the Reynolds number increases. The drag coefficients of balls changed rapidly from

about 0.5 to 0.2 at a Reynolds number in the range of 1.0×10^5 and 2.4×10^5, as shown here. This corresponds to the flow aspect change around the ball from the laminar separation to the turbulent separation. In order to explain these phenomena, the drag crisis was defined as the Starting and the Ending Reynolds number. The Starting Reynolds number and the Ending one was lowest at 1.0×10^5 and 1.2×10^5, respectively, on the Evopower, and they were highest at 1.8×10^5 and 2.4×10^5, respectively, on the Jabulani. It was found that the flow around the Evopower turned into a turbulent flow on about 5 m/s. however, the flow around the Jabulani turned into a turbulent flow on about 12 m/s. We considered that the cause of these phenomena was the difference in the panel shape of the ball.

Fig.4 shows the CD diagram of Vantaggio's smooth ball and the balls with dimple and pimple. In the subcritical region, the drag coefficient of all balls was not much changed, around 0.5. In the drag-critical region, the dimple ball has a large Reynolds number at the end of the transition. In the supercritical region, the smooth ball had the largest drag coefficient and the simple ball had the smallest CD. This indicates that the surface shape reduces the drag force of the balls. Also, the pimple ball has a smaller drag force than the dimple ball.

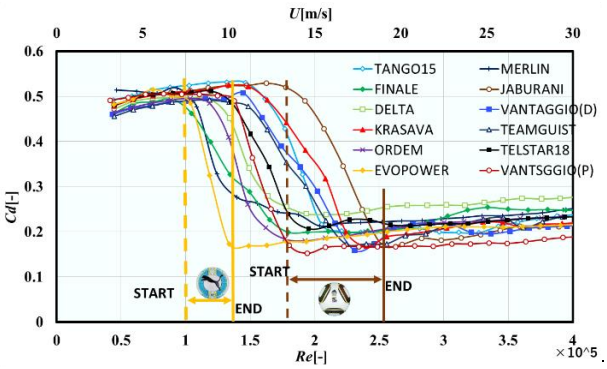

Fig.3 The C_D diagram of each ball

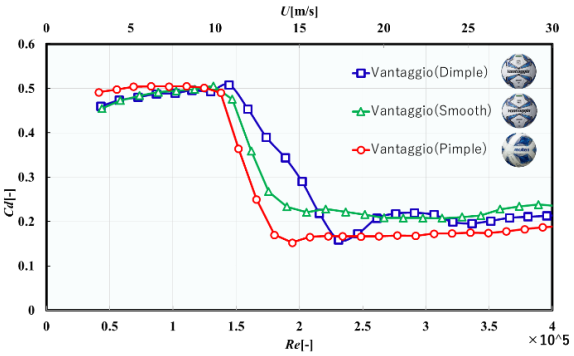

Fig.4 The C_D diagram of dimple, pimple and smooth ball

3.2 Groove shape measurement

The measurement results are shown in Fig.5. Large groove volume balls like Evopower have the small end-Reynolds number compared with the smaller volumes like Jabulani. It has a tendency that the larger the groove volume is, the smaller the end-Reynolds number becomes. The correlation between the total volume and the End-Reynolds number was strongly correlated with -0.83.

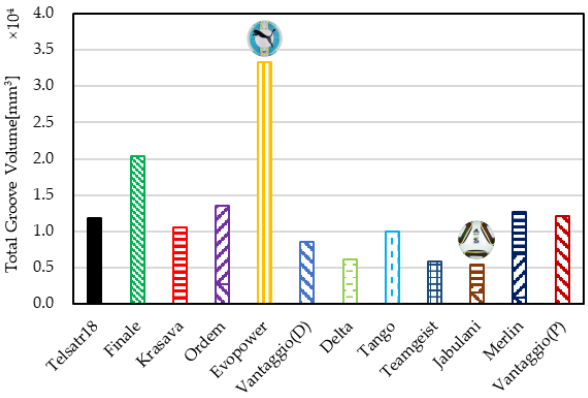

Fig.5 Total groove volume

3.3 Oil film experiment

Fig.6 showed the characteristic oil film results of balls. In the case of a true sphere, the true sphere had the first and second separation points Since the positions of the separation points of all the balls were almost the same, the C_D was almost the same at the wind speed 29.6 [m/s].

Fig.6 Oil film results of balls

3.3 2D-PIV measurement

Tables 1 and 2 show the 2D-PIV results of the Evopower and Jabulani. The separation point and the wake direction are indicated in each figure. In all cases of the subcritical and supercritical regions of drag crisis, it could be seen that the separation point and the flow direction of the wake flow were the same despite the change in the panel orientation. In the subcritical state of drag crisis, where *Re* was less than 1.8×10^5, the flow separation occurred around 90° when the center of the left front of the ball was defined as 0°. The C_D in this state was about 0.5 in the Reynolds number, less than 1.0×10^5. This was because the width of the turbulent ball wake became large on account of the separation occurred at around 90°. However, the separation point occurred in more than 90° in the supercritical state and the C_D became smaller to about 0.2. This was because as the Reynolds number increased the ball grooves stimulated the boundary layer, and the turbulent boundary layer, which was strong against flow separation, was created. Therefore, the flow separation was delayed, resulting in a narrow wake turbulence width.

In the drag crisis state, the position of the separation point and the flow expansion direction of the wake varied depending on the orientation of the

panel in any ball. Accordingly, it was found that the laminar separation and the turbulent separation were mixed depending on the panel in the drag crisis state, and the flow around the ball was partially different.

Finally, we compare the features of Evopower and Jabulani. In the subcritical state and supercritical state, the separation point shows the same tendency even if the types of ball are different. The C_D values are almost identical.

Table 1 The 2D-PIV Results of the Evopower

Panel Orientation & Laser position	Subcritical (5m/s) $Re = 7.3 \times 10^4$	Critical (8m/s) $Re = 1.2 \times 10^5$	Supercritical (15m/s) $Re = 2.2 \times 10^5$
	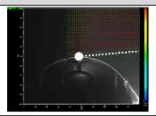	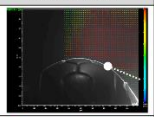	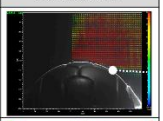
	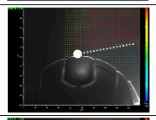	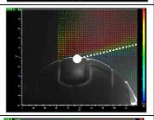	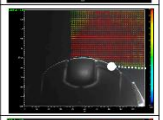
	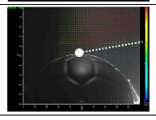	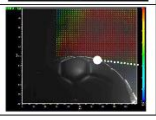	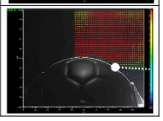

Table 2 The 2D-PIV Results of the Jabulani

Panel Orientation & Laser position	Subcritical (5m/s) $Re = 7.3 \times 10^4$	Critical (8m/s) $Re = 2.1 \times 10^5$	Supercritical (15m/s) $Re = 2.9 \times 10^5$
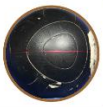	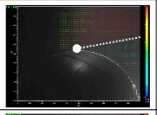	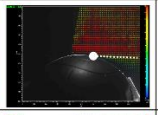	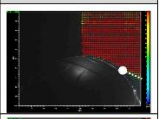
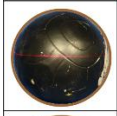	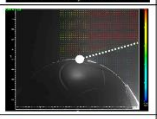	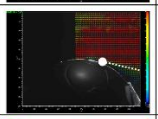	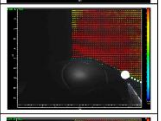
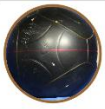	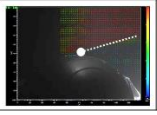	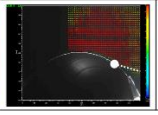	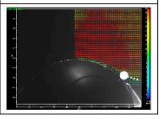

4 Conclusion

1. The total volume of the groove affects the Reynolds number at which the drag crisis occurs.
2. The panel groove affects the shape of the drag crisis.
3. The position of the flow separation point did not change in the subcritical and supercritical regions by the ball orientation. On the other hand, The aspect change of the drag crisis in panel difference causes the panel groove mixed with laminar and turbulent regions.

References

[1] Goff, J., Asai, T., Hong, S., J. Sports Eng. Technol, 228, 188–194 (2014).
[2] Hong, S., Asai, T., Seo, K., Procedia Eng.,112, 391–394 (2015).

FLOW CHARACTERISTICS AROUND A DOUBLE-SLOTTED CIRCULATION CONTROL WING

D. Yaguchi[1], T. Nakayama[2], and K. Sato[3]

[1]Graduate School of Engineering, Kogakuin University, Tokyo, Japan
[1]E-mail: am21064@ns.kogakuin.ac.jp
[2]Graduate School of Engineering, Kogakuin University, Tokyo, Japan
[2]E-mail: a218069@ns.kogakuin.ac.jp
[3]Department of Mechanical System Engineering, Kogakuin University, Tokyo, Japan
[3]E-mail: at12164@ns.kogakuin.ac.jp

Abstract

A circulation control wing (CCW) is an airfoil that uses tangential blowout from slots and the Coanda effect to generate circulation; it controls lift by the momentum of the blowout. Fundamental research has been conducted on tangential blowing cylinders. However, many basic parameters are used in a CCW, and conditions have been limited in previous studies. Therefore, claims that systematic research has been sufficiently conducted are dubious at best. The number of slots as well as the slot width and cylinder length are also critical parameters in the cylindrical shape. In this study, the deflection characteristics of the main jet were compared and investigated at the same momentum ratio using single- and double-slot cylinders placed downstream of the main jet.

Figure 1 shows a schematic of the experiment used in this study. A cylinder with a diameter of 50 mm was placed 200 mm from the wind tunnel.

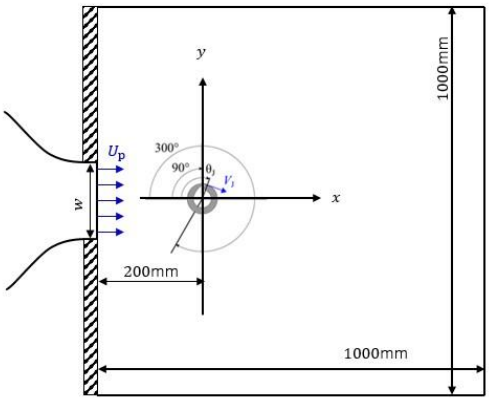

Fig.1. Schematic of the experiment.

In this study, two types of cylinders were prepared, namely, single- and double-slot.

Fig.2 and 3 show examples of single- and double-slot visualization observations, respectively. The experimental parameters were as follows. Fig. 2 shows the case of $C_{\mu 1} = 0.276$, $U_\mathrm{p} = 8.3\ \mathrm{m/s}, V_{\mathrm{j}1} = 62\ \mathrm{m/s}$, and $\theta_\mathrm{j} = 90°$.

Fig. 3 shows the case of $C_{\mu 2} = 0.276$, $U_\mathrm{p} = 8.3\ \mathrm{m/s}, V_{\mathrm{j}2} = 44\ \mathrm{m/s}$, and $\theta_\mathrm{j} = 90°, 270°$, respectively. The momentum coefficients C_μ are calculated using the following equations.

$$C_{\mu 1} = \frac{b}{w}\left(\frac{V_{j1}}{U_p}\right)^2 \qquad (1)$$

$$C_{\mu 2} = \frac{2b}{w}\left(\frac{V_{j2}}{U_p}\right)^2 \qquad (2)$$

The figure shows that the single-slot cylinder deflected the main flow to a greater extent than did the double-slot cylinder. This could be attributed to the effect of the 270° side-blowing flow rate of the double-slot cylinder on the flow field. In fact, in a previous study, it was confirmed that the direction of the main flow deflection was upward when the slot position was $\theta_\mathrm{j} = 270°$ in the case of a single-slot cylinder. In the present study, the deflection angle may have been different for the same momentum due to the same factor. However, because many parameters are used for the slot angle of a cylinder, finding the slot position at which the deflection angle is the maximum for a double-slot cylinder is required.

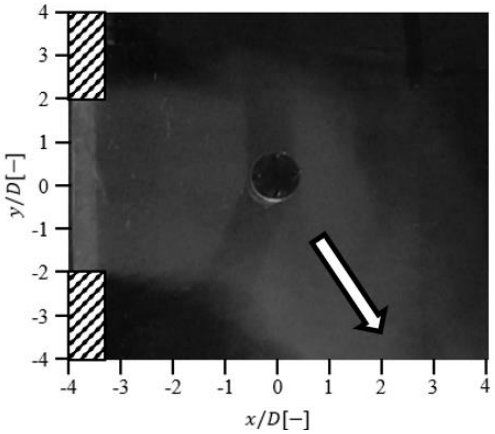

Fig.2. $C_\mu = 0.276$
$U_p = 8.3m/s, V_{j1} = 62m/s$, and $\theta_j = 90°$.

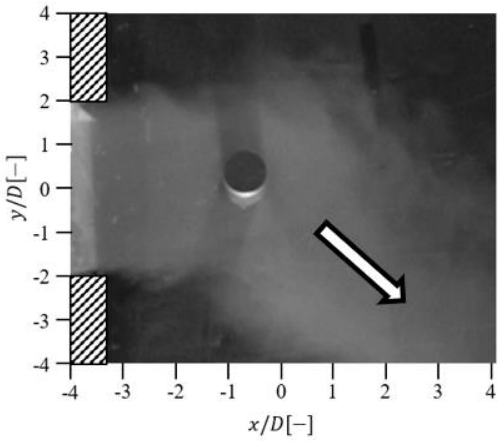

Figure. 3. $C_{\mu} = 0.276$ $U_{\mathrm{p}} = 8.3\mathrm{m/s}, V_{\mathrm{j2}} = 44\mathrm{m/s}$, and $\theta_{\mathrm{j}} = 90°, 270°$.

References:

[1] T. Shakouchi," Jet Flow Engineering", Fundamentals and Application, Morikita Publishing, 2004

[2] S. Okayasu, Y. Arakawa, K. Sato, T. Shakochi, and K. Furuya, "Influence of Ground Effect and Ceiling Effect on High Lift Device Using Tangential Blowout Cylinder", Proc. of the Japan Society for Aeronautical and Space Sciences, Vol, 56, no. 656, pp. 29–36, (2008)

[3] A. Fuji and K. Sato, "Directional Control of Jet Flow Using a Tangential Spray Cylinder", Proc. of the 72nd Gen. Meeting of the Kyushu Branch of the Japan Society of Mechanical Engineers

[4] Q. Zhang, F. Takahashi, K. Sato, W. Tsuru, and K. Yokota, "Jet Direction Control Using Circular Cylinder with Tangential Blowing Trans. Japan Soc. Aero", Space Sci., 64, no. 3, pp. 181–188, (2021)

VORTEX ARRANGEMENT OF SYNTHETIC JETS GENERATED BY ASYMMETRIC SLOTS

[*1]Takumi Ito, [*1]Kotaro Sato

[*1]Mechanical Engineering Program in the Graduate School of Engineering, Kogakuin University
1-24-2 Nishi-shinjuku, Shinjuku-ku, Tokyo 163-8677, Japan
E-mail: am21005@ns.kogakuin.ac.jp

Abstract

A fundamental study on the vortex arrangement of synthetic jets generated in asymmetric slots is presented. It was reported that two-dimensional synthetic jets generated in general symmetrical slots forms symmetrical vortex pairs and that the vortices propagate at each other's induced velocities, while asymmetrical slots such as beak-shaped ones form staggered vortices. However, the results reported thus far are limited, and many questions remain unaddressed. In this work, we focus on the transient behavior of synthetic jets generated in asymmetric slots and discuss the formation mechanism of staggered vortex arrays.

Over recent years, significant research has been devoted toward jet vectoring; studies on the directional control of single synthetic jets have also commenced. In a previous work, an asymmetric slot with a beak shape was proposed [1], and the behavior of the synthetic jet generated in the slot was investigated. However, owing to the limited range of conditions reported thus far, detailed flow characteristics and mechanisms have not been discussed comprehensively. In this study, the effect of asymmetric slots on a vortex array was investigated through numerical calculations.

Numerical simulations were performed using SCRYU/Tetra for Windows, assuming a two-dimensional incompressible viscous fluid with a mesh of 330,000 elements. The k-ε model was applied as the turbulence model. With regard to the boundary conditions, the flow velocity at the slot inlet, static pressure at the computational domain outlet, and total pressures at the upper and lower boundaries were set. Moreover, Non-slip conditions were applied to the slot sides and the rigid walls.

In this study, we focused on the transient phenomena of a synthetic jet formed under the condition of a dimensionless stroke length L_0 = 10 and a dimensionless beak length C = 6; we observed and analyzed the process of vortex train formation. Figure 1 presents an example of the observed behavior of the synthetic jet in each cycle. At (ii) t/T=2.0, a counterclockwise vortex is developed at the tip of the beak. In the case of the rectangular asymmetric slot, the counterclockwise vortex at the tip of the rectangle is absorbed by the developed clockwise vortex; consequently, this clockwise vortex becomes larger and is directed toward the counter-protrusion side. However, in the case of the beak shape, a counterclockwise vortex is developed at the tip of the beak, and it induces the clockwise vortex, resulting in the formation of a staggered array of vortices.

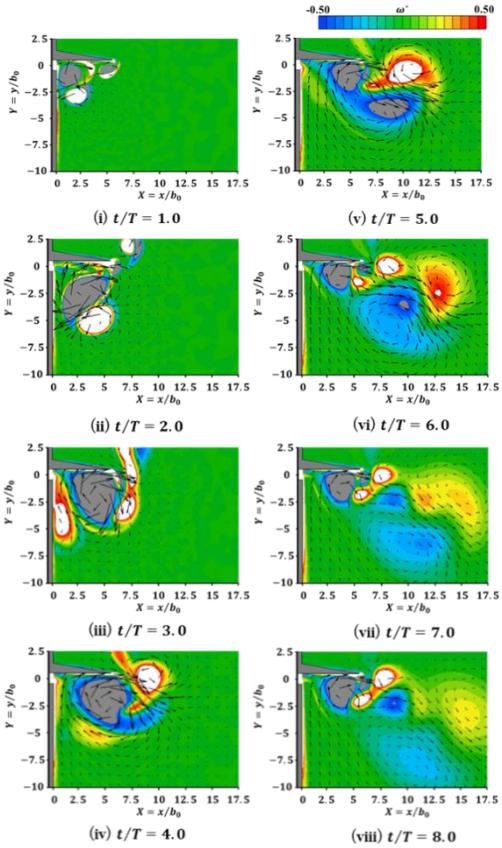

Fig. 1. Typical flow patterns of synthetic jet in numerical simulations (L_0 = 10, C = 6, f = 60 Hz, U_0 = 3.0 m/s, and Re = 990).

References:

[1] Kobayashi, R. et al., "Vector Control of Synthetic Jets Using an Asymmetric Slot" ASME, FEDSM2016-7648, (2016)

[2] Watabe, Y. et al., "Influence of an Asymmetric Slot on the Flow Characteristics of Synthetic Jets," Springer Proc. Phys., Vol.185(2016), pp.101-107

[3] Nishibe, K. et al., "Experimental and Numerical Study on the Flow Characteristics of Synthetic Jets" Journal of Fluid Science and Tecnology, Vol.6(2011), pp.425-436

INFLUENCE OF SECONDARY FLOW INDUCED ON COANDA SURFACE ON JET DEFLECTION CHARACTERISTICS

[*1]M. Nakagawa*, [*1]K. Sato

[*1]Mechanical Engineering Program in the Graduate School of Engineering, Kogakuin University
1-24-2 Nishi-shinjuku, Shinjuku-ku, Tokyo, Japan
E-mail: am21041@ns.kogakuin.ac.jp

Abstract

There is increasing interest in fluidic thrust vectoring, which can control the direction of a jet without changing its geometry. Thus far, the direction of primary flow has been controlled using steady secondary or synthetic jet flow with the coanda surface. The deflection characteristics of steady secondary flow are classified into three regions: dead zone, control region, and virtual saturation region. It has also been reported that the deflection angle can be set arbitrarily by combining the momentum ratio and the dimensionless frequency when synthetic jets are used[1] [2]. However, at present, the controllable range of these methods is not sufficiently wide. In this study, we attempt to control the direction of primary flow by installing a slot for secondary flow on the coanda surface located near the slot exit for the primary flow and adjusting velocity.

Fig. 1 shows the slot shape. The slot width h_1 and the coanda radius R of the primary flow slot are 1.0×10^{-2} m and 1.5×10^{-2} m, respectively. The slot width h_2 for the secondary flow on the coanda surface is 2.0×10^{-3} m. The secondary flow slot is located 30° clockwise from the y-axis with the center of the coanda cylinder as the rotation axis. The computational domain of the flow field was set to 1 m ×1 m. The x-axis was set at the center of the slot width in the direction of primary flow, and the y-axis was set on the solid wall. ANSYS Fluent (ANSYS Inc.) was used for numerical analysis. The working fluid was air, and unsteady analysis was performed assuming a two-dimensional incompressible flow. SST k-ω was applied to the turbulence model. For the boundary conditions, we have given velocity conditions for each inlet surface so that the velocities are arbitrary at the slot exit of the primary and secondary flows. A constant static pressure (p = 0 Pa) was applied to the outlet of the computational domain in the x- direction, and a constant total pressure was applied to the upper and lower boundaries. Here, we discuss the results obtained with Reynolds number $Re = 6.7\times10^3$.

Fig. 2(i) and (ii) show the velocity distribution plots when the suction secondary flow is added. The velocity distribution diagram plots the overall velocity $|\boldsymbol{v}| = \sqrt{u^2+v^2}$ measured on an arc of dimensionless radius r/h_1 = 10, where the velocity scale $|\boldsymbol{v}| / U_1$ ranges from 0 to 1. Fig. 2(i) and (ii) shows the results for U_2 = -0.707 m/s and U_2 = -2.24 m/s, respectively. In (i), the maximum velocity is recorded near the x-axis, indicating a straight-line jet structure, while in (ii), the maximum velocity is shifted downward along the y-axis, indicating that the jet is deflected downward by the secondary suction flow. It can be inferred from Fig. 2 that the deflection characteristics of the jet differ depending on the magnitude of the secondary flow suction velocity, and they change significantly between -2.24 m/s and -0.707 m/s.

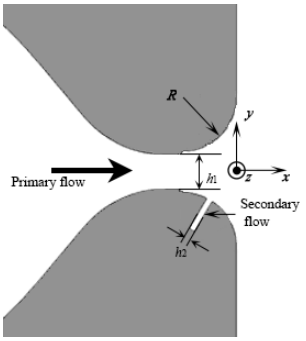

Fig.1. Magnified view of slot exit geometry.

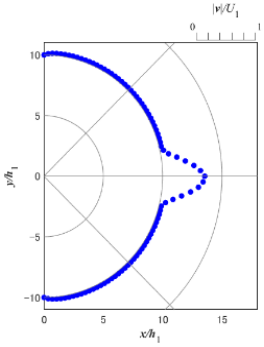

(i). U_1=10 m/s, U_2=-0.707 m/s

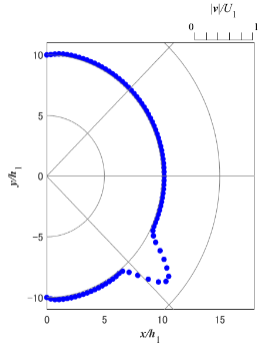

(ii). U_1=10 m/s, U_2=-2.24 m/s

Fig.2. Velocity distributions at different secondary flow velocities.
($h_1 = 1.0 \times 10^{-2}$ m, $h_2 = 2.0 \times 10^{-3}$ m, U_1 = 10 m/s)

Nomenclature

h	:	Slot width, m
R	:	Radius of Coanda surface, m
U	:	Velocity at slot exit, m/s
$\|\boldsymbol{v}\|$	:	Overall velocity, m/s
Re	:	Reynolds number
x, y, z	:	Coordinate axes

Subscripts

1	:	Primary jet
2	:	Secondary jet

References

[1] M. Trancossi, J. Stewart, S. Maharshi, and D. Angeli, “Mathematical Model of a Constructal Coanda Effect Nozzle”, JAFM, Vol. 9, No. 6 (2016), pp. 2813-2822.

[2] R. Kobayashi, Y. Watanabe, Y. Tamanoi, K. Nishibe, D. Kang, D, and K. Sato, “Jet vectoring using Secondary Coanda Synthetic Jets”, Bulletin of the JSME, Mechanical Engineering Journal, Vol. 7, No. 5 (2020), pp. 20-00215.

Interaction between Continuous Jet and Synthetic Jet under the Same Momentum Ratio Conditions

M. Mori[1], J. Matsuzaki[2], N. Ajino[3], K. Nisibe[4], and K. Sato[5]

[1] Graduate School of Engineering, Kogakuin University, Tokyo, Japan
E-mail: am21061@ns.kogakuin.ac.jp
[2] Mechanical Systems Engineering, Kogakuin University, Tokyo, Japan
E-mail: a217082@ns.kogakuin.ac.jp
[3] Graduate School of Engineering, Tokyo City University, Tokyo, Japan
E-mail: g2181001@tcu.ac.jp
[4] Department of Mechanical Engineering, Tokyo City University, Tokyo, Japan
E-mail: knishibe@tcu.ac.jp
[5] Department of Mechanical System Engineering, Kogakuin University, Tokyo, Japan
E-mail: at12164@ns.kogakuin.ac.jp

Abstract

Attempts have been made to control the direction of a continuous jet by interfering with it using a synthetic jet. However, because of the fragmentary nature of most previous studies, the flow field and deflection mechanism when continuous and synthetic jets interfere with each other remain unclear. In this study, the influence of varying the velocity and slot width of the continuous jet with a constant momentum ratio between the continuous jet and the synthetic jet on the flow field were investigated.

There have been many studies on the use of a synthetic jet for directional control of a continuous jet [1]–[3]. In this study, the effects on the flow field were studied when the velocity and slot width of the continuous jet are varied while keeping the momentum ratio between the continuous jet and the synthetic jet constant. The focus was on the flow field during the interference between a continuous jet and a synthetic jet, and an attempt was made to clarify the phenomena mainly by visualizing the flow.

Figure. 1(a) shows the experimental results obtained under the conditions of Uc = 7.00 m/s and bc = 3 mm and of Us = 7.00 m/s and bs = 3 mm. Figure. 1(b) shows the experimental results obtained under the conditions of Uc = 3.66 m/s and bc = 11 mm and of Us = 7.00 m/s and bs = 3 mm. In this experiment, the momentum ratio was unified to ξ = 1.00 by adjusting the velocity and slot width of the continuous jet. The synthetic jet flows from above and the continuous jet from below.

Figure. 1 shows an example of visualized observation of white smoke generated by a smoke generator flowing from a continuous jet generator blower and photographed by a camera (SONY ZV-1). In Fig. 1(a), the symmetry of the vortex pair formed in the synthetic jet is broken by the interference of the continuous jet, and the jet is deflected toward the synthetic jet. In Fig. 1(b), one can see that the jet is deflected toward the synthetic jet, as in the previous case. Comparing Figs. 1(a) and (b), there appears to be no significant change in the deflection of the jet. However, the vortices generated near the slot differ in size. This is thought to result from the difference in the size of the vortex when the two jets interfere with each other because the velocity of the continuous jet became smaller as the slot width of the continuous jet became larger.

These results show that, when the momentum ratio is kept constant and the velocity and slot width of the continuous jet are varied, there is no significant change in the deflection of the jet, but the size of the vortex is different.

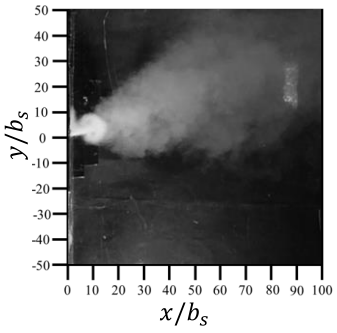

(a) U_c = 7.00 m/s, b_c = 3 mm
U_s = 7.00 m/s, b_s = 3 mm
L_0 = 46.7, f = 50 Hz

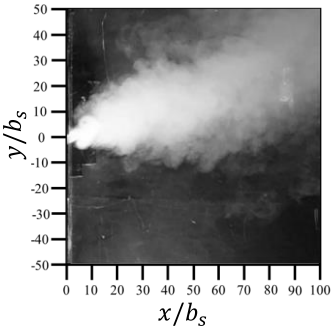

(b) U_c = 3.66 m/s, b_c = 11 mm
U_s = 7.00 m/s, b_s = 3 mm
L_0 = 46.7, f = 50 Hz

References:

[1] Smith, B. L., and Glezer, A., 2002, "Jet Vectoring Using Synthetic Jets," J. Fluid Mech., 458, pp. 1-34.
[2] Smith, B. L., and Glezer, A., 2005, "Vectoring of Adjacent Synthetic Jets," AIAA J., 43(10), pp. 2117-2124.
[3] Y, Suzuki., R, Kobayashi., K, Sato., K, Nishibe., and K, Yokota., "Interaction Between a Continuous Jet and Synthetic Jet," The 31st International Symposium on Transport Phenomena 13-16 October 2020, Honolulu, USA.

INFLUENCE OF SECONDARY SUCTION/BLOWING FLOWS ON PRIMARY JET

A. YAMADA[1], K. SATO[1] and D. KANG[2]

[1]Mechanical Engineering Program, Graduate School of Engineering, Kogakuin University
1-24-2 Nishi-Shinjuku, Shinjuku-ku, Tokyo 163-8677,
[2]Department of Mechanical Engineering, Saitama University
25 Shimo-Okubo, Sakura-ku, Saitama-shi, Saitama 338-8570, Japan
E-mail: am21066@ns.kogakuin.ac.jp

Abstract

A method for controlling the direction of a jet using a secondary flow with a coanda surface, called fluidic thrust vectoring, was proposed and some results have been obtained. However, few systematic studies have been reported, in particular studies using geometry as a parameter. Therefore, the effect of the radius of the coanda surface on the flow characteristics of the primary flow has not been sufficiently discussed. In this study, the effect of the radius of curvature of the coanda surface on the basic flow characteristics of the primary flow under the condition of secondary flow suction was investigated using the slot width of the primary flow as a representative length [1]-[5].

In this study, we attempted to clarify the relationship between the deflection characteristics of the primary jet and the non-dimensional radius of the coanda surface under the conditions of jetting and suction of the secondary flow. Moreover, the behavior of wall-attached jets is discussed under the condition of constant coanda radius, where the primary jet is deflected and sucked from above and below the slot suburbs.

NUMERICALANALYSIS CONDITIONS

ANSYS Fluent was used for numerical simulations. In this study, shear stress transport k-ω was adopted as the turbulence model, unsteady analysis of the flow field was performed assuming a two-dimensional flow, and the primary flow slot was calculated for a Coanda cylinder radius of R=70.0×10^{-3} m. The primary and sub-jet slot widths were h_1=10.0×10^{-3} m and h_2=10.0×10^{-3} m, respectively. Moreover, the slot widths for the primary and sub-jets were h_1=10.0×10^{-3} m and h_2=2.0×10^{-3} m, respectively.

Figure 1 shows the slot geometry and coordinate system near the slot, and a typical computational mesh example. The values considered were R=70.0×10^{-3} m, h_1=10.0×10^{-3} m, h_2=2.0×10^{-3} m, and h_3=2.0×10^{-3} m. In this case, the number of computational meshes was approximately 180,000.

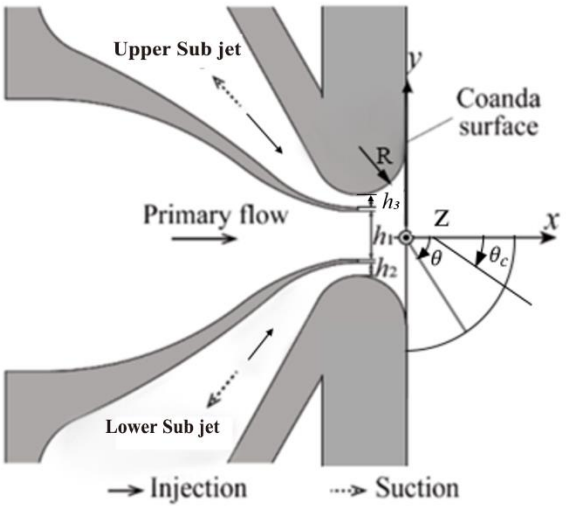

Fig 1. Magnified view of the slot exit geometry

RESULTS AND DISCUSSION

Typical flow patterns (primary jet only)

Figure 2 shows the calculation results for U_1=10 m/s for the primary jet only (no sub-jet). In Fig. 2, the velocity contour plot for R/h_2 =7 is shown. Because of the large coanda radius, the jet adheres to the coanda surface without a sub-jet. The surface to which the jet adheres depends on the calculation error and mesh accuracy; in this figure, it adhered to the bottom surface.

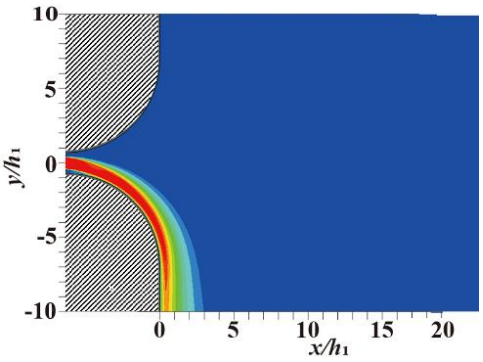

Fig. 2 Wall Adhesion Structure under Primary Jet Alone Condition
R/h_1 = 7, U_1= 10 m/s, U_{low}= 0 m/s, U_{up} = 0 m/s

Flow patterns of jet flow with sub-jet

Figures 3 and 4 show the calculation results for the case where the sub-jet is imposed under the conditions of jetting from above and below and suction. Figure 3 shows an example calculation for R/h_1 = 7, where (a) U_{low} = 7 m/s, U_{up}= -7 m/s, and (b) U_{low}= 7 m/s, U_{up} = -0.25 m/s. Figure 4 shows an example of calculation for R/h_1 = 7, with (a) U_{low} = -7 m/s, U_{up} = 7 m/s, and (b) U_{low} = 7 m/s, U_{up} = 12 m/s. In this range of calculation conditions, the wall adhesion occurred on the side with a lower pressure gradient near the slot under the conditions shown in Figs. 3(a) and 4(a). Therefore, the sub-jet U_{low} was kept constant, U_{up} was given as the amount of change, and U_{up} was confirmed to change the direction of wall adhesion.

Under the condition of Fig. 3, the direction of wall adhesion changed under U_{low} = 7 m/s,U_{up} = -0.25 m/s. Thus, the wall adhesion condition depended on U_{up} even when the suction condition of U_{up} was extremely low.

Under the condition of U_{low} = -7 m/s and U_{up} = 12 m/s in Fig. 4, the direction of wall adhesion changed. Thus, the jet characteristics changed when the jetting condition of U_{up} was lower than U_{up}/U_{low} = -1.7.

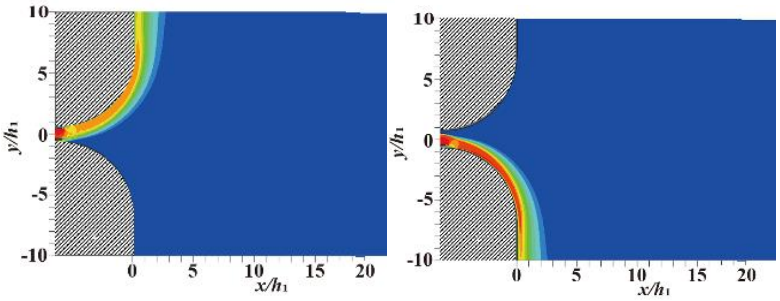

(a) U_{up} = -7 m/s (b) U_{up} = -0.25 m/s

Fig. 3 Flow patterns of jet flow with sub-jet

R/h_1=7, U_1 =10 m/s, U_{low} = 7 m/s

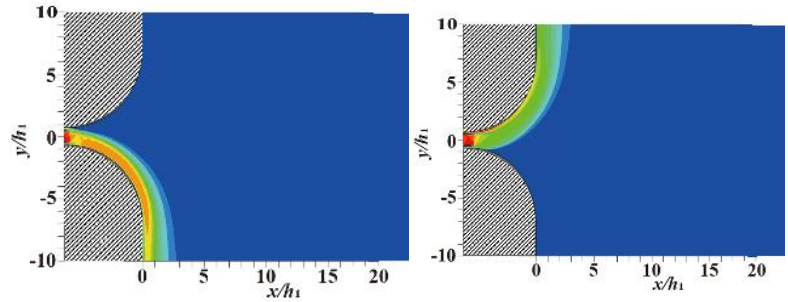

(a) U_{up} = 7 m/s (b) U_{up} = 12 m/s

Fig. 4 Flow patterns of jet flow with sub-jet

R/h_1 = 7, U_1 = 10 m/s, U_{low} = -7 m/s

CONCLUSIONS

In this study, we attempted to clarify the influence of the secondary jet and suction on the primary jet using numerical analysis.

It was found that the secondary jet and suction affected the jet deflection when the radius of the coanda surface was large.

NOMENCLATURE

h	Slot width, m
R	Radius of coanda surface, m
U	Velocity at slot exit, m/s
$\|v\|$	Overall velocity ($=\sqrt{(u^2+v^2)}$)
ν	Kinematic viscosity , m^2/s
Re	Reynolds number ($=\|U_1\| h_1/\nu$)
M	Jet momentum
ξ	Momentum ratio between primary and secondary jets
θ	Jet deflection angle
x, y, z	Coordinate axes

Subscripts

1	Primary jet
up	Upper sub-jet
low	Lower sub-jet

REFERENCES

[1] Trancossi, M., and Dumas, A., Coanda Synthetic Jet Deflection Apparatus and Control, pp. 1-14.

[2] Trancossi, M., Stewart, J., Subash, M., and Angeli, D., "Mathematical Model of a Constructal Coanda Effect Nozzle", *JAFM*, 9, No. 6 (2016), 2813-2822.

[3] Mason, M.S., and Crowther, W.J., 'Fluidic thrust vectoring of low observable aircraft', *CEAS Aerospace Aerodynamic Research Conference*, (June 10-12, 2002), Cambridge, UK.

[4] Al-Asady, A., and Abdullah, A.M., (2017), 'Fluidics Thrust Vectoring Using Co-Flow Method', *Al-Nahrain Journal for Engineering Sciences (NJES)*, Vol. 20, No. 1, pp. 5-18.

[5] Dores, D., Madruga, S.M., and Krothapalli, A., "Characterization of a Counterflow Thrust Vectoring Scheme on a Gas Turbine Engine Exhaust Jet", *AIAA*, San Francisco, California, 3516 (2006), 2006.

Development of a finite element model for mechanical analysis on colonic stent – organs interface

Minori Kunii, Kazuhiro Suga

Department of mechanical engineering, Graduate School of Engineering, Kogakuin University, Tokyo, Japan
E-mail: am21021@ns.kogakuin.ac.jp

Abstract

A colonic stent is a medical device that expands the colon that is obstructed by cancer or other diseases. By understanding the mechanical stimulus given to the colon during the expansion of the colon stent, we can improve various problems that may occur in stent treatment. Therefore, in this report, we have developed an optimal finite element model to understand the mechanical stimulus given to the colon.

The finite element model used in this report is shown in Figure 1. A two-dimensional model of the intestine and a single wire of the stent is used to analyze pushing the stent 1 mm into the colon. Based on the results of the analysis, it was confirmed which element size was optimal. The evaluation method was to plot the displacement in each of the xy directions at the nodes of the red and blue lines shown in Figure 1. The displacements in the xy direction at the red line and the blue line were plotted, and then compared with those at the finest 0.005 mm, which were also plotted. Figure 2-7 shows a selection of these plots.

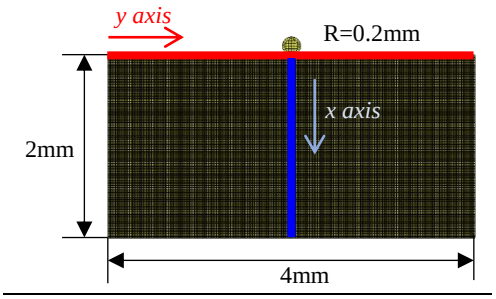

Fig 1. finite element model of 2D

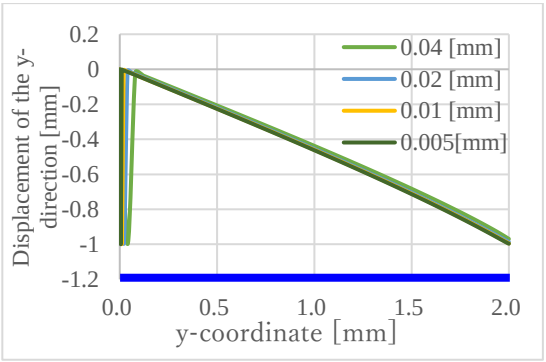

Fig 2. Displacement of the central part of the colon in the y-direction

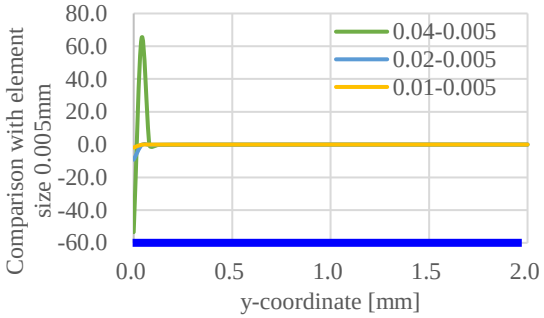

Fig 4. Comparison of element sizes of 0.04mm, 0.02mm, 0.01mm-0.005mm in the Y-direction displacement of the center of the colon

The y-axis in Figures 4 and 5 is the result of subtracting the result at 0.005 from the results at element sizes 0.01mm, 0.02mm and 0.04mm and dividing by the result at 0.005. The graph of the computation time for each element size is also shown.

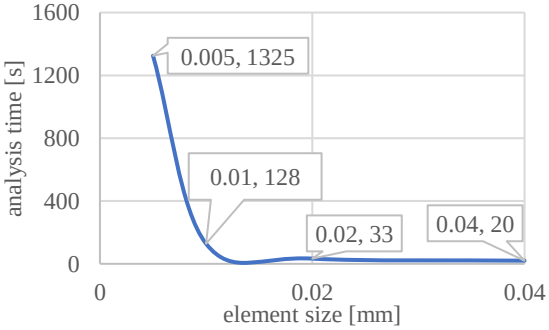

Fig 5. Relationship between element size and analysis time

Considering the results and the fact that it is not practical to use an element size of 0.005mm in a 3D model, we consider that 0.01mm or 0.02mm is better.

Measurement and Compensation of the 3D Printing using 2.5D Characterization

Yu-Sheng Lin*

Department of Mechanical Engineering, Southern Taiwan University of Science and Technology, Tainan, Taiwan
yushenglin@stust.edu.tw

Abstract

The technique of 3D printing, also referred as additive manufacturing, has been widely discussed in recent years due to less requirements for tooling or specialist programming skills. It has drawn much attention in various fields: engineering, medicine, food, cultural and creative industries. Despite the beauty of this technique is for customized designs and small quantity manufacturing, many people still consider applications or works manufactured by 3D printing as final products. Therefore, accuracy and precision are important in order to maintain consistent quality. In this study, a process of Digital Light Processing (DLP) 3D printing was evaluated and an example of a full denture model demonstrated variations in its shape after using 2.5D characterization. A pre-processing method to compensate for the systematic errors was applied symmetrically. As the results shown in Figure 1 and 2 that variations exist in between different printings, therefore, further studies of a pre-processing method are on-going.

Keywords: 3D printing, accuracy, digital light processing, 2.5D characterization.

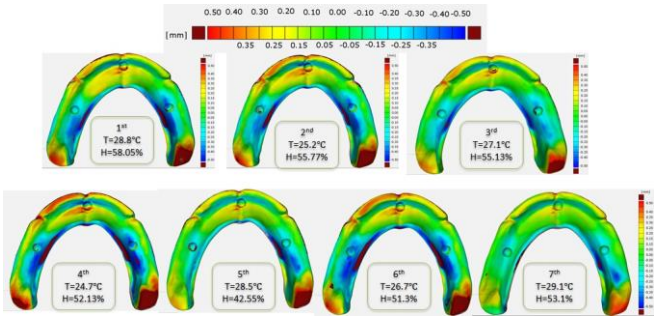

Fig. 1 An example of precision and accuracy measurements between 7 different 3D printings. This model is a maxillary record base for full denture

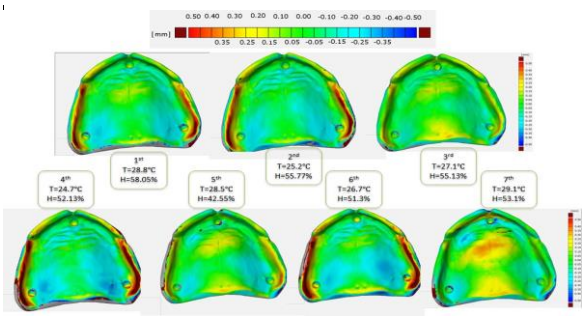

Fig. 2 An example of precision and accuracy measurements between 7 different 3D printings. This model is a mandibular record base for full denture

Oral Presentation

Advanced Functional Materials & Energy and Transportation

November 24th

Presentation No.	Title	Author	
AFM1.	Facile hydrothermal synthesis of interlayer-expanded MoS_2/rGO	Kien Nguyen-Ba, Huy Le-Quoc, Trang Nguyen-Thi-Thu, and Khan Dinh-Thanh	86
AFM2.	Fabrication of Anodic Aluminum Oxide Templates	Lance Tristan Oliver Roncal Pengson, M. Vasquez Jr	89
AFM3.	Carrier gas type dependence of Ga_2O_3 thin film grown by mist Chemical Vapor Deposition	Rie Yamada, S. Takahashi, A. Sekiguchi, T. Onuma, T. Honda, and T. Yamaguchi	91
AFM4.	A Study on Smart Fluid Technology and its Applications in Haptics	Aaron Raymond See, Kohila Chandramohan	93
AFM5.	Growth of GaInN multi quantum well on strain-controlled layer by RF-MBE toward realization of light emitting diodes operating in red spectral region	Masaki Matsuda, R. Yoshida, K. Tahara, T. Yamaguchi, T. Onuma, and T. Honda	98
AFM6.	Fluorescent immune-biosensor on the glass biochip used for albumin detection	Ying-Nien,Chou, Lien-Chiang,Hung	100
ET1.	Home Energy Management System Considering Stationary Storage and Electrical Vehicle	Jeeng-Min Ling, Firoj Ismail Mulani	102

Facile hydrothermal synthesis of interlayer-expanded MoS_2/rGO

Kien Nguyen-Ba*[a], Huy Le-Quoc[b], Trang Nguyen-Thi-Thu[b] and Khan Dinh-Thanh[c]

[a]Faculty of Mechanical engineering, University of Science and Technology - The University of Danang, Danang, Vietnam
[b]Faculty of Advanced Science and Technology, University of Science and Technology - The University of Danang, Danang, Vietnam
[c]Faculty of Physics, University of Science and Education - The University of Danang, Danang, Vietnam
*E-mail: nbkien@dut.udn.vn

Abstract

Expanded interlayer of MoS_2 nanosheets have great applications such as electrocatalyst, anode or cathode materials for rechargeable battery. Herein, a facile and scalable hydrothermal has been successfully used to synthesize the MoS_2/rGO composites, which results in significantly enlarged MoS_2 interlayers (from 0.62 nm to 0.89 nm). GO served as skeleton for the grow of MoS_2 nanoclusters, which dispersed and anchored on rGO sheets after the synthesis.

1. Introduction

Molybdenum disulfide (MoS2), with a well-defined layered structure similar to graphite, has been attracted considerable attention because of its unique electronic, optical, and electrochemical properties [1-2]. Usually, the 2H-MoS_2 semiconducting phase is thermodynamically stable. Nevertheless, the 2H-MoS_2 phase has low electrical conductivity, hindering its application for electrocatalysts and energy storage [3]. Coupling MoS_2 with graphene oxide (GO) is an effective approach to improve the electronic conductivity of MoS_2 [4]. Besides, compared to the standard interlayer distance of about 0.62 nm [4], the expanded interlayer of MoS2 shows many advantages, especially for the intercalation of guest ions such as Mg^{2+}, Zn^{2+} [5-6]. Therefore, simple, and scalable methods to synthesize expanded interlayer of MoS_2 nanosheets coupled with reduced graphene oxide (rGO) are highly desirable. Shengwei Li et al. prepared the MoS_2/rGO using a simple hydrothermal method, which results in significantly enlarged MoS_2 interlayers (from 0.62 nm to 1.16 nm). Their material showed excellent performance as cathode material for Zinc-ion battery [7] . Here, we report a facile and scalable hydrothermal synthesis to prepare the MoS_2/rGO composites with expanded interlayer of MoS_2 of about 0.89 nm. This unique structure would potentially be used as cathode materials for zinc-ion battery or anode materials for sodium-ion battery.

2. Experimental section

2.1. Materials synthesis

All chemicals were of analytical grade and directly used without further purification. Firstly, the graphene oxide (GO) was prepared by the oxidation of natural graphite flakes using a modified Hummers method described elsewhere [8]. Then, 30mg of the as-prepared GO was ultrasonically dispersed in 50 mL of double distilled water for 30 min., following by the addition of oxalic acid dihydrate (1 g), ammonium paramolybdate (0.3 g), and thiourea (0.323 g). Then the mixture was sonicated for an additional 30 min. and transferred into a 100 mL Teflon-lined stainless-steel autoclave. The autoclave was maintained at 210 oC for 24h in an oven. After being cooled naturally, the black powder (noted as MoS_2/rGO-10) was then collected and washed repeatedly with water and absolute ethanol, followed by drying at 60 oC for 12h. The MoS_2/rGO-25 sample was obtained by changing the molybdenum precursor to 750 mg. The molar ratio between Mo and S was maintained at 1: 2.5 for all samples. For comparison, the pristine MoS_2 was synthesized with the same process without adding GO.

2.2. Material characterizations

The crystal structure and morphology of all powders were characterized by an X-Ray diffractometer (Bruker D8 advanced, Germany), with Cu Kα radiation (λ = 1.5418 Å) at 40 kV, scanning electron microscopy (SEM, JEOL, JSM-IT200). Vibrational modes and defects of the materials was determined using Raman system (LabRaman, Horiba Scientific) with 532 nm laser excitation.

3. Results and disscusion

XRD patterns in Fig. 1a shows that the diffraction peaks at around 33.3o, 39.7o, and 57.9o, assigning to the (100), (103), (110) planes, are matched well to the hexagonal 2H-MoS_2 structure (JCPDS 73-1508) [9]. Moreover, a (002) peak shifts to low-angle region of 9.9o, corresponding to the expanded interplanar distance of 0.89 nm along the c axis (calculated using Bragg equation: $2d\sin\theta=\lambda$) [5]. The interlayer-expanded of all samples probably due to the intercalation of ammonium ions or the unreacted Mo-O bonds in the sulfidation process [5,8]. Compared to the MoS_2/rGO-25 and MoS_2 samples, the MoS_2/rGO-10 exhibits relatively weak intensity and broadened peaks, suggesting the formation of smaller amount of

MoS_2 and the well dispersed of MoS_2 particles on rGO sheets. Besides, the MoS_2/rGO-10 appeared an additional broad peak at about 26o, corresponding to the rGO[4]. While the rGO skeleton facilitates the electron transport, the interlayer expanded MoS_2 can lower the energy barrier of guest ions intercalation, such as Li^{+1}, Na^{+1}, Zn^{+2} [5]. As shown in Fig.1b, the Raman spectra of all prepared samples display the typical of 2H phase peaks at about 377.8 and 405.1, which correspond to E^1_{2g} (in-plane vibration) and A_{1g} (out of plane vibration) phonon mode, respectively [4-5]. The MoS_2/rGO-10 exhibits lower intensity and broaden peak, suggesting that the MoS_2 crystallites are smaller and dispersed well, agreeing with the XRD results.

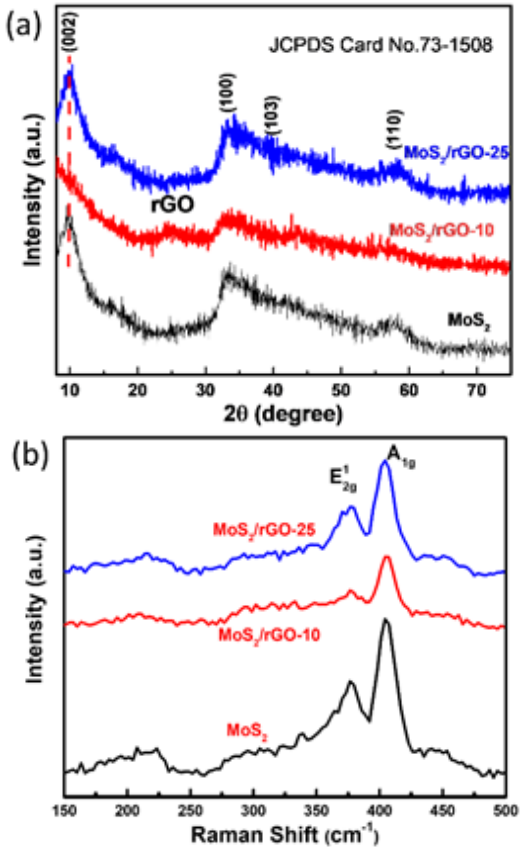

Fig. 1. XRD patterns (a) and Raman spectra of MoS2/rGO-25, MoS2/rGO-10, and MoS2

Scanning electron microscopy (SEM) was used to investigate the morphology of MoS_2/rGO-25, MoS_2/rGO-10, and MoS2. As shown in Fig.2a The SEM image of the pristine MoS_2 exhibits agglomerate flower-like nanoclusters, in contrast, when the GO is introduced, the nanocluster thoroughly dispersed and anchored on the rGO nanosheets, as can be seen in Fig.2b,c. When less Mo precursor is used, smaller MoS_2 nanoclusters are uniformly anchored on rGO nanosheets, as revealed in Fig.2c. In addition, the EDS mapping measurements clearly confirm the uniform distribution of Mo, S elements, as shown in Fig.3. The observed oxygen element uniformly distributed in all samples, suggesting the existence of unreacted Mo-O bond and the oxidation of MoS_2 surfaces exposed to air [5,10-11].

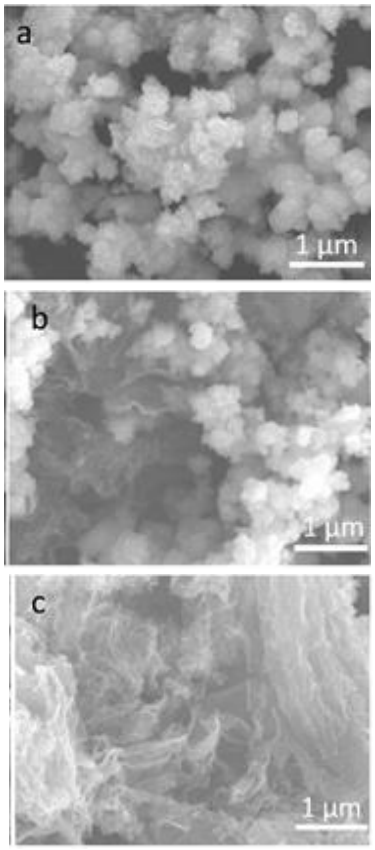

Fig. 2. SEM images of MoS_2, MoS_2/rGO-25, and MoS_2/rGO-10

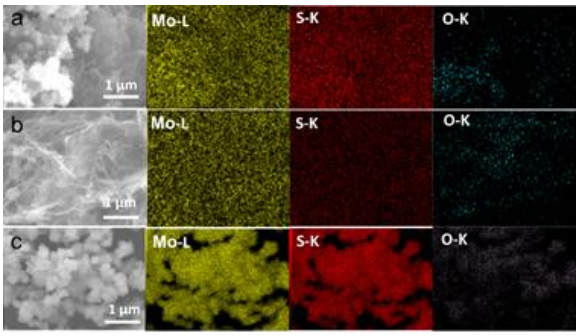

Fig. 3. Elemental mapping of MoS_2/rGO-25, MoS_2/rGO-10, and MoS_2

4. Conclusions

In summary, the MoS_2/rGO composites have been successfully synthesized using a facile hydrothermal method. XRD patterns confirmed that the interlayer spacing of all samples has been expanded from 0.62 nm to about 0.89 nm. Raman spectra and SEM images revealed that the MoS_2 nanoclusters are dispersed and anchored on the rGO nanosheets. Further studies are needed to understand the

mechanism of the formation of the expanded interlayer MoS_2 nanosheets and optimize the synthesis conditions.

Acknowledgement
This study was supported by Danang University of Science and Technology – The University of Danang under the Research Grant. Number T2021-02-10. Authors would like to thank researchers from the Faculty of Physics of Danang University of Science and Education – The University of Danang for supports with materials characterization.

References:

[1] X. Huang, M. Leng, W. Xiao, M. Li, J. Ding, T.L. Tan, W.S.V. Lee, J. Xue, Adv. Funct. Mater., 27, 1604943 (2017).
[2] C. Liu, D. Kong, P.C. Hsu, H. Yuan, H.W. Lee, Y. Liu, H. Wang, S. Wang, K. Yan, D. Lin, P.A. Maraccini, K.M. Parker, A.B. Boehm, Y. Cui, Nat. Nanotechnol., 11, 1098-1104 (2016)
[3] J. Liu, N. Gong, W. Peng, Y. Li, F. Zhang, X. Fan, Chem. Eng. J., 428, 130981 (2022).
[4] R. Wang, S. Gao, K. Wang, M. Zhou, S. Cheng, K. Jiang, Sci. Rep., 7, 1-9 (2017).
[5] X. Yu, G. Zhao, H. Huang, C. Liu, P. Lyu, N. Zhang, Chem. Eng. J., 428, 131214 (2022).
[6] H. Jia, M. Qiu, B. Tawiah, H. Liu, S. Fu, Compos. Commun., 27, 100841(2021).
[7] S. Li, Y. Liu, X. Zhao, Q. Shen, W. Zhao, Q. Tan, N. Zhang, P. Li, L. Jiao, X. Qu, Adv. Mater., 33, 2007480 (2021).
[8] W.S. Hummers, R.E. Offeman, J. Am. Chem. Soc., 80, 1339 (1958).
[9] J. Bai, B. Zhao, J. Zhou, J. Si, Z. Fang, K. Li, H. Ma, J. Dai, X. Zhu, Y. Sun, Small., 15, 1-11 (2019).
[10] J. Ye, W. Chen, S. Xu, Z. Yu, S. Hou, RSC Adv., 6, 104925–104932 (2016).
[11] J.D. Benck, Z. Chen, L.Y. Kuritzky, A.J. Forman, T.F. Jaramillo, ACS Catal., 2, 1916-1923 (2012).

Fabrication of Anodic Aluminum Oxide Templates

L.T.O. Pengson, M. Vasquez Jr*

Department of Mining, Metallurgical, and Materials Engineering, College of Engineering, University of the Philippines, Diliman

E-mail: lrpengson@up.edu.ph

I. Introduction

For the past years a lot of effort has been put into forming various kinds of nanomaterials. This is especially attractive due to different properties that nanomaterials exhibit as compared to the bulk version of the material. Each type of nanostructure formed can potentially be used for different kinds of applications in nanotechnology such as in alternative energy [1], nanoelectronics [2], biomedicine [3], and water treatment [4].

Among these nanostructures the synthesis rod shaped nanomaterials are particularly interesting for its applications in nano-electromechanical systems and devices. One such application is for zinc oxide (ZnO) where in having an ordered and uniform rod array can be characterized for gas sensing and piezoelectric applications [5].

Utilizing the pores produced by anodizing aluminum (Al), the produced anodic aluminum oxide (AAO) can be used as a low-cost template to ensure rod growth in an ordered fashion. In this study AAO was produced on top of a ZnO seed layer in preparation for rod growth.

II. Methodology

Glass substrates with a conductive indium tin oxide (ITO) film were cleaned using a standard degreasing process. ZnO films were reactively sputtered onto the ITO film for 1 h at 50 W with a 30:70 O_2 to Ar gas ratio where the working pressure is 0.7 Pa. Al films were then deposited onto the ZnO seed layer for 30 min at 100 W using a Radio Frequency (RF) magnetron system. The Al layer was then anodized for 1, 2, and 3 min, and a varying anodization voltage of 10, 20, and 30 V at 5°C in a 0.3M oxalic acid solution.

III. Results and Discussion

Before proceeding to the full layer sample of Al/ZnO/ITO/Glass, samples with layers of Al/ZnO/Glass were first tested for varying anodization voltages to confirm if the anodization process would have a detrimental effect on the underlying ZnO layer.

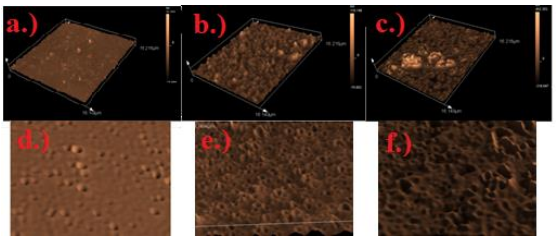

Fig. 1. 3D profile using an optical profilometer; a.)10V b.) 20V, c.) 30V; Surface image d.)10V e.) 20V, f.) 30V.

The Al layer of the samples were anodized in a 0.3 M oxalic acid solution for 1 min under varying anodization voltages. In Fig. 1 at 10 V the progression of the pore formation is too slow due to the low input power for the reaction. At 20 and 30V the pore formation is more pronounced due to the higher input.

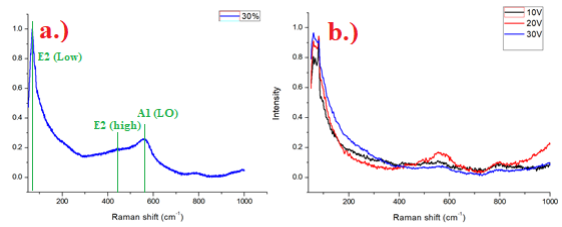

Fig. 2. Raman spectra; a.) ZnO reactively sputtered in a 30:70 O_2:Ar environment, b.) AAO/ZnO layer

From Fig. 2a the raman spectra of the ZnO layer is distinct with the E2 (Low), E2 (high), and A1 (LO) peaks present. After anodization the same peaks are still present in Fig. 2b. This shows that the ZnO layer survives after the anodization process and that this is a viable process for creating an AAO template on top of an existing layer.

After confirming the viability of anodizing a top Al layer deposited over other existing layers, the Al layer of the Al/ZnO/ITO/Glass samples were anodized in a 0.3 M oxalic acid solution for 1, 2, and 3 min at 30V.

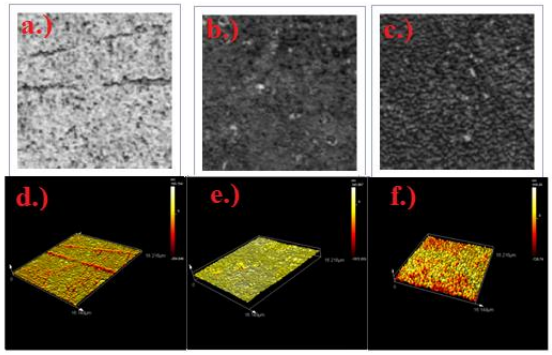

Fig. 3. Images and 3D profile using Optical Profilometer; Intensity map a.)1 min, b.) 2 min, c.) 3min; 3D profile d.) 1 min, e.) 2 min, f.) 3min.

As it can be seen in Fig. 3, as the time increases the anodization progresses until the template is formed.

Table 1. Surface roughness of AAO samples.

	1min	2min	3min
Sa (roughness)	23.098 ± 3.387nm	54.514 ± 15.845nm	108.758 ± 20.16nm

At 1 min we are past the barrier formation stage with initial pore initiation which explains why the surface roughness is only around 23 nm. At 2 min in can be seen that the pores are much deeper which suggests that we are at the steady pore growth phase of anodization this also coincides with the increase in surface roughness of the sample. At the 3 min mark we approach the end of the anodization step where most of the pores are through holes reaching ZnO layer underneath.

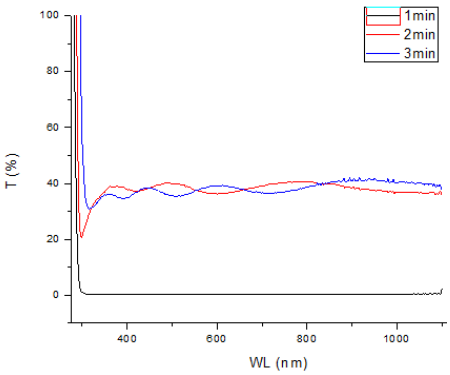

Fig. 4. UV-Vis transmittance spectra of AAO/ZnO/ITO/Glass samples.

For the 1 min sample it is evident that there is no transmission, which again supports the fact that the Al layer is still at the pore initiation stage and there are no through hole pores present. For the 2 min and 3min samples that transmittance increases to 40%. The values of transmittance are the same most likely due to through hole pores being present in both samples. The difference is that more pores are present in the 3 min sample and uniformly ordered.

IV. Conclusion

AAO can be anodized on top of an existing oxide layer in preparation for nanorod growth. Samples consisting of multiple layers AAO/ZnO/ITO/Glass were successfully synthesized. The samples also have some level of transparency since individually Glass and ITO are transparent and ZnO and AAO can be transparent depending on the synthesis method.

V. Acknowledgement

We would like to acknowledge the Nanoquench Project for the Raman Spectroscopy, the Discovery-Applied Research and Extension for Trans/Interdisciplinary Opportunities (DARETO) Project for the UV-vis Spectroscopy and the Vibrational Energy Harvesters for Resilient Sensor Nodes (VERSe) Project for the use of the optical profilometer.

References:

[1] A. Moezzi, A.M. McDonagh, M.B. Cortie: Zinc oxide particles: Synthesis, properties and applications, Chemical Engineering Journal Volumes 185–186, (2012) Pages 1-22

[2] G.R. Patzke, F. Krumeich, R. Nesper:Oxidic nanotubes and nanorods-Anisotropic modules for a future nanotechnology. Angewandte Chemie International Edition. (2002) 41:2446-2461

[3] J. Perez-Juste, I. Pastoriza-Santos, L. M. Liz-Marzan, and P. Mulvaney: Gold nanorods: Synthesis, characterization and applications. Coord. Chem. Rev. 249, 1870 (2005)

[4] S.P. Albu, A. Ghicov, J.M. Macak, R. Hahn, P. Schmuki: Self-organized, free-standing TiO2 nanotube membrane for flow through photocatalytic applications. Nano Lett. 7, (2007) 1286e1289

[5] M.S. Al-Ruqeishi, T. Mohiuddin, B. Al-Habsi, F. Al-Ruqeishi, A. Al-Fahdi, A. AlKhusaibi: Piezoelectric nanogenerator based on ZnO nanorods Arabian Journal of Chemistry (2017)

Carrier gas type dependence of Ga_2O_3 thin film grown by mist Chemical Vapor Deposition

R. Yamada[1*], S. Takahashi[1], A. Sekiguchi[2], T. Onuma[1], T. Honda[1], and T. Yamaguchi[1]**
[1]Department of Electronic Engineering and Electronics, Graduate School of Engineering, Kogakuin University, Tokyo, Japan
[2]Education Support Functions, Kogakuin University, Tokyo, Japan
[*]E-mail: cm21057@ns.kogakuin.ac.jp, [**]E-mail: t-yamaguchi@cc.kogakuin.ac.jp

Abstract

Gallium oxide (Ga_2O_3) has been attracted attention as a widegap semiconductor material for electrical and optical devices. The growth of high-quality α-Ga_2O_3 film is possible by mist chemical vapor deposition (mist CVD). In this study, influences of HCl as well as carrier gas type (O_2 or N_2) on the mist CVD growth of Ga_2O_3 on α-Al_2O_3 substrate were investigated. The importance of carrier gas type for the growth kinetics was confirmed from the viewpoint of redox reaction, especially at high HCl concentration region.

Introduction

Recently, gallium oxide (Ga_2O_3) has been focused as a widegap semiconductor material for electrical and optical devices such as deep ultraviolet detectors [1], metal-oxide-semiconductor field-effect transistor [2] and Schottky barrier diode [3]. Ga_2O_3 has six different crystal structures, α-, β-, γ-, δ-, ε-, and κ-phases [4]. Among six different crystal structures, we focused on α-phase. α-Ga_2O_3 is a metastable phase. The band gap energy of α-Ga_2O_3 is about 5.3 eV, which is the largest among the polymorphs. High quality α-Ga_2O_3 has been obtained by mist chemical vapor deposition (mist CVD) growth method [5].

Mist CVD is a growth technique working at atmospheric pressure. Mist is generated by ultrasonic transducer to atomize source solution and it is transferred to growth furnace by a carrier gas. Against the accomplishments in the successful growth of high quality α-Ga_2O_3 by mist CVD method, the growth mechanism has not fully clarified yet. We have used a small amount of HCl to enhance dissolution of source precursor. We have found that HCl not only enhanced the dissolution of source precursor but also gave significant impact on growth rate [6]. This result indicates that adding to a tiny amount of HCl into source solution is one of key factors for the growth of Ga_2O_3 film.

In this study, in addition to the impact of HCl, the impact of carrier gas type (O_2 or N_2) in the mist CVD growth of Ga_2O_3 on α-Al_2O_3 substrate was investigated.

Experiments

Ga_2O_3 thin films were grown for 1 hour on (0001)α-Al_2O_3 substrates by mist CVD. Tris(2,4-pentanedionato) gallium (III) ($Ga(C_5H_7O_2)_3$) was used as a source precursor. The precursor was first dissolved in deionized water to prepare a solution with precursor concentration of 0.05 mol/L, then 36% HCl was added so as to vary the HCl concentration from 0.10 mol/L to 0.47 mol/L. The growth temperature was set to be 460°C. The precursor solution was atomized by an ultrasonic transducer with a frequency of 2.4 MHz, and the aerosol was transferred to the substrate using oxygen or nitrogen gas. Surface morphology and film thickness were evaluated using scanning electron microscopy (SEM).

Results and Discussion

Figure 1 shows surface SEM images of Ga_2O_3 films grown at different carrier gas type (O_2 or N_2) and HCl concentrations of 0.10-0.47 mol/L. From these results, we found that the grain size became larger with increasing HCl concentration. These results suggest that surface migration is enhanced with the increase in HCl concentration. At high HCl concentrations, surface etching was confirmed for the samples grown with N_2 carrier gas. Figure 2 shows film thickness of Ga_2O_3 films as functions of HCl concentration and carrier gas type. Regardless of carrier gas type, film thickness was constantly increased with the increase of HCl concentration at low concentration region. At high HCl concentration region, on the other hand, a large difference of film thickness was observed depending on carrier gas type. The importance of carrier gas type for the growth kinetics was thus confirmed, especially at high HCl concentration region.

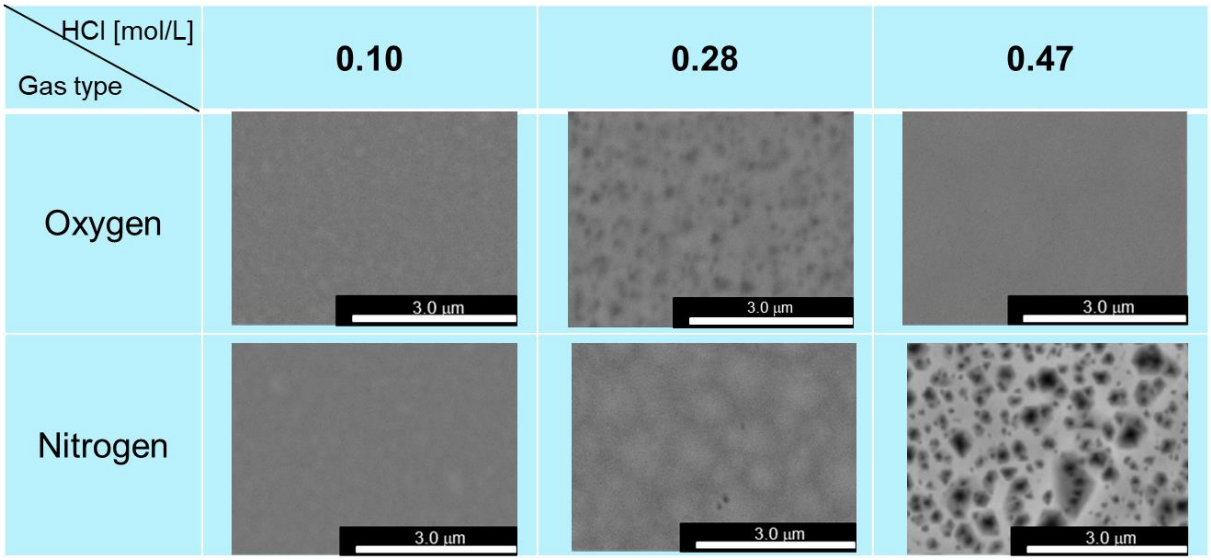

Fig. 1. Surface SEM images for Ga_2O_3 films grown with carrier gas type (N_2 or O_2) and various HCl concentration.

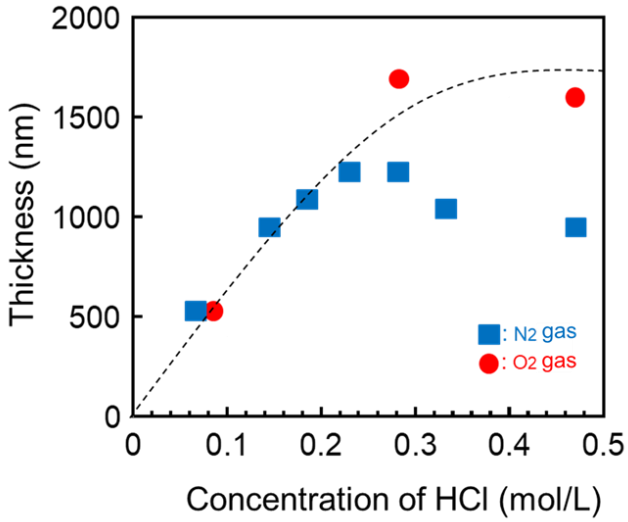

Fig. 2. Film thickness of Ga_2O_3 films grown at 460°C as functions of HCl concentration and carrier gas type.

Summary

In this study, influences of HCl as well as the carrier gas type on the mist CVD growth of Ga_2O_3 on α-Al_2O_3 substrate were investigated. The importance of carrier gas type for the growth kinetics was confirmed, especially at high HCl concentration region.

References:

[1] Y. Kokubun, K. Miura, F. Endo, and S. Nakagomi, Appl. Phys. Lett. **90**, 031912 (2007).
[2] News release, https://flosfia. com/20180713/.
[3] M. Oda, R. Tokuda, H. Kambara, T. Tanikawa, T. Sasaki, and T. Hitora, Appl. Phys. Express **9**, 021101 (2016).
[4] F. P. Sabino, Luiz Nunes de Oliveira, and Juarez L. F. Da Silva, Phys. Rev. B **90**, 155206 (2014).
[5] K. Akaiwa and S. Fujita, Jpn. J. Appl. Phys. **51**, 070203 (2012).
[6] S. Takahashi, K. Rikitake, T. Yamaguchi, H. Nagai, M. Sato, T. Onuma and T. Honda, JACG, 11th Division of Nanocrystalline Materials & Epitaxial Crystal Growth, Hiroshima Univ., Higashi Hiroshima Campas, Hiroshima (June 13-15, 2019), #Fr-P6.

A Study on Smart Fluid Technology and its Applications in Haptics

Aaron Raymond A. See and Kohila Chandramohan
Department of Electrical Engineering, Southern Taiwan University of Science and Technology, Tainan, Taiwan.
E-mail: aaronsee@stust.edu.tw

Abstract

In recent years increase interest in haptics research arose due to its numerous applications. For the haptic devices in the field of virtual reality, it is in a need to create realistic sensations of tactile and kinesthetic movements. A device with large size, poor dynamics, high inertia, and heavy weight can significantly affect the performance in rendering realistic sensation and degrees of freedom. Most of the existing wearable haptic feedback systems use tactile stimulation by vibrating motors for haptic feedback which lack a compelling sense of immersion with force feedback. The objective of this study is to address these challenges by revealing soft actuators in which the smart controllable fluids like Electrorheological (ER) fluid and magnetorheological (MR) fluid play a major role. These smart fluids are capable of transforming from liquid state to solid state in milliseconds due to its viscoelastic property under the controlled flow of electric and magnetic field respectively. Unlike electrostatic and electromagnetic motors, the soft actuators do not require any bulk hardware like motors, brakes, and clutches. It consists of thin elastomers, flexible electrodes, and controllable fluids for actuation. The mechanical properties of elastomers are close to that of human skin, allowing a more natural feel and interaction than using an external compressor and motor fixed glove. These fluids significantly contribute to improved stability and transparency of haptic devices. Due to its stability and transparency, MR and ER fluids have the application in sensitive domains like teleoperation in the medical field. As fluid technology continues to gain attention, the research and development of these fluids must keep pace. This review study covers the ER and MR fluid technology, its working modes, and its wide range of applications.

The magnetorheological (MR) fluids are basically non colloidal suspensions of micro sized magnetic particles in an inert base fluid along with surfactants to avoid sedimentation [1]. There are basically three components in an MR fluid [2], the base fluid, metal particles, and stabilizing additives.

A. Base fluid

The metal particles are suspended in a non-magnetic carrier fluid called the base fluid. The base fluid has natural lubrication and damping properties. The base fluids normally have low viscosity and are independent of temperature changes. When the magnetic field is applied to the MR fluid, the yield stress will make the base fluid thicker due to the presence of suspended ferromagnetic particles [3]. Commonly used base fluids are organic or aqueous liquids such as petroleum-based, synthetic hydrocarbon oils, mineral oils and Silicone oils.

B. Metal particles

For proper utilization of this magnetorheological technology, particles are chosen for their ability to achieve high magnetic saturation, allowing them to form a strong magnetizing chain. Therefore, the ferromagnetic or ferrimagnetic particles such as carbonyl iron, powder iron, iron cobalt alloys, nickel, cobalt, and ceramic ferrites are used. Those particles used in the MR- technology are micro sized. Size of the particle is approximately in the order of 1μm to 20μm [1].

C. Additives

The additives are required to control the viscosity of the liquid and the settling rate of the particles. These additives include stabilizers and surfactants[4]. Surfactants reduce the rate at which metal particles settle. Commonly used surfactants are oleic acid, tetramethylammonium hydroxide, citric acid, and soy lecithin, which serve to decline the rate of ferro particle settling in MR fluid [5]. Highly viscous materials such as grease or other thixotropic additives are used to improve settling stability [6]. Ferrous naphthenate and ferrous oleate can be used as dispersants. Metal soaps such as lithium stearate and sodium stearate as thixotropic additives [7]. Other roles of the additives include maintaining friction between metal particles and reducing the rate of fluid thickening due to long-term use and serves for anti-corrosion, thus the additives are importantly considered for the life of MR fluid.

Table 1. MR fluid versus ferrofluid [9].

Representative feature	MR fluid	Ferro fluid
Energy factor k	>1	<1
Maximum yield stress	100 kPa	10 kPa
Particle size	Some μm	Some nm
Particle material	Carbonyl iron	Iron oxide
Fraction by volume	Up to 50%	Up to 10%
Stability	Medium	Good
Functionality	Controllable shear stress	Controllable liquid flow

The magnetorheological behavior of an MR fluid is determined by all three components. The magnetorheological properties of the MR fluid will vary if any one component is changed. It is vital to have the best possible mix of all three elements. Because of differences in both the quality and quantity of metal particles, the magnetorheological behavior of MR fluids and ferrofluids differs [9]. Iron particles, a base fluid, and additives are all present in both. The size, number, and quality of the iron particles are the key differences. The iron particles in MR fluids are micrometer-sized. The iron oxide particles in ferrofluids are significantly smaller, around 30 nm [8,9]. The comparison of representative features is shown in Table 1.

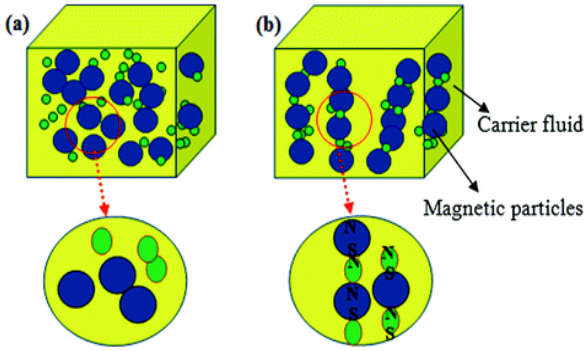

Fig. 1. a) Magnetic particle arrangement in the absence of a magnetic field (liquid-like) b) in the presence of an externally applied field (solid-like) [11]

In the absence of magnetic field, the magnetizable particles in the MR fluid are randomly suspended in the base fluid as shown in Fig. 1. a). On the other hand, When a magnetic field is applied, the magnetic particles interact and form chains-like structures due to dipole–dipole interactions (magnetic–polarization interaction) between particles in the direction of the applied magnetic field (as shown in Fig. 1. b). In this situation, the MR fluids would change from liquid to semi-solid or plastic in a millisecond. Simply put, the fluid flow is inhibited by the chain-like formation between particles, and the MR fluid has a viscoplastic behavior as measured by field-dependent yield stress. [11]

The MR fluid devices are normally intended to work in valve mode, shear mode, or squeeze mode, depending on the type of deformation used, function, and type of fluid flow [2]. These fluids greatly increase its apparent viscosity, to the point of becoming a viscoelastic solid from liquid state. In valve mode (fixed plate mode), the magnetic field is applied perpendicular to alter the viscosity of MR fluid which is located between the two static plates as shown in the Fig. 2 and this mode is used in commercial applications such as dampers for knee prosthesis, vibration dampers, seismic dampers for civil industry, active engine mounts and prop shaft mounts [8].

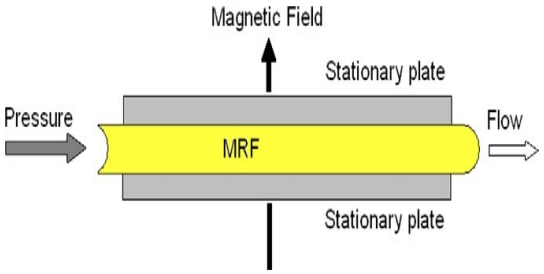

Fig. 2. Valve mode [8]

In shear mode (clutch mode), commonly known as direct shear mode, which is opposite to valve mode, the MR fluid flows between two plates or surfaces that have relative motion to each other as shown in Fig. 3. The applied magnetic field is in the same direction as the valve mode [8]. The applications of this mode are brakes, clutches, dampers and structural composites, and chucking and locking devices [11].

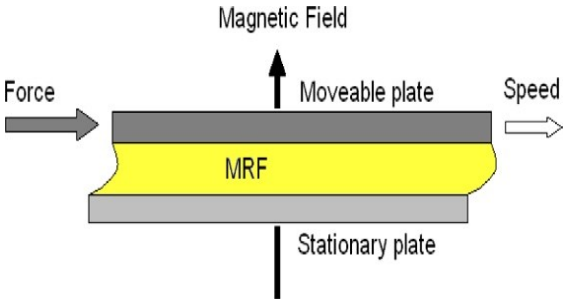

Fig. 3. Shear mode [8]

In squeeze mode (compression mode), the MR fluid flow between the two plates that are moving in a direction that is perpendicular to the planes [10]. It works by decreasing or expanding the spacing between parallel plates when a force is applied in the same direction as the magnetic field, resulting in squeezing flow of the fluid as shown in Fig. 4. The applied magnetic field to the MR fluid is in the same direction as the valve mode to change the MR fluid viscosity and, as a result, control the flow and create force [11]. The acting force is aligned with the particle chains and magnetic flux lines in this operational mode. In this mode, MR fluid devices often have little or no MR fluid flow due to the devices' construction. As a result, this mode is typically used in applications with minimal motion and high force [12]. This mode has fewer applications and is only employed in small-amplitude vibration and impact dampers [13]. The yield stress generated by this mode is around ten

times that generated by either the valve or the shear modes [2].

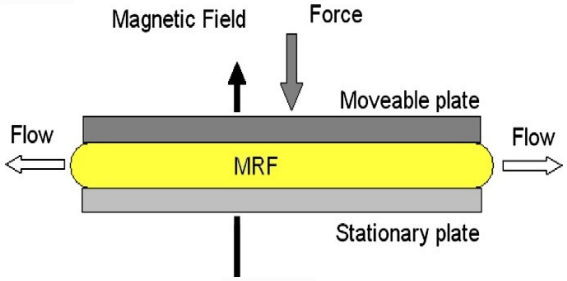

Fig. 4. squeeze *mode* [8]

Similar to MR fluids, The Electrorheological (ER) fluids are composed of solid particles suspended in nonpolar liquids. General particles used in preparing ER fluids are silica, titania, zeolites and the medium used in preparing ERF are silicone oil, mineral oil and castor oil. Size of the particle is approximately of the order of 1µm to 7µm. ER fluids are also able to change its viscosity when applying electric field. Like MR fluid, ER fluid features response times in the order of milliseconds, low power consumption [14].

Rather than MRF and ERF, simple dielectric fluids like silicon oil and mineral oils are also used and had better results in haptic actuation [15-17]. Hundreds of soft actuators on the skin of the fingers and palm are required for a haptic device to produce a believable feeling of touch, but these thin actuators must all be conveniently integrated into a glove or other wearable. Elastomers have mechanical qualities similar to human skin, providing for a more natural sensation and contact than an external compressor and motor-driven glove. Dielectric elastomer actuators (DEA) are soft actuators that deform elastomers using electrostatic forces [18]. They can be fabricated as arrays of addressable taxels [19,20] and as soft wearable interfaces [21]. Hydraulically amplified self-healing electrostatic (HASEL) devices use liquid dielectric instead of elastomers to provide integrated hydraulic amplification [22]. Peano-HASEL is a dielectric material with a high permittivity that is manufactured with inextensible shells and does not require stretchable electrodes. [16].

Haxel (HAXEL) is a hydraulically amplified taxel that allows for dense and adaptable cutaneous haptic feedback. HAXELs are constructed up of a fluid-filled hollow surrounded by a non-stretchable polymer shell on the periphery and bottom, and an elastomer center region on the top. The inextensible polymer contains electrodes [15]. When a voltage is placed between electrodes, the electrostatic pressure causes the fluid to zip, producing a big bump in the elastic central region as shown in Fig. 5. Similar to HAXEL, A. K. Han, et al., developed a miniature dielectric fluid transducer that is compliant and lightweight, and also capable of creating a maximum bump height of 1.45 mm and fast response of 50ms for 90% rise in bump height according to the voltage applied as shown in the Fig.6 [17]. These actuators can be arranged to create a compact multi-element array of controllable bumps. The array is intended primarily as a texture display, which users would explore using back-and-forth motions of the fingers.

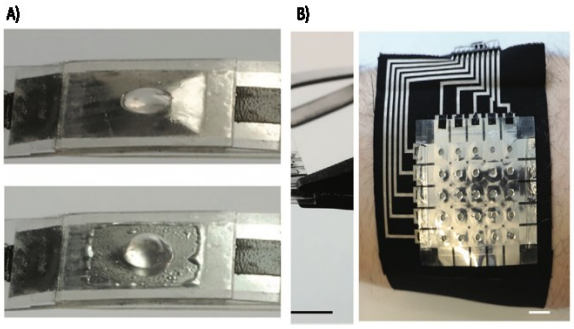

Fig. 5. A) HAXEL actuator in off-state (upper image) and actuated states (lower image) B) On a textile sleeve, a flexible HAXEL array is incorporated [15].

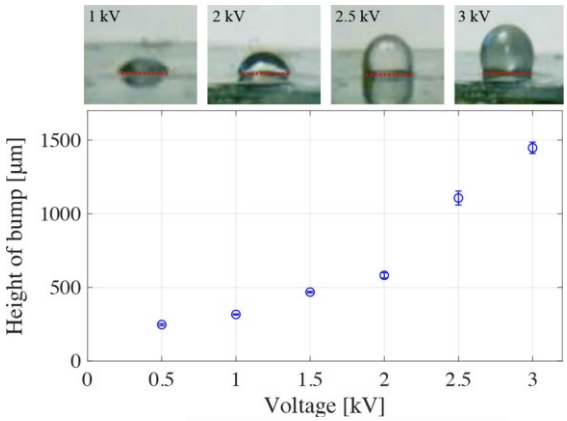

Fig. 6. Fluid bumps at different heights on various applied voltages [17].

Haptic applications like small consumer electronic products, the display units generally require miniaturization of tactile and kinesthetic modules. To minimize the size of kinesthetic actuators for hand-held device applications, the miniature tunable stiffness display actuated by MR fluids were designed [23]. The display is fabricated using MEMS technology and the three operating modes of MR fluids are used to maximize the resistive force. The stiffness change rate is measured nearly 30%, which is sufficient to create a stiffness sensation. These smart fluids are not only used for rendering haptic sensation in hands and fingers but also in foot. RealWalk achieves a novel interaction between the shoes and the ground surfaces while walking in Virtual world by using MR fluid actuators [24]. When a user steps on the ground in virtual environment with the shoes, the MR fluid actuators are depressed and changing its viscosity where its state is changed rapidly from liquid to solid and thus making the user could feel the variety of ground

Table 2. Various haptic devices using the smart fluid technologies are listed

Devices	Fluids used	haptic Feedback	working	Result
Haxel by Edouard et al., [15]	dielectric oil (Cargill Envirotemp FR3)	Tactile response	Electrostatic pressure leads to a zipping motion, pushing the fluid into a large bump	740 µm lateral displacement and 380 µm out-of-plane displacement
Haptic actuator by Mazursky et al., [14]	ER fluid	Both tactile and kinesthetic response	The actuator operates in pressure driven flow mode and the liquid–solid transition generates a yield stress with magnitude corresponding to the supplied voltage.	maximum force is about 2.5 N at 0 kV (off-state) and 3.6 N at 4kV DC
Soft robotic glove by Jadhav et al., [26]	Not mentioned	Kinesthetic response	Bell-crank lever mechanism for the soft actuation using Mckibben muscles	force of 16.66N at the pressure of 210 kPa
Miniature MR Fluid actuator by Savioz et al., [27]	MR Fluid-122EG	In the range of Hand kinesthetic response	Current in the coil induces the magnetic flux and produces yield stress in MR fluid enough to raise the piston.	force of 7.5 N at the current of 0.5 A and 10-12 mm of displacement
stiffness display by Tae-Heon et al., [23]	MR fluid	Kinesthetic response	MR fluid flow is controlled by the different modes (valve, shear and squeeze modes) The overflowing fluids make the PDMS membrane swollen.	Force of 5.9 N with the input current of 0 A, 7.5 N with the input current of 0.015 A, and 8.6 N with the input current of 0.03 A in the indented depth 1.5 mm.
Twin-driven actuator by Kikuchi et al., [28]	Compared the commercially available MR fluids (122EG, 132DG, and 140CG)	-	The twin-driven mechanism is used to reduce the basic friction of the actuators, and two multi-layered disc-type MR fluid clutches are used	torque error of 0.033 Nm for link type and 0.068 Nm for belt type 140CG is the best material, if maximum torque is required. 132DG is a better material for force control

Fig. 7. A person wearing RealWalk shoes experiences various types of land deformations in virtual [25]

material deformation such as snow, mud, and dry sand as shown in the fig. 7. The magnetic field intensity is designed to change based on the ground material in the virtual scene [25]. Various haptic devices using the smart fluid technologies are listed in table 2.

References:

[1] Park, Jong-Hyeok, and O-Ok Park. "Electrorheology and magnetorheology." *Korea-Australia Rheology Journal* 13.1 (2001): 13-17.

[2] Baranwal, Deepak, and T. S. Deshmukh. "MR-fluid technology and its application-a review." *International Journal of Emerging Technology and Advanced Engineering* 2.12 (2012): 563-569.

[3] Lord Corporation, Dr. Dave's Do-It-Yourself MR Fluid, Designing with MR Fluid, Magnetic Circuit Design, FAQs, Fluid specifications, 2006, www.lord.com.

[4] Huang J, Zhang JQ, Yang Y, Wei YQ. Analysis and design of a cylindrical magnetorheological fluid brake. J Mater Process Technol 2002;129:559–62.

[5] Ahamed, Raju, Seung-Bok Choi, and Md Meftahul Ferdaus. "A state of art on magneto-rheological materials and their potential applications." *Journal of Intelligent Material Systems and Structures* 29.10 (2018): 2051-2095.

[6] Magnetic fluid clutch, Technical news bulletin, National Bureau of Standards, 32/4 (1948), p. 54–60.

[7] [14] Wislow W. Field responsive fluid couplings, US Patent No. 2.886.151, 1959.

[8] Olabi, Abdul-Ghani, and Artur Grunwald. "Design and application of magneto-rheological fluid." *Materials & design* 28.10 (2007): 2658-2664.

[9] Vékás, Ladislau. "Ferrofluids and magnetorheological fluids." *Advances in science and technology*. Vol. 54. Trans Tech Publications Ltd, 2008.

[10] Najmaei, Nima, Mehrdad R. Kermani, and Rajni V. Patel. "Suitability of small-scale magnetorheological fluid-based clutches in haptic interfaces for improved performance." *IEEE/ASME Transactions on Mechatronics* 20.4 (2014): 1863-1874.

[11] Hajalilou, Abdollah, et al. "Models and Modes in MR Fluids." *Field Responsive Fluids as Smart Materials*. Springer, Singapore, 2016. 51-65.

[12] Carlson, J.D.: Magnetorheological fluid actuators. In: Janocha, H. (eds.) Adaptronics and Smart Structures, pp. 180–195. Springer, Berlin. ISBN 3-540-61484-2 (1999)

[13] Zhu, X., Jing, X., Cheng, L.: Magnetorheological fluid dampers: a review on structure design and analysis. J. Intell. Mater. Syst. Struct. **23**, 839–873 (2012)

[14] Mazursky, Alex, Jeong-Hoi Koo, and Tae-Heon Yang. "Design, modeling, and evaluation of a slim haptic actuator based on electrorheological fluid." *Journal of Intelligent Material Systems and Structures* 30.17 (2019): 2521-2533.

[15] Leroy, Edouard, Ronan Hinchet, and Herbert Shea. "Multimode hydraulically amplified electrostatic actuators for wearable haptics." *Advanced Materials* 32.36 (2020): 2002564.

[16] Kellaris, Nicholas, et al. "Peano-HASEL actuators: Muscle-mimetic, electrohydraulic transducers that linearly contract on activation." *Science Robotics* 3.14 (2018): eaar3276.

[17] Han, Amy Kyungwon, et al. "Haptic surface display based on miniature dielectric fluid transducers." *IEEE Robotics and Automation Letters* 5.3 (2020): 4021-4027.

[18] Pelrine, Ron, et al. "High-speed electrically actuated elastomers with strain greater than 100%." *Science* 287.5454 (2000): 836-839.

[19] Lee, Hyung Seok, et al. "Design analysis and fabrication of arrayed tactile display based on dielectric elastomer actuator." *Sensors and Actuators A: Physical* 205 (2014): 191-198.

[20] Marette, Alexis, et al. "Flexible zinc–tin oxide thin film transistors operating at 1 kV for integrated switching of dielectric elastomer actuators arrays." *Advanced materials* 29.30 (2017): 1700880.

[21] Mun, Seongcheol, et al. "Electro-active polymer based soft tactile interface for wearable devices." *IEEE transactions on haptics* 11.1 (2018): 15-21.

[22] Acome, Eric, et al. "Hydraulically amplified self-healing electrostatic actuators with muscle-like performance." *Science* 359.6371 (2018): 61-65.

[23] Yang, Tae-Heon, et al. "Development of a miniature tunable stiffness display using MR fluids for haptic application." *Sensors and Actuators A: Physical* 163.1 (2010): 180-190.

[24] Son, Hyungki, et al. "Realwalk: Haptic shoes using actuated mr fluid for walking in vr." *2019 IEEE World Haptics Conference (WHC)*. IEEE, 2019.

[25] Yang, Tae-Heon, et al. "Magnetorheological Fluid Haptic Shoes for Walking in VR." *IEEE Transactions on Haptics* 14.1 (2020): 83-94.

[26] Jadhav, Saurabh, et al. "Soft robotic glove for kinesthetic haptic feedback in virtual reality environments." *Electronic Imaging* 2017.3 (2017): 19-24.

[27] Savioz, Gregory, Valerian Ruchet, and Yves Perriard. "Study of a miniature magnetorheological fluid actuator for haptic devices." *2010 IEEE/ASME International Conference on Advanced Intelligent Mechatronics*. IEEE, 2010.

[28] Kikuchi, Takehito, et al. "Twin-driven actuator with multi-layered disc magnetorheological fluid clutches for haptics." *Journal of Intelligent Material Systems and Structures* 32.12 (2021): 1326-1335.

Growth of GaInN multi quantum well on strain-controlled layer by RF-MBE toward realization of light emitting diodes operating in red spectral region

M. Matsuda*[,1], R. Yoshida[1], K. Tahara[1], T. Yamaguchi[1,2], T. Onuma[1,2], and T. Honda[1,2]

[1]Department of Electrical Engineering and Electronics, Graduate School of Engineering, Kogakuin University, Tokyo, Japan
[2]Department of Applied Physics, School of Advanced Engineering, Kogakuin University, Tokyo, Japan
[*]E-mail: cm21047@ns.kogakuin.ac.jp

-Abstract-

The impact on $Ga_{1-y}In_yN$ underlayer (UL) for $Ga_{1-x}In_xN/Ga_{1-y}In_yN$ (x>y) multi quantum wells (MQWs) with high In composition grown by radio-frequency plasma-assisted molecular beam epitaxy (RF-MBE) was investigated. We observed a strong photoluminescence (PL) emission at 2.15 eV from the GaInN MQW on $Ga_{1-y}In_yN$ UL, though a broad peak at 1.40 eV~2.30 eV was observed for the MQW grown on the GaN UL. Therefore, the use of $Ga_{1-y}In_yN$ UL was found to contribute for improvement of performance of GaInN nitride-based red LEDs.

-Introduction-

GaInN ternary alloy is composed of InN and GaN binaries with bandgap energies varying from 0.7 eV to 3.4 eV at room temperature [1]. Commercialized blue light emitting diodes (LEDs) generally employ GaInN/GaN multiple quantum wells (MQWs) for their junction layer. However, the luminous efficacy degrades enormously as we increase the In composition due mainly to the quantum confined stark effect (QCSE) in the compressively strained MQWs. To overcome the issue and to establish improved-performance GaInN nitride-based red LEDs, $Ga_{1-x}In_xN/Ga_{1-y}In_yN$ (x>y) MQWs are promising candidates by virtue of their reduced lattice mismatch between the barrier and well layers [2]. However, the use of GaN UL degrades their emission efficiency. To take advantage of the use the $Ga_{1-x}In_xN/Ga_{1-y}In_yN$ MQWs, growth of thick $Ga_{1-y}In_yN$ UL having the same In composition with the barrier layer is indispensable. In this study, we grew the $Ga_{1-x}In_xN/Ga_{1-y}In_yN$ MQWs on $Ga_{1-y}In_yN$ UL by RF-MBE. Thier crystallinity and emission properties were studied by comparing the results for the $Ga_{1-x}In_xN/Ga_{1-y}In_yN$ MQWs grown on the GaN UL.

-Experiment-

An approximately 400-nm-thick $Ga_{1-y}In_yN$ film was grown by RF-MBE as an UL on the commercially available GaN/AlN/Al_2O_3 templates. The $Ga_{1-y}In_yN$ UL was grown at 680°C (monitored by a thermocouple) for 60 min. Subsequently, 5 periods of 2-nm-thick $Ga_{1-x}In_xN$/5-nm-thick $Ga_{1-y}In_yN$ MQWs were grown at 540℃ with fixed Ga/In flux ratio, nitrogen gas flow rate, and RF plasma power. $Ga_{1-x}In_xN$ wells ($Ga_{1-y}In_yN$ barriers) were grown for 15 sec. (45 sec.) with RF plasma power of 240 W (200 W), respectively. The samples were characterized by X-ray diffraction (XRD) and PL measurements. The PL was excited by the GaInN laser operating at 405 nm with an excitation power of 140 mW.

-Results and Discussion-

Figure 1 shows the XRD θ-2θ patterns near the (0002) diffraction peak measured for the MQW on GaN UL and MQW on GaInN UL. The pattern for the MQW on GaN UL exhibited apparent thickness fringes, indicating superior flatness of the surface and interface. Simulations for the experimental XRD patterns gave x=29% and y=22% for the $Ga_{1-x}In_xN/Ga_{1-y}In_yN$ MQW grown on the GaN UL, and x=48% and y=27% for the $Ga_{1-x}In_xN/Ga_{1-y}In_yN$ MQW grown on the $Ga_{1-y}In_yN$ UL. The simulation also gave the well thickness of 2.2 nm for the MQW on GaN UL, and 2.3 nm for the MQW on GaInN UL. Obviously, the MQW on GaN UL exhibited lower In composition due to the large lattice mismatch between the GaN and GaInN layers in the MQW. The PL spectra at 10 K are shown in Fig. 2. The MQW on GaN UL dominantly showed ruby luminescence at 1.74 eV and 1.79 eV from sapphire substrate [3]. The spectrum showed broad emission at 1.40 eV ~ 2.30 eV probably due to transition involving defect or impurity in the GaN UL. Unfortunately, PL from the MQW was not clearly observed reflecting the QCSE [4]. In contrast, MQW on GaInN UL showed a strong emission at 2.15 eV implying its superior emission property.

-Summary-

In conclusion, we grew the $Ga_{1-x}In_xN/Ga_{1-y}In_yN$ MQWs with high In composition on $Ga_{1-y}In_yN$ UL by RF-MBE. We observed a strong PL emission at 2.15 eV from the GaInN MQW on $Ga_{1-y}In_yN$ UL, though a broad peak at 1.40 eV~2.30 eV was observed for the MQW grown on the GaN UL. Therefore, the use of $Ga_{1-y}In_yN$ UL was found to contribute for improvement of performance of GaInN nitride-based red LEDs.

-Reference-

[1] J. Wu *et al.*, Appl. Phys. Lett. **80**, 3967 (2002).
[2] L. Zhang *et al.*, J. Appl. Phys. **51**, 030207 (2012).

[3] D. M. Adams *et al.*, J. Phys. E: Sci. Instrum. **9**, 1140 (1976).
[4] M. Auf der Maur *et al.*, Phys. Rev. Lett. **116**, 027401 (2016).

-Figures-

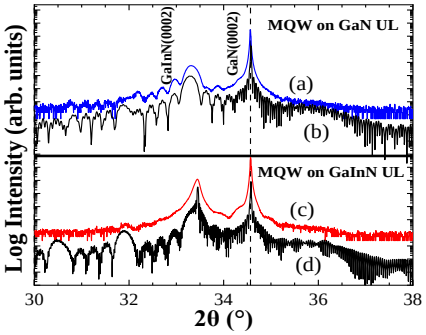

Fig. 1. (a)(c) Experimental and (b)(d) simulated XRD θ-2θ patterns.

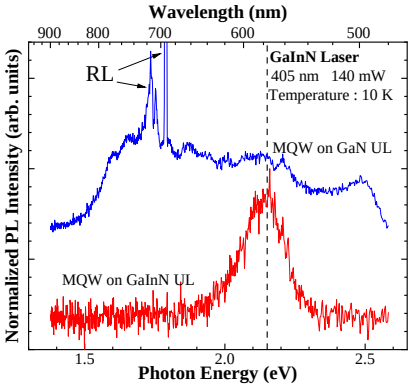

Fig. 2. PL spectra at 10 K of MQW on GaN UL and MQW on GaInN UL.

Fluorescent immune-biosensor on the glass biochip used for albumin detection

Ying-Nien,Chou* and Lien-Chiang,Hung

Department of Chemical and Materials Engineering, Southern Taiwan University of Science and Technology, Tainan, Taiwan
E-mail: ynchou@stust.edu.tw

Abstract

In this study, a glass-based fluorescent immunosensing chip was developed for rapid screening of recombinant urine protein. It combines surface self-assembly single-layer technology, and confirms the interface properties through the measurement of contact angle. And through the oxidation method to assist immunofluorescence sensing. This technology has the opportunity to become an effective urine protein sensing chip, and it is calibrated, accurate and fast. Through the optimization, manufacturing costs can be reduced again, and through cooperation with hospitals or government units around the world, it can be widely used to achieve early detection and early treatment effects.

The number of end-stage kidney disease in all countries is increasing. By 2020, the world's end-stage kidney disease population will exceed 2 million. The National Health Insurance Agency announced last year's top 10 most costly diseases. Chronic kidney disease burned NTD$53.3 billion a year and the number of kidney dialysis patients increased from 90,000 to 92,000.

The increase in the number of patients with end-stage renal disease is mainly from patients with diabetic nephropathy. It is estimated that by 2020, more than 80% of new cases will be from diabetic patients, and the number of diabetic nephropathy patients in the prevalence will also approach 60%. Among them, the content of urine protein in urine is a key indicator for determining kidney disease. The traditional quantitative detection of urine protein must be achieved through multi-step medical testing equipment, which is time-consuming and laborious and unfavorable for popularization.

Therefore, this research intends to develop a new type of glass substrate fluorescent immunosensing chip for rapid urine protein screening. This biochip uses a simple glass substrate as a chip carrier to specifically capture human protein by sandwich-type immune sensing. It uses fluorescent antibodies that can amplify the signal for fluorescent detection.

The first part is to modify the surface of the glass with the surface self-assembly monolayer technology. The pretreatment has a great influence on the monolayer film. When the wafer surface is cleaner, the monolayer film formed is denser. The change in the contact angle of the water droplets finds Optimize the modification conditions of APTES.

In the second part, the oxidation method is used to oxidize the primary antibody to bind the antibody to the amine group on the surface of the chip, detect the amount of protein adsorption through BCA, use the mechanism of antibody and antigen to grab the target, and then use the sandwich method of ELISA to connect to the secondary The antibody is connected to the tertiary antibody to strengthen the signal, and finally the fluorescence spectrum is used for quantitative analysis to know whether the patient has kidney disease problems.

Therefore, if patients with diabetes can actively control the development of chronic kidney disease and avoid the final stage of receiving dialysis treatment, it should effectively reduce the number of people receiving dialysis treatment for end-stage kidney disease. Even doctors can easily ignore it. A recent study published in the American Journal of Nephrology pointed out that many primary physicians cannot correctly diagnose kidney disease. The research suggests that the public should be more proactive in understanding the warning signs and undergo regular inspections. "Early detection is an important key to preventing or delaying chronic kidney disease."

CONCLUSIONS

This experiment develops a glass-based fluorescent immunosensing chip for rapid screening of recombinant urine protein.

The first part is to modify the surface of the glass with the surface self-assembly monolayer technology. The pretreatment has a great influence on the monolayer film. When the wafer surface is cleaner, the monolayer film formed is denser. The change in the contact angle of the water droplets finds Optimize the modification conditions of APTES.

In the second part, the oxidation method is used for primary antibody oxidation to bind the antibody to the amine group on the surface of the chip, detect the amount of protein adsorption through BCA, use the mechanism of antibody and antigen to grab the target, and then use the sandwich method of ELISA to connect to the secondary The antibody is connected to the tertiary antibody to strengthen the signal, and finally the fluorescence spectrum is used for quantitative analysis to find out whether the patient has kidney disease problems.

This experiment has the opportunity to become an effective urine protein test strip, which is calibrated, accurate and fast. After commercialization, the manufacturing cost can be reduced again, and through cooperation with hospitals or government units around the world, it can be widely used. Regardless of the gap between the rich and the poor or the regional problems, everyone can self-detect kidney disease to achieve early detection; Treatment; early healing effect.

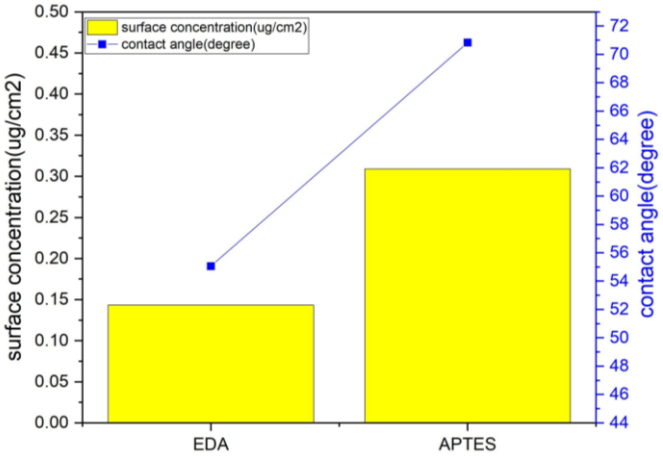

Figure 1. 1/500 BCA detects the difference between APTES and EDA

References:

[1] Schmidt SD, Mazzella MJ, Nixon RA, Mathews PM.(2012) "Aβ measurement by enzyme-linked immunosorbent assay. " Methods Mol Biol.2012;849:pp.507-527.

[2] Love, J. C., Estroff, L. A., Kriebel, J. K., Nuzzo, R. G., & Whitesides, G. M. (2005). Self-Assembled Monolayers of Thiolates on Metals as a Form of Nanotechnology. Chemical Reviews,105(4):pp.1103–1170.

[3] Weiland G.(1978),"Der Enzyme-Linked Immunosorbent assay (ELISA) [The enzyme-linked immunosorbent assay (ELISA)--a new serodiagnostic method for the detection of parasitic infections (author's transl)]."MMW Munch Med Wochenschr.3;120(44):pp.1457-1460

[4] Spence,Zachary (2018),"Biochemistry 8th ed - Jeremy M. Berg.":pp.83.

Home Energy Management System Considering Stationary Storage and Electrical Vehicle

Jeeng-Min Ling, Firoj Ismail Mulani*

Department of Electrical Engineering, Southern Taiwan University of Science and Technology, Tainan, Taiwan

*email: da82b205@stust.edu.tw

Abstract

To reduce the fossil fuel dependency and the gas emissions, Electrical Vehicles (EV) are used in recent years. The EVs are expected to be widely used in the Home Energy Management System (HEMS) infrastructures. HEMS is useful for minimizing the load on grid and optimal operation of a smart home in terms of minimizing the total energy cost. The main objective of this proposed study is to integrate the renewable energy sources (RES) and the grid with the electrical load and minimizing the overall cost of imported grid energy. Energy storage systems which includes stationary battery & EV battery can be charged during low demand period and stored power can be fed to home as well as grid during peak load hours.

Keywords: Electrical Vehicle, Home Energy Management System, Renewable Energy Sources

Introduction

Electric Vehicles (EVs) have grown in popularity over the last decade, with one of its main advantages being the reduction of greenhouse gas emissions in transportation networks. The charging load of electric vehicles powered by renewable energy sources can help to reduce transportation emissions even more. The photovoltaic (PV) powered EV technology has been reported to reduce greenhouse gas emissions by 47 to 78 percent, with the PV power feed-in rate and interest rate being utilized in policy making tools to promote low carbon transportation networks.

In the future, HEMS infrastructures and EVs are likely to be widely used in smart cities. Because several important users (i.e. RES, EVs, stationary batteries) are used in the EMS, it is necessary to govern the energy exchange between them. Also for accurately estimate of home electric demands, PV generation, EV and stationary battery storage is essential. For estimating the load demand & battery state, will have built a model which gives the information about the estimated parameters. These parameters are then useful in working of the EMS efficiently. The main function of this system is that the total buying cost from the grid is minimized, while at the same time the EV and the stationary battery is charged with the cheapest available energy.

Proposed System

Developing innovative techniques to lower a house or building's energy consumption while effectively integrating renewable energy sources (RES) into the power grid (primary source of electricity) looks to be a crucial topic that will significantly contribute to a more sustainable community. As a result, shifting building energy sources away from the power grid and toward on-site RES is a major notion for a sustainable building sector. In this context, the use of solar-based technologies, such as PV, to meet building energy demands is crucial among the various renewable energy sources (solar panels, wind turbines, etc.). Because the number of EVs are likely to rise in the near future, as is the level of building automation, intelligent energy management schemes to govern the energy exchange between all main users (EVs, buildings, and RES) will be critical. As a result, reliable predictions of building electric demands, EV use, and PV generation are required, as well as the ability to optimize the size of electrical storages, in order to increase the whole system's economic feasibility. Some future-oriented tariff scenarios, including different electricity charges and feed-in tariff (FiT) support in a net energy metering (NEM) environment, as well as reliability analysis, are considered in the proposed study to consistently deploy the uncertainty impacts. The goal of this study is to provide a long-term planning optimization methodology that takes into account the PV, battery bank (Stationary Battery (SB) and EV battery), and heat storage appliance's short-term scheduling features. Air conditioner with heat pump & water heater (ACWH), an advanced controlled electric heating/cooling appliance with a water tank to store heat energy, is integrated with a battery for electricity storage.

Figure 1 depicts the many components of the HEMS under investigation. An EV, PV array, SB storage, and home appliances make up the smart home. In this the HEMS is in charge of regulating energy flow between home components and the utility grid. The energy stored in both batteries is used at different times of the day depending on the needs of the home, the availability of solar PV, and the position of the electric vehicle. According to the storage devices capacities State of Charge (SOC), and to the maximum power constraints, the instantaneous

power demand of home, is satisfied by the distributed generation within the micro grid (i.e. PV generation produced), the power drawn by the batteries (both the SB, and the mobile one (EV Battery), and the power provided by the grid.

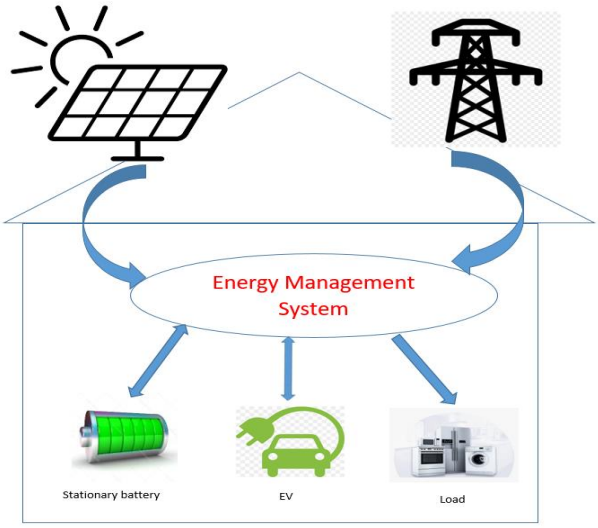

Figure 1. Home Energy Management System

The surplus of renewable energy is either constantly stored within the EV (if connected to the HEMS system) or delivered into the power grid once the SOC (SBmax) is achieved. If the EV is connected to the HEMS and its capacity is greater than the minimum constraint value SOC (EVmin), limited by driving needs, the EV operates as a source of electricity utilized to cover the electrical home needs when neither PV generation or stationary battery is available. Finally, the power grid serves as a backup system, supplying electricity. The HEMS decides on activities such as storing energy for future use and meeting current demand from available resources at any given time. These decisions are made with the goal of lowering the system's overall operating costs. PV energy is used first to power the household load in the proposed system since it is the cheapest available energy. To dispatch PV generation, a priority sequence of "House – SB – EV – Grid" is assumed. When the EV is disconnected from the house, the only available house energy sources are PV, SB, and the power grid. The amount of PV electricity generated is self-consumed by the house (for its energy needs), whereas the PV field's electricity surplus (PV production minus total house electricity need) is fed to and stored within the SB. When the SB is fully charged, any excess power generated is exported to the grid. In the event of no PV production (i.e. no solar radiation availability), the house is powered by the SB until it is completely discharged. When the EV is connected to the house, the excess electricity generated (i.e. PV production exceeds house needs and the SB, which has been preferentially charged, is full) is delivered to the EV. This stored energy is used to propel the EV.

Electrical Vehicle battery model

The battery is the most important part of an electric vehicle, and it has an impact on both the power grid and the home energy management system. The greater the capacity of an electric vehicle's battery and the demand for charging, the greater the grid's influence. The battery stores energy drawn from the charging station in charging mode, i.e. power output from PV or the grid functioning as an electricity load. In discharging mode, on the other hand, the battery functions as an electricity source, releasing stored energy to power the vehicle's electric engine or the residence to balance its load. The EV battery (Li-ion battery) is simulated in this proposed system using a modified Shepherd model. As a result, the behavior of a battery cell is modelled in terms of terminal voltage, discharge/charge current, and state of charge using this model.

Air Conditioner with Heat Pump Water Heater (ACWH) model

Instead of generating heat directly, a heat pump water heater uses electricity to transport heat from one location to another. As a result, the heat recovery mechanism is two to three times more energy efficient than a standard electric resistance water heater. Heat pumps act like a refrigerator in reverse to transport heat. In these systems, the heat pump is a tiny refrigerant-based direct expansion device that absorbs energy from the surrounding air and transfers it to water via an attached storage tank. Figure 2 shows the working principle and the schematic of the schematic diagram of ACWH. This system is projected to have a high performance coefficient. The coefficient of performance (COP) is the ratio of useable heat energy to electrical energy transferred.

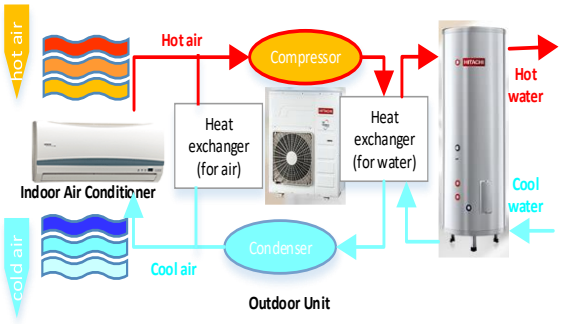

Figure 2. Schematic of air conditioner with heat pump water heater

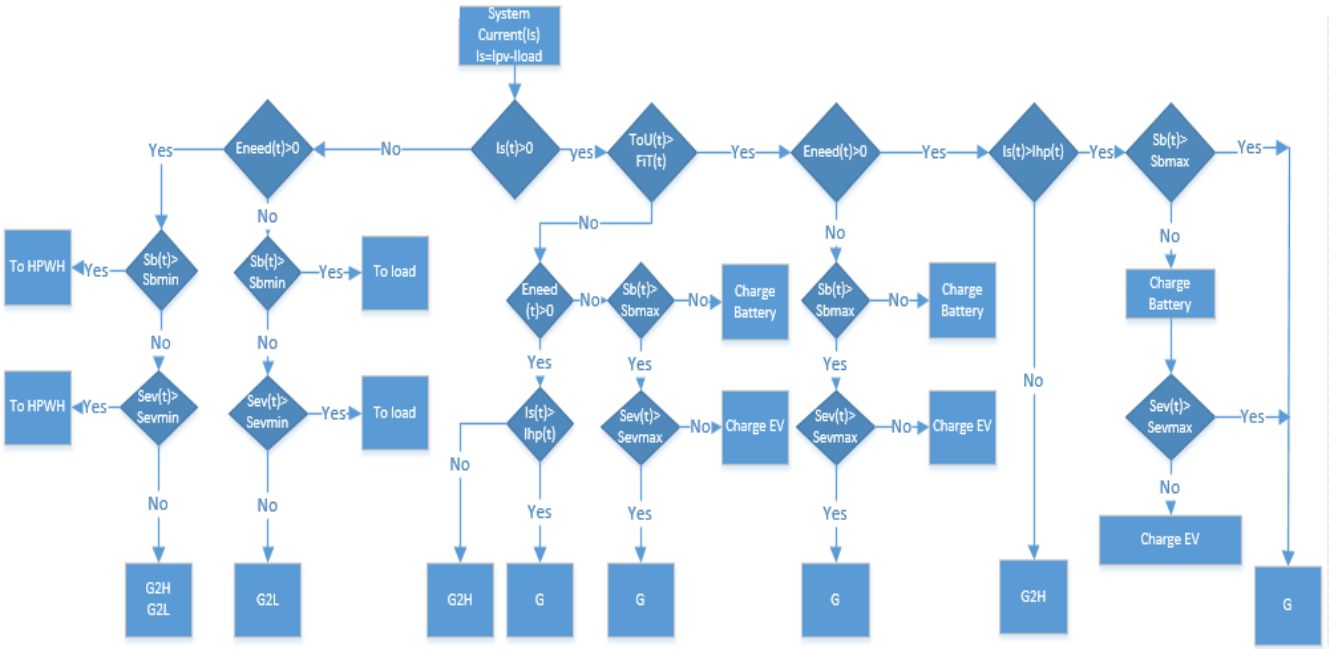

Figure 3. Flow chart of the proposed HEMS system

The flow char of the proposed of the HEMS system is shown in Fig.3. Depending on the availability of PV electricity and the demand for consumer hot water, the system will either draw energy from the grid or use a stationary battery or an electric vehicle battery to provide the power requirement. If there is no further demand for hot water, the batteries will be charged using low-cost energy, taking into account the FiT and Time of Use costs.

Conclusion

The implementation of the proposed HEMS reduces the cost of supplying electrical and thermal energy to the household load. The household stationary battery stores surplus energy and powers the load without PV generation. Any PV energy that is not absorbed by the load is stored in the battery for later use to reduce the cost of daily energy provision for the household load. Under the environment of NEM, the intermittence of PV energy can be optimally managed by the energy interactions between electrical and thermal energy storage devices by the proposed HEMS considering the program of demand response and the FiT.

REFERENCES

[1] M. Alirezaei, M. Noori, and O. Tatari, “Getting to net zero energy building: Investigating the role of vehicle to home technology,” *Energy and Buildings*, vol. 130, pp. 465-476, 2016.

[2] G. Barone, A. Buonomano, F. Calise, C. Forzano, A. Palombo, “Building to vehicle to building concept toward a novel zero energy paradigm: Modelling and case studies,” *Renew. Sustain. Energy Rev*, vol.101, pp.625–648, 2019.

Oral Presentation

Architectural and Civil Engineering

November 24th

Presentation No.	Title	Author	
ACE1.	Study on Optimum Room Temperature in Offices with Thermal Controllable Chairs	Shintaro Hanazono, Tatsuo Nobe	106
ACE2.	Optimized artificial neural network model to classify tasks in construction and project management field	Trang Thi Phuong Pham	107
ACE3.	Application of Biological Process for Enhancing Carbonation of MgO Cement	Huyen Thanh Do, Tung Hoang	112
ACE4.	Detachment diagnosis based on frequency characteristics using a tile specimen with a pseudo-dissociation part	Tatsuya Yamada, Masaki Tamura, Nobuyuki Sanjoba	114
ACE5.	Pineapple Core Sugar Extract as Set Retarder in Cement Paste	Rondel Arganza Dela Cruz	117
ACE6.	Non-Ergodic Probabilistic Seismic Hazard Analysis using Physics-Based Ground Motion Prediction: A Case of L'Aquila, Italy	Jedidiah Joel Carlos Aguirre, Bruno Rubino, Maurizio Vasallo, Guiseppe di Guilio, Francesco Visini	118
ACE7.	A mathematical model of two-dimensional vertical flow based on the dual approach	The-Hung NGUYEN	121

Study on Optimum Room Temperature in Offices with Thermal Controllable Chairs

Shintaro Hanazono and Tatsuo Nobe

Department of Architecture, Graduate School of Engineering, Kogakuin University, Tokyo, Japan
E-mail: dd21001@ns.kogakuin.ac.jp

Abstract

In this paper, we analyzed the practical use of thermal conditioning chairs that allow individuals to adjust their own thermal environment. As a result, it was found that individuals use TCCs to adjust their own warmness and coolness according to the room temperature. In addition, the results show that the indoor temperature range where the demand for temperature control occurs is below 23°C or above 25°C.

Individuals have different thermal requirements. Because, they have different metabolic rates, different amounts of clothing, and different preferences for thermal environments. Therefore, it is difficult to satisfy everyone by simply providing a uniform thermal environment. In order to reduce the dissatisfaction of occupants, it is necessary to provide a personal thermal conditioning systems or devices that allows each individual to adjust the thermal environment as needed.

For this reason, the authors developed a chair with cooling and heating functions (Thermal Conditioning Chair; TCC) and applied it to a practical building.

The TCC is a chair that allows individuals to freely adjust the warmness and coolness. For cooling, an isothermal airflow is used. The airflow is sucked in through the seat surface and blown out through an outlet located beside of the seat. This airflow acceleration effect improves the convective heat transfer coefficient of the body surface, thereby reducing the equivalent temperature by 1°C. For heating, a heater inside the seat surface heats the area in contact with the human body. This raises the equivalent temperature by 1°C.

The TCC was applied to a practical building and its usage was investigated. Fig. 1 shows the weekly average values of operation rate and indoor temperature. The upper row shows the data of female users (f2), and the lower row shows the data of male users (m5). The room temperature during the operation of the cooling function is above 25°C for both f2 and m5. This is due to the physiological reaction that sweating starts at this temperature. When the heating function is in operation, the room temperature is below 23°C in f2 and below 21°C in m5. We believe that this difference is due to the difference in metabolic rate and the amount of clothing worn by men and women.

This analysis revealed the following: 1) The TCCs have been manipulated according to the indoor temperature. 2) There are individual differences in the way it is used. 3) There were few requests to change the room temperature setting at 21-25°C, but when the room temperature deviated from that range, requests to change the room temperature were issued rapidly.

As the next development, we are planning to coordinate the air conditioning of the ambient area according to the usage of the TCCs. This means that the output of the room air conditioning is optimized by capturing the thermal demand of the occupants based on the usage of the TCC. Through this coordination, it is possible to minimize the input energy consumption of the air conditioning and eliminate occupancy discomfort.

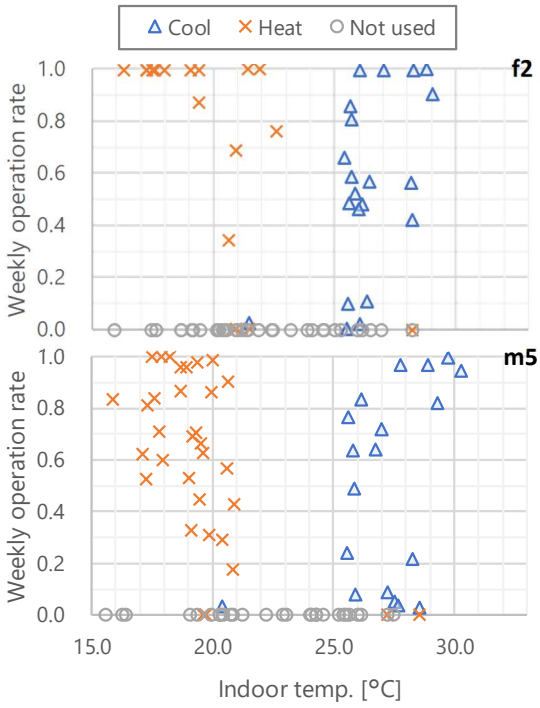

Fig. 1. Operation rate of TCC's user

Keywords:

Thermal comfort, Personal air-conditioning, Task and ambient air-conditioning

References:

[1] Lee S., Tanabe S., Nobe T.(2004). "Thermal Comfort of Task Air Conditioning with Isothermal Air Flow Unit", Journal of Environmental Engineering (Transactions of AIJ), Vol. 69, Issue 575, 75-82

[2] Vesely M., Zeiler W. (2014). "Personalized conditioning and its impact on thermal comfort and energy performance", Renewable and Sustainable Energy Reviews 34, pp.401–408

Optimized artificial neural network model to classify tasks in construction and project management field

Pham Thi Phuong Trang
Department of Civil Engineering, Danang University of Technology and Education, Danang, Vietmam
E-mail: ptptrang@ute.udn.vn

Abstract
Classification is one of the important tasks in the construction field. Classification has two main types, binary-class and multi-class classification that is more than two classes or problems. If classified correctly, managers can minimize the level of risk in the process of work. Therefore, creating a model that can simultaneously predict two-class and multi-class datasets with high efficiency is a concern of scientific researchers. Today, artificial intelligence (AI) models have been applied to handle most of problems in many fields including classification task. An intelligence created by humans with the goal of helping computers to automate intelligent behaviors like humans. The goal of this paper is to proposed optimized artificial neural networks (ANNs) model to solve both binary-class and multi-class classification in construction field. The author appied decompose algorithm optimizing ANNs model to create the best classification model. In the study, the author used three dataset concerning construction engineering including semic bump (binary class dataset), steel plate fault detection and urban land cover (multi-class datasets) to demonstrate the effficience of proposed model. Based on the provided engineering data, the analytical results confirm the proposed model has 85,917% predictive accuracy with semic bump dataset, 82,208% and 83,472% accuracy with steel plate fault detection and urban land cover datasets, respectively. The author also compared the resutls of the proposed model to basic ANN with the same three datasets.

Key words: Classification, artificial intelligence, artificial neural networks, construction field, decompose algorithm.

1. Introduction

Classification is the key helping human understand around the world. Classification related to the construction sector is diverse, rich and also very complex. There are two main types of classification: binary-class and multi-class classification. Some examples of classification in construction can be mentioned such as liquefaction of soil (liquefied or non-liquefied), classification of construction quality (good, medium, bad...), classification of public risks process, classifying the level of controversy in construction bidding (controversial, non-controversial, going to court...), classifying concrete strength (high, low or medium), classifying steel fault plates…

The purpose of classification is to forceast risks quickly and accurately, from which to propose solutions to overcome and solve these problems. Currently, in the world, there are many algorithms that have been applied to solve classification problem, however these algorithms do not have high accuracy and very few research works to solve the problem of binary-class and multiple-class classification at the same time. In addition, most of the calculation formulas are built on the perspective of each author and the measured results come from experiments, therefore the scope of calculation results of each formula are very different.

Recently, algorithms based on artificial intelligence (AI) are effective tools to solve problems in the field of construction, including classification [1, 2]. For example, Liu et al proposed a multi-objective support vector machine (SVM) for multi-class classification [3]. Besides, a new approach for classification of soil type based on laboratory tests using machine learning methods cluding Adaboost, Tree and artifical neural network (ANN) modeling [4].

In this study, the author used ANN model which is one of powerful tool of AI models to classify some classification datasets concerning civil engineering and project management. There are more and more studies proposed models based on basic ANN. Applications of ANN are used in many fields such as electricity, electronics, economics, military, construction ... to solve complex problems and require high accuracy such as automatic control, data mining, identification, etc. Chen et al provided a hybrid AI model, was developed utilizing the AI branches of ANN and Case Based Reasoning (CBR) that can be used to solve potential lawsuit problems caused by change orders in construction projects [5]. Maya et al develop an ANN model to predict construction projects performance [6]. The authors showed that ANN was designed to predict the project performance model using seven inputs that represented six factors that were prioritized as the most influencing factors.

To be honest, ANN is binary learning model, hence, the use of a single ANN can be inefficient in terms of accuracy and computational complexity when the data set is large, or the number of classes is high. This is the reason why in this study the author integrated decompose algorithm to ANN to optimize the ANN and yield the best resutls. Moreover, the proposed model can solve both binary class and muti

class classification in the same time. Decompose algorithms [7] are commonly used to solve classification problems with multiple classes. These methods spilit a multi-class classification problem into several binary classification problems and analyze each binary class problem [8]. Many studies [9, 10] demonstrated that one-against-one (OAO) [11] is one of the most effective decomposition strategies. Therefore, The proposed model in the research is called OVO-ANN.

The rest of this paper is organized as follow. Section 2 reviews the OVO, ANN and the classification evaluation methods. The collection dataset, and analytical results are mentioned in Section 3. And conclusion is given in Section 4.

2. Methodology

2.1. Decompose algorithm

Decomposition strategies have proven to be successful in improving classification performance in multi-class. These strategies decompose the original problem into several binary subproblems of a lower complexity [12]. One-vs-One (OVO) [8] is the most popular decomposition schemes. The OVO scheme divides an original problem into many binary problems as possible pair of classes. Then, each problem is faced by a binary classifier, which is responsible for distinguishing between each of the pair, and the outputs of these base classifiers are combined to forecast the final output.

2.2. Artifical neural network

ANN models are in accordance with biological neural networks or information processing models that are simulated based on the activity of the nervous system of an organism, consisting of a large number of connected neurons to process information. They consist of the first layer, hidden layers, and last layer. The ANN requires that the learning rate, number of nodes in a single hidden layer, and maximum number of training epochs are specified [13]. In which, the hidden layer consists of neurons, receives input data from nuerons in the previous layer and converts these inputs for the next processing layers. There can be many hidden layers in an ANN. The prediction accuracy of the ANN depends on the number of neurons in the hidden layer [14]. Figure 1 showed the ANN model structure.

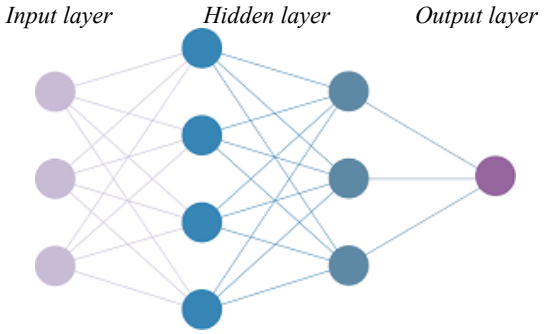

Fig. 1. The ANN model structure.

2.3. Performance measure

Evaluating model is an integral part of the model development process, helping to find the best model being suitable to research goal and type of data.

Confusion matrix is one of the best evaluated tools was used to evaluate the efficacy of an algorithm. Table 1 presents an example of a confusion matrix. From the table, the true positive (tp) value and true negative (tn) value represent accurate classifications. The false positive (fp) value or false negative (fn) value refers to erroneous classifications. The simplest and most commonly used way is accuracy. High values indicate favorable performance and vice versa. This evaluation simply calculates the ratio between the number of correctly predicted points and the total number of points in the test data set. Equation (1) mentioned the calculation of accuracy index.

Table 1. Confusion matrix

		Actual class	
		Positive	***Negative***
Predicted class	***Positive***	*true positive (tp)*	*false negative (fn)*
	Negative	*false positive (fp)*	*true negative (tn)*

$$Accuracy = \frac{tp + tn}{tp + fp + tn + fn} \quad (1)$$

3. Collection Datasets and analysis results

3.1. Seismic bump

An early warning model can be applied to forecast the occurrence of hazard events in monitoring seismic hazards in coal mines, reducing the risk of mechanical seismic impact to save the lives of mine workers. This dataset includes 170 samples, representing a hazardous state (Class 1) and 2414 samples, representing a non-hazardous state (Class 2). The binary-class dataset associated with seismic hazards in coal mines was taken from the literature [15]. Table 2 showed the parameter setting of seismic bump dataset.

Table 2. Parameter setting

Parameter	**Unit**	**Max. value**	**Min. value**	**Standard deviation**
Genergy	N/A	2,595,650.00	100.00	229,200.51
Gpuls	N/A	4518.00	2.00	562.65
Gdenergy	N/A	1245.00	-96.00	80.32
Gdpuls	N/A	838.00	-96.00	63.17
Energy	Joule	402,000.00	0.00	20,450.83
Maxenergy	Joule	402,000.00	0.00	19,357.45
Seismic bumps (1 = hazardous state, 2 = not)	N/A	2	1	

3.2. Steel plate fault detection

Fault diagnosis is important in industrial production. Clearly, producing defective products can

impose a high cost on a manufacturer of steel products and reduce risks in production process. The dataset was obtained from Semeion, Research of Sciences of Communication, Via Sersale 117, 00128, Rome, Italy. In this dataset, faults in steel plates are classified into 7 types, including Pastry, Zscratch, Kscratch, Stains, Dirtiness, Bumps and Other. The database contains 1941 data points with 27 independent variables. Table 3 presented the inputs and profile of categorical labels for data concerning faults in steel plates.

3.3. Urban land cover

Another multiple problem dataset is urban land cover (675 data points), was obtained from the UCI Machine Learning Repository [16]. The land cover dataset includes a total of 147 features, which include the spectral, magnitude, formal and textural properties of an image of land.

The spectral, magnitude, formal and textural properties of the image consist of 21 features. Afterwards, these features were repeated on each coarse scales (20, 40, 60, 80, 100, 120, and 140), yielding 147 features [17]. Table 3 listed attribute information and Table 4 presented attribute information and Table 5 showed number of data points concerning nine forms of land cover of urban land cover dataset.

Table 3. Parameter setting of faults in steel plates dataset

Parameter	Max. Value	Min. Value	Standard Deviation
Input			
Edges Y Index	1	0.048	0.234
Outside Global index	1	0	0.482
Orientation Index	1	−0.991	0.501
Edges X Index	1	0.014	0.243
Type of Steel_A300	1	0	0.490
Luminosity Index	1	−0.999	0.149
Square Index	1	0.008	0.271
Type of Steel_A400	1	0	0.490
Length of Conveyer	1794	1227	144.578
Minimum of Luminosity	203	0	32.134
X Maximum	1713	4	497.627
X Minimum	1705	0	520.691
Sigmoid of Areas	1	0.119	0.339
Edges Index	1	0	0.300
Empty Index	1	0	0.137
Maximum of Luminosity	253	37	18.691
Log of Areas	51,837	0.301	9704.564
Log Y Index	42,587	0	7273.127
Log X Index	30,741	0.301	7727.986
Steel Plate Thickness	300	40	55.086
Output—Type of fault			
Pastry (Class 1)			
ZScratch (Class 2)			
KScratch (Class 3)			
Stains (Class 4)			
Dirtiness (Class 5)			
Bumps (Class 6)			
Other (Class 7)			

Table 4. Attribute information of urban land cover dataset

Names of Attributes in the Dataset	Source of Information of the Segments
BrdIndx: border index	Shape
Area: area in m2	Size
Round: roundness	Shape
Bright: brightness	Spectral
Compact: compactness	Shape
ShpIndx: shape index	Shape
Mean_G: green	Spectral
Mean_R: red	Spectral
Mean_NIR: near Infrared	Spectral
SD_G: standard deviation of green	Texture
SD_R: standard deviation of red	Texture
SD_NIR: standard deviation of near infrared	Texture
LW: length/width	Shape
GLCM1: gray-level co-occurrence matrix	Texture
Rect: rectangularity	Shape
GLCM2: another gray-level co-occurrence matrix attribute	Texture
Dens: density	Shape
Assym: asymmetry	Shape
NDVI: normalized difference vegetation index	Spectral
BordLngth: border length	Shape
GLCM3: another gray-level co-occurrence matrix attribute	Texture

Note: These attributes are repeated for each coarse scale (i.e., variable 20, variable 40, ..., variable 140).

Table 5. Number of data points concerning nine forms of land cover in urban land cover dataset.

Names of the Land Cover in the Dataset	No. of Data Points
Trees (Class 1)	106
Concrete (Class 2)	122
Shadow (Class 3)	61
Asphalt (Class 4)	59
Buildings (Class 5)	112
Grass (Class 6)	116
Pools (Class 7)	29
Cars (Class 8)	36
Soil (Class 9)	34
Total	675

3.4. Analysis results

To demonstrate OVO-ANN model is the good model to slove not only binary class but also multiple class classification, the authors compared the results of the proposed model to basic ANN model with the same three datasets. Table 6 presented the comparision results.

Table 6. Comparion results

No	Dataset	ANN	OVO-ANN
1	Seismic bump	85,756	85,917
2	Steel plate fault	78,219	82,208
3	Urban land cover	80,186	83,472

From the table 6, we can see that with the binary class dataset (seismic bump), both ANN and OVA-ANN had the same resuls (85,756% for ANN and

85,917 for OVO-ANN). Therefore, it is clear that ANN had a good role in solving binary class problem. However, the OVO-ANN yielded the higher accuracy for multi-class problems (steel plate detection and urban land cover). Particulary, OVA-ANN had 82,208% for stell plate fault dectection and 83,472% for the remaining dataset.

4. Conclusion

AI is getting more and more attention and being applied in most fields: from high-tech, complex computing, to healthcare, the automotive industry and even smartphones…This study proposed the OVO-ANN model to classify both binary class and multiple class classification problems concerning civil engineering and management. ANN itseft plays an important role in handling binary class classification, however, to improve basic ANN model, the author optimizes it by decompose algorithm. This study used three dataset with different classification tasks to demonstrate the efficience of the proposed model. In the future work, the author hopes continue optimize OVO-ANN model to creat the new model which classify to more diverse datasets.

References:

[1] J.-S. Chou and C. Lin, "Predicting Disputes in Public-Private Partnership Projects: Classification and Ensemble Models," *Journal of Computing in Civil Engineering,* vol. 27, no. 1, pp. 51-60, 2013, doi: doi:10.1061/(ASCE)CP.1943-5487.0000197.

[2] M.-Y. Cheng and N.-D. Hoang, "Risk Score Inference for Bridge Maintenance Project Using Evolutionary Fuzzy Least Squares Support Vector Machine," *Journal of Computing in Civil Engineering,* vol. 28, no. 3, p. 04014003, 2014, doi: doi:10.1061/(ASCE)CP.1943-5487.0000275.

[3] L. Liu, B. Martín-Barragán, and F. J. Prieto, "A projection multi-objective SVM method for multi-class classification," *Computers & Industrial Engineering,* vol. 158, p. 107425, 2021, doi: https://doi.org/10.1016/j.cie.2021.107425.

[4] B. T. Pham *et al.*, "A novel approach for classification of soils based on laboratory tests using Adaboost, Tree and ANN modeling," *Transportation Geotechnics,* vol. 27, p.100508, 2021, doi:https://doi.org/10.1016/j.trgeo.2020.100508.

[5] J.-H. Chen and S. C. Hsu, "Hybrid ANN-CBR model for disputed change orders in construction projects," *Automation in Construction,* vol. 17, no. 1, pp. 56-64, 2007/11/01/ 2007, doi: https://doi.org/10.1016/j.autcon.2007.03.003.

[6] R. Maya, B. Hassan, and A. Hassan, "Develop an artificial neural network (ANN) model to predict construction projects performance in Syria," *Journal of King Saud University - Engineering Sciences,* 2021, doi: https://doi.org/10.1016/j.jksues.2021.05.002.

[7] A. C. Lorena, A. C. P. L. F. de Carvalho, and J. M. P. Gama, "A review on the combination of binary classifiers in multiclass problems," *Artificial Intelligence Review,* vol. 30, no. 1, p. 19, 2009/08/13 2009, doi: 10.1007/s10462-009-9114-9.

[8] M. Galar, A. Fernández, E. Barrenechea, H. Bustince, and F. Herrera, "An overview of ensemble methods for binary classifiers in multi-class problems: Experimental study on one-vs-one and one-vs-all schemes," *Pattern Recognition,* vol. 44, no. 8, pp. 1761-1776, 2011/08/01/ 2011, doi: https://doi.org/10.1016/j.patcog.2011.01.017.

[9] M. Galar, A. Fernández, E. Barrenechea, and F. Herrera, "DRCW-OVO: Distance-based relative competence weighting combination for One-vs-One strategy in multi-class problems," *Pattern Recognition,* vol. 48, pp. 28–42, 01/31 2015, doi: 10.1016/j.patcog.2014.07.023.

[10] S. Kang, S. Cho, and P. Kang, "Constructing a multi-class classifier using one-against-one approach with different binary classifiers," *Neurocomputing,* vol. 149, Part B, pp. 677-682, 02/01 2015, doi: 10.1016/j.neucom.2014.08.006.

[11] M. Hall, E. Frank, G. Holmes, B. Pfahringer, P. Reutemann, and I. H. Witten, "The WEKA data mining software: an update," *SIGKDD Explor. Newsl.,* vol. 11, no. 1, pp. 10–18, 2009, doi: 10.1145/1656274.1656278.

[12] L. P. F. Garcia, J. A. Sáez, J. Luengo, A. C. Lorena, A. C. P. L. F. de Carvalho, and F. Herrera, "Using the One-vs-One decomposition to improve the performance of class noise filters via an aggregation strategy in multi-class classification problems," *Knowledge-Based Systems,* vol. 90, pp. 153-164, 2015, doi: https://doi.org/10.1016/j.knosys.2015.09.023.

[13] D. J. Hill and B. S. Minsker, "Anomaly detection in streaming environmental sensor data: A data-driven modeling approach," *Environmental Modelling & Software,* vol. 25, no. 9, pp. 1014-1022, 2010, doi: https://doi.org/10.1016/j.envsoft.2009.08.010.

[14] B. B. Ashoor, A. Giwa, and S. W. Hasan, "Chapter 5 - Full-Scale Membrane Distillation Systems and Performance Improvement Through Modeling: A Review," in *Current Trends and Future Developments on (Bio-) Membranes*, A. Basile, E. Curcio, and Inamuddin Eds.: Elsevier, 2019, pp. 105-140.

[15] M. Sikora and Ł. Wróbel, "Application of rule induction algorithms for analysis of data collected by seismic hazard monitoring systems in coal mines," *Archives of Mining Sciences,* vol. 55, pp. 91-114, 01/01 2010.

[16] M. U. M. L. R. U. o. C. Lichman, School of Information and Computer Science: Irvine, CA, USA, Available online: http://archive.ics.uci.edu/ml (accessed on 20 December 2015), 2015.

[17] S. Durduran, "Automatic classification of high resolution land cover using a new data weighting procedure: The combination of k-means clustering algorithm and central tendency measures (KMC–

CTM)," *Applied Soft Computing,* vol. 35, pp. 136-150, 07/07 2015, doi: 10.1016/j.asoc.2015.06.025.

Application of Biological Process for Enhancing Carbonation of MgO Cement

Huyen Do[1*], Tung Hoang[2]

[1] Faculty of Project Management, The University of Danang - University of Science and Technology, Vietnam
E-mail: huyendt@dut.udn.vn
[2] Faculty of Road and Bridge Engineering, The University of Danang - University of Science and Technology, Vietnam
E-mail: hptung@dut.udn.vn

Abstract

This paper has proposed a new technique to enhance a carbonation process of MgO cement. The new method used reactions of microorganisms to release carbonation ions which could carbonated brucite products from MgO cement paste to generate hydrated magnesium hydroxy carbonates (HMHCs). The new component HMHCs increase strength of cement paste samples approximate 100% compared to control samples. The bio-carbonation technique could be used to shorted carbonation process of MgO cement in ambient environment.

Ordinary Portland (OP) cement was a main binding material which has been used for civil construction project around the world. However, the manufacture process of OP cement releases huge amount of CO_2 gas and consumed large energy due to using very high temperature (~1450 ^oC) to burn raw material. Recently, construction material engineers are going to use reactive MgO (RM) cement as an alternative binder of the OP cement. The manufacture process of RM cement only used lower calcination temperature (~700-900 ^oC), resulted in more environment friendly.

Although, the original strengths of RM cement were lower than OP cement, the strength of carbonated RM cement-based samples due to absorbed CO_2 gas could be higher than those of OP cement-based specimens. There are many methods to accelerate carbonation process of RM cement, most of them are using carbonation chambers and chemical additives, which were expensive, time and space consuming. This research work has investigate the use of biological reactions to generate carbonate ions for enhancing carbonation process of RM cement-based samples. The biological carbonation process follows a series of equations [2,3]:

$$CO(NH_2)_2 + 2H_2O \xrightarrow{\text{Urease}} CO_3^{2-} + 2NH_4^+ \quad (1)$$

$$MgO + H_2O + CO_3^{2-} \rightarrow \begin{cases} MgCO_3.3H_2O \text{ (nesquehonite)} \\ 4MgCO_3{\cdot}Mg(OH)_2.4H_2O \text{ (hydromagnesite)} \\ 4MgCO_3{\cdot}Mg(OH)_2.5H_2O \text{ (dypingite)} \end{cases} \quad (2)$$

The urease enzyme from microorganism hydrolyzed urea ($CO(NH_2)_2$) to release CO_3^{2-} ions (eq.1). The carbonate ions reacted with Mg^{2+} from RM cement to form hydrated magnesium hydroxy carbonates (HMHCs) including nesquehonite, hydromagnesite, and dypingite (eq.2). The HMHCs products were able to improve bonding within cement-based samples resulted in increasing compressive strengths.

The urease producing bacteria (UPB) used *Sporosarcina pasteurii* strain which were cultivated following process from [1]. The UPB contained approximate 15 U/ml (1 U = 1 μM of urea hydrolyzed/min of urease activity, ~1.7-2.0 of average optical density (OD600). The RM cement was from Richard Baker Harrison-UK. Three mixtures of cement paste were prepared. The control samples (CS) included RM cement and water with 0.65 of W/B (ratio of liquid solution to cement). The bio-mixture samples included RM cement, UPB, and urea (at 0.5 and 1 M). The mixtures were casted into cubic molds (5 × 5 × 5 cm), consolidated, and hardened under the ambient conditions.

The samples were demolded and performed compressive strength test at 2, 7, 14, 28 days. After mechanical test, the sub-samples were collected for microstructure analysis with SEM test. Fig. 1 shows steps of paste samples preparation including materials, casting, demolding.

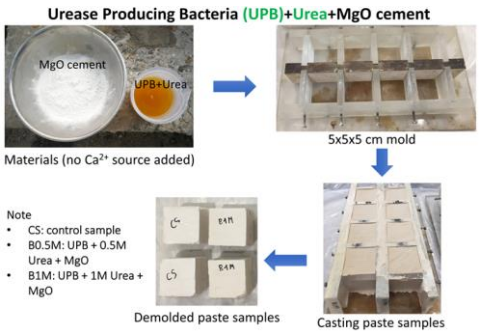

Fig. 1. Experimental work.

The compressive strengths results were shown in Fig. 2. The CS increased gradually from 600 kPa to 5200 kPa for 28 days. The strength gain of CS mainly depended on the hydration of MgO cement to form brucite ($Mg(OH)_2$). However, the initial strengths of biological-based samples (B0.5M and B1M) were significantly higher than CS at 2days. For example, the average strength of B0.5M reached 5100 kPa and B1M reached 6800 kPa at 2 days. The sharp increase in strength of biological-based samples might due to high amount formation of HMHCs by absorbed

carbonate ions released from urea hydrolysis process.

The trend of strength gain in both biological-based samples was similar to CS from 7 to 28 days curing. It reveals that the microorganism might not significantly impact on strength of samples for late age. The activity of microbes in samples might decrease after 7 days. However, the average final strength of biological-based samples was approximate double higher than strength of CS at 28 days. Interestingly, while the strengths of B1M were considerably higher than B0.5M at 2-14 days, the 28-day strength of B0.5M sample was slightly higher than B1M sample.

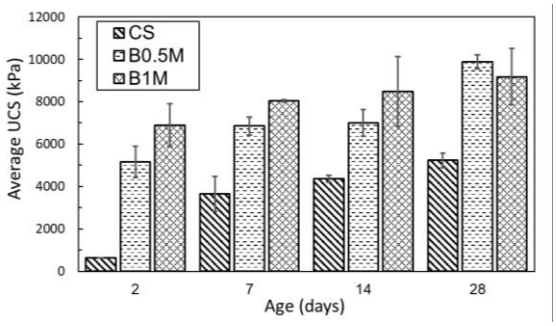

Fig. 2. Compressive strength of cubic samples.

SEM technique was employed for microstructure analysis. Because there was a significant change after 2 days curing, the SEM was performed on samples CS and B1M at 2 days. Fig. 3 showed the differences of microstructure between CS and B1M samples. The CS sample (Fig. 3(a)) presented the morphology of brucite formed by hydration. However, Fig. 3(b) provided a new formation mineral as hydromagnesite crystals which were not observed in CS. The formation of hydromagnesite crystals revealed that the carbonation process was occurred in biological-based samples [4].

The carbonated products were formed by reactions between CO_3^{2-} ions released from urea hydrolysis and Mg^{2+} from RM cement. The considerable differences in microstructure of B1M sample compared to CS sample which was not contained UPB and urea proved that the large amount of hydromagnesite crystals only formed within the biological-based sample. The strong bonding of new crystals increased strengths of biological-based samples significantly after 2 days (Fig. 2). However, the slow strength gain of biological-based samples from 7 to 28 days might resulted from reducing activity of bacteria in samples.

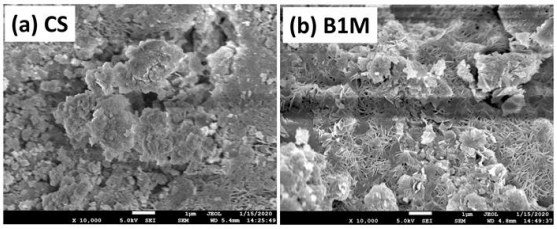

Fig. 3. SEM at 2 days: (a) CS sample, (b) B1M sample.

The results of this study proved that the carbonate ions released from hydrolysis of urea could significantly enhance carbonation process of RM cement-based samples. The new crystals of hydromagnesite were formed within biological-based samples, in order to provide stronger bonding to increase strength of samples. The strength of biological-based sample was 2 times higher than that of control samples. Although the strength gain biological-based samples was significantly high in early age (2 days), it increased gradually after 7 days, resulted from low urease activity of bacteria. The further research work should improve the activity of microbes in late age.

The new environment friendly method of bio-carbonation RM cement can apply to accelerate carbonation process of cement in ambient environment without carbonation chambers or chemical additivities. In addition, the quick strength gain (within 2 days) from the proposed technique can save time during construction process related to concrete casting phases.

References:

[1] T. Hoang, J. Alleman, B. Cetin, K. Ikuma, and S.-G. Choi, "Sand and silty-sand soil stabilization using bacterial enzyme induced calcite precipitation (BEICP)," Can. Geotech. J., pp. 1–66, 2018.

[2] T. Hoang, J. Alleman, B. Cetin, and S. G. Choi, "Engineering Properties of Biocementation Coarse- And Fine-Grained Sand Catalyzed by Bacterial Cells and Bacterial Enzyme," J. Mater. Civ. Eng., vol. 32, no. 4, pp. 1–15, 2020

[3] N.T. Dung, C. Unluer, Influence of accelerated hydration and carbonation on the performance of reactive magnesium oxide concrete, Adv. Cem. Res. (2018) 1–13.

[4] Tung Hoang, Nguyen Tien Dung, Cise Unluer, and Jian Chu, "Use of microbial carbonation process to enable self-carbonation of reactive MgO cement mixes", Cement and Concrete Research. (2020) 1-15.

Detachment diagnosis based on frequency characteristics using a tile specimen with a pseudo-dissociation part

Tatsuya Yamada[1, a*] Masaki Tamura[2] Nobuyuki Sanjoba[3]

[1] Master Course student, Dept.of Arch.,Graduate School of Engineering,Kogakuin Univ.,Tokyo,Japan
[2] Kogakuin University, Dr.Eng, School of Architecture Department of Architecture,Tokyo, Japan
[3] FBS Co., Ltd.,Tokyo ,Japan
[a*] dm21071@ns.kogakuin.ac.jp

Abstract

At present, the tapping sound inspection method, which is often used as an outer wall tile diagnostic method, cannot express the measurement result as an objective numerical value. Against this background, in order to examine the preparation of the standard, a tile test piece having a pseudo-dissociation portion was prepared, and the correlation between the frequency characteristics and the adhesive properties was evaluated. As a result, it was confirmed that the frequency characteristics and the adhesion strength are related to the decrease of the primary peak frequency as the adhesion strength decreases, and the possibility that the adhesion strength can be estimated from the primary peak is considered.

1. Introduction

At present, the tapping sound inspection method is often used as an outer wall tile diagnostic method. This is a diagnostic method in which an inspector hits a tile with a test hammer to distinguish and judge the difference in sound. This diagnostic method cannot express the measurement result as an objective numerical value. Therefore, there is a problem that the judgment accuracy varies[1]. Against this background, for the purpose of improving the judgment accuracy in the percussion test, a simulated test piece having a pseudo-dissociated portion (a state in which the adhesion strength is not sufficient although the adhesion portion is adhered) was prepared. Then, the anti-sound at the time of percussion was replaced with the frequency, and the judgment was made, and the creation of the correlation evaluation standard between the frequency characteristic and the tile adhesion property was examined.

2. Experiment outline

Table 1 shows the materials and contents used, and Table 2 shows the experimental factors and levels. Ten levels were prepared for the open time, and the divergence part was expressed by utilizing the decrease in adhesive strength due to the drying of the pasted mortar. Furthermore, 3 levels were set for the vibrato time, 2 levels were set for each type of mortar attached and the surface condition of the skeleton, and analysis was performed based on the results of the adhesion strength test and the frequency measurement at the time of consultation. Regarding the type of mortar to be attached, a field-prepared mortar that does not use a chemical admixture was prepared in order to confirm the effect of the hydration reaction of the polymer on the adhesion strength.

The mortar was prepared by mechanical kneading with a stirrer, and the tiles were attached after setting

Table 1. Materials and contents used

Classification	Item	Contents	
Finishing material	Exterior tiles	Ceramic tile (JIS A 5209)	
		Size	95 ㎜×45 ㎜ (Sole foot depth 1.39 ㎜)
			45 square two-chome tile
Sticking material	Ready-made mortar	Polymer cement mortar	
	On-site preparation mortar	Ordinary portland cement	
		Silica sand No. 5	
Structural material	Ordinary concrete	Flat plate (JIS A 5371)	
		Size	300×300×60 ㎜
measuring equipment	Frequency measurement	Tapping sound inspection machine	
	Adhesion strength measurement	Tensile tester	

Table 2. Experimental factors and levels

Cause	Level
Open time (min.)	0,5,10,15,20,40,60,80,100,120
Pasting method	Close contact
Vibrato time (sec)	1,3, Constant embedding time (After 40 minutes)
Types of pasted mortar	Ready-made, On-site preparation（cement : Sand aggregate =1:2）
surface treatment	Smooth surface, Sandblast surface
Wet with water	1.0 g constant
Tile type	45 square 2-chome tile constant
Curing	20℃ constant

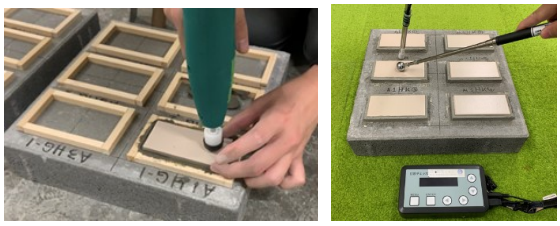

a) Adhesion construction status　　b) Frequency measurement status

Fig. 1. Test status of pseudo-dissociation tile test piece

an open time by close contact using the vibrato of the attachment tool. After curing for 28 days, frequency measurement and adhesion strength measurement were performed.

3. Adhesion strength measurement result

3.1 Adhesion strength depending on the surface condition of the skeleton

Figure 2 shows the adhesion strength of each type of mortar attached and the surface condition of the skeleton by vibrato time. Regarding the adhesion strength depending on the surface condition of the skeleton, no significant difference was confirmed between the two levels of surface treatment this time. The effect of the surface roughness of the contact interface, such as the increase in physical adhesion strength due to the contact interface between the mortar and the skeleton surface and the decrease in chemical adhesion strength due to insufficient adhesion surface, was small. I considered.

In addition, when the open time was 0 to 5 minutes, the adhesion strength was greater when the vibrato time was 1 second than when it was 3 seconds. On the contrary, when the open time was 5 to 20 minutes, the adhesion strength tended to be higher when the vibrato time was 3 seconds than when it was 1 second. Regarding this tendency, when tiles were attached within 5 minutes, if the vibrato time was increased, the cement and water were separated by vibration before the hydration reaction of the cement proceeded, and the progress of the hydration reaction was hindered. It was considered that this reduced the adhesion strength.

3.2 Adhesion strength depending on the type of mortar attached

From Fig. 2, when the open time was 0 to 20 minutes, the ready-mixed mortar had higher adhesion strength than the in-situ compounded mortar. This tendency was considered to be due to the fact that the premixed mortar was given a large amount of chemical adhesion strength due to the inclusion of the polymer in the initial stage. On the other hand, field-prepared mortar does not contain polymer. Therefore, the degree of expectation for the chemical adhesion strength at the initial stage is low, and the physical adhesion strength due to the engagement due to the unevenness of the contact interface shows a greater

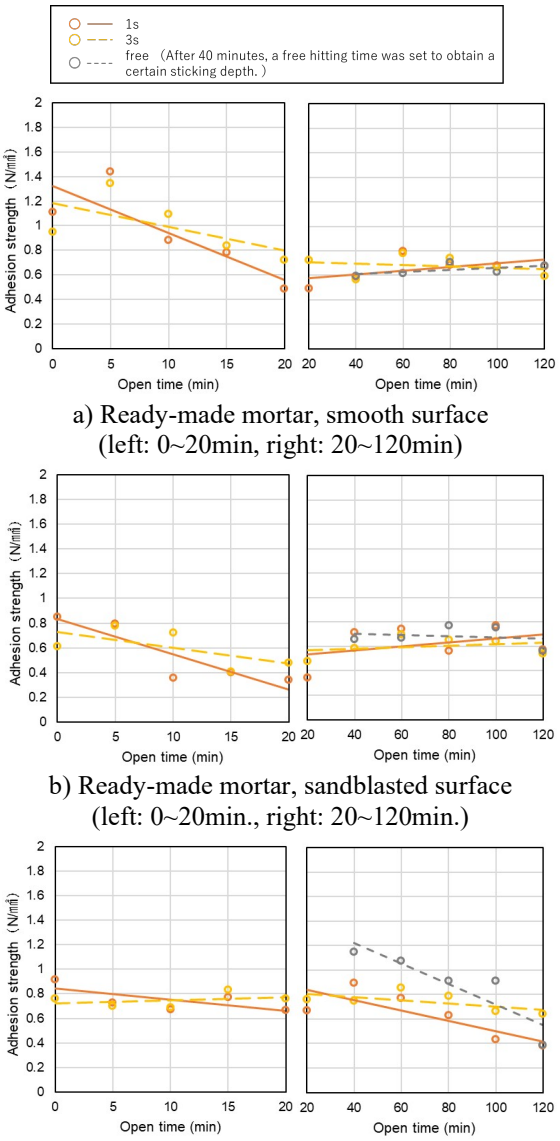

a) Ready-made mortar, smooth surface (left: 0~20min, right: 20~120min)

b) Ready-made mortar, sandblasted surface (left: 0~20min., right: 20~120min.)

c) On-site preparation mortar, sandblasted surface (left: 0~20min., right: 20~120min.)

Fig. 2. Adhesion strength by vibrato time for each type of mortar and surface condition of the skeleton

effect, so the adhesion strength does not increase so much at the open time of 0 to 20 minutes. It was considered that the result was obtained.

In addition, it was confirmed that the adhesion strength tends to increase as the vibrato time increases after 40 minutes in the on-site mortar. It can be pointed out that by taking a long vibrato time and sufficiently pressing the tiles into the mortar, the physical adhesion strength due to sufficient engagement between the tiles and the pasted mortar can be secured. On the other hand, in the prepared mortar, no difference was observed depending on the vibrato time. It is considered that this is because the influence of the chemical adhesion strength obtained by the hydration reaction of the polymer is large in the total adhesion strength, and the influence of the physical action such as engagement on the total adhesion strength is small.

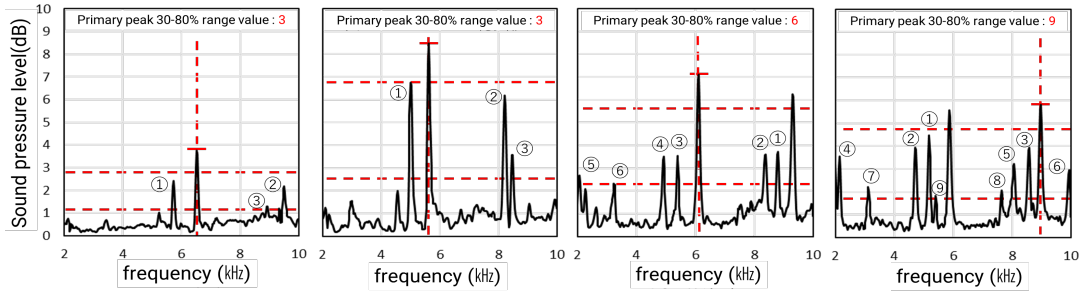

a)0 min. b)20 min. c)60 min. d)100 min.

Fig. 3. Frequency measurement results by open time and number of peeling part characteristic peaks (Ready-made/Vibrato time 3 seconds)

4. Frequency measurement result at the time of tile percussion

In Fig. 3, the measurement results of the premixed mortar and the vibrato time of 3 s were taken up with the frequency measurement results at the time of percussion and the number of peeled part characteristic peaks as the conditions having the adhesion characteristics with the least peeling. Since the number of detected frequencies with a strong sound pressure level increased to a maximum of 3 to 9 as the open time became longer, it was confirmed that the number of peak detections tended to increase as the open time became longer. It was considered that when the open time becomes long, the degree of hardening of the mortar varies, and the adhesion state is not uniform, so that the mortar is dispersed in various frequencies.

5. Correlation analysis of adhesion strength and frequency characteristics

Fig. 4 shows the adhesion strength due to the open time on the surface of all the preparations and the whole skeleton, and Fig. 5 shows the primary peak frequency due to the open time on the surface of all the preparations and the whole skeleton. From Fig. 5, the difference in the decrease in the adhesion strength was large from 0 to 40 minutes, and after 60 minutes, the change became small and almost constant, and from Fig. 6, the same tendency of change was observed in the primary peak frequency. Therefore, there is a relationship between the frequency characteristics and the adhesion strength that the primary peak frequency decreases with the same tendency as the adhesion strength decreases, and if the open time is within 20 to 40 minutes, the adhesion strength can be estimated from the primary peak. Gender was considered.

6. Conclusion

Since the prepared mortar contains a polymer, the chemical adhesion strength was greatly developed in the initial stage. Furthermore, it can be pointed out that the physical adhesion strength due to the engagement of the contact interface between the tile and the mortar can be sufficiently ensured by lengthening the vibrato time in the on-site prepared

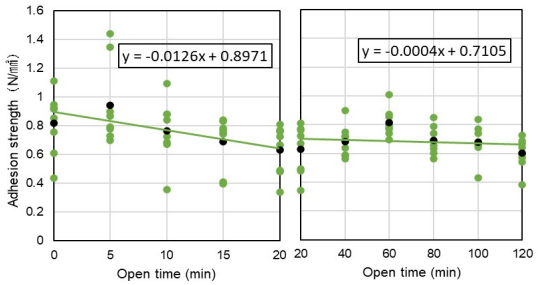

a)0~20 min. b)20~120 min.

Fig. 4. Adhesion strength due to open time on the surface of all formulations and all bodies

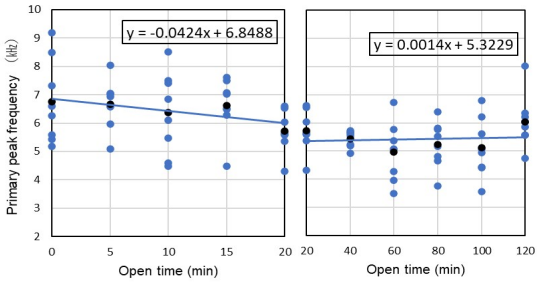

a)0~20 min. b)20~120 min.

Fig. 5. Primary peak frequency due to open time on all formulations and all skeleton surfaces

mortar. Therefore, it was clarified that the physical adhesion strength depends on the vibrato time. We also confirmed that the number of peak detections tends to increase as the open time increases. Then, the relationship between the frequency characteristics and the adhesion strength was found that the primary peak frequency decreased as the adhesion strength decreased, and it was considered that the adhesion strength could be estimated from the primary peak if the open time was within 20 to 40 minutes.

References:

[1] T. Soeda, T. Mikami, Basic research on the development of exterior tile peeling diagnostic equipment, Architectural Institute of Japan Structural Dissertation, 729-1779 (2016-11).

KEYWORDS:

Tile, Peeling, Tapping sound inspection, Adhesion strength, Frequency, Sound pressure level

ABSTRACT

DELA CRUZ, RONDEL ARGANZA, College of Engineering and Agro-Industrial Technology, University of the Philippines Los Baños, January 2021. **Pineapple Core Sugar Extract as Set Retarder in Cement Paste.**

Major Adviser: Dr. Richelle G. Zafra

Set retardation of concrete is essential in construction during hot weather conditions and during transfer since cement paste's plastic consistency should be maintained before casting and curing. Pineapple core is a bio-waste that contains sucrose, glucose and fructose which have set-retarding capacities. In this research, pineapple core sugar extract was used as a set retarder in cement paste. Varying percentages─0% (control), 0.2%, 0.4%, 0.6% and 0.8%─of the extract were used to determine the behavior of the setting time as the extract percentage changes. The delay in setting time of Type IP Portland cement was investigated having five cement paste groups with three replications per group. Vicat Needle Apparatus was used to determine the initial and final setting time of cement paste. The results exhibited that for both initial and final setting time, there is a significant difference between the control and the treatments, and that there is also a significant difference between one treatment and every other treatment. Accordingly, as the extract percentage increases, the initial and final setting time also increase even up to 248 min and 423 min, respectively.

Non-Ergodic Probabilistic Seismic Hazard Analysis using Physics-Based Ground Motion Prediction: A Case of L'Aquila, Italy

Jedidiah Joel C. Aguirre[1,2,a*], Bruno Rubino[2,b], Maurizio Vasallo[3,c], Guiseppe di Guilio[3,d], Francesco Visini[4,e]

[1] University of the Philippines – Los Baños, Laguna, Philippines
[2] Università Degli Studi Dell'Aquila, L'Aquila, Italy
[3]Istituto Nazionale di Geofisica e Vulcanologia – Sezione dell'Aquila, L'Aquila, Italy
[4]Istituto Nazionale di Geofisica e Vulcanologia – Sezione di Pisa, Pisa, Italy
[a]jcaguirre@up.edu.ph, [b]bruno.rubino@univaq.it, [c]maurizio.vassallo@ingv.it, [d]giuseppe.digiulio@ingv.it
[e]francesco.visini@ingv.it

Abstract

Earthquakes are sudden release of energy due to the shear failure of rocks in a causative fault [1]. The damages brought by earthquakes can be very overwhelming and it takes weeks, months, or even years for a site to recover after a tremor. In any kind of disaster risk planning and management, the estimation of earthquake occurrences and their impacts are concerns of any policy makers, engineers, and city planners. To estimate the feasible ground shaking levels in an area, a seismic hazard analysis (SHA) must be conducted [1].

At the present, there are two existing ways of estimating ground shaking levels: either deterministic (DSHA) or probabilistic (PSHA). DSHA aims to determine exactly the maximum controlling earthquake coming from a certain seismic source that can affect the site on a worst-case scenario basis. On the other hand, PSHA is a methodology that estimates the ground shaking hazard on a given place given the chances of exceeding a certain level of ground shaking that had occurred in the past within a specified period interval of validity. This approach considers the future earthquakes' occurrence which is uncertain in distance, time, magnitude, and ground motion. Also, this is more frequently utilized than the former since the worst-case controlling earthquake may not even occur during the design life of a structure.

The methodology of conducting an SHA has evolved several times during the past 50 years [2], [3], [4], [5]. A method which combines both approaches also known as Non-Ergodic Physics-Based PSHA, removes the reliance of the usual PSHA method to Ground Motion Prediction Equations (GMPEs) to avoid very high uncertainties in seismic hazard, especially in areas without existing GMPEs. This entails the simulation of an actual earthquake process through seismic wave propagation by solving the Elastodynamic Equation coupled with Hooke's Law, which is applied in a probabilistic framework [6].

The City of L'Aquila, Italy was severely affected by the M_w 6.1 earthquake last April 6, 2009, which caused the city approximately € 25 billion in damages, 300 casualties, and 1500 injured people [7]. As shown in Fig. 1, the city was surrounded by several active faults which makes the city very susceptible to seismic hazard.

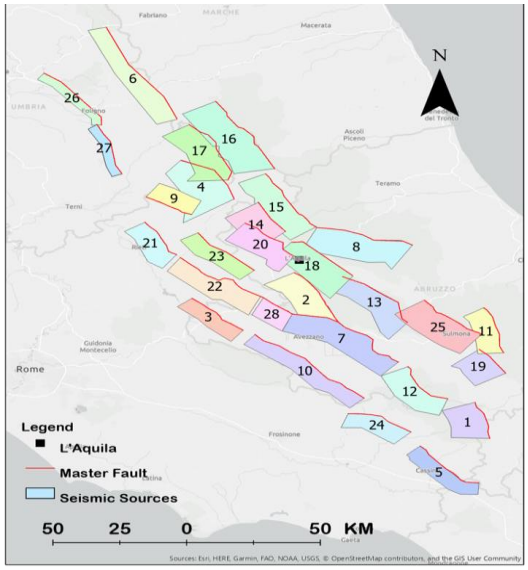

Fig.1. Seismic Sources within 100 km from L'Aquila, Italy

Recent PSHA of the entire Italy, including L'Aquila, was conducted using GMPEs to predict the ground shaking levels [8], [9]. Therefore, to minimize the increasing uncertainties due to the use of empirical equations, a non-ergodic probabilistic seismic hazard analysis (PSHA) was proposed in this study which utilizes the physics-based ground motion prediction. Other than the ground motion prediction and consideration of background seismicity (blind faults or area sources), all other steps in conducting PSHA are kept constant.

Methodology

As shown in Fig. 1, a total of 28 faults were identified in this study that are located within 100 km radius from the city of L'Aquila. All the sources in Fig. 1 are divided into 100 equal areas, whose centroids of the resulting smaller areas were located using ArcGIS Pro. Source-to-site distances were calculated from L'Aquila to each of these centroids, and the resulting distances were binned into 10 distance scenarios for each fault, thus creating a

Probability Mass Function (PMF) of the distance to show the uncertainty in the distance of future earthquakes. For illustration purposes, Fig. 2 shows the PMF for the Paganica Fault, the nearest fault in the city which caused the aforementioned tremor last 2009 [7].

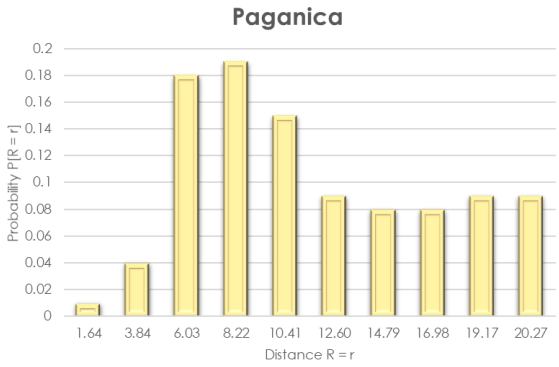

Fig. 2. Distance Probability Mass Function for Paganica Fault

Fault geometry, maximum magnitude, and occurrence rates were obtained from past studies [8], [9]. A minimum magnitude of 5.5 was set which is of engineering interest. Different magnitude scenarios from the minimum to maximum magnitude of earthquakes, with increments of 0.1 unit were considered.

A modified time-weakening friction law was proposed to model the seismic energy released by an earthquake, as shown in Fig. 3, which was based on the Friction Law model [10], modified in this study to account for the increase of shear stress τ in the fault immediately after the earthquake occurrence.

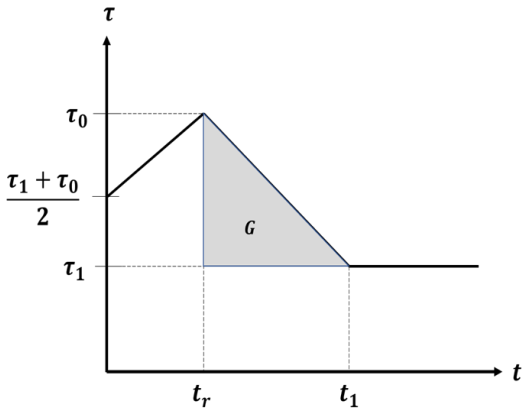

Fig. 3. Modified Time-Weakening Friction Law

The Fracture Energy G, Dynamic Stress Drop (τ_0–τ_1), Rupture Time t_r, and Characteristic Time t_1 were calculated for each magnitude scenario, whose values can be approximated using the empirical relations from the literature [10], [11]. Initial stress τ_1 was assumed to be zero, and τ_0 was estimated from Byerlee's Law [12]. In this study, the fault is assumed to undergo rupture that will increase the shear stress from the average of the minimum and maximum shear stresses to the maximum shear stress.

The one-dimensional elastodynamic equation coupled with Hooke's law was used to predict the peak ground acceleration (PGA), a measure of ground shaking level. Equation (1) below shows the partial differential equation problem setup with initial and boundary conditions in terms of wave velocity v and material shear stress τ, both of which are functions x and t which are source-to-site distance and time respectively.

$$\begin{cases} \rho\dfrac{\partial v}{\partial t}-\dfrac{\partial \tau}{\partial x}=0 & \mu=\rho V_s^2 & (x,t)\in[0,L_p]\times[t_r,t_1] \\ \dfrac{\partial \tau}{\partial t}-\mu\dfrac{\partial v}{\partial x}=0 & & \\ v(x,t_r)=0 & \tau(x,t_r)=0 & x\in[0,L_p] \\ v(0,t)=0 & \tau(0,t)=f(t) & t\in[t_r,t_1] \end{cases} \quad (1)$$

The shear stress function defined in Fig. 3 was used as the boundary shear stress *f(t)* in (1), which varies with the magnitude of the earthquake. Preliminary Reference Earth Model (PREM) Model of the Earth's crust was used to estimate the shear modulus μ, rock density ρ, and shear wave velocity V_s [12]. The approximate solution to (1) was solved using Staggered Finite Differences, employing a (trial) time step of Δt = 0.005 s and grid size of Δx = 20 m for each time t_r and t_1 per magnitude and earthquake distance L_p. This solution generates a synthetic ground motion (or seismogram), which is a plot of the velocity vs. time. The PGA was determined by taking the highest magnitude of the acceleration, which was obtained by taking the slope of the velocity vs. time plot.

Peak values of acceleration for each magnitude-distance pair were obtained for all seismic sources. These PGA are grouped according to their respective magnitude of occurrence and source-to-site distance, and the corresponding probability of exceedance $P[Y > y \mid rup_n]$ of a PGA value given its distance and magnitude were computed by taking the total number of distances whose PGA Y was greater than a reference PGA y for hazard calculations ($N[R_{Y>y}]$), divided by the total number of distances in each fault, which is N_R = 100. Mathematically, this is given by Equation (2):

$$P[Y > y \mid rup_n] = N[R_{Y>y}]/\, N_R \quad (2)$$

Reference PGAs (in terms of acceleration due to gravity $\boldsymbol{g}$) used for this study were as follows: 0.01 to 0.09 (in multiples of 0.01) and 0.10 to some upper limit, which is the maximum predicted PGA for all rupture scenarios.

The hazard rate of exceedance for all rupture scenarios in all seismic sources assuming that the sources are independent of each other and collectively exhaustive, is given by Equation (3):

$$\lambda_{IM}(im) = \sum_{n=1}^{N_{rup}} P[Y > y|rup_n]\lambda_{Rup}(rup_n) \quad (3)$$

where $P[Y > y \mid rup_n]$ is the probability of exceedance in (2), $\lambda_{Rup}(rup_n)$ is the hazard rate of the given rupture scenario (magnitude of occurrence) which is the probability of occurrence of the magnitude multiplied to the activity rates in a given magnitude [13], [14]. A series of reference PGA values were used to construct the hazard curve, the plot of PGA values vs. the hazard rate or the mean annual rate of exceedance for a given site [1], which is L'Aquila for this study.

Results and Discussion

A total of 325 magnitude scenarios and 2013 ground motion simulations were generated in this study. The smallest distance identified in this study came from Paganica Fault, which is 1.64 km. The highest and smallest PGA calculated in this study are 2.16*g* (which came from Paganica Fault) and 0.114*g* (which came from the farthest fault) respectively.

Fig. 4 shows the seismic hazard curve (solid line) for the city of L'Aquila, which was obtained by summing the individual hazard curves for each seismic source.

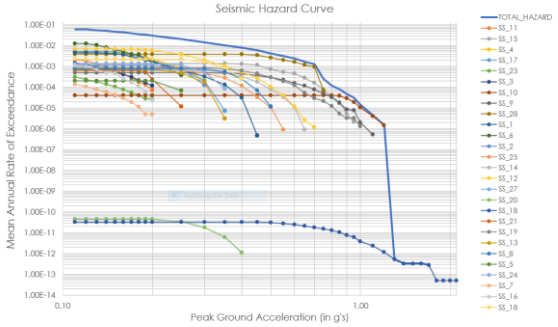

Fig. 4. Seismic Hazard Curve for the City of L'Aquila, Italy

The hazard curve generated in this study was compared to that of the recent PSHA [8], which is shown in Fig. 5.

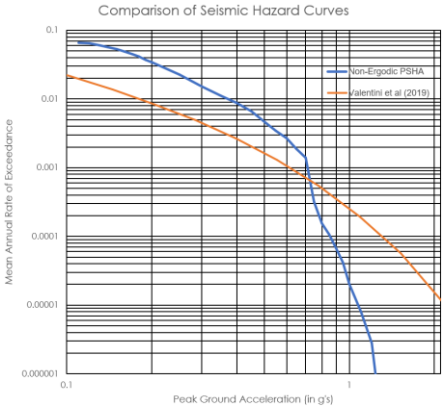

Fig. 5. Comparison to the Hazard Curve [8]

For PGAs less than 0.70*g*, higher hazard rates were observed, implying that the ground motion was overestimated for very far sources. Also, lower hazard rates were observed for PGAs greater than 0.70*g* which can be attributed to fewer seismic sources considered in this study.

Conclusion

Inclusion of background sources will increase the hazard in high-valued PGA. The grid size used in the simulations overestimates the PGA in very far sources, which can be improved by varying the grid size to be used in the approximate solution of (1). This will decrease the seismic hazard in low-valued PGA.

References:

[1] S.L. Kramer, *Geotech. Eq. Engg.*, Prentice-Hall Inc., New Jersey, 1-143 (1996).

[2] C.A. Cornell, *Bull. Seismo. Soc. Am.*, **58**, 1583-1606. (1968)

[3] R.K. McGuire, *Bull. Seismo. Soc. Am.*, **85**, 1275-1284. (1995)

[4] R.K. McGuire, *Eq. Engg. & Struct. Dynamics*, **37**, 329-338. (2007)

[5] J.G. Anderson, J.N. Brune, *Bull. Seismo. Soc. Am.*, **89**, 501-520. (1999)

[6] L. Hutchings, G. Viegas, *Eq. Res. & Anal. - New Frontiers in Seismo.*, Sebastiano D'Amico (Ed). IntechOpen, Available from: https://www.intechopen.com/books/earthquake-research-and-analysis-new-frontiers-in seismology/application-of-empirical-green-s-functions-in-earthquake-source-wave-propagation-and-strong-ground-m

[7] P. Monaco, G. Totani, G. Barla, A. Cavallaro, A. Costanzo, A. D'Onofrio, L. Evangelista, S. Foti, S. Grasso, G. Lanzo, C. Madiai, M. Maraschini, S. Marchetti, M. Maugeri, A. Pagliaroli, O. Pallara, A. Penna, A. Saccenti, F.S. De Magistris, S. Scasserra, F. Silvestri, A.L. Simonelli, G. Simoni, P. Tommasi, G. Vannucchi, L. Verrucci, *Eq. Geotech. Engg. Satellite Conf. XVIIth Int. Conf. Soil Mech. & Geotech. Engg.* (2009).

[8] A. Valentini, B. Pace, P. Boncio, F. Visini, A. Pagliaroli, F. Pergalani, *AGU 100: Advan. Earth & Space Sci* (2019).

[9] A. Valentini, F. Visini, B. Pace, *Nat. Haz. & Earth Sys. Sci.*, **17**, 2017-2039. (2017)

[10] A. Bizzari, *Rev. of Geophys.*, **49**, 1-32. (2011)

[11] M. Causse, L.A. Dalguer, P.M. Mai, *Geophys. J. Int.*, **196**, 607-620.

[12] P. Shearer, *Intro. to Seis.* 2nd ed. Cambridge University Press, New York. (2009).

[13] K. Tarbili, B. Bradley, J. Huang, V. Polak, D. Lagrava, J. Motha, S. Bae, *16th Euro. Conf. Eq. Engg.* – Thess. (2018)

[14] K. Tarbili, B. Bradley, J. Huang, R. Lee, D. Lagrava, S. Bae, V. Polack, J. Motha, M. Zhu, *2019 Pac. Conf. Eq. Engg.* – NZ. (2019)

A mathematical model of two-dimensional vertical flow based on the dual approach

The Hung Nguyen*

Faculty of Water Resources Engineering, University of Science and Technology,
The University of Danang, Vietnam
E-mail: ngthung@dut.udn.vn

Abstract

The mathematical model of two-dimensional vertical flow is commonly constructed using the classic average method by taking the integral from the right to the left riverbank (global averaged value - GAV [1,2]) of the three-dimensional Reynolds averaged Navier-Stokes equations [*Fig. 1.*]. Hence, the average quantities obtained from this approach do not generalize by means of dual approach (the global-local averaged value - GLAV [1,2]). This paper presents a dual approach to establish the two-dimensional vertical flow equations. The setup model will be more complex than the classic one because the integration can be done locally several times. In this paper, the author performed twice integrals: (i) the first, integration is from the right riverbank to the intermediate vertical surface layer between the right bank and the left bank (local averaged value – LAV [1,2]), and then (ii) the second, integration is from the right bank to the left bank (GAV) [1,2].

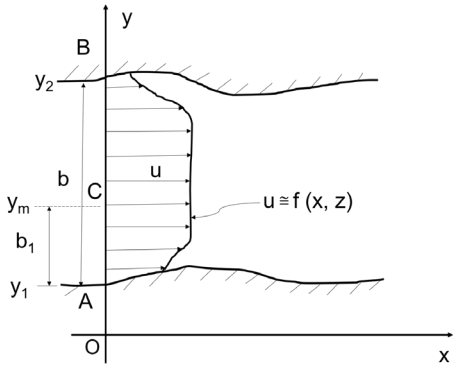

Fig. 1. Sketch of the construction of 2DV flow using the dual approach.

In this paper, the author has been built a system of equations to describe 2DV flow in open channel based on the dual approach as follows:

$$\gamma_{1c}.\frac{\partial}{\partial t}\left(y_2^2-y_1^2\right)+\beta_{1c}\frac{\partial}{\partial x}\left[\bar{u}.\left(y_2^2-y_1^2\right)\right]+$$
$$\delta_{1c}\frac{\partial}{\partial z}\left[\bar{w}.\left(y_2^2-y_1^2\right)\right]=0$$

$$\alpha_{1tx}.\frac{\partial}{\partial t}\left\{\bar{u}.(y_2^2-y_1^2)\right\}-\alpha_{1tx}.\bar{u}.\left\{\frac{\partial}{\partial t}(y_2^2-y_1^2)\right\}+$$
$$\beta_{1x}\frac{\partial}{\partial x}\left\{(\overline{uu}).(y_2^2-y_1^2)\right\}-\beta_{1x}(\overline{uu}).\frac{\partial}{\partial x}(y_2^2-y_1^2)$$
$$+\delta_{1x}\frac{\partial}{\partial z}\left\{(\overline{uw}).(y_2^2-y_1^2)\right\}-\delta_{1x}(\overline{uw}).\frac{\partial}{\partial z}(y_2^2-y_1^2)=$$
$$\frac{1}{\rho}.F_x.(y_2^2-y_1^2)-\frac{1}{\rho}.\frac{\partial p}{\partial x}.(y_2^2-y_1^2)+$$
$$\frac{1}{\rho}div(\vec{\tau})_x.(y_2^2-y_1^2)-\frac{1}{\rho}(\vec{\tau}.\vec{n})_x.(y_2+y_1)$$
$$\alpha_{1tz}\frac{\partial}{\partial t}\left\{\bar{w}.(y_2^2-y_1^2)\right\}-\alpha_{1tz}.\bar{w}.\left\{\frac{\partial}{\partial t}(y_2^2-y_1^2)\right\}+$$
$$\beta_{1z}\frac{\partial}{\partial x}\left\{(\overline{wu}).(y_2^2-y_1^2)\right\}-\beta_{1z}(\overline{wu}).\frac{\partial}{\partial x}(y_2^2-y_1^2)$$
$$+\delta_{1z}\frac{\partial}{\partial z}\left\{(\overline{ww}).(y_2^2-y_1^2)\right\}-\delta_{1z}(\overline{ww}).\frac{\partial}{\partial z}(y_2^2-y_1^2)=$$
$$\frac{1}{\rho}.F_z.(y_2^2-y_1^2)-\frac{1}{\rho}.\frac{\partial p}{\partial z}.(y_2^2-y_1^2)+ \qquad (1a)$$
$$\frac{1}{\rho}div(\vec{\tau})_z.(y_2^2-y_1^2)-\frac{1}{\rho}(\vec{\tau}.\vec{n})_z.(y_2+y_1)$$

Where: $\bar{u}$, $\bar{w}$ are the averaged velocity components along the river width in the Ox, Oz directions respectively; $\vec{n}$ is the boundary normal vector; $(\vec{\tau}.\vec{n})_x$, $(\vec{\tau}.\vec{n})_z$ is the side-wall friction in the Ox and Oz directions respectively; ρ is the density of water; α_{1tx}, α_{1tz}, β_{1x}, β_{1z}, δ_{1x}, δ_{1z} are correction factors with values close 1.

In the case of the origin of the axis Oy is chosen to coincide with point A (right riverbank), the system of equations (1a) is rewritten as follows:

$$\beta_{1c}\frac{\partial}{\partial x}\left[\bar{u}.b^2\right]+\delta_{1c}\frac{\partial}{\partial z}\left[\bar{w}.b^2\right]+\gamma_{1c}.\frac{\partial}{\partial t}\left(b^2\right)=0$$

$$\alpha_{1tx}.\frac{\partial}{\partial t}\left\{\overline{u}.(b^2)\right\}-\alpha_{1tx}.\overline{u}.\left\{\frac{\partial}{\partial t}(b^2)\right\}+$$
$$\beta_{1x}\frac{\partial}{\partial x}\left\{(\overline{uu}).(b^2)\right\}-\beta_{1x}(\overline{uu}).\frac{\partial}{\partial x}(b^2)+$$
$$\delta_{1x}\frac{\partial}{\partial z}\left\{(\overline{uw}).(b^2)\right\}-\delta_{1x}(\overline{uw}).\frac{\partial}{\partial z}(b^2)=$$
$$\frac{1}{\rho}.F_x.(b^2)-\frac{1}{\rho}.\frac{\partial p}{\partial x}.(b^2)+\frac{1}{\rho}div(\vec{\tau})_x.(b^2)-\frac{1}{\rho}(\vec{\tau}.\vec{n})_x.(b)$$
$$\alpha_{1tz}\frac{\partial}{\partial t}\left\{\overline{w}.(b^2)\right\}-\alpha_{1tz}.\overline{w}.\left\{\frac{\partial}{\partial t}(b^2)\right\}+$$
$$\beta_{1z}\frac{\partial}{\partial x}\left\{(\overline{wu}).(b^2)\right\}-\beta_{1z}(\overline{wu}).\frac{\partial}{\partial x}(b^2)+ \qquad (1b)$$
$$\delta_{1z}\frac{\partial}{\partial z}\left\{(\overline{ww}).(b^2)\right\}-\delta_{1z}(\overline{ww}).\frac{\partial}{\partial z}(b^2)=$$
$$\frac{1}{\rho}.F_z.(b^2)-\frac{1}{\rho}.\frac{\partial p}{\partial z}.(b^2)+$$
$$\frac{1}{\rho}div(\vec{\tau})_z.(b^2)-\frac{1}{\rho}(\vec{\tau}.\vec{n})_z.(b)$$

Remark: The system of equations (1a) and (1b) has adjustment coefficients α_i, β_i so it is easy to adjust the calculation results to be closer to reality. When the river width b changes slightly in time and space (along the river Ox and the depth Oz), then from the system of equations (1a) and (1b) we obtain the system of equations 2DV as follows:

$$\beta_{1c}\frac{\partial}{\partial x}\left[\overline{u}.b^2\right]+\delta_{1c}\frac{\partial}{\partial z}\left[\overline{w}.\left(b^2\right)\right]=0$$
$$\alpha_{1tx}.\frac{\partial}{\partial t}\left\{\overline{u}.(b^2)\right\}+\beta_{1x}\frac{\partial}{\partial x}\left\{(\overline{uu}).(b^2)\right\}+$$
$$\delta_{1x}\frac{\partial}{\partial z}\left\{(\overline{uw}).(b^2)\right\}=\frac{1}{\rho}.F_x.(b^2)-\frac{1}{\rho}.\frac{\partial p}{\partial x}.(b^2)+$$
$$\frac{1}{\rho}div(\vec{\tau})_x.(b^2)-\frac{1}{\rho}(\vec{\tau}.\vec{n})_x.(b)$$
$$\alpha_{1tz}\frac{\partial}{\partial t}\left\{\overline{w}.(b^2)\right\}+\beta_{1z}\frac{\partial}{\partial x}\left\{(\overline{wu}).(b^2)\right\}+$$
$$\delta_{1z}\frac{\partial}{\partial z}\left\{(\overline{ww}).(b^2)\right\}=\frac{1}{\rho}.F_z.(b^2)-\frac{1}{\rho}.\frac{\partial p}{\partial z}.(b^2)+$$
$$\frac{1}{\rho}div(\vec{\tau})_z.(b^2)-\frac{1}{\rho}(\vec{\tau}.\vec{n})_z.(b) \qquad (2)$$

From the equations (2) when linearizing along the width of the river b, we can easily get the system of 2DV flow equations set up according to the classical method.

From the 2DH flow equations derived using the dual approach [5] combined with 2DV equation (2), we obtain the 1D flow equation for the dual approach as follows:

$$\frac{\partial H^2}{\partial t}+\frac{\partial}{\partial x}(\alpha_{1c}uH^2)+\frac{\partial}{\partial x}(\beta_{1c}ub^2)=0$$
$$\frac{\partial}{\partial t}(\alpha_1.\overline{u}.H^2)+\alpha_{1tx}.\frac{\partial}{\partial t}(\overline{u}.b^2)+\frac{\partial}{\partial x}(\alpha_2.u^2H^2)+\beta_{1x}\frac{\partial}{\partial x}(\overline{uu}.b^2)$$
$$=-gH^2\frac{\partial Z_s}{\partial x}-g.b^2\frac{\partial Z_s}{\partial x}+\frac{1}{\rho}div(\vec{\tau})_x.(H^2)$$
$$-\frac{1}{\rho}(\vec{\tau}.\vec{n})_x.(H)+\frac{1}{\rho}div(\vec{\tau})_x.(b^2)-\frac{1}{\rho}(\vec{\tau}.\vec{n})_x.(b) \qquad (3)$$

Rewritting the system (3-27) according to the flow discharge Q and the water level elevation Z_s:

$$\frac{\partial(AH)}{\partial t}+\frac{\partial}{\partial x}(\alpha_{1c}HQ)+\frac{\partial}{\partial x}(\beta_{1c}bQ)=0$$
$$\frac{\partial}{\partial t}(\alpha_1.HQ)+\alpha_{1tx}.\frac{\partial}{\partial t}(bQ)+\frac{\partial}{\partial x}(\alpha_2.\frac{HQ^2}{A})+\beta_{1x}.\frac{\partial}{\partial x}(Q^2)=$$
$$-gAH\frac{\partial Z_s}{\partial x}-g.Ab\frac{\partial Z_s}{\partial x}+\frac{1}{\rho}div(\vec{\tau})_x.(H^2)+\frac{1}{\rho}div(\vec{\tau})_x.(b^2)$$
$$-\frac{1}{\rho}(\vec{\tau}.\vec{n})_x.(H)-\frac{1}{\rho}(\vec{\tau}.\vec{n})_x.(b) \qquad (4)$$

In the system of equations (4), the coefficients can be taken as follows:

$$\alpha_1\cong\alpha_{1tx};\ \alpha_2\cong\beta_{1x}$$

More simply, ignoring the effect of the width variation b, we receive the system of one-dimensional flow equations set up by the dual approach as follows:

$$\frac{\partial(AH)}{\partial t}+\frac{\partial}{\partial x}(\alpha_{1c}HQ)=0$$
$$\frac{\partial}{\partial t}(\alpha_1.HQ)+\frac{\partial}{\partial x}(\alpha_2.\frac{HQ^2}{A})= \qquad (5)$$
$$-gAH\frac{\partial Z_s}{\partial x}+\nu.H\frac{\partial^2 Q}{\partial x^2}-gAHS_f$$

Where: A is cross-sectional area; H is depth of flow; Q is discharge; Z_s is water surface elevation; ν is kinematic viscosity coefficient and S_f is frictional slope of the river bed.

Linearizing (5) with respect to H, we arrive at a system of classical 1D equations [3,7].

The improved two-dimensional vertical and one-dimensional flow models received from this dual approach allows the calculation of flow parameters is more accurate than the classical method. In other words, it provides some flexible parameters to adjust based on the field or experimental data.

Keywords: *classic average method, dual approach, two-dimensional vertical flow, average quantities.*

References:

[1] Nguyen Dong Anh, *Dual approach to averaged values of functions, Vietnam Journal of Mechanics, VAST*, Vol. 34, No. 3, pp. 211 – 214 (2012).

[2] Nguyen Dong Anh, *Dual approach to averaged values of functions: Advanced formulas, Vietnam Journal of Mechanics*, *VAST*, Vol. 34, No. 4, pp.

321 – 325 (2012).

[3] NGUYEN The Hung, *Salinity intrusion in Huong river network and the measure of hydraulic construction*, *The Journal of Science & Technology (Five University of Technology)*, No. 2, pp. 17-21 (1992).

[4] Hung NGUYEN The, *A dual approach to modeling solute transport, The International Conference on Advances in Computational Mechanics*, pp. 821-834 (2017).

[5] Tinh Ton That[1], The Hung Nguyen[1*], Dong Anh Nguyen[2], *A dual approach for model construction of two-dimensional horizontal flow, Proceedings of the 10th International Conference on Asian and Pacific Coasts, Hanoi, Vietnam, Sept. 25-28,* pp.115-120 (2019).

[6] Hung, NGUYEN The, *A dual approach for modeling two- and one-dimensional solute transport, The International Conference on modern mechanics and applications, Lecture notes in Mechanical Engineering,* pp 11-12, Springer (2020).

[7] Weiming Wu, *Computation river dynamics*, Taylor and Francis / Balkema (2007).

Oral Presentation

Information and Communications Technology (ICT) & Intelligent and Secure Systems

November 24th

Presentation No.	Title	Author	
ICT1.	Beautification Algorithm for Handwritten Characters Based on Deep Learning	Ko-Ting Wu, Qiu Chen	125
ICT2.	An approach for ceramic tile defects classification based on genetic algorithm and CNN	Nhat-To Huynh	128
ICT3.	Creating Strong AIWolf Agents using Systematic Tactical Evaluation	Shunsuke Hatta, Keisuke Takahashi, Kazunari Furukawa, Junji Yamato	129
ICT4.	A Study on Optical Burst Transfer Method in Torus Type Data Center Network	Yuya Ogino, Ken-ichi Baba	133
ICT5.	Effect of cell range expansion of picocells with a wide bandwidth in multiband HetNets	Ayumi Yoneyama, Hiroyuki Otsuka	135
ICT6.	Impact of phase noise for OFDM-based 1024-QAM transmission	Daisuke Kosuge, Hiroyuki Otsuka	136
ICT7.	A Study of QUIC and Application Development	Jiun-Yu Tu, Pei-Ying Tsai, Ya-Ting Zhuang	137
ISS1.	Verification of Dentition Shape Extraction Method	Yutaro Iso, Kazuhiro Suga	141

Beautification Algorithm for Handwritten Characters Based on Deep Learning

Ko-Ting Wu, Qiu Chen

Major of Electrical Engineering and Electronic, Graduate School of Engineering, Kogakuin University, Tokyo, Japan
E-mail: cm20021@g.kogakuin.jp, chen@cc.kogakuin.ac.jp

Abstract

With the development of artificial intelligence (AI), it has been able to makes the generated handwritten fonts similar to humans to a certain extent. In this paper, we propose a method to estimate the style of handwritten characters using deep neural networks, and reflect it to printed fonts to achieve the effect of beautifying the fonts. We use convolutional neural networks as the deep neural network architecture, perform font generation on the zi2zi model. The experimental results show that a good learning effect can be achieved on the zi2zi model, and beautified fonts can be generated to a certain degree.

1. Introduction

In recent years, with the spread of the Internet, the conversion of paper materials into digital data is developing at a high speed. Since electronic data signatures are more convenient than direct signatures, people have fewer and fewer opportunities to use pens.

So once they have the chance to write, many people write poorly. In this research, we propose a method to digitize someone's own font and beautify his handwritten font to some extent close to the printed font. The purpose of the research is to maintain the characteristics of handwritten characters and to approach the print font, aiming for an original in between.

In addition, traditional font creation is a time-consuming task, and related research is positive researching, they use GAN to create only a part of the font and automatically generate other fonts, it is considered to be useful. The purpose of this research is to generate full font like previous research.

2. Related Work and Challanges

First of all, as a previous research, research on the theme of font style conversion is active, and models such as pix2pix[1] and CycleGAN[2] have appeared one after another.

Among them, Multi-Content GAN (MC-GAN)[3], which was studied mainly for font image conversion, was also proposed, to create all of English letters , they use some font images (for example, A, B, C) and to generate all other font images (D to Z) . Such research is revolutionary for time-consuming font generation.

In this paper, we use zi2zi[4] (Master Chinese Calligraphy with Conditional Adversarial Networks), which is based on Chinese and Chinese characters, as one of the comparison targets, and estimate the process of changing one font to another.

In addition, zi2zi[4] is a model that learns for a print font data set, but it is not good at learning effects with handwritten characters, so the purpose of this research is fine-tuning with the zi2zi[4] model and hope to get the same results as handwritten font text, then when we get the proposed result, it means GAN has captured the features of printed fonts and handwritten fonts, we can produce original fonts that have both handwritten text features and beauty, and then achieve the goal of beautifying fonts.

3. Research Methodology

3. 1 zi2zi

As the main model of this research, we will build a system that learns from font images to font images end-to-end, and uses the trained model to generate original fonts. Estimate the process of changing one font to another font.

Zi2zi model is directly derived and extended from the popular pix2pix model. The network structure is illustrated below Fig.1.

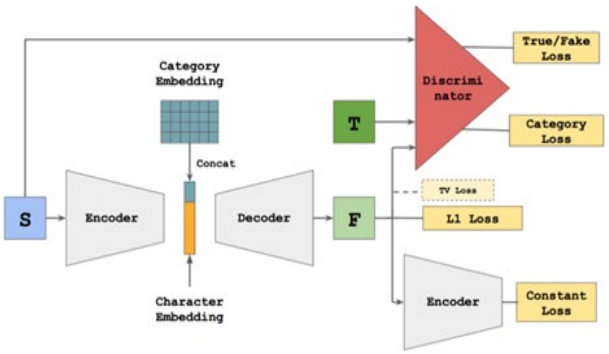

Fig. 1. zi2zi model

3. 2 Method

As shown in Fig. 2, the zi2zi model is learned by using the specified font as the learning target. In this experiment, the training target is 1000 images, each with 20 source fonts. The generative model trained in the first trained step, already has the power to generate font, but it also needs fine-tuning so as to get closer to handwriting rather than the trained source font.

In this experiment, the source font for fine-tuning

is 200 handwritten characters. In order to beautify, we used a fine-tuned model instead of just generating, and divided the handwritten characters to the target font into 10 stages, with 0 for the source font and 10 for the generated handwritten characters. When there is an interpolation feature from 0 to 10, we can adjust the feature arbitrarily to meet our needs.

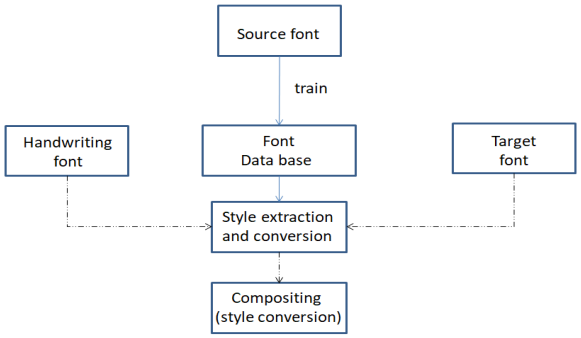

Fig. 2. Proposed method

3. 3 Fine-tuning

In fine-tuning, it is necessary to generate the same image data as the normal training. In this experiment, we used a box file to generate the characters of the handwritten image and the font characters. When creating the necessary box file, tesseract OCR was used to recognize fonts in handwritten images for fine-tuning the Japanese model.

In this experiment, wordlist is necessary, and we use tesseract OCR to automatic detect font position, and make a box around the word to generate box file. The resulting image is shown in Fig. 3.

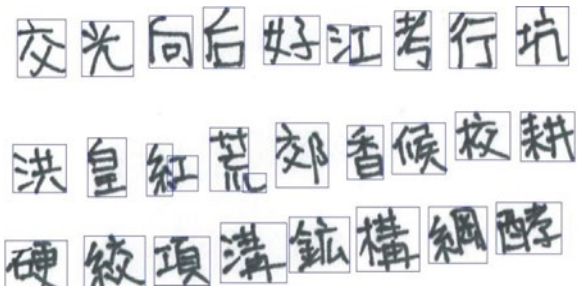

Fig. 3. Image of handwriting use OCR

In the image, the recognition result is quite high, but there is a slight deviation, some of the words cannot be recognized correctly, and will become "~" symbols.

In order to fix it completely, we fine-tuned the incomplete part as shown in Fig. 4 with the program jTessBoxEditor that can edit the box file. Finally, we use the fine-tuned box file and picture to generate the same data as the training data.

1	交	206	166	76	85
2	~	307	169	81	81
3	稿	413	161	68	76
4	合	498	148	65	90
5	洪	593	161	88	71
6	栽	693	174	37	56
7	~	728	176	50	58
8	黄	799	154	57	86
9	~	885	156	74	82
10	溝	990	147	82	87

Fig. 4. Adjustments in jTessBoxEditor

4. Experimental results

In our experiment, first, 20 fonts are used as training data, and the partial results of training with 40 epochs are shown in Fig. 5(a). The training effect is good because there are many source images and it is beautiful, and the partial results of fine-tuning data are shown in Fig. 5 (b), in which 10 epochs are fine-tuned for 200 handwriting font images, although the number of fine-tuned images is less than the training data, but it can be seen that they have been trained in some extent.

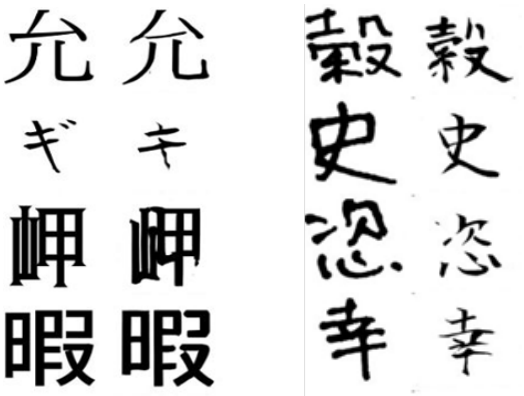

(a) (b)

Fig. 5. Comparison image

Next is the evaluation of the generated image. This time we chose the Chinese character "史", which has a large difference between the handwritten character and the source font "K Gothic". There are three pictures as shown in Fig. 6, from left to right are " handwritten", "Generated results", and "K Gothic (source font)".

Fig. 6. Comparison with source font image

From the overall glyph, the handwriting font is tilted left, which may be a feature of our handwriting.We think that the Chinese character "史" generated by the trained model is more tilted to the left than the source image. Therefore, it can be considered that the model has been effectively trained.

In addtion, in the local glyph, we can see that the part of "ノ" in th character "史" of source font is more curved than the handwriting font. From the generated fonts, the same part is straight, and the training data is also straight. Therefore, it can be considered that this is also evidence of training.

5. Conclusion

In this research, we have proposed a method to estimate the style of handwritten characters using deep neural networks, and reflect it to handwriting font to achieve the effect of beautifying the handwriting fonts. We conducted an experiment with zi2zi, and achieved a good training effect. The next goal is to adjust the parameters in zi2zi, so as to obtain a better generation quality, and to find other models to further improve.

References:

[1] P. Isola, J.-Y. Zhu, T. Zhou, and A.A. Efros, Image-to-image translation with conditional adversarial networks, arXiv preprint arXiv:1611.07004, 2016.

[2] P. Isola, J.-Y.Zhu, T. Zhou, and A.A. Efros. UnpairedImage-to-Image Translation using Cycle-Consistent Adversarial Networks. In *Proc. of IEEE Int. Conf. on Computer Vision*, 2017

[3] S. Azadi, et al., Multi-content GAN for few-shot font style transfer, in Proc. CVPR, 7564-7573 (2018)

[4] Y.Tian, zi2zi: Learning Chinese Character style with conditional GAN, https://github.com/kaonashi-tyc/zi2zi, 2017.

An approach for ceramic tile defects classification based on genetic algorithm and CNN

Nhat-To Huynh

Department of Project Management, The University of Danang – University of Science and Technology, Danang, Vietnam
E-mail: hnto@dut.udn.vn

Abstract

Ceramic tile industry has contributed significantly to the economy. Grading and classifying the finished products are required to guarantee the quality of products and the satisfaction of the customers. However, most of ceramic tile factoríe still have relied on human vision to deal with this problem.

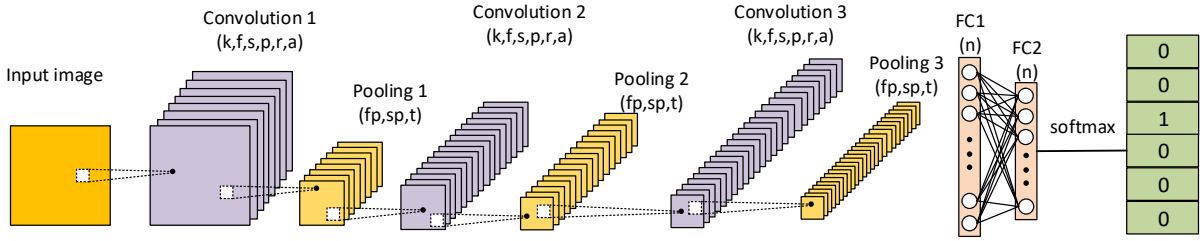

Fig. 1. general structure of CNN model

Classifying and grading the product relied on human vision has caused the quality problem due to inception and fatigue[1]. An automatic classifying system can enhance the quality control. However, there is a lack of studies for ceramic tile production. Thus, this study aims to propose a genetic algorithm based convolutional neural network (GA-CNN) which can automatically generate an optimal CNN for classification based on genetic algorithm. In particular, a general CNN structure is firstly determined including number of convolution layers, pooling layers, and fully connected layers. Then the parameters of each layers are optimized based on evolution process. Chromosome is designed that can represent efficiently all layers' parameters. The evolution proccess is implemented by crossover, mutation, and selection routines.

For ceramic tile defect classification problem, based on well-designed structure of some famous CNN and experts, the proposed GA-CNN consists of 3 convolutional layers, 3 pooling layers and 2 fully connection layers as Figure 1.

GA is used widely and efficiently for optimization problem[2][3]. The algorithms are designed based on evolution to find the optimal solution. General procedure of GA-CNN is designed as follows. Firstly, an initial population is generated based on encoding routine. Each chromosome represents a set of CNN structure parameters. To create new offspring, crossover and mutation routine are employed. A temporary population including parents and offspring is used to evaluate and select for next generation. The values of each chromosome in the temporary population are decoded and assigned to CNN model. The CNN models are optimized based on a given training dataset. Then the optimal CNN models are evaluated based on test dataset to generate fitness values of each chromosome. Based on the fitness values, selection routine is used to select chromosomes for next generation. This process is iterated until termination condition is met.

To validate, the proposed GA-CNN are compared to several well-known CNN algorithms. The results are shown as in table 1

Table 1. The accuracy of algorithms for different dataset.

Algorithm	Fashion_MNIST (%)	CTD (%)
ResNet	92.03	92.20
VGG	90.12	92.18
CNN-GA	87.22	90.55
Genetic CNN	82.81	90.73
GA-CNN	91.18	96.56

Defect detection and classification automatically can enhance the quality control in ceramic tile production. Due to different defect types of ceramic tile products, it is lack of models can deal with this problem completely. Thus, the study proposed an efficient algorithm to automatically generate an optimal CNN model for ceramic tile product. In particular, a general structure of CNN is constructed. Then, based on evolution process, genetic algorithm is designed to find optimal parameter of CNN layers automatically

References:

[1] S. H. Hanzaei, A. Afshar and F. Barazandeh, *Pattern Recognition*, **66**, 174-189 (2017).
[2] N. T. Huynh and C. F. Chien, *Computers & Industrial Engineering*, **125**, 615-627 (2018).
[3] N. T. Huynh, Y. C. Huang and C. F. Chien, *Computers & Industrial Engineering*, **125**, 221-231 (2018).

Creating Strong AIWolf Agents using Systematic Tactical Evaluation

Shunsuke Hatta, Keisuke Takahashi, Kazunari Furukawa, Junji Yamato

Department of Informatics, Graduate School of Engineering, Kogakuin University, Tokyo, Japan
E-mail: em21019@g.kogakuin.jp

Abstract

Artificial intelligence has surpassed humans in the games with perfect information, including GO and Shogi. On the other hand, artificial intelligence has not yet beaten humans in a game with imperfect information, and research is still ongoing. One of these games with imperfect information, the “werewolf game,” is attracting attention. The AI-based Werewolf Project is considered a good measure for the progress of Artificial General Intelligence. In this research, instead of creating agents by recombining the tactics of a single agent, we use a Simple Generation System to prepare multiple agents with different tactics. The purpose of this project was to evaluate the effectiveness of selecting a solid agent from among these agents and to use them to achieve excellent results in the protocol department of the 3rd International AI Werewolf Competition in conjunction with IJCAI2021. As a result, two of the agents we created made it to the finals and finished in 3rd and 6th place, confirming the effectiveness of this agent selection method.

1. Introduction

In 2016, artificial intelligence surpassed humans in Go, one of the most difficult "game with perfect information" as it defeated the world's top players. A "game with perfect information" is a game in which all players can observe all previous decisions made by all players at any point in time when they are making a decision. On the other hand, it is difficult to say that artificial intelligence has surpassed humans in "game with imperfect information," which is not a "game with perfect information." A "game with imperfect information"[1] is a game in which, at least at one point when one or more players are making a decision, it is not possible to observe the previous decisions made by one or more players. Examples include mahjong and poker.

Among the "game with imperfect information", the "Artificial Intelligence-based Werewolf Project"[2] is a project to conduct artificial intelligence research using the communication game "Are you a werewolf? ("werewolf game"), a communication game to research artificial intelligence.

To advance artificial intelligence technology, the Artificial Intelligence-based Werewolf Project is holding international competitions[3] once a year starting in 2019, inviting ordinary developers to compete for the strength of the Agents, or players, of artificial intelligence.

In this study, we created a variety of agents to achieve excellent results in the "Protocol divition"[4] of werewolf intelligence, a division in which programs play against each other with limited behavior in the form of protocols, and compared their winning rates and analyzed their tactics.

2. Objectives

The purpose of this study is to evaluate the effectiveness of selecting agents by evaluating their tactics[5]. To do this, we determine which tactics are effective for each role to decide which agents to submit. In doing so, instead of determining the direction of one agent and setting the tactics of that agent in detail, we prepare agents with several tactics and select a strong agent from among them.

We also aimed to achieve excellent results in the "3rd International AI Werewolf Competition".

3. Experimental Procedures

3.1 Agent Selection

We used aiwolf-server.jar, which is a file (aiwolf-ver0.6.2) containing tools and libraries for creating AI werewolf agents distributed by the Artificial Intelligence-based Werewolf Project, as the server. The roles used are the same as in the real tournament: 8 "villager", 3 "werewolf", 1 "seer", 1 "possessed", 1 "bodyguard", 1 "medium", and the role of each agent is chosen randomly in each game.

For each role, we created several agents with different combinations of tactics and compared their winning percentages. In this case, instead of implementing tactics that are considered to be strong , we selected strong agents through evaluation experiments from among several agents created using an agent creation system called the "Simple Generation System[6]" which was developed to lower the participation barrier to AI werewolf.

3.2 Evaluation Methods

The bases of the agents submitted to the tournament are Agent1, Agent2, and Agent3, respectively. We have prepared several different tactics for each of these roles that have been recombined.

We played 100 games, 10 times each, for each agent to be evaluated.

As the opposing agents, Agent1 played the game with four of the distributed source codes of the agents of the teams participating in the "the 1st International AI Werewolf Competition" and ten of the source codes of the agents of the teams participating in the "the 2nd International AI Werewolf Competition" for a total of 14 agents.

Agent2 played the game with three of the distributed source codes of the agents of the teams participating in the "the 1st International AI Werewolf Competition" and nine of the source codes of the agents of the teams participating in the "the 2nd International AI Werewolf Competition", one Agent1, and one agent prepared as a sample, for a total of 14 agents.

Agent3 played under almost the same conditions as Agent2, but with 14 agents in total, replacing one of the sample agents of Agent2 with one of Agent2.

In this way, the agents based on Agent1, Agent2, and Agent3, one each with the highest ratings, were submitted to the competition.

Hachi is an agent based on Agent1. In a 5-player village, based on agents in past tournaments, we selected the tactic of speaking out aggressively, since the total number of players is small, and it is thought to be easier to be trusted.

In the 15-player village, we focused mainly on the tactics of the werewolf team. We analyzed the concept of "Hiding," a tactic not often seen in werewolf intelligence but is often used in the original werewolf game. The tactic of "Hiding" is not to do many conspicuous actions such as deceive a role, and leave the early stages to other fellow werewolves. For this reason, it selected the tactic of cutting off relations with allies (abandoning when a fellow werewolf is about to be exiled in a vote). In addition, we paid particular attention to the reported results of deceiving a seer when it was a possessed agent. After analysis, we selected the tactic of behaving like a real role that had the highest win rate.

KP22 is designed based on Agent2. In a 5-player village, we selected the tactic of hiding when it was a werewolf because we thought it would be suspected and exiled if it predicted that werewolf multiple agents.

In a 15-player village, we analyzed the concept of taking the tactic of "disrupting the village," noting that the game would continue even if only one werewolf is exiled. In addition, we paid particular attention to the tactics of the werewolf to deceive a seer. After analysis, we selected the tactic of predicting that werewolf regardless of allied werewolves, which had the highest win rate.

Tomatoken is designed based on Agent3. In both the 5-player village and the 15-player village, we selected the tactic of Adjust to other players when it was a werewolf. This is because it is more advantageous to win the trust of the villager camp than to actively try to oust them and become suspicious due to differences in behavior.

We also paid particular attention to the medium's tactics, selecting not to act in a way that would protect his allies. This was to take advantage of the medium's ability to see the exiled agent's camp.

4. Results

4.1 Selection Results

As a result of the experiment, the tactical settings of the submitted agents are shown in Table 1 for the 5-player village and in Table 2 for the 15-player village. In this experiment, "Learning" refers to estimating the game state and making action decisions based on it. The state of the game is estimated by using Bayes' theorem to find the likelihood of the agent's action given the state of the game and the assignment of roles.

Table 1: Summary of agents in a 5-player village

5-player village	villager	seer	werewolf	possessed
1. Voting Policy	H,K: For werewolf T: Balance	H,K: For werewolf T: Balance	H,K: Adjust to other players T: Balance	H,K: Adjust to other players T: Balance
2. Protecting seer in voting	Yes	Yes	H,T: Yes K: No	H,T: Yes K: No
3. Speeching Policy	H,K: Express suspicious people T: Balance	H,K: Express suspicious people T: Balance	H: Express suspicious people K,T: Act like other players	H,T: Express suspicious people K: Act like other players
4. Predicting and Attacking Policy		Player who think is a werewolf	H: The seer K,T: Balance	
5. About 4 in the winning rate		H,K: Higher winning rate player K: No weighting	H,K: Higher winning rate player K: No weighting	
6. Predicting policy		Communicate honestly		
7. Deceiving seer policy			H: More predict that werewolf K,T: Behave like a real role	H,K: Predict that villager for werewolf T: Behave like a real role
8. Learning	H,K: More learning T: No learning	More learning	H,K: More learning T: Not much learning	More learning

Table 2: Summary of agents in a 15-player village

15-player village	villager	seer	werewolf	possessed	medium	bodyguard
1. Voting Policy	H,K: For werewolf T: Balance	H,K: For werewolf T: Balance	H: Adjust to other players K,T: Balance	H: Adjust to other players K,T: Balance	H,K: For werewolf T: Adjust to other players	H,K: For werewolf T: Balance
2. Protecting seer, medium, bodyguard in voting	Yes	Yes	H,T: Yes K: No	H,T: Yes K: No	H,K: Yes T: No	Yes
3. cut off relations with allies			H,K: Yes T: No			
4. Speeching Policy	H,K: Express suspicious people T: Balance	H,K: Express suspicious people T: Balance	H,T: Act like other players K: Express suspicious people	H: Act like other players K: Balance T: Express suspicious people	Express suspicious people	H,K: Express suspicious people T: Balance
5. Predicting and Protecting and Attacking Policy		H: A player of suspected K,T: Player who think is a werewolf	H,T: Balance K: The seer			H,K: The seer T: Balance
6. About 5 in the winning rate		H,K: Higher winning rate player K: No weighting	H,K: Higher winning rate player K: No weighting			H,K: Higher winning rate player K: No weighting
7. Predicting policy		Communicate honestly				
8. Deceiving seer policy			H: More predict that villager K: More predict that werewolf T:Behaving like a real role	H,T: Behaving like a real role K: More predict that villager		
9. Treatment of allied werewolf in 8			H: Not care werewolf or not K,T: Predict that villager for werewolf			
10. Learning	H,K: More learning T: No learning	More learning	H,K: More learning T: Not much learning	More learning	More learning	More learning

H: indicates the tactical settings of Hachi, K: indicates the tactical settings of KP22, and T: indicates the tactical settings of Tomatoken. No notation means that all tactics are the same. A blank field means that the role does not have any tactical setting.

In addition, KP22 was set to announce his role 80% of the time when it became a Power Play (when the werewolf camp surpassed the villagers, it would announce its role and force the villagers to exile themselves) when it was a werewolf and a possessed in a 15-player village.

4.2 Tournament Results

The results of the 3rd International AI Werewolf Competition are shown in Table 3.

Table 3: Results of the 3rd International AI Werewolf Competition

Rank	Agent Name	Programming Language	Using a Simple Generation System
1	toku/ICE	Java	
2	TOT	C#/ Java	
3	KP22	Java	✓
4	Syu	Java	✓
5	CanisLapus	Java	✓
6	Tomatoken	Java	✓
7	SORA	Java	✓
8	Hideto	Java	✓
9	HALU	python	
10	Tomato	Java	
11	OKAMI	python	
12	karma	Java	
13	wasabi	Java	
14	Sashimi	Java	

Because Toku and ICE were treated as the same agent, they tied for first place.

As for the results of the competition, Hachi did not qualify, KP22 finished 3rd, and Tomatoken finished 6th.

Of the 15 agents that participated in the tournament and advanced to the finals, six were created using the Simple Generation System, and all of the third through eighth places were created using the Simple Generation System, indicating that the overall results were good.

5. Discussion

The fact that KP22 and Tomatoken performed well suggests that the environment was stronger for agents with tactics to confuse the scene, such as actively identifying suspicious agent, proactively predicting that werewolf when deceiving a seer, and randomly attacking without learning much, than for agents with tactics to read deeply and take firm actions when in the werewolf camp.

For example, there were some agents who became the seer or the possessed only once or 14 times in 100 games, while the average number of times they became the roles was about seven times in 100 games. In addition, the range of winning percentages differed slightly depending on the combination of agents in each camp.

Because of the somewhat unconventional tactics used in this experiment, and because of the relationship between the combination of agents who are in the same camp and the winning rate, For example, we thought that there might be a kind of "Metagame" in which we take into account our own composition by predicting the composition of our opponents, as in the case of a rock-paper-scissors game in which we know in advance the tendency of the moves to be played by many players.

Therefore, as a future prospect, we would like to analyze the mainstream tactics from the current agents in the International AI Werewolf Competition and construct strategies corresponding to those tactics to improve the winning rate of the agents.

6. Conclusion

In order to improve the win rate of artificial intelligence in the "Protocol division" of AI werewolf and to aim for high rankings in the 3rd International AI Werewolf Competition, we created agents based on Agent1, Agent2, and Agent3 and analyzed the win rate.

As a result, two of them made it to the finals, and the best result was 3rd place, which is higher than the 5th place record set by Maruyama in the 2nd International AI Werewolf Competition last year, and we are very happy about that.

In addition, we would like to challenge research on the "Natural language division" that evaluates whether artificial intelligence is capable of natural dialogue, with the aim of having artificial intelligence and humans fight in werewolf game.

And if the 4th International AI Werewolf Competition is held, I would like to consider participating in it in order to achieve a higher rank.

References:

[1] Game with perfect information and Game with imperfect information | game-WIIS https://wiis.info/economics/game-theory/game/game-of-perfect-infomation-and-game-of-imperfect-information/ (2021.10.21).

[2] Kosuke Shinoda, Daisuke Katagami, Masamichi Inaba, Fujio Toriumi, Hirotaka Osawa, Hitoshi Matsubara, AIWolf Project 2015, JSAI SIG-SLUD-B502-20, Vol.75, pp.80-85.

[3] Artificial Intelligence based Werewolf Project http://aiwolf.org/ (2021.10.21).

[4] Takashi Otsuki, Yukiya Konda, Evaluation of the AI-based werewolf game player agent which can persuade and can be persuaded, The 34th Annual Conference of the Japanese Society for Artificial Intelligence (2020), 1P3-GS-7-05.

[5] Hiroaki Doguro, Hitoshi Matsubara, Performance Evaluation of AI Wolf Using Neural Network, The 32th Annual Conference of the Japanese Society for Artificial Intelligence (2018), 1H1-OS-13a-02.

[6] Atsushi Takeda, Fujio Toriumi, Development of a simple generation system of the werewolf AI agent, The 34th Annual Conference of the Japanese Society for Artificial Intelligence (2020), 2F5-OS-20b-02.

A Study on Optical Burst Transfer Method in Torus Type Data Center Network

Yuya Ogino and Ken-ichi Baba*

Electrical Engineering and Electronics Program, Graduate School of Engineering,
Kogakuin University, Tokyo, Japan
E-mail: cm21008@ns.kogakuin.ac.jp

Abstract

In data center networks, their architectures and device technologies are studied based on optical network and optical label processing in order to reduce the rejection rate of data required immediate response. In this paper, we propose a data transfer method using optical burst transfer based on this architecture. Our proposed method basically selects a path with the least probability of collision.Simulation results show that the signal rejection rate is reduced.

1. Introduction

As part of the increase in the Internet services, the communication traffic flowing in data center networks is increasing [1]. Therefore, it is important to reduce the power consumption and increasing bandwidth demand. In order to resolve these problems, we utilize optical communication in data center network actively. Optical packet switching has been proposed for nodes in a torus ring as a way to construct an optical data center network. [2] However, optical packet switching requires OEO conversion during switching, which incurs overhead and makes it difficult to provide an immediate response.

In order to suppress the rejection rate of data required immediate response, conventional research [3] has proposed an architecture and device technology that utilize optical label processing. In this paper, we propose a data transfer method according to this architecture. We use optical burst transmission to select a path with the least probability of signal collision.

2. Related technology

In conventional research [3], a method of constructing a torus network using wavelength allocation and optical labeling has been proposed. When transmitting data, each node in the torus topology broadcasts an optical burst signal to the nodes in the torus ring using a unique transmission wavelength. The optical label containing the destination information is attached to the transmitted optical burst signal. Each node reads the destination information in the optical labels of all wavelengths of the received signals and receives the data addressed to its own node. In the above network configuration method, the preamble is not required because the optical label is processed at the time of reception. Therefore, the waiting time for signal processing can be reduced compared to OCS and OPS.

3. Optical Burst Transfer Method

In the proposed architecture in [3], the node sends only predetermined wavelength signal and receives all wavelength signals. So in torus ring networks, the wavelength signal can be sent from the certain node and all wavelength signals can be received by all nodes. Then if the node sends data to the node belong other torus ring, data is exchanged at the node considered the relay node to change the torus ring. In this case a relay node cannot relay multiple signals to the same torus ring at the same time. Therefore, if a signal arrives later at a relay node, the later signal will be rejected.

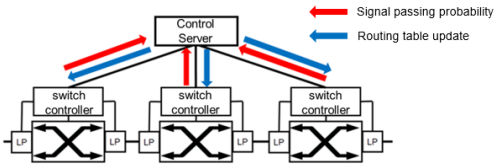

Fig. 1. Control server function diagram

In this paper, we propose an optical burst forwarding method that uses the signal passing probability to suppress the signal rejection. In the proposed method, the signal passing probability p is obtained from the utilization of the transmission port of each node. The signal passing probability p is given by Equation (1). where t_p is the time when data is transmitted or forwarded after t millisecond at the transmission port of the wavelength unique to each node. Figure 1 shows that the control servers collect the signal passing probability of each node and perform routing control based on the signal passing probability of the nodes in the network.

$$p = 1 - \frac{t_p}{t} \tag{1}$$

We denote the path control algorithm as follows.

I. Calculate the shortest hop path from the source node to the destination node.
II. Multiply the signal pass rate of the outgoing port of the sending node by the signal passing probability of the outgoing port of each relay node in each shortest path.
III. Of the values obtained by multiplying the signal passing probability of each shortest path, the one with the largest value is selected as the path

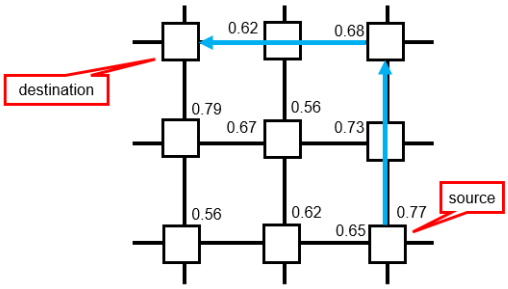

Fig. 2. route selection diagram

least likely to cause signal rejection.

IV. When a signal passes from a source node to a destination node, the routing table is updated so that the signal passes through the selected route.

V. The operations I through IV are performed for all combinations of source to destination nodes.

Figure 2 shows an example of path selection. Each value represents the signal transit ratio. The signal transit ratio is calculated for each shortest path, and the path indicated by the blue arrow is selected as the path with the largest signal transit ratio multiplier.

4. Performance evaluation

In order to investigate the basic characteristics, simulations were performed in a 4 × 4 torus topology. The arrival of requests follows a Poisson distribution, and the path duration follows an exponential distribution with an average of 300 msec. t is 200 msec, and the number of wavelengths is 4. As a comparison, we use a method that randomly selects a path from the shortest path.

Figure 3 shows the results of the signal rejection ratio for the random route selection method and the proposed method using the signal passing probability. Figure 3 shows that the proposed method reduces the request rejection rate by about 3.3 points when the load is 1.5 compared to the random route selection method. This can be attributed to the fact that the shortest path with the highest signal passing probability is selected.

Figure 4 shows the number of changing torus rings , From Fig. 4, it can be seen that the method applying the route selection method based on the signal passing rate has fewer torus ring changes than the random route selection method. When the number of torus ring changes is reduced, the number of burst signals broadcasted by relay nodes in the entire network can be suppressed, thus reducing signal contention in the entire network. Therefore, the reduction in the number of torus ring changes can be considered as one of the factors that reduce the signal rejection rate of the entire network.

5. Conclusion

In this paper, we proposed an optical burst

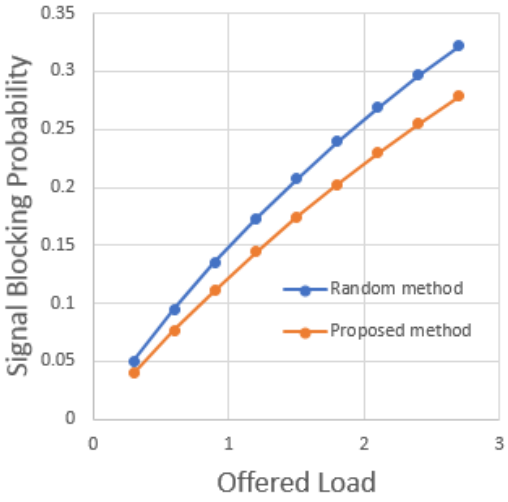

Fig. 3. Comparison of signal rejection rates

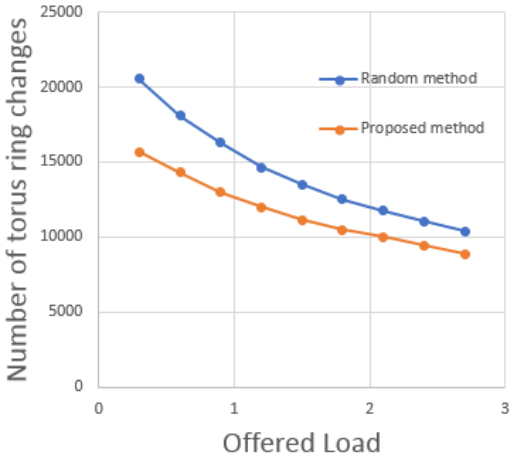

Fig. 4. Number of changing torus ring

forwarding scheme for torus data center networks. The simulation results show that the signal rejection rate is reduced. In order to investigate the basic characteristics, a small network was used, which resulted in a large rejection rate. In the future, we will study the control method to obtain an appropriate rejection rate in a realistic scale.

References:

[1] A. Singh, et al., “Jupiter rising: A decade of clos topologies and centralized control in google’s datacenter network”, *ACM SIGCOMM computer communication review*, vol. 45, no. 4, pp. 183–197, Aug. 2015.

[2] B. Uscumlic, et. al., “Cost efficient network slicing for optical packet switched torus data centers”, *in Proc of IEEE ICC*, pp. 1– 7, May 2017.

[3] H. Toshikazu, et. al., “Low-latency optical label switch networks and device technology using high-speed optical switches." *IEICE Technical Report (PN2019-20)*, vol. 119, no. 180, pp.67-72, Aug.2019.

Effect of cell range expansion of picocells with a wide bandwidth in multiband HetNets

Ayumi Yoneyama and Hiroyuki Otsuka

Graduate School of Engineering, Kogakuin University, Tokyo, Japan
E-mail: cm20056@ns.kogakuin.ac.jp

Abstract

5G NR NSA deployments combine with 4G macrocells and 5G NR picocells in the same coverage, which is the same configuration as a heterogeneous network (HetNet). In HetNets, cell range expansion (CRE) technology is important that can allow more user equipment (UE) to access the picocell, i.e., virtually expand the picocell coverage. In this paper, we clarify the optimal transmission (Tx) power of a pico eNB for multiband HetNet combined with a macro eNB operating at 2 GHz band and pico-eNB having a wider signal bandwidth operating at 4.5 GHz band picocell. Then, we investigate the user throughput of the HetNet when CRE is applied to picocells under the conditions of around the optimal Tx power.

Table I shows the configuration of multiband HetNet and primary simulation parameters [1]. The carrier frequencies used in the macro- and pico-eNB are 2.0 and 4.5 GHz, respectively. The sicnal bandwidth for the macro- and pico-eNB are 10 MHz and 100 MHz, respectively.

We investigate the average and 5-percentile user throughput using system-level computer simulations.

Table 1. Primary simulation parameters

Parameter	Macro eNB	Pico eNB
Cell layout	Hexagonal grid, 19 cell sites, 3 sectors per site	4 picos per sector
Cell radius	289 m (ISD = 500 m)	-
Carrier frequency	2.0 GHz	4.5 GHz
System bandwidth	10 MHz	100 MHz
Tx power	46 dBm	31,37 dBm
Tx height	32 m	10 m
Tx antenna gain	14 dBi	5 dBi
UE distribution	2/3 clustered distribution, 30 UEs per sector	
CSO	From 0 to 39 dB, 3dB step	
Link adaptation	25 MCS (QPSK to 1024-QAM)	
Traffic model	Full buffer	

Figure 1 shows the average and 5-percentile user throughput as a function of the Tx power of the pico-eNB. Based on these results, we confirmed that the Tx power of 37 dBm can provide the best performance. Figure 2 shows the average and 5-percentile user throughput as a function of CSO when the Tx power is 37 dBm. Figure 3 shows the average and 5-percentile user throughput when the Tx power is 31 dBm. From the average user throughput perspective, CRE does not work when the Tx power is 37 dBm. While, CSO of 6 dB in CRE provides best performance when the Tx power is 31 dBm.

In summary, we first clarified the optimal Tx power of the pico-eNB for multiband HetNets. Then, we investigated the effect of CREas a function of CSO for around the optimal Tx power.

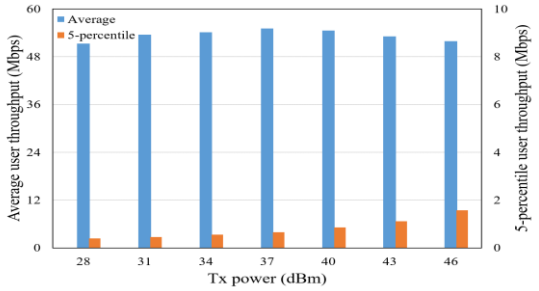

Fig. 1. Average and 5-percentile user throughput as a function of Pico-eNB Tx power.

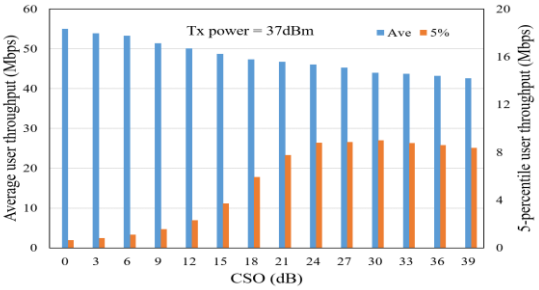

Fig. 2. Average and 5-percentile user throughput as a function of Tx power of 37 dBm.

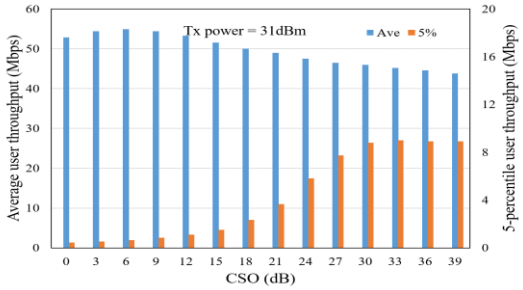

Fig. 3. Average and 5-percentile user throughput as a function of Tx power of 31 dBm.

References:

[1] A. Yoneyama, F. Kemmochi, and H. Otsuka, "Pico-eNB Tx Power Optimization for Multiband HetNets with MCS Incorporating 1024-QAM," *in Proc. ICOIN2021*, O-8-5, Jan 2021.

Impact of phase noise for OFDM-based 1024-QAM transmission

Daisuke Kosuge* and Hiroyuki Otsuka

Graduate School of Engineering, Kogakuin University, 1-24-2, Shinjuku-ku, Tokyo, 163-8677 Japan
cm20019@ns.kogakuin.ac.jp, otsuka@cc.kogakuin.ac.jp

Abstract

The use of millimeter wave bands is promised to achieve higher data rates because the available amount of signal bandwidth is enormous. However, the phase noise of millimeter wave oscillator degrades the transmission performance of OFDM. In particular, OFDM signal with high-order QAM will be sensitive to phase noise. In this paper, we investigate the transmission performance of OFDM-based 1024-QAM in the presence of phase noise as a function of a subcarrier spacing of OFDM signal.

In 5G, the use of high frequency bands is being considered to meet the requirements of high speed and high capacity. For wideband transmission using high-frequency bands, OFDM signals need to support multiple subcarrier spacing, and especially when using high carrier frequencies such as millimeter wave, the subcarrier spacing needs to be widened to reduce the effect of phase noise. The authors have previously evaluated the transmission performance of 256/1024/4,096-QAM under LTE-based subcarrier spacing conditions [1].

In this paper, we discuss Impact of phase noise for OFDM-based 1024-QAM transmission against five different types of subcarrier spacings.

Table 1 shows Primary Simulation Parameters. The OFDM signal bandwidth is assumed to be 100 MHz. The subcarrier spacing of OFDM is 15, 30, 60, 120, 240 kHz. The phase noise model was set to the values in the table in reference to 3GPP TR 38.803[2]. Figure 1 shows the transmission model. In this simulation, phase noise is added on the frequency axis before IFFT processing for the convenience of the simulation.

Table 1. Primary Simulation Parameters

Symbol modulation		1024-QAM				
Encoder		Turbo encoding Coding rate, R = 1/3 Constraint length = 4				
Signal mapping		Gray code				
Bandwidth (MHz)		100				
OFDM	subcarrier spacing (kHz)	15	30	60	120	240
	Cyclic prefix length (ns)	4760	2380	1190	595	298
Phase noise	level (dBc/Hz)	-70, -88, -95, -100				
	Frequency offset (kHz)	10^3, 10^4, 10^5, 10^6				
Decoder		Soft decision Viterbi decoding				

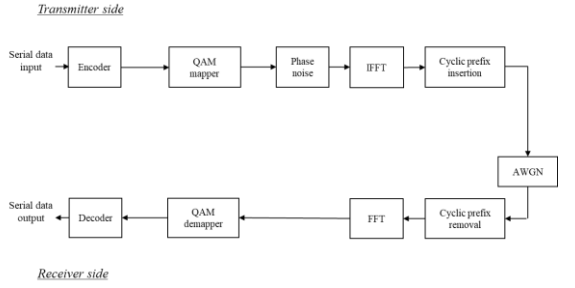

Fig. 1. Transmission model.

Figure 2 shows the BER performance of impact of phase noise for OFDM-based 1024-QAM transmission. When subcarrier spacing = 240 kHz, the required SNR to satisfy BER = 10^{-4} increases by about 4 dB during no phase noise. This is because the inter-subcarrier interference due to phase noise can be reduced by increasing the subcarrier spacing. When subcarrier spacing = 15, 30, 60, 120 kHz, 1024-QAM can no longer achieve a BER of 10^{-4} even if the SNR is increased. Also, the narrower the subcarrier spacing, the larger the value of BER floor became.

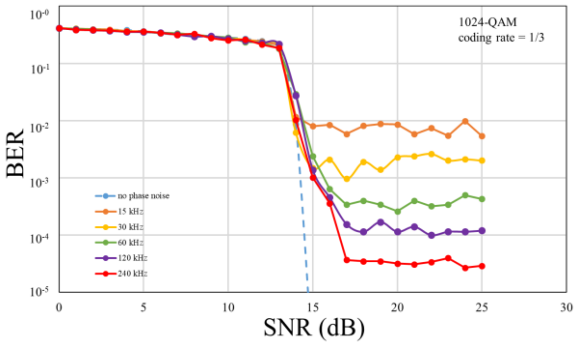

Fig. 2. SNR vs. BER performance.

In this paper, we clarified the BER performance of OFDM-based 1024-QAM as a function of subcarrier spacing in the presence of phase noise.

REFERENCE

[1] D. Kosuge and H.Otsuka, "Transmission Performance of 256-QAM for Subcarrier Spacing of OFDM under Fading Environment," IEICE Communications Society Conference , B-5-2, Sept. 2020.

[2] 3GPP TR 38.803, "Radio Frequency (RF) and co-existence aspects," V14.2.0 Release 14.

A Study of QUIC and Application Development

Pei-Ying Tsai, Ya-Ting Zhuang and Jiun-Yu Tu*

Department of Computer Science & Information Engineering, Southern Taiwan University of Science and Technology, Tainan, Taiwan, R.O.C.

E-mail: duketu@stust.edu.tw

Abstract

What is QUIC proposed by Google? It will be faster, safer and more stable than previous network protocols. Below we will explain the difference between QUIC and the previous agreement, and make a web case for the application of QUIC in the future

Before explaining QUIC, we want to talk about its predecessor, even the predecessor http 1.0 and http 2.0

First is http 1.0. It can only have a short connection with the server.

Every time you want to connect to the server, you must create a TCP connection, and it will not record past requests. In other words, each connection is a new connection, and every request will go through a high-latency three-way handshake, which is a waste of resources and time.

Next, http 2.0 solves http 1.0 Stream Multiplexing, binary framing, header compression and server push, it can disport more efficiently without changing http1.0

Then why does QUIC still appear?

The reason is that the TCP and UDP used by http are too extensive, and it is impossible to change them all at once. If you change them, I am afraid that many things will not be changed!

Let's talk about the advantages and disadvantages of TCP and UDP

TCP

Sequential numbering:

Add a number to each packet, so that even if the packets are not sent to the destination in the original order, the destination can still use this number for correct reassembly.

Three-way Handshake:

When the client wants to connect to the server, it must actively send a packet requesting connection to the server.

When the server receives and confirms this packet, it will also send a corresponding packet back to the client for confirmation and start waiting for the client's response.

When the client receives the response packet from the server, it can confirm that the previously sent packet has been correctly received. If the client also agrees to establish a connection with the server, it will send back a confirmation packet to inform the server.

After the above three conversations, the server receives and confirms it, it completes the three-way handshake and enters the connection establishment state.

Head-of-line blocking:

The first data packet of a column is blocked, which causes the whole column of data packets to be blocked.

UDP

UDP is fast and has a large traffic because it does not have a three-way handshake like TCP, there is no problem of chain building and unchaining, and there is no problem of line head blocking. Relatively speaking, UDP lacks security in order to be fast.

UDP is an unreliable non-connected data streaming service. The non-connection type refers to the unilateral transmission of messages when different transmission destinations want to start the transmission of messages. Therefore, the reliability of communication is relatively low, but it is also faster and suitable for real-time service.

UDP does not guarantee that the data is delivered exactly, the data is not received in order, and it will not search for lost packets.

QUIC & HTTP/3.0

Next, we will introduce our understanding of QUIC.

QUIC is a brand-new network protocol and a new multiplexing protocol based on UDP.

QUIC is the abbreviation of Quick UDP Internet Connections.

Google proposed QUIC to improve the user experience, especially to shorten the page load time.

HTTP/3.0 is HTTP Over QUIC, which is used to implement the QUIC protocol based on the UDP protocol.

The QUIC working group defined a clear boundary between the transport (QUIC) and application (HTTP/3) layers in the IETF, and TLS 1.3 replaced QUIC Crypto.

The architecture is shown in Fig. 1

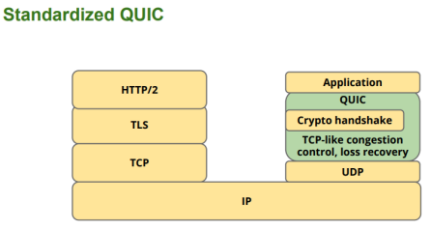

Fig. 1. QUIC architecture

QUIC features: connection establishment, multiplexing, packet loss recovery, flow control, connection migration

1. Connection establishment

QUIC proposes a new connection mechanism, the initial connection handshake and key exchange, it only takes 1 RTT.

By caching the key of the initial connection handshake on the client, starting from the second connection, each subsequent connection can directly start to transmit data, as shown in Figure 2, to achieve 0-RTT handshake detention, data is transmitted directly in an authenticated and encrypted channel.

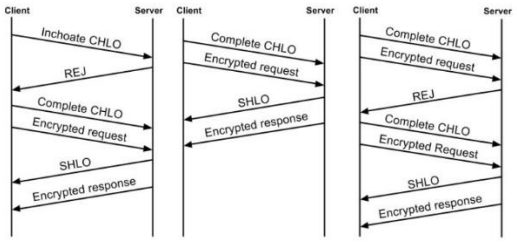

Fig. 2. New connection mechanism

2. Stream Multiplexing

When a packet transmitted by a TCP connection is lost, the transmission of the entire connection will be blocked before the sender actively discovers it and retransmits it. This is the problem of TCP HOL blocking.

Because QUIC performs data transmission of multiple streams in the same connection, when a packet in a stream is lost, only the transmission of this stream will be affected, and other streams can continue data transmission without being affected to avoid HOL blocking.

Multiplexing characteristics of QUIC:
Each Stream has its own Stream ID. In order to avoid conflicts, the Stream ID initiated by the client is an odd number, and the Stream ID initiated by the server is an even number.

The QUIC packet transmitted in the QUIC connection can carry multiple stream frames at the same time. Each stream frame may come from a different stream.

In order to avoid retransmission problems in QUIC, when sending, both the initial and retransmitted packets will be the unique packet number. In this way, when an ACK is received, the receiving end can clearly determine whether it is initial or retransmission.

3. Flow Control

Through flow control, the amount of data transmitted by the client can be limited.
In order to avoid this potential HOL blocking, QUIC uses connection flow control and stream flow control to limit the maximum buffer size that a single stream can occupy.

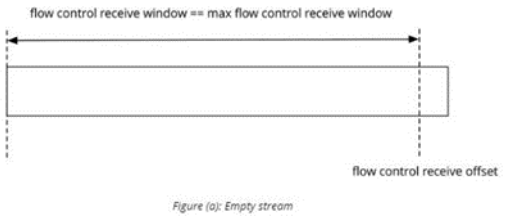

Fig. 3. Stream flow control

The receiving end can set the stream according to its own needs. For the newly created stream, the size of the receive window will be the same as the size of the max receive window. Flow control restricts the sender to only send data whose offset is within the receive window, that is, it can only send data in this interval, to ensure that the sender will not send more data than the receiver's buffer can withstand.

4. Connection Migration

To identify the TCP connection, four parameters are needed to distinguish which TCP the received packet belongs to. The disadvantage of this mechanism is that when the client's IP changes, the original connection will all fail.

Therefore, in order to handle the Connection Migration problem, QUIC uses the Connection ID to identify the connection, which is randomly generated by the client when the connection is established. The receiving end can continue the connection through the ID.

Where can QUIC be used?
Browse social web pages, watch videos, and video conferences to make web pages faster.
In this epidemic, we can obviously find that the delivery was running everywhere, but my order was delayed in delivery or was filtered by the system. Although there was a late discount, it greatly reduced our desire to use it.
Many browsers already support QUIC, so we used it to implement an online ordering integration system.

Online ordering integration system functions:
Use QUIC to improve the problem of missing orders, GPS positioning of delivery personnel is more

accurate, and save more waiting time.

Unify the two delivery platforms (Uber Eat, Foodpanda)

Platform: Receive customer orders without missing orders. The store will deliver them to the delivery staff before they are done. They will ship multiple times, estimate the production time, and calculate the waiting time more accurately.

Consumer: One-click comprehensive comparison of various discounts in the store menu.

Delivery staff: The positioning of the order is more clear, the order is received with the closest store, and the AI decide the similar route to stack the order, but no more than 3 orders.

When receiving a high amount, first evaluate the weight of the unit. If the unit is too heavy, split the bill directly to save the delivery staff from reporting time.

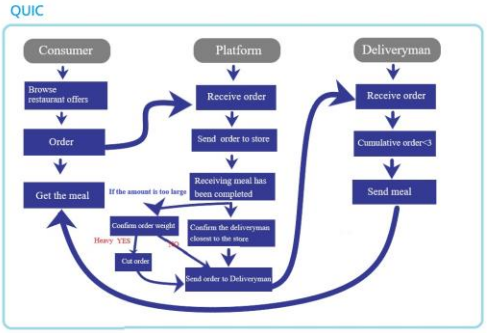

Fig. 3. Online ordering integration system flow chart

References:

[1] The QUIC Transport Protocol: Design and Internet-Scale Deployment.

[2] Flow control in QUIC Robbie Shade. May 2016

[3] QUIC, a multiplexed transport over UDP

[4] QUIC Tutorial A New Internet Transport

[5] QUIC WIKI Page

Verification of Dentition Shape Extraction Method

Yutaro ISO[1)], Kazuhiro SUGA[2)]

1) Graduate School of Engineering, Kogakuin University, JAPAN
E-mail: am20008@ns.kogakuin.ac.jp
2) Department of Mechanical Engineering, Faculty of Engineering, Kogakuin University, JAPAN
E-mail: ksuga@cc.kogakuin.ac.jp

Abstract

In order to realize safe and effective orthodontic treatment, it is important to understand the intraoral 3D shape. Currently, the problem is that the optical impression used to grasp the intraoral 3D shape is expensive and can only be measured at a specific dental clinic. Therefore, in order to grasp the intraoral 3D shape in a short time and inexpensively, we propose a method of reconstructing the intraoral 3D shape using NeRF (Neural Radiance Fields for View Synthesis). In this report, we propose a method to remove the spatial density other than the object by using the increase / decrease of the color distribution when performing 3D reconstruction using NeRF.

INTRODUCTION

In order to realize safe and effective orthodontic treatment, it is important to understand the intraoral 3D shape. Currently, the problem is that the optical impression used to grasp the intraoral 3D shape is expensive and can only be measured at a specific dental clinic. Therefore, in order to grasp the intraoral 3D shape in a short time and inexpensively, we propose a method of reconstructing the intraoral 3D shape using NeRF (Neural Radiance Fields for View Synthesis). We will conduct an experiment to reconstruct the dentition model and clarify the problems of the reconstruction. We also propose solutions to the problems.

3D Reconstruction Result by NeRF

Reconstruct the 3D shape of the dentition model using NeRF. NeRF reconstructs density and color information at a certain position in space from a photograph. Table 1 shows the shooting conditions. Figure 1 shows a part of the photographs used for the reconstruction. Figure 2 shows a three-dimensional reconstruction in STL format.

Examination of Density Removal Method Based on Color Information

We will examine a method for removing densities other than the dentition model from the distribution of color information. This time, the dentition shape is extracted by dividing the section by increasing or decreasing the distribution from the three types of color information of red, green, and blue, and removing the density existing in the section. Figure 3 shows an example of the extracted results. Figure 3 shows the result of removing the section where the green color increases. Compared with Fig. 2, green does not affect the dentition model and can remove a lot of noise.

Table 1. Photo Shooting Condition

Shooting Equipment	iPhone 12
Image Size	1920 × 1080px
Number of Images	179

Fig1. Images Used for 3D Reconstruction

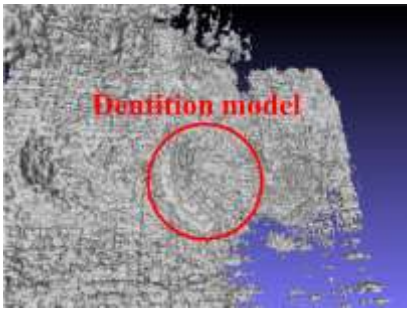

Fig2. 3D Reconstruction Results by NeRF

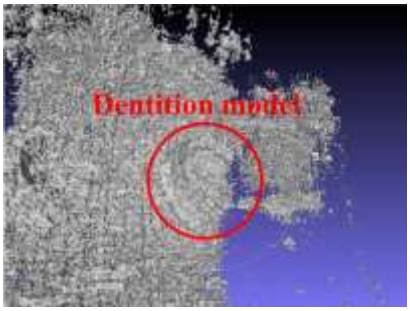

Fig3. Noise Removal Based on Color Information

References:

[1] Ben Mildenhall, Pratul P. Srinivasan, Matthew Tancik, Jonathan T. Barron, Ravi Ramamoorthi, Ren Ng NeRF: Representing Scenes as Neural Radiance Fields for View Synthesis – ECCV 2020

Oral Presentation

Education and Human Studies

November 24th

Presentation No.	Title	Author	
EHS1.	Evaluation of internal rotation gait and normal gait based on the interarticular coordination	Natsuki Sai, Tatsuro Sato, Shinichiro Morichi, Satoru Kizawa, and Ayuko Saito	143
EHS2.	A study on coordination between a line of sight and motion of body during hitting a ball with a racket	Toshikazu Yagi, Satoru Kizawa, and Ayuko Saito	146
EHS3.	Study on the movement during walking beautifully and the perception of beauty	Yura Honda, Shogo Takeuchi, Jun Muramatsu, Satoru Kizawa, Masaki Tamura, and Ayuko Saito	150
EHS4.	Research on recognition of movement using an optical motion capture system	Shun Shiotani, Satoru Kizawa, Masaki Tamura, and Ayuko Saito	153

November 24th

Presentation No.	Title	Author	
EHS5.	A New Perspective on English Education for Engineering Majors −Optimizing English Education at Kogakuin University–	Tomoko Wada	157
EHS6.	A Practical Report on English Education at Kogakuin University: A Lesson from Basic English I/II	Takayuki Akimoto	159
EHS7.	English Education in the Age of SDGs: A Survey on English Learning among Kogakuin University Students	Tomomi Yamada, Kazunori Suzuki	160
EHS8.	An Application of CNN in Answer Analyzing and Estimation Education Advanced Technology	Nguyen Hoang Mai	163

Evaluation of internal rotation gait and normal gait based on the interarticular coordination

Natsuki Sai, Tatsuro Sato, Shinichiro Morichi, Satoru Kizawa, and Ayuko Saito

Department of Mechanical Science and Engineering, School of Advanced Engineering, Kogakuin University, Tokyo, Japan
E-mail: s519022@ns.kogakuin.ac.jp

Abstract

This study investigates the coordination between the joint angles of lower limbs during normal gait and internal rotation gait by applying singular value decomposition. The results indicated that the ankle abduction, the ankle internal rotation, the hip flexion were generated during internal rotation gait.

The symptoms of the disorder in central nervous system patients such as cerebral palsy change due to growth [1]. The tests for cerebral palsy include imaging of the brain, such as ultrasound, CT scan, or MRI. These tests help to distinguishing between cerebral palsy and other possible causes. Sedatives may be used to keep body stationary during those tests. However, sedative use may lead to side effects for children [2]. On the hand, motion analysis can be used to detect abnormal gait caused by central nervous disorder. The optical motion capture system used for motion analysis requires many markers to be attached to the body. Moreover, distinguishing internal rotation gait from spastic gait caused by central nervous system disorder is not easy. Detecting gait characteristic of children with spastic cerebral palsy by simple motion analysis enables to find disease in the early-stage such as regular checkups for infants. Therefore, in this research, as a first step to build a method of identifying internal rotation gait and spastic gait, we attempt to detect the characteristics of normal gait and internal rotation gait of healthy people. This study investigates the coordination between the joint angles of lower limbs during normal gait and internal rotation gait by applying singular value decomposition. The dominant coordination pattern is obtained by applying singular value decomposition on the joint angles of lower limbs measured during the experiment [3].

Healthy participant is examined during the experiment. Following an explanation of the purpose and requirements of the study, the participants gave their written informed consent to participate. Study approval was obtained from the Research Ethics Board, Kogakuin University, and the National Institute of Technology, Akita College.

During the experiment kinematic and kinetic data were collected simultaneously using an optical motion capture system (Bonita 10; Vicon Motion Systems, Ltd.) and two force plates (9286; Kistler Japan Co., Ltd.). The two force plates were placed on the walking path shown in Fig. 1. During the experiment, the participant stepped with their left foot on the first force plate and their right on the second. The sampling frequencies of the optical motion capture system and the force plates were 100 Hz.

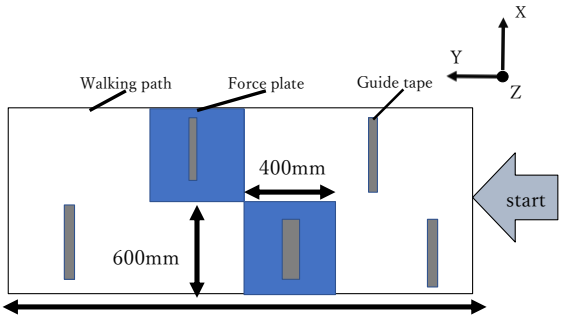

Fig.1 Walking path.

The positions of the reflective markers for the optical motion capture system were set in accordance with the Plug-in Gait lower body marker set.

Markers were placed at the heel contact point on the walking path based on each participant's natural stride length. The participants were instructed to walk using a natural stride in time with a metronome (110 bpm). They performed the task with a normal gait and a internal rotation gait three times each. After the experiment, markers were labeled using analysis software (Nexus2, manufactured by Vicon). Knee joint angles were obtained by running the Plug-in Gait Dynamic pipeline.

The joint angles of the participant are depicted in Figs. 2 to 4. Black solid curves represent the average values of five trials during normal gait. Red solid curves represent the average values of five trials during internal rotation gait. The dashed curves represent the standard deviations of five trials. The walking cycle is 100%, which extends from the beginning of the stance phase until the end of the swing phase. Figure 2 represents that the ankle joint angle during internal rotation gait was much more abduction and internally rotated than the result during normal gait. Figure 3 represents that there was no clear difference in flexion and extension of the knee joint. Figure 4 represents that the hip joint angle during internal rotation gait was much more adducted and internally rotated than the result during normal gait. The results indicate that there are clear differences in

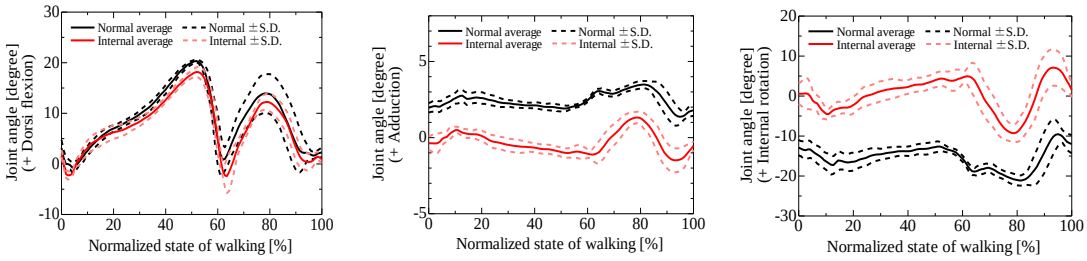

(a) Dorsi - plantar flexion (b) Adduction - abduction (c) Internal - external rotation

Fig. 2 Left ankle joint angle obtained from 3D motion capture system.

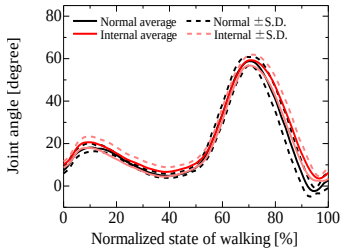

Fig.3 Left knee joint angle obtained from 3D motion capture system (Flexion - extension).

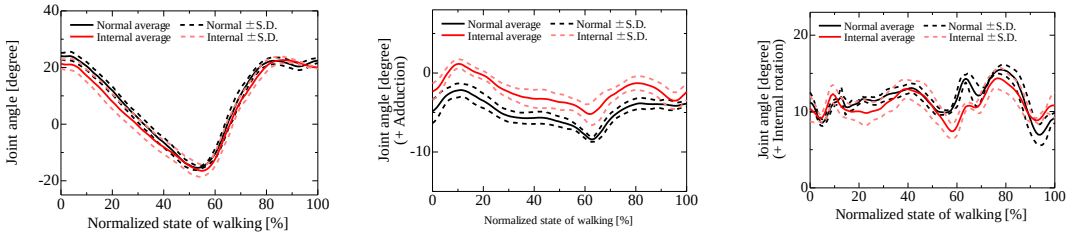

(a) Flexion - extension (b) Adduction - abduction (c) Internal - external rotation

Fig. 4 Left hip joint angle obtained from 3D motion capture system.

the results between normal gait and internal rotation gait of a healthy subject.

The coordination between the lower limbs of a person walking normally and internal rotationally was examined by applying singular value decomposition.

Lower limb joint angles were converted into dimensionless quantities of -1 to 1 as follows:

$$\theta(t) = \frac{2(\theta_{raw} - \theta_{min})}{\theta_{max} - \theta_{min}} - 1 \qquad (1)$$

where θraw (t) represents the joint angles obtained from an optical 3D motion capture system; θmax, and θ min respectively represent the maximum, and minimum joint angles for each joint.

The observation matrix consists of dimensionless quantities of lower limb joint angles. The observation matrix R(θ, t) is composed in Fig.2.

Where θ_{Lxank}, θ_{Lyank}, θ_{Lzank}, θ_{Rxank}, θ_{Ryank} and θ_{Rzank} respectively represent the angles of drosal, abduction, and internal rotation in the left and right ankle; θ_{Lxkne} and θ_{Rxkne} respectively represent the angles of flexion in the left and right knee; θ_{Lxhip}, θ_{Lyhip}, θ_{Lzhip}, θ_{Rxhip}, θ_{Ryhip} and θ_{Rzhip} respectively represent the angles of flexion, abduction, and internal rotation in the left and right hip; and *m* represents the number of time-series data points.

The observation matrix [Eq. (2)] is decomposed into the basis vectors as

$$(\theta, t) = \begin{pmatrix} \theta_{Lxank}(t_1) & \theta_{Lyank}(t_1) & \theta_{Lzank}(t_1) & \theta_{Lxhip}(t_1) & \theta_{Lyhip}(t_1) \\ \vdots & \vdots & \vdots & \vdots & \vdots \\ \theta_{Lxank}(t_m) & \theta_{Lyank}(t_m) & \theta_{Lzank}(t_m) & \theta_{Lxhip}(t_m) & \theta_{Lyhip}(t_m) \end{pmatrix}$$

$$\begin{pmatrix} \theta_{Lyhip}(t_1) & \theta_{Lzhip}(t_1) & \theta_{Rxank}(t_1) \cdots \theta_{Rzhip}(t_1) \\ \vdots & \vdots & \vdots \quad \vdots \quad \vdots \\ \theta_{Lyhip}(t_m) & \theta_{Lzhip}(t_m) & \theta_{Rxank}(t_m) \cdots \theta_{Rzhip}(t_m) \end{pmatrix} \qquad (2)$$

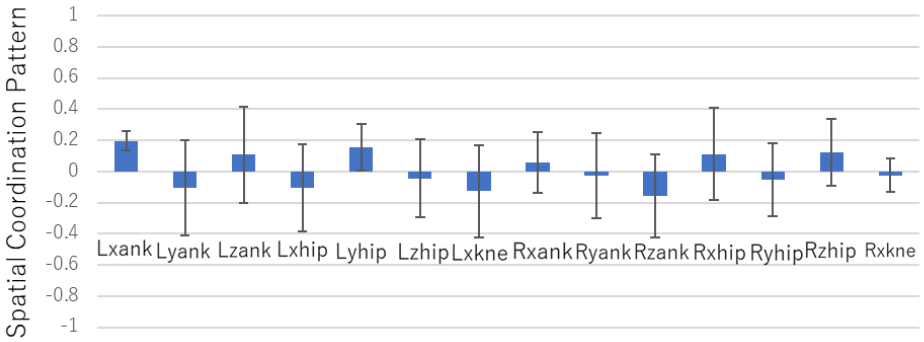

Fig. 5 Spatial coordination pattern of the fist mode of the normal gait..

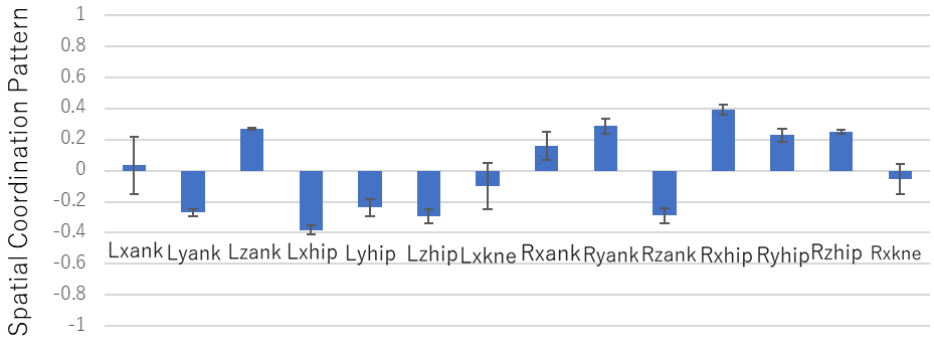

Fig.6 Spatial coordination pattern of the fist mode of the internal rotation gait..

$$R(\theta,t)=\sum_{i=1}^{n}\lambda_i V_i(t)Z_i{}^T(\theta) \qquad (3)$$
$$(i=1,\ldots,n,\ \ n=14)$$

where λ_i is a singular value; Z_i is a dominant coordination pattern. The motion modes are defined in descending order of λ_i.

The contribution ratioγ_i of the singular value in the i-th motion mode is

$$\gamma_i=\frac{\lambda_i}{\sum_{i=1}^{n}\lambda_i{}^2} \quad (i=1,\ldots,n,\ \ n=14) \qquad (4)$$

where i is the number of columns in the observation matrix.

The contribution ratio of the first mode was calculated to be about 34~54%. Consequently, we concluded that the first mode was the dominant motion mode in each trial. The spatial basis results, which represent the coordination patterns, are shown in Figs. 5 and 6. Figure 5 is the result of the normal gait. Figure 6 is the result of the internal rotation gait. In the case of the normal gait, there was no significant change in the value difference. However, in the internal rotation gait result, the abduction angle of the ankle, the internal rotation angle of the ankle, the flexion angle of the hip joint, the abduction angle, and the internal rotation angle were generated. As a result, we concluded that those results were coordination patterns during normal gait and internal rotation gait.

References:

[1] M. Nakajima et al., Developmental changes in the Collis horizontal reaction analyzed using a three-dimensional video motion analysis system. I. Examination of techniques for inducing Collis horizontal reaction, Japanese society of child neurology, Vol. 37, No. 6 (2005), pp. 479-485 (in Japanese).

[2] E. Suzuki et al., Evaluation on spastic gait caused by cervical myelopathy with gait analysis, Proceedings of annual meeting of Japanese society for clinical biomechanics and related research, Vol. 23(2002), pp. 447-451 (in Japanese).

[3] T. Funato et al., Quantitative evaluation of the intersegmental coordination during human locomotion, Journal of the Robotics Society of Japan, Vol. 28, No. 8 (2010), pp. 996-1003 (in Japanese).

A study on coordination between a line of sight and motion of body during hitting a ball with a racket

Toshikazu Yagi*, Satoru Kizawa, and Ayuko Saito

Department of Mechanical Science and Engineering, School of Advanced Engineering, Kogakuin University, Tokyo, Japan
E-mail: your_s518066@ns.kogakuin.jp

Abstract

investigate the coordination between a line of sight and motion of body during hitting a ball with a racket. As a result The result was different with or without instructions.

Integrating the information on visual, vestibular sense, and proprioception, and perceiving them are important to control human motion. Vision is the sense which perceives the external environment. Vestibular is the sense which perceives the inclination of the body. Proprioception is the sense of self-movement and body position. A person integrates those senses to sustain a standing position. Vision is different from other senses because it is a sense which obtains information about the external environment away from the body. When humans move their bodies in daily life or exercise, recognizing the positional relationship between space and destination using vision is needed. Analyzing coordination between the visual and body-sense systems contributes to improve the efficiency of sports practice and instruction. We focused on the movement of the line of sight during hitting a ball with a racket. A gaze measurement system and an optical motion capture were used in the experiment. A gaze measurement system converted the center position of the pupil to two-dimensional coordinates. An optical motion capture was used to measure the upper limb joint angles. The coordination between the line of sight and upper limbs of a person hitting a ball is examined by applying singular value decomposition [1][2]. Furthermore, we verify the result for the condition in which the thrower throws a ball after stating the direction in which the ball will be passed. We also verify the result for the condition in which the thrower throws the ball without stating the intended direction. This allows us to verify the difference in visual-motor coordination of a player depending on the presence or absence of advance notice of the direction in which he or she needs to move.

The line-of-sight positions were acquired using a gaze measurement system. The upper limb joint angles were measured using an optical 3D motion capture system. The positions of reflective markers for the motion capture system were determined by reference to the Helen Hayes marker set. The definitions of upper limb joint angles are shown in Table 1. The definitions of shoulder joint angles and elbow joint angles are shown in Figs. 1 and 2 respectively. The player's line-of-sight positions were obtained as pixel coordinates on the visual field plane (X-Z plane) shown in Fig. 3. The horizontal X-axis ranged from -319 pixels to 319 pixels. The vertical Z-axis ranged from -239 pixels to 239 pixels. healthy adult (height 1.63m, weight 53.0 kg) participated in the experiment. After receiving an explanation of the purpose and requirements of the study, the participant gave his written informed consent to participate. Study approval was obtained from the Research Ethics Board, National Institute of Technology, Kogakuin University (Approval number 2020-B-1).

The reference coordinate system in the laboratory and the standing positions of a thrower and a player are shown in Fig. 4. They stood 2.7 m apart on the Y-axis of the reference coordinate system. The thrower was instructed to throw the ball 5 seconds after the thrower's signal. The direction to throw the ball was

Fig.1 Definitions of upper limb joint angles.

Angles	Associated movement	Angles	Associated movement
Left shoulder angle (LSX)	Flexion	Right shoulder angle (RSX)	Flexion
Left shoulder angle (LSY)	Abduction	Right shoulder angle (RSY)	Abduction
Left shoulder angle (LSZ)	Internal rotation	Right shoulder angle (RSZ)	Internal rotation
Left elbow angle (LE)	Flexion	Right elbow angle (RE)	Flexion

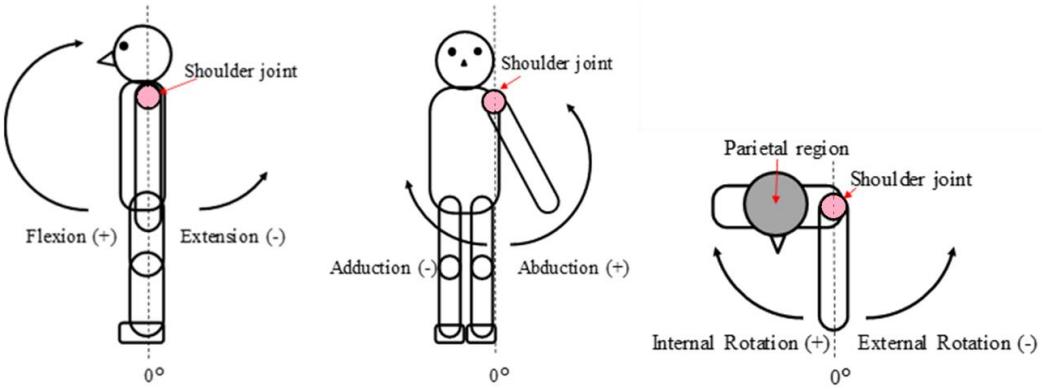

(a) Flection-Extension *(b)Abduction-Adduction* *(c)Internal Rotation-External Rotation*

Fig. 1 Definitions of shoulder joint angles.

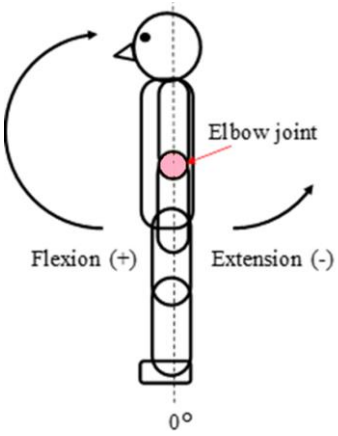

Fig. 2 Definitions of elbow joint angles.

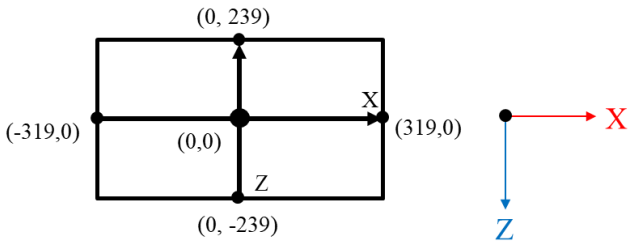

Fig. 3 Definition of pixel coordinate system.

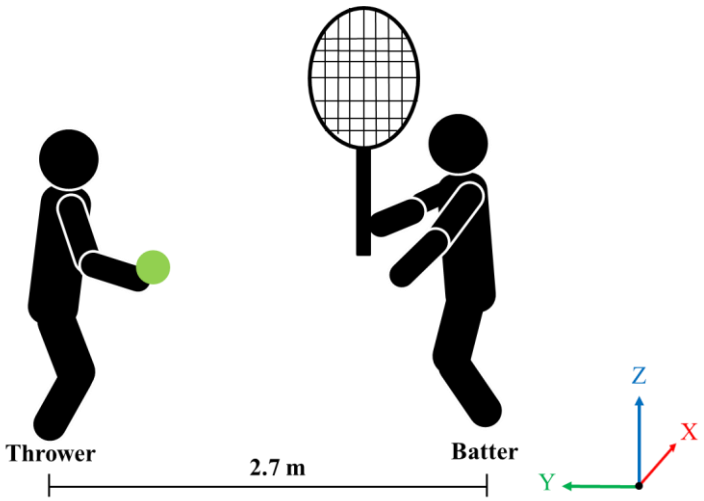

Fig. 4 Definition of the reference coordinate system and standing positions.

to either the right or left side of the batter. The thrower held the ball in his right hand, and threw the ball using an underhand toss in all trials. The experiment aimed to confirm visual-motor coordination from the common features of the results of repeated similar movements by the player. Thus, we conducted two trials under each condition. The trials, in which the thrower threw the ball after stating the intended direction the ball, were performed twice each on the left and right sides. Then, trials in which

the thrower tossed the ball without stating the intended direction were performed twice each on the left and right sides. Because the purpose of this study was to analyze visual-motor coordination of basic motion as a ball is hit, the player was instructed to maintain a standing position and hit the ball without moving his feet to eliminate complicated motions. Sampling frequencies of the gaze measurement system and the optical motion capture system were each 60 Hz.

Upper limb joint angles and pixel coordinates of the line-of-sight positions were converted into dimensionless quantities of -1 to 1 as follows:

$$\theta(t) = \frac{2(\theta_{raw}(t) - \theta_{min})}{\theta_{max} - \theta_{min}} - 1 \quad (1)$$

where $\theta(t)$ represents the normalized joint angles; $\theta_{raw}(t)$ represents the joint angles obtained from an optical 3D motion capture system; θ_{max}, and θ_{min} respectively represent the maximum, and minimum joint angles for each joint. The normalized coordinates of line of sight were calculated in the same way. The observation matrix consists of dimensionless quantities of upper limb joint angles and pixel coordinates of the line-of-sight positions. The observation matrix $R(\theta, G, t)$ is composed as follows:

$$R(\theta, G, t) = \begin{pmatrix} \theta_{LSX}(t_1)\ \theta_{LSY}(t_1)\ \theta_{LSZ}(t_1)\ \theta_{LE}(t_1) \\ \vdots \quad \vdots \quad \vdots \quad \vdots \\ \theta_{LSX}(t_m)\theta_{LSY}(t_m)\theta_{LSZ}(t_m)\theta_{LE}(t_m) \end{pmatrix}$$

$$\begin{pmatrix} \theta_{RSX}(t_1)\ \theta_{RSY}(t_1)\ \theta_{RSZ}(t_1)\ \theta_{RE}(t_1)\ G_x(t_1)\ G_z(t_1) \\ \vdots \quad \vdots \quad \vdots \quad \vdots \quad \vdots \quad \vdots \\ \theta_{RSX}(t_m)\theta_{RSY}(t_m)\theta_{RSZ}(t_m)\theta_{RE}(t_m)G_x(t_m)G_z(t_m) \end{pmatrix} \quad (2)$$

where $\theta_{LSX}(t)$, $\theta_{LSY}(t)$, $\theta_{LSZ}(t)$, $\theta_{RSX}(t)$, $\theta_{RSY}(t)$, and $\theta_{RSZ}(t)$ respectively represent the angles of flexion, abduction, and internal rotation in the left and right shoulders; $\theta_{LE}(t)$ and $\theta_{RE}(t)$ respectively represent the angles of flexion in the left and right elbows; $Gx(t)$ and $Gz(t)$ respectively represent the pixel coordinates of the line-of-sight positions for the x and z axes in consideration of the flexion, extension, internal rotation, and external rotation of the subject's head; and m represents the number of time-series data points.

The observation matrix [Eq. (2)] is decomposed into the basis vectors as

$$R(\theta, G, t) = \sum_{j=1}^{n} \lambda_j V_j(t) Z_j^T(\theta, G)$$
$$(j = 1, \ldots, n,\ \ n = 10) \quad (3)$$

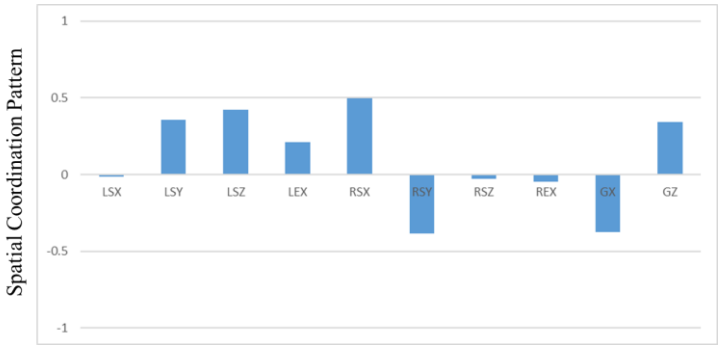

(a) The first mode.

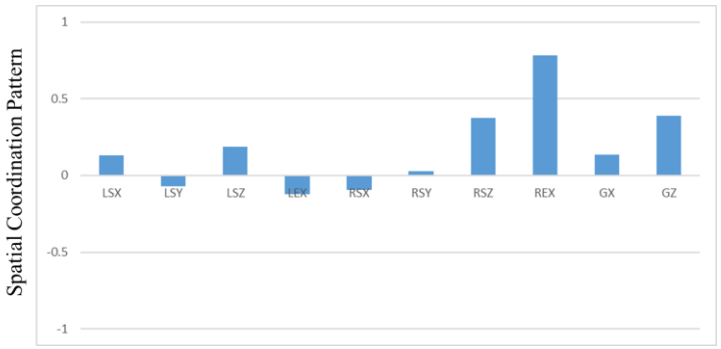

(b) The second mode.

Fig. 5 Spatial coordination pattern of the lines of sight and upper limb joint angles when the thrower threw the ball after stating the throwing direction.

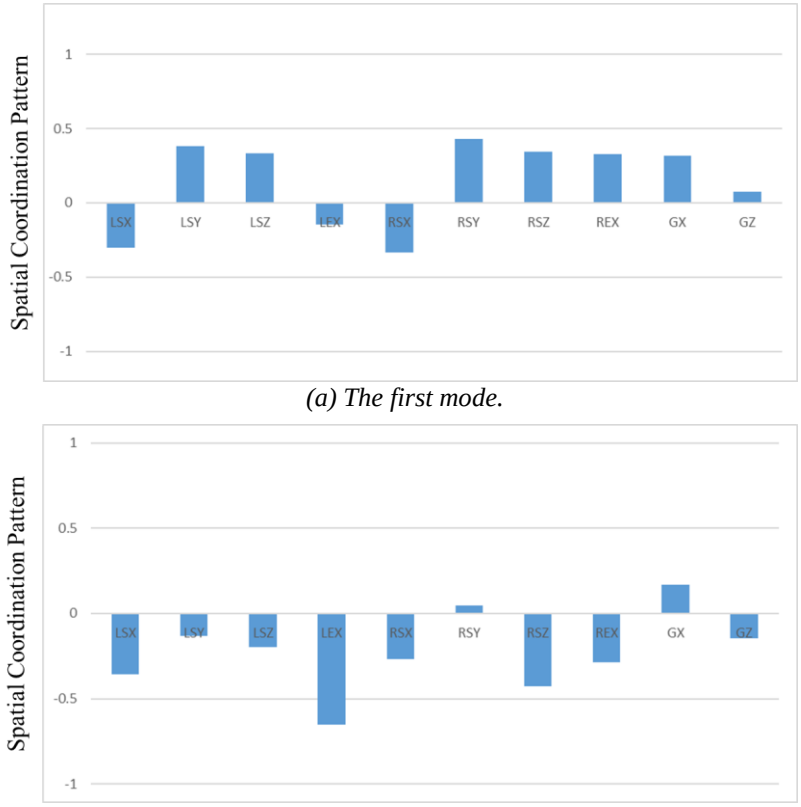

(a) The first mode.

(b) The second mode.

Fig. 6 Spatial coordination pattern of the lines of sight and upper limb joint angles when the thrower threw the ball without stating the throwing direction.

where λ_j is a singular value. The motion modes are defined in descending order of λ_j.

The contribution ratio β_j of the singular value in the *j*-th motion mode is

$$\beta_j = \frac{\lambda_j}{\sum_{j=1}^{n} {\lambda_j}^2} \quad (j = 1, \ldots, n, \ n = 10) \tag{4}$$

where *j* is the number of columns in the observation matrix.

The contribution ratio of the first mode was calculated to be about 40%, the second mode 20%, and the third and later modes less than 10% in all trials of the subject. Consequently, we concluded that the first mode was the dominant motion mode in each trial. The second mode accounted for about 20% of the motion, including characteristic coordination patterns. Therefore, the results for the first and second modes were examined in detail.

The spatial basis results, which represent the coordination patterns, are shown in Figs. 6 and 7. Figure 6 is the results of the trial in which the thrower tossed the ball to the subject's right side after stating the intended direction. Figure 6 is the result of the trial in which the thrower tossed the ball to the subject's right side without stating the intended direction. In Figs. 6 and 7, panel (a) provides the result for the first mode; panel (b) presents the second mode.

References:

[1] Funato, T., Aoi, S. and Tsuchiya, K., Quantitative evaluation of the intersegmental coordination during human locomotion, Journal of the Robotics Society of Japan, Vol. 28, No. 8 (2010), pp. 996-1003 (in Japanese).

[2] Hayashi, Y., Tsujiuchi, N. and Matsuda, Y., Quantitative evaluation concerning principal gait locomotion pattern of a trans-femoral amputee with a prosthetic limb based on the intersegmental coordination, Transactions of the JSME (in Japanese), Vol. 81, No. 825 (2015a), DOI : 10.1299/transjsme.15-00020.

Study on the movement during walking beautifully and the perception of beauty

Yura Honda*, Shogo Takeuchi, Jun Muramatsu, Satoru Kizawa, Masaki Tamura, and Ayuko Saito

Department of Mechanical Science and Engineering, School of Advanced Engineering, Kogakuin University, Tokyo, Japan.
E-mail: s519046@ns.kogakuin.ac.jp

Abstract

This study aimed to show the evaluation criteria of beauty when a person looks at a man who walks beautifully. We examined the relation between the kinematic factors during walking. The psychological factors when a person evaluates beauty were evaluated by using a questionnaire survey.

1. Introduction

"Beautiful walking" that a person walks elegantly while maintaining the correct posture is gaining popularity mainly among women [1]. In addition to the health benefits of exercise, "Beautiful walking" improves mental health by looking beautiful [2]. "Beautiful walking" could be accepted by many people as a form of exercise that supports mental and physical health [3].

The elements that are perceived as beautiful in the beautiful walking are based on personal sensibility. In addition, it is possible that gender differences are related to sensibility. For example, a person feels "fresh" and "neat" rather than "beautiful" as a first impression when looking at a man who walks beautifully. Kinematic features during walking beautifully that transcend gender may exist. This study aimed to show the evaluation criteria of beauty when a person looks at a man who walks beautifully. We examined the relation between the kinematic factors, such as joint angles during walking, and the psychological factors when a person evaluates beauty. Firstly, the 3D motion capture system measured the walking exercise of a participant who was a male professional walking instructor. The two types of gait were measured during the experiment; "Beautiful walking" that a person walks while maintaining his pelvis straight, "Not-beautiful walking" that a person walks while maintaining his pelvis backward. Secondly, the subjective evaluation experiment was conducted. The evaluators watched the video that was taken in the gait measurement. A questionnaire survey on the " Beautiful walking" and "Not-beautiful walking" was conducted.

2.Gait measurement experiment

The experiment was conducted at Kogakuin University, Shinjuku campus. A healthy male (height 1.76m, weight 58kg) participated in the experiment. Study approval was obtained from the Research Ethics Board, Kogakuin University. The participant gave his written informed consent to participate after understanding the purpose and requirements of the study. Kinematic date were collected using an optical motion capture (MAC3D; Motion Analysis). The sampling frequencies of the optical motion capture was 100 Hz. 29 reflective markers were attached to the participant's body by referring to the Helen Hayes Marker Set (Fig. 1). The participant was instructed to walk using a natural stride in time with a metronome 90 bpm (Fig.2). The two types of gait were measured during the experiment; "Beautiful walking" that a person walks while maintaining his pelvis straight, "Not-beautiful walking" that a person walks while maintaining his pelvis backward.

This study focused on the joint angles of the sagittal plane. The results of the head angle, trunk angle, pelvis tilt angle, right shoulder joint angle, right elbow joint angle, right wrist joint angle, right hip joint angle, right knee joint angle, and right ankle joint angle are shown in Fig. 3. The solid red lines represent the results of "Beautiful walking", and the blue solid red lines represent the results of "Not-beautiful walking". The horizontal axis is 100% for one gait cycle that includes one stance phase and one swing phase. The toe-off time of "Beautiful walking" was at about 60%, and the toe-off time of "Not-beautiful walking" was at about 63%.

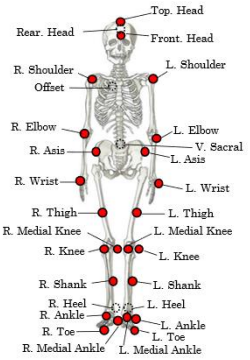

Fig. 1. Marker positions.

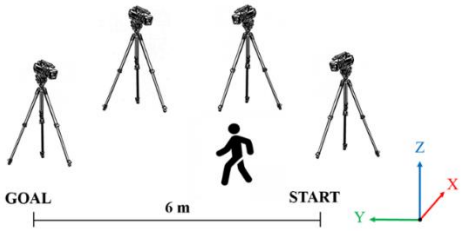

Fig.2.Walking path

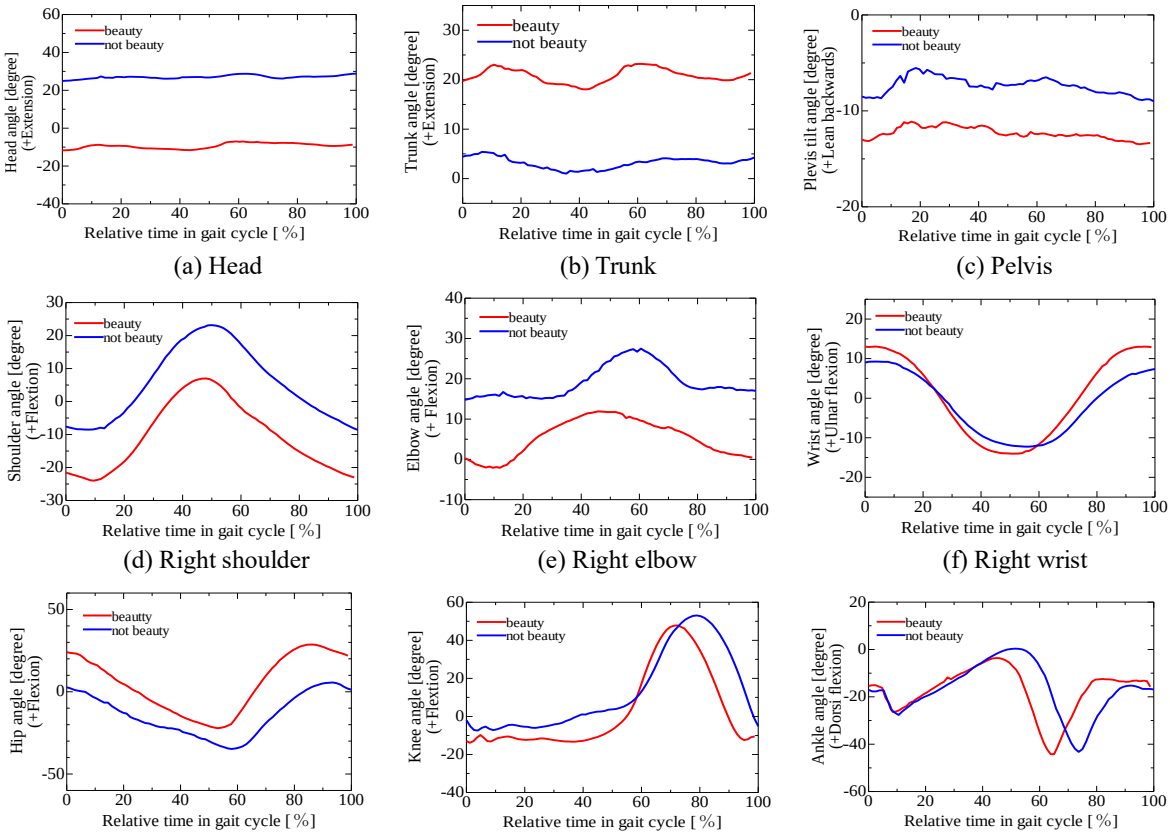

(a) Head (b) Trunk (c) Pelvis

(d) Right shoulder (e) Right elbow (f) Right wrist

(g) Right hip (h) Right knee (i) Right ankle

Fig.3 The sagittal joint angles during walking obtained from the 3D motion analysis system

The head angles did not change throughout the gait cycle in both two types of walking. The trunk angles, pelvic tilt angles, right shoulder angles, right wrist angles, and right hip angles of the two types of walking were almost the same. The right elbow angles, right knee angles, and right ankle angles of the two types of gait walking show differences. Therefore, these three joints' motions may influence the subjective evaluation.

3.Subjective evaluation experiment

The subjective evaluation of the two types of walking was conducted referring to the previous study. 10 evaluation words were selected for the evaluation of walking. We asked 34 evaluators including men and women to watch the video which was taken in the gait measurement. A questionnaire survey on the video using the selected evaluation words was conducted. The evaluators answered 1 to 5 for each evaluation word (1: Very XXX 2: Slightly XXX 3: Neither 4: Slightly ○○○ 5: Very○○○). Fig.1 shows the evaluation sheet used in the experiment.

4.Result

Table 2 shows the questionnaire results. The results show the mean values and standard deviations of each word. The mean of all words for "Beautiful walking" was 2.97. We determined that 3.05 or higher was a high evaluation and less than 2.70 was a low evaluation. "Beautiful walking" results which were 3.05 or higher were "beautiful," "elegant," "unusual," and "healthy. The mean of all words for "Not-beautiful walking" was 1.73. We determined that less than 1.40 was a low evaluation. "Not-beautiful walking" results which were less than 1.40 were "beautiful," "elegant," "attractive," and "healthy. The results indicate that the three words, "beautiful," "elegant," and "healthy",

Table 1 Table1 Evaluation word pairs.

Like	⇔	Dislike
Beauty	⇔	Not beauty
Elegant	⇔	In elegant
Stability	⇔	Instability
Soft	⇔	Hard
Calm	⇔	Restless
Rare	⇔	Commonplace
Pleasant	⇔	Unpleasant
Attractive	⇔	Unattractive
Health	⇔	Unhealthy

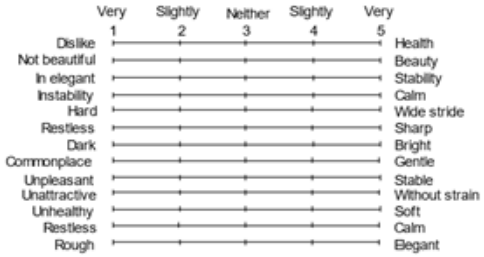

Fig.4 Evaluation sheet

Table2 Average points and standard deviations of questionnaire results

Evaluation word	Beauty	Not beauty
Like	2.76(1.21)	1.49(0.92)
Beauty	3.07(1.24)	1.30(0.70)
Elegant	3.05(1.25)	1.16(0.43)
Stability	3.02(1.34)	1.56(0.79)
Soft	2.60(1.05)	2.44(1.39)
Calm	2.71(0.92)	1.84(0.99)
Rare	3.64(0.97)	3.49(1.13)
Pleasant	2.86(1.15)	1.72(0.87)
Attractive	2.60(1.35)	1.19(0.44)
Health	3.38(1.19)	1.09(0.36)

showed a particularly large difference in the evaluation of the two types of walking. We concluded that these three keywords were particularly strongly related to the evaluation of the two types of walking.

References:

[1] S. Saito, N. Ushifusa, H. Sakai, M. Kondo, Y. Kobayashi, "Kinematic characteristics of aesthetic gait patterns", Journal of the Society of Biomechanisms. 25, 195-209, (2020).

[2] Y. Nakatani, I. Sato-Suzuki, N. Tsujino, A. Nakasato, Y. Seki, M. Fumoto, H. Arita, "Augmented brain 5-HT crosses the blood-brain barrier through the 5-HT transporter in rat", Eur J Neurosci, 27(9), 2466-2472, (2008).

[3] Y. Ryu, T. Maekawa, D. Yoshino, N. Sakitani, A. Takashima, T. Inou, J. Suzurikawa, J. Toyohara, T. Tago, M. Makuuchi, N. Fujita, K. Sawada, S. Murase, M. Watanave, H. Hirai, T. Sakai, Y. Yoshikawa, T. Ogata, M. Shinohara, M. Nagao, Y. Sawada, "Mechanical Regulation Underlies Effects of Exercise on Serotonin-Induced Signaling in the Prefrontal Cortex Neurons", iScience, 23(2), https://dx.doi.org/10.1016/j.isci.2020.100874, (2020).

[4] S. Takeuchi, J. Muramatsu, M. Tamura, and A. Saito, "Experiment on selecting evaluation words for sensory evaluation of beautiful walking", 19th International Symposium on Advanced Technology, (2021).

Research on recognition of movement using an optical motion capture system

Shun Shiotani*, Satoru Kizawa, Masaki Tamura, and Ayuko Saito

Department of Mechanical Science and Engineering, School of Advanced Engineering, Kogakuin University, Tokyo, Japan
E-mail: s518028@ns.kogakuin.ac.jp

Abstract

The batter's motion during batting was measured using an optical 3D motion capture system. As a result, coordination of these specific body parts may be used as a criterion when a person recognizes the movement of swinging a bat.

We recognize human movements by detecting the human body parts motions. Recognition is the identification of something as having been previously seen, heard or known. Even in the case of a rigid link model, where joints are connected by straight lines, a person can recognize its movements by detecting the links motions. Even when the marker trajectories obtained from an optical motion capture are seen, a person can detect the changes in the marker positions and identifies them as having been previously seen, heard, or known. Therefore, a person seems to be able to recognize the characteristics of human movements by detecting the point cloud motion.

In this study, we attempted to extract the features of marker trajectories during hitting a baseball obtained from an optical motion capture system. During a baseball game, a batter faces a pitcher. A batter recognizes the motion of the pitcher and anticipates the pitch. A pitcher also recognizes the batter's motion and decides how to pitch. It is useful to develop effective coaching techniques by clarifying how and when a pitcher and a batter recognize each other's motion.

The batter's motion during batting was measured using an optical 3D motion capture system. We focused on the trajectories of reflective markers attached to the batter and obtained the characteristics of the marker trajectories. The singular value decomposition was applied to the marker coordinates to verify the coordination between marker motions [1][2]. This study could be useful for clarifying the cognitive structure of human vision.

The experiment was conducted at Kogakuin University, Hachioji campus. A healthy male participated in the experiment. Study approval was obtained from the Research Ethics Board, Kogakuin University. The participant gave his written informed consent to participate after understanding the purpose and requirements of the study. Kinematic date were collected using an optical motion capture (MAC3D; Motion Analysis). The sampling frequencies of the optical motion capture was 100 Hz. The positions of reflective markers for the motion capture system were determined by reference to the Helen Hayes Marker set (Fig.1). The reference coordinate system in the laboratory and the standing positions of a batter is shown in Fig. 2. The batter was instructed to swing a

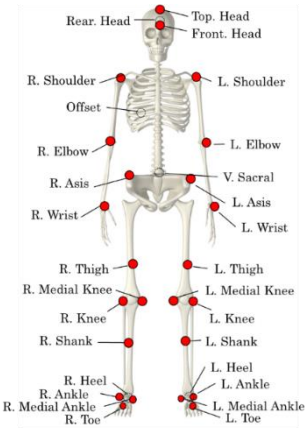

Fig.1 Helen Hayes marker set.

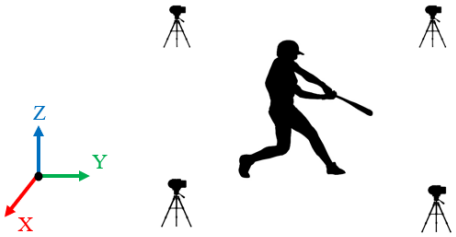

Fig.2 Reference coordinates and batter's position.

bat 5 seconds after the start of measurement. The purpose of this study is to analyze the motion when swinging a bat. In order to eliminate complicated movements that are likely to show individual differences, the batter was instructed to swing a bat without changing the standing position.

During the experiment, the batter swung a bat in the positive direction of the Y-axis. In order to detect the characteristics of the batter's motion when viewed from the pitcher, we focused on the reflection marker coordinates on the X-Z plane in Fig. 2. Figure 3 shows the results of the reflection marker trajectories on the X-Z plane. The horizontal axis is the X-coordinate and the vertical axis is the Z-coordinate. The result indicates that the batter's motion is clearly left-right asymmetrical. The result also indicates that both the left and right wrists rotate on the X-Z plane when

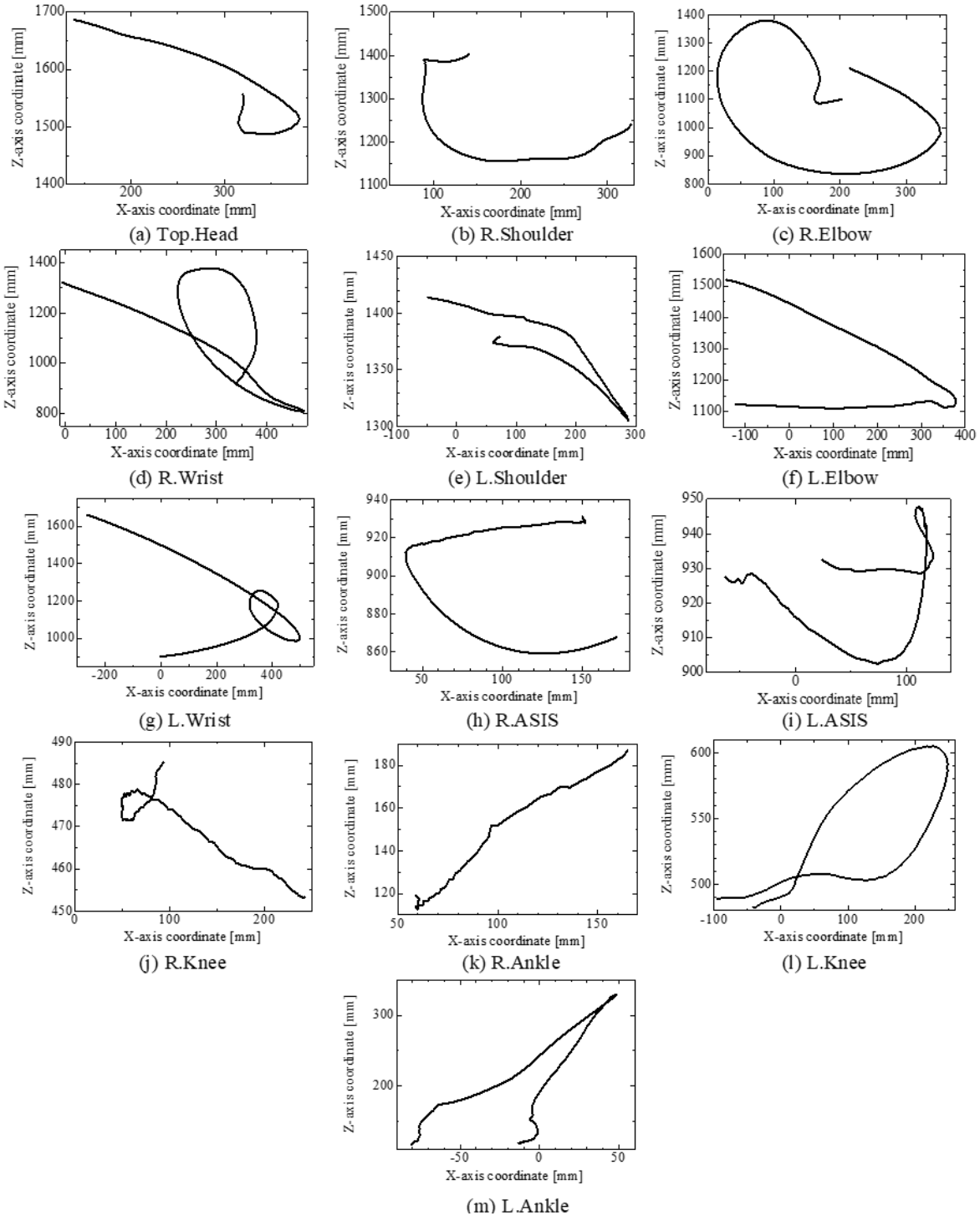

Fig.3 Marker trajectories in X-Z plane during batting obtained from the 3D motion analysis system.

swinging a bat. Therefore, we determined that the left and right wrists' movements had similar trajectories.

The coordination between the marker coordinates of a person swinging a bat was examined by applying singular value decomposition.

The marker coordinates were converted into dimensionless quantities of -1 to 1 as follows:

$$X(t) = \frac{2(X_{raw} - X_{min})}{X_{max} - X_{min}} - 1 \qquad (1)$$

where $X(t)$ represents the normalized X-coordinates; $X_{raw}(t)$ represents the X-coordinates obtained from an optical 3D motion capture system; X_{max}, and X_{min} respectively represent the X-coordinates for each body part. The normalized Z-coordinates were calculated in the same way.

The observation matrix consists of dimensionless quantities of the normalized X- and Z-coordinates. The observation matrix $R(X,Z,t)$ is composed as follows:

$$R(X,Z,t) = \begin{pmatrix} X_{TH}(t_1)\ Z_{TH}(t_1)\ X_{LS}(t_1)\ Z_{LS}(t_1)\ X_{LE}(t_1)\ Z_{LE}(t_1)\ X_{LW}(t_1)\ Z_{LW}(t_1) & \dots & X_{RW}(t_1)\ X_{LAS}(t_1)\ Z_{LAS}(t_1)\ X_{RAS}(t_1)\ Z_{RAS}(t_1) \\ \vdots \quad \vdots \quad \vdots \quad \vdots \quad \vdots \quad \vdots \quad \vdots \quad \vdots & & \vdots \quad \vdots \quad \vdots \quad \vdots \quad \vdots \\ X_{TH}(t_m)Z_{TH}(t_m)\ X_{LS}(t_m)Z_{LS}(t_m)X_{LE}(t_m)Z_{LE}(t_m)X_{LW}(t_m)Z_{LW}(t_m) & & X_{RW}(t_m)X_{LAS}(t_m)Z_{LAS}(t_m)X_{RAS}(t_m)Z_{RAS}(t_m) \end{pmatrix}$$

$$\begin{pmatrix} X_{LK}(t_1)\ Z_{LK}(t_1)\ X_{LA}(t_1)\ Z_{LA}(t_1) & \dots & X_{RA}(t_1)\ Z_{RA}(t_1) \\ \vdots \quad \vdots \quad \vdots \quad \vdots & & \vdots \quad \vdots \\ X_{LK}(t_m)Z_{LK}(t_m)X_{LA}(t_m)Z_{LA}(t_m) & & X_{RA}(t_m)\ Z_{RA}(t_m) \end{pmatrix} \quad (2)$$

Here, $X_{TH}(t)$ and $Z_{TH}(t)$ are the *X*- and Z-coordinates of the Top.Head marker, $X_{LS}(t)$, $Z_{LS}(t)$ are the *X*- and Z-coordinates of the L.Shoulder marker, $X_{LE}(t)$, $Z_{LE}(t)$ are the *X*- and Z-coordinates of the L.Elbow marker, $X_{LW}(t)$, $Z_{LW}(t)$ are the *X*- and Z-coordinates of the L.Wrist marker, $X_{RS}(t)$, $Z_{RS}(t)$ are the *X*- and Z-coordinates of the R.Shoulder marker, $X_{RE}(t)$, $Z_{RE}(t)$ are the *X*- and Z-coordinates of the R.Elbow marker, $X_{RW}(t)$, $Z_{RW}(t)$ are the *X*- and Z-coordinates of the R.Wrist marker, $X_{LAS}(t)$, $Z_{LAS}(t)$ are the *X*- and Z-coordinates of the L.ASIS marker, $X_{RAS}(t)$, $Z_{RAS}(t)$ are the *X*- and Z-coordinates of the R.ASIS marker, $X_{LK}(t)$, $Z_{LK}(t)$ are the *X*- and Z-coordinates of the L.Knee marker, $X_{LA}(t)$, $Z_{LA}(t)$ are the *X*- and Z-coordinates of the L.Ankle marker, $X_{RK}(t)$, $Z_{RK}(t)$ are the *X*- and Z-coordinates of the R.Knee marker, $X_{RA}(t)$, $Z_{RA}(t)$ are the *X*- and Z-coordinates of the R.Ankle marker.

The observation matrix [Eq. (2)] is decomposed into the basis vectors as

$$R(X,Z,t) = \sum_{j=1}^{n} \lambda_j V_j(t) Z_j{}^T(X,Z) \quad (3)$$
$$(j = 1, \dots, n,\ \ n = 26),$$

where λ_j is a singular value. The motion modes are defined in descending order of λ_j.

The contribution ratio β_j of the singular value in the j-th motion mode is

$$\beta_j = \frac{\lambda_j}{\sum_{j=1}^{n} \lambda_j{}^2} \quad (j = 1, \dots, n,\ \ n = 26) \quad (4)$$

where j is the number of columns in the observation matrix.

Fig. 4. First mode result.

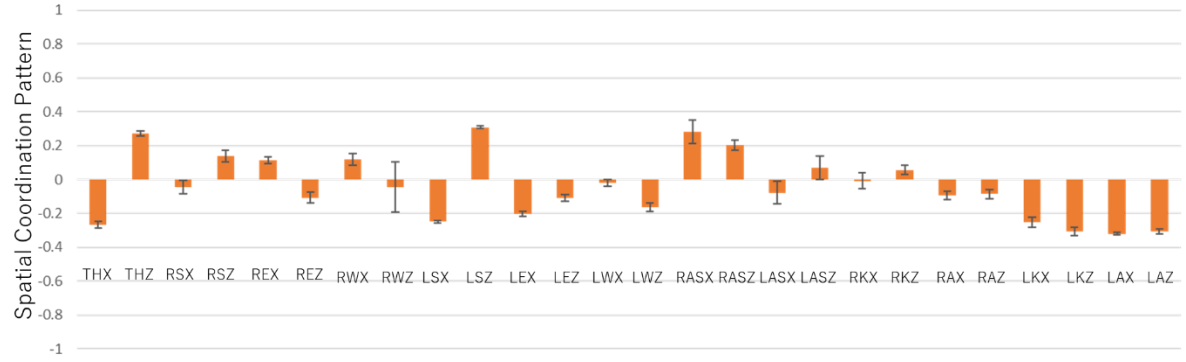

Fig. 5. Second mode result.

The results of singular value decomposition of the marker locus of the body part are shown in Fig. 4 and Fig. 5. The movements of specific joints (right shoulder, left elbow, left wrist, left pelvis, right knee, and right ankle) were generated in the first mode shown in Fig.4. The movements of specific joints (head, left shoulder, right hip, left knee, and left ankle) were generated in the second mode shown in Fig.5. Coordination of these specific body parts may be used as a criterion when a person recognizes the movement of swinging a bat.

References:

[1] Funato, T., Aoi, S. and Tsuchiya, K., Quantitative evaluation of the intersegmental coordination during human locomotion, Journal of the Robotics Society of Japan, Vol. 28, No. 8 (2010), pp. 996-1003 (in Japanese).

[2] Hayashi, Y., Tsujiuchi, N. and Matsuda, Y., Quantitative evaluation concerning principal gait locomotion pattern of a trans-femoral amputee with a prosthetic limb based on the intersegmental coordination, Transactions of the JSME (in Japanese), Vol. 81, No. 825 (2015a), DOI : 10.1299/transjsme.15-00020.

A New Perspective on English Education for Engineering Majors –Optimizing English Education at Kogakuin University–

Tomoko WADA

Center for Promotion of Higher Education, Kogakuin University, Tokyo, Japan
E-mail: tmkwada0720@gmail.com

Abstract

In this presentation, a new concept of what should be aimed in English education at engineering university will be provided from the perspective of communication education. In the process, a typology of what needs to be taught will be provided along with a model which illustrates how all these subject matters are incorporated.

1. Introduction

In developing an English (taught as a foreign language) program for students of engineering majors, one needs to start from setting its objectives and goals. The objectives and goals of an English program at engineering university are for students to be able to utilize and efficiently communicate in the language and to be able to function as a capable engineer or researcher in the field. In the world where international cooperation has become a requisite to engage in solving global issues, such as the attainment of Sustainable Development Goals (SDGs), it does not suffice to teach English as just an independent subject. English needs to be taught in the way that stimulates students to open their eyes to the fundamental system of knowledge and motivate them to actively utilize what they learn to advance their studies.

In this presentation, a new concept of what should be aimed in English education at engineering university will be provided from the perspective of communication education that is required in university education. In the process, a typology of what needs to be taught for prospective engineers at university will be provided along with a model which illustrates how all these subject matters are incorporated in university education.

2. What is taught in university education: a typology

Figure 1[1] illustrates how the contents of university education can be conceptualized in terms of communication education. Education provided at university can be broadly classified into three categories: "education that specializes knowledge" provided by faculty of students' major, "education that generalizes knowledge" provided by the faculty of liberal arts or general education, and "education that personalizes knowledge" provided by the faculty of career education and development[2]. "Education that specializes knowledge" is education that deepens knowledge in the student's own field of expertise and makes the student proficient in it. "Education that generalizes knowledge" is education that exposes students to a wide range of academic disciplines and allows them to apply the understanding of "people, society, and nature" that they have gained to the context of their own field of specialization, while at the same time allowing them to consider the cultural and social significance of that knowledge to their major. Based on these two types of education, career education (education that personalizes knowledge) helps students recognize their own aptitude and focus on their aspirations and values in finding a job.

Of the above three categories, liberal arts education (education to generalize knowledge), when applied to the education at engineering universities, is aimed to help students enhance their expertise by recognizing it in a broader social context. Engineers need to understand and be able to apply and integrate their expert knowledge and skills to the situation they are put in and be able to complete their assignments. Furthermore, with regard to the communication skills, engineers need both verbal and non-verbal knowledge and skills in communication to efficiently complete their tasks, especially when they are working as a team or with clients. From these aspects, "education to generalize knowledge" plays a prerequisite role in university education and should run alongside the education provided in students' major and career development.

Meanwhile, looking at the current state of liberal arts education at universities, even though the goals of each subject are clearly established as mentioned above, the actual classes are offered in the ways that make it difficult for students to understand them[3]. Students seem to not recognize why they need to take liberal arts classes and how they can use what they learn there in their future as engineers. For such classes in general education programs, more efforts needs to be made to design curricula and lessons so that intentions explained above can be more easily conveyed to students.

3. A new perspective on liberal arts education curricula design: the three aspects

When "education to generalize knowledge," as defined here, is interpreted so that it can better be applied to the development of a curriculum design, the three aspects that outline what is to be achieved are raised[2]:

a. Understanding "WHAT" of the subject matter
b. Understanding "WHY&HOW" of the subject matter
c. Understanding "WHICH" of the subject matter

Conventionally, the contents of liberal arts and general education has been taught in the form of independent knowledge which made it difficult for students to understand why it is necessary to learn it and how it will be utilized in their future. In the modern age, with ever-progressing globalization and the occurrences of disasters and challenges such as the outbreak of COVID-19 or attainment of SDGs, "the ability to confront unprecedented problems" is becoming increasingly necessary. In order to work ways out of such predicaments, one needs to be able to actively engage oneself and logically and critically think through problems to seek solutions. Reevaluating and redesigning course contents of liberal arts and general education from the three aspects introduced above will nurture these skills in students and help present the subject matter in relation to their major and career.

4. Optimizing English education with the new perspective

The situation of teaching independent knowledge in the subject area has been the same in English education, and various improvements have been made in this field. In Japan, English has conventionally been taught as independent knowledges, such as that of grammar, vocabulary, and pronunciation, with little reference to meaning. Observing the improvements made in the research field of English language teaching, the English section in the Division of Global Career Education has optimized its English curriculum to accommodate the demand to develop students' English ability to cope in the modern society (see Table 1)[1]. In the current curriculum, English is taught as the communication tool by making students conceptualize WHAT, WHY, HOW and WHICH of what they learn.

References:

[1] Wada, T., Promoting a new perspective on liberal arts education for engineering majors: using a practice item taken from TOEIC textbook as an example. Proceedings of 69th JSEE Annual Conference. (2021).

[2] Wada, T., Setting a goal for undergraduate English curriculum in Japan: factors to be considered in developing English programs for engineering majors. Kogakuin University Treatises **59-1**. (in print).

[3] Erickson, H.L., Lanning, L.A. & French, R., *Concept-based curriculum and instruction for the thinking classroom*, London: Corwin. (2017).

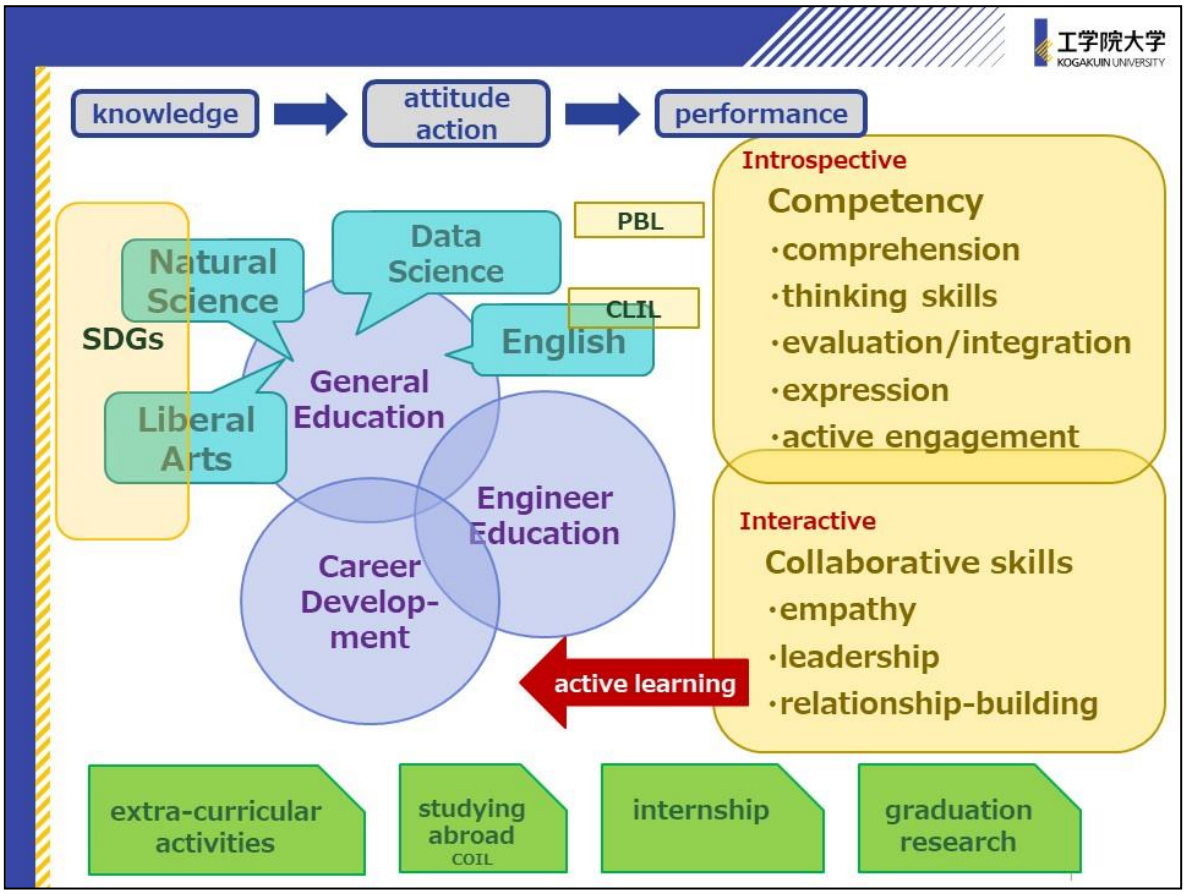

Fig. 1. Contents of university education conceptualized in terms of the suggested perspective

A Practical Report on English Education at Kogakuin University: A Lesson from Basic English I/II

Takayuki Akimoto

Center for Promotion of Higher Education, Kogakuin University, Tokyo, Japan
E-mail: t.akimoto@cc.kogakuin.ac.jp

Abstract

In this talk, I will report on what kind of lessons are offered in Basic English I/II, one of the compulsory English courses at Kogakuin University, what kind of changes are made after the Corona pandemic, how they are reflected in students' TOEIC-IP scores, and how their scores are used in Kogakuin's English education.

1. Introduction

In the age of the SDGs, international partnerships are becoming more and more important. Therefore, engineering universities like Kogakuin University are aiming to foster the next generation of leaders who specialize in science and technology and who can work on achieving the SDGs on their own. Against this backdrop, it is becoming even more important for students to acquire English as a communication tool to connect people internationally. English education at Kogakuin University (KU) aims to enable students to handle English as a communication tool, to recognize it in a broad social context, and to understand it in relation to various fields.[1] By doing this, we offer three compulsory English courses (Basic English, Basic Communication, and Basic Academic English), and our ultimate goal is for students to be able to write sentences in English in which they raise problems based on objective facts and evidence, analyze and clearly explain the causes, and then propose their own solutions. In this talk, I will report on (a) what kind of lessons are offered in Basic English I/II, one of the compulsory English courses at KU for 1st year students, (b) what kind of changes are made in the Corona pandemic, (c) how they are reflected in students' TOEIC-IP scores, and how they are used in our English education.

2. Basic English I/II before/after the Corona pandemic

In Basic English I/II (henceforth, BE), students practice questions based on the TOEIC® reading section. We not only provide students with knowledge of English grammar and vocabulary, but also develop students' independent and critical thinking skills necessary for communication e.g., through an understanding of English-speaking cultures and the linguistic differences between Japanese and English with a view to eventually enabling students to use English as a communication tool. Before the Corona pandemic, explanations of grammar and vocabulary were given individually by each teacher; as a matter of course, the level of students' understanding varied from class to class. However, since the university's classes have been online since the Corona pandemic, more detailed explanatory materials on grammar and vocabulary have been prepared for students so that they can study on their own, and these materials have been uniformly distributed to all classes. As will be explained below, this effect is clearly seen in the increase in students' TOEIC-IP scores.

3. Practice and use of TOEIC-IP

BEII (the second semester) includes TOEIC-IP score as one of the student's performance evaluation, and students are required to take the TOEIC-IP test held in January every year. Fig.1 shows the transition of the average TOEIC-IP scores of first-year university students from 2016 to 2020.

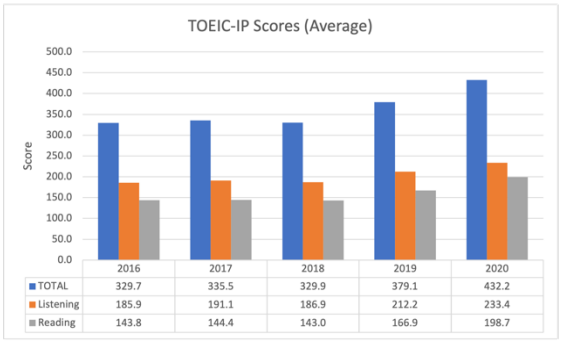

Fig. 1. TOEIC-IP Average Scores from 2016-2020

By 2018, the average score was about 330, rising to about 380 in 2019, and then to about 430 in 2020, when classes went online due to the Corona pandemic. It is noteworthy that the 2020 score was higher than the average score for new employees in the fields of engineering and architecture (396).[2] As such, the English proficiency of our university's first-year students has been on the rise since 2019, and we believe that the uniform teaching practices at BE have contributed to this. Currently, the scores are used to allocate students to classes according to their proficiency level in the compulsory English courses in the second year and to improve class materials.

References:

[1] Wada, Tomoko. Setting a Goal for Undergraduate English Curriculum in Japan. *Kogakuin University Bulletin,* **59(1)**, (to appear).
[2] IIBC, New Employees in 2019 TOEIC® Listening & Reading Latest Data, (2019).

English Education in the Age of SDGs: A Survey on English Learning among Kogakuin University Students

Tomomi Yamada[1] and Kazunori Suzuki[2]

[1]Center for Promotion of Higher Education, Kogakuin University, Tokyo, Japan
E-mail: tyamada@cc.kogakuin.ac.jp
[2]Educational Development Center, Kogakuin University, Tokyo, Japan
E-mail: k.suzuki@cc.kogakuin.ac.jp

Abstract

In this talk, we will give an overview of the two compulsory English courses at Kogakuin University: Basic Communication and Basic Academic English, and report on the results of a questionnaire of students' attitudes towards English in these two classes. Further, based on the results, we will talk how English teaching can be improved in the age of SDGs.

1. Introduction

Although more than two decades have passed since the beginning of the 21st century, the problems we face, such as the environment and poverty, remain unresolved and in some respects, they are becoming more serious. Urgent action is now needed if we are to continue to live on Earth. In this context, the Sustainable Development Goals (SDGs) were formulated by the United Nations in 2015, and they differ from previous international efforts in that they require countries in different stages of development and situations to work together to solve common problems. Further, there's an emphasis on the fact that social, economic, and environmental issues which have been recognized separately in the past, be interconnected and deeply interdependent. In other words, in the age of SDGs, it will be important for students to have the ability to understand and communicate with people who have different backgrounds and ideas, and to have a broad perspective that places their own field of expertise in the context of solving global problems[1].

As an engineering university, Kogakuin university regards English as a communication tool for engineers and aims to provide English courses that enable students to learn about different cultures and the social and economic systems that create problems. To achieve this, our university offers three compulsory English courses: Basic English, Basic Communication and Basic Academic English. In this talk, we will report on how classes are taught in Basic Communication: a compulsory course for first-year students, and Basic Academic English: a compulsory course for second-year students, students' attitudes towards learning English, and how English teaching can be improved to develop human resources, which can contribute toward the building of a sustainable society.

2. A Brief Summary of Basic Communication and Basic Academic English

Basic Communications is a compulsory course for first-year students and is taught once a week for 105 minutes. In this class, students watch news clips from Voice of America (VOA) to learn about the daily lives of students in America and their approaches toward global issues. At the same time, students will learn about paragraph writing and practice explaining their ideas in a convincing manner, rather than merely stating their feelings, to people from different cultural backgrounds[2].

Basic Academic English is a compulsory course for second-year students and is also taught one a week for 105 minutes. In this class, students read articles on issues such as gender, immigration and globalization to learn about social systems and their problems. At the same time, through learning essay writing skills, students improve their ability to raise issues based on objective facts and evidence, analyse and explain the causes clearly, while proposing their own solutions[3].

3. A Survey on Kogakuin University Students' English Learning

Despite the increasing importance of English, the English language skills of students at Kogakuin University are insufficient. Therefore, we conducted a questionnaire on Basic Communication I and Basic Academic English I to learn about their attitude toward learning English. Figures 1 and 2 show the students' "likes" and "dislikes" of English. 59% of students taking Basic Communication I responded to the questionnaire. 48.7% of them said they "like" or "somewhat like" English. Regarding Basic Academic English I, 65% of students taking the class responded to the questionnaire. 45.7% of those respondents said that they "like" or "somewhat like" English. In order to find out the reasons why students "like" or "dislike" English, text mining by a KH Coder[4] was conducted and co-occurrence network analysis was performed. Figures 3 to 6 illustrate the results: the students who "like" or "somewhat like" English mentioned "people", "to be able to take" and "communication" as their reasons, as well as "to

watch", "Western movies" and "Western music". This may indicate that students see English as a means of communication with people and experiencing foreign cultures. In contrast, the words in reasons given by the group who "dislike" or "somewhat dislike" English include "to memorise", "vocabulary", "grammar" and "a lot". This suggests that, unlike the students who "like" English, they perceive it only as a "subject" to be studied in the classroom[5].

4. Further Improvement of English Teaching in Kogakuin University

From these results, it can be said that the future challenge for teaching English is to make students aware that English is not just a subject, but it is also a communication tool. For example, it would be useful to provide more opportunities for students to study abroad and to interact with people from a variety of backgrounds in the classroom, so that they can experience the joy of communication. The development of communication skills and intercultural understanding through English is also important in the development of engineers who can contribute to the building of sustainable world.

References:

[1] H. Minami and M. Inaba. *SDGs: A Guide in Time of Crisis* (in Japanese). Iwanami Shoten, Publishers. (2021).

[2] T. Wada. Setting a Goal for Undergraduate English Curriculum in Japan: Factors to Be Considered in Developing English Programs for Engineering Majors (in Japanese). *Kogakuin University Bulletin*, **59**(1), (forthcoming).

[3] *Ibid.*

[4] K. Higuchi. *Quantitative Text Analysis for Social Researchers: A Comtribution to Contenet Analysis (2nd ed.)* (in Japanese). Nakanishiya. (2020).

[5] T. Yamada. A Survey on English Learning of Students in Kogakuin University (in Japanese). *Kogakuin University Bulletin*, **59**(1), (forthcoming).

Appendices:

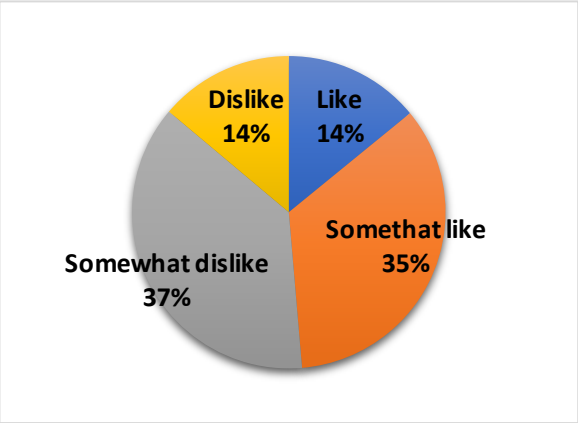

Fig. 1. "Likes" and "Dislikes" of BC I students

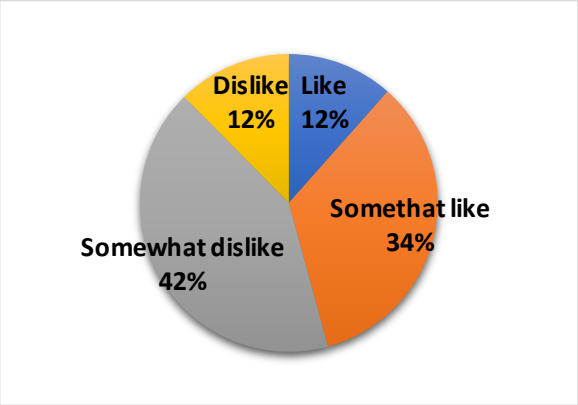

Fig. 2. "Likes" and "Dislikes" of BAE I students

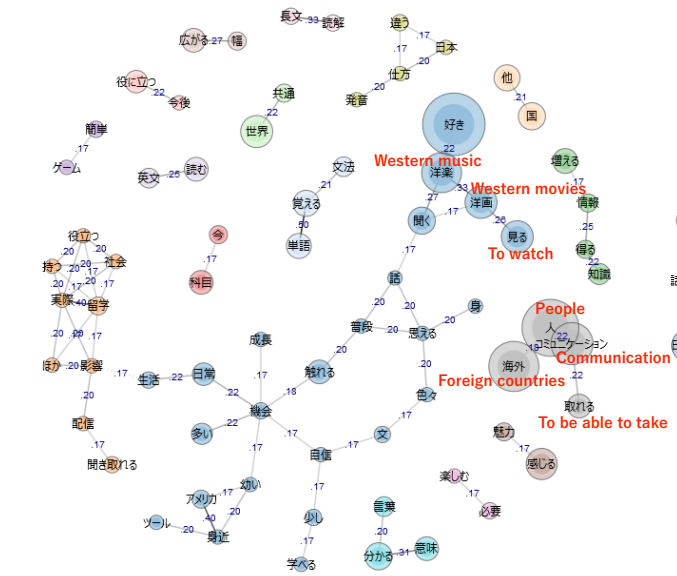

Fig. 3. Co-occurance for "Likes" (BC I students)

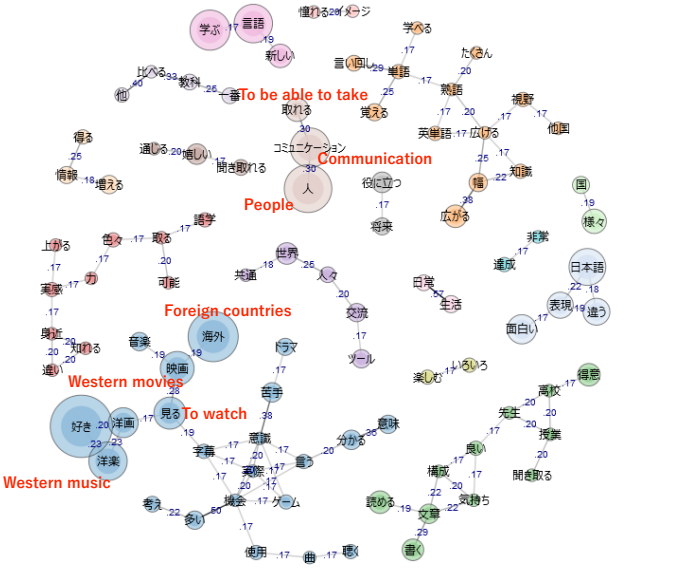

Fig. 4. Co-occurance for "Likes" (BAE I students)

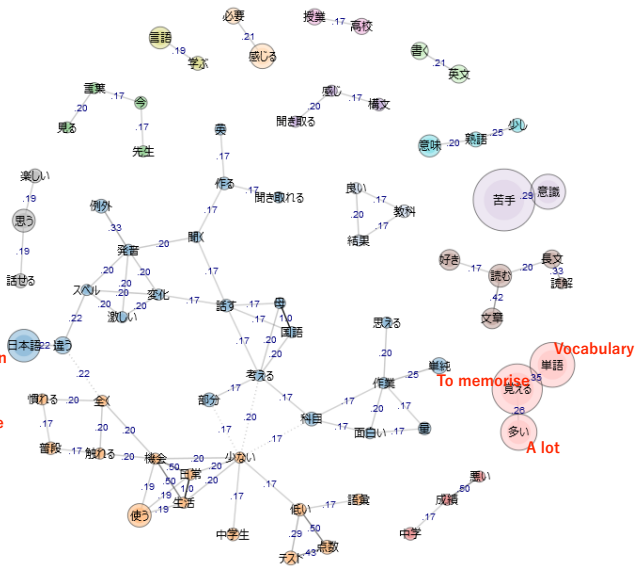

Fig. 5. Co-occurance for "Dislikes" (BC I students)

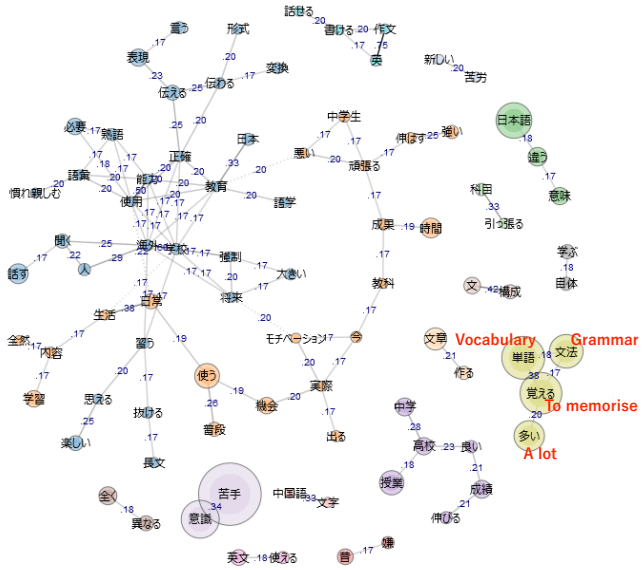

Fig. 6. Co-occurance for "Dislikes" (BAE I students)

An Application of CNN in Answer Analyzing and Estimation Education Advanced Technology

N. H. Mai

Department of Electrical Engineering, University of Danang, The University of Science and Technology Danang, Vietnam
E-mail: nhmai@dut.udn.vn

Abstract

A key issue in distance learning in a distributed university system is the ability to ask questions and evaluate answers. Due to the lack of close contact and the large number of students, a teacher is unable to ask and hear every teacher's answer, leading to an unfair and incomplete assessment. Therefore, it is very necessary to come up with a solution so that every student has the opportunity to communicate with the teacher and vice versa, the evaluation from the teacher for all students is essential. In this way, we need to analyze the question to automatically generate the question and evaluate the answers through lessons, so that the questions are not the same for each student, as well as the answers are independent. There are many methods of analyzing sentences, each of which has certain advantages and disadvantages. The research in this article uses the method of predicate-parametric analysis, combined with artificial neural networks to find the most reliable response direction, thereby properly assessing students' abilities and creating maximum learning self-awareness. The simulation results are given to be able to organize and apply widely on the number of coagulants and simultaneously.

Keyword: higher education, ANN, CNN, analyzing, grammar, fuzzy, sentence

INTRODUCTION

Introduction of the predicate – argument method (PAM) Currently there are four types of sentence analysis as follows: - Analysis by functional grammar
- Analysis according to traditional grammar
- Analysis according to information theory
- Analysis by semantic grammar.

In which, the analytical method according to semantic grammar means the method of structural analysis is relatively new and highly effective, especially when using computers to analyze sentences of arbitrary length. This method is also known as the predicate-parameter analysis method. This method has the strength of identifying high-focused semantics, short analysis time and improving objective reality, but has the disadvantage of poorly exploiting new information, or in other words, understanding. The sentence concept is not high, because it focuses on dissection to find the sentence core. The PAM method can be used to analyze both Vietnamese and English sentences, and can be extended to many other languages. A tightly structured sentence always includes the predicator-centered verb and surrounding reference element entities, called arguments or arguments. Based on this structure we will consider the evaluation from the core factor. A predicate can have one or more parameters, in which there will be primary, secondary, and external, but also may not have any.

In fact, there is also a predicate that does not require an argument (eg in French: verb pluit: il pleut (rain) has no argument; il is a subject that does because, not argument). In Vietnamese, a special type of predicate can be seen as a proof for the predicate case does not require arguments. In addition, the predicates require arguments. The number of arguments required by the predicate is not equal. • The predicate requires an argument (the state predicate, the property predicate, the feature, some active predicates ... These predicates only need the subject object of the action.) For example: It sings. / She is quite fat. • The predicate requires two arguments (impact predicates, speech predicate, relationship predicate…) For example: The teacher has corrected the English exercise/ This wall is made of bricks. • The predicate requires three arguments (predicates with the meaning of inducing, giving). Example: I told him to boil water/I gave you the book. • Predicates require four arguments (predicates change, buy, sell…). These predicates require the objects of exchange, the changer, and two things for exchange. This is the case that probably exists only in theory. In fact, depending on the circumstances, these four parameters may not appear simultaneously.

Required: Are entities surrounding the predicate whose presence is required by the predicate. For example, in the sentence: "I gave him a book." I am, a book and he is obligatory. The opening element: Are the entities that appear in the situation, but their presence is not required by the predicate, but by the situation or circumstance. For example: in the sentence: "This afternoon, I gave him a book." this afternoon is ambition to expand. Compulsory division of parameters - extended or denominational parameters - element is only relativistic. A required argument in one predicate framework can be an extension argument in another predicate framework.

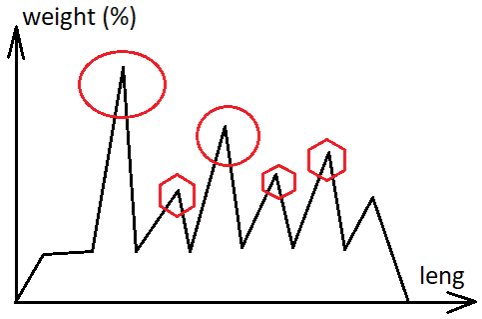

Fig. 1. The weight of central answer

In this figure 1 we see that the predicate is placed in the function with the highest weight. So, if the predicate has not been found yet, the weights can initially be sown randomly and then reevaluated. This algorithm will be discussed in the next section. "Adjectives are words such as verbs, adjectives, modal adjectives, hieroglyphs, onomatopoeia ..." The evaluation of the weights of the predicates and the argument are through the fuzzy algorithm of the n-state association function. However, the difficult problem is that the number of input variables is not constant. This is different from conventional fuzzy systems. The number of variables varies with each answer, despite the same question. Therefore, in order to reduce the computation time, the inclusion of group optimization theory to group words and phrases is essential. Group optimization algorithm to localize the number of variables Thus, for an answer with n words, the first thing is to arrange to create N phrases that combine meaning, for example: - Current is the directional flow of electric charges in the electric field In this case n = 15 But we will sort by clusters: Current / is / current / displacement / directional / of / the / charge / in / electric field Thus, according to this analysis, N = 10 will be produced. In those 10 phrases, considering each phrase as a variable, we will determine the predicate. Clearly in this sentence, displacement is active, thus posing the questions: what current? current; How current? the charge; What line do? in relocation; Where is the line? electric field. So, the question ideas to answer here are: - What? - How? - What? - Where? The predicate will be on the second question. The first sentence is the subject, so it gives direction to the predicate. The parameters are in the following questions. For cases where the central predicate is adjective, the determination is similar to the verb. (Because in Vietnamese, adjectives have many similarities with verbs). Therefore, when determining the variable as the predicate, we give the weight or the membership function that has a value of 1, similarly for the central argument [6]. By using the fuzzy variable in this case, we will divide the reference areas into the center as shown in Figure 2 [9].

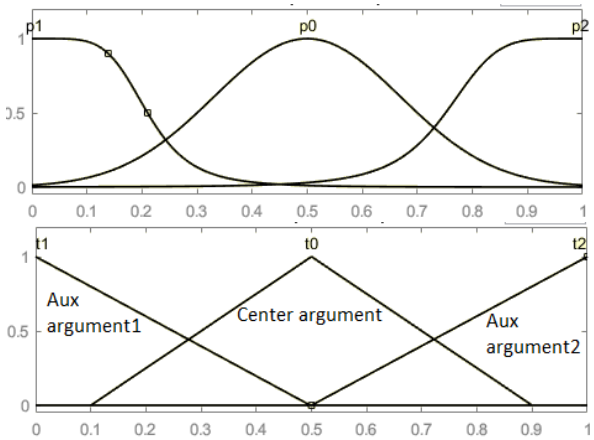

Fig. 2. Fuzzification of central solution

Looking at such a variable division, we can see that there can be 3 predicate regions and 3 parameter regions. It is of course possible to change the number of regions because each variable has the same number of regions. If the system has N variables and each variable has a maximum of m zones, the maximum number of zones is M = N.m. The number of answers depends on the rating of the output, usually 0.25 points, so we will have the output divided into 40 variable regions as shown in Figure 3.

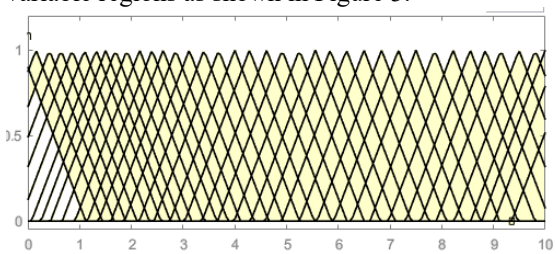

Fig. 3. Divide variable regions of answer.

BASIC OF APPLICATION OF CNN

Based on such a classification structure, the application of the ANN in network is a reasonable calculation and satisfies the assessment of responses [2],[4],[5],[7],[8]. The problem here is that the number of input variables is not constant, that is, N changes, so according to the normal fuzzy structure, N must be fixed. That architecture is not suitable for this object class. Then we need to offer another reference algorithm. In order to reduce the input variable, the conjunctions are not put in the variable, such as, tense, and, but ... So, in the case of the above sentence, only N = 9. Such division is still difficult, so Here we will apply the principle of consecutive halving. Assuming the answer has n initial words, then call vector: x [n] = (x [0], x [1],… x [n-1]) = (x [k]) where k = 0… n-1 after the first split, we get two sets, assuming the phrase is equally divided.

$$x_1[n] = (x_1[k])$$
$$x_2[n] = (x_2[k])$$
$$k = 0...n/2 \quad (1)$$

If the phrase is not evenly divided, it doesn't matter, because then we will At this point, we will have 2 new variables x1 and x2 are two phrase vectors.

$$x_1[n] = (x_1[k]); k = 0...n/2 - 1$$
$$x_2[n] = (x_2[k]); k = 0...n/2 \quad (2)$$

If these variables have formed the minimum phrase, the division stops, and if the phrase is not minimalistic, we will further divide it into smaller phrases. At that time, the number of variables increases gradually, until the phrases are all minimalistic.

$$x \to \begin{cases} x_1 \to \begin{cases} x_{11} \to \begin{cases} x_{111} \\ x_{112} \end{cases} \\ x_{12} \to \begin{cases} x_{121} \\ x_{122} \end{cases} \end{cases} \\ x_2 \to \begin{cases} x_{21} \to \begin{cases} x_{211} \\ x_{212} \end{cases} \\ x_{22} \to \begin{cases} x_{221} \\ x_{222} \end{cases} \end{cases} \end{cases} .....N-1 \quad (3)$$

In which some intermediate variables may be empty, so in fact the number of input variables is not always a multiple of 2. After reaching the critical variable state, applying fuzzy logic to the above input variables, the associated functions μ (x) are also a vector:

$$\boldsymbol{\mu}(\mathbf{x}) = [\mu(x_0), \mu(x_1), ..., \mu(x_{N-1})] \quad (4)$$

When determining the value of the membership function, it is necessary to get data from the library to evaluate and teach AI. Therefore, it is necessary to build a complete database library, as complete as possible.

Library issue:

This library is not just a pile of data. Lectures are gathered from a variety of sources, with each teacher providing a complete lecture. However, if you rely on just one person, you cannot satisfy universal, even if it is the best teacher. Therefore, we need to analyze and evaluate the lectures of the library. The algorithm for building the library is based on the following filters:

- Filter the keywords of the content: include words, phrases, explain phrases and extended phrases
- Filter the conjunctions - Save phrases to separate folders
- Link directories with the reference area of the fuzzy variable in and out.

Those are the basic steps, in each step there will be detailed steps to concretize the implementation. Each course is a 3-dimensional matrix, with each element being a lesson in a class or lesson:

$$\mathbf{A} = \begin{bmatrix} \mathbf{C}_1 \\ \mathbf{C}_2 \\ ... \\ \mathbf{C}_n \end{bmatrix} = \begin{bmatrix} [\mathbf{C}_{11}, \mathbf{C}_{12}, ..., \mathbf{C}_{1m}] \\ [\mathbf{C}_{21}, \mathbf{C}_{22}, ..., \mathbf{C}_{2m}] \\ ... \\ [\mathbf{C}_{n1}, \mathbf{C}_{n2}, ..., \mathbf{C}_{nm}] \end{bmatrix} =$$

$$\begin{bmatrix} \begin{bmatrix} c_{111} \\ c_{112} \\ ... \\ c_{11j} \end{bmatrix} & \begin{bmatrix} c_{121} \\ c_{122} \\ ... \\ c_{12j} \end{bmatrix} ... & \begin{bmatrix} c_{1m1} \\ c_{1m2} \\ ... \\ c_{1mj} \end{bmatrix} \\ ... & ... & ... \\ \begin{bmatrix} c_{n11} \\ c_{n12} \\ ... \\ c_{n1j} \end{bmatrix} & \begin{bmatrix} c_{n21} \\ c_{n22} \\ ... \\ c_{n2j} \end{bmatrix} ... & \begin{bmatrix} c_{nm1} \\ c_{nm2} \\ ... \\ c_{nmj} \end{bmatrix} \end{bmatrix} \quad (5)$$

In each lesson there will be key issues and the teacher will use these keywords to create situations for students to answer. The questions can be arbitrarily long or short. But the answer should be clear and correct with keywords.

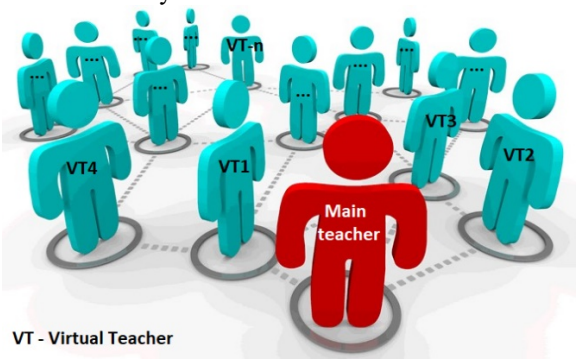

Fig. 4. The virtual teachers

Thus, it is possible to implement a Point-to-Point strategy, i.e. a teacher - a student. Teacher clone makes it feel like learning in a real environment without expensive virtual reality for the poor students. Thus, a main professor of the university can create his own copy and those VT will teach as MT. Copying is not If the answer is not clear then fuzzy's judgment will be fuzzy and of course the results will be poor. Situation generates questions: The question was created by the virtual instructor by surprise. VT-Virtual Teacher receive lectures from the library, along with the real teacher (MT-Main Teacher) to teach each student. The teacher model can be illustrated as follows: difficult, just a basic graphic design tool can do it. VT's work consists of three main things:

- Lectures according to the schedule
- Ask students case questions
- Get answers and student quality assessment.

APPLY CNN INTO ESTIMATE ANSWER

Go back to definition of input and output variables, we use CNN to evaluate input weight number. After analyzing predicator and argument in sentence, we

compare the results to library data and calibrate weight value function. Denote $x_p[n] \in R^m$ is a set of predicators, $x_a[n] \in R^h$ is a set of arguments, convolution neural network y[n] of two input sets is follow:

$$y[n] = x_p[n] * x_a[n] = \sum_{k=0}^{m+h} x_p[k] x_a[n-k] \text{ with n = 0 …m+h-1} \quad (6)$$

The lecture is very simple because it is accessed from the memory or the cloud. The point here is to ask a question and get an answer. Obviously, we can't ask questions first, because then the problem becomes stiff. So, the question raised in this situation is: - The question keyword, is the predicate - Add the parameters. For example, while giving a lecture on "electromagnetic sensors", the two keywords "sensor" and "electromagnetic" are used as the main predicate. The keyword set of the question is focused on the main phrase.

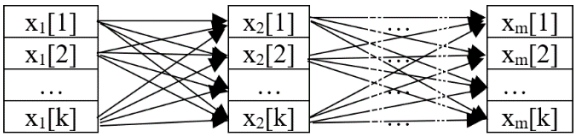

Fig. 5. The model of procession

If the sets $\mathbf{x}_1 = [x_1[1], x_1[2],\ldots,x_1[k]]^T$, …, $\mathbf{x}_m = [x_m[1], x_m[2],\ldots,x_m[k]]^T$ then we could write output signal **y** as same convolution:

$$\mathbf{y} = \mathbf{x}_1 * \mathbf{x}_2 * \ldots * \mathbf{x}_m$$

is a *k* elements vector. However, if we do convolution with *m* class then there are many results of calculation and can't focus roots. The simple method of answer is use two direction of matrix with row and column are topics of the question.

0	1	1	1	1	1	1
1	1	1	0	0	1	1
0	0	1	1	1	1	1
1	0	1	1	1	0	0
0	0	1	1	1	1	1
1	1	1	1	1	1	0
0	0	0	1	1	1	0

Fig. 6. The start matrix of answer

With the above matrix, according to the subject of the row, there will be a certain number of reasonable answers when the value 1 is at most. However, it does not necessarily mean that we get the date because the learner can answer any sentence, meaning that the correct number of predicates and verbs can change. Here we denote the predicates and the false predicates as the number 0 and the correct number 1. The same goes for the argument in the column topic. With this structure, it is possible to use the convolutional neural network CNN to evaluate the response level and give score for the answer. By using features of [1 1; 1 1] or [1 1 1; 1 1 1; 1 1 1] which are the simplest sub-answers including the predicate and the central argument, CNN for answers with a rating of 0 to 10. The evaluation result is the highest weight of the final computed vector. How many topics are given to the question is up to the questioner [3]. For example: - Let's analyze the meaning of A, it means that students must state two topics: "Meaning" and "Analysis". But if: - If the meaning of A, then there is only one topic and in this case we just treat the matrix as a vector and evaluate according to the standard phrase without regard to the level of true / false, that is the evaluation score. there are only two levels of pass / fail - With such a concept, it can be extended to a question with more topics, then the answer matrix will have more dimensions because each topic is one dimension of the matrix. However, the assessment will then take more time without increasing the quality of the review. The practice of teaching for many years shows that questions bring the best rating of 2 or 3 topics. Single-topic questions apply only to multiple-choice questions and do not reflect reality. The questions with more topics often fall into the essay test and will show the sharpness of students' thinking when assessing answers. Obviously, if to achieve the best evaluation results, a one-time comparison is not effective because the number of responses is very much and depends on the student's performance. Therefore, if performing a multi-tier CNN, it will give the best evaluation results. That is deep learning applied in this case.

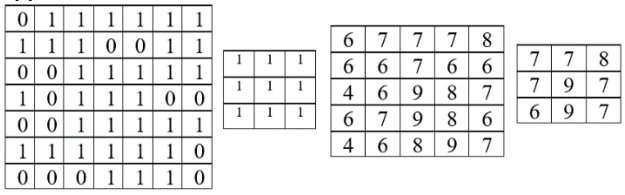

Fig 7. The result of CNN

At this point, it is possible to deduce the answer results of students after a CNN process equivalent to level 7 when using the sigmoi function to evaluate max pooling.

THE SENSITIVE FUNCTION METHOD

Although this is a simple example, it shows that applying CNN combined with AI inference allows a rapid assessment of student quality from time to time. Therefore, in a lesson, it is possible to evaluate students many times and finally use the average formula to get results. Accordingly, we give a number of calculation methods as follows:

Method 1:

$$N = \frac{\sum_{i=1}^{m} N_i}{m} \quad (7)$$

Use sensitive integrated criterion function to decide minimum time to answer and maximum score as follow equation:

$$J = \sum_{i=1}^{m} \int_0^t \frac{2\tau}{N_i} d\tau = \sum_{i=1}^{m} \frac{t_i^2}{N_i} \to \min \quad (8)$$

Will allow for a quick assessment of the quality of students' learning without having to deal with

complicated and unfair statistical calculations. Describe this integral as shown below.

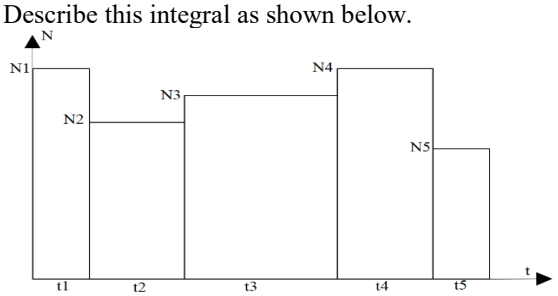

Fig 8. Description of integrated

As fig.5, with difference scores and think tine and answer time then estimation of result is:

t	2	4	7	4	2
N	8	6	7	8	5

Hence we have:

$$J_1 = \frac{4}{8} + \frac{16}{6} + \frac{49}{7} + \frac{16}{8} + \frac{4}{5} = 12,967$$

If other student has answer time as table 2:

t	4	4	10	4	7
N	8	6	7	8	5

Then $J_2 = 30,752$

If student has score as table 3:

t	2	4	7	4	2
N	10	7	5	7	8

Then $J_3 = 15,271$

So with the above 3 students, the second student is of the worst quality, and the third student has a higher GPA than the first student but wasted time on question 3 with low scores (5) So, although the third student has a score of 10 in question 1 and 8 in question 5, the quality of learning through the sensitivity index is worse than the first student.

Method 2

We take out second sensitive function by maximum scale as following:

$$J = \sum_{i=1}^{m} \frac{N_i}{t_i} \to \max \qquad (9)$$

This means that if students get good grades with short thinking time, they are judged to do better. Specifically, for the three above cases, they are listed as follows:

$$J_1 = \frac{8}{2} + \frac{6}{4} + \frac{7}{7} + \frac{8}{4} + \frac{5}{4} = 11$$

$$J_2 = \frac{8}{4} + \frac{6}{4} + \frac{7}{10} + \frac{8}{4} + \frac{5}{7} = 6,914$$

$$J_3 = \frac{10}{2} + \frac{7}{4} + \frac{5}{7} + \frac{7}{4} + \frac{8}{2} = 13,214$$

Under this approach, the third student had better results than the first. This shows that when the functional indicators are close to each other, the human assessment is only relative. These sensitivity functions are really meaningful when the standard values differ greatly, at least over 30%. Then how to have a relatively accurate assessment without violating educational principles. Method 3 The problem that the author raises next is amplifying positive deviations to increase the "good" index or amplifying the non-positive deviations to increase the "poor" index. Here:

- Non-positive difference is the difference between the point value and 10 (the highest score): $\Delta N = 10 - N$
- Positive deviation is the time difference between the minimum thought time allowed and the real time answering the question: $\Delta t = t_0 - t$.

In the time t used, it will happen that t is less than or greater than t0, meaning that the time deviation can be positive or negative, but the point deviation has only one side. Therefore, the author gives the point of using the exponential function with the natural base and the amplification function here is:

$$K_t = K_0 e^{-at\,an(\Delta t)} + \psi$$

Here K0 is the coefficient to be used to adjust the scale value and ψ is the coefficient for adjustment of deviation. These coefficients are chosen arbitrarily but always ensure positive so as not to lose the spontaneity of the exponential. The graph shows the variation Kt according to the time deviation as shown

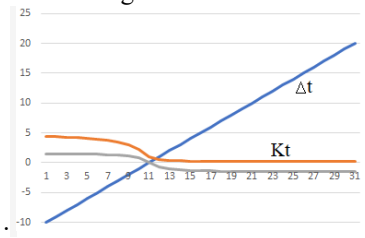

Fig. 9. Describe change of functions

Thereby, we see that the use of the function Kt has ensured the fairness in the evaluation without losing the generality, but amplified the small time zone very well with a large amplitude, while in the time domain large positive deviation , the equilibrium value is smaller and it is also appropriate because when the required time has been exceeded, poor performance is evident. From there we build up the formula for the sensitivity function:

$$J = N.K_t = N\left(K_0 e^{-a\tan(\Delta t)} + \psi\right) \to \max$$

Apply this formula with $K_0 = 1$; $\psi = 0$ then we have results of three students as:

$J_1 = 107,1$

$J_2 = 83,7$

$J_3 = 124,9$

So the third student has better results than the first student, while the first student is better than the second student. This result is consistent with the formula in the second method but the difference is clearer so it will be more reliable.

DISCUSSION

The application of predicate and argument is sentence analyzing to analyze structure of answer in teaching is a good method now. This is a modern method to fast

and exactly understand answer of student in classroom without real teacher.
The fuzzification central answer and apply CNN to estimate quality of answer and use sensitive function method also new good method to do fast estimate ability of student at online classroom. The method has convenience with virtual teacher and comfortable state for student.

CONCLUSION

This is a study in higher education to apply into DUSM (Distributed University Systems Model) [1], which is a digitalization university modern in near future. The studies are start results to approximate education modern with target: “one teacher for one student” with highest collaboration. We hope the application of this study in future.

REFERENCE

[1] N.H.Mai, Application of Artificial Intelligence in Distribution of University System Model, SIE conference 2020, Riga in Latvija, p516-526.
[2] Byra Michal, Galperin Michael, Ojeda-Fournier Haydee (2018) Breast mass classification in sonography with transfer learning using a deep convolutional neural network and color conversion. Medical physics, 10.1002/mp.13361 723
[3] Stephen Victor, (2016). Distributed Learning: A Flexible Learning and Development Model, *E-Learn: World Conference on E-Learning in Corporate, Government, Healthcare, and Higher Education*, At Washington, DC US.
[4] Kim D H, MacKinnon T (2017) Artificial intelligence in fracture detection: transfer learning from deep convolutional neural networks. Clinical radiology, 10.1016/j.crad.2017.11.015
[5] Kim Tackeun, Heo Jaehyuk, Jang Dong-Kyu (2018) Machine learning for detecting moyamoya disease in plain skull radiography using a convolutional neural network. EBioMedicine, 10.1016/j.ebiom.2018.12.043
[6] Yiming Zhou1,a and Yongmei Su1, Development of CNN and its Application in Education and Learning, 2019 9th International Conference on Social Science and Education Research (SSER 2019), p720-724
[7] Jinwei Wan, Bo Chen, Bin Xu, Hongwei Liu, Lin Jin (2019) Convolutional neural networks for radar HRRP target recognition and rejection. EURASIP Journal on Advances in Signal Processing, 10.1186/s13634-019-0603-y
[8] Mingyuan Xin, Yong Wang (2019) Research on image classification model based on deep convolution neural network. EURASIP Journal on Image and Video Processing, Vol.2019 (1), pp.1-11
[9] Ibrahim A. Hameed and Claus G. Sorensen, Fuzzy Systems in Education: A More Reliable System for Student Evaluation**,** DOI: 10.5772/7216, IntechOpen access

Lightning Talk Session

Advanced Functional Materials

November 23rd

Presentation No.	Title	Author	
AFML1.	Effect of visible light for photocatalytic property of TiO_2/Cu_2O thin films	Katsuyuki Takeda, Ichiro Takano	170
AFML2.	Dependence on Ar incident angles of PTFE surface treated by plasma	Yoshitaka Nakayama, Ichiro Takano	171
AFML3.	Analysis of High Thermal Conductivity Mechanism of Naphthyl Benzoate-Twin Mesogenic Epoxy Polymers with Alkyl Chain Length 2 Having 2,7-Naphthyl Benzoate as the Mesogenic Skeleton	Yuu Miyama, T. Kawai, and Y. Itoh	172
AFML4.	Hardness of alumina film formed on aluminum by anodic oxidation with oxalic acid and alcohol	Takuma Sano, Hidetaka Asoh	174
AFML5.	Study on high thermal conductivity mechanism of phenyl benzoate twin-mesogen epoxy polymers by vibrational spectroscopy	Takeru Ishizawa, T. Kawai, and Y. Itoh	177
AFML6.	Influence of a CuO layer for conversion efficiency of CuO/TiO_2 thin films	Masaki. Yanagisawa, Ichiro. Takano	179
AFML7.	Theoretical calculation of infrared absorption spectra of hydrogen in various polymers under high-pressure hydrogen	Masayoshi Tsuji, T. Kawai and Y. Itoh	180
AFML8.	Improvement of Electrical Property of α-In_2O_3 Films Grown by Mist Chemical Vapor Deposition Using In_2O_3 Powder as Source Precursor	Akito Taguchi, T. Onuma, T. Honda, and T. Yamaguchi	181
AFML9.	Study on thermal conductivities of poly(methacrylic acid ester) having azobenzene as a mesogen with different spacer carbon numbers and the end group carbon numbers	Nanako Sakai, Tadatomo Kawai, and Yuzo Itoh	183

Effect of visible light for photocatalytic property of TiO_2/Cu_2O thin films

Katsuyuki Takeda*, Ichiro Takano**

*Graduate school of engineering, Electrical engineering and electronics, Kogakuin university, Tokyo, Japan
E-mail: cm21035@ns.kogakuin.ac.jp
**Faculty of engineering, Department of electrical and electronic engineering, Kogakuin university, Tokyo, Japan
E-mail: ct97912@ns.kogakuin.ac.jp

Abstract

In our previous study, TiO_2/Cu_2O multilayer thin films on a glass substrate were fabricated to expand a light-absorbing region and it was confirmed that the photocatalytic property of the TiO_2 thin film with the Cu_2O layer was improved. In this study, the effect of the Cu_2O layer was investigated by each photocatalytic measurement of TiO_2, TiO_2/Cu and TiO_2/Cu_2O thin films.

In recent years, there has been various reports related to artificial photosynthesis. Most of those researches have reported about hydrogen generation as a preliminary step toward organic matter production. The photocatalytic effect of TiO_2 as a typical photocatalysis has strong antifouling and antibacterial property, while the problem is that the photoenergy absorption wavelength is limited to the ultraviolet region below 380 nm. In this study, TiO_2 multilayer thin films with Cu_2O as a bottom layer was fabricated to obtain the photocatalytic property in visible light. In addition, the photocatalytic property of TiO_2/Cu_2O was compared with those of TiO_2/Cu and TiO_2, and the effect of the Cu_2O layer for visible light was investigated. By the expansion of an absorption wavelength, it is anticipated that an application of TiO_2 is also expanded.

The multi-process coating system was used for TiO_2 and Cu_2O thin film deposition on glass substrates of 15 mm x 9 mm (Micro slide glass) in a size. The substrates were ultrasonically cleaned with ethanol for 10 min. After the substrates were introduced into a vacuum chamber, those were sputter-cleaned in an Ar gas atmosphere for 5 min. The TiO_2 thin film was deposited by reactive sputtering with an O_2 flow rate of 1.5 sccm, an Ar flow rate of 20 sccm, and an RF input power of 100 W. The Cu_2O thin film was also deposited by reactive sputtering with an O_2 flow rate of 10 sccm, an Ar flow rate of 15 sccm and a DC input power of 30 W. The both films were 200 nm in a thickness. The Cu thin film was deposited by sputtering with an Ar flow rate of 15 sccm and a DC input power of 30 W to achieve a thickness of 200 nm. The surface composition of the thin films was measured by X-ray photoelectron spectroscopy (JPS-9030, JEOL Co., Ltd.). The optical properties of the thin films on glass substrates were measured by UV-Visible spectrophotometer (UV-2550, Shimadzu Co., Ltd.) to determine the transmittance of a methylene blue solution. The immersion test using methylene blue solution was carried out by light irradiation to a quartz cell filled with 3 ml of 10 ppm methylene blue solution. After the sample was immersed in the solution, the cell was irradiated with an artificial solar lamp for 6 hours.

Figure 1 shows the transmittance change of a methylene blue solution of a glass substrate without a film, TiO_2/glass, TiO_2/Cu_2O/glass, and TiO_2/Cu/glass. The transmittance of a methylene blue solution was evaluated as the photocatalytic property of samples. The transmittance change of the glass substrate was decoloration by artificial sun-light irradiation itself. The TiO_2/Cu_2O/glass among all samples exhibited the highest photocatalytic effect of over 90 % at 6 hours. Because the TiO_2/Cu_2O/glass with the Cu_2O layer showed the higher effect than the TiO_2/Cu/glass in the transmittance, the inserted Cu_2O layer enhanced the photocatalytic effect of the TiO_2 layer. In addition, It was suggested that the Cu_2O layer played the role of

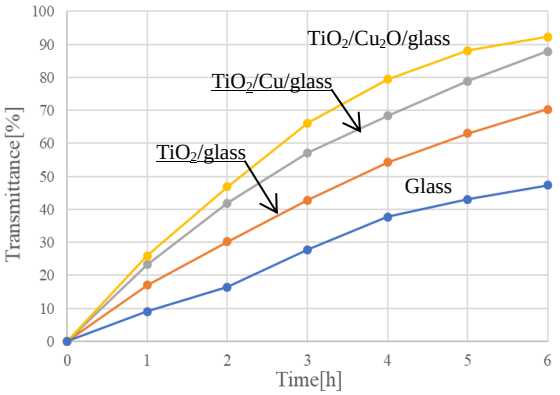

Fig. 1. Transmittance of the methylene blue solution for the immersion time.

p-type semiconductor for n-type of TiO_2. Because the TiO_2/glass had higher transparency than that of TiO_2/Cu/glass, it was considered that the difference of TiO_2/Cu/glass and TiO_2/glass occurred by reflection of the Cu layer for light irradiation.

In this investigation, it was found that the multilayer thin film of TiO_2/Cu_2O exhibited the higher photocatalytic property than that of the single layer of TiO_2. Furthermore to improve the photocatalytic property, the control for the structure of Cu_2O was important.

References

[1] Akihiro Joichi, Ichiro Tkano: 2018 Japan Surface Vacuum Society Academic Lecture, 1P51S (2018.11.19).

Dependence on Ar incident angles of PTFE surface treated by plasma

Yoshitaka Nakayama*, Ichiro Takano*

*Graduate School of Engineering, Electrical engineering and electronics, Kogakuin university, Tokyo, Japan
E-mail: cm21038@ns.kogakuin.ac.jp
**Faculty of engineering, Department of electrical and electronic engineering, Kogakuin university, Tokyo, Japan
E-mail: ct97912@ns.kogakuin.ac.jp

Abstract

In order to utilize PTFE with various excellent properties as a high-frequency printed circuit board, surface modification of PTFE was carried out by Ar plasma treatment. In this study, the tape shaped PTFE was attached to a semicircular substrate and dependence of Ar incident angles for the chemical state of PTFE was investigated by X-ray photoelectron spectroscopy.

Polytetrafluoroethyene (PTFE) exhibits excellent electrical properties due to the strong bonding energy of F and C atoms. In addition, PTFE is chemically stable and is attracting attention as a material for printed circuit boards. However, due to its chemical stability, it is difficult to obtain sufficient adhesion to copper as a wiring material. Therefore, it is necessary to improve the adhesion of PTFE by surface modification.

Ar plasma is classified as a low-energy surface treatment that has been applied to the functionalization of textiles and glass surfaces. This surface treatment can be applied to PTFE without polar groups, to break the chemical bonds on the surface and produce functional groups that contribute to the adhesion. In this study, The authors investigated the effect of the Ar plasma treatment on the surface chemical state of PTFE for the incident angle of ions.

Fluoroplastic adhesive tape (Nitto Denko Corporation, No.903UL) was used as the sample PTFE, and it was attached to a semicircular acrylic substrate to change the incident angle continuously. For Ar plasma treatment, an opposed plasma generator for surface cleaning installed in the intermediate chamber of the multi-process coating system (ULVAC Co., Ltd.) was used. Under the condition of an achieved pressure below 5×10^{-5} Pa in the intermediate chamber, The plasma treatment was carried out at the introduced Ar gas flow rate of 5.0 sccm, the RF input power of 150 w and the processing time of 180 s. The surface chemical state of the modified PTFE was measured by X-ray photoelectron spectroscopy (Kratos Ultra, Shimadzu Corp.) and evaluated mainly by waveform separation of C 1s spectra.

The C1s XPS spectra of raw PTFE and PTFE treated at 90°, 45°, and 15° in an incident angle are shown in Fig. 1. C1s spectrum of raw PTFE is showed at a factor of 10. The results of the waveform separation of the C1s spectra are shown in Fig 2. The Ar plasma treatment removed fluorine atoms from PTFE and increased the C-C bonds at all incident angles. In addition, COOH and OH adsorbed to functional groups that contribute to adhesion because the sample PTFEs were exposed in the air after the plasma treatment. Fluorine atoms of the surface were mostly removed at an angle of 15°. In other words, fluorine atoms were preferentially etched by the low-angle ion bombardment, and the C-C bonds in the bulk appeared on the surface layer.

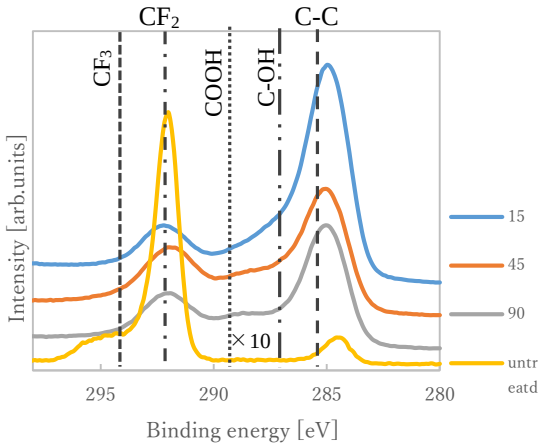

Fig. 1. C1s XPS spectra of Ar plasma treated PTFEs

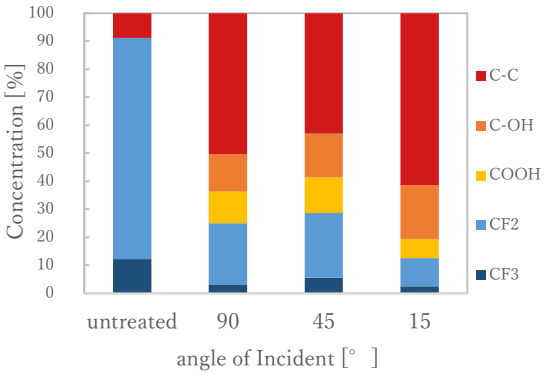

Fig. 2. Surface concentration for incident angles calculated from C1s waveform separation

In this study, it was found that fluorine atoms on the surface could be efficiently removed by low-angle ion bombardment in the Ar plasma treatment. Under the condition without the air exposure in the vacuum, the adhesive effect of copper coating by sputtering will be investigated in the future.

References:

[1] K. Iesaka, I. Takano, IEEJ Transactions A, Vol.141, No.1, pp34-39(2021)

Analysis of High Thermal Conductivity Mechanism of Naphthyl Benzoate-Twin Mesogenic Epoxy Polymers with Alkyl Chain Length 2 Having 2,7-Naphthyl Benzoate as the Mesogenic Skeleton

Y. Miyama, T. Kawai and Y. Itoh

Department of Applied Chemistry, Graduate School of Engineering, Kogakuin University, Tokyo, Japan
E-mail: bm20037@ns.kogakuin.ac.jp

Abstract

2,7-Naphthylbenzoate twin-mesogen epoxy polymers with alkyl chain length 2 are synthesized and analyzed, and the effects of differences in alkyl chain length and mesogen backbone on the higher-order structure and thermal conductivity are analyzed.

Introduction

In recent years, the performance and miniaturization of electric and electronic devices have been remarkably developed, and the heat generated from the inside of these devices has been steadily increasing. Since this heat adversely affects the equipment such as malfunction, it is important how efficiently the heat is released. As insulating materials, epoxy polymer is typically used in these kinds of devices, but the thermal conductivity of the epoxy polymer is small (around 0.2 $Wm^{-1}K^{-1}$). The addition of filler increases the thermal conductivity, but the viscosity also increases at the same time. Therefore, the increase of thermal conductivity of epoxy polymer itself is required. The liquid crystalline epoxy polymer which includes two mesogens, the twin-mesogen epoxy polymer has shown recently to have a relatively large thermal conductivity, and such a large thermal conductivity of the liquid crystalline epoxy polymer has been explained qualitatively to come from its higher orderliness of liquid crystalline structure [1].

In this study, we synthesized and analyzed twin-mesogen epoxy polymers with alkyl chain length 2, where the mesogen is 2,7-naphthylbenzoate (2,7-twin NB2), and clarified the effects of differences of alkyl chain length and mesogen backbone on the liquid crystal structure, higher-order structure, and thermal conductivity, being compared with those of 2,7-naphthylbenzoate twin-mesogen epoxy polymers with alkyl chain length 4 (2,7-twinNB4) [2]and 8 (2,7-twinNB8) [3] and the other mesogen polymers.

Experimental

Ethyl 4-hydroxybenzoate and 1,2-dibromoethane were reacted to synthesize 1,2-bis (4-carbethoxyphenoxy) ethane (1). Potassium hydroxide was reacted with (1) to synthesize 1,2-bis (4-carboxyphenoxy) ethane (2). Thionyl chloride was reacted with (2) to synthesize 1,2-bis (4-chloroformylphenoxy) ethane (3). 2,7-dihydroxynaphthalene was reacted synthesize 1,2-bis (4- (2-hydroxynaphthalene-7-oxycarbonyl) phenoxy) ethane (4). Epichlorohydrin was reacted with (4) to synthesize 2,7-TwinNB2.

Twin-mesogen epoxy polymer (TME2,7-NB2) was obtained by curing the mixture of 2,7-TwinNB2 and 4,4'-diaminodiphenyl methane (DDM) (molar ratio is 2:1) at 168 ℃ for 4 hours.

Result and Discussion

As a result of polarization microscope observation of the synthesized 2,7-Twin NB2, a liquid crystal was shown at around 188.4 ° C and an isotropic liquid was shown at around 204.0 ° C. DSC measurement showed a crystal-liquid crystal transition at 161.3 ° C and a liquid crystal-isotropic liquid transition at 174.7 ° C.

The DSC measurement results are shown in Table 1 together with the results with alkyl chain lengths of 4 and 8.

Table.1. Epoxy monomer transition temperature and liquid crystal temperature range

	T_{C-L}/°C	T_{L-I}/°C	Temperature range /°C
2,7-TwinNB2	161.3	174.7	13.3
2,7-TwinNB4	131.0	157.2	26.2
2,7-TwinNB8	136.7	155.7	19.0

X-ray diffraction pattern of TME2,7-NB2 was shown in Fig.1.

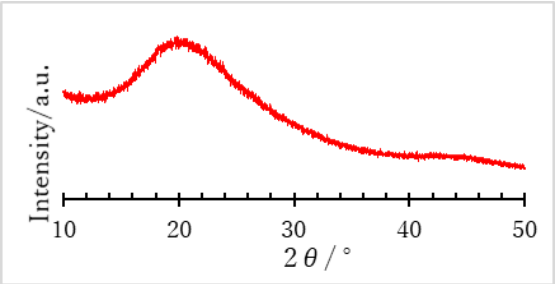

Fig.1.Results of XRD analysis of TME2,7-NB2

The d spacings and coherent length D were calculated from the X-ray data using the Bragg and Scherrer equation. The results are shown in Table 2 together with the results with alkyl chain lengths of 4 and 8.

Table.2. Epoxy polymer d spacings and coherent length D

	d / Å	**D / Å**
TME2,7-NB2	4.46	23.6
TME2,7-NB4	4.55	20.2
TME2,7-NB8	4.42	23.3

The thermal conductivities of the TME2,7-NB2 were measured. The thermal conductivities measurement results are shown in Table 3 together with the results with alkyl chain lengths of 4 and 8. The detailed discussion will be given in the presentation.

Table.3. The thermal diffusivity and thermal conductivity of epoxy polymer.

	thermal diffusivity / m^2 S^{-1}	**thermal conductivity /W m^{-1} K^{-1}**
TME2,7-NB2	2.10×10^{-7}	0.421
TME2,7-NB4	2.05×10^{-7}	0.411
TME2,7-NB8	1.53×10^{-7}	0.305

References:

[1] M. Akatsuka, Farren and Y. Takezawa, J. Apply. Polym. Sci.,89 (2003) 2464
[2] M. Furukawa , T. Kawai and Y. Itoh, Polysolvat 10, Sarerno Italy 2014
[3] Y.Itoh, K. Nakahira, and T. Kawai, MRS Advances, DOI:10.1557/adv.2018.46

Hardness of alumina film formed on aluminum by anodic oxidation with oxalic acid and alcohol

Takuma Sano and Hidetaka Asoh

Applied Chemistry and Chemical Engineering,
Graduate School of Engineering, Kogakuin University, Tokyo, Japan
asoh@cc.kogakuin.ac.jp

Abstract

Porous anodic films have attracted much attention due to their potential applications in various industrial fields. By reducing the porosity, the hardness is expected to be improved. In this study, the effect of electrolyte composition on the hardness of anodic film formed on aluminum by anodic oxidation under mild conditions was evaluated. Specifically, the effect of the addition of alcohols (ethanol and ethylene glycol) to the oxalic acid based electrolyte was investigated. The voltage-time curve, formation efficiency, morphology, and Martens hardness of the obtained anodic films were clearly affected by the type and amount of alcohol added. The addition of alcohol effectively suppressed the chemical dissolution of the anodic film during anodic oxidation without lowering the temperature of the electrolyte, resulting in the formation of a high-strength film with low porosity and thick pore walls. The Martens hardness of the formed film increased by 18% with the addition of 50 vol% ethanol and by 25% with the addition of 50 vol% ethylene glycol.

Introduction

Porous-type anodic films are generally formed by anodic oxidation of aluminum in an acid electrolyte. They have attracted wide attention as a host material, template, or mask for the fabrication of various objects at the nanometer scale. Many studies have investigated the structural features of porous alumina films, especially self-ordered pore arrays. In parallel, the formation efficiency of anodic films and the effects of the chemical composition of the electrolyte on their growth and structure have also been studied extensively. For practical application, an important objective is to improve the production efficiency of anodic films and properties such as the hardness, wear resistance, and corrosion resistance.

The properties of anodic porous alumina films are influenced by the dimensions of their structure, such as the interpore distance, pore diameter, pore walls, porosity, and film thickness. Industrially, hard anodic films on aluminum are obtained by anodic oxidation in a sulfuric acid solution kept at low temperature (below 10°C) to avoid chemical dissolution of the formed oxide film. The suppression of chemical dissolution of the pore walls is expected to result in the formation of an anodic film with low porosity and improved film hardness. Previous studies have focused on the addition of alcohols to the electrolyte to avoid chemical dissolution of the oxide film during anodic oxidation [1,2]. For example, anodic oxidation was carried out using sulfuric acid electrolytes containing monovalent alcohols (methanol, ethanol) and polyvalent alcohols (ethylene glycol, glycerol) at a constant current of 100 A m^{-2} to investigate the effect of alcohol added on the Coulombic efficiency. As a result, regardless of the type of alcohol, the formation voltage, the coating ratio (formation efficiency of anodic film), and the maximum achievable film thickness all increased with the amount of alcohol added. Although the addition of alcohol to the electrolyte may improve the properties of the films, few studies have focused on its effect on the hardness of the films. In this study, the effects of added monovalent or polyvalent alcohols to oxalic acid-based electrolytes on anodic oxidation behavior and related properties, especially hardness, were investigated. The purpose of this study was to develop an anodic oxidation process that can achieve high strength anodic films under mild conditions.

Experimental

A high purity (99.99%) aluminum plate with a working area of 10 cm^2 was used for the anodic oxidation. A 20 cm^2 aluminum plate was also used for the formation efficiency measurement. Before anodic oxidation, each sample was degreased with 5 wt% NaOH at 60°C for 20 s, washed with ion-exchange water, and immersed in 30 vol% HNO_3 at room temperature for 1 min. The concentration of oxalic acid was set at 0.3 mol dm^{-3}. Ethanol and ethylene glycol were used as additives. The effect of the type of alcohol on the formation of porous alumina films by anodic oxidation and on their structural and mechanical properties was investigated. Anodic oxidation was carried out at a constant current density of 100 A m^{-2}, and the electrical conductivity and viscosity of the mixed solution of oxalic acid and each alcohol at 20°C were evaluated. The efficiency of anodic film formation by anodic oxidation was evaluated by the coating ratio, which represents the conversion efficiency of aluminum to alumina. The thickness of the anodic film was measured using an eddy current film thickness gauge. The surface structure of the anodic film was observed using a field emission scanning electron microscope. To

evaluate the hardness of the anodic film, an indentation hardness test was performed. The hardness of the anodic film was evaluated by Martens hardness, which was obtained from the relationship between the applied load and the displacement (load-displacement curve). A dynamic ultra micro hardness tester (Shimadzu, DUH-211) was used for the hardness test.

Results and discussion

Figures 1(a) and 1(b) show the voltage-time (V-t) curves of anodic oxidation using a mixture of oxalic acid and alcohol at a constant current density of 100 A m^{-2}. When any alcohol was added to the oxalic acid-based solution, the voltage increased compared to the case of anodic oxidation using a solution without alcohol. In all cases, the voltage increased as the alcohol concentration increased. When 50 vol% alcohol was added to oxalic acid, the final voltage after 60 min of anodic oxidation was 85 V for ethanol and about 100 V for ethylene glycol.

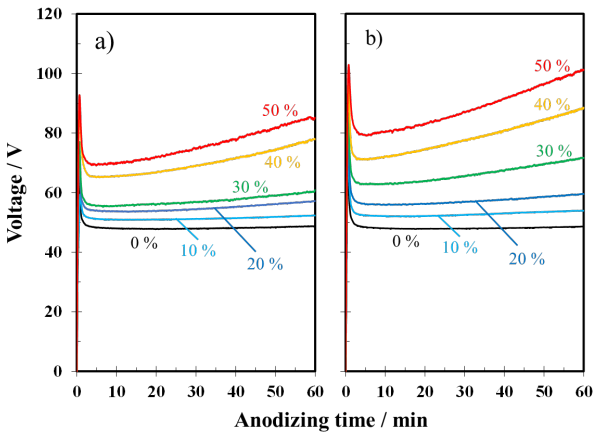

Figure 1 Voltage–time curves for the anodic oxidation in 0.3 mol·dm^{-3} oxalic acid with various concentrations of (a) ethanol and (b) ethylene glycol at a constant current density of 100 A·m^{-2} and temperature of 20 °C.

Figure 2 shows the physical properties of the solution consisted of oxalic acid with alcohol. As the amount of alcohol added increased, the viscosity increased and the electrical conductivity decreased. This increase in voltage can be attributed to the higher solution resistance caused by the addition of alcohol.

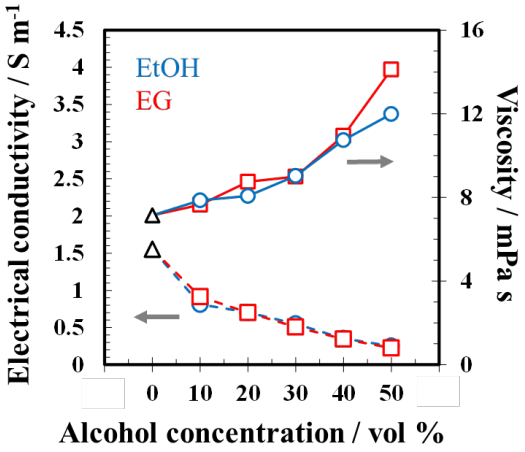

Figure 2 Viscosity and conductivity of a 0.3 mol·dm^{-3} oxalic acid–water–alcohol system as functions of the alcohol concentration: ethanol (EtOH) and ethylene glycol (EG).

Figure 3 shows the surface SEM images of alumina films formed with oxalic acid and 10-50 vol% ethylene glycol. With the addition of alcohol, the ratio of pore diameter to interpore distance in the film clearly decreased. From these SEM images, it was clear that the chemical dissolution of the outer surface of the anodic film was suppressed by the addition of alcohol.

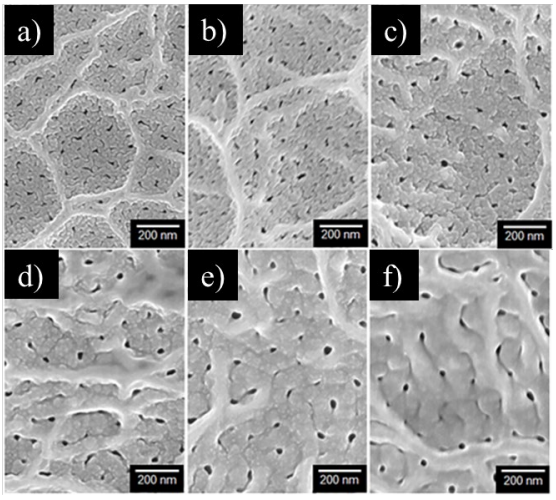

Figure 3 SEM images of alumina films formed with oxalic acid and 10-50 vol% ethylene glycol. *(a) no ethylene glycol, (b) 10% ethylene glycol, (c) 20%, (d) 30%, (e) 40%, and (f) 50%.*

Figure 4 shows the effect of ethanol or ethylene glycol concentration on the coating ratio. Anodic oxidation was performed for 60 min with constant current density in all cases (i.e., the charge was the same). The coating ratio was 1.35 for oxalic acid alone, but increased by about 3% (from 1.35 to 1.39)

for 50 vol% ethanol and by about 8% (from 1.35 to 1.46) for 50 vol% ethylene glycol. This is due to the fact that the addition of alcohol suppressed the chemical dissolution of the film during electrolysis.

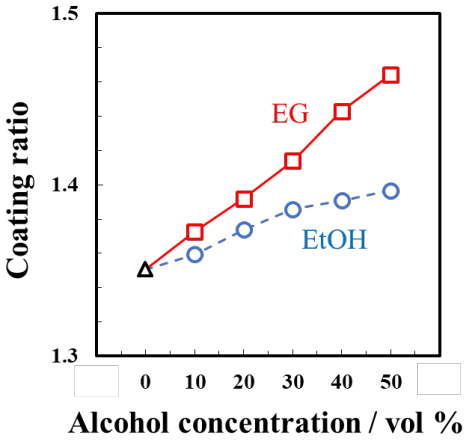

Figure 4 Relationship between the coating ratio and alcohol concentration. Anodic oxidation was conducted in 0.3 mol·dm^{-3} oxalic acid added 10–50 vol% of each alcohol at a current density of 100 A·m^{-2} and temperature of 20 °C for 60 min.

Figure 5 shows the relationship between the amount of alcohol added and the Martens hardness of the film. When ethanol was added, the hardness of the film was up to 1.18 times higher than that of the reference sample (without alcohol). When ethylene glycol was added, the hardness of the film increased up to 1.25 times compared to the reference sample. This increase in hardness is in good agreement with the trends in formation efficiency and surface structure shown in Figs. 3 and 4. The addition of alcohol effectively suppressed the chemical dissolution of the anodic film into the electrolyte without lowering the temperature of the electrolyte, resulting in a low porosity and high strength of the formed film.

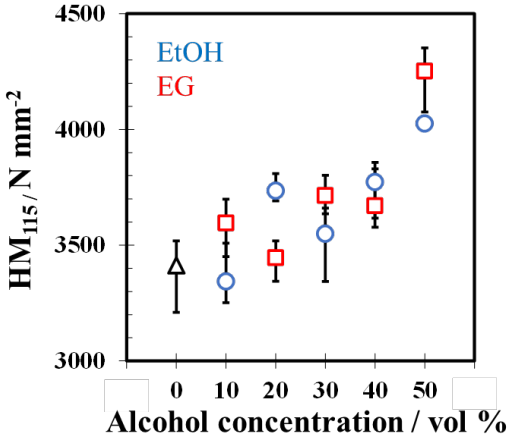

Figure 5 Relationship between the Martens hardness (HM_{115}) and alcohol concentration.

Conclusion

The effects of the addition of alcohols (ethanol and ethylene glycol) to oxalic acid electrolyte on the V-t curve, formation efficiency, morphology, and hardness of the resulting anodic film were investigated. Both alcohols showed similar effects, but ethylene glycol (polyvalent alcohol) was more effective than ethanol (monovalent alcohol) in improving film formation efficiency and hardness. The Martens hardness of the film increased by 25% when 50 vol% ethylene glycol was added. Our process using a mixture of oxalic acid and alcohol is clearly different from the anodic oxidation conditions used in previous studies: moderate current density (100 A m^{-2}), moderate temperature (20°C), and gentle agitation (300 rpm). However, we obtained similar results to the conventional method of lowering the temperature of the electrolyte. Our approach provides a new strategy to fabricate hard anodic films with low porosity under mild condition of anodic oxidation.

References:

[1] H. Asoh, M. Matsumoto, H. Hashimoto, *Surf. Coat. Technol.*, **378**, 124947 (2019).
[2] M. Matsumoto, H. Hashimoto, H. Asoh, *J. Electrochem. Soc.*, **167**, 041504 (2020).

Study on high thermal conductivity mechanism of phenyl benzoate twin-mesogen epoxy polymers by vibrational spectroscopy

T. Ishizawa*, T. Kawai, Y. Itoh
Department of applied chemistry, Graduate School of Engineering, Kogakuin University, Tokyo, Japan
E-mail: bm20005@ns.kogakuin.ac.jp

Abstract

In this study, we synthesized phenyl benzoate twin-mesogen epoxy polymer which have ester group in mesogen, and we investigated the effects of high order structure changes due to the direction of the ester group on the thermal conductivity, comparing with those of the reverse direction ester group of twin-mesogen epoxy polymer and tried to clarify the quantitative high thermal conductivity mechanism of twin-mesogen epoxy polymers.

Introduction

Recently, due to the higher performance and miniaturization of electronic devices, the amount of heat genereted inside the devices increase and cause increasing power consumption of cooling and malfunctions. The epoxy porymers are widely used for the insulation materials of these devices due to their heat resistance and insulation properties. However, the thermal conductivity of the conventional epoxy polymers is lower than metal and ceramis. If it is possible to increase theramal conducitivity of these polymers, it brings about higher performance and miniaturization of the device. In general, thermal conductivity of the polymers is proportional to the order of the arrangement of molecules. Therefore, we focused on the liquid crystal structure in which the molecules have a regular arrangement.

The liquid crystalline epoxy polymer which include twin mesogens, the twin-mesogen epoxy polymer has shown to have a relatively large thermal conductivity, five times larger than those of conventional epoxy polymers and such a large thermal conductivity of the liquid crystalline epoxy polymer has been explained qualitatively to come from its high oreder of liquid crystalline structure [1].

In this study, we synthesized phenyl benzoate twin-mesogen epoxy polymer which have ester group in mesogen, and we investigated the effects of high order structure changes due to the direction of the ester group on the thermal conductivities.

Experimental

The synthetic scheme of twin-mesogen epoxy monomer with spacer carbon number of 2 (twinPB2R) was shown in Fig. 1. 1,2-Bis(4-ethoxy-carbonylphenoxy)ethane (1) was synthesized from 4-hydroxybenzoic acid and 1,2-Dibromoethane. 1,2-Bis(4-carboxyphenoxy)ethane (2) was Hydrolyzed and synthesized from (1) and potassium hydroxide. 1,2-bis(4-chloroformylphenoxy)ethane (3) was obtained from (2) and thionyl chloride after excess of thionyl chloride was removed by evaporation. 3 was used in the next reaction without purification because of its instability. 1,2-bis(4-(4'-hydroxyphenyl-4-oxycarbonyl) phenoxy)ethane (4) was synthesized from (3) and hydroquinone. Finally twinPB2R was synthesized from (4) and Epichlorohydrin. Twin-mesogen epoxy polymer with two spacer carbons (TMEPB2R) was obtained by curing the mixture of twinPB2R and 4,4'-diaminodiphenyl sulfone (DDS) (molar ratio is 2:1) for 4 hours.

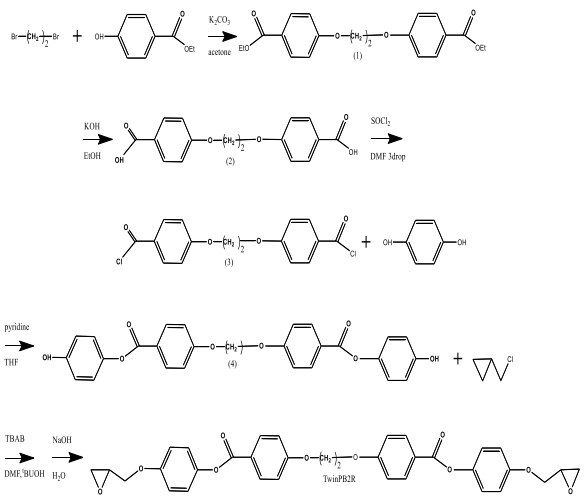

Figure. 1. The synthetic scheme of twin-mesogen epoxy monomer with spacer carbon number of 2 (TwinPB2R)

Result and Discussion

The liquid crystal temperature range and transition temperature of twinPB2R and other monomers, measured by differential scanning calorimetry, were shown in Table 1.

Table. 1. The liquid crystal temperature range and transition temperature of twinPBnR

sample	$T_{c\rightarrow L}$ /℃	$T_{L\rightarrow L}$ /℃	T_{L-I} /℃	Temperture Range /℃
twinPB2R	208.3	228.5	283.2	74.9
twinPB2	176.1	—	231.9	55.8
twinPB4R	187.8	191.5	222.5	34.7
TwinPB4	180.6	—	215.5	34.9
TwinPB8R	132.1	141.5	176.5	44.4
TwinPB8	153.0	—	182.0	29.0

From the above, it is considered that the R-type molecule whose ester group bond order is closer to the alkyl chain side has a wider liquid crystal temperature range than the conventional type, and has a molecular structure that stably forms a liquid crystal and has a high order.

In the X-ray diffraction pattern of TMEPB2R, the broad peak around 20 degrees was observed, showing some orderliness in the materials. With equations of Bragg and Scherrer, d spacings and dimensions of the crystallite (coherent length), D were calculated from the X-ray data, and the thermal conductivity were shown in Table 2.

The detailed discussion will be given in the presentation.

Table. 2. d, D and thermal conductivity of TMEPB2R

sample	**d spacing /Å**	**Coherent length D/Å**	**Thermal diffusivity /m^2 s^{-1}**	**Thermal conductivity /W m^{-1} K^{-1}**
TMEPB 2R	4.59	25.9	1.59×10-7	1.23

Reference

[1]M. Akatsuka, Farren and Y. Takezawa, *J. Apply. Polym. Sci*. **2003**, 89,2464.

Influence of a CuO layer for conversion efficiency of CuO/TiO_2 thin films

Masaki. Yanagisawa*, Ichiro. Takano**

*Graduate school of engineering, Electrical engineering and electronics, Kogakuin university, Tokyo, Japan
E-mail: cm21054@ns.kogakuin.ac.jp
**Faculty of engineering, Department of electrical and electronic engineering, Kogakuin university, Tokyo, Japan
E-mail: ct97912@ns.kogakuin.ac.jp

Abstract

An approach for the decarbonized society has been proposed in various fields. The spread in the market of the solar power generation is remarkable, while Si-based solar cells have suffered the problem from its high manufacturing energy. From the viewpoint of its energy reduction, oxide solar cells attracts attention. In this study, CuO/TiO_2 thin films were fabricated by sputtering deposition and the conversion efficiency were measured. It was confirmed that the conversion efficiency was affected by the structure of a CuO layer.

As the demand for the renewable energy system increases, the utilization of solar cells is also expanding. The mainstream Si-based solar cells are characterized by high photo-conversion efficiency and reliability, but due to the shortage of Si raw materials and high manufacturing energy, new solar cells are required.

Wet dye-sensitized solar cells consisting of semiconductor electrodes (TiO_2), ruthenium-sensitized dye and electrolyte, and solid-state dye-sensitized solar cells in which these electrodes are replaced by metal oxides have been reported. The authors focused on solid-state solar cells because of their long-term stability, and fabricated oxide solar cells with CuO thin films as the p-type semiconductor and TiO_2 thin films as the n-type semiconductor. In comparison with Cu_2O[1], which plays the role of an electromotive force layer in oxide solar cells, CuO has the problem of being an indirect transition type, while it has the advantage of having a band gap energy of about 1.4 eV and a wider absorption edge than that of Cu_2O.

The deposition conditions of CuO and TiO_2 fabricated by sputtering deposition using the multi-process coating system are shown in Table 1. In this

Table 1 Experimental conditions

Substrate	Glass with FTO,EAGLE XG	
Film material	CuO	TiO_2
Base pressure [Pa]	$<1.0\times10^{-5}$	
O_2 flow rate [sccm]	0	1.5
N_2 flow rate [sccm][2]	0	0.2
Ar flow rate [sccm]	20	20
Input power [W]	100,150	100
Film thickness [nm]	300	300

experiment, TiO_2 thin films with slight nitrogen are utilized. N-doped TiO_2 is a wider absorption edge than that of the stoichiometry TiO_2. The substrates were ultrasonically cleaned with ethanol for 10 min and then Ar plasma cleaning in a vacuum chamber for 10 min before the film formation.

The I-V measurement was performed using a solar simulator (HAL-320 ASAHI SPECTRA) with the

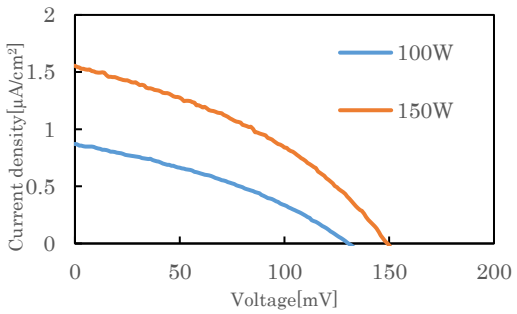

Fig 1. I-V characteristics

condition by applying an electronic load and irradiating with artificial-sunlight of 100 mW/cm^2.

Figure 1 shows the I-V properties using different input powers to form a CuO layer. The short circuit current increased from 0.87 μA/cm^2 to 1.6 μA/cm^2 and also the open circuit voltage increased from 130 mV to 150 mV by increasing an input power to form the CuO layer. The conversion efficiency of the CuO/TiO_2 thin film with 100 W in an input power was 3.96×10^{-5} % and that of 150W was 8.60×10^{-5} %.

In general, solar cells show a higher conversion efficiency with direct bandgap semiconductors, however, CuO is an indirect bandgap semiconductor, which is the cause of its low conversion efficiency. On the other hand, CuO has several merits such as the absorption edge of CuO is wider than that of Cu_2O and CuO can absorb light in a wide range.

In this experiment, the compound CuO target was used for forming the CuO thin films because of keeping homogeneity in composition of formed thin films, while the CuO thin films with an oxygen defect may be formed in the sputtering process. In the future, the detailed investigation of the structure will be necessary.

References

[1]-K. Ishizaka，Anmar H. Shukor，I. Takano：Vacuum and Surface Science，63, 7(2020) pp348–351
[2]-K. Takayama，I. Takano，Y. Sawada: Vacuum, 46, 5 (2003) pp457-461

Theoretical calculation of infrared absorption spectra of hydrogen in various polymers under high-pressure hydrogen

M. Tsuji, T. Kawai and Y. Itoh

Department of Applied Chemistry, Graduate School of Engineering, Kogakuin University, Tokyo, Japan
E-mail:bm20028@ns.kogakuin.ac.jp

Abstract

Mechanism of fracture in rubber materials for high pressure hydrogen vessels is highly affected by the hydrogen dissolved in rubber during high-pressure hydrogen exposure[1]-[3]. In order to clarify the state of the hydrogen molecules dissolved in the polymers and the interaction between hydrogen molecules and polymer molecules, we analyzed the IR spectra of the hydrogen dissolved in the polymers under high-pressure hydrogen by the theoretical calculation, ab initio MO calculations of hydrogen molecules interacting with polymer model molecules.

Introduction

Mechanism of fracture in rubber materials for high pressure hydrogen vessels is highly affected by the hydrogen dissolved in rubber during hydrogen exposure. Therefore, the state of hydrogen molecules dissolved in the polymer materials under the hydrogen exposure is very important. Infrared absorption spectra show the detailed state of the molecule. Ordinary conditions, the hydrogen stretching vibration is IR inactive. It has been known that the high-pressure hydrogen has become IR active, and IR inactive molecular vibration has become IR active under the electric field, known as Stark effect. The hydrogen stretching vibrational peak has appeared in the IR spectra of polymers under the high-pressure hydrogen exposure and it has been thought that it has come from Stark effect caused by the electric field in the polymer materials because of the sharp IR peaks.

In this study, in order to clarify the state of hydrogen dissolved in polymer materials, we analyzed the IR spectra of the hydrogen dissolved in the polymers under high-pressure hydrogen by the theoretical calculation, ab initio MO calculations of hydrogen molecules interacting with polymer model molecules.

Experimental

Monomer and dimer molecular models of polystyrene, polymethyl methacrylate, and polyethylene terephthalate were prepared for structural optimization by ab initio MO Hartree-Fock calculation, and then vibrational calculations were performed using HF/6-31(G) for two molecules, interacting hydrogen molecule and polymer model molecule above.

Results and discussion

The calculated IR spectra of H_2 interacting with the monomer model were shown in Table 1, and the calculated IR spectra of H_2 interacting with the dimer model were shown in Table 2. The all H_2 frequencies interacting with polymer molecules shifted lower frequencies than that of H_2 mono-molecule. The detailed discussion will be given in the presentation.

Table 1 The calculated H_2 stretching frequencies of the hydrogen molecule interacting with the monomer model of polymers

	H_2 stretching frequencies/cm^{-1}	**$\Delta\nu$/cm^{-1}**
H_2	4159.72	0.0
PMMA	4150.26	-9.46
PS	4155.60	-4.12
PET 1	4144.16	-15.56
PET 2	4150.94	-8.78

Table 2 The calculated H_2 stretching frequencies of the hydrogen molecule interacting with the dimer model of polymers

	H_2 stretching frequencies/cm^{-1}	**$\Delta\nu$/cm^{-1}**
H_2	4159.72	0.0
PMMA 1	4148.84	-10.88
PMMA 2	4148.49	-11.23
PMMA 3	4151.60	-8.12
PS 1	4154.00	-5.72
PS 2	4157.53	-2.19

References

[1] Briscoe, B. J. , Savvas, T. and Kelly, C. T. , *Rubber Chemistry and Technology*, 67, 384-416(1994)
[2] Embury, P. , *Sealing Technology*, 2004, 6-11(2004)
[3] Briscoe, B. J. and Liatisis, D. , Rubber Chemistry and Technology, 65, 350-373(1992)

Improvement of Electrical Property of α-In_2O_3 Films Grown by Mist Chemical Vapor Deposition Using In_2O_3 Powder as Source Precursor

A. Taguchi[1,*], T. Onuma[1,2], T. Honda[1,2] and T. Yamaguchi[1,2]

1. Department of Electrical Engineering and Electronics, Graduate School of Engineering, Kogakuin University, Tokyo, Japan
2. Department of Applied Physics, School of Advanced Engineering, Kogakuin University, Tokyo, Japan

*E-mail: cm21033@ns.kogakuin.ac.jp

Abstract

Pure α-In_2O_3 films were successfully grown on (0001) α-Al_2O_3 substrates by mist CVD using In_2O_3 powder as a source precursor. Polycrystalline growth of cubic phase In_2O_3 was completely suppressed by increasing the HCl concentration in the source solution. The resultant pure α-In_2O_3 film grown with a concentration of over 1.2 mol/L showed better electrical properties than those using In(acac)$_3$, i.e., Hall mobility of about 200 cm^2/Vs and residual carrier concentration of about 1×10^{18} cm^{-3} were obtained.

1. Introduction

Amorphous and polycrystalline In_2O_3 films doped with Sn are widely used as transparent conductive oxides for flat panel displays and solar cells [1,2]. On the other hand, research interest has been directed towards single crystalline In_2O_3 due to its potential for active element in the electronic devices. In_2O_3 has two types of crystal structures: one is a cubic bixbyite structure (c-In_2O_3) as the most stable phase, and another is a rhombohedral corundum structure (α-In_2O_3) as a metastable phase. The α-In_2O_3 films have been grown on (0001) α-Al_2O_3 substrates by the mist chemical vapor deposition (mist CVD) [3].

The mist CVD method has been attracting attention as a new generation epitaxial growth method because it can be performed under atmospheric pressure, and it is a solution-based growth method using a simple system configuration.

In the growth of α-In_2O_3 films by mist CVD, In(acac)$_3$ [$In(C_5H_7O_2)_3$] and HCl have been widely used as source solusions [3-5]. We have shown that HCl was found to have influence on not only dissolution but also the growth of α-In_2O_3 [5]. Concerning the use of In(acac)$_3$, however, carbon atoms in the In(acac)$_3$ would affect the electrical properties of α-In_2O_3 [6]. From this point of view, the use of carbon-free In_2O_3 powder dissolved in the HCl solution can be proposed to suppress the carbon impurities in the films.

In this study, α-In_2O_3 films were grown on (0001) α-Al_2O_3 substrates by mist CVD using carbon-free In_2O_3 powder as a source precursor. Impact of the use of In_2O_3 powder as a source precursor on their growth were clarified in terms of their structural and electrical properties.

2. Experiment

In_2O_3 films were grown by mist CVD. In_2O_3 powder (4N: 99.99%) was used as the source precursor. The In_2O_3 powder was first dissolved in 36% HCl(aq.). Then, deionized water was added to prepare the source precursor solution. The In_2O_3 concentration was fixed at 0.05 mol/L and the HCl concentration [HCl] was varied in between 0.82 and 2.3 mol/L. The solution was atomized using a 2.4 MHz ultrasonic transducer and the formed aerosol was transferred to the substrates using a carrier O_2 gas. The In_2O_3 films were grown at 550°C for 60 min. on (0001) α-Al_2O_3 substrates. X-ray diffraction (XRD), scanning electron microscopy (SEM) and Hall effect measurements at room temperture, and secondary-ion mass spectrometry (SIMS) were utilized as evaluation methods.

3. Results and Discussion

The XRD 2θ-ω profiles of In_2O_3 films grown using the source solusions with different HCl concentrations are shown in Fig. 1. The diffraction peak intensity from c-In_2O_3 decreased with increasing the HCl concentration and the peak were completely suppressed for the films grown using the source precursor solutions with concentrations over 1.2 mol/L, resulting in the observation of single-phase α-In_2O_3. These results have similar tendency with those using the In(acac)$_3$ [5].

Figure 2 shows the results of Hall effect measurements at room temperture for the films grown with In_2O_3 powder. The data plots for the films with In(acac)$_3$, which were grown under comparable grown conditions, are also shown for comparison [5]. Obviously, the α-In_2O_3 films grown with In_2O_3 powder shows better electrical properties than those grown with In(acac)$_3$ [3-5], i.e., Hall mobility of about

200 cm^2/Vs and residual carrier concentration of about 10^{18} cm^{-3} were obtained.

Figure 3 shows the depth profile of carbon measured by SIMS for the sample grown with 1.2 mol/L HCl concentration, where the sample exhibited the lowest residual carrier concentration. The carbon concentration was in the order of 10^{17} cm^{-3}, which was one order of magnitude lower than those grown using $In(acac)_3$ [5]. It is reported that carbon atom can become a shallow donor in In_2O_3 film [6]. Therefore, the superior electrical properties in the samples grown with In_2O_3 powder would be associated with reduction in carbon impurities.

4. Summary

In this study was that α-In_2O_3 films were grown on (0001) α-Al_2O_3 substrates by mist CVD using carbon-free In_2O_3 powder as a source precursor. The result shows an enhancement in α-phase formation were observed with increasing HCl concentration. Indeed, the α-In_2O_3 films grown with In_2O_3 powder show better electrical properties and lower carbon concentration than those grown with $In(acac)_3$. These superior electrical properties would be associated with effectiveness of using In_2O_3 powder as a source precursor.

Acknowledgement

The authors would like thank Prof. S. Fujita and Dr. K. Kaneko of Kyoto University, and Profs. M. Sato, H. Nagai and A. Sekiguchi of Kogakuin University for their fruitful discussion. The authors would also like to thank Dr. S. Numao of Toray Research Center for the SIMS analysis.

References:

[1] B. G. Lewis and D. C. Paine, *MRS Bulletin* **25**, 22 (2000).
[2] T. Koida, *Phys. Status Solidi A* **214**, 1600464 (2017).
[3] N. Suzuki, K. Kaneko, S. Fujita, *J. Cryst. Growth* **364**, 30 (2013).
[4] K. Kaneko, M. Kitajima, and S. Fujita, *MRS Adv. Mater. Research Society* **99**, 301 (2017).
[5] T. Yamaguchi, S. Takahashi, T. Kiguchi, A. Sekiguchi, K. Kaneko, S. Fujita, H. Nagai, M. Sato, T. Onuma, and T. Honda, *Appl. Phys. Express* **13**, 075504 (2020).
[6] J. L. Lyons, D. Steiauf, A. Janotti, and C. G. Van de Walle, *Phys. Rev. Applied* **2**, 064005 (2014).

Figures

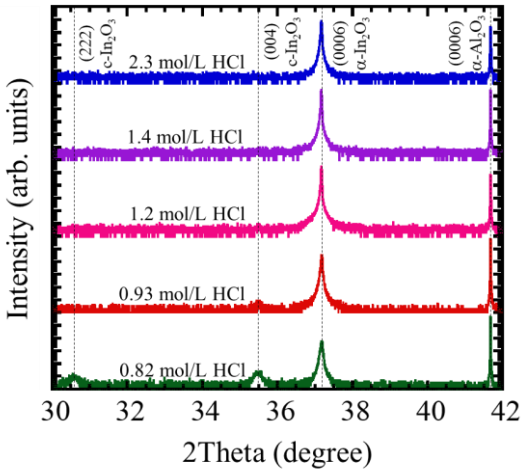

Fig. 1. 2θ-ω profiles of In_2O_3 films grown using the source solutions with different HCl concentrations.

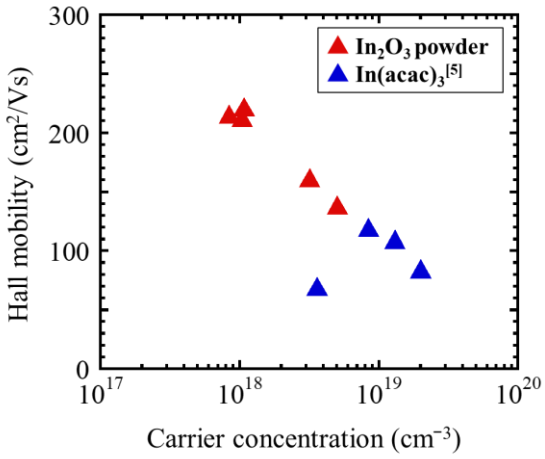

Fig. 2. Hall mobility at room temperature as a function of carrier concentration for In_2O_3 films grown using In_2O_3 powder and $In(acac)_3$ as source precursors.

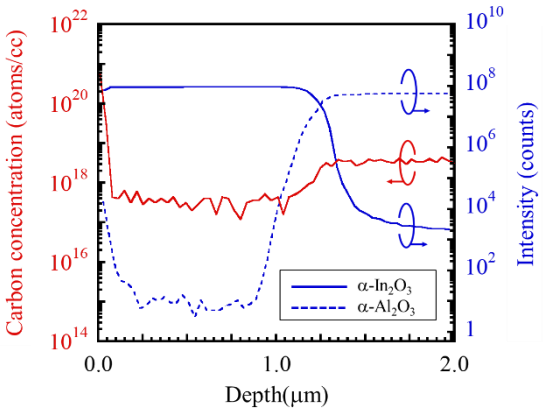

Fig. 3. Depth profile of carbon measured by SIMS in α-In_2O_3 film grown with 1.2 mol/L HCl concentrations on α-Al_2O_3 substrate.

Study on thermal conductivities of poly(methacrylic acid ester) having azobenzene as a mesogen with different spacer carbon numbers and the end group carbon numbers

Nanako SAKAI, Tadatomo KAWAI, Yuzo ITOH

Graduate School of Engineering Kogakuin University,
E-mail: bm20021@ns.kogakuin.ac.jp

1. Introduction

In recent years, electronic devices have become increasingly compact. Electronic devices, which always require insulators, have difficulty in dissipating heat due to the low thermal conductivity of insulators. Since heat buildup inside electronic devices can cause problems such as malfunction, how to dissipate the heat has become an issue.

In the research on polymethacrylate esters with spacer carbon number 2, 4 and 6, which have azobenzene as a mesogen, it was found that the liquid crystal temperature range was wider and the thermal diffusivity was greatest with spacer carbon number 6 [1].

In this study, we synthesized side chain type liquid crystal methacrylate polymers with spacer carbon number 4, and the end group carbon numbers of 6 and CN of azobenzene as mesogen and investigated their higher-order structures and thermal conductivities, compared to those of the previously synthesized methacrylate type liquid crystal polymer with spacer carbon number 4 and the end group carbon numbers of 1.

2. Experimental

4 - Hydroxy - 4' - cyanoazobenzene (A) was synthesized by the reaction of p-anisidine with sodium nitrite. (A) was reacted with 1 , 4-dibromobutane to synthesize 1 - bromo - 4 (cyanoazobenzene - 4' - oxy) butane (B). (B) was reacted with potassium methacrylate to form 4 - (4 - cyanoazobenzene - 4'-oxy) butyl (B) and potassium methacrylate to synthesize 4-(4 - cyanoazobenzene-4'-oxy- azobenzene) butylmethacrylate (C, monomer).

3. Results and Discussion

The transition temperatures and liquid crystal temperature ranges of those with the end group carbon numbers of 6 and CN were shown in Table 1, comparing with the end group carbon numbers 1.

Table1. The transition temperatures liquid crystal temperature ranges of monomers

end group carbon numbers	T_g / °C	T_{SN} / °C	T_{NI} / °C	ΔT / °C
1	66.0	—	67.7	1.7
6	60.5	67.5	84.6	24.1
CN	106.8	—	107.8	1.0

T_{SN} : smectic - nematic transitional temperature, T_{NI} : nematic - Isotropic liquid transitional temperature

The liquid crystalline temperature range of end group carbon numbers 6 was larger than end group carbon numbers 1 and CN. In addition, a smectic phase was confirmed for the monomer with end group carbon numbers of 6.

we plan to carry out polymerization of the monomers and perform XRD measurements and thermal diffusivity measurements on the polymers to analyze how the end groups influence on the thermal conductivities.

[1] Naho MITHUISHI *Graduation Thesis, Kogakuin University* **2018** Thermal Conductivity of Methacrylic Polymers Having Azobenzene as a Mesogen in the Side Chain

Lightning Talk Session

Biochemistry and Food Science

November 23rd

Presentation No.	Title	Author	
BFSL1.	Investigation of extraction method for antimicrobial substances accumulated in aerial microalgae	Toshihiro Sekizawa, Nobuhiro Aburai, and Katsuhiko Fujii	185
BFSL2.	Isolation of lichen photobionts by a density gradient centrifugation	Kotomi Hirose, Nobuhiro Aburai, and Katsuhiko Fujii	186
BFSL3.	Development of microflora which produces hydrogen from digested sludge	Yuhei Hayakawa, Nobuhiro Aburai, and Katsuhiko Fujii	187
BFSL4.	The ability of wild Bacillus sp. to produce polyglutamic acid	Suzuka Sato, Nobuhiro Aburai, and Katsuhiko Fujii	188
BFSL5.	Screening of carotenoid-rich aerial microalgae	Yuta Hiki, Nobuhiro Aburai, and Katsuhiko Fujii	189
BFSL6.	Functional Properties of Chitin Deacetylase from *Aspergillus fumigatus*	Hidetoshi Suzuki, Masashi Ohkura, Kazuaki Okawa and Fumitaka Oyama	190
BFSL7.	Mechanistic insights of inactivation of YKL-40, a chitinase-like protein	Keita Suzuki, Kazuaki Okawa, and Fumitaka Oyama	191
BFSL8.	Component imaging of spheroids by using an FIB-TOF-SIMS	Tomoki Goto, Hyogo Takeuchi, Mizuki Shu, Reiko Saito, Kazuya Matsushima, Makoto Saito, Sanshiro Hanada, Nobuhiko Kojima, Masato Morita, and Tetsuo Sakamoto	192

Investigation of extraction method for antimicrobial substances accumulated in aerial microalgae

Toshihiro Sekizawa, Nobuhiro Aburai, and Katsuhiko Fujii

Applied Chemistry and Chemical Engineering, Graduate School of Engineering, Kogakuin University, Tokyo, Japan
E-mail: bm21028@ns.kogakuin.ac.jp

Abstract

It has been reported that lipid fraction of microbial mats, mainly composed of aerial microalgae, contain antimicrobial substances. However, the substances are unstable and can be obtained only in small amounts, making structural analysis difficult. The purpose of this study was to develop the extraction method of antimicrobial substances accumulated in cultured aerial microalgae. We examined the following methods to grind microbial mats: grinding by a pestle, grinding by a pestle with addition of alumina beads, and grinding by a bead homogenizer with addition of glass beads. As a result, employment of a bead homogenizer and glass beads was most effective to extract antimicrobial substances.

With the emergence of drug-resistant bacteria, there is an urgent need to search for new antimicrobial substances. It has been reported that lipid fraction of microbial mats, mainly composed of aerial microalgae, contain antibacterial substances. However, the substances were unstable and could only be obtained in small amounts, making structural analysis difficult. The purpose of this study was to investigate the extraction method of antimicrobial substances accumulated in cultured aerial microalgae.

The aerial microalgal strain BRCK-006 was cultured in Bold's Basal medium for at least 21 days at a temperature of 25 ± 2°C, a flow rate of aeration at 100 mL min^{-1}, a light intensity of 40 µmol photons m^{-2} s^{-1}, a pH of 8.00 ± 0.05. An initial turbidity of microalgal inoculant (Abs 750nm) was 0.05. After 3-week cultivation, the algal cells were harvested, freeze-dried, grinded with a pestle, a pestle and alumina beads, or bead crusher. The mixture of chloroform and methanol in the ratio of 2:1(v/v) was employed to extract total lipid [2]. The lipid obtained by pestle and bead crusher were applied to a silica gel chromatography to prepare three fractions and tested their antimicrobial activity using a paper disc method against *Kocuria rhizophila* (BRC 12708).

By 21-day cultivation, 125 mg of dried microalgal cells was obtained from 500 mL culture. The total lipid was prepared from 50 mg dry cell, according to three grinding method, as described above, and chloroform/methanol extraction, The highest recovery of lipid was observed by grinding cells with bead crusher among tested method. The total lipid was applied to a silica gel chromatography to obtain three fractions, which were followingly subjected to the antimicrobial activity assay. Antimicrobial activity was detected in the fraction-C of the lipid sample prepared by grinding cells by a pestle (Fig. 1). In contrast, antimicrobial activity was not found in lipid sample prepared by other grinding methods (Fig. 2). Therefore, grinding of cells with alumina or glass beads seem useful for efficient lipid preparation, but frictional heat generated by bead crushing might partly reduce antimicrobial substances. Purification and identification of the antimicrobial active substances in algal cells are in progress.

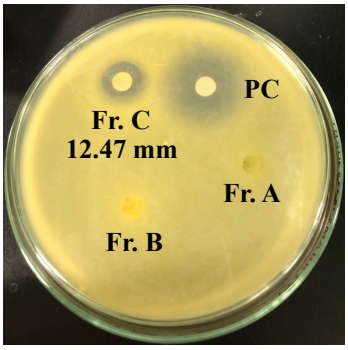

Fig. 1 Evaluation of antimicrobial activity of lipid obtained from pestle-ground cells. (PC : Chloramphenicol)

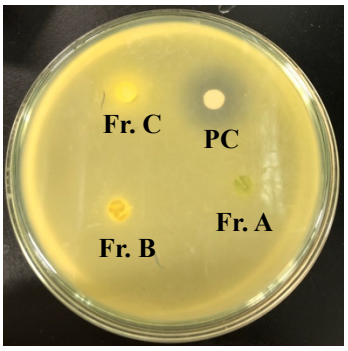

Fig. 2 Evaluation of antimicrobial activity of lipid obtained from glass bead-ground cells. (PC : chlorampenicol)

References:

[1] A. E. Abomohra, W. Jin, M. E. Sheekh, *Energy Conversion and Management*, **108**, 23−39 (2016).

Isolation of lichen photobionts by a density gradient centrifugation

Kotomi Hirose, Nobuhiro Aburai, and Katsuhiko Fujii

Department of Applied Chemistry and Chemical Engineering, Graduate School of Engineering, Kogakuin University, Tokyo.
E-mail: bm21040@ns.kogakuin.ac.jp

Abstract

We investigated the separation of symbiotic algae from symbiotic fungi in order to search for bioactive substances in the symbiotic algae that compose lichens. we succeeded in separating the symbiotic algae by making a gradient of Ficoll and centrifuging them in a density gradient. In the future, we will cultivate the symbiotic algae isolated by this method and search for bioactive substances possessed by the symbiotic algae.

Lichens are a mutualistic symbiotic community of fungi and algae. In the lichen community, photobionts photosynthetically produce organic carbons such as carbohydrates, a part of which nourishes fungi. As its consideration, photobionts are protected from harsh environment like dryness by the fungal mycelium, which also gather moisture and nutrients, and provide an anchor to their habitat. Water and mineral nutrients are obtained mainly from rain, dust, or the substrate. If cyanobacteria are present, they can fix atmospheric nitrogen. [1].

While free living microalgae are known to produce a variety of biologically active substances, there is a lack of research on the biologically active substances possessed by the photobionts, because of a difficulty to disrupt lichen tissue and separate photobiont from fungi. Therefore, we examined the conditions for separation of photobiont and symbiotic fungi using a density gradient centrifugation.

Lichen samples (Fig. 1) were collected in the University campus using a toothbrush. Subsequently, the lichen sample was suspended in 25 mL of sterile water and allowed to stand for 10 minutes. After that, 20 mL of the supernatant was transferred to a new 50 mL centrifuge tube and centrifuged at 10,000 × *g* for 1 min. The supernatant was removed and pellet was suspended in 2 mL of sterile water. The pellet suspension containing lichen (1 mL), 1.0 mm glass beads (60 mg), and 0.5 mm zirconia beads (80 mg) are transferred to microtube and ground for 30 seconds by a bead crusher. The homogenate was centrifuged at 10,000 × *g* for 1 min. The supernatant was then removed and a pellet containing crushed lichen was suspended in 0.5 mL of sterile water. Crushed lichen suspensions were then overlaid on layers of 10%, 25%, and 35% (w/w) Ficoll solution in a microtube and centrifuged at 50 × *g* for 30 min. The 25% (w/w) Ficoll layer in which photobiont accumulated was overlaid on the Ficoll layer (10%, 25%, 35% (w/w)) prepared in another microtube and centrifuged at 10,000 × *g* for 1 minute. The 25% Ficoll layer containing photobionts was collected, mixed with 1 mL of sterile water, and centrifuged at 10,000 × *g* for 10 min. The supernatant was removed and the resulting precipitate was dissolved in sterile water to obtain the fraction of photobiont.

Microscopic observation after density gradient centrifugation showed no significant contamination of fungal mycelium in photobiont feaction, and thus the photobiont seemedsuccessfully isolated (*Fig. 2a and 2b*).

Since a density gradient centrifugation can centrifuge photobionts simply and quickly. In the future, we will cultivate the photobiont obtained by a density gradient centrifugation to search for bioactive substances and study their possible industrial applications.

Fig. 1 lichens used in this study.

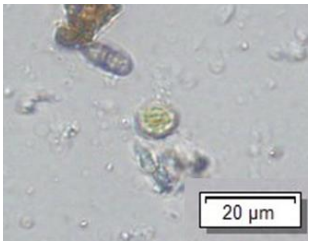

Fig. 2a. lichen homogenate containing photobiont and fungal mycelium

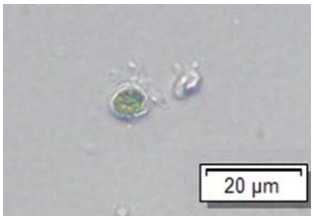

Fig. 2b. photobiont recovered by a density gradient centrifugation.)

References:

[1] S. Inaba et al.. *Mistery of Fungus.* Toukai University publishing department 81-87 (2014).

Development of microflora which produces hydrogen from digested sludge

Yuhei Hayakawa, Nobuhiro Aburai, and Katsuhiko Fujii

Applied Chemistry and Chemical Engineering, Graduate School of Engineering, Kogakuin University, Tokyo
E-mail: bm21038@ns.kogakuin.ac.jp

Abstract

The parent microflora which produces methane from digested sludge was transformed into hydrogen-producing microflora by heat treatment. Cellulase and chitinase activities were retained in the culture supernatant of the hydrogen-producing microflora to the same extent as in the parent microflora, suggesting that its enzymatic activities are derived from thermostable hydrolytic microorganisms. Comparison of the bacterial members of the hydrogen-producing microflora with those of parent microflora by the PCR-DGGE showed that bacteria which are minor population in the parent microflora became dominant species in the hydrogen-producing microflora.

Domestic wastewater is generally treated by the activated sludge method in Japan. This method generates excess sludge, the biomass of growing microorganisms. Even if anaerobic digestion is used to reduce the volume of excess sludge, only about 40% of the organic matter of the sludge can be decomposed [1]. As a result, persistent residue (digested sludge, DS) is generated after digestion. Therefore, development of a recycling method for DS is an important issue for contribution to the SDGs.

While aerobic DS-degrading fungi were first reported as a DS degrader, methanogen is strict anaerobe [2]. Therefore, the conversion of DS into methane requires a two-step reaction: an aerobic process for DS hydrolysis and an anaerobic process for methane production from DS hydrolysate. We enriched an anaerobic soil microflora that can decompose DS and produce methane. Since anaerobic digestion is accomplished by three groups of microorganisms, hydrolytic microbes, acid- and hydrogen-producing microbes, and methanogens, we attempted to develop microflora which can produce hydrogen from DS, by inactivating the methanogens [3].

Hydrogen produces water when burned, but does not produce greenhouse gases, so it is expected to be a new renewable energy source to reduce global warming.

The culture of the parent flora inoculated into a vial containing 100 mg DS and 10 ml sterile deionized water. Gas phase in the vial was replaced with nitrogen gas to maintain an anaerobic condition and cultivated for 4 weeks. After 4-week cultivation, grown microbial culture was heat-treated at 30, 50, 60, 80, 100 or 121°C for 15 or 30 minutes. The heat-treated culture was inoculated into a fresh DS suspension, and cultivated for 4 weeks. After cultivation, the gas phase in the vials was analyzed by the GC-TCD. The cellulase and chitinase activities of the microflora culture supernatant were measured using cellulose azure and chitin azure as a substrate, while protease activity was measured by the BCA method. Microbial composition of the flora was analyzed by the PCR-DGGE.

The biogas yield of the heat-treated microflora is shown in Fig.1. Methane was produced by the microflora treated at 30°C, 50°C, and 60°C, suggesting that those temperature are not sufficient to inactivate the methanogens. In contrast, treatment at 80°C and 100°C, methane was not produced and hydrogen was accumulated, suggesting that methanogens were completely inactivated. The PCR-DGGE analysis showed that the bacterial members of the microflora were dramatically changed in comparison to the parent flora, implying that thermotolerant hydrolyzing and hydrogen-producing microorganisms became dominant in the microflora. Enzymatic activities of hydrolase for cellulose, chitin, and protein, major components of DS, were detected, suggesting that microflora retains DS-degrading activity.

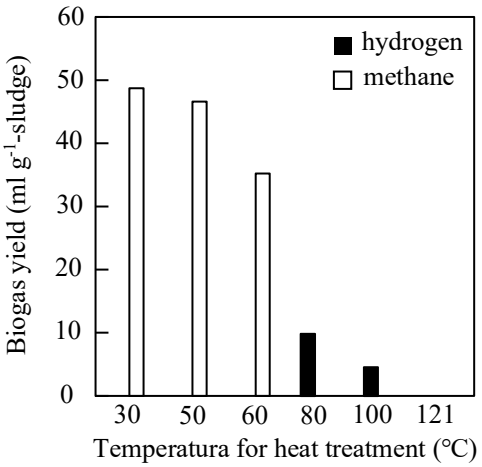

Fig.1 Biogas production by heat-treated microflora (cultivated at 30°C for 4weeks)

References:

[1] E. Athanasoulia, et al, *Renewable Energ.*, **47**, 147−151 (2012).
[2] K. Kuribayashi, et al, *Int. Biodet. Biodegrad.,* **120**, 58-65 (2017).
[3] T. Shigematsu, Y. Tang, K. Kida, *Seibutsu-kogaku*, **87**, 570–596 (2009).

The ability of wild *Bacillus* sp. to produce polyglutamic acid

Suzuka Sato, Nobuhiro Aburai, Katsuhiko Fujii

Applied Chemistry and Chemical Engineering, Graduate School of Engineering, Kogakuin University, Tokyo, Japan

E-mail: bm21020@ns.kogakuin.ac.jp

Polyglutamic acid (PGA) has attracted an attention owing to application potential in various fields such as cosmetics and medicinal. We searched for wild *Bacillus* strains that produced more PGA, and characterized using an amino acid analyzer, an HPLC equipped with a refractive index detector and thin layer chromatography. Results showed that mucilage of the strain 8H is composed of PGA and glucan. Molecular weight for 8H PGA was determined to be 9655 kDa.

Generally, petroleum-derived water-absorbent polymers are used in diapers and sanitary products, but because of concerns about depletion of petroleum in the future, frequent skin problems such as rashes, and the difficulty of biodegradation, there is growing interest in naturally derived polymers that are friendly to the environment and the skin. Its water-absorbing and moisture-retaining properties are expected to be utilized in a variety of fields. The mucilage of *Bacillus subtilis* var. *natto* are a viscous matrix containing polyglutamic acid (PGA), which is known to form water-absorbing hydrogel by chemical treatment. In this study, we searched for wild *Bacillus* strains that produced more PGA than *B. subtilis* var. *natto*, or strains that produced characteristic polyglutamic acid, and characterized the PGA produced.

Soil and litter samples were collected in and around University campus. After boiling for 10 min., the samples were inoculated to Basal, E, and MSgg media, and cultivated at 25℃ for 3 days. The emerging colonies were isolated, subcultured, and their 16S-rRNA gene and the 16S-23S intergenic spacer (IGS) region DNA are analyzed for classification. Mucilage of the isolates was collected from the grown biofilm on agar medium, and bacterial cells were removed by a centrifugation. Mucilage was precipitated by adding ethanol, and freeze dried. The viscosity of the mucilage solution was measured using the Ostward's viscometer. The protein and carbohydrate concentrations of the samples were then determined by the BCA and phenol sulfate methods, respectively. Reduced viscosity the matrix was calculated and the strains which produce viscous mucilage were screened. Amino acid analysis for mucilage protein was carried out by a Waters UPLC system. Thin layer chromatography and an HPLC equipped with a refractive index detector was employed to analyze mucilage polysaccharide.

Environmental samples were cultured using three different agar media, and 35 bacterial colonies were obtained. After repeated isolation and subculture, the isolates were narrowed down to 13 strains based on the viscosity of their mucilage. Phylogenetic analysis showed that the isolates belong to the genus *Bacillus*. Viscosity for mucilage of most isolates was lower than that of *B. subtilis* var. *natto*, but mucilage of the strain 10Q had a viscosity close to that of *B. subtilis* var. *natto*, and that of the strain 8H had a viscosity higher than *B. subtilis* var. *natto*. DNA analysis showed that 16S-rRNA entire gene and IGS region DNA showed high similarity to those for *B. simplex*. Chemical analysis showed that the mucilage of the strain 8H contains protein which has molecular mass of 9655 kDa and was rich in glutamic acid, suggesting that it is PGA. Unlike *B. subtilis* var. *natto*, major polysaccharide in the matrix was glucan. It is the first report for PGA production by *B. simplex*. Viscosity for matrix of *B. simplex* type strain was hence measured, but the type strain could produce trace amount of viscous matrix, implying that the strain 8H is *B. simplex* variant with high PGA producing ability.

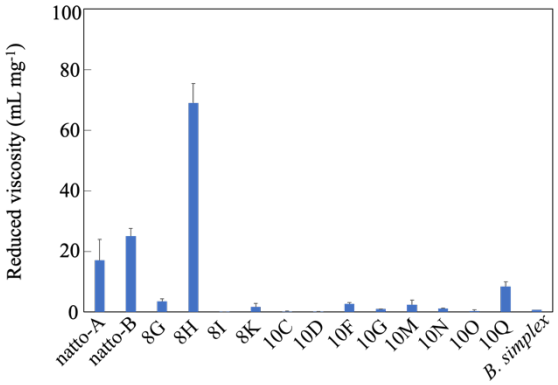

Fig. 1. Reduction viscosity of environmental samples.

Screening of carotenoid-rich aerial microalgae

Yuta Hiki, Nobuhiro Aburai, and Katsuhiko Fujii

Applied Chemistry and Chemical Engineering, Graduate School of Engineering, Kogakuin University, Tokyo
E-mail: bm21039@ns.kogakuin.ac.jp

Abstract

Carotenoid content for 79 aerial microalgal strains was examined, by measuring absorbance derived from carotenoid. Amongst the isolates, 9strains showed relatively high carotenoid accumulation.

Microalgae generally grow in the hydrosphere, and aerial microalgae that grow on substrates such as concrete on land. Aerial microalgae grow in severe environments with such as dryness, strong sunlight and temperature differences, and accumulate various carotenoids under stressful condition. Carotenoids are bioactive substances with antioxidant activity, and are expected to be applied in the fields of pharmaceuticals, cosmetics, and foods. Trace amounts of various carotenoids are present in plant cells, some microalgae that grow in the hydrosphere were reported to accumulate large amounts of some carotenoids. On the other hand, aerial microalgae have been isolated so far, the carotenoid accumulating ability has not been clarified in most strains. Therefore, the purpose of this study is to screen carotenoid-rich aerial microalgae with a whole-cell-based screening method.

The algal strains used in this study were collected from the outdoor unit of the air conditioner and a surface of tree in Kogakuin University (Hachioji Campus). Of 79 isolates, 42 strains were collected at the outdoor unit and 37 strains at the tree surface. These algal strains were cultured in a 96-wells microtiter plate under a various light intensity, temperature, nitrogen source, and pH. At this time, the culture conditions at 40 μmol photons m^{-2} s^{-1}, 25 °C, nitrogen source (NO_3^-), and pH 8.0 were set as a standard conditions (SC) for comparison. Bold's Basal medium (BBM) was employed to cultivate algal strains, and the initial turbidity of algal culture was adjusted to absorbance 750 nm of 0.05. The absorption spectrum of the grown algal strains was measured with a microplate reader.

Coelastrella sp. KGU-Y002 was employed to establish formulae to estimate cellular carotenoid content of aerial microalgae. Absorbance spectrum of 350-750 nm with 10 nm interval for microalgal culture was measured with a plate reader. Using the established formulae 1, 2, and 3, as shown below, cellular carotenoid content for 79 strains were compared based on carotenoid-derived absorbance at 490 nm ($A_{490\ Car}$)[1].

$$A_{650\ Chlb} = A_{680}/2.38 \quad (1)$$

$$A_{490\ Chlb} = A_{650\ Chlb} \times 2.89 \quad (2)$$

$$A_{490\ Car} = A_{490} - A_{490\ Chlb} \quad (3)$$

Based on the previous method, the absorbance at 480 nm derived from carotenoids was calculated. Fig.1 shows the absorbance at 480 nm for evaluation carotenoid accumulation when the outdoor unit algae strain was cultured for 21 days under 170 μmol photons m^{-2} s^{-1}, 25 °C, pH 8, with BBM. Under the high light intensity, two strains (no. 2 and 42) showed efficient carotenoid accumulation with an absorbance of over 0.9 by 3 weeks cultivation (Fig. 1). The absorbances for the strains no. 2 and no. 42 culture were 1.7 and 2.9 times, compared with the SC, respectively. In BBM at pH 3, two strains (no. 37 and 42) showed an absorbance of more than 0.8, which is 2.44 times higher than that for SC. At pH 10, four strains (no. 37, 38, 41, and 42) showed an absorbance of over 0.8. Of the four strains, strains no. 38 and 42 showed an absorbance of over 1.5 times compared with the SC. Under low or high temperature (5 or 35°C), the absorbance for evaluation carotenoid accumulation of all algal strains was about 0.6 times compared with SC. Of the 42 strains obtained from the outdoor unit, five were determined as potential carotenoid-rich strains. In the future, these strains will be cultivated in a large scaled and be evaluated their carotenoid production.

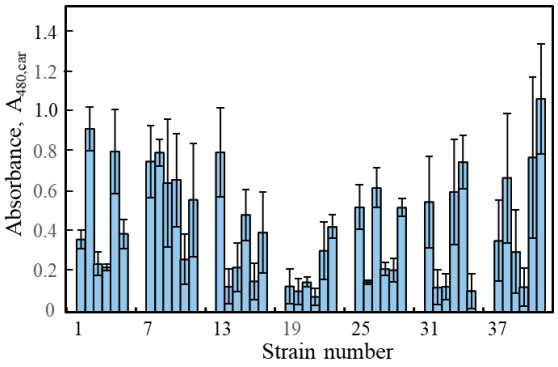

Fig.1 Absorbance at 480 nm for evaluation of carotenoid accumulation

References:

[1] N. Aburai, H. Kazama, A. Tsuruoka, M. Goto, K. Abe, *J. Biotechnology*, **268**, 6-11 (2018).

Functional Properties of Chitin Deacetylase from *Aspergillus fumigatus*

Hidetoshi Suzuki*, Masashi Ohkura, Kazuaki Okawa and Fumitaka Oyama

Department of Chemistry and Life Science, School of Advanced Engineering, Kogakuin University, Tokyo, Japan

E-mail: bm20026@ns.kogakuin.ac.jp

Abstract

Aspergillus fumigatus, a filamentous fungus ubiquitous in the environment, causes several human pulmonary disorders, such as invasive aspergillosis and allergic bronchopulmonary aspergillosis. *Aspergillus fumigatus* possesses chitin deacetylase genes, but their enzymatic function remains unclear. We expressed *Aspergillus fumigatus* chitin deacetylase as a fusion protein in *E. coli* and analyzed its enzymatic function using p-chitin as a substrate. Recombinant *Aspergillus fumigatus* chitin deacetylase released acetic acid from p-chitin at pH 3.0~6.0. The recombinant protein showed a peak of activity with maximum was observed at pH 5.0. This recombinant protein can be used to elucidate detailed biomedical functions of the *Aspergillus fumigatus* chitin deacetylase.

Chitin, a polymer of (β-1,4)-linked *N*-acetyl-D-glucosamine, confers structural rigidity to fungi, crustaceans, helminths and insects [1]. Fungal cell wall chitin acts as a pathogen-associated molecular pattern and is reported as a potential inducer of allergic inflammation [2]. *Aspergillus fumigatus*, a filamentous fungus ubiquitous in the environment, causes several human pulmonary disorders [2]. Chitin deacetylase produces chitosan by deacetylation of chitin. *Aspergillus fumigatus* has seven putative chitin deacetylase genes [3]. However, the functional properties of *Aspergillus fumigatus* chitin deacetylase remain unknown. Here, we describe an *E. coli*-expression system that allows for the production of active chitin deacetylase fused to Protein A at the N-terminus and V5 epitope and $(His)_6$ tag (V5-His) at the C-terminus (Protein A-chitin deacetylase-V5-His) (Fig. 1).

The chitin deacetylase cDNA was cloned into the expression vector and expressed in *E. coli*, followed by purifying using the Ni Sepharose column. The recombinant enzyme was incubated with p-chitin (Megazyme) and 1 mM $ZnCl_2$ for 1 hour. We evaluated chitin deacetylase activity by quantifying the released acetic acid from p-chitin using the K-ACETRM kit (Megazyme).

To examine the expression of Protein A-chitin deacetylase-V5-His in *E. coli*, we analyzed the expressed protein by Western blotting using an anti-V5 antibody. We detected a major band, which corresponded to that for the mature Protein A-chitin deacetylase-V5-His (the expected size for the mature Protein A-chitin deacetylase fusion, i.e., 68 kDa). Recombinant *Aspergillus fumigatus* chitin deacetylase released acetic acid from p-chitin at pH 3.0~6.0. The recombinant protein showed a deacetylation activity with a maximum observed activity at pH 5.0. Thus, the *E. coli*-expressed Protein A-chitin deacetylase-V5-His fusion protein possesses chitin deacetylase activity. This recombinant protein can be used to elucidate detailed biomedical functions of the *Aspergillus fumigatus* chitin deacetylase.

Fig. 1. Schematic representations of the *E. coli*-expressed Protein A-chitin deacetylase-V5-His. The *E. coli*-produced proteins contain the affinity tail of Protein A (yellow) at the N-terminus, whereas the proteins contain V5-His (green) at the C-terminus. Newly synthesized recombinant proteins contain the Protein A signal sequence (blue).

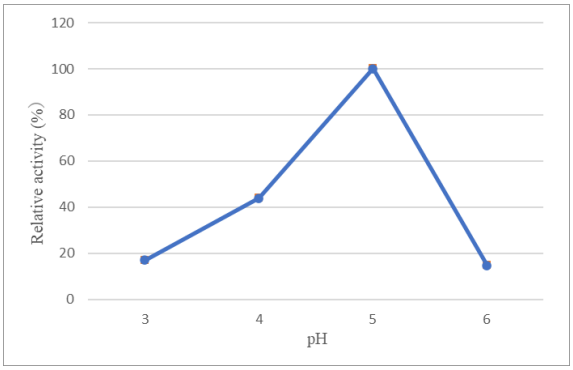

Fig. 2 Evaluation of chitin deacetylation activity of recombinant cda.

References:

[1] Reese et al., *Nature* 447, 92–96 (2007).
[2] Muraosa et al., *Scientific Reports* 9, 3345 (2019)
[3] Mouyna et al., *Cell. Infect. Microbiol*., 06 (2020)

Mechanistic insights of inactivation of YKL-40, a chitinase-like protein

Keita Suzuki*, Kazuaki Okawa, and Fumitaka Oyama

Department of Chemistry and Life Science, School of Advanced Engineering, Kogakuin University, Tokyo, Japan
E-mail: bm20025@ns.kogakuin.ac.jp

Abstract

YKL-40, one of the chitinase-like proteins, is expressed in mice and humans. Its levels are elevated in many diseases. Thus, YKL-40 is thought to play an important role. However, it is still unclear how this protein contributes to the pathophysiology of related diseases. Although YKL-40 has sequence homology to chitotriosidase (CHIT1), it lacks chitinase activity. Here, we attempted to activate YKL-40 by introducing two amino acid substitutions in the active center of the wild-type YKL-40. However, mutant YLK-40 remained inactive. This result indicates that multiple amino acids substitutions are required to activate YKL-40.

Chitinase-like proteins (CLPs) are structurally similar to chitinases but cannot degrade chitin. Mice mainly express Chitinase 3-like-1 (Chi3l1), Ym1 and Ym2, while humans express YKL-40(CHI3L1) and YKL-39 (CHI3L2)[1]. YKL-40 levels are increased in asthma, COPD, inflammatory bowel disease, Alzheimer's disease, and malignant tumors[2],[3],[4],[5],[6]. Thus, YKL-40 may play important roles under the pathophysiological conditions in humans. However, the contribution of the protein to the pathophysiology of the related diseases remains to be determined.

YKL-40 has relatively high sequence homology to human chitotriosidase (CHIT1) but does not have chitinase activity. Based on sequence similarities, CLPs belong to the family 18 of the glycosyl hydrolases. The active site motif DxxDxDxE, essential for the activity of GH18 chitinases, is not conserved in YKL-40. In YKL-40, catalytic residues of the active site are substituted to an alanine (Ala138) and a leucine (Leu140) residue (Fig. 1). The lack of chitinase activity in YKL-40 is assumed to be due to the mutation of crucial residues within the conserved catalytic sequence.

This study attempted to activate YKL-40 by reverting its two non-conservative substitutions in the active site to those of the active chitinases. Two substitutions of the amino acid (A138D and L140E) were introduced in the active center of the wild-type YKL-40 (WT-YKL-40) and YKL-40 mutant (MT-YKL-40) cDNAs were constructed (Fig. 2).

Although human CHIT1 shows chitinolytic activity, WT- and MT-YKL-40 did not show the activity (Fig. 3). These results suggest that the lack of chitinase activity in YKL-40 is not due to the simple amino acid substitution in the conserved catalytic motif. This result indicates that it is necessary to substitute multiple amino acids in addition to the two amino acid substitutions to activate YKL-40.

Fig. 1. The catalytic residues in the active site are substituted.

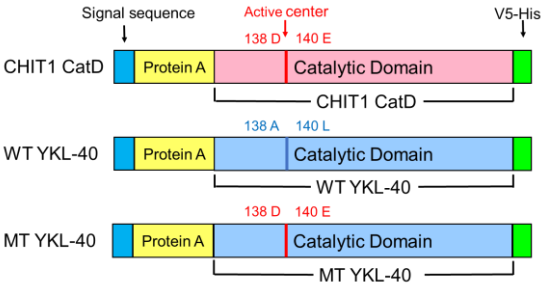

Fig. 2. Schematic representation of a fusion protein expressed in E. coli.

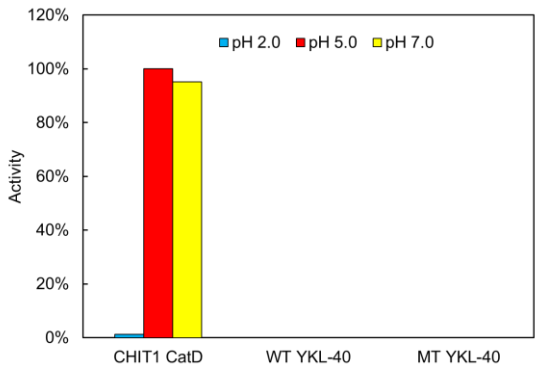

Fig. 3. Comparison of the chitinolytic activities of recombinant proteins using the fluorogenic substrate.

References:

[1] Hakala BE, et al., *J Biol Chem.* **268**, 25803-25810 (1993)
[2] Chupp GL, et al., *N. Engl. J. Med.* **357**, 2016-2027 (2007)
[3] Létuve S, et al., *J. Immunol.* **181**, 5167-5173 (2008)
[4] Vos K, et al., *Ann. Rheum. Dis*. **59**, 544-548 (2000)
[5] Choi J, et al., *J Neurol.* **258**, 2181-2185 (2011)
[6] Johansen JS, *Eur J Cancer*. **31A**, 1437-1442 (1995)

Component imaging of spheroids by using an FIB-TOF-SIMS

Tomoki Goto[1], Hyogo Takeuchi[2], Mizuki Shu[1], Reiko Saito[2,3], Kazuya Matsushima[4], Makoto Saito[4], Sanshiro Hanada[4], Nobuhiko Kojima[4], Masato Morita[1], and Tetsuo Sakamoto[1,2*]

[1]Department of Applied physics, School of Advanced Engineering,
Kogakuin University, Tokyo, Japan
[2]Department of Electrical and Electronic Engineering, Graduate School of Engineering,
Kogakuin University, Tokyo, Japan
[3]Corporate Manufacturing Engineering Center, Toshiba Corporation,
Yokohama City, Kanagawa, Japan
[4] Department of Life and Environmental System Science, Graduate School of Nanobioscience,
Yokohama City University, Yokohama City, Kanagawa, Japan
*ct13087@ns.kogakuin.ac.jp

Abstract

In recent drug discovery, three-dimensional cell cultures (called "spheroid") have received much attention. In addition, spheroids with internal channel-like structures are used to create a pathway for drug transportation. For this purpose, spheroids are made by mixing cells and alginate hydrogel beads. In this study, a cross section of such spheroid was cut and analyzed by FIB-TOF-SIMS (Focused Ion Beam Time-of-Flight Secondary Ion Mass Spectrometer). The result confirmed the distribution of cells and beads inside the spheroid. This result is expected to observe the distribution of drugs in medication.

Cell culture technology has been widely used in many fields such as drug discovery, medicine, cosmetics, and foods. Particularly, in drug discovery, culturing cells in a spherical shape makes it possible to evaluate cells with functions and structures closer to those of living organisms. For this reason, in recent years, spheroids have been attracted attention instead of two-dimensional cell culture in drug discovery [1]. Most of the drug distributions within a spheroid have been observed by fluorescent-labeling and confocal laser microscopy, so far. However, some kinds of drugs cannot be fluorescently-labeled, and excess labeling may alter the dynamics of the drug. Therefore, there is a need to device a new method to visualize the distribution of drugs in spheroids without fluorescent-labeling. In addition, spheroids with an internal channel-like structure have been used to improve substance exchange [2]. Therefore, cross-sectional imaging is also needed for the development of a novel spheroid with channel-like structure for medication.

Our FIB-TOF-SIMS was developed in our lab has the highest lateral resolution of 40 nm, which enables simultaneous mass imaging of multiple elements [3]. In addition, the high resolution enables the analysis of intracellular structures.

The spheroid was made from a mixture of alginate hydrogel beads. The beads are made to the same size as cells using SPG (Shirasu Porous Glass) membrane. The spheroid was created by mixing 2,000 cells and the beads to make channel-like structure. In addition, cesium, which is not present in cells, was added to the beads so that the beads could be clearly distinguished from cells.

A flat surface for internal structure of the spheroid was prepared with a cross-section polisher (IB-19530CP, JEOL) and analyzed using the FIB-TOF-SIMS. The images showing the distribution of both cells and beads were obtained based on specific mass peaks of them. The result is shown in Fig. 1. The red area represents Na^+, and its distribution allows us to see each of the cells one-by-one. The green area represents organic component ($C_nH_m^+$ fragment ions) derived from the beads. In addition, the result of Cs distribution was shown in Fig. 2. Comparison of Fig. 1 and Fig. 2 shows that the distribution of organic components (beads) and Cs (added into beads) is consistent.

This component imaging allowed us to confirm the shape and distribution of the beads in the spheroid. It is expected that the mechanism of medication is visualized by drug distribution in spheroids.

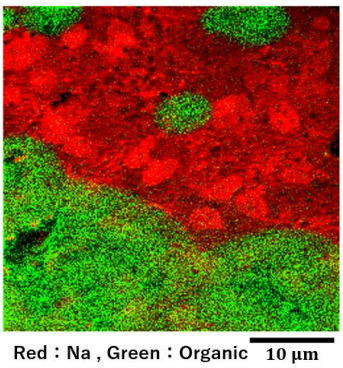

Fig. 1. Cross-sectional mapping of the spheroid. The red area represents Na^+, and the green area represents organic component ($C_nH_m^+$ fragment ions).

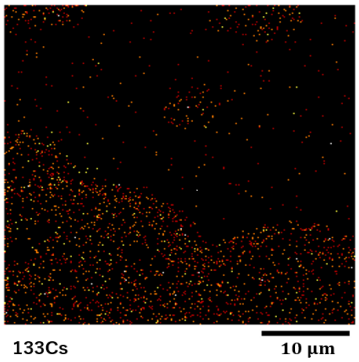

Fig. 2. Cross-sectional mapping of the spheroid. The red pixels represent Cs.

References:

[1] Y. Miyamoto *et al.*, *Organ Biology*, **27**, 37 (2020).
[2] N. Kojima *et al.*, *Sensor. Actuat. B-Chem.*, **198**, 249 (2014).
[3] T. Sakamoto *et al.*, *Appl. Surf. Sci.*, **255**, 1617 (2008).

Lightning Talk Session

Electric Engineering and Electronic Engineering

November 23rd

Presentation No.	Title	Author	
EEEL1.	UV-irradiated fabrication of SWCNT/SiO_2 Composite thin film at room temperature via Molecular Precursor Method	Naoki Ogawa, Hiroki Nagai, and Mitsunobu Sato	196
EEEL2.	Fabrication of visible-light responsive WO_3 Thin Film *via* Molecular Precursor Method	Taichi Murayama, H. Nagai, and M. Sato	197
EEEL3.	Remarkable mechanical flexibility of intentionally strain-induced amorphous B-doped In_2O_3 transparent conductive film	Shun Mori, Yukiya Ichinoseki, Kotaro Watanabe, Kaito Murano, Kaito Oe and Shinya Aikawa	198
EEEL4.	Understanding the switching mechanism of stacked ZrO_2-based ReRAM by insertion of SiO_x thin layer at the electrode interfaces	Keito Toyama, Ryusuke Akiyama, Kento Yuki and Shinya Aikawa	200
EEEL5.	Residual strain in GaN nanocolumns grown on Si(111)	Naoki Goto, Y. Hosoya, T. Onuma, T. Yamaguchi, and T. Honda	202
EEEL6.	Identification of Killer Defects in β-Ga_2O_3 Schottky Barrier Diodes by Raman Mapping Measurements	Masahiko Nakanishi, K. Shoji, S. Masuya, M. Kasu, T. Yamaguchi, T. Honda, K. Sasaki, A. Kuramata, and T. Onuma	204
EEEL7.	p-type behavior of lattice-expanded SnO_x by post-deposition N2 annealing	Kotaro Watanabe, Takuma Kawaguchi, and Shinya Aikawa	206
EEEL8.	Relationship between resistivity of NiO thin films and oxygen plasma condition at different deposition pressures	Mamoru Murayama, A. Ishikawa, T. Yamaguchi, T. Honda, K. Sasaki, A. Kuramata, and T. Onuma	208
EEEL9.	Measurement of Flexoelectric Coefficient (e_{11}-e_{33}) Using HAN Cells with Concentric-shaped Interdigitated Array Electrodes	Hiroki Shimoda, Yukihiro Kudoh, and Taiju Takahashi	210
EEEL10.	Well width dependence on residual strain in high In composition GaInN/GaInN MQW by RF-MBE	Kaigo Tahara, J. Yamada, T. Yamaguchi, Y. Nanishi, T. Onuma, T. Honda, and K. Kishino	212
EEEL11.	Micro scale analysis of LFP cathode of all solid state battery by FIB TOF SIMS	Akihiro Kawasugi, Naoki Gomyo, Linchun He, Masato Morita, and Tetsuo Sakamoto	215
EEEL12.	Development of resonance ionization mass spectrometry imaging method for radioactive Sr isotopes analysis	Takeru Yoshida, Takumi Umedate, Masato Morita, Tetsuo Sakamoto, Yue Zhao, Vollker Sonnenschein, Hideki Tomita, Toshihide Kawai, Takeo Okumura, Yukihiko Sato, Masabumi Miyabe and Ikuo Wakaida	216
EEEL13.	Trade-off relation of F concentration in CaF_2 co-sputtered In_2O_3-based transparent conductive film	Kaito Oe, Shun Mori, Kotaro Watanabe and Shinya Aikawa	217
EEEL14.	Emission Properties of Rocksalt-structured MgZnO Microcrystals for VUV Light Emitter	Wataru Kosaka, S. Hoshi, K. Kanta, K. Kaneko, T. Yamaguchi, T. Honda, S. Fujita, and T. Onuma	219
EEEL15.	Analysis of aerosol in urban city air using FIB-TOF-SIMS	Kentaro Sakai, Shokei Tsuchida, Noa Kato, Masato Morita, and Tetsuo Sakamoto	222

EEEL16.	Validation of Spray Droplets by ESD for a New Technique of Single Cell Rapid Freezing	Takayuki Umemura, Kenta Shirasu, Masato Morita, Kumiko Nagase, Wakako Hamanaka, Masatoshi Kakihana, Tatsuo Ohira, Norihiko Ikeda and Tetsuo Sakamoto	223
EEEL17.	Anatase Thin-Film Fabrication by Novel Precursor Solution Involving Stable Trisoxalato Complex of Ti (IV) without O_2^{2-} Coordination	Takuro Murayoshi, H. Nagai, and M. Sato	225
EEEL18.	Humidity dependency of the ionic conductivity of $Li_{1+x}Al_xTi_{2-x}(PO_4)_3$ transparent thin films fabricated by molecular precursor method	Kazuma Aochi, H. Nagai, and M. Sato	226
EEEL19.	Impact on InN Buffer Layer Inserted into GaInN/GaN Interfaces By RF-MBE	Daiki Itabashi, Ryosuke Yoshida, Tomohiro Yamaguchi, Takeyoshi Onuma, Tohru Honda	227

UV-irradiated fabrication of SWCNT/SiO_2 Composite thin film at room temperature via Molecular Precursor Method

Naoki Ogawa[a], Hiroki Nagai[b], and Mitsunobu Sato[a, b]*

[a] Electrical Engineering and Electronics, Graduate School, Kogakuin University, Tokyo, Japan
E-mail: cm20014@ns.kogakuin.ac.jp
[b] Department of Applied Physics, School of Advanced Engineering, Kogakuin University, Tokyo, Japan
*E-mail: lccsato@cc.kogakuin.ac.jp

Abstract

Single-walled carbon nanotube (SWCNT)/silica composite thin film was fabricated by Molecular Precursor Method (MPM) which is a wet chemical process. The obtained thin film shows electrical resistivity of 7.7×10^{-3} Ω cm, a thickness of 60 nm, and the transmittance is higher than 80% in the range of 178–2600 nm, in the exception of 220–352 nm in which the value is 73–79%. This unprecedented transparent conductive film that has transparency from vacuum ultraviolet (VUV) to the infrared region (IR) is promising as the transparent conductive film of new optoelectronic devices.

Transparent conductive films (TCF) are used as transparent electrodes for light-emitting diodes (LED), solar cells, and others. Indium tin oxide (ITO) and fluorine tin oxide (FTO) films are generally used for TCF because these materials have electrical resistivity under 10^{-3} Ω cm and transmittance over 80% in the visible light region [1]. However, these TCFs are not adoptable to devices utilizing UV, such as a deep-UV (DUV) LED due to their band gap. Therefore, TCF transparent to light in wide-range wavelength should contribute to develop novel optoelectronic devices.

Recently, we reported the fabrication of MWCNT/SiO_2 composite thin film through UV irradiation at ambient temperature using MPM [2]. The thin film has a pencil hardness of 8H, an electrical resistivity of 0.7 Ω cm, and transmittance over 80% in both visible and UV regions. Here, we attained a fabrication of SWCNT/SiO_2 composite thin film having high transparency and conductivity by using the MPM.

A SiO_2 precursor solution (**S_{Silica}**) was prepared according to our previous work [2]. The **S_{Silica}** was obtained by the reaction of 1.3 g of tetraethyl orthosilicate (TEOS) with 1.1 g of oxalic acid in 10 g of ethanol under reflux for 1 h. The concentration of Si^{4+} ion was 0.5 mmol g^{-1}. A diluted solution (**S_{CNT}**) of the ethanol dispersion of SWCNT (eDIPS-INK) was prepared by adding ethanol, to adjust the concentration of 0.1 mass%. Then, the SWCNT/SiO_2 composite precursor solution, in which the C/Si molar ratio is 0.4, for SWCNT/SiO_2 composite thin film was prepared by mixing the **S_{Silica}** and **S_{CNT}** at room temperature. This mixed solution was mechanically stirred for 1 h. The obtained solution are denoted as **S_{COMP}**.

Three hundred micro-litter of **S_{COMP}** was dropped onto a quartz glass substrate, and then spin-coated. The precursor film (**P_{COMP}**) was obtained by preheating the spin-coated film at 70°C for 10 min. The SWCNT/SiO_2 composite thin film was formed by irradiating UV light at 254 nm (with a corresponding intensity of 4 mW cm^{-2}) for 64 h onto precursor film in a clean bench. The UV-irradiated films are denoted as **F_{COMP}**. The **F_{COMP}** was heat-treated to yield the **F'_{COMP}** at 500°C for 1 h in air using an electric furnace.

The film thickness, electrical resistivity, and pencil hardness of **F_{COMP}** were 60 nm, 7.7×10^{-3} Ω cm, and 4H, respectively. The transmittance of **F_{COMP}** was more than 80% in the wavelength region from 178 to 2600 nm, and more than 73% in the range of 220–352 nm. Furthermore, the conductivity of **F'_{COMP}** could be maintained on 10^{-3} Ω cm level, and the pencil hardness of **F'_{COMP}** increased to 9H.

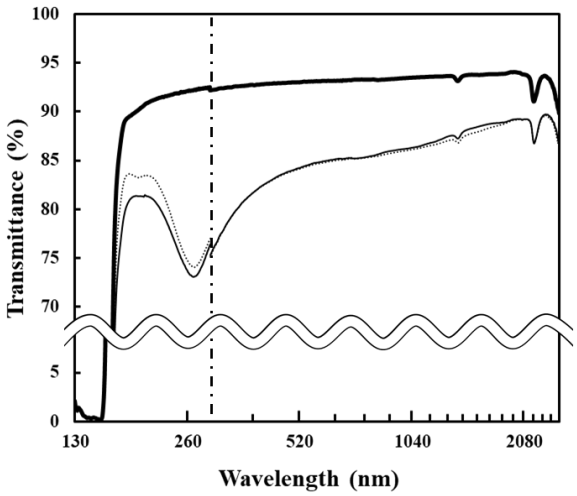

Figure 1 Transmittance spectra of **F_{COMP}** (—), **F'_{COMP}** (⋯), and quartz glass substrate (—).

References:

[1] K. L. Chopra, S. Major, and D. K. Pandya, *Thin Solid Films*, **102,** 1–46 (1983).
[2] H. Nagai, N. Ogawa, and M. Sato, *Nanomaterials*, **11**, 1348 (2021).

Fabrication of visible-light responsive WO_3 Thin Film *via* Molecular Precursor Method

T. Murayama, H. Nagai, and M. Sato*

Electrical and Electronic Engineering Program, Graduate School of Engineering,
Kogakuin University of Technology and Engineering, Tokyo, Japan
E-mail: lccsato@cc.kogakuin.ac.jp

1. Introduction

Tungsten oxide (WO_3) thin film has attracted attention as an electrode of the electrochromic device (ECD) and photocatalyst.[1,2] Many researchers reported the formation of WO_3 thin films using the dry and wet processes.[1,3] The wet process with no need of complicated vacuum systems has many practical advantages as compared to dry one. The molecular precursor method (MPM) developed by our study is a wet chemical process to fabricate metal oxide, metal, and metal phosphate thin films. In this study, a dibutylammonium salt of W^{6+} complex with citrate ligand was newly isolated. A transparent WO_3 thin film was successfully fabricated on a quartz glass substrate using a novel precursor solution involving the complex.

2. Experimental

2.1. Preparation of $(Bu_2NH_2)_3[WO_3(cit)]\cdot H_2O$

To 200 g of pure water was added 11.64 g (60 mmol) of citric acid. After 5 min stirring, the solution was added with 23.74 g (180 mmol) of dibutylamine and stirred for 5 min. Into the mixed solution, 15.01 g (120 mmol) of tungstic acid was added at 70°C with stirring. After 2 h, a solution with a small amount of white powder was obtained. After the white powder was filtered off using a filter paper, the solution was evaporated to ca. 70 mL under reduced pressure. The solution with white powders newly precipitated was kept overnight at 23°C. The obtained powders **PP** were collected on a paper filter and air-dried.

2.2. Preparation of WO_3 precursor solution

Into 3 g of ethanol, 0.78 g (0.94 mmol) of **PP** was added. A precursor solution **PS**, in which W^{6+} ion concentration is 0.25 mmol g^{-1}, was obtained by stirring for 1 h at 23°C.

2.3. Coating and heat-treating procedures

The precursor film was formed on a quartz glass substrate of 20 × 20 mm^2 by dropping 100 μL of **PS**, spin-coating (1st step 500 rpm/5 sec, 2nd step 2000 rpm/30 sec), and preheating at 70°C in a drying oven for 10 min. The precursor film was heat-treated in a muffle furnace at 550°C for 30 min in air. The obtained thin film is denoted as $\mathbf{F_{550}}$.

2.4. Measurements

Elemental analysis of **PP** was performed on a Perkin Elmer 2400 Series II CHN analyzer. The TG and DTA curves of **PP** were measured on a TG-2010s instrument (Bruker AXS). The α-Al_2O_3 powder in a Pt crucible was used as a reference. The temperature was raised from 25 to 1000°C at a rate of 5°C min^{-1} in air at a flow rate of 0.1 L min^{-1}. IR spectra of **PP** and the ligand were acquired from disks diluted with KBr using the FT-IR 600 spectrophotometer. The crystal phase of $\mathbf{F_{550}}$ adhered to the quartz glass substrate was examined using a SmartLab (Rigaku) X-ray diffractometer using Cu *Kα* radiation-source at a power of 45 kV and 200 mA. The film thickness of $\mathbf{F_{550}}$ was measured by a stylus profilometer, DEKTAK-3 (Sloan). The surface morphology of $\mathbf{F_{550}}$ was observed using an FE-SEM (JSM-6701F, JEOL). The transmittance spectra of $\mathbf{F_{550}}$ was measured in the wavelength region of 200−1100 nm using a Shimadzu UV-1900i spectrophotometer in double-beam mode and the substrate was used as a reference.

3. Results and Discussion

The result of elemental analysis on **PP** obtained by the reaction of tungstic acid and citric acid under the presence of dibutylamine in water was as follows; 43.49 (43.43); H, 8.13 (8.14); N, 5.10 (5.06) %. The calculated values for $WC_{30}H_{67}N_3O_{11}$ are given in parentheses and well consistent to the experimental data. Therefore, the yield of the compound can be determined as 46% from the mass of the product, 23.0 g. In the IR spectrum of **PP**, characteristic bands assignable to ν_a(C=O) were observed at 1583 and 1635 cm^{-1}. The endothermic peaks up to 125°C in the DTA curve of **PP** with the loss of 4 mass% are owing to the removal of water molecules. The TG curve shows that **PP** decomposed completely up to 480°C, with a final residue of 28 mass%. It was thus elucidated by these results that the chemical formula of the product is $(Bu_2NH_2)_3[WO_3(cit)]\cdot H_2O$.

The film thickness of $\mathbf{F_{550}}$ was ca. 100 nm. The XRD peaks at 2θ = 23.5, 24.5, 27.0, 29.1, 34.2, 42.1, 45.7, 47.4, 50.0, 50.8, 54.1, 55.8, 61.0, 63.0, 72.0 and 76.6° for $\mathbf{F_{550}}$ are assignable to the (020), (200), (120), (112), (202), ($\bar{1}$23), ($\bar{3}$21), (004), (400), ($\bar{1}$14), (042), (142), (043), (224), (400) and (116) phases of monoclinicWO_3. The transmittance of $\mathbf{F_{550}}$ in the visible region is higher than 82%. The optical band-gap of $\mathbf{F_{550}}$ obtained by a Tauc plot was 2.8 eV. An FE-SEM image indicates that the surface of $\mathbf{F_{550}}$ is smooth. When visible light whose wavelength is longer than 400 nm and 1.0 mW cm^{-2} was irradiated onto $\mathbf{F_{550}}$, the photo-induced hydrophilicity could be repeatedly observed as the water contact angle changes. Details will be discussed in the presentation.

4. References

[1] Kun Wang *et al.*, *J. Alloys Compd*., **889**, 861 (2021).
[2] Imre M. Szilagyi *et al.*, *J. Catal*., **294**, 119 (2012).
[3] Maksasithorn *et al.*, *Chinese J. Catal*., **35**, 233 (2014).

Remarkable mechanical flexibility of intentionally strain-induced amorphous B-doped In_2O_3 transparent conductive film

Shun Mori, Yukiya Ichinoseki, Kotaro Watanabe, Kaito Murano, Kaito Oe and Shinya Aikawa

Department of Engineering, Graduate School of Engineering, Kogakuin University, Tokyo, Japan

E-mail: aikawa@cc.kogakuin.ac.jp

1. INTRODUCTION

Highly transparent and flexible conductive films that can be deposited at room temperature are demanded for next-generation energy and information devices. However, since the current ITO requires post-deposition annealing, there is a limitation in terms of room temperature process. On the other hands, In_2O_3-based transparent conductive film reduces the electron scattering probability by reducing ionic radius of dopant[1], thus, carrier mobility can be improved. Based on this work, we focused on B specie, which has very small ionic radius of 0.027 nm, and have developed boron-doped In_2O_3 (IBO)[2]. We found that the mobility of an as-deposited IBO was improved than that of non-doped In_2O_3 but the optimum dopant concentration is still unknown. Here, we investigate B concentration dependence of electrical and optical properties of IBO as well as the crystal structure, and clarify the optimum concentration in the film. In addition, IBO deposited on a PET substrate as a potential for flexible transparent conductive film will be discussed.

2. EXPERIMENTS

A glass substrate was ultrasonically cleaned in acetone and IPA, and then irradiated with an excimer lamp to remove organic residue. An IBO thin-film with a different B concentration was deposited at room temperature using an RF magnetron sputtering equipment. The RF power and total pressure during deposition was 100 W and 0.24 Pa, respectively. Ar was used as a carrier gas. A ceramic In_2O_3 target was used as the starting material. Incorporation of B was carried out by co-sputtering technique using B grains (purity 99.999 %). To examine an effect of annealing treatment, the IBO film was performed with and without the treatment. The annealing conditions were for 30 min in the range between 150 to 600 °C in O_2, Ar/H_2, and N_2 atmosphere. The sheet resistance was measured using a four-probe method. The carrier mobility and electron density were estimated using Hall-effect measurement system (ACCENT HL5500PC) at room temperature. The optical transmittance was measured using an UV-vis-NIR spectrophotometer (Shimadzu UV-3600). The film thickness was measured using a surface profiler (Dektak XT-E). The film composition was analyzed using an energy dispersive X-ray spectrometer (EDS) at an acceleration voltage of 10 kV. To examine the flexibility, IBO films deposited on a PET was measured the resistance during the film bending using lab-made equipment.

3. RESULTS & DISCUSSION

Figure 1 shows the electron density, carrier mobility, and resistivity of the as-deposited IBO as a dependence of dopant concentration. In the IBO with 0.2 at.% of B/In ratio, the resistivity, carrier density and mobility was 3.09×10^{-4} Ω·cm, 4.02×10^{21} cm^{-3} and 9.12 cm^2/V_S, respectively, was obtained. These values are better than the non-doped In_2O_3. Therefore, we considered the IBO with 0.2 at.% of B/In ratio was optimum. However, the resistivity of IBO increases with more than 0.2 at.% doping. Excess B concentration inhibits the sharing of oxygen atoms in the InO_6 polyhedral and decreases carrier mobility[3].

Figure 2 shows the change in the resistivity of IBO as a function of annealing temperature. The O_2 concentration during the deposition was 0 %. The resistivity increased to 2.36×10^{-1} Ω·cm with increasing temperature in the O_2 annealing. This is due to the reduction of electron density by compensation

of oxygen vacancies. In the Ar/H_2 annealing atmosphere, the resistivity was not decreased. This means the film did not reduced as expected. Change in the resistivity was not significant up to 300 °C in the N_2 condition but it increased to 1.27×10^{-3} Ω·cm at 600 °C. We believe that weakly-bonded oxygen causes the reduction of electron density by incorporation into vacancy sites[4][5]. We found that no annealing treatment is necessary for IBO film, thus it can be applicable use of plastics as a substrate.

Figure 3 shows a photograph of the bending measurement of the fabricated IBO on a PET substrate. The inset is the schematic diagram. The results showed that the resistance was sensitive to the curvature of the film. We will discuss the bending angle dependences and comparison to an ITO film.

4.CONCLUSIONS

We investigated the dependence of B concentration in IBO and examined its application of flexible transparent conductive film. In the optimum conditions, 3.09×10^{-4} Ω·cm, 4.02×10^{21} cm^{-3}, 9.12 cm^2/Vs and 80.1 % for resistivity, electron density, mobility and average optical transmittance in the visible region were obtained. The IBO film showed better electrical and optical properties in spite of deposition at room temperature. This feature can be applicable for flexible electronics.

REFERENCES

[1] N. Mitoma, et al., App. Phys. Lett., 106, p.042106 (2015).

[2] S. Aikawa, et al., Proc. of the IEEE 20th Int. Conf. Nanotechnol. (IEEE-NANO), pp.202-206 (2020).

[3] X. Zhang, et al., J. Am. Chem. Soc., 140, pp.12501-12510 (2018).

[4] K. Ide, et al., App. Phys. Lett., 99, p.093507 (2011).

[5] S. Aikawa, et al., App. Phys. Lett.,106, p. 192103 (2015).

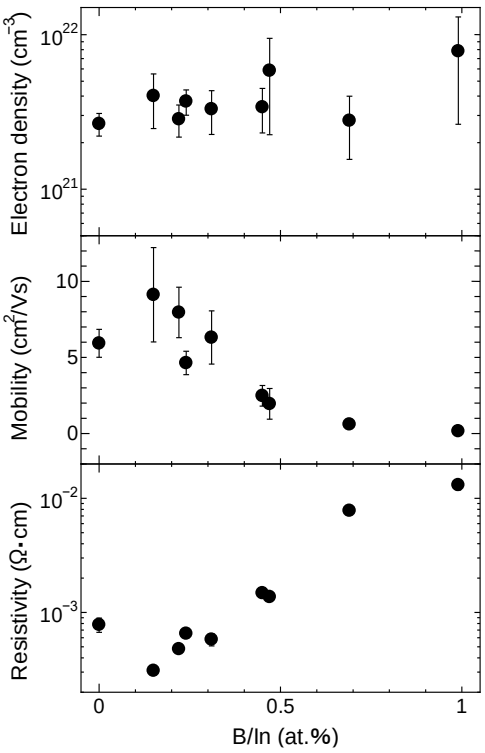

Fig.1 Electron density, mobility and resistivity of deposited IBO thin films as a dependence of dopant concentration.

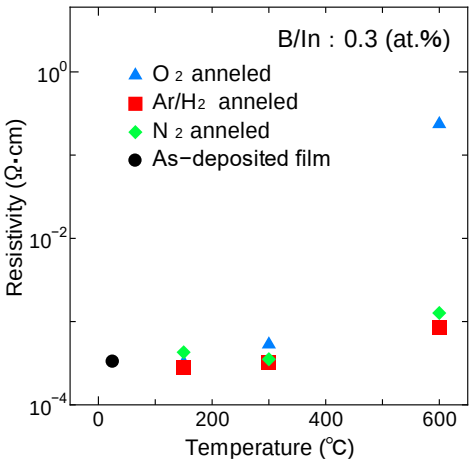

Fig.2 Resistivities of IBO films as a function of annealing temperature.

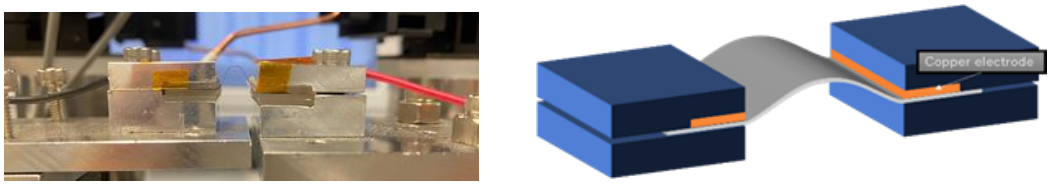

Fig.3 Bending measurement of the IBO film deposited on a PET substrate.

Understanding the switching mechanism of stacked ZrO_2-based ReRAM by insertion of SiO_x thin layer at the electrode interfaces

Keito Toyama, Ryusuke Akiyama, Kento Yuki and Shinya Aikawa

Department of Electrical and Electronic Engineering, Graduate School of Engineering,
Kogakuin University, Tokyo, Japan
E-mail: cm20037@ns.kogakuin.ac.jp

1.INRTODUCTION

Resistance-change random-access memory (ReRAM) has attracted much attention in the advanced information society because of its simple structure that enables miniaturization and multi-bit operation by stacking different materials. However, since typical ReRAMs use Pt for electrodes[1], the use of alternative metals is required to reduce the manufacturing cost of the devices. Cu is used as an alternative metal, but it causes ion migration to the ZrOx resistance change layer and degrades the switching operation due to mixing with oxygen vacancies.[2] In recent study by Dohee Lee et al [3], a SiO_2 DLL (diffusion limiting layer) was inserted into the Cu/ZrO_2 interface. In the study by Dohee Lee et al [3], it was found that the insertion of a SiO2 DLL (diffusion limiting layer) at the Cu/ZrO_2 interface suppressed Cu ion implantation and resulted in stable resistance change. However, a completely noble metal-free ReRAM has not yet been developed.

In this study, we report the results of the I-V characteristics of a ReRAM fabricated using Mo as an electrode, which is highly compatible with the CMOS fabrication process, and a SiOx layer inserted at the electrode/ZrO_x interface to suppress ion migration. The degradation characteristics of the fabricated devices in this experiment will also be reported.

2. EXPERIMENTS

Fig. 1 shows a cross-sectional schematic diagram of the fabricated ReRAM.A Si substrate wasultrasonically cleaned in acetone and IPA, and was irradiated using an excimer lamp to remove organic residue. An electron beam evaporation was used for whole deposition processes in this study. After 50 nm of Mo was deposited by electron beam evaporation at a rate of 0.04 nm/s to 0.1 nm/s, 10 nm of SiO_x and 20 nm of Zr were deposited at a rate of 0.04 nm/s. Then, it was annealed under O_2 atmosphere for 30 minutes at 600 °C. The SiO_x layer at the top electrode interface was deposited at 5 nm, and annealed under the same conditions. Finally, 50 nm Mo was deposited through the shadow mask at a rate of 0.04 nm/s to 0.1 nm/s. *I-V* measurement was performed at least 10 times for each device. During the measurements, the bottom electrode was grounded.

3. RESULTS & DISCUSSION

Figure 2 shows the I-V characteristics of the fabricated ReRAM. A typical set/reset operation with an on/off ratio of 10^2 was observed at +2V and -3V. The forming voltage at this time was 5V. The set/reset operation was confirmed for about 21 cycles. Figure 3 shows the I-V characteristics of the 22nd and 23rd cycles, and it can be seen that the current does not fall steeply around -3V in the 22nd cycle. In the 23rd cycle, the operating voltage and current increased around 3V. This is because the conductive filament was not fully broken in the 22nd cycle, and the reset operation did not occur. The reason for this is that Mo diffuses into the SiO_x layer of the fabricated ReRAM because it is deposited from the bottom electrode to the resistance change layer and then annealed. Therefore, it is necessary to optimize the thickness of the SiO_x layer on the bottom electrode side.

Regarding ion implantation, Cu has a diffusion coefficient of $5.6\times10^{-21}cm^2/s$ at 1000°C [4] against SiO_2, while Mo has a diffusion coefficient of $8\times10^{-19}cm^2/s$ [5]. Without the SiO_2 layer, ions would be directly implanted into the resistance change layer, but the SiO_2 layer suppresses ion implantation. Without the SiO_2 layer, ions are directly implanted into the resistance change layer, but the SiO_2 layer suppresses the ion implantation.

4. SUMMARY

We investigated the effect of SiO_x layer between electrode/ZrO_x/electrode resistive switching layer. The ReRAM sandwiched between SiO_x layers showed good operation with an on/off ratio of two orders of magnitude. As a degradation characteristic, it was found that the conductive filament could not be fully broken due to the diffusion of Mo ions into the SiO_2 layer on the bottom electrode side.

References:

[1] Schroeder, Herbert, and Doo Seok Jeong. "Resistive switching in a Pt/TiO_2/Pt thin film stack a candidate for a non-volatile ReRAM." Microelectronicengineering 84.9-10 (2007): 1982-1985.

[2] Zhai, Haifa, et al. "Resistive switching properties

and failure behaviors of (Pt, Cu)/amorphous ZrO_2/Pt sandwich structures." Journal of Materials Science & Technology 32.7 (2016): 676-680.

[3] Dohee Lee, et al. "Imporoved switching and synapse characteristics using PEALD SiO_2 thin film in Cu/SiO_2/ZrO_2/Pt device. " Journal of Applied Surface Science 547 (2021): 149140

[4] Gupta,D. et al. "Copper diffusion in amorphous thin films of 4% phosphorus-silicated. " Journal of Applied Physicss 61(1992):2178-2180

[5] H, G, Francois Saint Cyr. et al. "Diffusion of 18 elements implanted into thermally grown SiO_2 " Journal of Applied Physicss 94 7443 (2003)

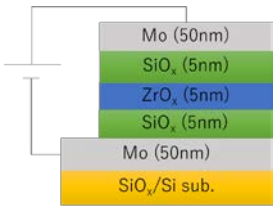

Fig.1 Cross-sectional schematic diagram of fabricated ReRAM.

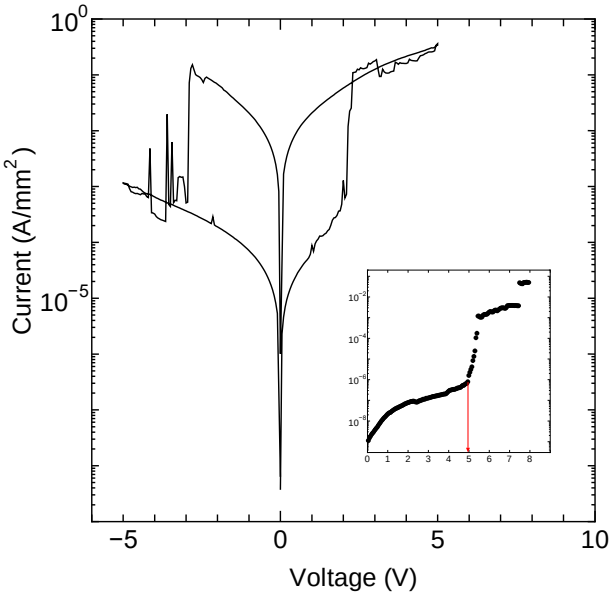

Fig.2 RS behavior of Mo/SiO_2/ZrO_2//SiO_2/Mo device.

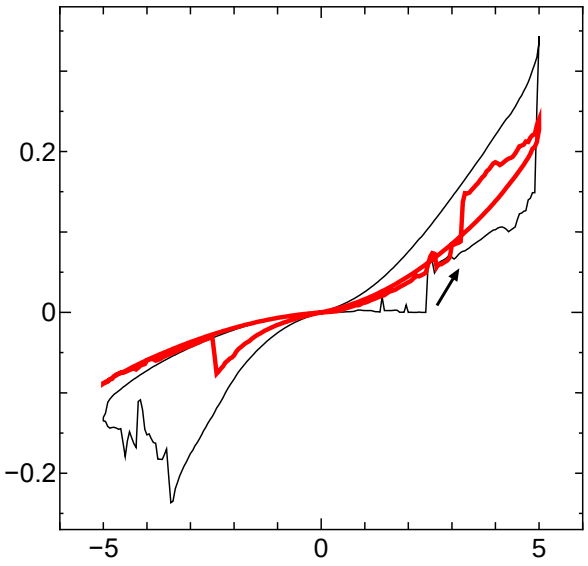

Fig.3 Degradation characteristics Mo/SiO_2/ZrO_2//SiO_2/Mo device.

Residual strain in GaN nanocolumns grown on Si(111)

N. Goto*, Y. Hosoya, T. Onuma, T. Yamaguchi, and T. Honda

Department of Electrical Engineering and Electronics, Graduate School of Engineering, Kogakuin University, Tokyo, Japan
*E-mail: cm20022@ns.kogakuin.ac.jp

Abstract

Residual strain in the GaN nanocolumns was investigated using Raman scattering spectroscopy. The E2 peak shift was observed from the GaN layer grown on sapphire, while the peak observed from the GaN nanocolumns showed a frequency close to that of the GaN bulk, which means that GaN nano columns have a low residual strain. The nanocolumn structure is one of the effective methods to realize stress-free GaN crystals grown on the Si substrate.

Small-size micro-LED display (μLEDD) has been investigated for augmented reality (AR) applications. In this case, a high dense integration of μLEDs is required. Their cost-effective fabrication requires "popular" substrates such as Si. The high dense integration also requires a top-to-bottom contact scheme for μLEDs. Although Si substrates have a conductivity with a doping technique, generally, GaN/Si growth needs to insert an AlN layer, which is an isolator. This means that a carrier injection into the GaN through Si substrates is difficult. On the other hand, the nanocolumn (NC) structure is one of the growth forms of the GaN crystals [1] without AlN or its related buffer layers. It is a columnar crystal made of nanoscale nitride semiconductor, and the strain relaxation effect makes it possible to obtain a GaN crystal suitable for light emitting devices [2]. In addition, it has been reported that E2 mode frequency in Raman scattering is sensitive to lattice strains in the c-plane as confirmed in hexagonal GaN [3]. In this study, Raman scattering was used to investigate whether GaN nanocolumns are stress-free or not.

Self-organized GaN nanocolumns were grown on n-Si(111) substrate using plasma-assisted molecular beam epitaxy (RF-MBE), as shown in Fig. 1. Growth time was 60 minutes, Growth temperature was 980 °C, Ga flux was 7.5×10^{-7} Torr, N_2 flow rate was 2.0 ccm, and RF power was 400 W. The samples were observed using Raman scattering. For comparison, GaN layers grown on sapphire and GaN bulk crystals grown by HVPE.

The results of Raman scattering shown in Fig. 2. The dotted line in the figure shows the reported E2 position (565 cm^{-1}) [4]. It is reported that residual strain makes the E2 peak shift in GaN [4]. It was confirmed that the E2 peak of the GaN nanocolumns shows a wavenumber close to that of the GaN bulk. In contrast, it was confirmed that the E2 peak of the GaN film is shifted in the direction of high frequency. This means that the lattice mismatch between GaN and Al_2O_3 caused compressive strain in the a-axis direction of GaN, which leads to the change in atomic positions [5]. On the other hand, the E2 peak observed from the GaN nanocolumns was same as that from GaN bulk.

Generally, GaN layers grown on Si substrate have a large tensile residual strain, which is an obstacle for their device applications. However, GaN nano columns grown on Si show their strain-free conditions. These results indicate that GaN NCs grown on Si have a potential for the application to μLEDD with strain-reduced light-emission layers.

In summary, Raman spectra of GaN NCs were observed. The E2 peaks shift was compared with GaN epilayers and GaN bulk crystals. It is clarified that GaN NCs were residual strain-free.

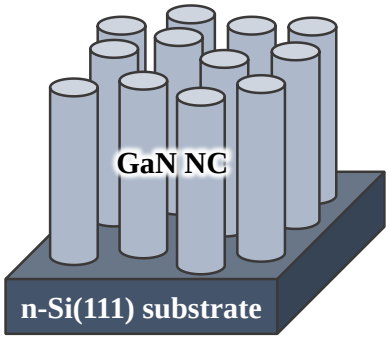

Fig. 1. The assumed structure of GaN nanocolumns on Si(111) substrate.

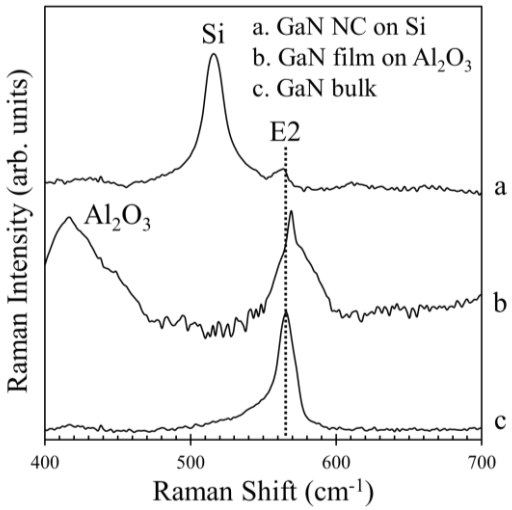

Fig. 2. Raman spectra of GaN nanocolumns, GaN film on Al_2O_3 and GaN bulk.

References:

[1] H. Sekiguchi, *et al*., *Appl. Phys. Express*, **1**, 124002 (2008).
[2] V. Ramesh, *et al*., *J. Appl. Phis*., **107**, 114303 (2010).
[3] F. Demangeot, *et al*., *Solid State Commun*., **100**, 207 (1996).
[4] V. Yu. Davydov, *et al*., *Phys. Rev. B*, **58**, 19 (1998).
[5] S. Nakashima, *et al*., *J. Appl. Phys*., **92**, 053512 (2006).

Identification of Killer Defects in β-Ga_2O_3 Schottky Barrier Diodes by Raman Mapping Measurements

M. Nakanishi[1,*], K. Shoji[1], S. Masuya[2], M. Kasu[3], T. Yamaguchi[1], T. Honda[1], K. Sasaki[2], A. Kuramata[2], and T. Onuma[1]

1 Department of Electrical Engineering and Electronics, Graduate School of Engineering, Kogakuin University, 2665-1 Nakano, Hachioji, Tokyo 192-0015, Japan
2 Novel Crystal Technology, Inc., Sayama, Saitama 350-1328, Japan
3 Department of Electrical and Electronic Engineering, Saga University, Saga 840-8502, Japan
*E-mail: cm20039@g.kogakuin.jp

Abstract

Raman mapping measurements were performed on β-Ga_2O_3 Schottky barrier diode (SBD) to identify a possible origin of the killer defects. All of the Raman peaks for β-Ga_2O_3 were observed below 800 cm^{-1}. In addition, a broad peak was observed around 1300 cm^{-1}. The peak was quite similar to the peaks for powdered cluster nano-diamond. Clear observations of arcuate lines in Raman mapping images at 1300 cm^{-1} and correspoding emission spots in the emssion maicoroscopy image cofirmed that polishing marks could be a killer defect of the SBDs.

Introduction

Monoclinic β-Ga_2O_3 is attracting attention as an alternative candidate for power electronics because of its ultra-wide bandgap (E_g) of 4.5 to 4.8 eV, high breakdown electric field of 8 MV/cm, and good chemical and thermal stability [1]. Availability of edge-defined film-fed growth (EFG) grown large single crystalline wafers will be a big advantage. For further improvements in device performance, identification of killer defects is essential. So far, dislocations, stacking faults, and other characteristic defects have been identified using X-ray topography and transmission electron microscopy [2-5]. However, the observations need sample processing and destruction. Therefore, it is desired to establish a non-destructive microstructure evaluation technique. In this study, Raman mapping measurements were employed for β-Ga_2O_3 crystals to figure out measuring condition for crystal defect visualization.

Experiments

To correlate the Raman mapping image and killer defects, the (001) β-Ga_2O_3 Schottky barrier diode (SBD) after the emission microscopy observation was used. The SBD initially consisted of a 500-μm-diameter Ni/Au Schottky electrode on top of the halide vapor phase epitaxy (HVPE) grown epilayer and a Ti/Au ohmic electrode formed on entire back face of EFG substrate. For the emission microscopy observation, center of the Ti/Au ohmic electrode was etched to observe the image from back face of the SBD. Then, to observe the Raman mapping image from the surface, the area around the Ni/Au electrode pad was etched followed by removing the electrode. Raman spectra was measured using a HORIBA LabRAM HR800 at room temperature. The sample was irradiated using a cw YAG: Nd laser at 532 nm with a power of 12 mW. The back-scattered light was dispersed by a monochromator with a spectral resolution of 6.9 cm^{-1}. An objective lens with a magnification of 15x and a spot diameter of 1 μm was used. The mapping step was se as 3 or 10 μm.

Results and Discussion

Representative Raman spectrum is shown in Fig. 1. The unpolarized Raman spectrum consists of 10 A_g mode and 5 B_g mode peaks, all of which were observed below 800 cm^{-1}. In addition, a broad peak was observed around 1300 cm^{-1}. Fig. 2(a) shows the enlarged Raman spectrum around 1300 cm^{-1}. The peaks around 1300 and 1600 cm^{-1} are quite similar to those for the powdered cluster nano-diamond in Fig. 2(b) [6].

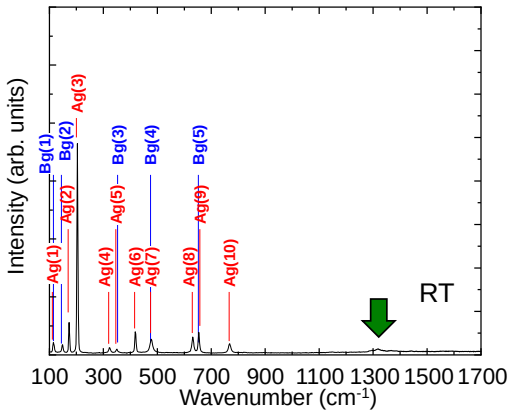

Fig. 1. Representative Raman spectrum at RT for β-Ga_2O_3.

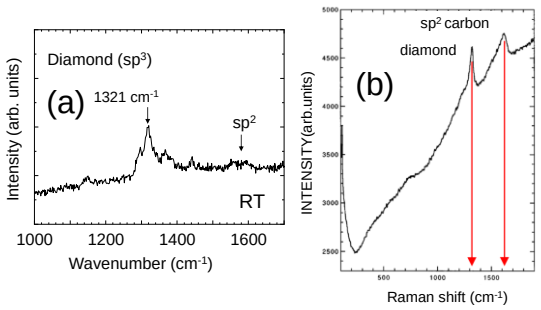

Fig. 2. (a) Enlarged Raman spectrum around 1300cm^{-1} for β-Ga_2O_3. (b) Raman spectrum of cluster nano-diamond [6] is shown for comparison.

Optical microscope image and Raman mapping images are summarized in Fig. 3. For the optical microscope image in Fig. 3(a), characteristic structures were not observed except for a large dark spot at the top and several small dark spots. On the contrary, dark lines extending along the [010] direction were additionally observed in the Raman mapping image as shown in Fig. 3(c). They are attributed to the plate-shaped nanovoids along the (100) plane [4,5]. In Fig. 3(d), arcuate lines were observed. As mentioned above, the Raman Peak around 1300 cm^{-1} is quite similar to the peaks for cluster nano-diamond. The arcuate lines are thus considered to be originated from the polishing marks during manufacturing the substrate.

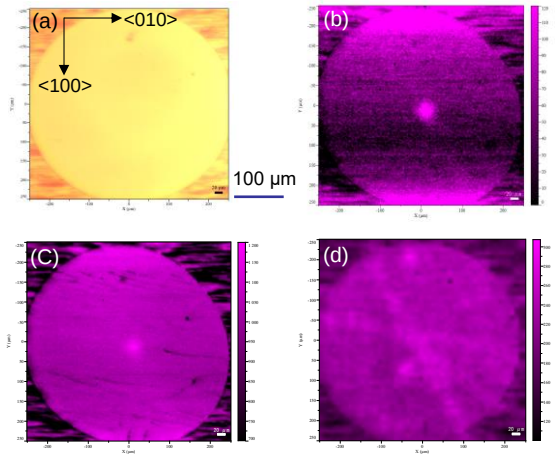

Fig. 3 (a) Optical microscope and Raman mapping images at (b) $B_g(2)$, (c) $A_g(3)$, and (d) 1300 cm^{-1}.

Raman mapping image at 1300 cm^{-1} and the emission microscopy image are shown for comparison in Fig. 4. The emission microscopy image was taken under reverse bias of 200 V. The emission spots are considered to be induced by the leakage current. It is confirmed that the emission spots appeared along the the arcuate line. The emission microscopy image observations have confirmed that the emission spots are often identified at the surface void defects for the substrate [5] and at the polycrystalline defects for the HVPE-grown epitaxial layer [7]. Present results imply that the polishing marks could also be killer defects of the SBDs.

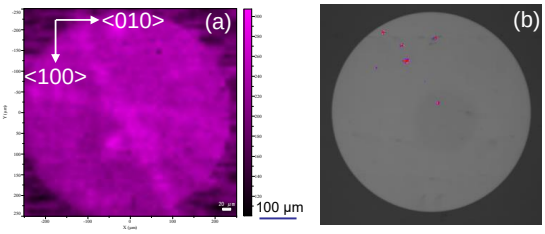

Fig. 4. (a) Raman mapping image at 1300 cm^{-1}. (b) Emission microscopy image under reverse bias of 200 V.

Summary

Raman mapping measurements were performed on β-Ga_2O_3 crystals, and an attempt was made to visualize the crystal defects. By comparing the optical microscope and Raman mapping images, characteristic dark lines and arcuate lines could be visualized. The results indicated usefulness of Raman mapping measurement as a non-destructive microstructure evaluation technique for β-Ga_2O_3 crystals.

Acknowledgements

This work was supported in part by the New Energy and Industrial Technology Development Organization (NEDO), subsidized by project No. 0624003.

References:

[1] M. Higashiwaki and G. H. Jessenet, Appl. Phys. Lett. **112**, 060401 (2018).
[2] M. Kasu, K. Hanada, T. Moribayashi, A. Hashiguchi, T. Oshima, T. Oishi, K. Koshi, K. Sasaki, A. Kuramata and O. Ueda, Jpn. J. Appl. Phys. **55**, 1202BB (2016).
[3] K. Hanada, T. Moribayashi, T. Uematsu, S. Masuya, K. Koshi, K. Sasaki, A. Kuramata, O. Ueda and M. Kasu, Jpn. J. Appl. Phys. **55**, 030303 (2016).
[4] O. Ueda, N. Ikenaga, K. Koshi, K. Iizuka, A. Kuramata, K. Hanada, T Moribayashi, S. Yamakoshi and M. Kasu, Jpn. J. Appl. Phys. **55**, 1202BD (2016).
[5] S. Sdoeung, K. Sasaki, K. Kawasaki J. Hirabayashi, A. Kuramata, T. Oishi and M. Kasu,, Appl. Phys. Lett. **117**, 022106 (2020).
[6] M. Yoshikawa, Y. Mori, H. Obata, M. Maegawa, G. Katagiri, H. Ishida and A. Ishitani, Appl. Phys. Lett. **67**, 694 (1995).
[7] S. Sdoeung, K. Sasaki, K. Kawasaki, J. Hirabayashi, A. Kuramata and M. Kasu, Appl. Phys. Express **14**, 036502 (2021).

p-type behavior of lattice-expanded SnO_x by post-deposition N2 annealing

Kotaro Watanabe, Takuma Kawaguchi, and Shinya Aikawa
Kogakuin University, Japan
E-mail: aikawa@cc.kogakuin.ac.jp

1. INTRODUCTION

SnO_x-based oxide semiconductors exhibit both n- and p-type conductions, depending on the ionic state of Sn, making it possible to realize all-oxide CMOS circuits[1]. Although an n-type conduction can be easily fabricated and its electrical properties are superior to p-type behavior[1-3], p-type SnO_x thin films are very difficult to obtain because of narrow sputtering conditions. The reason for the difficulty is based on the presence of dense subgap defects originating from oxygen vacancies (V_O)[4]. Thus, they should be reduced as well as controlling the hole density in order to enhance p-type properties. Here, we focus on N_2 annealing to fill V_O because N atom does not strongly compensate holes compare to group-III metal doping, and investigate change in the electrical properties of SnO_x films by post-deposition N_2 annealing.

2. EXPERIMENTS

SnO_x thin films (thickness: 100 nm) was deposited on a Si substrate with a thermal SiO_2 using RF magnetron sputtering at room temperature. A ceramic SnO_2 target was used for sputtering deposition. The oxygen ratio (O_{PP}) was varied between 2 and 10%. The total pressure and RF power were fixed at 0.12 Pa and 100 W, respectively. After the deposition, the films were annealed for 1 h under N_2 atmosphere in the range of 150 to 600 °C using a rapid thermal annealer. The electrical properties of the film were measured at room temperature using a Hall effect measurement system. The binding states were also characterized by X-ray photoelectron spectroscopy.

3. RESULTS & DISCUSSION

Figure 1 shows the annealing temperature dependence of the mobility, carrier density and sheet resistance of the SnO_x film deposited under 10% of O_{PP}. It was confirmed that the resistance decreased up to 300 °C, but increased after 300 °C. We suppose that the conductivity improvement is caused by crystallization and reduction of subgap density. On the other hand, more than one digit decrease in carrier density was observed after annealed at 300 °C, suggesting that the binding state was changed. Hsu et al. reported that increase in Sn^{4+} content in the SnO_x thin film and deterioration of the crystallinity was occurred in vacuum annealing at 400 °C or higher[4]. Since the correlation between decrease in carrier density and crystallization is quite low, we speculate that change in the binding states is more dominant than the crystal structure in our case.

Figure 2 shows a histogram of the carrier types of the film before and after N_2 annealing. The carrier type was extracted from the results of Hall measurement. 40 samples were measured for as-deposited films, and 47 samples were measured for N_2 annealed SnO_x. The yield of p-type SnO_x thin films increased from 7.2% to 31.9%. This indicates that the N_2 annealing is contributed to convert the SnO_x film to p-type conduction. Such conversion to p-type behavior is considered to be caused by the following reactions in the film [5]: $2N_O^X + O_L^X \rightarrow 2N_O^- + V_O^{++} + 1/2O_2$. Here, N_O indicates the O^{2-}-site is replaced by N^{3-}. According to Stavale et al.'s discussion, hole generation originated from the substitution of N^{3-} is possible in the case of N-doped ZnO. Based on the above discussion, Nguyen et al. showed that the reaction scheme can be applied to a sputter deposited SnO_x thin film fabricated in N_2 environment, and exhibited p-type behavior [6]. This means that similar reaction mechanism occurs in post-deposition N_2 annealing, and thus we believe that the p-type conversion is caused by hole generation. A schematic image of the reaction is illustrated in the inset of Fig. 2.

XPS analysis was performed to characterize the chemical binding states of N, Sn and O in the SnO_x film. Figure 3 shows the XPS spectra of as-deposited and N_2-annealed SnO_x films deposited at 4% of O_{pp}. In the Sn $3d_{5/2}$ spectrum, the deconvoluted peaks located at the lowest and highest energy of 484.3, 485.8 and 486.1 eV come from Sn^0, Sn^{2+} and Sn^{4+}, respectively. For the N_2 annealed film, the larger Sn^{2+} component indicates the presence of SnO phase. In addition, the overall peaks of the N_2 annealed film is shifted to the lower energy. Fan et al. mentioned the peak shift is originated from surface charge

transfer in 2D materials and the shift to the lower direction is due to the hole doping[8]. Thus, in the case of SnO_x partially substitution by N, it is possible to occur charge transfer and resulting hole doping. On the other hand, Sn^0 peak, which did not appear in as-deposit films, is confirmed in the annealed films. This peak comes from metal-Sn, which was generated by reducing the SnO_2 due to the N2 annealing. For the O1s spectra [Fig. 1(b)], three peaks can be seen at 529.8, 530.3, and 531.4 eV, correspond to lattice oxygen (O_L), oxygen vacancy (O_V), and chemisorbed oxygen (O_C), respectively. After N_2 annealing, O_V intensity was decreased, suggesting that density of V_O reduced. The N1s spectrum shown in the bottom of Fig. 1(c) can be deconvoluted into two peaks. No signal can be detected for the as-deposited film. The lower energy peak (N_I) is derived from oxynitride[7], while the higher peak (N_O) is that appears when N^{3-} is substituted at the O^{2-}-site. These results showed hole generation.

4. SUMMARY

We investigated the conduction-type conversion of n-type SnO_x to p-type by post-annealing in N_2 atmosphere. The XPS analysis revealed that the decreased carrier density annealed at 600 °C is caused by N^{3-} substitution into O^{2-}-site. This substitution generated holes, resulting in the reduction of electron density. Furthermore, the component of the film changed to SnO-rich phase. Thus, n-type SnO_x could be successfully convert to p-type by the post-deposition N_2 annealing.

1) R. Barros, *et al.*, Nanomaterials **9**, 320 (2019).
2) J. Um, *et al.*, Mater. Sci. Semicond. Process. **16**, 1679 (2013).
3) P.-C. Hsu, *et al.*, ACS Appl. Mater. Interfaces **6**, 13724 (2014).
4) P.-C. Hsu, *et al.*, Jpn. J. Appl. Phys. **52**, 05DC07 (2013).
5) T. T. Nguyen, *et al.*, Ceram. Int. **45**, 9147 (2019).
6) F. Stavale, *et al.*, J. Phys. Chem. C **118**, 13693 (2014).
7) X. Ding, *et al.*, Surf. Coat. Technol. **231**, 67 (2013).
8) S. Fan, *et al.*, Nanoscale, **11**, 15359-15366(2019).

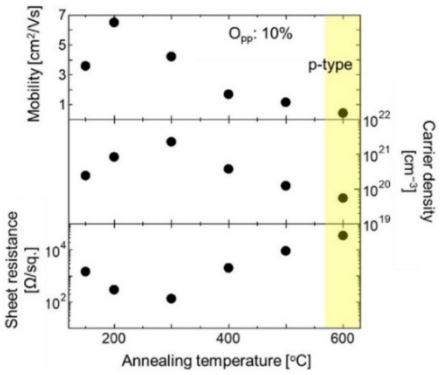

Fig. 1 Typical electrical properties (mobility, carrier density, and sheet resistance) of the fabricated SnO_x thin films as a function of annealing temperature.

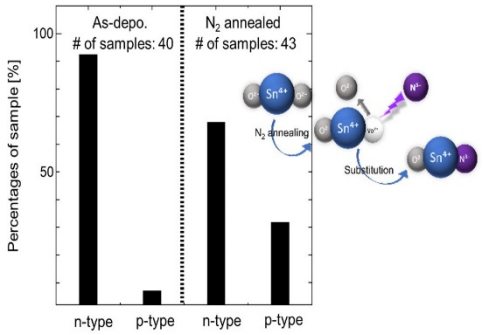

Fig 2. Histogram of carrier types of as-deposited and N_2 annealed SnO_x thin films. The inset shows a schematic illustration of substitution reaction in which N^{3-} replaces O^{2-}-site after N_2 annealing.

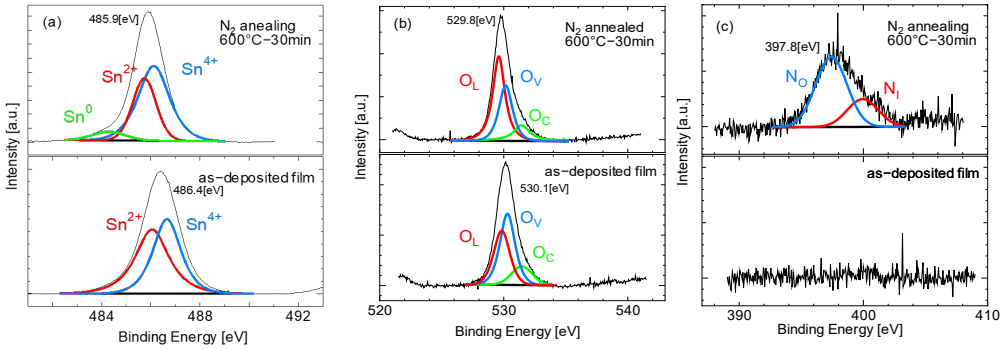

Fig3. Typical XPS spectra of as-deposited and N_2 annealed SnO_x films: (a) $Sn3d_{5/2}$, (b) O1s, (c) N1s, respectively

Relationship between resistivity of NiO thin films and oxygen plasma condition at different deposition pressures

M. Murayama[1*], A. Ishikawa[1], T. Yamaguchi[1], T. Honda[1], K. Sasaki[2], A. Kuramata[2], and T. Onuma[1]

1 Department of Applied Physics, School of Advanced Engineering and Department of Electrical Engineering and Electronics, Graduate School of Engineering, Kogakuin University, 2665-1 Nakano, Hachioji, Tokyo 192-0015, Japan
2 Novel Crystal Technology, Inc., Sayama, Saitama 350-1328, Japan
E-mail: cm21050@g.kogakuin.jp

Abstract

NiO films were deposited by RF magnetron sputtering. A p-type conductivity was achieved with a minimum resistivity ρ of 39 mΩ·cm at 0.6 Pa. By monitoring the RF plasma spectra, we recognized clear correlation between ρ and I_{O^*}. Spectroscopic plasma monitoring was found to be a useful tool for further improvement in p-type conductivity.

Introduction

Nowadays, power electronics is getting attention to realize carbon-free society. β-Ga_2O_3 is emerging as a primary material for power electronics[1] with a reasonably low cost by virtue of an availability of large-area single-crystalline substrates grown by melt-growth methods. β-Ga_2O_3-based Schottky barrier diodes have already achieved high breakdown voltage with maintaining low leakage current. For further improvements on device performance, integration of p-type layer is indispensable as is the case for 4H-SiC and GaN-based devices. In this study, we selected NiO as one of the p-type candidates to fabricate junction barrier Schottky diode. NiO films were fabricated by Radio Frequency (RF) magnetron sputtering. The RF plasma was monitored during the process, and a relation between oxygen radical emission and film properties are studied.

Experimental

60-160-nm-thick NiO films were deposited by RF magnetron sputtering (Canon-Anelva: L-332-FH) at an ambient temperature. A 99.9 mol% purity NiO target and c-plane sapphire substrate were set with a distance of 3 cm. RF power and oxygen flow rate was fixed with 25 W and 5 sccm, respectively. A chamber pressure was varied by adjusting a pumping speed. Resistivity ρ was determined by the Hall-effect measurement (Nanometrics: HL5500PC-SK) at room temperature. The plasma spectra were monitored by the fiber spectrometer (Ocean Optics: USB2000+UV-VIS-ES). The carrier type was determined by the Seebeck coefficient measurement. Morphology of film surface was investigated by atomic force microscopy (OLYMPUS: OLS4500).

Results

As shown in Fig. 1, sputtering rates slightly increased with pressure, but were almost the same. Pressure dependencies of spectrally integrated emission intensity of oxygen radical O* (I_{O^*}) at 777 nm[2] and resistivity of NiO films are plotted in Fig. 2

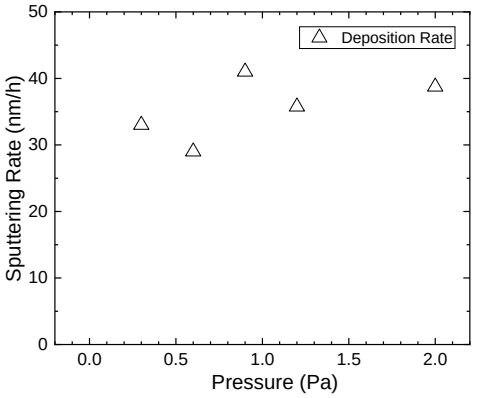

Fig. 1. Sputtering rate of NiO films with different pressure.

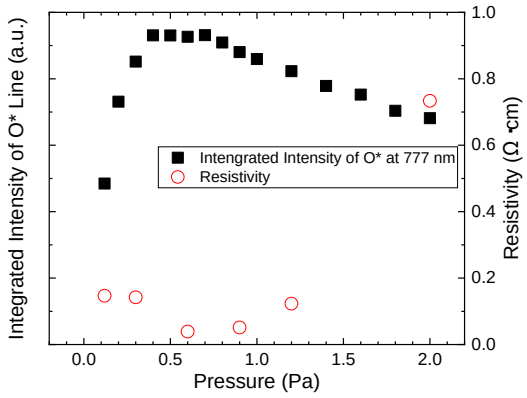

Fig. 2. Spectrally integrated emission intensity of oxygen radical at 777 nm and resistivity of NiO films as a function of pressure.

with open circles and solid squares, respectively. ρ values were in a range 39-734 mΩ·cm, and showed a minimum at 0.6 Pa. In contrast, I_{O^*} increased at 0.12-0.4 Pa, then saturated at 0.4-0.7 Pa, and decreased at 0.7-2.0 Pa. The carrier types are summarized in Table 1. Typical surface AFM images for the films deposited at 0.12, 0.9, ad 2.0 Pa are shown in Fig. 3. The root mean square (RMS) values of surface roughness show a monotonical increase with the pressure as shown in Fig. 4.

Table 1. Carrier type of NiO films determined by Seebeck coefficient measurements.

Pressure (Pa)	0.12	0.3	0.6	0.9	1.2	2.0
Carrier type	n	p	p	p	p	n

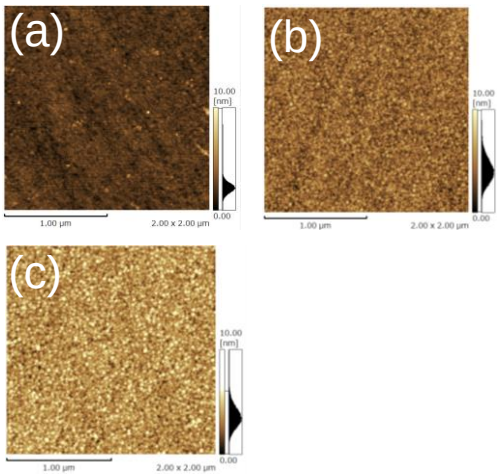

Fig. 3. Surface AFM images of NiO films deposited at pressures of (a) 0.12 Pa, (b) 0.9 Pa, and (c) 2.0 Pa.

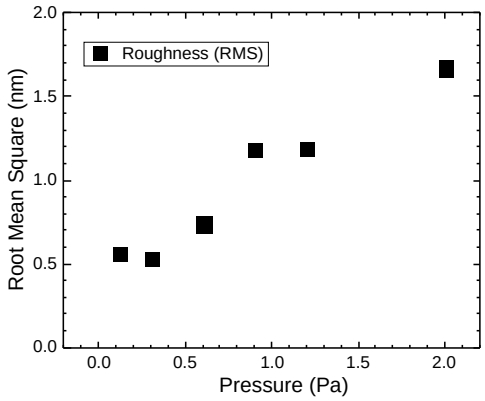

Fig. 4. Root mean square values of surface roughness of NiO films as a function of pressure.

Discussion

The pressure dependency of ρ in Fig. 2 is similar with the previous report[3], but its origin has not been elucidated, yet. Here, we focused on the opposite dependencies of ρ and I_{O^*} with the pressure. The increase of I_{O^*} reflects the increase in the O* supply. The O* has strong reactivity, and is preferentially incorporated into the films. At the constant sputtering rates, the decrease in ρ at 0.12-0.6 Pa is attributed to increase in the acceptor-type Ni vacancy reflecting the oxygen rich condition. The increase in ρ at 0.6-2.0 Pa seems again reflecting the decrease in O* supply. Indeed, carrier type change in Table 1 can be understood with the same manner. But, the monotonical increase of the RMS values in Fig. 4 implys the grain boundary scattering more or less influences on the resisitivity above 0.6 Pa. It is generally known that collisions between the sputtered species and the plasma species at elevated presures cause the coating atoms to arrive at the substrate in randomized directions that promote shadowing and rough surface of the films [4]. Therefore, the shadowing effect may induce the monotonical increase of the RMS values in Fig. 4.

Conclusion

In summary, we prepared NiO films by the RF magnetron sputtering. A p-type conductivity was achieved with a minimum ρ of 39 mΩ·cm at 0.6 Pa. By monitoring the RF plasma spectra, we recognized clear correlation between ρ and I_{O^*}. Spectroscopic plasma monitoring was found to be a useful tool for further improvement in p-type conductivity.

Aknowledgement

We would like to thank Prof. S. Aikawa for his help with the sputtering equipment. This work was supported in part by the New Energy and Industrial Technology Development Organization (NEDO), subsidized by project No. 0624003.

References:

[1] M. Higashiwaki and G. H. Jessen, *Appl. Phys. Lett*. **112**, 060401 (2018).
[2] P. H. Krupenie, *J. Phys. Chem. Ref*. Data 1, **423** (1972).
[3] H. Sato, T. Minami, S. Takata, and T. Yamada, *Thin Solid Films* **236**, 27 (1993).
[4] J. A. Thornton and D. W. Hoffman, *Thin Solid Films* **171**, 5 (1989).

Measurement of Flexoelectric Coefficient (e_{11}-e_{33}) Using HAN Cells with Concentric-shaped Interdigitated Array Electrodes

Hiroki Shimoda[1]*, Yukihiro Kudoh[2], and Taiju Takahashi[2]

[1] Department of Electrical Engineering and Electronics, Graduate School of Engineering, Kogakuin University, Tokyo, Japan
[2] Department of Information and Communications Engineering, Faculty of Informatics, Kogakuin University, Tokyo, Japan
E-mail: cm20027@ns.kogakuin.ac.jp

Abstract

We have proposed a method to evaluate the difference e_n (= e_{11} - e_{33}) of the flexoelectric coefficients in nematic liquid crystals (LCs) by using the disclination lines due to the reverse twist caused by the flexoelectric effect, which is induced by applying the DC voltage to a hybrid aligned nematic (HAN) cells. In this study, we measured e_n and investigated the influence of impurity ions on the flexo coefficient measurement.

1. Introduction

As higher definition of liquid crystal display (LCD) pixels progresses, light leakage and flicker at the pixel electrode edges have been reported [1,2], and the flexoelectric effect [3] (hereinafter referred to as the flexo effect) has been pointed out as one of that cause. The flexoelectric effect is a phenomenon in which polarization occurs due to the distorted orientation of LC molecules, and the polarization responds to the polarity of the applied electric field. There are e_{11} and e_{33} as coefficients indicating the degree of flexoelectric polarization, which are caused by spray and bend distortions, respectively. It is not easy to evaluate e_{11} and e_{33} individually due to the continuity of the LC director orientation. Therefore, $e_p = e_{11} + e_{33}$ or $e_n = e_{11} - e_{33}$ is evaluated, however, it is generally difficult to detect them in the same sample cell because it is necessary to detect the flexo effects from another direction regarding the distortion of the LC orientation.

We have proposed the following two cases of combination as measurement methods of e_n. Case A: concentric rubbing treatment and linear interdigitated array electrodes [4,5], and Case B: linear rubbing treatment and concentric interdigitated array electrodes. [6] (see Fig. 1.) Case B is an improved version of Case A, *i.e.*, it has an advantage of not requiring special rubbing equipment since linear rubbing treatment is a general method to fabricate LC devices. In both cases, a HAN cell applying the DC voltage is used, and discontinuous defects due to reverse-twist caused by the influence of the flexo effect are used. This defect appears in every other interdigitated electrode, and it is recognized as a quasi-disclination line (hereinafter referred to as quasi-DL) because those looked like a continuous line when the cell was viewed from a distance. Two quasi-DLs are observed in the cell, and the angle formed by them is measured, then e_n is determined by comparison with theoretical calculations [4,5]. Such quasi-DL is not induced when the AC voltage is applied. The advantage of our method is that it does not require a special optical system nor fine optical axis adjustment.

We attempted to evaluate e_n using Case B this time since we had not carried out experiments using the Case B method so far.

2. Experiment

The HAN cell was assembled with two types of glass substrates: one side was with concentric interdigitated electrodes of ITO and the rubbing treatment was done on the covered with a horizontal alignment film, and the other side was without any electrodes and a vertical alignment film was formed. The cell thickness was approximately 3 µm, and L/S = 100 µm / 20 µm of the interdigitated electrode pitch. The nematic mixture ZLI-4792 (Merck) was injected into the empty cell. Then, a DC voltage was applied up to approximately 90 V to the sample cell sandwiched between the polarizers for observing the quasi-DLs. Since quasi-DLs were formed when a low voltage was applied, it was necessary to particularly slow the voltage rise rate at a low voltage. After that, in order to avoid the influence of impurity ions, the voltage was switched to the AC and downed to approximately 60V.

In addition, since the sample cell was not sealed, impurity ions might invade the cell from the outside after a lapse of days after injecting the LC materials,

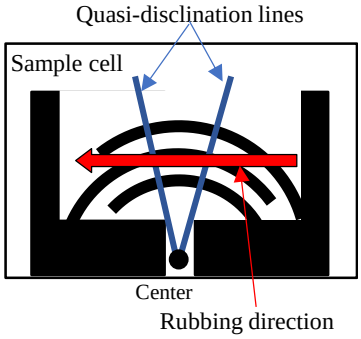

Fig. 1. Schematic model of the sample cell with concentric electrodes.

which might affect the measurement of the flexo coefficient, that is, it was expected that the measuring angle formed by quasi-DLs would change. In other words, by measuring the angle of DLs again after a

few days after the sample cells were prepared, it was possible to investigate the effect of the inclusion of impurity ions from the outside on the measurement of the flexo coefficient.

3. Result and Discussion

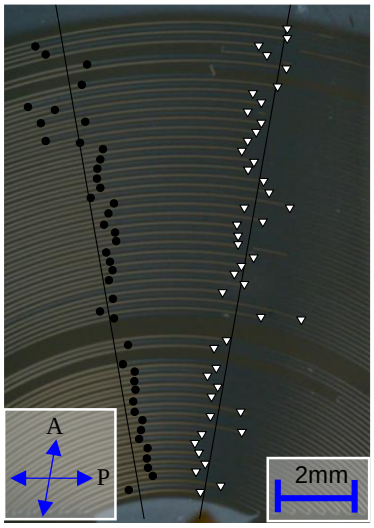

Fig. 2. Appearing of quasi-DLs under applying the DC voltage.

Figure 2 shows an example of the DLs in the cell induced by the above procedure and observed. It can be seen that two DLs are generated symmetrically in a fan shape. Six sample cells were prepared and the flexo coefficient of each was evaluated. As a result, e_n = -5.7 ± 1.1 pC/m with ZLI-4792 was obtained. In addition, as a result of measuring e_n again using a cell that had been fabricated for several days, the average value changed up to -6.78 ± 0.78 pC/m. From this, it could be seen that the measured value of e_n increases as the number of days elapses after injecting LC in the cell and the cause of this was impurity ions that had entered from the outside. Furthermore, there was a high possibility that impurity ions were contained even in the freshly prepared sample cell, which means that the removal of impurity ions would be an important issue.

Tab.1. Measurement values of e_n for each cell depending on elapsed days after injecting LC.

Days after	Measurement value of e_n for each cell [pC/m] Cell No.						
	1	2	3	4	5	6	Avg.
0	-1.93	-6.84	-5.96	-5.76	-9.87	-3.81	-5.77 ±1.1
6				-6.12	-8.05	-4.47	-6.21 ±1.03
9				-6.55	-8.24	-4.72	-6.5 ±1.02
15	-7.69	-7.43	-5.23				-6.78 ±0.78
18	-6.57	-7.36	-5.44				-6.46 ±0.56

In addition, the previous measurement result using Case A leaded e_n= -1.3 pC/m [7]. In case B this time, e_n larger. It seems that the cause of these results was the problem of the radius of the concentric electrodes or concentric rubbing. The maximum radius of the measurement part in case A was 12 mm, and that of the concentric electrodes in this measurement (Case B) was 16.5 mm. Since the curvature of this time was smaller than in Case A, the position where discontinuous defects occur could be detected more sensitively with slight differences. However, it was expected that the position would be easy to shift by the influence of impurity ions, for example.

4. Conclusion

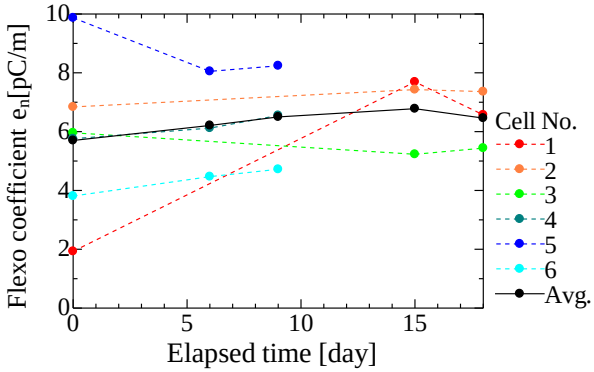

Fig. 3. Flexo coefficient e_n of each cell by the number of days elapsed.

The flexo coefficient e_n of the nematic LC, ZLI-4792, was measured using a HAN cell with concentric interdigitated electrodes, and e_n = -5.7 ± 1.1 pC/m was obtained. As the number of days passed after the cell was fabricated, a change in the flexo coefficient was observed, and that cause was thought to be impurity ions.

As a future subject, we would like to improve the measurement accuracy by removing impurity ions.

References:

[1] T. Suzuki and M. Suzuki: *Proc. of Japanese Liquid Crystal Society Meeting, 3D06*, 514, 1999. [in Japanese]

[2] I. H. Jeong, I. W. Jang, D. H. Kim, J. S. Han, B. V. Kumar, S. H. Lee, S. H. Ahn, S. H. Cho, and C. Yi: SID Symp. Digest of Technical Papers, 44, 1, pp. 1368-1371, 2013.

[3] R. B. Meyer: Physical Review Letters, 22, 18, pp. 918-921, 1969.

[4] N. Shirai: *Proc. of Japanese Liquid Crystal Society Meeting*, PA31, 2018. [in Japanese]

[5] N. Shirai, Y. Kudoh, T. Takahashi: *Proc. of IDW*, LCTp1-4, 2019.

[6] H. Shimoda, Y. Kudoh, and T, Takahashi: *Proc. of Japanese Liquid Crystal Society Meeting*, PC01, 127, 2020. [in Japanese]

[7] N. Shirai: Master's Thesis, Dept. of Electrical Engineering and Electronics, Kogakuin University, 2018.

Well width dependence on residual strain in high In composition GaInN/GaInN MQW by RF-MBE

K. Tahara[1,*], J. Yamada[2], T. Yamaguchi[1,], Y. Nanishi[3], T. Onuma[1], T. Honda[1], and K. Kishino[2]**
[1]*Department of Electrical Engineering and Electronics, Graduate School of Engineering, Kogakuin University, Tokyo, Japan*
[2]*Sophia University, Tokyo, Japan*
[3]*Ritsumeikan University, Kyoto, Japan*
[*]E-mail: cm20035@ns.kogakuin.ac.jp, [**]E-mail: t-yamaguchi@cc.kogakuin.ac.jp

Abstract

High-In-composition $Ga_{1-x}In_xN/Ga_{1-y}In_yN$(x>y) multiple quantum wells were grown by RF-plasma-assisted molecular beam epitaxy. Their X-ray diffraction patterns and photoluminescence spectra were measured to assess an impact of well width on the structural and optical properties. Blue-shift of the emission peak with the well width was attributed to the In composition pulling effect during the relaxation process of MQWs.

Introduction

Gallium-indium nitride (GaInN) [1], which is widely used as a material for blue and green light-emitting diodes (LEDs), has a potential to expand its emission wavelength from ultraviolet to infrared spectral range by controlling In composition. Not only blue and green LEDs, which are commercially availed, but also red LED using GaInN/GaN multiple quantum wells (MQWs) has been challengingly fabricated by Metal Organic Chemical Vapor Deposition (MOCVD) [2]. However, the internal quantum efficiency (IQE) drops drastically compared to the blue or green LEDs. This is mainly due to the quantum confinement Stark effect (QCSE) induced by strained quantum wells [3]. Phase separation also occurs in the MOCVD growth of GaInN alloys with high In composition.

Behind this background, we have been proposing to use $Ga_{1-x}In_xN$ / $Ga_{1-y}In_yN$ (x>y) MQWs grown by RF-plasma-assisted molecular beam epitaxy (RF-MBE) for future realization of LEDs. In contrast to MOCVD, RF-MBE realizes low temperature growth, and it is an advantage when growing GaInN and other materials containing InN. Recently, *in situ* monitoring of strain during the growth of GaInN by synchrotron X-ray diffraction (XRD) reciprocal space mapping (RSM) measurements led us to find In compositional pulling by reducing strain in GaInN layer [4].

In this study, high In composition $Ga_{1-x}In_xN$/ $Ga_{1-y}In_yN$ MQWs are grown by RF-MBE. Their XRD patterns and photoluminescence (PL) spectra are measured to assess an impact of well width on the structural and optical properties.

Experiment

GaN was initially grown at a growth temperature (thermocouple temperature) of 1120°C for 4 min. on the commercially available GaN-template. Then, approximately 1-μm-thick GaInN layer was grown at 865°C for 90 min. After that, five periods of $Ga_{1-x}In_xN/Ga_{1-y}In_yN$ (x>y) MQWs were grown at 765°C. The well thickness *L* was varied from 1 to 5 nm with fixed barrier thickness of 5 nm. Note that the In compositions in the well and barrier layers were controlled using the dual Ga Knudsen-Cells. Finally, the MQWs were capped by growing an approximately 15-nm-thick GaInN layer having the same In composition with the barrier layer. The MQWs were characterized by XRD and PL measurements. The PL spectra were mesured at room temperature (RT) using the 325.0 nm line of cw He-Cd laser as the excitaiton source.

Results and Discussion

RSM around the $\bar{1}05$ diffraction spot for the GaInN MQW with the well width of 5 nm is shown in Fig. 1. The diffraction spots for GaN-template, GaInN underlayer, and the 0th order of MQWs [abbreviated as MQW (0)] were apparently observed. From the reciprocal coordinates for the diffraction peaks of GaInN layer and MQW (0), in-plane and out-of-plane lattice constants were determined.

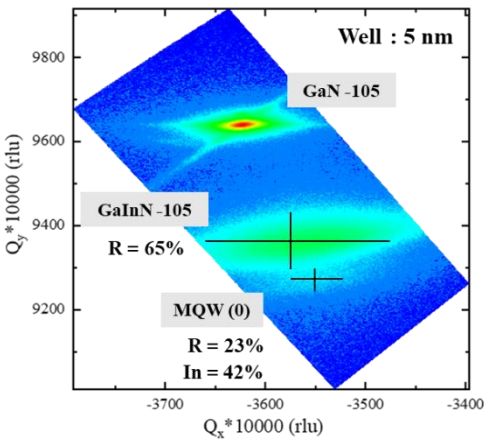

Fig. 1. XRD RSM for sample with well width of 5 nm.

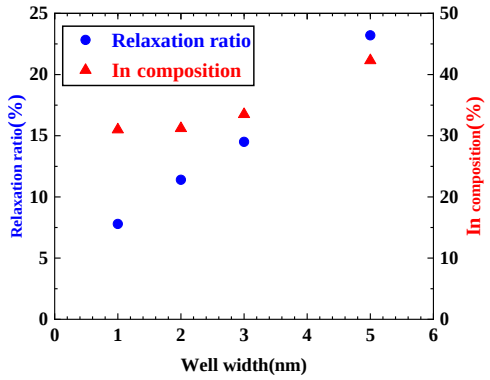

Fig. 2. Relationship between averaged relaxation ratio and In composition of MQWs estimated from RSM mesurements.

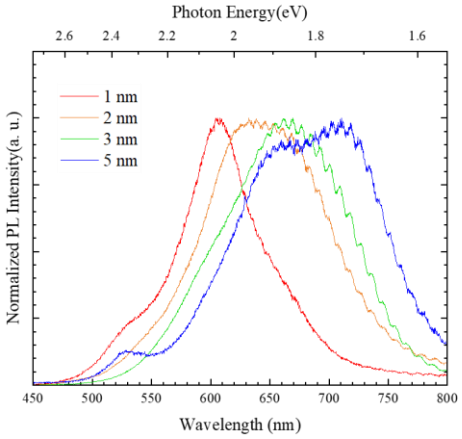

Fig. 4. Normalized PL spectra at RT for MQWs with well widths of 1, 2, 3, and 5 nm.

From the definition of Poisson's ratio, In composition and the relaxation ratio R were estimated.

The In composition of 25% and R=65% was obtained for the GaInN underlayer, and the In composition of 42% and R=23% were obtained as averaged ones for the well and barrier layers in the MQWs. Note that the relaxation ratios were estimated as; $R=100\times(a_{strain}-a_{UL})/(a_{relax}-a_{UL})$ (%), where a_{strain} and a_{relax} represent, respectively, the measured and relaxed in-plane lattice constant for the overlayer, and a_{UL} represents the measured in-plane lattice constant for the underlayer. The measured in-plane lattice constant for GaN-template was used as a_{UL} to evaluated the R in the GaInN underlayer, and that for the GaInN underlayer was used in the case of the MQWs.

By applying the analyses for three other MQWs having well widths of 1, 2, and 3 nm, the averaged relaxation ratio and In composition were obtained as a function of well width as shown in Fig. 2. Obviously. the averaged In composition increased with increasing R. The results may be due to the In compositional pull effect [4].

Extrapolation to the vertical axis gave the In composition of the barrier layers to be y=31%. Then, the In composition of the well layers x was estimated from the well and barrier thicknesses. The XRD 2θ-ω patterns for (002) diffraction peaks are shown in Fig. 3. The simulated patterns are also shown for comparison. The simulated results well reproduce the 2θ-ω pattern. The In compositions of the well layers were determined to be x=39% for *L*=1 nm, x=41% for *L*=2 nm, x=44% for for *L*=3 nm, and x=48% for *L*=5 nm.

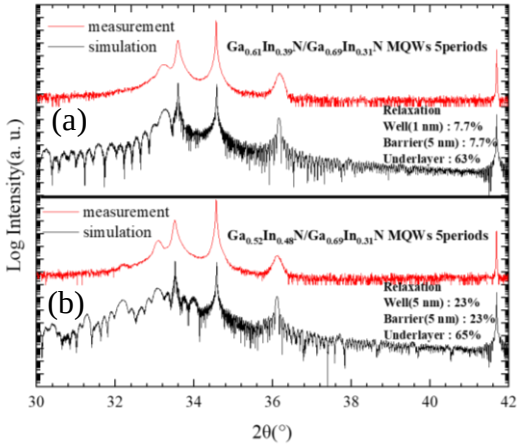

Fig. 3. XRD 2θ-ω patterns for MQWs with well widths of (a) 1 nm and (b) 5 nm. Simulated patterns are also shown for comparison.

PL spectra measured at RT for the GaInN MQWs are shown in Fig. 4. The PL peak wavelength showed a blue-shift from 710 nm (1.75 eV) for 5 nm to 610 nm (2.03 eV) for 1 nm. It is considered that the blue-shift of 280 meV cannot solely be attributed to the quantum-confined effect. Indeed, the In composition showed relatively large change of Δx=9% with the well width as discussed above. Overall results indicate that the In compositional pull effect [4] was attributed to the PL blue-shift in the present MQWs.

Summary

In summary, the high In composition GaInN MQWs grown by RF-MBE exhibited a relatively large blue-shift in the PL emission peaks with decreasing the well width. From the simultaneous evaluation of In composition and relaxation ratio in the MQWs by the XRD analyses, the blue-shift was attributed to the In composition pulling effect during the relaxation process of the MQWs.

Acknowledgement

This work was supported in part by Grants-in-Aid for Scientific Research Nos. 20K05348 and 19H00874 from MEXT, Japan.

References:

[1] J. Wu, W. Walukiewicz, K. M. Yu, J. W. Ager III, E. E. Haller, Y. Saito and Y. Nanishi, Appl Phys. Lett. **80**, 21 (2002).

[2] T. Mukai, M. Yamada and S. Nakamura, Jpn. J. Appl. Phys. **38**, 3976 (1999).

[3]T. Takeuchi, C. Wetzel, S. Yamaguchi, H. Sakai, H. Amano, I. Akasaki, Y. Kaneko, S. Nakagawa, Y. Yamaoka and N. Yamada, Appl. Phys. Lett. **73**, 1691 (1998).

[4] T. Yamaguchi, T. Sasaki, S. Fujikawa, M. Takahasi, T. Araki, T. Onuma, T. Honda and Y. Nanishi, Crystals **9**, 631 (2019).

Micro-scale analysis of LFP cathode of all-solid-state battery by FIB-TOF-SIMS

Akihiro Kawasugi[2], Naoki Gomyo[1], Linchun He[3], Masato Morita[1], Tetsuo Sakamoto[1,2,*]

[1]Grad. Sch. of Electrical and Electronic Eng., Kogakuin Univ., Tokyo, Japan
[2]Department of Applied Physics, Graduate School of Engineering, Kogakuin University, Tokyo, Japan
[3]Department of Materials Science and Engineering, National University of Singapore, Blk EA, Singapore
[*]E-mail: ct13087@ns.kogakuin.ac.jp

Abstract

All-solid-state Li-ion batteries (ASS-LIB) are considered as one of the promising candidates for the next-generation of energy storage devices, and hence is currently attracting a lot of attention. Among the various explored solid-state electrolytes (SSEs) including sulfide, oxide, polymer, and their composites, ceramic-polymer composite materials shows high Li-ion mobility[1]. However, there are limited analytical methods to understand the operating and degradation mechanism, and the details have not been clarified.

In this study, ASS-LIBs are analyzed with a high-resolution focused ion beam secondary ion mass spectrometer (FIB-TOF-SIMS), which was originally developed by our laboratory. We attempt to elucidate the interaction between LFPs and SSE by means of visualization of Li and other elements in small areas.

An ASS-LIB was prepared, it consists of a solid electrolyte (SSE) composed of a polymer Li salt containing $LiAl_{0.5}Ge_{1.5}(PO_4)_3$ (LAGP) and $LiN(SO_2CF_3)_2$（LiTFSI）, a cathode containing $LiFePO_4$ (LFP), $(CH_2CF_2)_n$（PVDF） and SSE components. For comparison, fresh samples and 200 charge-discharge cycled samples were prepared. They were sectioned smoothly by Ar^+ ion beam using Cross Section Polisher™ (JEOL, Japan). The cross-sections were analyzed by the FIB-TOF-SIMS apparatus[2] developed in our laboratory, and the components were mapped.

The positive ion spectrum by the FIB-TOF-SIMS apparatus is shown in Fig.1. In the literature, little changes in the shape of LFPs due to charging and discharging have been observed [3]. Therefore, the intensity of Fe signal, which is the framework of LFP, was normalized and compared.

As the result of comparing the fresh and 200 cycled samples, no significant difference was observed, and only a little more Li was detected in the fresh sample. Therefore, the spectrum was extracted by limiting the range to LFP particles. The center of the figure shows the map of Fe, which indicates the location of LFP particles. The spectrum was extracted in the area enclosed by the square within the particle, and the spectrum shown on the right of the figure was obtained. As a result, it was confirmed that the amount of Li detected inside the particle was higher after 200 cycles.

From the above results, it can be considered that, the amount of Li decreased in the SSE of the 200-cycled sample. This may be due to the fact that not only Li from the electrode but also Li from the SSE becomes de-inserted into the electrode by charging and discharging. This may lead to an increase in the amount of Li stored in the electrode, thereby increasing the capacity.

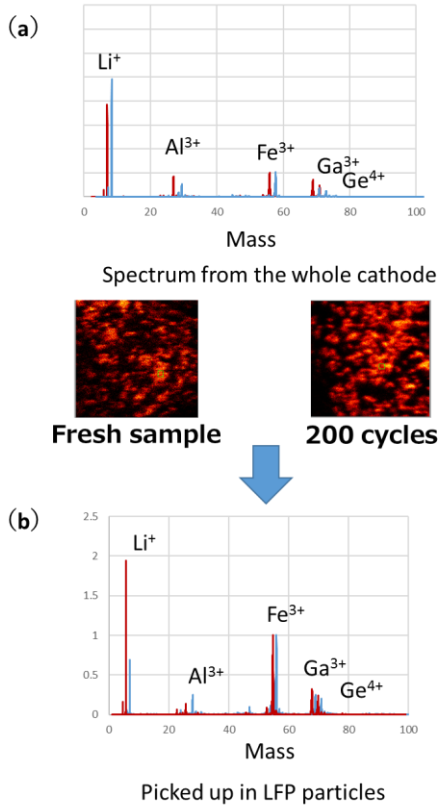

Fig. 1: positive ions spectra （a）from the whole cathode（b）from LFP particle

References:

[1] Xiaokun Zhang *et al*., *Nano Lett.*, **18**(6), 3829-3838 (2018).
[2] T. Sakamoto *et al.*, *Appl. Surf. Sci.*, **255**, 1617-1620 (2008).
[3] P. Hovington *et al*., *J. NanoLett*, **17**, 15, 4, 2671-2678 (2015).

Development of resonance ionization mass spectrometry imaging method for radioactive Sr isotopes analysis

Takeru Yoshida[1)], Takumi Umedate[1)], Masato Morita[2)], Tetsuo Sakamoto[1, 2 *)], Yue Zhao[3)], Vollker Sonnenschein[4)], Hideki Tomita[4)], Toshihide Kawai[5)], Takeo Okumura[5)], Yukihiko Sato[6)], Masabumi Miyabe[6)] and Ikuo Wakaida[6)]

[1)] Grad. Sch. of Electrical and Electronic Eng., Kogakuin Univ.,
2665-1 Nakano-machi, Hachioji, Tokyo, 192-0015 Japan
[2)] Department of Applied Physics, Kogakuin University,
2665-1 Nakano-machi, Hachiouji, Tokyo, 192-0015 Japan
[3)] Toyota Technological Institute, 2-12-1 Hisakata, Tempaku-ku, Nagoya, 468-8511, Japan
[4)] Nagoya University, Furo-cho, Chikusa-ku, Nagoya, 464-8601 Japan
[5)]Japan Neutron Optics Inc., 20-5, Takeshima-cho, Gamagori, Aichi, 443-0031, Japan
[6)]Japan Atomic Energy Agency, 790-1, Motooka Otsuka, Tomioka, Futaba-gun, Fukushima, 979-1151, Japan
*ct13087@ns.kogakuin.ac.jp

Abstract

Radioactive Sr is a β-ray-emitting nuclide and doesn't emit γ-rays. Therefore, it is difficult to analyze by radiation measurements such as imaging plate and γ-ray camera. Time-of-flight secondary ion mass spectrometry (TOF-SIMS) is suitable for the analysis of multi-elements and isotope ratio. However, it has a problem of isobaric interference which derives from non-element-specific-ionization. Resonance laser sputtered neutral mass spectrometry (R-SNMS) is a very effective method for radioactive materials with high element selectivity. In this method, isobaric interference is avoided. In this study, the images of Sr isotopes were obtained selectivity and efficiently by R-SNMS. Additionally, it was confirmed that the accuracy of the isotope ratio measurement was improved. This result provides a useful reference for the future analysis of radioactive ^{90}Sr in real sample.

1. Introduction

In Fukushima Daiichi nuclear power plant accident, large amounts of radioactive species were released into the air. Some fraction of these radioactive species exists in environment as particulate matters[1]. Among them, some nuclides are difficult to analyze, if they do not radiate γ-rays. Time-of-flight secondary ion mass spectrometry (TOF-SIMS) is effective for analyzing particles. However, it has a serious problem of isobaric interference due to non-element-selective ionization with focused ion beam (FIB) sputtering. For example, it is very difficult to distinguish ^{90}Sr (radioactive) and ^{90}Zr (stable) by the mass spectrum of SIMS owing to the limitation of mass resolution. The resonant laser ionization sputtered neutral mass spectrometry (R-SNMS) can overcome this problem[2]. It was reported that the isotopes of radioactive Cs were analyzed successfully by using R-SNMS[2]. In this study, we report an R-SNMS result of another element Sr. Here, we evaluated the R-SNMS of non-radioactive $SrCO_3$ reagent.

2. Results and Discussion[3]

A mixture of powders of non-radioactive $SrCO_3$ and Zr was used as the sample. We tuned a wavelength of lab-made Ti:Sapphire laser[4] to the Sr transition level to selectively ionize the target element. Here, we selected the $5s^2$ (ground state) to 5s5p orbital and the 5s5p to $5p^2$ (autoionizing state) orbital as the resonance absorption scheme of Sr by using the two tunable Ti:Sapphire lasers. The resonance absorption occurs when the photon energy was matched to the energy levels of Sr, and subsequent absorption of another photon results in ionization. The lasers were incorporated into our FIB-TOF-SIMS apparatus. We succeeded in obtaining the mapping of Sr particles with selectivity by R-SNMS. In addition, We confirmed that the isotope ratio measurement accuracy of Sr was improved. Figure 1 shows the images of the reagent of $SrCO_3$ at the same field of view by SIMS and R-SNMS.

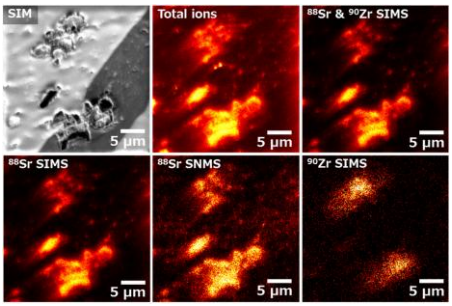

Figure 1. The images of the reagent of $SrCO_3$ mixed with Zr at the same of view by SIMS and R-SNMS

References

[1] K. Adchi, *et al*., *Sci. Rep*., **3**, 2554 (2013)
[2] T. Sakamoto, *et al., Anal. Sci.* **34**, 1265 (2018)
[3] Y. Zhao, *et al*., *J. Vac. Sci. Technol. B*., **38**, 044001 (2020)
[4] H. Tomita, *et al*., *Prog. Nuck. Sci. Techol.* **5**, 97 (2018)

Trade-off relation of F concentration in CaF_2 co-sputtered In_2O_3-based transparent conductive film

Kaito Oe, Shun Mori, Kotaro Watanabe and Shinya Aikawa

Department of Electrical and Electronic Engineering, Kogakuin University, Tokyo, Japan
E-mail: aikawa@cc.kogakuin.ac.jp

1. INTRODUCTION

Transparent conductive film with high transmittance and low resistivity is demanded for enhancing the quality of liquid crystal displays, touch panel sensors, solar cells, and so on [1]. For these applications, high transparency and conductivity are required for transparent conductive film, thus, it is necessary to improve both properties simultaneously. Sn-doped In_2O_3 (ITO) has a low electrical resistivity (~1×10^{-4} Ωcm) because of its high carrier density (10^{21} cm^{-3}) and is widely used for commercial applications [2]. We have two main reasons for focusing on In_2O_3 even with In known as a rare metal. First, the trap density of the In_2O_3 grain boundary is one order of magnitude lower than that of the ZnO system [3]. A low trap density should theoretically lead to mobility improvement. Second, In_2O_3 has structural flexibility that allows atoms with different ionic radius to be readily incorporated in the lattice [4].

Since conductivity is obtained from the product of the carrier density and mobility, increase in either parameter improves conductivity. However, cation doping has limitation to further increase electrical conductivity [5], thus F^- doping is an alternative way to enhancing the electrical and optical properties of In_2O_3-based transparent electrodes. Shigesato et al. reported that the F-doped In_2O_3 thin film was fabricated by RF magnetron sputtering using an In_2O_3 ceramic target co-sputtered with InF_3 pellets [5]. The carrier density was successfully increased from 3.1×10^{19} to 2.9×10^{20} cm^{-3} by placing optimum number of InF_3 pellets. In this case, F/In at.% was observed about 30% and the resulting resistivity obtained 1×10^{-3} Ωcm. However, the conductivity is poor compared to ITO. In addition, they did not mention in the optical transparency of the film. Thus, the influence of F doping on optical properties of In_2O_3 transparent conductive film is still unclear.

In this study, we focused on CaF_2, which is widely known as an optical lens material, as an F dopant into In_2O_3 because CaF_2 has high transparency, and is inexpensive and safe material. The CaF_2-doped In_2O_3 film (In_2O_3:CaF_2) was deposited on a glass substrate by means of sputtering and was characterized its electrical and optical properties depending the deposition conditions. We also investigated influence of Ca in the film in addition to the F doping.

2. EXPERIMENTS

A fused-quartz glass (10×10 mm^2, 0.5-mm thick) was used as the substrate for thin-film fabrication. The substrate was ultrasonically cleaned in acetone and isopropyl alcohol and irradiated using an excimer lamp (wavelength: 172 nm) for 5 min to remove organic residue. The In_2O_3:CaF_2 film was then deposited at room temperature by RF magnetron sputtering using 4N purity, 3-inch diameter In_2O_3 ceramic target. CaF_2 doping was performed by placing CaF_2 grains (99.9% purity) on the erosion region of the target. By changing the number of CaF_2 pellets on the erosion region, films with different CaF_2 concentration were fabricated. The RF power, total pressure during sputtering deposition and oxygen partial pressure were fixed at 100 W, 0.5 Pa and 1.9 mPa, respectively. The background pressure was evacuated below ~5×10^{-4} Pa. By optimizing the deposition time, the thickness of the film was adjusted to be 100 nm.

3. RESULTS & DISCUSSION

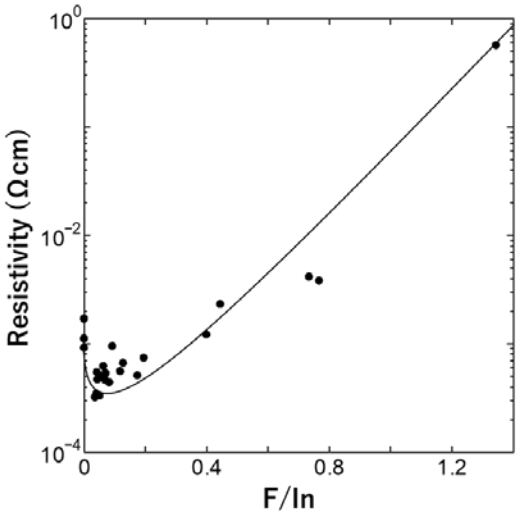

Fig. 1 Relationship between resistivity and F/In atomic ratio in the fabricated films.

Figure 1 shows the change in the resistivity as a function of F/In atomic ratio in the films, which is estimated by EDX results. The resistivity becomes low when F/In is around 0.04 at.%, and then it increases as the F content increases. This tendency is caused by the Ca content in the film, which will be discussed later.

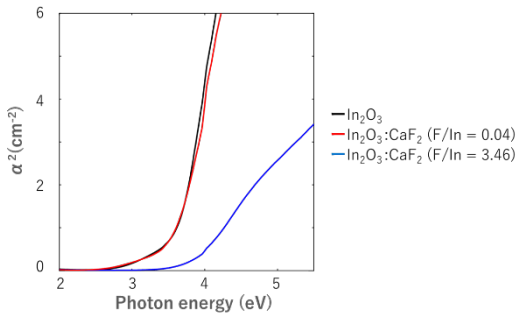

Fig. 2. Absorption coefficient as a function of photon energy of typical In_2O_3 and In_2O_3:CaF_2 films.

Fig. 2 shows the comparison of the In_2O_3, In_2O_3:CaF_2 (F/In = 3.46), and In_2O_3:CaF_2 (F/In = 0.04). The vertical axis is the square of the absorption coefficient (α^2), and the horizontal axis is the photon energy. The absorption coefficient α is calculated using the following equation:

$$\alpha = \ln(100T)^{-1}/d \qquad (1)$$

where T is the transmittance, and d is the film thickness.

The optical band gaps were estimated from Fig. 2 and were obtained 3.59, 3.82, and 3.61 eV for In_2O_3, In_2O_3:CaF_2 (F/In = 3.46), and In_2O_3:CaF_2 (F/In = 0.04), respectively. It is known that the transmittance in the visible region increases as the band gap increases, and the average transmittance in the visible region is 81.5, 89.5, and 83.1 % for In_2O_3, In_2O_3:CaF_2 (F/In = 3.46), and In_2O_3:CaF_2 (F/In = 0.04), respectively. Because CaF_2 has large band gap of 10 eV, the CaF_2 doping plays a role of increasing the transmittance of In_2O_3. [6]

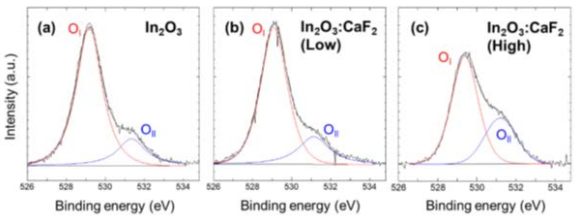

Fig. 3 Typical O1s XPS spectra of the fabricated films: (a) In_2O_3, (b) In_2O_3:CaF_2 (F/In = 0.04), (c) In_2O_3:CaF_2 (F/In = 0.77).

Figure 3 shows typical O1s XPS spectra of the fabricated films for (a) In_2O_3, (b) In_2O_3 (F/In concentration: 0.04, Low), and (c) In_2O_3: CaF_2 (F/In concentration: 0.77, High), respectively. The peak area ratio of In_2O_3, In_2O_3: CaF_2 (Low), and In_2O_3:CaF_2 (High) are 15.54, 19.43, and 32.76 %, respectively. The amount of O_{II}, derived from oxygen vacancy (V_O), tends to increase as the F/In at.% increases. This might be caused by Ca ions of CaF_2. The bond-dissociation energy of Ca-O (383.3 kJ/mol) is stronger than that of In-O (346 kJ/mol) [7]. This means Ca takes over O from In, thus V_O density increases. In the case of low F content ratio, F^- ions generate electrons by substitution of O_2^-, thus, sheet resistance decreased as shown in Fig. 1. On the other hand, in the high F concentration film, Ca and F are bound each other based on the bond-dissociation energy of Ca-F (556.5 kJ/mol), which is stronger than that of both Ca-O and In-O, then CaF_2 phase are formed and the film becomes CaF_2-rich insulator. We suppose that the phase change is obviously appeared at the F/In content of 0.2 .

4. SUMMARY

In this study, we focus on CaF_2 as a dopant into In_2O_3. The obtained resistivity and transmittance showed 3.1×10^{-4} Ωcm and 83.1 %, respectively, which are comparable to ITO. The XPS results showed that V_O content increases as the CaF_2 concentration increases. We believe that this is due to the strong bond-dissociation energy of Ca-O than In-O. As the F content increases, the optical band gap becomes larger, which is due to the increase in the amount of CaF_2 in the film.

References:

[1] B. G. Lewis, et al., MRS Bull. 25, 22 (2000).
[2] T. Minami, Thin Solid Films 516, 5822 (2008).
[3] K. Ellmer, et al., Thin Solid Films 516, 4620 (2008).
[4] F. Utsuno, et al., Thin Solid Films 496, 95 (2006).
[5] Y. Shigesato, et al., Jpn. J. Appl. Phys. 39 (b) 242, No. 10, 2041–2050 (2005),.
[6] H.Shi, et al., phys. stat. sol.2041, (2005)
[7] Y.-R. Luo, Comprehensive Handbook of Chemical Bond Energies (CRC Press, New York, 2007).

Emission Properties of Rocksalt-structured MgZnO Microcrystals for VUV Light Emitter

W. Kosaka[1,*], S. Hoshi[2], K. Kanta[1], K. Kaneko[2,3,4], T. Yamaguchi[1], T. Honda[1], S. Fujita[2,3] and T. Onuma[1]

[1] Department of Applied Physics, School of Advanced Engineering and Graduate School of Engineering, Kogakuin University, 2665-1 Nakano, Hachioji, Tokyo 192-0015, Japan
[2] Department of Electronic Science and Engineering, Kyoto University, Nishikyo-ku, Kyoto 615-8520, Japan
[3] Engineering Education Research Center, Kyoto University, Kyoto University, Nishikyo-ku, Kyoto 615-8530, Japan
[4] Photonics and Electronics Science and Engineering Center, Kyoto University, Nishikyo-ku, Kyoto 615-8520, Japan
*E-mail: cm21022@g.kogakuin.jp

Abstract

Rocksalt-structured (RS) MgZnO crystals are grown on quartz glass substrates by the mist chemical vapor deposition (mist CVD) method. Cathodoluminescence (CL) emission properties are comparatively studied with those for the RS-MgZnO epitaxial film prepared on MgO substrate to explore their potential for vacuum ultraviolet (VUV) emitter. Growths of RS-MgZnO on quartz glass substrate indicate formation of microcrystals (MCs). The MCs dominantly exhibit a near-band-edge VUV emission at 5.97 eV (208 nm) at 6 K and 5.77 eV (215 nm) at 300 K. Moreover, the MCs show a noticeable higher energy shoulder at 6.6 eV (188 nm) at 6 K and 6.4 eV (194 nm) at 300 K. The results ensure potential of RS-MgZnO crystals for active element in VUV emitter regardless of the substrate material.

Introduction

Deep ultraviolet (DUV) and vacuum ultraviolet (VUV) lights are expected to be utilized in various fields; such as virus inactivation, ozone generator, and nanofabrication. To develop the light emitters covering widely in DUV and VUV spectral regions, we are focusing on rocksalt-structured (RS) MgZnO alloys. Recently, we have succeeded in growth of atomically flat RS-MgZnO thin films on MgO substrates by the mist chemical vapor deposition (mist CVD) method. The epitaxial films exhibited cathodoluminescence (CL) peaks located in the DUV and VUV regions. [1,2] However, the use of MgO substrate still has some drawbacks, such as limitations in size and shape and its cost. Alternative use of quartz glass substrate has some advantages such as shape flexibility, lower cost, and applicability of traditional technology.

In this study, RS-MgZnO crystals are grown on quartz glass substrates by the mist CVD method. The RS-MgZnO film is also grown on the MgO substrate. Their emission properties are comparatively studied to correlate their crystallinity and optical properties.

Experiment

RS-MgZnO crystals were grown on quartz glass substrates by the mist CVD method.[1] The precursor solution was prepared by mixing magnesium chloride hexahydrate and zinc chloride as solute, and ultrapure water and acetic acid as a solvent in a ratio of 8:2.[1] The molar concentration ratio was set to [Mg]:[Zn]=9:1 with fixing a total molar concentration ratio [Mg]+[Zn] of 0.04 mol/L. Growth temperatures T_g were set as 700 and 750ºC. Oxygen gas was utilized as carrier and dilution gas. For comparison, a 270-nm-thick RS-MgZnO film was also grown on (100) MgO substrate with [Mg]:[Zn]=9:1, [Mg]+[Zn]=0.03 mol/L, and T_g=700ºC. The MgO molar fraction x in the RS-MgxZn1-xO was quantified by the energy dispersive X-ray (EDX) spectrometry. An acceleration voltage was set to be 15 kV.

Surface and panchromatic CL images were measured by a scanning electron microscope (SEM)-CL (SEM-CL) system at room temperature (RT). Acceleration voltage was set at 3 kV and the wavelength range in 190-800 nm was measured. The VUV transmittance and VUV CL were measured using a custom-built VUV spectroscopy system, [3] in which the optical path was filled with nitrogen gas. The VUV transmittance spectra were measured at RT using a monochromatic light in a wavelength range of 110-300 nm from deuterium lamp dispersed. A quartz glass longpass filter was used in a wavelength range longer than 200 nm to exclude the 2nd-order lights. The VUV CL spectra were measured in a wavelength range of 160-320 nm. The CL was excited by an electron beam operated at 5 kV with an emission current of 41 μA. The transmitted light and CL were detected using a solar-blind photomultiplier tube. Temperature was varied from 6 to 300 K.

Results and discussion

As shown in the surface SEM images in Figs. 1(a) and 1(b), RS-MgZnO crystals on the quartz glass substrates formed octahedral-shaped microcrystals (MCs). The 700ºC sample shows sparse growth of MCs with a size of about 1 μm. Meanwhile, the 750ºC sample shows dense growth of MCs with sizes

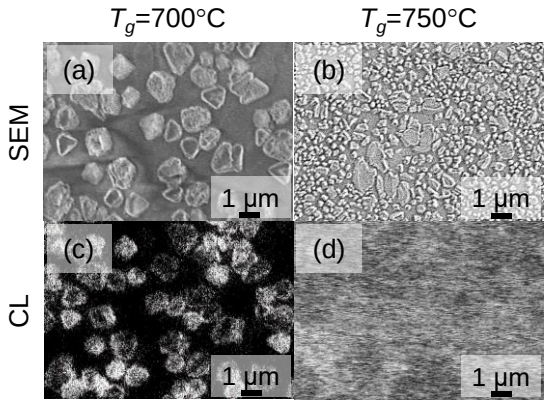

Fig. 1. (a) SEM and (c) RT panchromatic CL images of RS-$Mg_{0.93}Zn_{0.07}O$ MCs grown on quartz glass substrate at T_g=700 ℃. Corresponding data for RS-$Mg_{0.95}Zn_{0.05}O$ MCs grown at T_g=750 ℃ are shown in (b) and (d).

in a range of 100 nm to 1 μm. The averaged x for the MCs distributed in the range of 1 μm in diameter was evaluated by measuring about a hundred points by the EDX spectrometry. Histograms show a Gaussian distribution (data not shown). The averaged x for the 700ºC sample was 0.93 with a standard deviation of 0.01, and that for the 750ºC sample was 0.95 with a standard deviation of 0.03. As shown in Figs. 1(c) and 1(d), the panchromatic CL images represent similar features with the SEM images, confirming that the MCs produce the CL. Transmittance spectrum at RT for the 750ºC sample is shown in Fig. 2. Spectrum for the RS-MgZnO film grown on MgO substrate is also shown for comparison. Although the sparse growth for the 700ºC sample inhibits observation of the transmittance spectrum, the 750ºC sample allows us to observe the transmittance through the densely distributed MCs as follows. Partial gaps in between the MCs resulted in constantly 20% transmittance in the whole measured wavelength range (data not shown). To exclude the influence of the partial gaps on the spectrum, the lower end of 20% was subtracted. Then, all the spectra are normalized so that the transmittance is 100% at the maximum value. While the transmittance spectrum for the RS-$Mg_{0.92}Zn_{0.08}O$ film showed a sudden increase above 185 nm, the spectrum for the RS-$Mg_{0.95}Zn_{0.05}O$ MCs showed a gradual increase above 180 nm.

CL spectra of the MgZnO MCs grown on the quartz glass substrates at T_g=750°C are shown in Fig. 3(a). CL spectra for the RS-$Mg_{0.92}Zn_{0.08}O$ film grown on MgO substrate are also shown in Fig. 3(c) for comparison. Note that the spectrum at 300 K is multiplied by 10. All the spectra dominantly exhibit a deep UV luminescence (DUVL) band at around 5.7-6.0 eV. Strictly, the CL peak energies at 6 K (300 K) were 5.97 eV (5.77 eV) for the 750°C RS-$Mg_{0.95}Zn_{0.05}O$ MCs and 5.86 eV (5.66 eV) for the RS-$Mg_{0.92}Zn_{0.08}O$ film. Here, noticeable feature is observation of shoulders in a higher energy side for

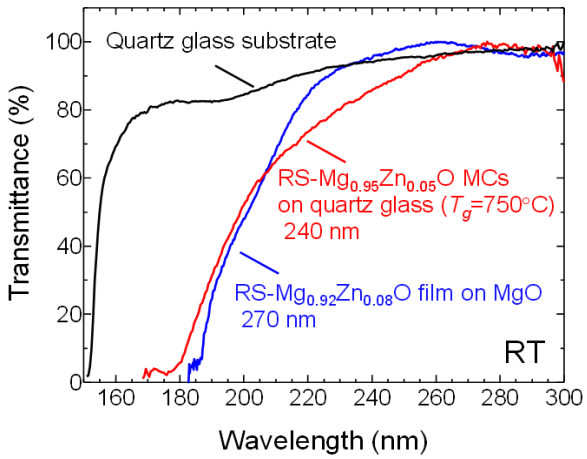

Fig. 2. Transmittance spectra at RT for quartz glass substrate, RS-$Mg_{0.95}Zn_{0.05}O$ MCs grown on the quartz glass substrate at Tg=750ºC and RS-$Mg_{0.92}Zn_{0.08}O$ film grown on MgO substrate.

the MCs grown at 750°C. i.e., the shoulders appeared

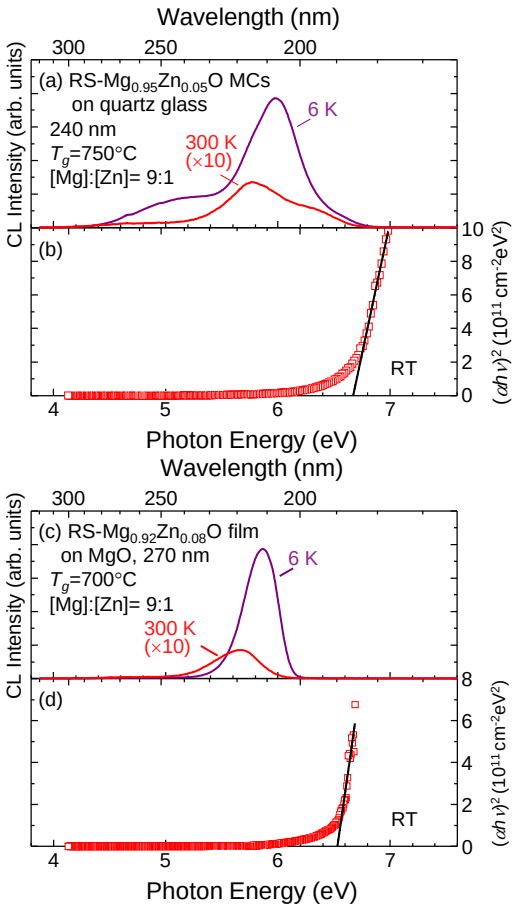

Fig. 3. (a) CL spectra at 6 and 300 K and (b) Tauc plot at RT for RS-$Mg_{0.95}Zn_{0.05}O$ MCs grown on quartz glass substrate at Tg=750°C. Corresponding data for RS-$Mg_{0.92}Zn_{0.08}O$ film grown on MgO substrate is also shown in (c) and (d) for comparison.

at 6.6 eV (6.4 eV) at 6 K (300 K). Obviously, the RS-$Mg_{0.95}Zn_{0.05}O$ MCs showed distinct near-band-edge emission in the VUV region, which has hardly been realized for the epitaxial films grown on the MgO substrates.

The Tauc plots for the RS-$Mg_{0.95}Zn_{0.05}O$ MCs grown at 750°C and the RS-$Mg_{0.92}Zn_{0.08}O$ film are comparatively shown in Figs. 3(b) and 3(d), respectively. The absorption coefficient α was calculated by the optical transmittance spectra at RT in Fig. 2 as $\alpha=\ln[(1-R)^2/T]/d$, where R, T, and d represent the reflectance, transmittance, and film thickness, respectively. Averaged thickness for the 750°C MCs was confirmed by cross-sectional SEM measurement to be 240 nm. The linear regressions give absorption edge energies as 6.67 eV for the RS-$Mg_{0.95}Zn_{0.05}O$ MCs and 6.53 eV for the RS-$Mg_{0.92}Zn_{0.08}O$ film. We found relatively large Stokes-like shift for the DUVL bands being 0.90 eV for the MCs and 0.87 eV for the film, where the Stokes-like shift was obtained by subtracting the CL peak energy at 300 K from the absorption edge energy at RT. The results are quite similar to those for the RS-MgZnO films grown on MgO substrates. [2,4] The observation of similar Stokes-like shift in MCs and film imply existence of deep tail state in MCs. However, observation of the higher-energy shoulder at 6.6 eV (6.4 eV) at 6 K (300 K) may be attributed to local fluctuation of x in between the RS-$Mg_{0.95}Zn_{0.05}O$ MCs. Distinct observation of the higher-energy shoulder at 300 K may imply a beneficial feature of MCs, i.e., self-organization of defect-free crystal may be promoted by the MC growth on the quartz glass substrate. Further studies are necessary to correlate the crystallinity and the emission properties in the MCs.

Conclusion

RS-MgZnO crystals were grown on quartz glass substrates by the mist CVD method. Formation of MCs was confirmed by the SEM-CL measurements. The VUV transmittance and VUV CL were measured using a custom-built VUV spectroscopy system. CL spectra showed noticeable differences in between the MCs and epitaxial film prepared on (100) MgO substrate: higher energy shift of the NBE DUVL band and observation of higher energy shoulders for the MCs. Obviously, the MCs showed distinct NBE emission in the VUV region, which has hardly been realized for the epitaxial films grown on the MgO substrates. The results ensure potential of RS-MgZnO crystals for active element in VUV light emitter regardless of the substrate material.

Acknowledgements

This work was supported in part by Grants-in-Aid for Scientific Research No. 20H00246 from MEXT, Japan. T.O. is grateful to Prof. A. Yoshikawa of Chiba University for his continuous encouragements.

References:

[1] K. Ishii, M. Ono, K. Kaneko, T. Onuma, T. Honda, S. Fujita, Appl. Phys. Express **12**, 052011 (2019).

[2] M. Ono, K. Ishii, K. Kaneko, T. Yamaguchi, T. Honda, S. Fujita, T. Onuma, J. Appl. Phys. **125**, 225108 (2019).

[3] T. Onuma, W. Kosaka, K. Kudo, Y. Ota, T. Yamaguchi, K. Kaneko, S. Fujita, T. Honda, Appl. Phys. Lett. **119**, 132105 (2021).

[4] T. Onuma, M. Ono, K. Ishii, K. Kaneko, T. Yamaguchi, S. Fujita, T. Honda, Appl. Phys. Lett. **133**, 061903 (2018).

Analysis of aerosol in urban city air using FIB-TOF-SIMS

Kentaro Sakai[1)], Shokei Tsuchida[1)], Noa Kato[2)], Masato Morita[2)], and Tetsuo Sakamoto[1, 2 *)]

[1)] Department of Electrical and Electronic Engineering, Graduate School of Engineering, Kogakuin University, Tokyo, Japan
2) Department of Applied physics, School of Advanced Engineering, Kogakuin University, Tokyo, Japan
*ct13087@ns.kogakuin.ac.jp

Abstract

There are many fine particles in atmosphere are called aerosol. We analyzed aerosol collected at Shinjuku Campus of Kogakuin University using an aerosol sampler. Our FIB-TOF-SIMS apparatus can analyze individual aerosol particles. The component distribution of both the surface and interior of each particle. Therefore, we obtained detailed nature of several types of aerosols in urban city air. This study can reveal the information of aerosol concerning its origin and impacts on human health.

There are many fine particles in the atmosphere. Those fine solid or liquid particles floating in air are called aerosol. Aerosols come from natural origin, such as pollen and yellow sand, and also from artificial activities in urban areas, such as railways and cars. For the analysis of aerosol particles, bulk analysis methods have been traditionally used. In the bulk analysis, the information of averaged element ratio with high accuracy can be obtained. However, the information of individual particles is disappeared. Therefore, it is difficult to compare the data of individual particle analysis with bulk analysis data and discuss the abundance ratio of particles [1]. In our laboratory, we developed an FIB-TOF-SIMS (focused ion beam time-of-flight secondary ion mass spectrometry) apparatus that can analyze individual particles of aerosol. The component distribution of the surface structure and internal structure of individual particles has been analyzed [2].

The other hands, many types of artificial aerosol were included urban air. In addition, it is known that various particles have health effects [3,4]. But the relationship between the type of aerosols and the impact of human health has not been clarified so far. In this study, we analyzed aerosols in urban air using the FIB-TOF-SIMS, and obtained specific structure of several types of aerosols.

In this study, aerosol particles were collected on a flat Si substrate (Nilaco, 0.5 mm thickness, 6x6 mm^2) by the lab-made aerosol sampler which can collect aerosol on flat substrate with uniformly by movable stage [5]. Then, detailed structural and component analysis were performed used by the FIB-TOF-SIMS.

Figure 1 shows an example of the TOF-SIMS imaging of some elements of a particle. This particle was mainly consisted of Fe, Cr and Mn. Therefor, we considered this was stainless steel particle. Other types of aerosol will be show at the conference.

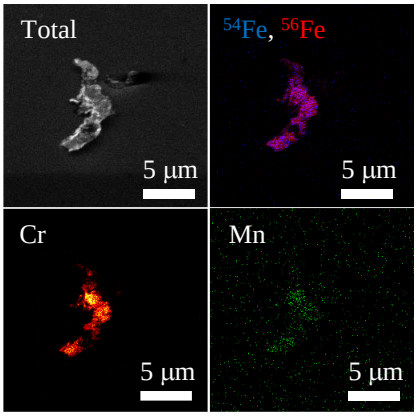

Fig. 1. Aerosol particle sampled in Shinjuku Campus.

References:

[1] N. Takegawa, A. Takami, *Earozoru Kenkyu*, **32**, 118-124 (2017).
[2] T. Sakamoto, M. Koizumi, J. Kawasaki, J. Yamaguchi, *Appl. Surf. Sci.*, **255**, 1617-1620 (2008).
[3] E. Vidrio, H. Jung, C. Anasatasio, *Atmos. Environ.*, **42**, 4369-4379 (2008).
[4] C. Arden Pope, R. Burrnet, M. Thun, E. Calle, D. Krewski, K. Ito, G. Thurston, *JAMA*, **287**, 1132-1141 (2002).
[5] K. Otsuka, M. Esaka, Y. Miura, T. Sakamoto, *BUNSEKI KAGAKU*, **63**, 317-322 (2014).

Validation of Spray Droplets by ESD for a New Technique of Single Cell Rapid Freezing

Takayuki Umemura[1], Kenta Shirasu[1], Masato Morita[2], Kumiko Nagase[3], Wakako Hamanaka[3], Masatoshi Kakihana[3], Tatsuo Ohira[3], Norihiko Ikeda[3] and Tetsuo Sakamoto[1,2*]

[1] Grad. Sch. of Electrical and Electronic Eng., Kogakuin Univ.,
2665-1 Nakano-machi, Hachioji, Tokyo, 192-0015 Japan
[2] Department of Applied Physics, Sch. of Advanced Eng., Kogakuin University,
2665-1 Nakano-machi, Hachiouji, Tokyo, 192-0015 Japan
[3]Tokyo Medical University Division of Thoracic & Thyroid Surgery,
6-7-1 Nishishinjuku, Shinjuku-ku, Tokyo, 160-0023 Japan
*ct13087@ns.kogakuin.ac.jp

Abstract

The need of the analysis of biological samples is increased recently. In medical field, the visualization of distribution of chemical elements and drugs in tissues are quite important. The application of TOF-SIMS analysis to biological material is expected as a high special resolution imaging technique. However, the TOF-SIMS apparatus is maintained under vacuum condition. Therefore, samples cannot be maintained natural living state. In this study, we developed a new rapid freezing method of biological sampale by ESD (Electro Spray Deposition). In addition, we varified the spray droplets using this system. We show that it is possible to rapidly freeze of cells by using this method .

1, Introduction

It is known that inorganic ions plays important roles of activity of cells[1]. In recent years, visualization of constituents has large demands. In fact, various kinds of both bulk analysis and local imaging analysis techniques have been developed[2]. However, micro-imaging of organelle-level has not been realized except fluorescent microscopy imaging. In our research group, a high lateral resolution Focused Ion Beam Time-of-Flight Secondary Ion Mass Spectrometer (FIB-TOF-SIMS) has been developed. This apparatus has the highest resolution of 40 nm in the world[3]. It promises element-imaging of organelle in a single cell for various inorganic species simultaneously.

The most important thing when a cell is analyzed with the TOF-SIMS is water in the cell, because the inside of the TOF-SIMS is high vacuum around 10^{-6} Pa. It is needed to perform a pretreatment for fixation of water, other than chemical fixative.

In this study, we devised a new rapid freezing method by combining electro-spray deposition (ESD) and metal-touch freezing. In this method, individual cells are sprayed as droplets emitted from the electro-spray tip, and each cells impact on the cooled metal surface, then frozen rapidly.

2. Experimental

First, the ESD was used to experiment with the spraying of a solution containing cells. 4-(2-hyrdroxyethyl)-1-piperazineethanesulfonicacid)(HEP-ES) is used as the medium at 0.1 M in water. Cultured human lung cancer cells (A549) were used in the experiment. Density of the cells in HEPES buffer solution was 1.0 x 10^5 cells/mL.

Next, we sprayed cells (droplets) on the cooled substrate and observed the droplets on the substrate with the TOF-SIMS. The spray was done twice at different distances.

3.Results and Discussion

Cells sprayed by the ESD was confirmed by viewing FIB-induced secondary electron images. However, the ESD spray at this high cell density was not stable. This is because of Taylor cone formation at the tip was affected by the excess cells.

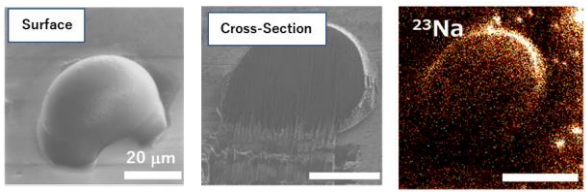

(a) Distance from the drawer electrode to the substrate : 4 cm

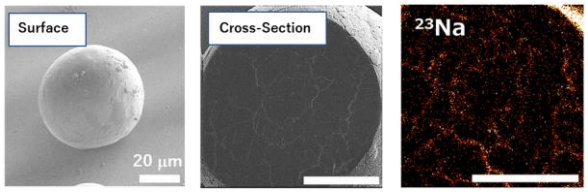

(b) Distance from the drawer electrode to the substrate : 6 cm

Fig1 : Droplets by ESD in SIMS

Figure 1 shows the difference between droplets when the distance from the ESD extractor electrode to cooled substrate was changed. In case of (a), where the distance was short, the droplet shape was not sphere but like a dome showing that the droplet col-

lided with the surface at a high speed. This resulted in also higher cooling (freezing), because the interior has no crystalline structures. In case of (b), the shape as changed to spherical. This means that the droplet was changed to ice before contacting with the surface. In this case, many grain boundary depicted by Na^+ ions were observed on the cross-section. This result shows that the difference in distance has a significant effect on the location of the droplet components. Detailed discussion will be included in the short presentation.

References:

[1] T. A. Stewart *et al*., *Biochimica et Biophysica Acta*, **1848**, 2502-2511 (2015).
[2] K. Ogasawara, *Plant Morphology*, **26** , 13-17(2014).
[3] T. Sakamoto *et al*., *Applied Surface Science*, **255**, 1617 (2008).

Anatase Thin-Film Fabrication by Novel Precursor Solution Involving Stable Trisoxalato Complex of Ti(IV) without O_2^{2-} Coordination

T. Murayoshi, H. Nagai, and M. Sato*

Electrical and Electronic Engineering Program, Graduate School of Engineering,
Kogakuin University of Technology and Engineering, Tokyo, Japan
E-mail: lccsato@cc.kogakuin.ac.jp

1. Introduction

Anatase, one of the most popular photoreactive materials, has long been investigated for degradation of organic pollutants, dissociation of water, and solar energy conversion [1]. However, the efficiency of photoreactions is limited by the absorption capability for visible (vis) light. Fabrication and their photo-reactivity of vis light-responsive thin films by the physical and/or chemical modification of anatase films has been investigated by many researchers, because of the importance of photoreaction with high reactivity under vis light. The fabrication of visible light-responsive films with enhanced UV sensitivity was achieved by our study [2]. Layer-structured anatase films were prepared by using a molecular precursor method (MPM), which uses coating solutions including the alkylammonium salts of an anionic Ti complex of EDTA and OX ligands in an Ar gas flow, where EDTA and OX represent ethylenediamine-*N*, *N*, *N*', *N*'-tetraacetic acid and oxalic acid, respectively.

However, this precursor solution with oxalato ligand had a problem to yield precipitates within one week, even though hydrogen peroxide (H_2O_2) was used as a usual stabilizer. In this study, we examined two kinds of titania precursor solution involving Ti^{4+} complex with oxalato ligand. We here report that a newly prepared solution with no use of H_2O_2 is stable for more than one week, and a transparent anatase thin film was successfully fabricated on a quartz glass substrate using the novel precursor solution.

2. Experimental

2.1 Preparation of Titania precursor solution (S_1; Ti : ox : H_2O_2 : $BuNH_2$ = 1 : 2.2 : 1 : 2)

Titania precursor solution **S_1** was prepared according to the procedures previously reported with slight modification [2]. First, 1.73 g (22.6 mmol) of butylamine, 3.28 g (24.9 mmol) of oxalic acid dihydrate, and 3.23 g (11.3 mmol) of $Ti(O^iPr)_4$ were mixed in 20 g of ethanol. The mixed solution was refluxed for 2 h and then cooled to room temperature. After adding 1.34 g (11.3 mmol) of 30% H_2O_2, the clear solution was refluxed for 0.5 h. The concentration of Ti^{4+} ion was 0.4 mmol g^{-1}. The white precipitates (**P_1**) formed after one month were collected on a paper filter and air-dried.

2.2 Preparation of Titania precursor solution (S_2; Ti : ox : Bu_2NH = 1 : 3 : 2.1)

In 20 g of ethanol, 3.46 g (26.3 mmol) of Bu_2NH and 4.75 g (37.5 mmol) of oxalic acid dihydrate were mixed. The mixed solution was refluxed for 1 h and then cooled to room temperature. After adding 3.66 g (12.5 mmol) of $Ti(O^iPr)_4$ the clear solution was refluxed for 3 h. The concentration of Ti^{4+} ion was 0.4 mmol g^{-1}. No precipitation appeared in the solution for more than one week.

2.3 Coating and heat-treating procedures

The solution **S_2** (200 μL) was dropped and spin-coated on a 20 × 33 mm^2 area of the quartz glass substrate. A spin-coating method at room temperature was used for forming precursor films with a double step mode; first at 500 rpm–5 sec and next at 2000 rpm–30 sec. The precursor film was pre-heated in a drying oven at 70°C for 10 min and then heat-treated at 500°C for 30 min in air. The obtained thin film is denoted as **$F_{Titania}$**.

2.4. Measurements

Elemental analysis of **P_1** was performed on a Perkin Elmer 2400 Series II CHN analyzer. The crystal structure of **$F_{Titania}$** adhered to the substrate was examined using an X-ray diffractometer using Cu *Kα* radiation-source at a power of 45 kV and 200 mA. The thickness of **$F_{Titania}$** was measured by a stylus profilometer. The transmittance spectrum of **$F_{Titania}$** was measured in the wavelength region of 200−1100 nm using a spectrophotometer in double-beam mode, and quartz glass substrate was used as a reference.

3. Results and Discussion

The elemental analysis result on **P_1** was as follows; C, 37.39 (37.11); H, 6.33 (6.23); N, 7.13 (7.22) %. The calculated values for $TiC_{12}H_{24}N_2O_9$ are given in parentheses and consistent with the found data. Therefore, the chemical formula of the insoluble **P_1** might be a chargeless complex, $[Ti(BuNH_2)_2(ox)_2]\cdot H_2O$. However, no precipitate was formed in another precursor solution **S_2**. It suggests that the chemical formula of this soluble complex is $(Bu_2NH_2)_2[Ti(ox)_3]$. Thus, the stable titania precursor solution involving Ti^{4+} complex of oxalato ligand without H_2O_2 was obtained.

The XRD peaks at 2θ = 25.5, 37.1, 38.0,48.2, 54.2, 55.3, 63.0, 69.1, 70.5, and 75.4° for **$F_{Titania}$** are assignable to (101), (103), (004), (200), (105), (211), (204), (116), (220), and (215) phases of anatase, respectively. The film thickness of **$F_{Titania}$** was 100 nm. The transmittance of **$F_{Titania}$** in the visible region is higher than 80%. The optical bandgap obtained by a Tauc plot was 3.4 eV. Thus, well-adhered and transparent anatase film was formed by heat-treating of the precursor film spin-coated on a quartz glass substrate, by applying the molecular precursor solution **S_2** with no use of H_2O_2.

References:

[1] K. Hashimoto, *et al*., *Jpn. J. Appl. Phys.*, **44**, 8269 (2006).
[2] H. Nagai, *et al*., *Sol. Energy Mater. Sol. Cells*, **92**, 1136 (2008).

Humidity dependency of the ionic conductivity of $Li_{1+x}Al_xTi_{2-x}(PO_4)_3$ transparent thin films fabricated by molecular precursor method

K. Aochi, H. Nagai, and M. Sato*

Electrical Engineering and Electronics Program, Graduate School of Engineering,
Kogakuin University of Technology and Engineering, Tokyo, Japan
E-mail: lccsato@cc.kogakuin.ac.jp

1. Introduction

All-solid-state (ASS) rechargeable lithium-ion-batteries (LIBs) have been received much attention, because they can provide safer LIBs with higher thermal and electrochemical stabilities than those using organic electrolytic solutions. $Li_{1+x}Al_xTi_{2-x}(PO_4)_3$ (LATP) is one of the Li-ion conductive ceramics with NASICON (Na super-ion-conductor) structure and of a promising candidate as a solid electrolyte.

We recently reported a photovoltaic lithium-ion-battery (PV-LIB), which can be also charged by solar-light irradiation, by using titania and $LiCoO_2$ (LCO) on fluorine doped tin oxide (FTO) pre-coated glass electrodes and an organic electrolytic solution involving Li^+ ion [1]. The thin films were fabricated by the molecular precursor method (MPM) developed by the present authors [2]. We here report the thin film fabrication of LATP (x = 0.3) and ASS-PV-LIB by using thin films fabricated with the MPM. The humidity dependence of the ionic conductivity of LATP thin fillm and charge/discharge voltage of ASS-PV-LIB was examined.

2. Experimental

2.1 Preparation of LATP precursor solution

The LATP precursor solution was prepared by mixing of the precursor solutions for Li_2O, TiO_2, Al_2O_3, and a source of PO_4^{3-}. These solutions were mixed according to the stoichiometric ratios of each ion. The obtained solution is denoted as **S$_{LATP}$**.

2.2 Coating and heat-treating procedures

The FTO glass substrate (20 × 33 × 1.1 mm^3) was etched using Zn powder and 20% HCl to separate the FTO layer into two equal parts. The LATP precursor films were obtained on the etched FTO glass substrate and quartz glass substrate (20 × 20 × 1.5 mm^3) by dropping 100 μL of **S$_{LATP}$**, spin-coating (1st step 500 rpm/5 s, 2nd step 2000 rpm/30 s), and preheating at 70°C in a drying oven for 10 min. The precursor film was heat-treated at 600°C for 180 min in air. The obtained film is denoted as **F$_{LATP}$**.

2.3 Measurements

The crystal phase of **F$_{LATP}$** adhered onto the FTO glass substrate was examined using an X-ray diffractometer using Cu *Kα* radiation-source at a power of 45 kV and 200 mA. The film thickness of **F$_{LATP}$** was measured by a stylus profilometer. The Li^+ ion conductivity of the thin films was measured by the AC impedance analyzer with FFT method. Impedance measurements of **F$_{LATP}$** at frequencies from 1 MHz to 0.1 Hz were performed using a Solartron 126096W under ambient temperature and the humidity of 20, 30, 50, 70, and 80%.

3. Results and Discussion

The film thickness of **F$_{LATP}$** on the quartz glass and FTO glass substrate was 60 and 40 nm, respectively. The XRD peaks at 2θ = 14.8, 21.0, 24.6, 29.7, 33.3, 44.5, 47.7, 50.2, and 57.5° for **F$_{LATP}$** fabricated on the quartz glass substrate are assignable to the (012), (110), (113), (024), (122), (200), (134), (315), and (410) phases of $LiTi_2(PO_4)_3$, respectively. The peaks at 2θ = 32.7, and 36.8° are assignable to the ($\bar{4}$12) and (215) phases of $LiPO_3$. However, the XRD patterns of **F$_{LATP}$** on the FTO substrate indicated only SnO_2 peaks. Figure 1 shows the Nyquist plots for **F$_{LATP}$**. The Nyquist plots under the humidity of 20, 30, and 50% were not useful to estimate the ion conductivity. On the other hand, in the cases of 70 and 80% humidity, the ion conductivity of 1.27×10^{-3} and 4.11×10^{-3} S cm^{-1} respectively could be determined by using the Nyquist plots. The dependence of the ionic conductivity of **F$_{LATP}$** on the humidity is agreed with that of the LATP (x = 0.3) powder reported very recently [3]. The humidity dependence of ASS-PV-LIB using the **F$_{LATP}$** will be discussed in the presentation.

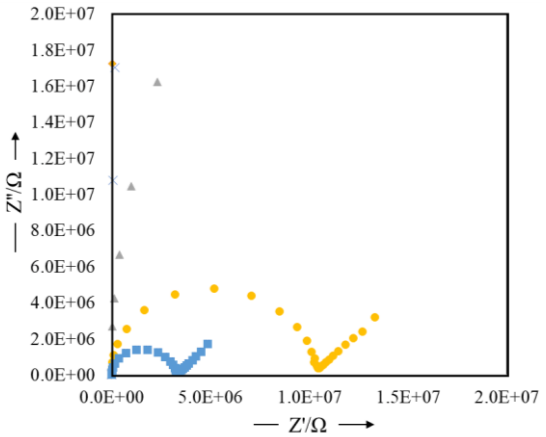

Fig. 1 Nyquist plots for **F$_{LATP}$** measured under ambient temperature and the humidity of ∗: 20, ◆: 30, ▲: 50, ●: 70, and ■: 80%.

References

[1] H. Nagai, et al. Funct. Mater. Lett., 9 (2016).
[2] H. Nagai, M. Sato, Adv. Coat. Mater. Wiley, (2018).
[3] H. Yamada, et al. J. Power Sources, 511 (2021).

Impact on InN Buffer Layer Inserted into GaInN/GaN Interfaces By RF-MBE

Daiki Itabashi, Ryosuke Yoshida, Tomohiro Yamaguchi, Takeyoshi Onuma, Tohru Honda
Department of Electrical Engineering and Electronics, Graduate School of Engineering, Kogakuin University, Tokyo, Japan
E-mail: cm21003@ns.kogakuin.ac.jp

Abstract

GaInN alloys are candidate materials for photovoltaic receiver in blue-light optical wireless power transmission (OWPT) system. In this study, GaInN films were grown on the GaN template by the RF-plasma-assisted molecular beam epitaxy for future application as an absorption layer in the OWPT system. Relaxation ratio of the GaInN films as high as 80% was achieved by inserting a thin InN buffer layer. The larger lattice of InN buffer layer was found to be favorable to enhance relaxation ratio of GaInN films.

Optical wireless power transmission (OWPT) is an innovative technology to supply electricity with a simple set up including light source and light receiving device [1]. GaInN based blue laser diode (LD) and light emitting diode (LED) are promising candidates for light sources in the OWPT system. It has been reported that GaInN with In composition of 20% is suitable for the photovoltaic receiver due to its high responsivity for blue light [2]. GaInN films have typically been grown on GaN on sapphire templates because of the unavailability of bulk GaInN substrates in the market. Although thick GaInN film is indispensable to sufficiently absorb the blue light in OWPT system, heteroepitaxial growth of GaInN on the GaN template induces plenty of crystal defects due to the lattice mismatch between GaInN and GaN. Therefore, it is necessary to fabricate a lattice-matched GaInN template. However, the relaxation ratio of high In composition GaInN has been achieved as high as 65% when the GaN is used as a substrate [3]. Therefore, it is necessary to develop a technique for growth of fully-relaxed GaInN on the GaN template.

In this study, GaInN films were grown on the GaN template by inserting a thin InN layer. The idea originates from the GaInN growths on sapphire (0001) substrates using an InN buffer layer [4]. Here, we employ the InN buffer layer as thin as a critical layer thickness to promote further relaxation of GaInN films.

The growths started from a10-nm-thick InN buffer layer at a growth temperature (thermocouple temperature) of 500°C for 2 min on the GaN templates by the RF-plasma-assisted molecular beam epitaxy (RF-MBE). Then, a 60-nm-thick GaInN layer was grown as a cap layer at a growth temperature of 500°C for 15 min. After that, a 400-nm-thick GaInN layer was grown for 60 min at different temperatures between 500 and 680°C. For comparison, GaInN layers were also grown without inserting the InN and GaInN cap layers at the same growth temperature range.

The films were evaluated by XRD reciprocal space mapping (RSM) measurement for GaInN diffraction spot to estimate In composition and relaxation ratio, simultaneously [5]. The samples were also evaluated by measuring X-ray rocking curve (XRC) profiles for the diffraction peaks to evaluate mosaicity of the crystal from the full width at half maximum (FWHM) values. Surface morphology was characterized by Field-emission scanning-electron-microscope (FE-SEM).

Relaxation ratio and XRC FWHM of GaInN (104) peak are shown as a function of growth temperature in Fig. 1. For the GaInN films grown at the lower growth temprature range, the relaxation ratio tends to increase and the FWHM values follow the same trend. The values gradually decreased with increasing the growth tenperature. By inseting the InN buffer layer, further relaxation of GaInN films were achieved up to the growth temperature of 675°C. The achievement may be due to the the fact that InN, which has a larger lattice constant than GaInN, is used as the buffer layer. The large lattice may enlarge the GaInN lattice resulting in the futher relaxation. As for the XRC FWHM in Fig. 1(b), values tend to decrease with increasing the growth temperature. But, further increase in the temperatre over 620°C caused an increase for the GaInN films using the InN buffer layer. Thermal decompositon of InN buffer is considered to be a major reason for the degradation. Currently, growth at around 620°C is an optimal condition. The results indicate that the InN buffer layer is favorable to enhance relaxation ratio of GaInN films.

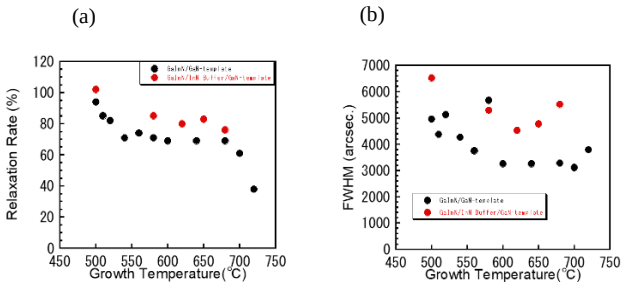

Fig. 1. (a) Relaxation ratio and (b) XRC FWHM of GaInN (104) peak as a function of growth temperature. Black and red symbols represent the data for the films with and without employing the InN buffer layer, respectively.

References:

[1] Y. Katsuta and T. Miyamoto, Jpn. J. Appl. Phys., **57**, 08PD01(2018).
[2] S. Valdueza-Felip *et al*., Sol. Energy Mater. Sol. Cells, **160**, 355(2017).
[3] Y. Nakajima Kogakuin University, M. D. Thesis(2019).
[4] AM. Hori et al., Phys. Stat. Sol. (b), **234**, 750(2002).
[5] S. Pereira et al., Appl. Phys. Lett., 80, 3913(2002).

Lightning Talk Session

Information and Communications Technology (ICT) & Intelligent and Secure Systems

November 23rd

Presentation No.	Title	Author	
ICTL1.	Design Thinking-based Requirements Elicitation Method using Role-Based Prototyping and its Evaluation	Senju Nakajima, Takayuki Kitagawa, Tadahisa Kondo, and Mari Inoki	230
ICTL2.	The bottleneck of MTD System Operation	Shintaro Kawamura, Osamu Mizuno	233
ICTL3.	A Study on Access Control Methods in IoT Data Distribution using Fog Computing	Masaki Yoshii, Ryohei Banno, and Osamu Mizuno	234
ICTL4.	Non-functional Requirements Summarization Method Using Convolutional Neural Network and Domain Ontology	Yuta Saikawa, Takeshi Nagaoka, Takayuki Kitagawa, and Mari Inoki	235
ICTL5.	Determination of intermittent defects by a method that focuses on the rows before and after the defective shot	Yusuke Takada, Yoshio Miki	239
ICTL6.	Transmission Control in DTN Considering Data Amount	Hiyu Suzuki, Osamu Mizuno	240
ICTL7.	Fast Adjacent Communication with RDMA and Double Buffering	Kota Yoshimoto, Akihiro Fujii, and Teruo Tanaka	242
ICTL8.	Preliminary Experiments for the Realization of ICN based Wireless Sensor Networks	Eishin Nagaoka, Masaki Yoshii, Ryohei Banno and Osamu Mizuno	245
ICTL9.	Personalization of Service Controller for Home Network Devices	Taich Kimura, Osamu Mizuno	247
ICTL10.	Parallelization of Automatic Tuning using Multiple Jobs for Machine Learning Programs	Sorataro Fujika, Teruo Tanaka, Akihiro Fujii, Yuka Kato, Satoshi Ohshima, andTakahiro Katagiri	248
ICTL11.	A Method for Detecting Anomalies in IoT Devices Using LSTM	Yutaro Nakamura, Osamu Mizuno	252
ICTL12.	A Study of Applying Plumtree Algorithm for Blockchain Networks	Yusuke Kitagawa, Kazuyuki Shudo, Osamu Mizuno, Ryohei Banno	253
ICTL13.	PAPR Reduction Effect by Applying Clipping in Spectrum Suppressed Transmission	Teppei Kanke, Takatoshi Sugiyama	254
ICTL14.	Performance Analyses of Efficient Belief Propagation Bit-flip Decoding Schemes for Polar Codes with Permutated Factor Graphs	Hidetoshi Saito, Naoya Takahashi	255
ICTL15.	Interleaving Depth Optimization for Concatenated FEC in 2.4GHz Ingenu System	Kentaro Yamamoto, Takatoshi Sugiyama	259
ICTL16.	Calculated Distance Error Performances by Relay Type GPS in Shinjuku Area	Kouhei Yoshida, Takatoshi Sugiyama	261
ICTL17.	The Child's Residual Limb Model Reconstruction by using Point Cloud Data	Ding-Horng Chen, Qiao-Ting Shen	263
ICTL18.	An Image Segmentation Method based on Unsupervised Learning Algorithms	Zong-Xian Yin	266
ISSL1.	Wired cable proposal on the feasibility of a stratospheric platform -Background and wired connections and strategies for orbital elevators-	Koichiro Murata	267

Design Thinking-based Requirements Elicitation Method using Role-Based Prototyping and its Evaluation

Senju Nakajima[1, a *], Takayuki Kitagawa[2, b], Tadahisa Kondo[1, c], and Mari Inoki[1, d]

[1]Department of Informatics, Graduate School of Engineering, Kogakuin University, Tokyo, Japan
[2]Toshiba Digital Solutions Corporation, Tokyo, Japan
E-mail: [a] em20013@ns.kogakuin.ac.jp, [b] Kitagawa.Takayuki@toshiba-sol.co.jp, [c] tkondo@cc.kogakuin.ac.jp, [d] m_inoki@cc.kogakuin.ac.jp

Abstract

This paper proposes a requirements elicitation method based on design thinking to substantiate customer empathy by combining design thinking and requirements engineering. In the proposed method, customer journey map creation, use-case modeling, and prototyping are incorporated into the problem-solving process using design thinking. The insights derived from customers using the customer journey map are substantiated via prototyping during the definition of software requirements. The proposed method was implemented at two workshops, and its performance in both cases was evaluated. The proposed method was demonstrated to be effective for discussions that not only reinforce solutions but also propose solutions from fragments of ideas.

In software product development, it is extremely important to improve the requirements definition process, which is used to clarify the customer's desires.

Conventional requirements elicitation methods utilize stakeholder analysis, scenario analysis, and use-case modeling to identify customer requirements from software products [1]. On this basis, the development process is performed by engineers. However, such methods suffer from the risk that the functional and non-functional requirements desired by the customer may not be satisfied by the final product.

Design thinking has emerged as a promising alternative to elicit customer requirements accurately. This creative problem-solving methodology was introduced by Tim Brown [2].

Design thinking comprises five steps—Empathize, Define, Ideate, Prototype, and Test (Fig. 1(a)). These steps are often repeated in practical applications of design thinking [3]. Even for beginner engineers, accurate elicitation of requirements from the user's perspective is essential to develop appropriate solutions.

Hehn et al. analyzed the artifacts created during the development process using design thinking and requirements engineering. Accordingly, they proposed an artifact model that considers connectivity using both methods [4]. However, the proposed procedure was not adequately detailed, even for beginner engineers to elicit user requirements accurately.

In this study, we propose a requirements elicitation method based on a combination of design thinking and requirements engineering to substantiate customer empathy.

The proposed method involves the construction of artifacts corresponding to a customer journey map, a use-case model, and a prototype, which Hehn et al. considered to be a bridge between design thinking and requirements engineering.

Fig. 1(b) depicts the role-based prototyping process, which combines design thinking and requirements engineering. The prototyping stage of the design thinking framework is repeated thrice while improving the created prototype. Each prototyping process comprises the following tasks—customer journey map (CJM) creation, use-case modeling, and prototyping.

During the prototyping step, the prototypes are classified into three categories corresponding to separate objectives based on the state of the requirements elicitation method. The first prototype involves substantiating ideas and confirming the actual desires of customers. The second prototype involves confirming whether the improvements being made are aligned with the customer's requirements. The final prototype is to support the decision regarding the ultimate resolution.

Fig. 1(c) illustrates the creation of the CJM and an example of a CJM (d).

Creation of the customer journey map consists of the following subtasks:

(c1) Defining the target persona and the scenario.

(c2) Extracting actions of the persona, assuming the behavior of the persona in that scenario.

(c3) Eliciting opponents that are contacted by the persona in the scenario.

(c4) Imagining the thoughts and feelings of the persona in that scenario.

(c5) Identifying the problems faced by the persona and evaluating their causes, prospective solutions, and the conclusions of other analysts.

During the creation of the CJM, the insights gathered from customers are analyzed and identified to comprehend the thought process and emotion of each persona. Accordingly, the obtained results are used to identify the problems faced by customers and develop suitable solutions. In this method, the insights obtained based on the CJM are substantiated using prototyping during the definition of software requirements.

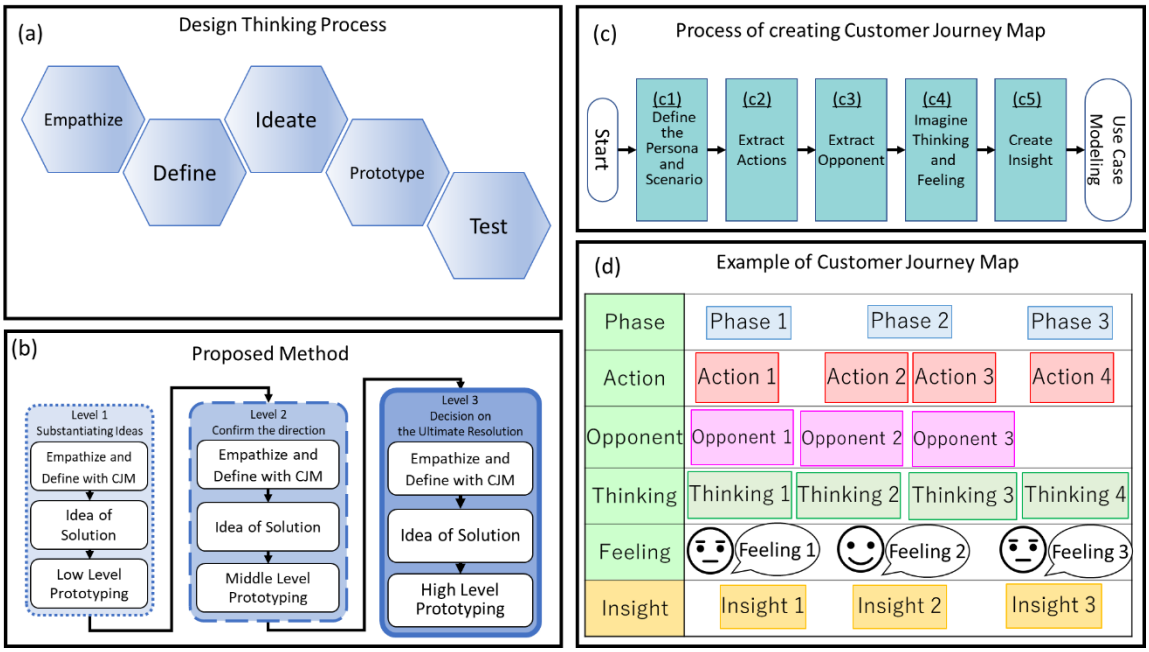

Fig. 1. Overview of the proposed method.

The proposed method was evaluated at the following two workshops:

- (w1) After defining personas, creating CJMs, and organizing ideas, prototypes were created and verified to provide feedback for further addition or modification of insights.
- (w2) The workshop process depicted in Fig. 1(b) was applied. In addition, a questionnaire-based survey was conducted after the workshop.

The participants at the workshops were engineers. Each participant was assigned a developer or customer role. The theme of both workshops was "Solving telecommuting telework problems by applying IoT-based services." The common goal was to create new business ideas to support telecommuting teleworkers. Table 1 lists the attributes of each workshop.

Table 1. Attributes of each workshop.

Workshop	Format	Duration	Number of Teams	Total number of participants
(w1)	Face-to-face	3 h	4	16
(w2)	Online	9 h	5	19

During the evaluation of the performance of the proposed method in the two cases, the insights obtained via the CJM were targeted. They were categorized as problems, solutions, or others. The insights gathered by the (w1) and (w2) teams are depicted in Fig. 2 and Fig. 3, respectively. In (w1), 47 insights were extracted in total by all teams. The average number of insights extracted by each team was 11.75.

In (w2), 75 insights were extracted in total by all teams. The average number of insights extracted by each team in (w2) was 10.71. The average percentage of extracted solutions was 9.5 and 7.43 for the (w1) and (w2) teams, respectively. In both cases, most of the extracted insights corresponded primarily to the solutions. In terms of the number of insights, no palpable difference was noticed between the two workshops.

Furthermore, the relationships between the insights appearing at Levels 1–3 in (w2) were analyzed. An insight is defined to be a "derived insight" if it is obtained via redefinition based on discussions at a subsequent level, in accordance with the insights defined at a lower level or by adding branching and new information. A total of 16 Level 3 derived insights were extracted from teams in (w2), at an average of 2.28 per team. The overall derivation rate was 21%.

The history of these insights at Level 1 and Level 2 were analyzed, and the following four patterns were identified:

(1) Problem → Problem → Solution
(2) Problem → Solution → Solution
(3) Solution → Solution → Solution
(4) Other → Other → Solution

The total number of insights corresponding to the four aforementioned patterns was 14, at an average of 2.00 per team.

In (w1), a task to improve the solution insights was also performed. The total number of derived insights was 8, at an average of 2.00 per team. The only pattern that emerged was solution → solution. This indicates that the solution was improved.

In (w1), the history of the consideration of insights was only discussed in a manner that reinforced the solution. However, in (w2), the discussion was based on the multiple perspectives of patterns (1)–(4).

A questionnaire-based survey was conducted after the completion of (w2). The respondents were asked to indicate their level of understanding and their capability of using the method in the future on a

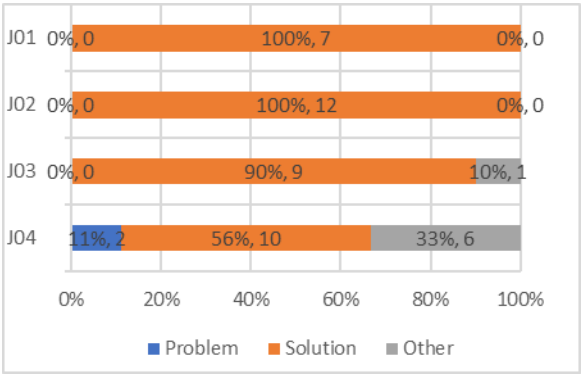

Fig. 2. Number of insights in (w1).

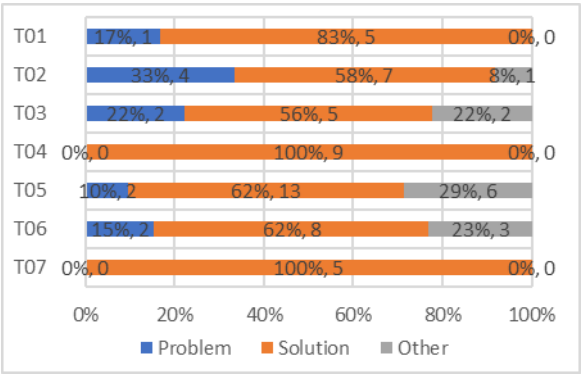

Fig. 3. Number of insights in (w2).

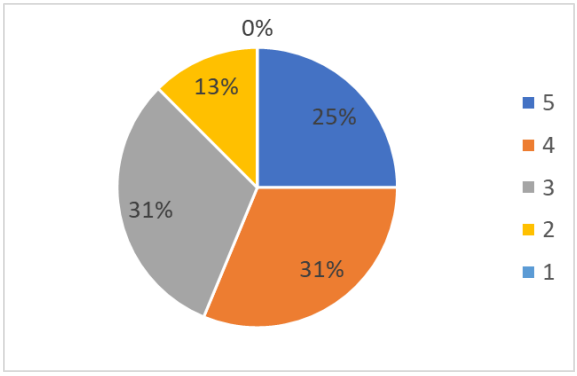

Fig. 4. Survey results on comprehension.

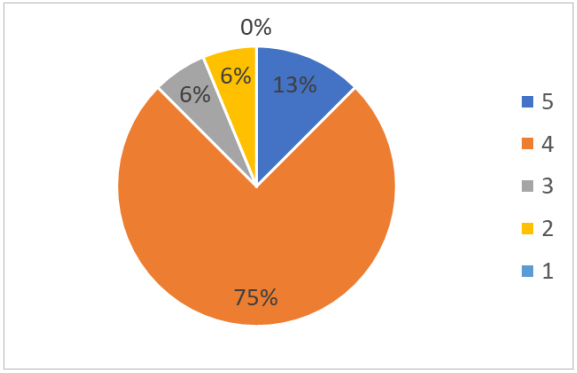

Fig. 5. Survey results on ease of future use.

5-point scale, with higher scores corresponding to better evaluation. The results are depicted in Figs. 4 and 5, respectively. With regard to comprehension, more than 80% of the respondents reported scores between 3 and 5. When asked if they could use the method in the future, more than 90% of the respondents reported scores between 3 and 5, which indicates superior performance.

Although the application of the proposed method in (w2) required more time for discussion than in (w1), it enabled the engineers to conduct active discussions and subsequently, review the discussion process. Therefore, the proposed method was more effective and reasonable in the second case in terms of obtaining requirements in a rational manner.

Herein, we proposed a method for eliciting requirements by combining design thinking and requirements engineering to create a confluence of empathy and co-creation. The proposed method was demonstrated to be effective for discussions that not only reinforce solutions but also propose solutions from fragments of ideas. In the future, we intend to continue using the method in other cases to improve it further.

Acknowledgements

This research was supported by the MEXT enPiT-Pro Smart SE: Smart Systems and Services Innovative Professional Education Program and the Research Organization of Information and Systems at Inter-University Research Institute Corporation.

References:

[1] Iso/IEC/IEEE 29148:2018, Systems and Software Engineering — Life Cycle Processes — Requirements Engineering, (2018).

[2] T. Brown, Change by Design, Revised and Updated: How Design Thinking Transforms Organizations and Inspires Innovation, Harper Business, (2019).

[3] Hasso Plattner Institute of Design at Stanford, An Introduction Design Thinking Process Guide, https://dschool.stanford.edu/resources/getting-started-with-design-thinking

[4] J. Hehn, D. Mendez, F. Uebernickel, W. Brenner, M. Broy, *IEEE Software*, **37**(2), 25–31 (2020).

The bottleneck of MTD System Operation

Shintaro KAWAMURA, Osamu MIZUNO

Department of Graduate School of Engineering, Kogakuin University, Tokyo, Japan
E-mail: cd20001@ns.kogakuin.ac.jp

Abstract

Moving Target Defense (MTD) is configured with heterogeneous web servers. In MTD, the webserver becomes the bottleneck in request processing capacity. It may cause a problem that reduces the entire system's performance. This paper reports that the bottleneck appears using the Apache webserver.

1. Introduction

Moving Target Defense (MTD) is an architecture that uses heterogeneous web service middleware to improve security performance. Sending random requests to heterogeneous middleware is expected to reduce the probability of success of attacks targeting vulnerabilities in specific middleware.

Zhang et al. [1] proposed heterogeneous database servers. They conducted experiments to determine the probability of a successful SQL query targeting a specific vulnerability. They reported that MTD could reduce the probability of a successful attack by 90% compared to the existing architecture.

In this paper, assuming that the results of [1] guarantee the security performance of MTD, we study the system operation issues applying MTD to webservers. There are many ways to implement daemons that provide web services, such as single-threaded and multi-processing.

2. Practical Experiment

The single-threaded method processes a particular request in parallel, so it can process requests at a higher speed. The multi-processing method processes requests sequentially by spawning child processes, so the request processing capacity varies depending on the number of processes. Nginx is a single-threaded web server, and Apache is a multi-processing web server.

If MTD is configured with Nginx and Apache, there is a risk of a difference in request processing capacity. In particular, if the request processing capacity of one of the web servers is lower than the other, the average processing capacity of the entire system is restricted.

To demonstrate whether such a problem occurs, we conducted a benchmark using the ab command [2] in the experimental environment shown in Figure 1. As shown in Figure 1, the client sends 100,000 requests to the MTD server with 100 users, and the MTD server manages Apache and Nginx running on different ports. By overriding the Port Forwarding setting at 60-second intervals, the MTD switches the web server that processes the requests from Apache to Nginx. To evaluate the difference in request processing capacity, the memory assignment for Apache and Nginx is limited to 100MB by *cgconfig*.

Figure 2 shows the benchmark results.

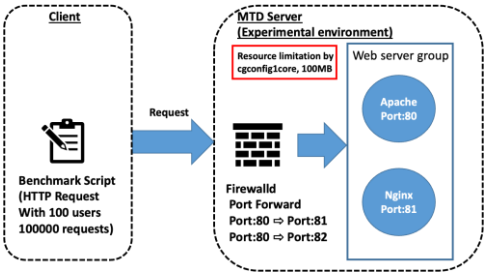

Fig. 1 Environment of the demonstration experiment

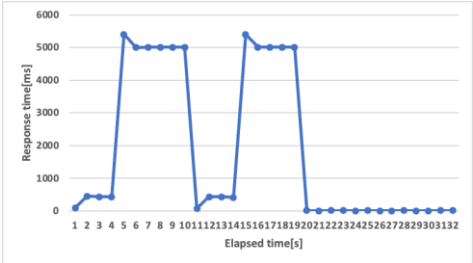

Fig. 2 Results of the demonstration experiment

3. Results

Figure 2 shows that Apache's maximum request processing time is 5403 [ms], and the maximum request processing time for Nginx is 8 [ms]. From the demonstration experiment, Apache becomes the bottleneck and reduces the processing capacity of the entire system. In summary, the performance of MTDs is degraded by the difference in request processing capacity that depends on the implementation method of the daemon. In future research, we will investigate methods to correct the difference in request processing capacity.

References

[1] Zhang J., Feng, X., Wang, D. and Ming, L., "Web Service Applying Moving Target Defense," IEEE International Conference on Data Science in Cyberspace (DSC), 2018.

[2] " ab - Apache HTTP server benchmarking tool",https://httpd.apache.org/docs/2.4/programs/ab.html (Reference 2021-09-22)

A Study on Access Control Methods in IoT Data Distribution using Fog Computing

Masaki Yoshii[1)], Ryohei Banno[2)], and Osamu Mizuno[1, 2)]

[1)] Department of Electrical Engineering and Electronics, Graduate School of Engineering, Kogakuin University, Tokyo, Japan
[2)] Department of Information and Communication Engineering, Faculty of Informatics, Kogakuin University, Tokyo, Japan
E-mail: cm20053@ns.kogakuin.ac.jp, banno@cc.kogakuin.ac.jp, omizuno@cc.kogakuin.ac.jp

Abstract

New services can use fog nodes to distribute Internet of Things (IoT) data. To distribute IoT data, we apply the publish/subscribe messaging model to a fog computing system. A service provider assigns a unique identifier, called a Tag ID, to a player who owes data. A Tag ID matches multiple IDs and resolves the naming rule for data acquisition. However, when the users set their fog nodes and distribute IoT data through multiple players, the distributed data would include private information. We propose a Table-based Access Control (AC) to manage data transmission permissions to solve this issue. This paper discusses two kinds of access control methods, Table-based AC and Ticket-based AC.

1. Introduction

Fog computing has been proposed to apply preprocessing techniques, such as machine learning and data cleansing of Internet of Things (IoT) data on fog nodes between IoT devices and cloud servers. Fig. 1 shows an overview of fog computing. Some cloud applications deploy on fog nodes to reduce congestion and transmission delay. Fog nodes analyze IoT data without sending the data to the cloud, and they send obtained results to service users. In addition, distributing IoT data via multiple fog nodes may lead to new services using IoT data.

However, it is possible that a user's published data, including private information, could be delivered to a service provider via a fog node without the user's permission. We propose a Table-based Access Control (AC) [1] and Ticket-based AC to solve this issue. The user can protect unintentional data distribution by setting "permit/deny" of data transmission for each service provider in the Table-based AC.

2. Table-based Access Control

Table-based Access Control has the elements of topics, the destination of IoT data in a User Fog Node (UFN), and permit/deny for data transmission.

By registering permission/denial of IoT data transmission in advance, the distribution of private data can be reliably protected.

Equation (1) gives the size of the table, where the size of the table is T_t, the number of IoT devices is T_{pub}, and the destination of the data is T_{sub}.

$$T_t = T_{pub} \times T_{sub} \quad (1)$$

The search time is $O(\log(T_t))$ using the binary search algorithm.

3. Ticket-based Access Control

Table-based AC requires the user to operate the Access control himself. Also, it is not possible to implement uniform access control among different players.

UFN and Service Fog Nodes (SFN) have a contractual relationship with the Ticket Authentication and Authorization Infrastructure (TAI). When SFN wants to receive IoT data from UFN, it generates a ticket and sends it to TAI. The TAI authenticates the ticket and stores it in its database. The UFN receives the ticket addressed to itself from the TAI and sends the IoT data to the SFN based on the content of the received ticket.

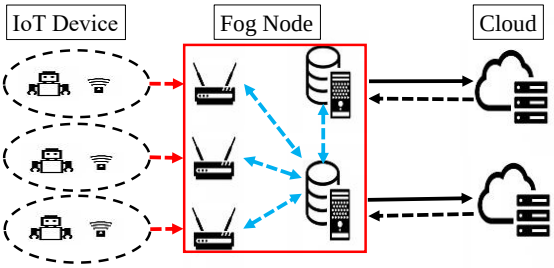

Fig. 1. Overview of Fog Computing.

4. Qualitative Evaluation

When comparing Table-based AC and Ticket-based AC in terms of security, Table-based AC requires users to register ACLs, which may be troublesome. In Ticke-based AC, if each player maintains a contractual relationship with TAI, TAI mediates Access Control.

Ticket-based AC is effective in preventing unauthorized access and spoofing because it authenticates and authorizes each player.

5. Conclusion

Table-based AC and Ticket-based AC are proposed and give qualitative evaluation. For future study, we will conduct evaluation by simulation.

Acknowledgments

Part of this research was supported by JSPS KAKENHI Grant Number JP18K11276.

References:

[1] M. Yoshii, R. Banno and O. Mizuno, "Evaluation of Table-based Access Control in IoT Data Distribution Method using Fog Computing," IEICE Communications Express, Vol.10, No. 10, Oct. 2021. DOI: 10.1587/comex.2021XBL0134.

Non-functional Requirements Summarization Method Using Convolutional Neural Network and Domain Ontology

Yuta Saikawa[1, a *], Takeshi Nagaoka[2, b], Takayuki Kitagawa[2, c], and Mari Inoki[1, d]

[1]Department of Informatics, Kogakuin University, Tokyo, Japan

[2]Toshiba Digital Solutions Corporation, Tokyo, Japan

E-mail: [a] j118093@ns.kogakuin.ac.jp, [b]Nagaoka.Takeshi@toshiba-sol.co.jp,

[c]Kitagawa.Takayuki@toshiba-sol.co.jp, [d] m_inoki@cc.kogakuin.ac.jp

Abstract

Technology that aids the summarization of documents is highly significant in accelerating the understanding of requirement specifications of large-scale information systems. The requirements specification of an information system include functional and non-functional requirements. This study focuses on the non-functional requirements, and proposes an automatic summarization method from a quantitative perspective. The proposed method is constructed by combining two automatic text classification technologies based on a convolutional neural network and domain ontology. It provides summarized data using the results of classification and quantitative visualization. Based on the evaluation, the proposed method is considered effective in risk prediction for insufficient non-functional requirements.

1. Introduction

Acceleration of social realization of digital transformation is essential [1][2][3]. Hence, it is important to analyze the requirements specification of existing information systems to propose a new digital business, based on current issues. In a complicated information society, there are multiple related information systems, and the scale of requirements specification for each system tends to be substantial. It is highly inconvenient for engineers, who are not involved in the development of such complicated and considerable systems, to understand and obtain the necessary information from the requirements specification. Generally, requirements specification are written in native language. Consequently, efforts to summarize requirements specification using summarization technology based on natural language processing technology have been studied [4][5]. Summarization using natural language processing technology often utilizes the semantic similarity and frequency of occurrence of words [6][7].

The requirements specification include functional and non-functional requirements [8]. Consider the following non-functional requirements: "This system must operate 24 h a day, 365 days a year." This is only a single sentence requirements; however, if it were to be overlooked in development, it would have a significant effect on the system operations. Among the non-functional requirements, there are various other significant requirements, even if the amount of description is small. Therefore, if non-functional requirements are summarized based on the frequency of the occurrence of a word, there is a substantial risk that important content would be missed. In addition, even if it is not explicitly defined in the requirements specification, there are non-functional requirements, such as usability and performance, that are implicitly required by the user in an actual operation. In the summarization of non-functional requirements, information that quantitatively and concisely depicts the situation is effective, such as which non-functional requirements are defined to what extent and which non-functional requirements are not defined. Therefore, in this study, the authors have proposed a non-functional requirements summarization from a quantitative aspect.

2. Problem and solution approach on automatic summarization of non-functional requirements

To understand the extent of the description of non-functional requirements of each type in the requirements specifications, the automatic classification technology of non-functional requirements is considered effective. Shreda and Hanani proposed a method for automatic classification based on Word2Vec and a convolutional neural network (CNN) for each type of non-functional requirements [9]. Younas et al. proposed a method of classifying non-functional requirements using ontology, to reduce the difficulty of preparing a significant amount of training data [10]. As the former method employs a general pre-trained model based on information including news articles, there is a risk that the accuracy of classification, specialized for non-functional requirements, will not improve. In the latter method, the defined ontology is limited; it is suggested that the accuracy of the classification would be further improved by enhancing the ontology. These methods are limited to classifying documents, and do not correspond to summarizing the entire requirements specification. Therefore, in this research, the authors have proposed (1) to combine three tasks for accurately classifying non-functional requirements into types—construct a CNN pre-trained model, integrate ontology, and extend the ontology to realize the automatic classification of non-functional requirements—and (2) to provide summarization data

using the results obtained from the classification and quantitative visualization.

3. Summarization from a quantitative aspect using CNN and domain ontology

Fig. 1 shows the outline of the proposed non-functional requirements in an automatic summarization method. In the proposed method, when requirement specification documents are provided, the non-functional requirements are classified into 12 types such as availability, operational, usability, and security, depending on the description of its contents. The number of non-functional requirements are quantitatively visualized based the types.

To classify the description of requirements based on the type of non-functional requirements, the authors used a consensus algorithm from the results of two methods: classification based on (a) CNN and (b) ontology.

3.1 Classification based on CNN

CNN is a machine learning technology that adds convolution to a CNN; it is widely used in the fields of image and video recognition and identification. Zhang et al. proposed a CNN pre-trained model that is effective for sentence classification [11]. In this study, the authors created a CNN pre-trained model using the training data labeled in advance, and classified the input non-functional requirements using the model.

3.2 Classification based on domain ontology

An ontology is a method that obtains semantic similarities between words, by defining the concepts that express the words and the relationships between the concepts. The pre-trained Word2Vec model was used as a synonym for the keyword defined in the ontology. Word2Vec, which is a natural language processing technology, is a library that can learn the semantic similarity of each word using a neural network and output the meaning of the input word as a multidimensional vector. In this study, the definition proposed by Younas et al. [10], non-functional requirements grade [12], and opinions of experts were used to define the ontology specific to non-functional requirements.

3.3 Summarization based on quantitative aspect

To improve the accuracy of the automatic summarization of non-functional requirements, the authors combined classification methods based on the CNN and domain ontology. Fig. 1 shows the processing flow using the proposed method. In CNN, the convolution is performed with four different filter sizes, which is followed by flattening, and eventually, each requirement is classified. Subsequently, the keywords of each type, defined in advance, are compared using the ontology. The classification result of the CNN is weighted to classify the requirements. Then, the number of non-functional requirements for each type is visualized from the quantitative perspective. According to the visualized summarization, the types of non-functional requirements with a small number of definitions or those that are undefined are clarified.

4. Evaluation

4.1 Evaluation method

The proposed method was evaluated using the following method.

Objective: The authors will clarify the effectiveness of the summarization using a quantitative perspective method according to the consensus of the CNN and the domain ontology.

Target data: Labeled requirements that included in "PROMISE Software Engineering Repository Dataset" [13] (hereinafter, referred to as "PROMISE").

Procedure:

(1) The authors conducted an experiment on data classification. The experiment comprised three tasks: Task1, Task2 and Task3. The authors compared the classification results of the three tasks. Task1, Task2 and Task3 classify the non-functional requirements using CNN, ontology, and the proposed consensus method of CNN and ontology, respectively.

(2) The precision, recall, and F-value of each task were calculated.

(3) The summarization of the non-functional requirements from a quantitative aspect is visualized based on the result of the consensus method.

4.2 Results

Table 1 shows the experimental results of applying this method. As shown in Table 1, the recall rate and precision rate of Task3 were improved compared to Task1. The recall rate of Task3 was improved compared to Task2. In Task3, the accuracy rate of the top three cases was improved by identifying requirements that are otherwise difficult to identify using CNN, let alone with ontology.

The summarization of Task3 from a quantitative aspect is shown in Fig. 2. The test data contain 99 non-functional requirements. In Task3, the method was applied to these test data.

5. Discussion

As shown in Table 1, in Task1 of only CNN, the accuracy of the classification decreased owing to the bias of the training data, such as an imbalance of definitions in some types of non-functional requirements. However, it was confirmed that the classification in Task3, combining the CNN and ontology, improved the accuracy of classification, and enabled summarization from a quantitative aspect even with a small amount of training data.

According to the summarization from a

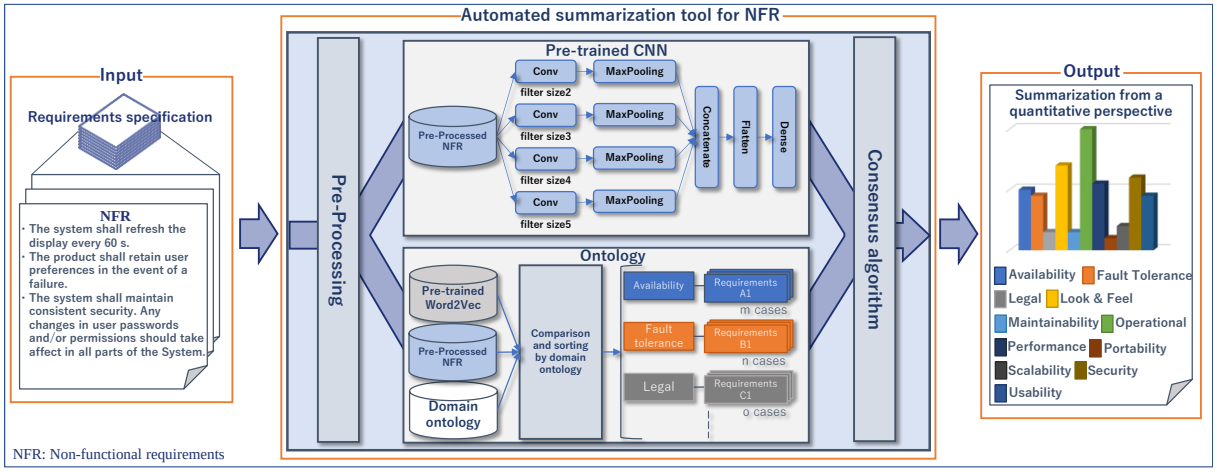

Fig. 1. Overview of the non-functional requirements summarization method.

Table 1. Results of the evaluation.

	Task1	Task2	Task3
Recall	0.343	0.490	0.495
Precision	0.345	0.395	0.389
F-value	0.324	0.332	0.377
Accuracy	0.464	0.313	0.464
Top 3 Rates of Accuracy	0.696	0.606	0.747

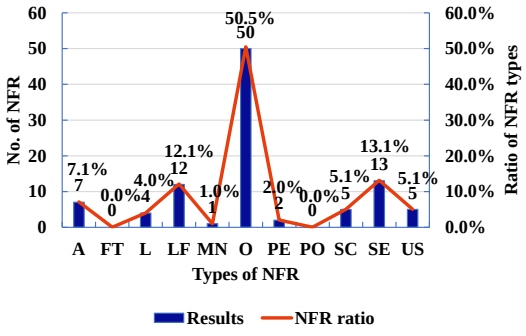

Fig. 2. Non-functional requirements summarization from a quantitative perspective produced by Task3.

quantitative perspective, resulting in non-functional requirements in Fig. 2, the requirements for fault tolerance and portability (PO) are less than other types in the requirements specification of the test data. The authors enquired an actual experienced engineer regarding the situation of PROMISE; the engineer pointed out "Compared to the requirements of other types, the definition of type PO is insufficient." The result of the summarization from a quantitative perspective includes the same points as those made by the engineer.

In addition, by visualizing the definition status of the non-functional requirements, as shown in Fig. 2, it is easy to identify the types of non-functional requirements that are insufficiently defined. Therefore, this method is considered effective for risk prediction for the omission of definitions for the non-functional requirements in requirements specification.

6. Conclusion

The authors proposed a method for automatic summarization of non-functional requirements. The proposed method is constructed by combining two automatic text summarization technologies based on CNN and domain ontology. The proposed method summarizes data using the results of classification, and visualizes it from a quantitative aspect. As the situation of description of non-functional requirements is clarified from the quantitative perspective, it is possible to highlight the risk of omitting definitions for non-functional requirements, inherent in the requirements specification. In the future, in addition to increasing the training data of the requirements specification, by expanding the keywords used in the ontology, the accuracy of the classification of non-functional requirements and high-quality summarization from a quantitative perspective will be improved.

Acknowledgment

This work was supported by JSPS KAKENHI (Grant No. JP19K11907).

References:

[1] B. Tabrizi, Put Employees at the Center of Your Post-Pandemic Digital Strategy, Harvard Business Review (2020).

[2] G. Doukidis, D. Spinellis and C. Ebert, *IEEE Softw.*, **37**, 13–21 (2020).

[3] The Ministry of Economy, Trade and Industry (METI), DX Report 2 (Interim Report), Compiled as Interim Report by Study Group for Acceleration of Digital Transformation, https://www.meti.go.jp/press/2020/12/20201228004/20201228004-1.pdf (Accessed 2021-10-6).

[4] A. Ferrari, *2018 ACM/IEEE 40th International Conference on Software Engineering: Companion Proceedings*, 536–537 (2018).

[5] F. Dalpiaz, A. Ferrari, X. Franch, and C.

Palomares, *IEEE Softw.*, **35**, 115–119 (2018).
[6] G. Goth, *Commun. ACM*, **59**, 13–16 (2016).
[7] M. Day and C. Chen, *2018 IEEE International Conference on Information Reuse and Integration (IRI)*, 478–484 (2018).
[8] ISO/IEC/IEEE 29148:2018, Systems and software engineering - Life cycle processes - Requirements engineering (2018).
[9] Q. Shreda and A. Hanani, *IEEE Access*, **4**, 1–22 (2016).
[10] M. Younas, K. Wakil, D. Jawawi, M. Shah and A. Mustafa, *IJACSA*, **10**, 539–547 (2019).
[11] Y. Zhang and B. Wallace, A Sensitivity Analysis of (and Practitioners' Guide to) Convolutional Neural Networks for Sentence Classification (2015).
[12] Information-Technology Promotion Agency, Japan, Non- functional requirements grades, https://www.ipa.go.jp/sec/softwareengineering/reports/20130311.html (Accessed 2021-10-03)
[13] PROMISE Software Engineering Repository Dataset http://promise.site.uottawa.ca/SERepository/ (Accessed 2021-04-23)

Determination of intermittent defects by a method that focuses on the rows before and after the defective shot*

Yusuke Takada[1-a], Yoshio Miki[1-b]

Department of Informatics, Graduate School of Engineering, Kogakuin University, Tokyo, Japan
E-mail: em21016@ac.kogakuin.ac.jp

Abstract

The purpose of this study is to identify the causes of intermittent defective products in injection molding machines using data analysis. An overall view of the injection molding machine is shown in Figure 1.

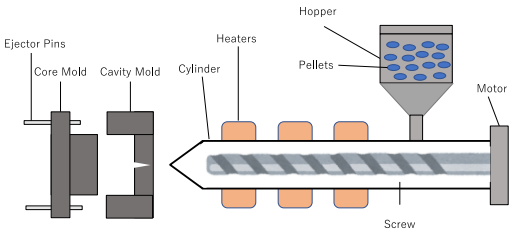

Fig. 1. Injection molding machine figure.

In recent years, there have been many scandals caused by inadequate quality assurance in product design and manufacturing, which has become a major social concern. The size of the product is not constant, but varies, and this variation causes a serious quality problem when defective products are not routinely produced and shipped as good products. The purpose of this study is to identify the cause of intermittent defective products in injection molding machines after the parameters are tuned and the machine enters the mass production stage. A simplified view of intermittent defective products is shown in Figure 2.

Fig. 2. Intermittent defective products figure.

In the past, Nakata et al. used the MT method to diagnose and predict the defects in hydraulic injection molding machines[1]. In addition, research has been conducted by Fukushima et al[2]. to study the determination of defective products by applying the MT method to image analysis data of products generated from injection molding machines.

However, the method using the MT system is not suitable for the prediction of intermittent defects. The reason is that there is no change in the parameters when a defective product is generated, but a defective product is generated. Therefore, the proposed method focuses on the rows before and after the defective shot in the numerical data with the aim of estimating the cause of defective products. By using this method, we were able to successfully identify several defective shots, and it became clear that we could estimate the cause of a defective shot not only by focusing on the explanatory variables at the same time as the result of the shot, as previously thought, but also by focusing on the time before and after the shot.

In the future, we will estimate the cause of defects based on parameters that change after a defect occurs. In addition to the average of the time before and after, we will also consider methods to identify when there is some kind of change in the time before and after.

References:

[1] M. Nakata, A. Sugiyama, H. Yamamura, N. Saito, S. Xu, H. Yano, “Determination and prediction of hydraulic injection molding process using MT system” *Quality Engineering*, **19-5**, 30-36 (2011).

[2] S. Fukushima, Z. Zhao, N. Kawata, “A Study on Shape Defect Discrimination of Molded Products Using Image Analysis” *Society for Precision Engineering*, **6-4**, 86-87(2018)

Transmission Control in DTN Considering Data Amount

Hiyu SUZUKI and Osamu MIZUNO

Graduate School of Engineering and Electronics Engineering Kogakuin University, Tokyo, Japan
E-mail: cm20030@ns.kogakuin.ac.jp

Abstract

DTN which provide direct communicates between mobile terminals is known as a useful method in the large-scale disaster. It is necessary to give priority to data which transmit in DTN at the time of disaster. Therefore, we propose the attribute-based transmission order control method (ATOC). However, since ATOC does not suppress transmission, there is a possibility of excessive data transmission and reception. In this paper, we propose a new data transmission control method based on ATOC. Simulation results show that the number of data transmissions of high-importance data is suppression to about 76 % and average about 75 %.

1 Introduction

Delay Tolerant Networking (DTN)[1] is one of the communication systems without using communication infrastructure in a large-scale disaster. DTN is “store and forward” data when the terminals pass each other. Epidemic Routing[2] is a typical routing method for DTN. We proposed that the attribute-based transmission order control method (ATOC)[3] that is a routing method using the importance of the data to be transfer under the limited condition. However, ATOC generates excessive transmission and reception of data. We improved ATOC to suppress amount of transmit data[4]. In this paper, the evaluation by the simulation is discussed.

2 Data Priority

We define data to be transmitted and received into the following two types.

・High-Importance data: Data created by public organizations, including data to be spread to disaster victims such as evacuation orders. It is evaluated by the data propagation rate of the proportion that there is no destination and spreads to the whole.

・Low-importance data: Data created by non-public organizations, such as personal safety confirmation messages, can be said to be important between users concerned, but the priority is lowered from the viewpoint of all participants. Since it is important to reach a specific destination, it is evaluated by the data arrival rate at the destination.

3 The attribute-based transmission order control method (ATOC)

By determining the transmission probability according to the importance of the data, high-importance data can be preferentially transmitted[5]. Here, the transmission probability is defined as the number of transmitted times divided by the number of transmission opportunities. However, since the data transmission order is defined randomly, there is a possibility of sending low-importance data first or retransmitting already spread high-importance data. ATOC can spread the high-importance data which has not spread by the former method. However, the transmission and reception of the excess data are carried out.

4 The modified attribute-based transmission order control method (MATOC)

4.1 Overview

In this paper, we propose a modified data attribute-based transmission control method (MATOC) which improves ATOC. The transmission probability is given in the preparation of the data, and it is changed by the existence of the request of the data.

To confirm the effectiveness of MATOC, we evaluate using The Opportunistic Network Environment simulator[6]. The evaluation objects are two of a transmission order control system according to ATOC and MATOC. The evaluation indexes are two of data propagation rate and data transmission number of the high-importance data.

We assume that 300 mobile nodes moving randomly at 0 ~ 1.0 m/s in a space of 250 × 250 m. The fixed node acts as a public institution in the center of the simulation area. It creates high-importance data. The low importance data is created and transmitted by two mobile nodes which are likened to the victim. The simulation time is 12 hours.

4.2 Data propagation rate results for high-importance data

Fig.1 shows the relationship between the data propagation rate of high-importance data and the number of data transmissions. In Fig.1, the X-axis indicates the number of data transmissions of high-importance data, and the Y-axis indicates the data propagation rate of high-importance data. The number of the high-importance data in Fig.1 is an average value extracted from several nodes. The darker color markers indicate older data, and the lighter colors indicate newer data. When MATOC is used, the data propagation rate of high-importance data is about 100 % compared with ATOC. Concretely, it was shown that the data propagation rate of the high-importance data decreased about 13 % at the largest and about 3 % on the average, when the increase value of the transmission probability is 40 % by MATOC.

4.3 Result of the number of high-importance data transmissions

As shown in Fig.1, MATOC suppresses the number of data transmissions compared with ATOC. Concretely, it was proven that the data transmission number of the high-importance data could be suppressed about 38 times at the maximum and about 26 times on the average, when MATOC with the increase value of transmission probability of 40 % was used.

5 Discussion

5.1 Data propagation rate for high-importance data

From 4.1, the data propagation rate of high-importance data is suppressed by using MATOC. This is because MATOC performs transmission control unlike ATOC. Moreover, the data propagation rate of the high-importance data is difficult to be 100 % in MATOC. The transmission control of MATOC becomes stronger as the data spreads. Therefore, the data propagation rate of the data made in the latter half of the simulation did not reach 100 %.

5.2 Number of high-importance data transmissions

From 4.2, by using MATOC, the suppression effect of the data transmission number of high priority data was confirmed. Nevertheless, since the data propagation rate of the high-importance data to be prepared at first is approximately equivalent to that of MATOC, the over-transmitted data could be suppressed.

5.3 Proper transmission probability

From the results in Section 4, we discuss the increase in the transmission probability of appropriate high-importance data. From the result of data propagation rate and data transmission number of the high-importance data, the appropriate increase value of the transmission probability is 40 %. Because the data propagation rate of the high-importance data is improved more than the increase value of 20 %, and the result is almost equivalent to 60 %. From Fig. 1, the results of data propagation rate of high-importance data are almost equivalent between 40 % and 60 %. Therefore, the transmission opportunity of the spread high-importance data is increasing, and the propagation of the unspread high-importance data is hindered. When the transmission probability is 20 %, the data propagation rate of the high-importance data is lower than when the transmission probability is 40 % even if the error bar is referred. Because the increase value is small, and the case in which the data is not sent, even if it is requested, increases. Therefore, 40% is appropriate for the increase value of the transmission probability.

Additionally, the increase value 40 % of the transmission probability is effective from the point of the data transmission number of the high-importance data. The increase of the transmission probability of 40 % can suppress the data transmission number of the high-importance data compared with ATOC. Also, the data transmission number of the high-importance data can be suppressed even if the data propagation rate of the high-importance data is compared with the rise value 60 %, which is almost equivalent. Therefore, to reduce the excessive resource consumption of smartphones, it is recommended to increase the transmission probability to 40 %.

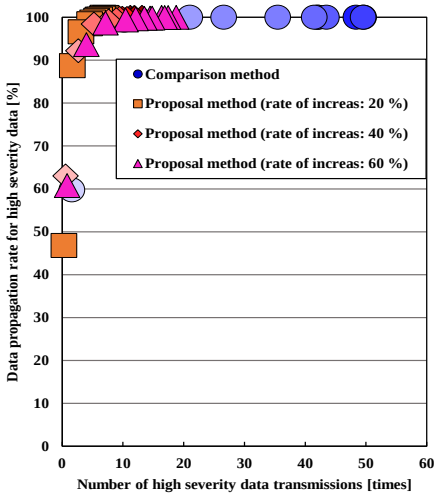

Fig. 1. Results of data propagation rate and number of data transmissions for high-importance data

6 Conclusion

In this paper, we propose MATOC for DTN data transmission and show suitable increase value of transmission probability is 40%/ As a future study, whether the rise value of the appropriate transmission probability is equivalent, when the simulation area is changed.

Acknowledgements

Part of this research was funded by JSPS Grant-in-Aid JP18K11276.

References:

[1] S. Farrell et al., "When TCP breaks: Delay-and d isruption-tolerant networking, " IEEE Internet C omputing, vol.10, no.4, pp.72-78, 2006.

[2] A Vahdat and D. Becker, "Epidemic routing for partially connected ad hoc networks," Technical report, CS-2000-06, Duke University, 2000.

[3] H. Suzuki at el., "Queuing Method in DTN Focusing on the Importance of Data, " IEICE Technical Report, vol. 120, no. 297, NS2020-87, pp. 1-6, 2020.

[4] H. Suzuki at el., "Suppression for Replication Number in Transmission Order Control Method by DTN, " IEICE Gen. Conf. Mar., 2021.

[5] H. Suzuki at el., "Data Transmission Control Met hod in DTN Focusing on the Importance of Data, " IEICE Gen. Conf. Mar., 2020.

[6] Ari Keränen at el., "The ONE simulator for DTN protocol evaluation, " Simutools '09: Proceedings of the 2nd International Conference on Simulation Tools and Techniques, Article 55, pp.1-10

Fast Adjacent Communication with RDMA and Double Buffering

Kota Yoshimoto, Akihiro Fujii, Teruo Tanaka

Department of Informatics, Graduate School of Engineering, Kogakuin University, Tokyo, Japan
E-mail: k221013@ns.kogakuin.ac.jp

Abstract

We are researching interprocess communication used in highly parallel computers. RDMA is one of the methods for speeding up it. In this research, RDMA with double buffering was applied to one-to-one communication and adjacent one to evaluate the performance. It was found out that RDMA with double buffering was the fastest compared it to MPI etc. in both one-by-one communication and adjacent one to multiple processes.

1. Introduction

In large-scale scientific computing programs, parallelization by MPI communication is widely used. MPI is convenient because it can be run on many computers. However, interprocess communication often becomes a bottleneck in highly parallel computers. [2] RDMA (Remote Direct Memory Access) is an interface to reduce the delay caused by communication. RDMA communication can be performed at high speed by writing data directly to the memory of the destination node. However, it is asynchronous communication and data may be overwritten during calculation. Therefore, synchronization is required to maintain data consistency. Double buffering is a method that can maintain data consistency without synchronizing it. In this research, the performance of RDMA communication and double buffering were measured. MPI, RDMA, RDMA with double buffering were compared in performance by one-to-one communication and adjacent communication.

2. Interprocess data communication

2.1 Adjacent communication

Fig. 1 shows the model of adjacency communication used in this experiment. When the number of adjacencies is 4, it communicates with the two before and the two after the process.

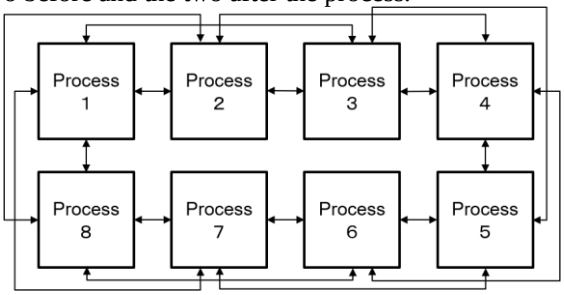

Fig. 1. Adjacent communication model

2.2 MPI_Isend/Irecv

Communication completion is done by MPI_Waitall call that waits for all communication calls finished.

2.3 RDMA

RDMA communication can read and write data without the intervention of the program of the destination node by using a dedicated memory, and it is possible to communicate at a higher speed than that by MPI. With the computer used in this experiment, it is possible to select transmission completion notification and reception completion notification. However, this time, the completion of transmission was confirmed by providing a notification area in the memory and waiting for the completion of the change with a spin wait.

3. RDMA with double buffering (RDMA_DB)

In normal RDMA communication, the source node writes data, ignoring the status of the destination node. The data may be overwritten without its consistency. Therefore, it is necessary to synchronize in order to maintain it. In RDMA with double buffering, two buffers for communication are prepared: when the data in the buffer is read, the other buffer communicates. The destination node does not send the next data until the data has been read. In addition, the source node waits for the data sent by the destination node to be received. There is no delay in sending and receiving data more than once, and data is not overwritten by using double buffers. As a result, data consistency can be maintained without synchronization processing, and high speed can be achieved. Fig. 2 shows a flowchart of the operation image.

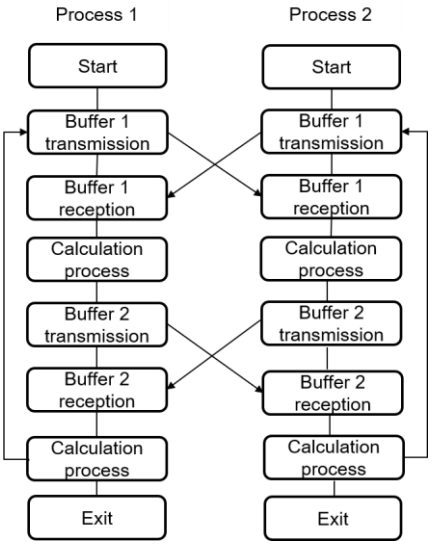

Fig. 2. Flow chart of double buffering

4. Numerical experiment

4.1 Experimental conditions / computer

In this experiment, MPI communication, RDMA one, and RDMA one with double buffering were evaluated by one-to-one communication and adjacent one, respectively. In one-to-one communication, one

process per node was measured by changing the number of data for two processes. In adjacent communication, evaluation was made in two cases. In one case, the number of adjacent processes was fixed and the total number of processes was changed. In another case, the total number of processes was fixed and the number of adjacent processes was changed. In both cases, the data size is fixed at 160. When the whole process was changed, the adjacent processes were fixed at two. In addition, the number of nodes was adjusted so that there were 4 processes per node. When the number of adjacent processes was changed, the total number of nodes was fixed at 16 and the number of processes was fixed at 128. Table 1 shows the computing environment. Table 2 shows the experimental conditions.

Table 1. Computer used for the experiment [1]

System	FUJITU PRIMEHPC FX1000
CPU	A64FX
Compiler	Fujitsu C / C ++ compiler
Communication Library	Fujitsu MPI

Table 2. Experimental conditions

	Double precision data	Total number of processes	Adjacent processes
Fig.3	From 10 to 1280	2	1
Fig. 4	160	From 8 to 64	2
Fig. 5	160	128	From 2 to 32

4.2 Experimental Results / Discussion

Fig. 3 shows the results of one-to-one communication. Its vertical axis represents time, while its horizontal axis represents the number of double-precision data. It shows that RDMA with double buffering was the fastest, followed by MPI normal RDMA, and finally normal RDMA. RDMA with double buffering is the fastest because it does not require synchronization. MPI and RDMA were faster than MPI is that in one-to-one communication. This is probably because the programs written in MPI are also optimized by the compiler like the one written in RDMA.

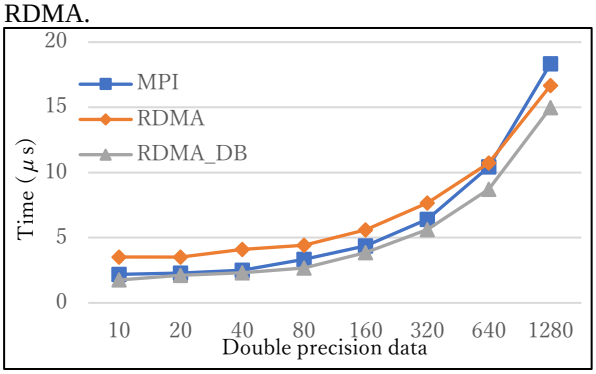

Fig. 3. One-to-one communication

Fig. 4 shows the case where the total number of processes is changed by adjacent communication. Its vertical axis represents time, while its horizontal axis represents the number of processes. The communication time did not change much though the total number of processes was changed. This is because the amount of communication per process does not change even if the total number of processes is increased. In addition, unlike one-to-one communication, RDMA with double buffering was the fastest in adjacent one, followed by RDMA, and finally MPI. RDMA communication with double buffering was the fastest for the same reason as one-to-one one. As a result of comparing RDMA and MPI, it is presumed that what was described by MPI was not corrected like the one described by RDMA. It is because adjacent communication is more complicated than one-to-one one.

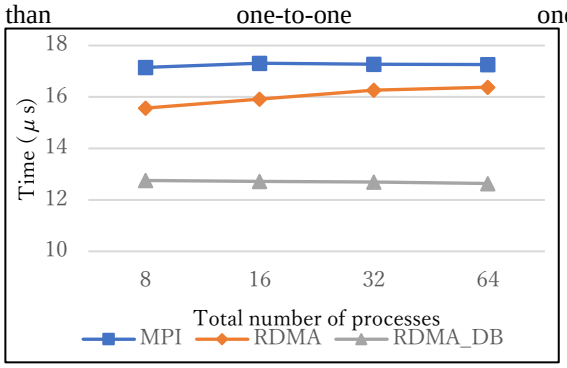

Fig. 4. when the total number of processes is changed by adjacent communication

Fig. 5 shows the case where the number of adjacent processes is changed by adjacent communication. Its vertical axis represents time, its horizontal axis represents the number of adjacent processes. As a result, the communication time increased proportionally when the number of adjacent processes was changed. It is because changing the number of adjacent processes increases the amount of communication per process. In addition, in RDMA, MPI, and RDMA with double buffering, the time difference widened as the number of neighbors increased.

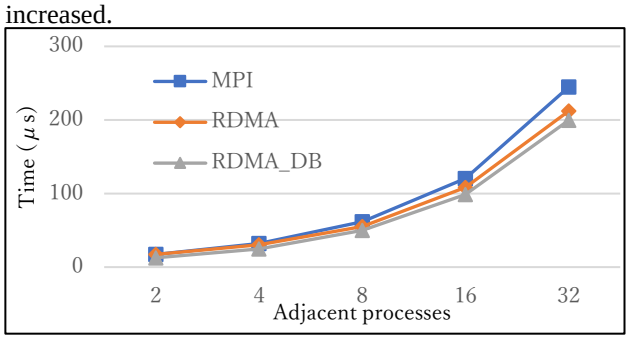

Fig. 5. When the number of adjacent communication adjacent processes is changed

5. Conclusion

MPI, RDMA and RDMA, with double buffering were evaluated using one-to-one communication and adjacent communication. It showed that RDMA was faster than MPI as the number of adjacent processes increased. In addition, RDMA with double buffering reduced synchronization and was the most efficient communication method of the three.

Further research on the way to apply this technique

to application programs using adjacent communication.

References:

[1] Super computer “Flow Type I subsystem”, Nagoya Univerisyty <https://icts.nagoya-u.ac.jp/ja/sc/>

[2] Kanamori Issaku, et al., *Acceleration of communication with low latency uTofu interface in LQCD application*, IPSJ SIGHPC report, Vol.2020-HPC-177 No.22 (2020).

Preliminary Experiments for the Realization of ICN based Wireless Sensor Networks

Eishin Nagaoka[1)], Masaki Yoshii[1)], Ryohei Banno[2)] and Osamu Mizuno[1, 2)]

[1)] Department of Electrical Engineering and Electronics, Graduate School of Engineering, Kogakuin University, Tokyo, Japan
[2)] Department of Information and Communication Engineering, Faculty of Informatics, Kogakuin University, Tokyo, Japan
E-mail: cm21037@ns.kogakuin.ac.jp, cm20053@ns.kogakuin.ac.jp, banno@cc.kogakuin.ac.jp, omizuno@cc.kogakuin.ac.jp

Abstract

We have proposed an Information-Centeic Networking based Wireless Sensor Network (ICSN) to provide multiple Internet of Things (IoT) services. Also, we have proposed an ICSN Platform (ICSNP) that provides the functions of executing IoT services in sink nodes. To implement ICSN, it is necessary to clarify the characteristics of RTT in the communication between sink nodes and sensor nodes. This paper measured the latency of sensor data acquisition in ad-hoc communication between sink node and sensor node to realize ICSN using Cefore. As a result, there are no harmful effects of acquisition delay due to the variation of communication distance. the RTT characteristics of ICSN with the variation of 1m communication distance are clarified.

1. Introduction

Internet of Things (IoT) services are attracting attention because sensors collect data autonomously and send them to the cloud via gateways. Ordinary IoT services need individual sensor networks. When a new IoT service is provided, a new sensor network is required. Therefore, each time a new IoT service is introduced, the number of sensor networks increases. As a result, construction and management costs are rising. To solve this problem, we have proposed Information-Centric Networking based Wireles Sensor Network (ICSN), which applies Information-Centric Networking (ICN) to sensor networks, to provide multiple IoT services on existing sensor networks[1]. Also, we have proposed an ICSN Platform (ICSNP) as a platform to execute user requests for IoT services[2]. These enable the early deployment of an environment where multiple IoT services exist in a single sensor network. We have shown the effectiveness of ICSN through simulation and emulation. However, it is necessary to clarify the characteristics of RTT between sink node and sensor node to implement the ICSN. This paper evaluated the delay time of sensor data acquisition when the distance between the sink node and the sensor node was varied.

2. ICSN

ICSN is a network that applies ICN to sensor networks. Fig. 1 shows ICSN. The sensors are dispatched to several areas. One of the dispatched sensors acts as Cluster Head (CH) in each area.

Fig. 1 shows an example of ICSN operation. First, the sink node sends "*B/temperature*" on Interest to a temperature sensor in Area B through the CH in Area A (CH_A). When the CH_B receives Interest, it checks required kind of data. After confirming that the request is for a sensor in the area, it sends Interest to

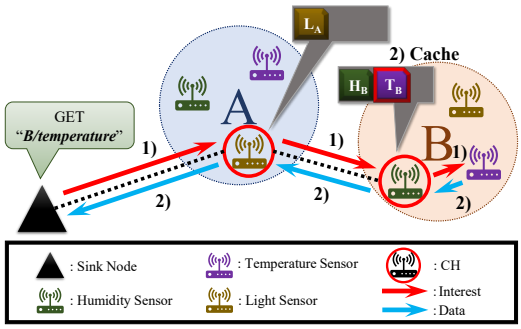

Fig. 1. ICSN.

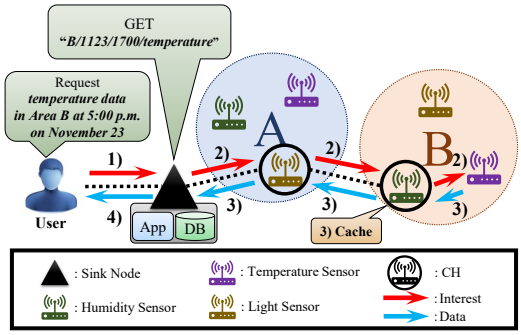

Fig. 2. ICSNP.

the target sensor and acquires the data for Data message. At this time, the received data is cached and then transferred. When the CH_A receives data, it transfers the data without caching because the sensor data came from another area.

3. ICSNP

ICSNP is a platform that realizes the processing of user requests and the execution of IoT services in ICSN. The sink node includes the application and the database. The user accesses the application and requests to acquire or refer sensor data. Also, it converts such user's request to interest message for ICSN.

Fig. 2 shows an example of ICSNP operation. First, the user accesses the application in the sink node and she/he inputs the request information to acquire sensing data. For example, she/he wants to acquire temperature in Area B at 5 p.m. on November 23. The sink node converts the request information into data ID, such as "*B/1123/1700/temperature*", and it sends an Interest to the sensor device. The following operation of the sensor device is the same as ICSN. After receiving the sensor data, it registers the data in the database. After that, it outputs the result to the user in the application.

4. Evaluation

To realize ICSN, we execute preliminary experiments to communication between sink nodes and sensor nodes. Table 1 indicates the experimental parameters. For each node, we used Cefore[3], an OSS that realizes the communication environment of ICN. Moreover, we use XAMPP[4] and MariaDB[5] for the web application and database in ICSNP. We vary the distance between the sink node and the sensor node 1 to 11m by 1m. The evaluation index is RTT. Fig. 3 and Fig. 4 are the experimental results.

As shown in Fig. 3, the RTT is relatively long when the first Interest is sent, and it becomes almost constant after that. Also, there was almost no change in RTT due to changes in communication distance. The delay is caused by establishing a new session with the sensor node when sending the first Interest. As shown in Fig. 4, the RTT for each communication distance showed almost no variation in RTT for all communication distances. These results confirmed that the communication between sink node and sensor node in ICSN has almost no delay effect on RTT even when the variation of 1m occurs.

5. Conclusion

In this paper, we have conducted preliminary experiments to formulate the communication between sink nodes and sensor nodes for the realization of ICSN. From the results, it was confirmed that there was almost no delay in the RTT due to the variation of the communication distance, and the RTT was almost unaffected by the variation of 1m.

In the future, we will measure the resource load, processing load, and RTT of each node to realize ICSN in a field.

Acknowledgements

Part of this research was funded by Japan Society for the Promotion of Science (JSPS) research grant JP18K11276.

Table1. Experimental Environment.

Node	Sink Node	Sensor Node
Product	HP ProBook 430 G1	Raspberry Pi Model 3B+
OS	Ubuntu 16.04	Raspbian 9
Middleware	Cefore[3], XAMPP[4], MariaDB[5]	Cefore[3]
Memory	4 [GB]	1 [GB]
Core	2	4
Processer	Intel Core i5-4200U CPU 1.60GHz	Broadcom BCM2837B0 Cortex-A53 (ARMv8) 1.4 GHz

Parameters	Values
Number of Nodes	Sink Node : 1, Sensor Node : 1
Measurement Time	15 [min]
Acquisition Interval	1 [min]
Communication Distance	1 ~ 11 [m]

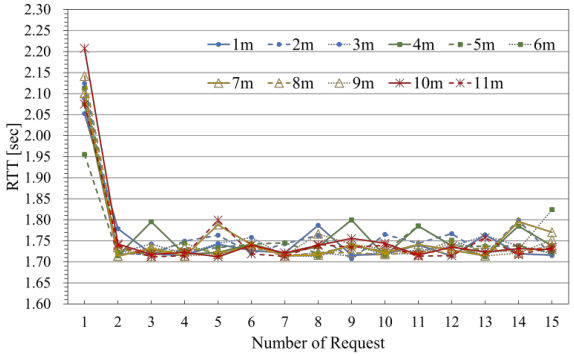

Fig. 3. RTT results for each elapsed time.

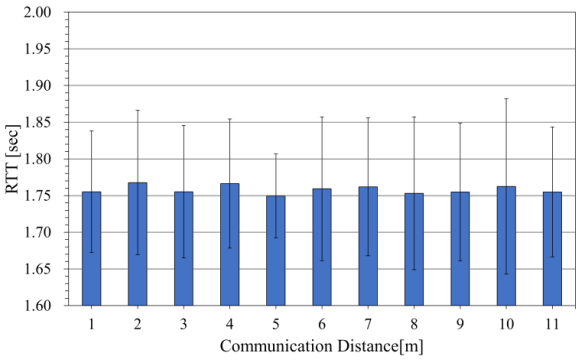

Fig. 4. RTT results for each communication distance.

References:

[1] T. Kaida, M. Koike and O. Mizuno, "The Data Cache Method on Sensor Networks Applied Information-Centric Network," IEICE Trans. Commun. (in Japanese), Vol. J100-B, No. 2, pp. 48-58, Feb. 2017.

[2] K. Kimura and O. Mizuno, "Performance Requirements Evaluation of Network Functions in Information-Centric Networking based Wireless Sensor Network", IEEJ Trans. Information and Systems. (in Japanese), Vol.140, No. 6, pp. 583-584, June 2020.

[3] Cefore, https://cefore.net/, (accessed Oct. 10th 2021).

[4] XAMPP, https://www.apachefriends.org/jp/index.html, (accessed Oct. 10th 2021).

[5] MariaDB, https://mariadb.com/, (accessed Oct. 10th 2021).

Personalization of Service Controller for Home Network Devices

Taichi Kimura, Osamu Mizuno

Electrical Engineering and Electronics Program, Graduate School of Engineering, Kogakuin University, Tokyo, Japan
E-mail: cm21018@ns.kogakuin.ac.jp

Abstract

This paper shows the control method for multiple home network services to prevent unwanted operation. This method uses operation priority and the execution judgement rules. Evaluating this method by questionary, the controller applied the method got different results from users in some cases. This paper discusses new functions to personalize operation priority.

Home network devices are home appliances that can connect to a network. They can be operated remotely or automatically. However, the home network device may perform an operation that the user does not want. In particular, such a situation may occur when operating multiple home network services at the same time.

Therefore, this paper aims to establish a control method that maintains the state of home network device that the user wants when operating multiple home network services.

For home network device operations, the controller accepts operation request at any time. Then, it is impossible to prevent new operations in situations where the status should be maintained. For example, "when you want to keep the window closed, open the window automatically on a sunny day." A control method to maintain the user's operation is shown in Fig. 1 [1] to solve this problem. In this method, the 5 levels of priority are defined. It determines which situations should be maintained, and the operation is executed or prevented. This method uses a motion sensor to judge the presence or absence of a person in the vicinity of the device.

When an operation request happens, the controller refers to the current operation. Whether maintain operation or not is determined based on the operation priority and the execution judgment rules. The rules include "When there is a person, any physical operations get prioritized" and "When the fire sensor reacts, automatic operations regarding fire get prioritized." When the motion sensor detects that a person goes out of the room, the operation judgment works based on the same criteria as above. Suppose it decides that the current operation is rejected. In that case, the requested operation is accepted. Otherwise, if the current operation is accepted maintained, the requested operation is rejected. When the automatic operation is not executed, it goes into the "waiting for re-execution state." Also, suppose the operation waiting for re-execution is not necessary. In that case, the status of waiting for re-execution is released.

To evaluate the proposed method, the questionnaire survey that research differences of judgment between the controller and users was conducted [1]. There are 10 questions. As a result, in seven questions, controller decisions and majority users' decisions were matched. Still, in two questions, the percentage of majority users is under 2/3. The other controller decision and the majority of user decisions were not matched. Therefore, the proposed method is not enough to reproduce the user's decision.

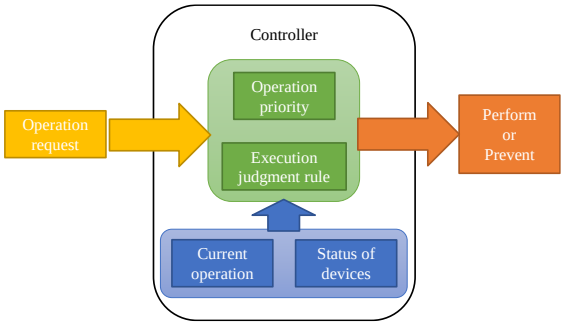

Fig. 1. A control method maintaining the operation that the user wants.

To solve this problem, it is necessary to improve the execution judgment rule [1]. However, it is difficult to make personalized decisions because many user decisions are always matched. Accordingly, a personalized function is required. The function changes the priority by the operation using machine learning. In this function, when an operation is rejected, the controller sends notifications to registered control device. The notifications include requests to choose between "ignore," "execute" for the user. The controller learns from the choices; then, the controller changes the priority when a similar operation request comes. There are some well-known learning ways. Unsupervised learning is suitable for making a personalized decision, but there are various configurations among users. Therefore, reinforcement learning is more suitable than unsupervised learning.

In this paper, how to improve a control method maintaining the operation that the user wants was discussed. In the future, we design detail of the controller, and evaluate it.

References:

[1] T. Kimura, O. Mizuno, “A system and user judgment in home network device operation,” *2021 IEICE General Conference*, BS-4-3, Mar. 2021.

Parallelization of Automatic Tuning using Multiple Jobs for Machine Learning Programs

Sorataro Fujika[†1*], Teruo Tanaka[†1], Akihiro Fujii[†1], Yuka Kato[†2], Satoshi Ohshima[†3], Takahiro Katagiri[†3]

†1 Department of Informatics, Graduate School of Engineering, Kogakuin University, Tokyo, Japan
* E-mail: em21021@ns.kogakuin.ac.jp
†2 Division of Mathematical Sciences Department of Information and Sciences, School of Arts and Sciences, Tokyo Woman's Christian University, Tokyo, Japan
†3 Information Technology Center, Nagoya University, Aichi, Japan

Abstract

We are working on the study of simultaneous estimation of multiple parameters by automatic tuning using iterative one-dimensional search, and this time we applied it to a machine learning program. This machine learning program is an application for pedestrian route prediction that takes about 20 minutes for one actual measurement. This report shows that automatic tuning, which takes 3.7 days for sequential execution, can be completed in about 4 hours by parallelizing. In addition, it is shown that the automatic tuning is searching for a superior value by comparing the actual measurement results with randomly selecting points from the space searched by the automatic tuning.

1. Introduction

Automatic tuning is a technology that automatically searches for the optimum performance parameters (parameters that affect the performance to be optimized by tuning such as execution time and power consumption) according to the computer environment and program[1][2][3]. We are studying automatic tuning using iterative one-dimensional search[4][5][6][7].

Currently, we are working on research to optimize hyperparameters when a machine learning program trains in an environment where multiple GPUs that are effective for machine learning can be used. The machine learning program to be tuned takes several hours for one training, and it takes an enormous number of days for tuning.

The purpose of this study is to parallelize the actual measurements required for automatic tuning and reduce the execution time. Parallelization uses a method in which the actual measurement of the user program required for automatic tuning is executed multiple times at the same time. For the execution environment, we use the Nagoya University supercomputer "Flow" Type II subsystem, which can use multiple GPUs that are effective for machine learning[8]. In addition, automatic tuning is performed by sequential execution, and the execution time and estimation results are compared.

2. Automatic tuning method and parallelization

2.1. The Iterative one-dimensional search

The iterative one-dimensional search is a method of repeating the direction search and the one-dimensional search in the parameter space in order to estimate multiple performance parameters at the same time. Figure 1 shows the flow of parameter estimation by iterative one-dimensional search. The parameter space consists of possible values (discrete points) of each parameter with multiple parameters as axes. In the direction search, one reference point is first determined, and the points adjacent to each direction of the reference point are examined to find the point with the best performance. In the one-dimensional search, the points in the direction of the points found in the direction search are examined, and the point with the best performance is set as the new reference point. These two searches are repeated until there is no movement of the reference point. However, the points checked once will not be checked after the second time.

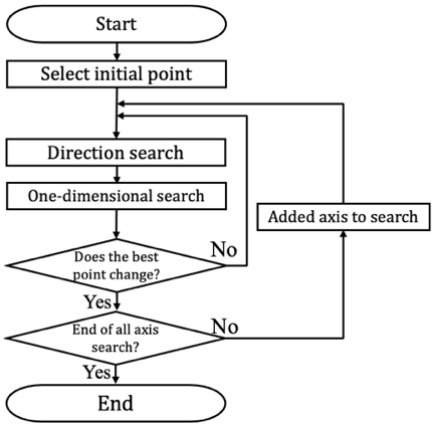

Fig. 1. Flow of Iterative One-dimensional Search

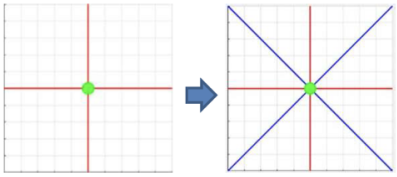

Fig. 2. An Example of Expanding the Search Axis in a Two-Dimensional Search Space

Since the pattern becomes large when searching in all directions from the beginning, only a limited direction is searched. Figure 2 shows an example of expanding the search range in the two-dimensional parameter space. Initially, only the direction of each axis is searched, and if the point to be searched is not found, the point on the diagonal line composed of the combination of each two axes is added and evaluated. This diagonal line is gradually increased to gradually expand the search area. With this method, it is possible to search for as many points as possible without investigating the points at which the execution result deteriorates.

2.2. Parallelization method

In the conventional iterative one-dimensional search, hyperparameter estimation of a machine learning program, which takes a long time to train, takes several days. Therefore, as shown in Fig. 3, the execution time is reduced by parallelizing the actual measurement of the direction search and the one-dimensional search.

Parallelization is done for an environment where multiple jobs can be executed in parallel. The execution environment uses the "Flow" Type II subsystem, which is a supercomputer of Nagoya University. This supercomputer can run up to 50 jobs for each user at the same time. Only one GPU can be used for each job, and the nodes used are shared among users.

The parallelization of actual measurement is realized by simultaneously executing (submitting a job) the hyperparameters of the machine learning program with different values. Since Flow can execute up to 50 jobs at the same time, the maximum number of parallels possible this time is 50. This makes it possible to save a lot of time.

3. Application to the program to be evaluated

3.1. Program to be evaluated

The program targeted for automatic tuning is a pedestrian route prediction application using machine learning[9]. This application predicts the future route and arrival point of the pedestrian from the past movement trajectory data of the target person by the training phase and the prediction phase.

In the training phase, pedestrian position information is extracted from images randomly selected from the dataset, and a predictor is generated using the constructed training data. Social LSTM, which is a recurrent neural network method, is used to generate predictors[10].

In the prediction phase, LiDAR measures the locus of pedestrian movement, generates input data from the measurement data to the predictor, and predicts the route with the predictor.

For the figure of merit, FDE (Final Displacement Error), which is the error between the actual pedestrian's arrival point and the arrival point

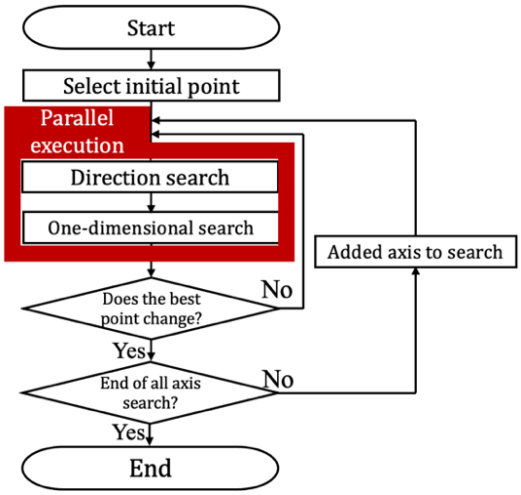

Fig. 3. Perform directional search and one-dimensional search together

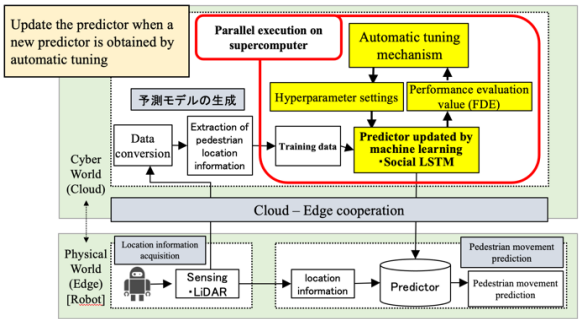

Fig. 4. Positioning of automatic tuning mechanism and pedestrian route prediction application

predicted by the predictor, is used. The smaller the FDE, the better the accuracy. In this study, we estimate the combination of hyperparameters that reduce FDE.

3.2. Positioning of automatic tuning and pedestrian route prediction applications

Figure 4 shows the positioning of the automatic tuning mechanism and the pedestrian route prediction application. The target system consists of Physical world and Cyber World. In the Physical world, a robot uses a prediction model to predict the movement of people around it and operate. The data is sent to Cyber World, and the prediction model is updated as needed by machine learning. Hyperparameters are automatically tuned on this Cyber World.

The automatic tuning mechanism optimizes the machine learning hyperparameters used to generate the predictor. The automatic tuning mechanism actually measures with a predictor using the set hyperparameters and acquires the performance evaluation value (FDE in this case). At this time, the hyperparameter used first is called the initial parameter. The automatic tuning mechanism sets the combination of hyperparameters to be searched by iterative one-dimensional search from the acquired performance evaluation value. The predictor actually measures using the set hyperparameters. This

procedure is repeated until the iterative one-dimensional search is completed. Here, the proposed method actually measures the combination of multiple hyperparameters in parallel on a supercomputer that can use multiple GPUs.

4. Hyperparameter estimation result

4.1. Issue setting

In order to investigate the effect of parallelizing automatic tuning, we conducted an experiment and analyzed using the data of "hotel", which takes less time for training. This data requires about 20 minutes for one training. There are 5 types of hyperparameters to be tuned in total, and 5 patterns of possible values are set for each. Therefore, the combination of hyperparameters is 3125 patterns in total.

4.2. Estimated result

Table 1 shows the estimation results of hyperparameters in parallel execution and sequential execution. At the time of parallel, 205 trainings were performed while changing the combination of hyperparameters. The execution time is 4 hours, which is about 1/22 times that of sequential execution. Initial parameters are a combination of hyperparameters that are currently empirically considered to be the best and used. Compared with the initial parameters, the FDE obtained this time is reduced by about 0.71 m.

Since machine learning has a stochastic element, performance evaluation value (FDE in this case) may fluctuate each time it operates. Therefore, we performed additional measurements 10 times using the hyperparameters and initial parameters estimated by parallel execution and sequential execution. The distribution is shown in Fig. 5. It can be seen that the estimation results of parallel execution and sequential execution differ in the three hyperparameters, but the difference in distribution is not large. In addition, it can be seen that the estimated hyperparameters are changing at a superior value compared to the initial parameters.

Figure 6 shows the transition of the search during parallel execution. In the figure, each blue dot is the FDE obtained as a result of executing the machine learning program. The area between the orange vertical lines is the range of simultaneous executions in parallel, and the numbers in □ are the number of simultaneous multiple executions. First, execute all the points on the five axes and find the point with the smallest FDE among them. Let that point be the next reference point. The point that becomes the smallest FDE found is indicated by a red dot in the figure. When the reference point does not change, the axes to be searched are expanded in the order of 2 axes, 3 axes, and so on. The green horizontal line is the FDE value of the initial parameter. Compared with this axis, it can be seen that 85% of the points searched this time have better FDE than the initial parameters.

The number of times of training by estimation by automatic tuning of parallel execution was 205 times. For comparison, we examined the distribution of FDE by randomly changing the hyperparameters the same number of times. The results are shown in Fig. 7. The green horizontal line is the FDE of the initial parameter, and 41% of the total points have a better FDE than the initial parameter. Compared with the above, 85% of the points examined by automatic tuning were better than the initial parameters, indicating that the iterative one-dimensional search efficiently improves the figure of merit.

Table 1. Hyperparameter estimation results for parallel and sequential execution

		Parallel execution	Sequential execution	Initial parameters
Hyper parameters	rnn_size	512	512	128
	Grad clip	10	11	10
	Learning rate	0.003	0.01	0.003
	dropout	0.3	0.3	0.5
	Lambda param	0.002	0.0002	0.0005
FDE (m)		1.14	1.13	1.85
Execution time		4 hours	3.7 days (89.5 hours)	
Number of trainings		205	264	
Average execution time per training		1240seconds(20 minutes)		

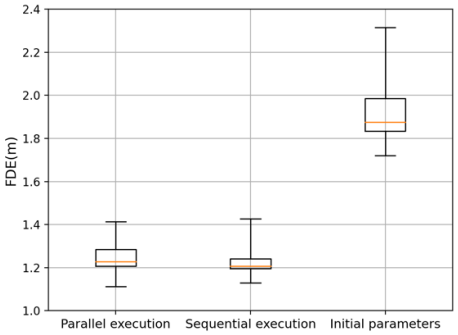

Fig. 5. Distribution of the results of 10 additional measurements with hyperparameters estimated by automatic tuning

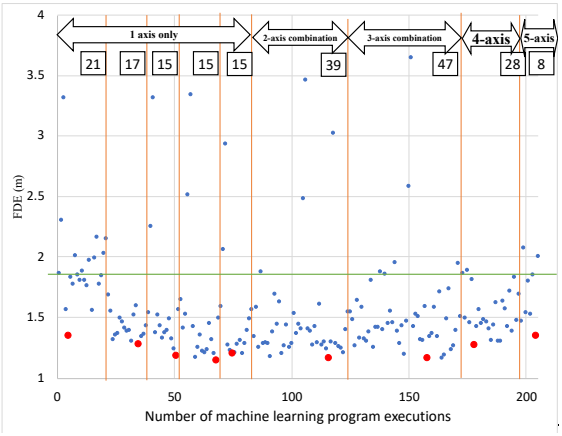

Fig. 6. Transition of search during parallel execution

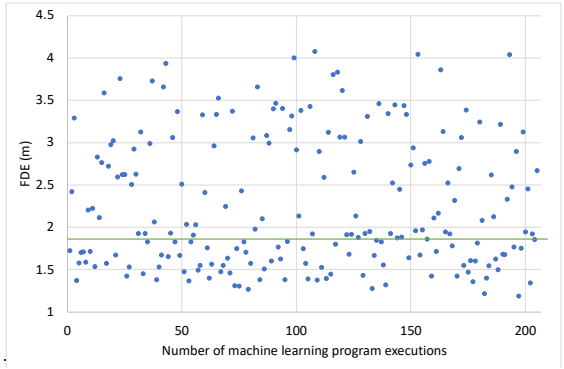

Fig. 7. Result of executing with randomly set hyperparameters

5. Conclusion

In this research, an automatic tuning mechanism using iterative one-dimensional search was made possible to measure in parallel by submitting multiple jobs at the same time using the environment of a supercomputer that can use multiple GPUs. We applied the improved automatic tuning mechanism to hyperparameter estimation of machine learning programs.

The conclusions of this report are the following two points.

· By parallelization, the time required for hyperparameter estimation of the target machine learning program was reduced from 89.5 hours (3.7 days) to 4 hours.

·Compared with the random search, the automatic tuning using the iterative one-dimensional search efficiently investigates the points that are better than the initial parameters.

The training data used this time was a simple one in which one training was completed in 20 minutes. In addition, it is possible that the optimal combination of hyperparameters may change due to changes in training data. The next subject is to apply it to data that takes several hours for one training, and to clarify the difference of optimal hyperparameters due to changes in the training data set.

Acknowledgments:

This work is supported by "Joint Usage/Research Center for Interdisciplinary Large-scale Information Infrastructures" in Japan (Project ID: jh210019-NAH) and JSPS KAKENHI Grand Number JP 18K11340.

References:

[1] T. Katagiri and D. Takahashi, Japanese Auto-tuning Research: Auto-tuning Languages and FFT, Proceedings of the IEEE, Vol. 106 , Issue 11, pp. 2056-2067 (2018)

[2] H. Kuroda, K. Naono, T. Iwashita, Special feature: Automatic software tuning in scientific computing, Academic journal "Information processing", vol. 50, Information Processing Society of Japan (2009) (in Japanese).

[3] J. Bilmes, K. Asanovic, C.W. Chin, J. Demmel, Optimizing Matrix Multiply using PHiPAC: a Portable, High-Performance, ANSI C Coding Methodology, in Proc. the 11 th international conference in Supercomputing, Vol.97, pp.340-347 (1997).

[4] T. Tanaka, R. Otsuka, A. Fujii, T. Katagiri, T. Imamura, Implementation of d-Spline based Incremental Performance Parameter Estimation Method with ppOpen-AT, Scientific Programming 2014, IOS Press, 22 4 pp.299-307, (2014).

[5] M. Mochizuki, A. Fujii, T. Tanaka, T. Katagiri, Fast Multidimensional Performance Parameter Estimation with Multiple One-dimensional d-Spline Parameter Search, International Workshop on Automatic Performance Tuning (iWAPT2017), (2017).

[6] T. Tabeta, N. Seki, A. Fuji, T. Tanaka, H. Takizawa, An Optimization Technology of Software Auto-Tuning Applied to Machine Learning Software, Poster Session on HPCAsia2020 (2020).

[7] S. Fujika, T. Tabeta, A. Fujii, T. Tanaka, Y. Kato, S. Ohshima, T. Katagiri, Application and Stability Verification of Parallelized Automatic Tuning to Machine Learning Programs on GPU Cluster, IPSJ Technical Report, vol.2021-HPC-178, No.16, pp.1-8 (2021) (in Japanese).

[8] Information Technology Center, Nagoya University, Introducing the supercomputer "Flow", http://www.icts.nagoya-u.ac.jp/ja/sc/overview.html, (Last access: October 19, 2021)

[9] R Akabane, Y Kato, Pedestrian Trajectory Prediction Based on Transfer Learning for Human-Following Mobile Robots, IEEE ACCESS, Vol.9, pp.126172-126185 (2021).

[10] A. Alahi, K. Goel, V. Ramanathan, A. Robicquet, Li Fei-Fei, S. Savarese, Social LSTM: Human Trajectory Prediction in Crowded Spaces, Proc. IEEE Conference on Computer Vision and Pattern Recognition (CVPR 2016), pp.961-971 (2016).

A Method for Detecting Anomalies in IoT Devices Using LSTM

Yutaro Nakamura, and Osamu Mizuno

Department of Electrical Engineering and Electronics, Graduate School of Engineering, Kogakuin University, Tokyo, Japan
E-mail: cm20040@ns.kogakuin.ac.jp

Abstract

The Internet of Things (IoT) is attracting attention. The collection and utilization of data, including sensor data, is becoming increasingly important. However, IoT devices are prone to anomalies such as failure or theft, which reduce the system's reliability. This paper aims to realize a system that detects anomalies in IoT systems when the data received from sensors fluctuates rapidly. This paper proposes an anomaly detection system by building a predictive model of the data using Long Short-Term Memory (LSTM).

The IoT is attracting attention, and the collection and utilization of data, including sensor data, is becoming more important. However, IoT devices are susceptible to failures, theft, and other anomalies that reduce the system's reliability. Therefore, in this paper, the research objective is to realize a system that can detect abnormalities in IoT systems when data received from sensors fluctuates suddenly.

Since device anomalies reduce data and system reliability, a mechanism to support the regular operation of the device itself is necessary. Dead-activity support is a way to check for abnormalities in devices. However, devices are required to save power. The dead-activity response may cause the device to run out of battery. Therefore, it is necessary to be able to detect abnormalities using data obtained from sensors.

This paper proposes a method to detect abnormalities in devices using received sensor data to detect abnormalities when the data fluctuates unexpectedly. In this paper, we use temperature data as sensor data.

The term "abnormality" includes multiple cases. We focus on the case where the data fluctuates rapidly. This case appears of a time-series data waveform, which includes values not appearing ordinary. We used the Autoregressive model (AR model) to predict the observed values from sensors [1]. However, there were some problems such as low accuracy in determining anomalies in areas where anomalous values occur frequently.

This paper proposes a method to identify anomalies by building a data prediction model using LSTM [2] and distributing the degree of anomaly. LSTM model is a deep learning method suitable for analyzing time series of data. Parameter "e" is the difference between the predicted and actual values calculated by LSTM, and all the differences are distributed. 5% on one side of the normal distribution is set as the anomaly threshold. The anomaly above the threshold is judged as an anomaly.

Figure 1 shows the application of the LSTM model to the anomalous data. The data is room temperature in our laboratory, and added a 5% probability of outputting a sudden anomalous value, as shown in [1].

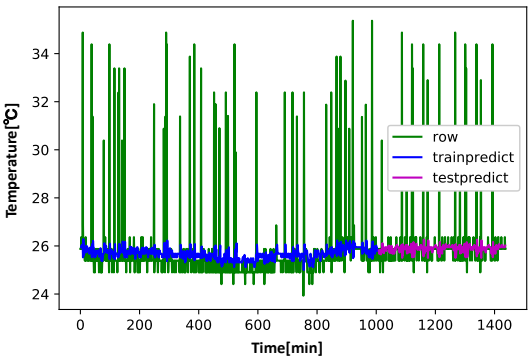

Fig. 1. Anomaly data and prediction results by LSTM.

The predicted values are close to the standard values in the areas where the data values fluctuate rapidly. Also, the truth rate is 97.2%, which is higher than the accuracy of the AR-model. LSTM can predict plausible values from both long-term and short-term aspects. In contrast, existing methods learn from past data before predicting values.

We applied LSTM to build an appropriate model for the sensor data and detect anomalies. As a future study, we will compare and evaluate the previous anomaly detection methods.

References:

[1] Y. Nakamura, K. Kimura, Y. Amano and O. Mizuno, "Anomaly detection methods for devices in IoT systems," The 2020 IEICE General Conference, BS-2-7, Mar. 2020 (in Japanese)

[2] Gers, Felix A., Jurgen Schmidhuber, and Fred Cummins. "Learning to forget: Continual prediction with LSTM." Neural computation 12.10 (2000): 2451-2471.

A Study of Applying Plumtree Algorithm for Blockchain Networks

Yusuke Kitagawa†, Kazuyuki Shudo††, Osamu Mizuno†, and Ryohei Banno††

† Kogakuin University, Tokyo, Japan.
†† Tokyo Institute of Technology,Tokyo, Japan.
E-mail: cm21016@ns.kogakuin.ac.jp

1. Introduciton

Blockchain technology continues to attract considerable attention as the basis for cryptocurrency. Such technology shares a ledger to record transactions among multiple computers on a network designed to prevent tampering. However, in practice the use of blockchain technology involves the consumption of communication resources, because information may be delivered to the same node more than once through different neighbors. In this study, we propose a method to reduce duplicate messages in blockchain networks by applying an algorithm called Plumtree.

2. Proposed method

In this study, we solve the problem of communication resource consumption using the ability of Plumtree to reduce redundant message transmissions based on the Bitcoin network. Plumtree[1] is a combination of tree-based and gossip-based approaches to reduce redundancy while maintaining high message reliability. Plumtree is a combination of tree-based and gossip-based approaches to reduce redundancy while maintaining high message reliability. In the proposed method, blocks are first broadcasted using the same mechanism as Bitcoin. Based on the routing information used in the broadcast, each node is given information about its neighbors in the spanning tree. For subsequent broadcasts, we use the constructed tree.

3. Evalution

We measured the number of messages and the number of hops based on SimBlock[2], which can simulate the information propagation of a blockchain. The experimental parameters of the SimBlock used in this experiment are shown in Table 1.The number of nodes and block size are set to 8370 and 803.565 Kbytes, respectively. These are the values as of December 15, 2020. We did not use Compact Block Realy (CBR) to simulate block propagation up to four blocks, and used the default values of SimBlock for the rest. The number of trials was set to 10. Figure 1 shows the number of messages for the proposed method and the existing method when the number of blocks is simulated up to 4. The vertical axis is the total number of messages received by all nodes, and the horizontal axis is the measurement item. It can be seen that the proposed method reduces the number of messages by more than 75% compared to the existing method. Next, we investigate the hop count when messages by more than 75% compared to the existing method. Next, we investigate the hop count when Plumtree is applied to the blockchain.

Table1 SimBlock parameters

Parameter	Value
NUM_OF_NODES	8370
BLOCK_SIZE	803.565 Kbyte
CBR_USAGE_RATE	0
CHURN_NODE_RATE	0

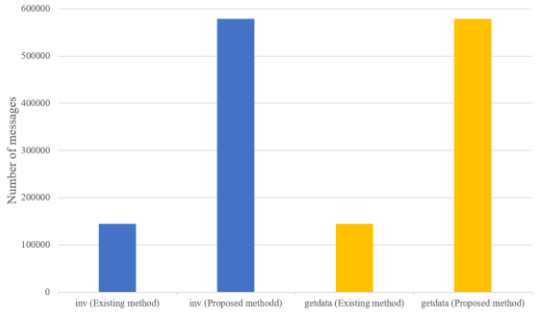

Fig.1 Number of inv and getdata messages in Bitcoin

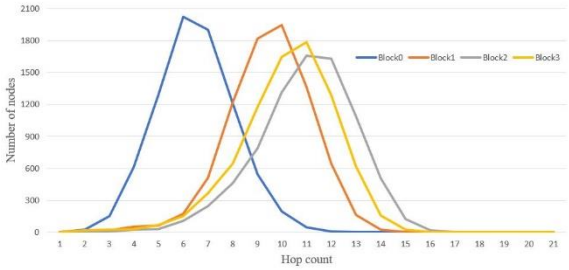

Fig.2 Number of hops in each blocks

Figure2 shows the hop count for each block. The vertical axis is the number of nodes, and the horizontal axis is the number of hops. it can be seen that the number of hops becomes larger than the initial transmission by applying Plumtree.

4. Conclusion

In this study, we found that the number of messages can be reduced, but the number of hops tends to increase with the application of the Plumtree. As future work, we plan to study methods to improve the construction of the spanning tree in order to reduce the number of hops.

References:

[1] Joao Leitao et al., "Epidemic Broadcast Trees", IEEE SRDS, pp.301-310, 2007.
[2] Yusuke Aoki et al., "SimBlock: A Blockchain Network Simulator", CryBlock, pp. 325-329, 2019.

This is an unrefereed paper.

PAPR Reduction Effect by Applying Clipping in Spectrum Suppressed Transmission

Teppei Kanke, Takatoshi Sugiyama

Graduate School of Engineering, Kogakuin University, Tokyo, Japan
E-mail: cm21014@ns.kogakuin.ac.jp

Introduction

In recent years, the frequency bands for assigning new wireless systems are exhausted. To solve this problem, spectrum suppressed transmission[1] has been proposed. It reduces its required bandwidth while maintaining throughput as possible to increase frequency utilization efficiency. However, its PAPR performances would increase due to spectrum suppression[1]. In this paper, we propose a new spectrum suppressed transmission scheme applied by clipping[2].

Proposal

The block diagram of the proposed scheme is shown in Fig.1. It reduces PAPR by the clipping after spectrum suppression. The definition of the clipping threshold is shown in Fig.2. The horizontal axis is I-channel amplitude of QPSK signal and the vertical axis is Q-channel amplitude. The clipping threshold is β times of the average power of QPSK modulated signal. If the transmission power exceeds the clipping threshold, it must be restricted to the threshold as shown by (A). Otherwise, in the case that it is smaller than the threshold, it is maintained like can of (B). However, smaller β leads to larger non-linearity distortions due to clipping. Therefore, it is necessary to determine the optimum β without BER performance degradation.

Simulation Evaluation

In this simulation, spectrum suppressed transmission with a suppression ratio of 20% for 10M [symbol/s] single carrier QPSK modulation, and convolutional coding with coding rate of 1/2 and constraint length of 7 – 3 bits soft decision Viterbi decoding are used, respectively.

The relationship between β and required Eb/No at BER $= 10^{-4}$ is shown in Fig.3. As β becomes smaller, the BER performance deteriorates due to non-linear distortion by the clipping. However, as β over 1.7, the BER performances have no degradation compared to that without the clipping. Therefore, the optimum β is 1.7 in this condition.

The relationship between β and PAPR at CCDF $= 10^{-2}$ is shown in Fig.4. CCDF means complementary cumulative distribution function. It can be seen that PAPR is more reduced as smaller β. Applying the optimum β of 1.7, compared to the conventional scheme without the clipping, the proposed scheme can reduce PAPR by 2.8dB without BER performance degradation.

Conclusion

In this paper, we have proposed a new spectrum suppressed transmission scheme applied by clipping. For example of single carrier QPSK with 20% spectrum suppression, by the clipping with the optimum threshold, the proposed scheme can reduce PAPR by 2.8dB without BER performance degradation.

References:

[1] M. Shirai, T. Sugiyama, J. Abe, K. Suzaki and H. Shiba, "PAPR characteristics in spectrum suppressed transmission and transmission quality improvement by equalization," WPMC 2017, pp. 52-56, Dec. 2017.

[2] X. Li, and J. Cimini, L.J, "Effects of clipping and filtering on the performance of OFDM," in Proc.VTC97, vol.3, pp.1634-1638, May 1997.

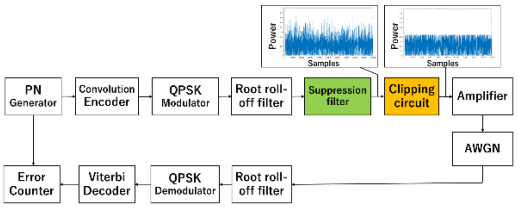

Fig. 1. Block diagram of the proposed scheme.

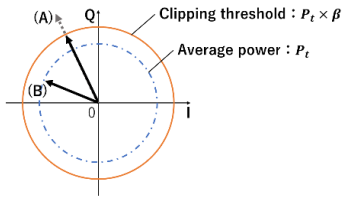

Fig. 2. Definition of clipping threshold.

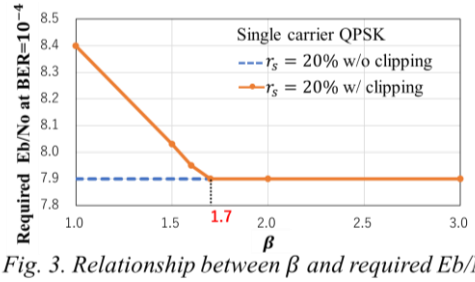

Fig. 3. Relationship between β and required Eb/No.

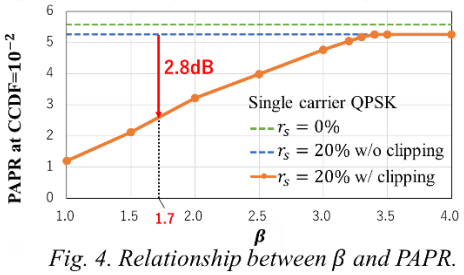

Fig. 4. Relationship between β and PAPR.

Performance Analyses of Efficient Belief Propagation Bit-flip Decoding Schemes for Polar Codes with Permutated Factor Graphs

Hidetoshi Saito* and Naoya Takahashi

Graduate School of Engineering, Kogakuin University, Tokyo, Japan
E-mail: h-saito@cc.kogakuin.ac.jp

Abstract

It is known that a polar code is a channel coding standard for the fifth generation mobile communications system (5G). We take a parallel decoding method for belief propagation (BP) decoding of a polar code such as decoding of a low-density parity check code or turbo code. However, it is pointed out that the error-correction performance of a polar code using BP decoding is far from the requirements of 5G mobile technologies. So far as known, we can improve the error-correction performance of a polar code with BP decoding if BP decoding is performed on multiple permutated factor graphs of the polar code for estimating erroneous codewords. In this research, we show that the permutations on the factor graph can be mapped into suitable permutations on the codeword positions by using Arikan's Bhattacharyya bounds of bit channels. We propose a new BP decoding scheme with cyclic redundancy check coding, bit flipping and multiple permutated factor graphs. As a result, the error-correction performance of the proposed BP decoding for the 5G polar code of length 1024 and rate 1/2 shows significant improvement over that of the conventional BP decoding with the same number of random factor graph permutations at the signal-to-noise ratio of 3.0 dB or more.

I. Introduction

Polar codes are the error-correction codes that were proved to achieve channel capacity over a memoryless binary-input output-symmetric channel or binary erasure channel with practicable encoding and decoding algorithms [1]. It is known that the third generation partnership project choose polar codes for the enhanced mobile broadband control channel of the fifth generation wireless communications system (5G) [2], [3]. In decoding of polar codes, we use successive cancellation (SC) or belief propagation (BP) decoding scheme which is a typical decoding algorithm [4], [5]. However, the frame error rate (FER) performance of a polar code with a moderate finite length is inferior to that of a low-density parity-check code or turbo code with the same length if the polar code is decoded by a SC decoding scheme. Thus, it is pointed out that the error-correction performance of a polar code with a shortened length under SC decoding is insufficient for many practical ICT applications in the information and communications technology sectors. To improve the SC decoding performance, a successive cancellation list (SCL) decoding scheme was proposed [6]. The SCL decoding scheme maintains a list of most likely several codeword candidates. We make a substantial improvement in the SCL decoding performance if we use a cyclic redundancy check (CRC) code which is concatenated to the polar code and select a correct codeword in the candidates. This decoding scheme is called the CRC-aided SCL decoding scheme [7].

On the other hand, if we use a BP decoding scheme for a polar code, every message passing process can be executed in parallel. Unlike the above sequential decoding schemes such as SC and SCL decoding schemes, parallel processing in the decoding process allows the BP decoding scheme to obtain high throughput. But, the BP decoding scheme has the disadvantage that the error-correction performance of a polar code under BP decoding cannot achieve low error probability within a practicable number of message passing iterations. Then, it is pointed out that we utilize the redundant factor graph representations to improve the error-correction performance of a polar code under BP decoding [8]. These redundant representations can be constructed by different any permutations of the original factor graph of the given polar code. The permutations in the factor graph of the polar code are selected randomly or predetermined to detect a codeword candidate as correctly as possible if the decoding fails on the original permutation [9], [10]. When a CRC code is concatenated to a polar code, the error correction performance of the polar code using BP decoding on the permuted factor graph outperforms the performance of non-CRC-aided SCL decoding for some cases.

In this research, we propose a new BP decoding scheme with CRC coding and bit-flipping techniques. If we use permutated factor graphs of the original polar code for our proposed BP decoding, we show that the error rate performances of our proposed decoding scheme outperform the conventional BP decoding schemes defined by [9]. This report is organized as follows. In the Sections II and III, we review the knowledge of a polar code and BP decoding algorithm briefly. Section IV shows our proposed BP decoding algorithm. The specific construction process of permutated factor graphs and the algorithm of proposed BP decoding with permutated factor graphs are described. Simulation results and analyses are presented in Section V. Section VI gives some conclusions.

II. Polar coding scheme

The concept of channel polarization transforms independent channels into polarized channels by

channel combining and splitting [1]. The code rate is $R = k/N$, where the notation of k is information bits and the notation of N is the block length (or codeword length). From the idea of channel polarization, the k reliable channels are used to transmit information bits, while the other $N - k$ channels are used for frozen bits and set to zeros. For a given polar code with the rate R, the k information bits and the other $N - k$ frozen bits are determined by Bhattacharyya parameters [11]. The block length of a polar code is given by $N = 2^m$ and the generator matrix $\boldsymbol{G}_N$ of this (N, k) polar code which can be recursively defined as

$$\boldsymbol{G}_N = \boldsymbol{F}^{\otimes \mathrm{m}}, \boldsymbol{F} = \begin{bmatrix} 1 & 0 \\ 1 & 1 \end{bmatrix}, \quad (1)$$

where $\boldsymbol{F}^{\otimes m}$ denotes the m-th Kronecker power of $\boldsymbol{F}$. The message $\boldsymbol{u}$ is composed of K information bits and encoded to a codeword $\boldsymbol{x} = \boldsymbol{u} \cdot \boldsymbol{G}_N$.

III. Belief propagation decoding

The BP decoding algorithm is well known as the message passing algorithm and usually described in terms of operations on factor graphs. BP decoding of a polar code is based on the factor graph representation of the given polar code's generator matrix $\boldsymbol{G}_N$, where subsequent iterations are conducted on the polar encoding factor graph [12]. BP decoding iteratively propagate messages in parllel and can estimate the codeword $\widehat{\boldsymbol{x}}$ and the message $\widehat{\boldsymbol{u}}$. The factor graph of the polar code can be obtained by adding N check nodes to each column of the first $m = log_2 N$ columns from left to right in the polar encoding factor graph. Thus, this factor graph consists of an $m + 1$ stages containing N node per stage. The nodes of the factor graph are labeled with pairs of integers (i, j), $1 \le i \le N$, $1 \le j \le m + 1$. Soft messages (LLRs) $\widehat{\boldsymbol{x}}_{LLR}$ and $\widehat{\boldsymbol{u}}_{LLR}$ are updated and propagated among adjacent nodes from the rightmost column to the leftmost column during the whole BP iteration process. Then, the decoder reverses the course and updates schedule toward the rightmost column. This procedure makes one round of BP iteration. In the concrete, BP decoding treats associating two messages with each node (i, j) for every round of BP iteration: a right-propagating message $R_{i,j}^t$ and a left-propagating message $L_{i,j}^t$, where $t = 0,1, \ldots$ is a time index. These two messages correspond to LLRs at time t and are initialized as follows:

$$L_{i,m+1}^0 = \ln \frac{P(y_i|x_i = 0)}{P(y_i|x_i = 1)},$$

$$R_{i,m+1}^0 = \ln \frac{P(u_i = 0)}{P(u_i = 1)}$$

$$= \begin{cases} 0, & \text{if } i \text{ is the index of an information bit,} \\ \infty, & \text{if } i \text{ is thr index of the frozen bit.} \end{cases} \quad (2)$$

All other $R_{i,j}^0$ and $L_{i,j}^0$ are set to equal 0. During BP decoding, these messages are propagated and updated among adjacent nodes using min-sum algorithm as follows [13]:

$$L_{i+2^{m-j},j}^t = L_{i+2^{m-j},j+1}^{t-1} + \alpha \cdot f\left(L_{i,j+1}^{t-1}, R_{i,j}^t\right),$$

$$R_{i,j+1}^t = \alpha \cdot f\left(R_{i,j}^t, L_{i+2^{m-j},j+1}^{t-1} + R_{i+2^{m-j},j}^t\right),$$

$$L_{i,j}^t = \alpha \cdot f\left(L_{i,j+1}^{t-1}, L_{i+2^{m-j},j+1}^{t-1} + R_{i+2^{m-j},j}^t\right),$$

$$R_{i+2^{m-j},j+1}^t = R_{i+2^{m-j},j}^t + \alpha \cdot f\left(L_{i,j+1}^{t-1}, R_{i,j}^t\right), \quad (3)$$

where $\alpha = 0.9375$ and $f(a, b) \triangleq \text{sign}(a) \cdot \text{sign}(b) \cdot \min(|a|, |b|)$ for any real values a,b [12], [14]. In BP decoding processes, messages are passed along the factor graphs in an iterative manner from right to left and from left to right until the maximum number of iterations N_{max} is reached. The notations of $\boldsymbol{L}_{N\times(m+1)}$ and $\boldsymbol{R}_{N\times(m+1)}$ denote the matrix that store total left-propagating messages and the matrix that store total right-propagating messages, respectively. After reaching the predefined number of BP iteration, the decision sequence $\boldsymbol{x}$ is determined based on the hard decision of messages from the nodes in the leftmost column. Alternatively, we terminate BP iteration if following early termination conditions are satisfied in the decoding process [12].

1. $\boldsymbol{G}$-based: $\widehat{\boldsymbol{x}} = \widehat{\boldsymbol{u}} \cdot \boldsymbol{G}_N$ is satisfied.
2. CRC-based: parity checks of the concatenated CRC calculation are satisfied.

IV. Improved belief propagation decoding scheme and permutated factor graphs

If BP decoding is performed on the permutated factor graphs, there are several existing methods to choose the factor graph permutations that improves the error-correction performance of polar codes. In this research, we propose another method to choose the factor graph permutations. In our method, we define that

$$w = \left|\overline{\boldsymbol{A}_c \cup \boldsymbol{A}_c^p}\right|, \quad (4)$$

where the notations of $\boldsymbol{A}_c$ and $\boldsymbol{A}_c^p$ are the set of frozen bits corresponding to the original factor graph of the polar code and the set of frozen bits corresponding to the permutated factor graph of the same polar code, respectively. We use Bhattachayya parameters [15], [16] to choose the elements of $\boldsymbol{A}_c$ and $\boldsymbol{A}_c^p$. Algorithm 1 provides the method to choose elements of the set of frozen bits base on Bhattachayya parameters where the notation of $\boldsymbol{z}$ is the bit-channel metrics given by $\boldsymbol{z} = \left(z_0, \ldots, z_j, \ldots . z_{N-1}\right)$.The index set of layers of the original and permutated factor graphs is given by $\boldsymbol{L} = \{l_0, \ldots, l_{m-1}\}$ and $\boldsymbol{L}^{\mathrm{p}} = \left\{l_{k_0}, \ldots, l_{k_{m-1}}\right\}$, respectively. If $l_i = l_{k_i} (0 \le i \le m - 1)$, it is found that $\boldsymbol{L} = \boldsymbol{L}^p$. We randomly choose $\mathbf{A}_c^p$ which is allocated in the ascending order of w.

When the symbol of q_{max} denotes the total

number of permutated factor graphs, [9] proposes BP decoding with permutated factor graphs and each permutated factor graph is used in predetermined order among q_{max} factor graphs. If BP decoding fails on the original factor graph and we change the structure of the factor graph, we have a chance to estimate the correct codeword candidate [17], [18]. Therefore, the greater q_{max} will be, the higher the polar code has flexibility in design of permutated factor graphs. If we use more permutated factor graphs, it is possible to improve the error-correction performance of the polar code under BP decoding. Algorithm 2 shows our designed decoding algorithm for a polar code using the proposed BP decoding scheme and permutated factor graphs based on Bhattacharyya parameters. In this decoding process, when $\hat{\boldsymbol{x}}$ is satisfied with the decoding termination conditions, decoding exits and the remaining permutated factor graphs are unused. In the other case, LLRs of $\boldsymbol{L}$ and $\boldsymbol{R}$ at time t are inherited by the next decoding process at time $t+1$. Here, in Algorithm 2, the notations of $N_{it,max}^{P}$, $\boldsymbol{l}_{\text{scheduled}}$ and ``LLR2Bit''denote the maximum number of iterations for each permutated factor graph which satisfies $N_{it,max}^{P} > N_{it}$, the column index of the factor graph, and the hard decision function for the estimated sequence.

Algorithm 1: Selection method of a set of frozen bits

Input: $N, K, \boldsymbol{L}^{P} := \{l_{k_0}, \ldots, l_{k_{m-1}}\}, SNR$
Output: $\boldsymbol{\mathcal{A}}_c$ *with* $|\boldsymbol{\mathcal{A}}_c| = N - K$

$z_0 = \exp(-SNR)$
for $i = 1 : m$ **do**
  $k_i = \texttt{GetSuffixNumber}(l_{k_i})$
  $S \leftarrow 2^{k_i}$
  for $j = 0 : S/2 - 1$ **do**
    $T = z_j$
    $z_j = 2T - T^2$
    $z_{j+S/2} = T^2$
  end for
end for
$\boldsymbol{\mathcal{A}}_c := \texttt{GetGoodCapacity}(\boldsymbol{z}, N - K)$
return $\boldsymbol{\mathcal{A}}_c$

Algorithm 2: Proposed BP decoding with permutated factor graphs

Input: $y_{LLR}, \boldsymbol{\mathcal{A}}_c, M, N_{it}, N_{it,max}^{P}, \boldsymbol{G}, q_{max}, l_{scheduled}$
Output: $\hat{u}$

$N \leftarrow \texttt{Length}(y_{LLR})$
$n \leftarrow \log_2 N$
for $iq = 0$ to q_{max} **do**
  $schedule \leftarrow l_{scheduled}(iq)$
  $(\boldsymbol{L}, \boldsymbol{R}) \leftarrow \texttt{InitializeLandR}(y_{LLR}, \boldsymbol{\mathcal{A}}_c)$
  for $itr = 1$ to $N_{it,max}^{P}$ **do**
    if $itr \pmod{N_{it}} = 0$ **then**
      $y_{LLR} \leftarrow \texttt{ChangetoFixedBit}(y_{LLR}, \hat{x}, itr, N_{it})$
    end if
    $(\boldsymbol{L}, \boldsymbol{R}) \leftarrow \texttt{OneBPIteration}(N, n, \boldsymbol{L}, \boldsymbol{R}, schedule)$
    $\hat{u} \leftarrow \texttt{LLR2Bit}(\boldsymbol{L}(0,:) + \boldsymbol{R}(0,:))$
    $\hat{x} \leftarrow \texttt{LLR2Bit}(\boldsymbol{L}(n,:) + \boldsymbol{R}(n,:))$
    if $\texttt{EarlyStopCriterion}(\hat{u}, \hat{x}, \boldsymbol{G}, M)$ **then**
      return $\hat{u}$
    end if
    $itr \leftarrow itr + 1$
  end for
  $iq \leftarrow iq + 1$
end for
$\hat{u} \leftarrow \texttt{LLR2Bit}(\boldsymbol{L}_m(0,:) + \boldsymbol{R}_m(0,:))$
return $\hat{u}$

V. Error rate performance evaluations of various belief propagation decoding schemes

In this section, we evaluate the error rate performances of (1024, 512) polar codes [4] under the original BP decoding, conventional BP decoding with permutated factor graphs given by [9] and our designed BP decoding scheme defined by the previous section. We evaluate the bit error rate (BER) performances, the FER performances and the average iteration numbers of each decoding scheme. Furthermore, we compare our designed decoding scheme with the CA-SCL decoding scheme with list size $L = 4$ or 8. We use CRC-10 and the other CRC code whose generator polynomial is given by $M'(x) = x^8 + x^7 + x^6 + x^4 + x^2 + 1$. The other CRC is referred to as CRC-8 and we use both of CRC-10 and CRC-8 for the computer simulation of each BP decoding scheme. From Figs. 1 and 2, the error rate performances of our designed BP decoding schemes with permutated factor graphs are close to those of the part of CRC-aided SCL decoding schemes (notations of ``SCL CRC-8 $L$=4", ``SCL CRC-8 L=8", and ``SCL CRC-10 L= 4"). It is found that our proposed BP decoding scheme with 10 permutated factor graphs exhibits the superior performance compared to the other schemes. Thus, if we use the permutated factor graphs given by the previous section, our designed BP decoding scheme gives the significant performance improvement compared to the other conventional BP decoding schemes. Fig. 3 shows average iteration numbers of several BP decoding schemes. Our proposed BP decoding scheme with 10 permutated factor graphs shows the smallest numbers. Furthermore, it is found that all proposed BP decoding

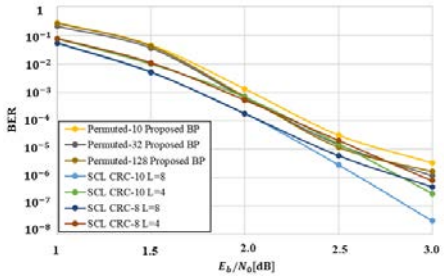

Fig. 1. BER performances of CRC concatenated (1024, 512) polar codes under several BP and SCL decoding schemes.

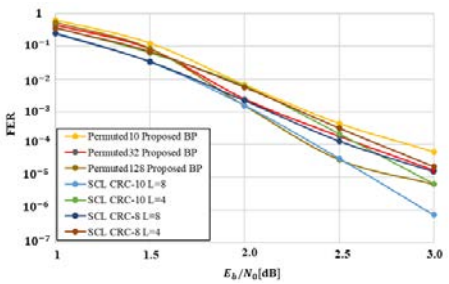

Fig. 2. FER performances of CRC concatenated (1024, 512) polar codes under several BP and SCL decoding schemes.

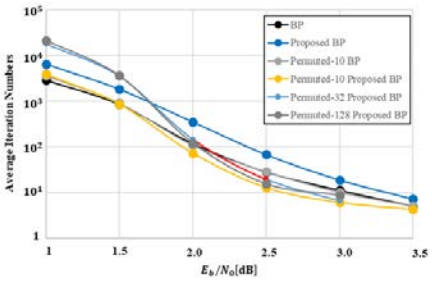

Fig. 3. Average iteration numbers of several BP decoding schemes for CRC concatenated (1024, 512) polar codes.

schemes with permutated factor graphs improve average iteration numbers without depending on q_{max} in signal-to-noise ratio (SNR) regions higher than 2.5 dB. But, average iteration numbers of each proposed BP decoding scheme with permutated factor graphs are almost the same as numbers of the original BP decoding scheme in those SNR regions.

VI. Conclusions

In this research, we propose an effective modified BP decoding scheme with CRC coding and bit flipping methods. Moreover, we combine the modified BP decoding scheme with permutated factor graphs. We design the new selection method of permutated factor graphs using Bhattacharyya parameters to maximize the elements of the union of the frozen bit sets corresponding to the original factor graph and the permutated factor graph. As a result, this proposed BP decoding scheme with permutated factor graphs can improve the SNRs in both of the BER and FER performances compared with the conventional BP decoding with permutated factor graphs. Furthermore, simulation results demonstrate that the FER of the proposed BP decoding for a (1024,512) polar code with permutated factor graphs can approach that of CRC-aided SCL decoding with CRC-10 and L = 8 in SNR regions lower than 2.5 dB.

References:

[1] E. Arikan, ``Channel polarization: a method for constructing capacity achieving codes for symmetric binary-input memoryless channels,'' *IEEE Trans. Inf. Theory*, vol. 55, no. 7, pp. 3051–3073, Jul. 2009.

[2] 3GPP TR38.913 v14.1.0, ``Study on scenarios and requirements for next generation access technologies,'' Dec. 2016.

[3] 3GPP Technical Specification 36.212, ``Evolved universal terrestrial radio access (E-UTRA); multiplexing and channel coding,'' ver. 14.2.0, release 14, Apr. 2017.

[4] V. Bioglio, C. Condo, and I. Ingmar, ``Design of polar codes in 5G new radio,'' *IEEE Commun. Surveys Tuts.*, vol. 23, no. 1, pp. 29-40, First Quarter 2021.

[5] E. Arıkan, ``Polar codes: a pipelined implementation,'' *4th International Symposium on Broadband Communication (ISBC 2010)*, Melaka, Malaysia, 11-14 July, 2010.

[6] I. Tal and A. Vardy, ``List decoding of polar codes,'' *IEEE Trans. Inf. Theory*, vol. 61, no. 5, pp. 2213–2226, May 2015.

[7] K. Niu and K. Chen, ``CRC-aided decoding of polar codes,'' *IEEE Commun. Lett.*, vol. 16, no. 10, pp. 1668–1671, Oct. 2012.

[8] A. Elkelesh, S. Cammerer, M. Ebada, and S. ten Brink, ``Mitigating clipping effects on error floors under belief propagation decoding of polar codes,'' *in Proc. 14th Int. Symp. Wireless Commun. Syst. (ISWCS' 2017)*, pp. 384–389, Bologna, Italy, 28-31 Aug. 2017.

[9] N. Doan, S. A. Hashemi, M Mondelli, W. J. Gross, ``On the decoding of polar codes on permuted factor graphs,'' *2018 IEEE Global Communications Conference (GLOBECOM 2018)*, WCS-I2, Abu Dhabi, United Arab Emirates, 9-13 Dec. 2018.

[10] L. Li, and L. Liu, ``Belief propagation with permutated graphs of polar codes,'' *IEEE Access*, vol. 8, pp. 17632-17641, 2020.

[11] S. Zhao, P. Shi, B. Wang, ``Designs of Bhattacharyya parameter in the construction of polar codes,'' *in Proc. 7th International Conference on Wireless Communications, Networking and Mobile Computing (WiCOM 2011)*, Wuhan, China, 23-25 Sept. 2011.

[12] B. Yuan and K. K. Parhi, ``Early stopping criteria for energy-efficient low-latency belief-propagation polar code decoders,'' *IEEE Trans. Signal Process.*, vol. 62, no. 24, pp. 6496-6506, Dec. 15, 2014.

[13] Y. Yu, Z. Pan, N. Liu, and X. You, ``Belief propagation bit-flip decoder for polar codes,'' *IEEE Access*, vol. 7, pp. 10937–10946, 2019.

[14] A. Balatsoukas-Stimming, M. B. Pariz, and A. Burg, ``LLR-based successive cancellation list decoding of polar codes,'' *IEEE Trans. Signal Process.*, vol.63, no.19, pp.5165-5179, Oct. 2015.

[15] H. Li and J. Yuan, ``A practical construction method for polar codes in AWGN channels,'' *in Proc. TENCON Spring Conference*, pp. 223-226, Sydney, NSW, April 2013.

[16] H. Vangala, E. Viterbo, and Y. Hong, ``A comparative study of polar code constructions for the AWGN channel,'' arxiv:1501.02473, Jan. 11, 2015.

[17] S. Sun, S. G. Cho, and Z. Zhang, ``Error patterns in belief propagation decoding of polar codes and their mitigation methods,'' *in Proc. Asilomar Conf. on Sig., Syst. and Computers (Asilomar 2016)*, pp. 1199-1203, Nov. 2016.

[18] O. Afisiadis, A. Balatsoukas-Stimming; and A. Burg, ``A low-complexity improved successive cancellation decoder for polar codes,'' *in Proc. 48th Annual Asilomar Conference on Signals, Systems, and Computers (Asilomar 2014)*, pp. 2116-2120, Pacific Grove, CA, USA, 2-5 Nov. 2014.

Interleaving Depth Optimization for Concatenated FEC in 2.4GHz Ingenu System

Kentaro Yamamoto, Takatoshi Sugiyama

Graduate School of Engineering, Kogakuin University, Tokyo, Japan
Email: cm20051@ns.kogakuin.ac.jp

Abstract

In recent years, IoT (Internet of Things) is attracting a lot of attention and it's enabled by various wireless communication standards called LPWA (Low Power Wide Area)[1]. This paper focus on Ingenu[2], [3], which uses the 2.4GHz band among LPWA. We propose a new concatenated FEC (Forward Error Correction) in Ingenu system to more improve the transmission quality. The proposed concatenated FEC consists of convolutional encoding-Viterbi decoding as an outer FEC and differential encoding-differential detection with nonredundant error correction[4] as an inner FEC. The optimal interleaving depth can obtain the best BER(Bit Error Rate) performance of Ingenu system applied by the proposed concatenated FEC.

Proposed concatenated FEC

The proposed concatenated FEC in Ingenu system consists of convolutional encoding-Viterbi decoding as an outer FEC and differential encoding-differential detection with nonredundant error correction as an inner FEC. Interleaving of vertical writing and horizonal reading between two FECs. The reasons for these choices are as follows. Ingenu standard specifies both differential encoding-differential detection and convolutional encoding-Viterbi decoding. In order to more improve the BER performance of Ingenu systems, our proposed concatenated FEC selects the differential detector with nonredundant error correction[4] because it is unnecessary to change the specification of Ingenu. The circuit diagram of differential detector with nonredundant error correction[4] is shown in Fig.1. Differential encoding might be recognized as a kind of convolutional encoding and the its constraints are used for nonredundant error correction[4]. It is accomplished by both one and two symbols differential detections. Afterwards, the output of one and two symbols differential detections calculate a syndrome to eliminate non-existent error patterns. This allows for error correction with nonredundant bits and can improve the BER by about 1dB at 10^{-4} in AWGN[4].

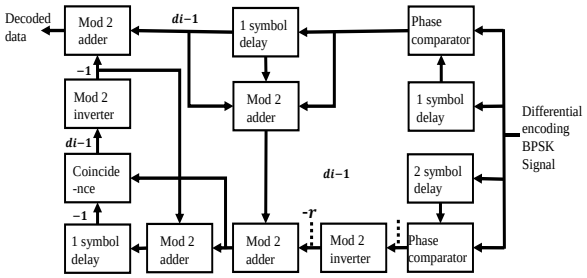

Fig.1 Circuit diagram of differential detector with nonredundant error correction

Simulation diagram

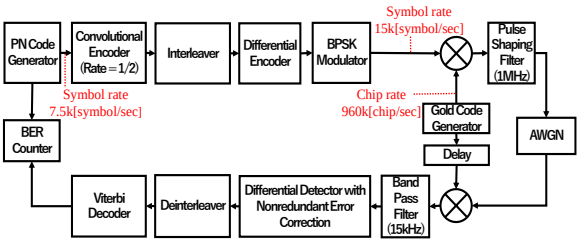

Fig.2 Simulation block diagram

The simulation block diagram of the proposed concatenated FEC in Ingenu system is shown in Fig.2. In this block diagram, in the transmitter, convolutional encoder (coding rate of 1/2, constraint length of 7) is performed as an outer FEC encoder. After interleaving, differential encoder as an inner FEC encoder is used. The signals are fed to BPSK modulator to generate 15kbps modulated signals. This modulated signal is spread by the Gold Code to about 1MHz bandwidth. This means 64times direct sequence spectrum spreading. The spread signal is transmitted after pulse shaping by a pulse shaping filter. In the receiver, the receiving signal is multiplied by the de-spreading code as same as spreading code. After that, the de-spread signal passes through a 15kHz bandwidth band pass filter. Afterwards, there are differential detector with nonredundant error correction, de-interleaver and Viterbi decoder with hard decision.

Simulation results

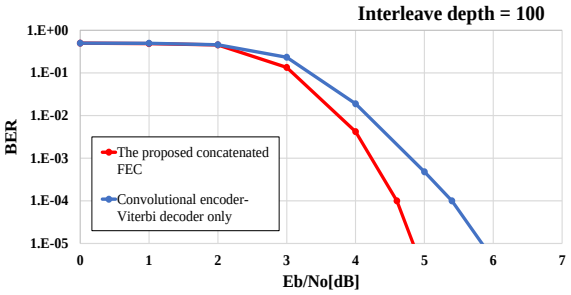

Fig.3 BER performance of the proposed concatenated FEC in Ingenu system

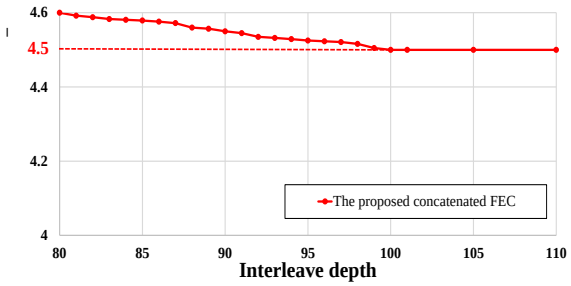

Fig.4 Interleave depth of the proposed concatenated FEC in Ingenu system

Fig.3 shows the BER performance of the proposed concatenated FEC in Ingenu system when the interleaving depth is 100. Compared to convolutional encoding-Viterbi decoding only, the proposed concatenated FEC can improve Eb/No at BER = 10^{-4} by about 1dB. Next, the interleaving depth is optimized. The interleaving depth of the proposed concatenated FEC in Ingenu system is shown in Fig.4. As the interleaving depth becomes deeper, it is obvious that the BER performance becomes better. The interleaving depth is saturated at more than 100, and the Eb/No at BER = 10^{-4} is 4.5dB at that depth. Therefore, the optimal interleaving depth is detected to be 100.

Conclusion

In this paper, we have proposed concatenated FEC that consist of convolutional encoding-Viterbi decoding and differential encoding-differential detection with nonredundant error correction in Ingenu system to more improve BER performances. We have evaluated the interleaving depth for the proposed concatenated FEC. The optimal interleaving depth of 100 can obtain the best BER performance of Ingenu system applied by the proposed concatenated FEC.

References:

[1] Zheng Li, “IoT Network LPWA Basics -Sigfox, LoRa, NB-IoT- “, June 2017.

[2]” https://www.ingenu.com”, Dec. 2020

[3] P. Kim et al, “Performance Analysis of Direct Sequence Spread Spectrum Aloha for LEO Satellite IoT System”, VTC2019-Fall, Sept. 2020.

[4] Samejima, et al, “Differential PSK System with Nonredundant Error Correction”, IEEE JSAC Vol.1 pp74-81, Jan. 1983.

Calculated Distance Error Performances by Relay Type GPS in Shinjuku Area

Kouhei Yoshida, Takatoshi Sugiyama

Graduate School of Engineering, Kogakuin University, Tokyo, Japan
E-mail: cm20054@ns.kogakuin.ac.jp

Abstract

It is difficult to receive GPS signals directly from GPS satellites in urban areas because many tall buildings block GPS signals. To solve this problem, we have proposed relay type GPS. In the relay type GPS, it is possible to calculate the GPS receiver's position assisted by the many mobile terminals. In this paper, we measure the calculated distance errors using a commercial GPS receiver in Shinjuku area. Moreover, we evaluate the calculated distance error performances and the number of received GPS satellites by the relay type GPS using the measured GPS positioning results.

INTRODUCTION

Currently, GPS (Global Positioning System) [1] has been used widely. However, GPS receivers cannot receive GPS signals from GPS satellites in urban areas because many tall buildings block GPS signals. GPS positioning is not possible unless four or more signals are received [2]. To solve this problem, relay type GPS has been proposed [3],[4]. In the relay type GPS, it is possible to calculate the target GPS receiver's position assisted by the many mobile terminals around it, which transmit their own position information via the same GPS signal format. The mobile terminal transmitting its own position information is called G-MT [5]. In this paper, we measure the calculated distance errors using a commercial GPS receiver in Shinjuku area. Moreover, we evaluate the CCDF (Complementary Cumulative Distribution Function) of the calculated distance errors and the number of receivable GPS satellites including the G-MTs by the relay type GPS in the Shinjuku model using the position information measured with a commercial GPS receiver.

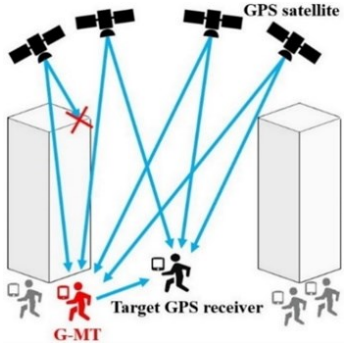

Fig. 1. The system diagram of the relay type GPS.

SIMULATION PARAMETERS

The measured environment and the simulation model of Shinjuku area are shown in Fig.2, 3, and the simulation parameters are shown in Table 1. The measurement area is around Kogakuin University, and a target GPS receiver is placed in front of it. In this measurement, three G-MTs for relay type GPS are used, and they are placed at the intersection within the line of sight from the target GPS receiver.

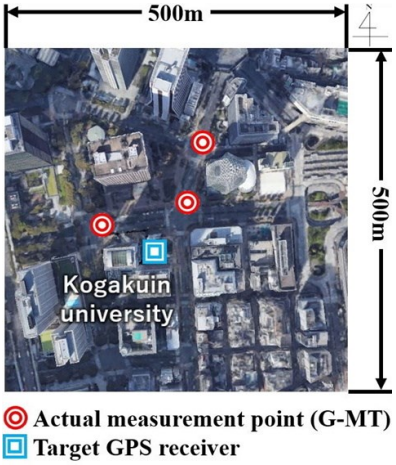

Fig. 2. The measurement area (Shinjuku).

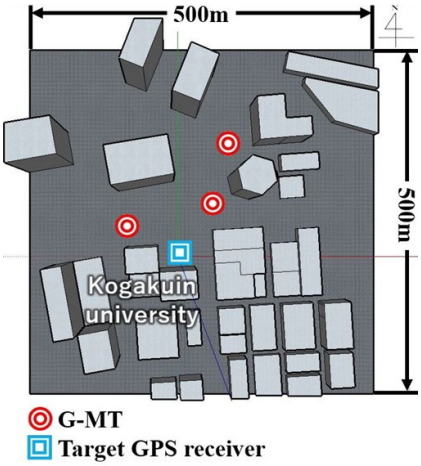

Fig. 3. The simulation model.

Table 1. The simulation parameters.

Parameter	*Value*
Number of G-MTs	1~3
Number of GPS satellites	32
Model size	500m × 500m
Simulation time	24 hours
Position calculation interval	5 minutes

SIMULATION RESULTS

The CCDF of calculated distance errors of the target GPS receiver by the relay type GPS is shown in Fig.4. The calculated distance error of the target GPS receiver is more improved by increasing the number of G-MTs. For example with the number of G-MTs = 3, the calculated distance error improvement of 95.23 m has been achieved by using relay type GPS when CCDF is 50%. Furthermore, the number of receivable GPS satellites including the G-MTs is shown in Fig.5. The target GPS receiver can always receive four or more GPS signals by using relay type GPS. This leads the positioning of the target receiver possible always.

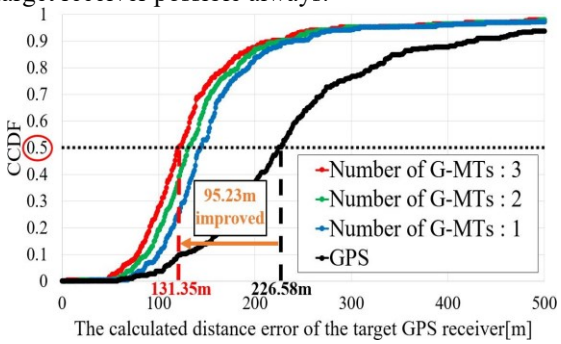

Fig. 4. The CCDF of calculated distance error by the target GPS receiver.

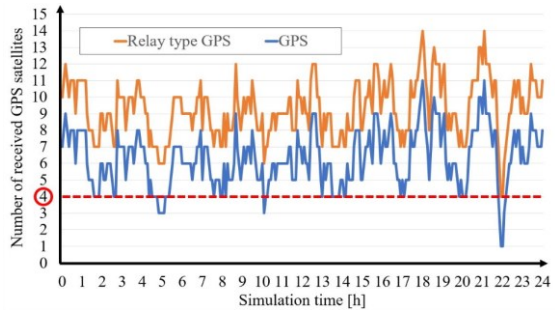

Fig. 5. The number of received GPS satellites.

CONCLUSION

We have evaluated the CCDF of the calculated distance error by the relay type GPS in the models simulating Shinjuku area using the position information obtained by a commercial GPS receiver. Compared with the conventional GPS, the calculated distance error of the target GPS receiver is reduced by using relay type GPS. In addition, the positioning of the target receiver is always possible by the relay type GPS.

References:

[1] Pratap Misra and Per Enge, "Global Positioning System: Signals, Measurements, and Performance", Syoyo Bunko, 2004.

[2] Bradford W. Parkinson, "Introduction and Heritage of NAVSTAR, the Global Positioning System", Global Positioning System: Theory and Applications, Vol. I, AIAA, 1996.

[3] Kouhei Yoshida and Takatoshi Sugiyama, "Calculated Distance Error Improvement by Using Drones in Relay Type GPS", KICS ICTC2020, VI-6.4, Oct. 2020.

[4] Kouhei Yoshida and Takatoshi Sugiyama, "GPS positioning accuracy improvement by using drone in relay type GPS", P128-129, ISAT-19, Jan. 2021.

[5] Norifumi Murai and Takatoshi Sugiyama, "Calculated Distance Error Improvement by Using Elevation Mask in Relay Type GPS," KICS ICTC2018, I-1.2, Oct. 2018.

The Child's Residual Limb Model Reconstruction by using Point Cloud Data

Ding-Horng Chen*, and Qiao-Ting Shen

Department of Computer Science and Information Engineering, Southern Taiwan University of Science and Technology, Tainan, Taiwan
E-mail: chendh@stust.edu.tw

Abstract

This paper proposes a three-dimensional reconstruction for young children's residual limbs point cloud data based on ORB algorithm. The proposed system is divided into four subsystems. First retrieve multi-angle point cloud information by a handheld Intel RealSense LiDAR depth camera. Second, perform the feature extraction and matching from 2D image by using ORB algorithm. Third, register the partial point cloud data fragments to a complete 3D model. And the last, implement the surface reconstruction of the points clouds by optimizing the parameters similarity of the transformation matrices to obtain a smooth surface.

Introduction

According to the World Health Organization's Disability Report, the number of people with disabilities worldwide exceeds one billion and is increasing. Children born with amputated limbs will face many difficulties and challenges in the growth period. Nowadays, traditional plaster models are still used to make prosthetic sockets, and this process requires repeated measurement, adjustment, and modification. The process is quite complicated and requires a lot of manpower and time. To solve the problem, this paper uses the point cloud data obtained by the depth camera to reconstruct the three-dimensional model of the child's residual limb.

This paper builds the system architecture of 3D reconstruction of residual limbs, as shown in Figure 1. According to the system architecture, the proposed system is divided into several subsystems. The first subsystem is image acquisition, which is implemented by a handheld depth camera by capturing the multi-view images. The second subsystem is 2D image feature extraction and matching by using ORB (Oriented FAST and Rotated BRIEF) algorithm to calculate the significant key-points in the image. The key descriptor is found by using the feature algorithm of ORB to calculate the Hamming distance. The third subsystem is the point cloud data registration which is implemented to find the transformation matrix between the two corresponding images by minimizing the internal parameters differences of point cloud of the color and depth image information. The last subsystem is to perform the surface reconstruction of the point cloud model to obtain a smooth surface of the model. In this paper, the open-source library PCL (Point Cloud Library) is used for development.

Image Acquisition

In this paper, a handheld Intel RealSense LiDAR Camera L515 depth camera is used to record images in 360 degrees around the model. Through the GUI of the RealSense Viewer provided by Intel, users can adjust image parameters and obtain images that include color (RGB) images, depth (Depth) images, and infrared (Infrared) images. The color image, the depth image and the json file that records the information of the camera's internal matrix will be stored separately for use in subsequent image processing steps. In this paper, we record 24 second images (with .bag file format) and generates 433 color images and 433 depth images respectively. The program developed in this paper will read the bag file to generate sequential color images and depth images. The image acquisition UI is shown in Figure 2.

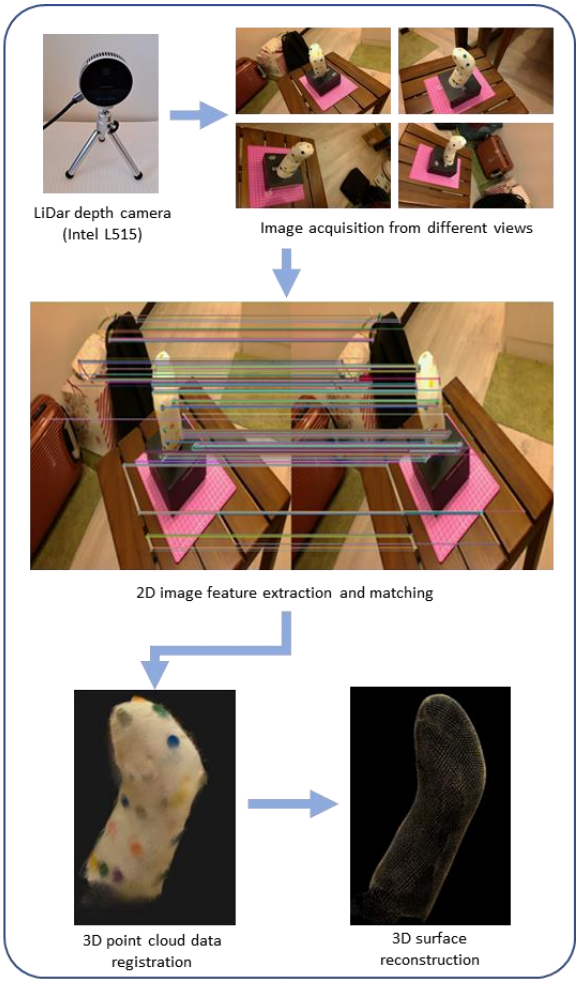

Fig. 1. System architecture

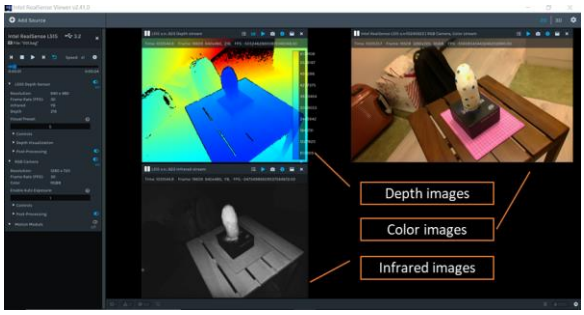

Fig. 2. Image acquisition by Intel L515 camera

2D image feature extraction and matching

In order to effectively and accurately extract the correlation between two images, we must perform image feature point extraction and matching. The feature points in the image refer to the prominent regional features in the image. After extracting the salient features in an image, it can be used as an important basis for identifying image similarity for subsequent feature matching. In this paper, ORB algorithm is used as the feature extraction method. The advantage of the algorithm is fast and stable extraction of features, anti-noise ability and rotation invariant. The ORB corner detection and feature descriptor algorithm is derived from the original FAST (Features from Accelerated Segment Test) corner feature detection and the BRIEF (Binary Robust Independent Elementary Features) descriptor.

The feature points of the image sequence are extracted by ORB algorithm, and salient features are obtained. Feature matching is mainly based on the Hamming distance of ORB feature descriptors between two images. Given a matching threshold to calculate the best match between the images. The matching result is shown in Figure 3.

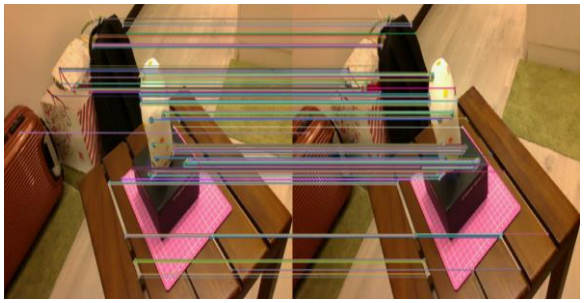

Fig. 3. The best matching result of corresponding images

3D point cloud data registration

In order to construct a complete residual limb model, we perform point cloud stitching. This step converts color images and depth images into point clouds (with .pcd file format), and then stitch multi-view point cloud files to find the key points and feature descriptors between the two images. The Hamming distance is calculated to find the best image pairing, and sequentially reconstruct the complete model data from the image fragment information.

In order to improve the efficiency of point cloud stitching, point cloud filtering, point cloud segmentation and outlier removal methods are used. The implementation is described in detail as follows. The purpose of point cloud filtering is to reduce the amount of computation. We adopt a passthrough filter to set the area range to remove the background and retain the point cloud information. We implement the point cloud segmentation algorithm to separate the foreground and background point cloud objects. In this paper, we use the random sampling consensus (RANdom SAmple Consensus, RANSAC) algorithm proposed by Fischler and Bolles in 1981 to detect and remove planar objects in the point cloud. Since the original point cloud information usually contains a lot of noise, outliers, etc., the matching process is susceptible to interference and affects the accuracy of the matching. Therefore, this paper adopts a statistical outlier removal filter to remove outliers and reduce noise interference for the subsequent feature matching processing. The experimental results are shown in Figure 4.

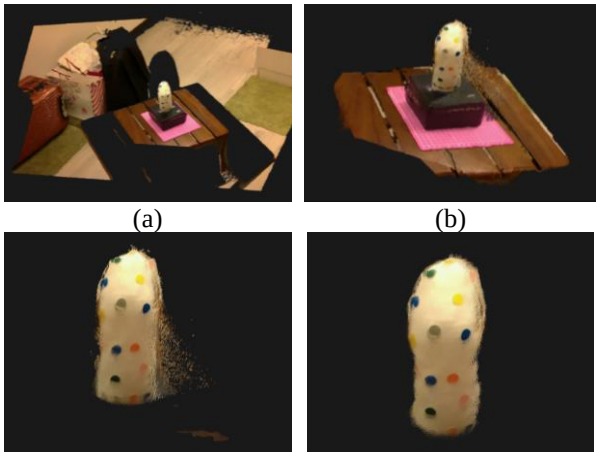

Fig. 4. The experimental results of 3D point cloud data registration. (a) The stitching result of 10 point cloud files; (b) The result of point cloud using passthrough filter; (c) The result of point cloud using RANSAC segmentation; (d) The result of point cloud using statistical outlier removal filter.

3D surface reconstruction

After completing the previous steps, a point cloud model can be constructed. To obtain a smooth three-dimensional object surface for subsequent adjustment, this paper conducts three-dimensional surface processing and surface reconstruction with PCL library. First, a down sampling method is used to reduce the amount of computation. For the point cloud data points, the moving least square method (MLS) is used to calculate the minimum error between the smooth surface and the point cloud data points. Finally, we use the point cloud greedy algorithm to generate the model.

The down sampling algorithm adopted in this paper is the *pcl::VoxelGrid* function provided by the

PCL library. With this method, we can assign the size and resolution of the XYZ coordinate in space. For the data points of the point cloud, use the *pcl:: MovingLeastSquares* function of the PCL library to achieve point cloud smoothing and surface reconstruction. This step was performed twice to achieve the best smoothing effect. To generate the final surface model, we use the greedy algorithm to triangulate the surface mesh. Here we use the PCL library's *pcl::GreedyProjectionTriangulation* method to calculate the normal vector of the point cloud, then perform the Delaunay triangulation algorithm. Finally, the three-dimensional points are connected according to the points of the plane projection, and the surface model is reconstructed by the triangular mesh.

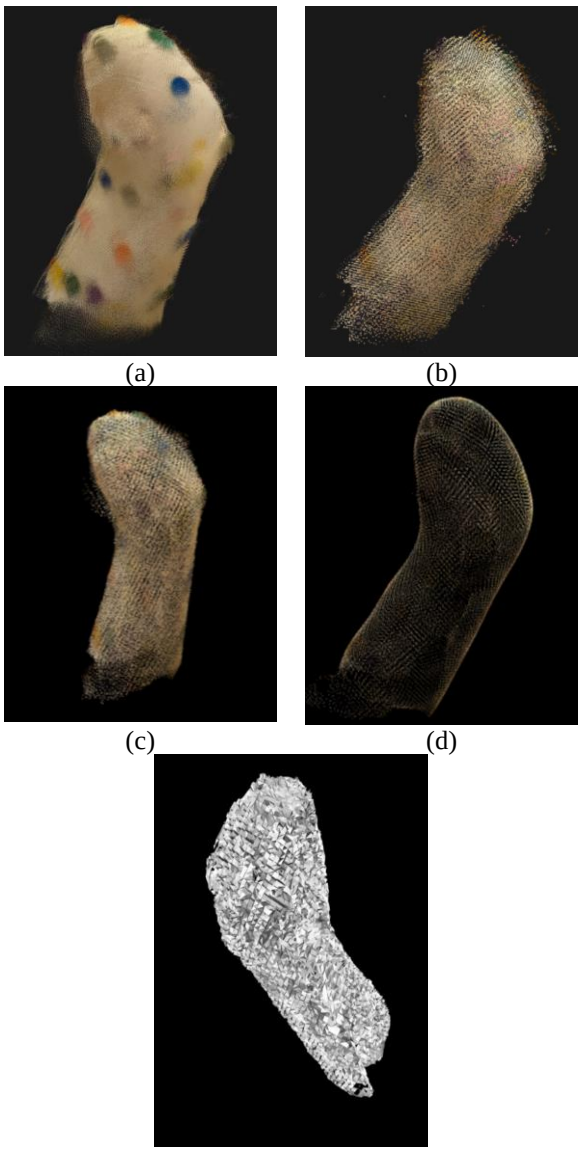

Fig. 5. The experimental results of 3D surface reconstruction. (a)(b) The point cloud before and after the down sampling method; (c)(d) The surface reconstruction result of the first and the second MLS smoothing; (e) The surface reconstruction result of the greedy projection triangulation.

Conclusion

In this paper, a depth camera is used to obtain the multi-view point cloud information of the child residual limb model, and the ORB algorithm matching technology and three-dimensional reconstruction are combined to obtain a complete residual limb model. Manufacturers will be able to use this as a basis for making prosthetic sockets, and it can also reduce the inconvenience of traditional model-taking of children's residual limbs.

Remark

This research is supported by the Ministry of Science and Technology, Taiwan, Grant MOST 109-2622-E-218-006-CC2.

References

[1] R. Ismail *et al.*, "Affordable and Faster Transradial Prosthetic Socket Production Using Photogrammetry and 3D Printing," *Electronics*, vol. 9, no. 9, p. 1456, Sep. 2020, doi: 10.3390/electronics9091456.

[2] E. Rublee, V. Rabaud, K. Konolige, and G. Bradski, "ORB: An efficient alternative to SIFT or SURF," in *2011 International Conference on Computer Vision*, Barcelona, Spain, Nov. 2011, pp. 2564–2571. doi: 10.1109/ICCV.2011.6126544.

[3] M. Alexa, J. Behr, D. Cohen-Or, S. Fleishman, D. Levin, and C. T. Silva, "Point set surfaces," in *Proceedings Visualization, 2001. VIS '01.*, San Diego, CA, USA, 2001, pp. 21–537. doi: 10.1109/VISUAL.2001.964489.

[4] M. Alexa, J. Behr, D. Cohen-Or, S. Fleishman, D. Levin, and C. T. Silva, "Computing and rendering point set surfaces," *IEEE Trans. Vis. Comput. Graph.*, vol. 9, no. 1, pp. 3–15, Jan. 2003, doi: 10.1109/TVCG.2003.1175093.

[5] B. Mederos, L. Velho, and L. H. De Figueiredo, "Moving least squares multiresolution surface approximation," in *16th Brazilian Symposium on Computer Graphics and Image Processing (SIBGRAPI 2003)*, Sao Carlos, Brazil, 2003, pp. 19–26. doi: 10.1109/SIBGRA.2003.1240987.

[6] Xiao-Shan Gao, Xiao-Rong Hou, Jianliang Tang, and Hang-Fei Cheng, "Complete solution classification for the perspective-three-point problem," *IEEE Trans. Pattern Anal. Mach. Intell.*, vol. 25, no. 8, pp. 930–943, Aug. 2003, doi: 10.1109/TPAMI.2003.1217599.

[7] R. B. Rusu, N. Blodow, and M. Beetz, "Fast Point Feature Histograms (FPFH) for 3D registration," in *2009 IEEE International Conference on Robotics and Automation*, Kobe, May 2009, pp. 3212–3217. doi: 10.1109/ROBOT.2009.5152473.

[8] P. J. Besl and N. D. McKay, "A method for registration of 3-D shapes," *IEEE Trans. Pattern Anal. Mach. Intell.*, vol. 14, no. 2, pp. 239–256, Feb. 1992, doi: 10.1109/34.121791.

An Image Segmentation Method based on Unsupervised Learning Algorithms

Zong-Xian Yin*

Department of Computer Science and Information Engineering, Southern Taiwan University of Science and Technology, Tainan, Taiwan
E-mail: yinzx@stust.edu.tw

Abstract

Computer visual systems can rapidly obtain a large amount of data and automatically process them with ease. The precision of image segmentation, which plays a critical role in computer visual systems, directly affects the quality of processing results. The paper proposed an image segmentation methods involving unsupervised classification and region growing–based image segmentation methods. This method can effectively segment image areas containing a complex background or uneven light and shadow.

An image usually only has certain regions, called the foreground or the target, that are meaningful or interesting for their capture of people or objects. The remainder of the image is called the background. Image segmentation precision affects subsequent image processing and analysis. The main image segmentation methods are classified as region based, edge based, and segment based. For the accurate segmentation of the object from the complex background, Kulathilake et al. [1] proposed computing the difference between two consecutive frames to generate a foreground mask. Morphological erosion and flood filling were then used to isolate and extract the object regions from the mask. AbdelRaouf et al. [2] integrated the Frangi filter with the region growing algorithm for image segmentation. Wang et al. [3] applied a Hessian filter to clarify vascular structure in images. Subsequently, k-means and region growing algorithms were used for the segmentation of vessel-containing regions from the images. Huang et al. [4] used a statistics-based threshold segmentation algorithm to compute image threshold values and divide images into regions.

In this paper, we introduce an unsupervised learning method which can effectively segment image areas containing a complex background or uneven light and shadow. The method conjoins the regional parameter expansion and the optimal cover tree algorithm. The regional parameter expansion algorithm first identifies regional characteristics which can be used to segment the object regions in the images. Next, the optimal cover tree algorithm is used to establish the sequential relationships between the object regions. Figure 1 presents a flow chart of the method. In step 1, images are divided into sub-images of fixed size for image recognition. In step 2, deep learning is used for object region recognition. In step 3, a regional parameter expansion algorithm is used to segment the object regions in the sub-images. In step 4, an optimal cover tree algorithm is used to examine and connect the object regions in the adjacent sub-images.

Applying image segmentation techniques to medical image processing can facilitate the identification of lesions, as well as diagnosis and treatment decision-making. Our method was simple and effective overall, in both the theoretical and practical contexts. Future research directions can involve integrating the coronary artery disease grading system and quantitative indexes with the present algorithm for lesion classification.

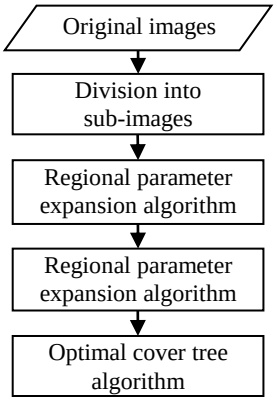

Figure 1. flow chart of our proposed method

References:

[1] K. A. S. H. Kulathilake, L. Ranathunga, G. R. Constantine, N. A. Abdullah, “A segmentation method for extraction of main arteries from Coronary Cine-Angiograms”, in 2015 Fifteenth International Conference on Advances in ICT for Emerging Regions (ICTer), 24-26 Aug. 2015

[2] S. Sameh, M. A. Azim, A. AbdelRaouf, “Narrowed coronary artery detection and classification using angiographic scans”, in 2017 12th International Conference on Computer Engineering and Systems (ICCES), 19-20 Dec. 2017

[3] S. Wang, B. Li, S. Zhou, ”A Segmentation Method of Coronary Angiograms Based on Multi-scale Filtering and Region-Growing”, in 2012 International Conference on Biomedical Engineering and Biotechnology, 28-30 May 2012

[4] J. Huang, W. Qu, L. Meng, C. Wang, “Based on statistical analysis and 3D region growing segmentation method of liver”, in 2011 3rd International Conference on Advanced Computer Control, 18-20 Jan. 2011

Wired cable proposal on the feasibility of a stratospheric platform -Background and wired connections and strategies for orbital elevators-

Koichiro Murata
Department of SystemDesign, Graduate School of Engineering, Kogakuin University, Tokyo, Japan
E-mail: gm20005@ns.kogakuin.ac.jp

Abstract

Many private companies, led by SpaceX, have entered the space industry and have been successful, attracting a lot of investment. The use of space has become so familiar to us that we are not even aware of it. These are mainly rocket-based industries such as space travel and docking to the ISS. However, there is an urgent need for proposals that are more environmentally and financially effective, and I have focused on orbital elevators that connect the ground and space. I summarized the stratospheric platform necessary for this realization.

Since the end of the Cold War, many countries other than the U.S. and Russia have been engaged in space development, but the focus has been on rocket and satellite development. Therefore, we propose a new platform to connect the ground and space. As a general concept, space elevators exist, but there are structures that extend to geostationary satellites, but the platform here will be a wired connection between the ground and the stratosphere. Prior research has brought to light a wide range of issues, from stability and operational efficiency to safety. Optimistic hopes for the future exist, especially for sturdy materials and methods to make it self-sustaining. Therefore, we propose a quantitative and novel construction method and evaluate it in comparison with existing platforms. For this purpose, we will conduct experiments on a small scale to clarify the above possibilities. We will also conduct additional research on economic effects, as we consider them important for our proposal. As a research method, we will conduct several self-sustaining methods on a small scale to check the buoyancy and safety from external factors such as wind.

Table 1 R & D segment

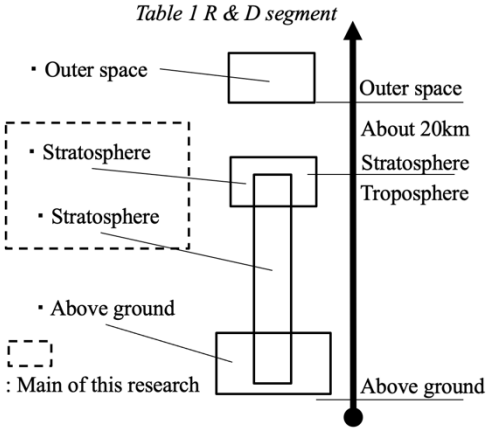

The space section is the front line for utilizing the space environment for solar power generation and transmission. The stratosphere is the place to receive energy, conduct experiments, and transmit communications, taking advantage of its fixed location. The cable section is wired to the stratosphere to ensure stable construction. The ground section is the interconnection point for communication lines and electric power. Based on the above, we are looking for a way to construct the stratosphere and the cable section.

As an experiment, we will conduct a small experiment on a university campus. We will prepare multiple shapes and materials to explore external factors such as wind [1]. In addition, there are similar studies on imagining ideas that can be used for reference[2].

Table 2 Parametric

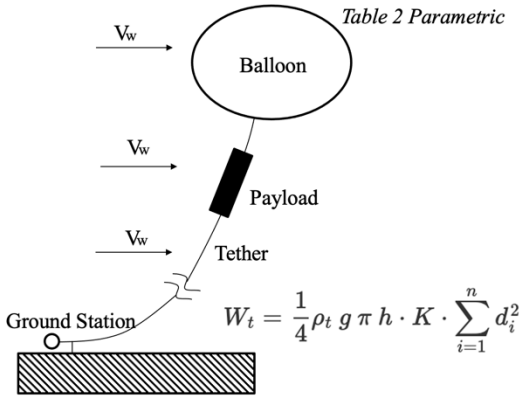

References:

[1] K. Izet-Ünsalan and D. Ünsalan, "A low cost alternative for satellites- tethered ultra-high altitude balloons," *Proceedings of 5th International Conference on Recent Advances in Space Technologies - RAST2011*, 2011, pp. 13-16, doi: 10.1109/RAST.2011.5966806.

[2] McKuin, B., Zumkehr, A., Ta, J. *et al.* Energy and water co-benefits from covering canals with solar panels. *Nat Sustain* **4,** 609–617 (2021). https://doi.org/10.1038/s41893-021-00693-8

Lightning Talk Session

Simulation Science, Measurement Science, Computational Science

November 23rd

Theoretical study on interfacial interaction of zig-zag carbon nanotubes/epoxy resin nanocomposite

Yurika Serizawa[1]*, Tomoe Yayama[1], and Fumiko Akagi[1]

Department of Electrical Engineering and Electronics, Graduate School of Engineering, Kogakuin University, Tokyo, Japan
E-mail: cm21029@ns.kogakuin.ac.jp

Abstract

We studied the effect of point defects in carbon nanotubes (CNTs) and epoxy nanocomposite on the interface between a CNT and epoxy resin using first-principle calculations based on density functional theory (DFT). The point defect changed the interfacial interaction between the CNTs/epoxy resin because the peak state of the Fermi level decreased.

Structural components used in space mission, such as rockets or satellites, require lightweight and high mechanical strength. Carbon fiber-reinforced composites are attracting attention in aerospace industries because they have excellent mechanical performances, such as higher specific strength, than conventional metals and alloys [1]. CNTs, which possess high tensile strength due to covalent bonds, are promising next-generation reinforcing materials for composites. However, the interfacial adhesion between CNT and epoxy resin is low and the growth of cracks at the interface can cause the material fracture [2]. Therefore, we should investigate the CNT/resin interface from the microscopic electrons and atoms perspective. In this study, the interface models of the CNT/epoxy resin nanocomposites were designed using atomic-scale structures and the effects of point defects in CNTs on the interface between CNTs and epoxy resin were investigated using the first-principle calculation based on density functional theory. The electronic structure calculations were conducted within the framework of DFT as implemented in the Vienna Ab initio Simulation Package (VASP) [3]. Further, the Perdew-Burke-Ernzerhof (PBE) generalized-gradient approximation for exchange-correlation energy function was used. The cutoff energy was set to 400 eV and the number of k-points was 1 × 1 × 6. Fig. 1 shows the computational model of CNTs with epoxy resin. Fig. 1(a) shows the "perfect model", in which the epoxy molecules are placed over defect-free CNTs. Fig. 1(b) shows the "defected model," in which the epoxy molecules are placed over the CNT with a point defect. A diglycidylether of bisphenol A (DGEBA) molecule was used as the model for epoxy resin. For the CNT, a zig-zag (7,0) single-wall carbon nanotube was used. The partial density of states (PDOSs) of electrons is shown in Fig. 2. Fig. 2(a) and (b) are the CNT-only PDOSs, without and with a defect, respectively, and Fig. 2(c) and (d) are the PDOSs for the perfect and defected model, respectively. Comparing Fig. 2(a) and (b), the CNT with a point defect has the electron levels partially occupied in the gap. Thus, these electron levels are defect levels caused by a point defect.

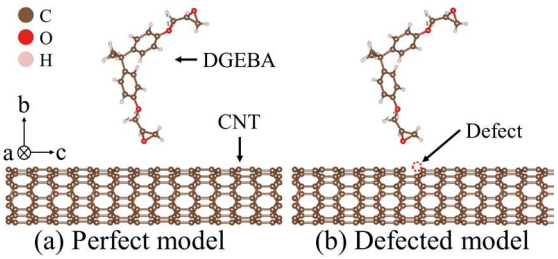

Fig. 1. Computational models.

These are almost the same for (a) and (c); however, the PDOS for the defect levels of (d) is smaller than that of (b). This is because the interface interaction between DGEBA and CNT changed due to the point defects. Moreover, when the charge-density distributions were investigated, the sharing of orbitals between CNTs and epoxy resin was observed. This result suggests the feasibility of enhancing the interfacial adhesion between CNT and resin.

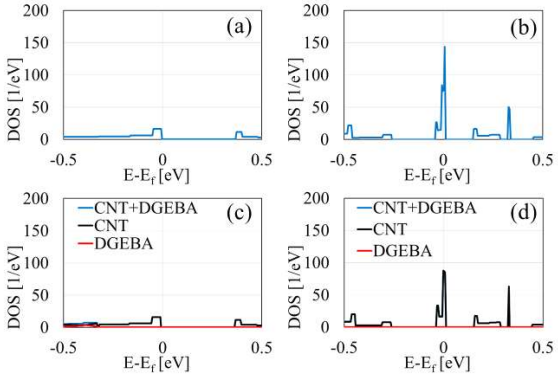

Fig. 2. Partial density of states: (a) CNT (b) Defected CNT (c) Perfect model (d) Defected model.

References:

[1] K. Mori, N. Matsumoto, S. Nomoto, and K. Tsuruta, *OJCM*, **7**, 179–184 (2017).
[2] W. Jian, D. Lau, *Compos. Sci. Technol.*, **191**, 108076 (2020).
[3] G. Kresse, J. Furthmüller, *Phys. Rev. B*, **54**, 11169–11186 (1996).

Predicting of Pedestrian Trajectory Using Sequence to Sequence Learning with Neural Networks

Tomoya Ono[1] and Takashi Kanamaru[2]

[1] Major of Mechanical Engineering, Kogakuin University,
Tokyo 192-0015, Japan (am20015@ns.kogakuin.ac.jp)
[2] Department of Mechanical Science and Engineering, Kogakuin University,
Tokyo 192-0015, Japan (kanamaru@cc.kogakuin.ac.jp)

Abstract

Recently, development of navigation robots and autonomous cars is rapidly progressing. When such robots become popular in our daily life, their collisions with humans should be avoided for safety. To avoid such collisions, we predicted pedestrian trajectories using three methods of machine learning including sequence to sequence learning, and we compared their results.

Recently, development of navigation robots and autonomous cars is rapidly progressing. When realizing such robots, safety for humans is highly important. Therefore, in this study, we predict pedestrian trajectories to avoid collisions of robots with humans.

When applying the prediction of pedestrian trajectories to realistic mobile robots, predicting multiple steps of data would be useful. Therefore, we predict the future sequential data $p_{t+1}, p_{t+2}, \cdots, p_{t+n}$ with n steps from the past sequential data $x_{t-m+1}, x_{t-m+2}, \cdots, x_{t-1}, x_t$ with m steps where $m = 15$ and $n = 10$.

For that purpose, we investigated the following three methods.

I. Predicting n steps of data with n models.
II. Predicting n steps of data with a model by applying one-step prediction several times.
III. Predicting n steps of data with Seq2Seq (sequence to sequence) model.

In the method I, n models are trained in which the kth model predicts p_{t+k} from the past sequential data $x_{t-m+1}, x_{t-m+2}, \cdots, x_{t-1}, x_t$ where $k = 1,2, \cdots, n$. By collecting n results of predictions, we obtain $p_{t+1}, p_{t+2}, \cdots, p_{t+n}$.

In the method II, only a model that predicts p_{t+1} from $x_{t-m+1}, x_{t-m+2}, \cdots, x_{t-1}, x_t$ is trained. The subsequent predictions are obtained by appending the prediction p_{t+i} to the past sequential data.

In the method III, a Seq2Seq model [1] is trained that can predict n steps of data from m steps of the past sequential data.

In the following, we treat pedestrian trajectories represented by two dimensional coordinates (x_t, y_t).

In the both methods I and II, we used long short-term memory (LSTM) networks [2] and conventional multi-layer neural networks (NN), and we compared their results. In the method I, the significant difference ($p < 0.05$) between the results of LSTM and NN was not observed. In the method II, the results of LSTM were significantly better than those of NN ($p < 0.05$).

The predicted trajectories of the method I (LSTM), the method II (LSTM), and the method III (Seq2Seq) are shown in Fig. 1. It is observed that the predicted trajectories of the method III (Seq2Seq) were closest to the original data. It is also observed that the trajectories of the method I is not smooth because the predictions $p_{t+k}(k = 1,2, \cdots, n)$ were obtained from the independently trained n models.

The detailed results of the experiment will be shown in the presentation.

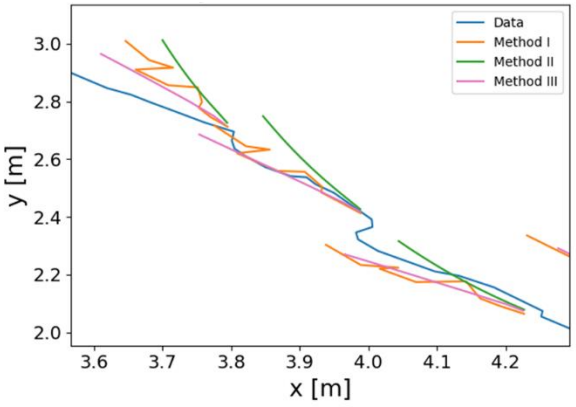

Fig. 1 Comparison of the predicted trajectories.

References:

[1] N. Sakata, Y. Kinoshita and Y. Kato, "Predicting a Pedestrian Trajectory Using Seq2Seq for Mobile Robot Navigation", The 44nd Annual Conference of the IEEE Industrial Electronics Society, pp. 4300-4305, 2008.
[2] A. Alahi, K. Goel, V. Ramanathan, A. Robicquet, Li Fei-Fei, S. Savarese, "Social LSTM: Human Trajectory Prediction in Crowded Spaces", Proceedings of the IEEE Conference on Computer Vision and Pattern Recognition (CVPR), pp. 961-971, 2016.

Separation Control around NACA0015 Airfoil using Vortex Generator Type Plasma Actuator over Low Reynolds Number Conditions

Shota Mayahara* and Makoto Sato

Department of Mechanical Science and Engineering, Graduate School of Engineering, Kogakuin University, Tokyo, Japan
E-mail: s518057@ns.kogakuin.ac.jp

Abstract

This presentation shows the separation control around a NACA0015 airfoil using vortex generator type plasma actuators (VG-PA) at a Reynolds number of 63,000. As a result of numerical simulations, it is confirmed that VG-PA can suppress the separated-flow in this Reynolds number from the instantaneous flow fields and the lift and drag coefficients.

To control a separated-flow, plasma actuators (PA) have been expected [1]. The PA is a micro device that can induce a wall-jet flow by applying AC and high voltage. As a result, separated flows can be suppressed by the control. In the previous researches, two setting types of PA have been investigated. One is a spanwise type PA(SP-PA), which is installed in the span direction, and the other is a vortex generator type PA(VG-PA), which is installed in the chord direction. Many researches have been conducted on the separation control using the SP-PA and effective control methods (acting style, setting location and so on) have been found over a wide Reynolds number conditions (Re=O (10^3-10^6)) [2]. On the other hand, there are no researches on separation control using the VG-PA over wide Reynolds number conditions.

In this study, we have conducted large-eddy simulations on the separation control using the VG-PA at $5000 \leq Re \leq 63000$ in order to clarify the control mechanisms and control effects using the VG-PA.

The target Reynolds numbers, angles of attack and grid points are shown in Table 1. In this abstract, the case of Re=6.3×10^4 is shown. The length of the VG-PA (lp) toward chord direction is set as 0.5c or 0.95c. The distance between each VG-PA is 0.1c. The numerical simulations have been conducted by super computer "Oakforest-PACS" of the University of Tokyo. Approximately 390 cores are used in one case.

Figure 1 shows the instantaneous flow fields and Fig. 2 shows lift and drag coefficients. From Fig. 1, the flow separation occurs in the no control case. On the contrary, the streamwise vortex can be observed near the leading edge and the separation is suppressed in VG-PA acting cases. When the length is long (lp:0.95c), the VG-PA can suppress the separation to trailing edge of the airfoil. Form this result, it is found

Table 1. Target Reynolds numbers (Re), angle of attack (AoA) and grid points.

Re	AoA	Grid points
5.0×10^3	10°	33 million
1.0×10^4	10°	33 million
6.3×10^4	12°	33 million

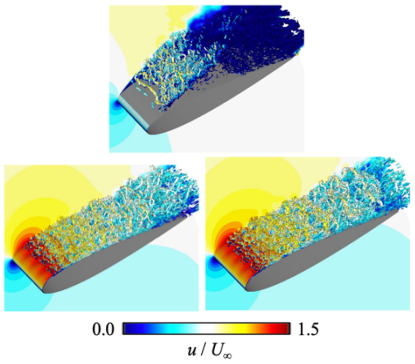

Fig. 1. Instantaneous flow fields. (Upper: No control, left: lp0.5, right: lp0.95)

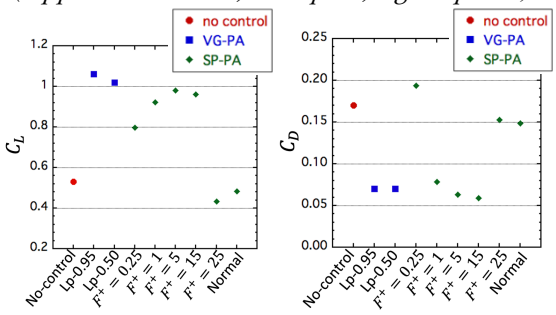

Fig. 2. Lift (left) and drag (right) coefficients.

that the long VG-PA shows higher control effect compared with the short (lp:0.5) VG-PA.

The lift and drag coefficients show control effects by the VG-PA. The lift is greatly improved and its effect is higher than that of the SP-PA [3]. The drag coefficient is improved in the VG-PA, however, the effect of the SP-PA is more effective.

References:

[1] Post, M. L. and Corke, T. C., *AIAA J.*, **42**, 2177–2184, (2004).

[2] M. Sato, K. Okada, K. Asada, H. Aono, T. Nonomura, K. Fujii, *Physics of Fluids*, **32**, 025102 (2020).

[3] M. Sato, T. Nonomura, K. Okada, K. Asada, H. Aono, A. Yakeno, Y. Abe, K. Fujii, *Physics of Fluids*, **27**, 117101(2015).

GPS Positioning Error Improvements by Number of Reflections and Incident Angle Estimations

Koichi Saito, Takatoshi Sugiyama

Graduate School of Engineering, Kogakuin University, Tokyo, Japan
E-mail: cm21025@ns.kogakuin.ac.jp

INTRODUCUTION

In GPS, the pseudo ranges calculated by propagation times of GPS signals are used the positioning calculation [1]. However, when reflection signals are received from building walls, the pseudo ranges are observed to be longer than the original linear distances. These deteriorate the GPS positioning accuracies. So as to unravel this problem, pseudo range correction method has previously been proposed [2]. Although it must estimate the number of reflections and incident angle of the received GPS signal, the estimation accuracies by the conventional estimation are not enough to improve GPS calculated distance errors. In this paper, we propose new estimation models that estimate the number of reflections and incident angle by using the pseudo ranges before the correction in addition to the conventional received GPS signal power. It is clarified that the pseudo range correction method applied by the proposed estimations more improves GPS calculated distance errors than those with the conventional estimations.

PSEUDO RANGE CORRECTION METHOD

The pseudo range correction method [2] is shown in Fig.1. In order to use the equation described below, GPS satellite A is intentionally transformed from three-dimensional coordinates to a two-dimensional plane and A is placed on the same plane as reception point B, Temporary reception point C and reflection point D [2]. Fig.1 shows an example of the number of reflections n of 1. The point where the GPS signal is received at 0 m above the ground when it travels straight ahead is defined as the temporary reception point C. Since DB equals DC in triangle BCD, using the cosine theorem in triangle ABC, the original linear distance AB between the GPS satellite and the reception point can be obtained from the observed pseudo range AC by using r and θ, as shown in Equation (1). r is defined as the distance from the reception point to the reflective surface of the east building and θ is defined as the incident angle of the GPS signal, respectively. The number of reflections n from 2 to 4 can be calculated in the same way [2].

$$n = 1: \quad AB^2 = AC^2 + (2r)^2 - 2AC(2r)\cos\theta \qquad (1)$$

In this paper, r is assumed to be known distance because it is a relatively short distance and may be measured visually by commercial smart phone applications such as Ref. [3]. In the conventional estimation model, the number of reflections and the incident angle were estimated using only the received power [2], but the estimation accuracies were insufficient. Fig.2 shows the conventional estimation model for n and θ. In this paper, to estimate the number of reflections more precisely. We use the fact that different numbers of reflections lead different received powers even in the equivalent pseudo range conditions. Moreover, the incident angle is estimated by using the relationship that smaller incident angle has longer delay. This is because longer propagation time through the ionosphere and troposphere leads longer pseudo range, even for the same the number of reflections.

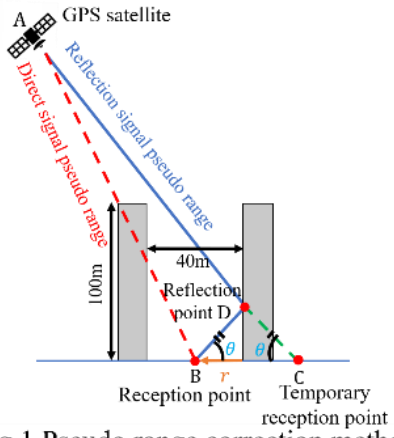

Fig.1 Pseudo range correction method

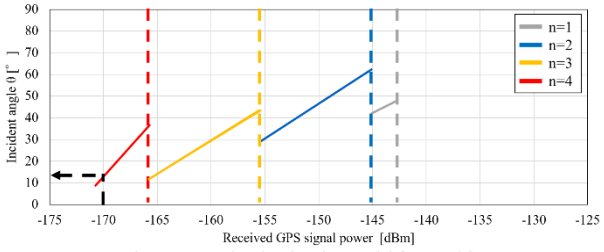

Fig. 2 Conventional estimation model for n and θ.

SIMULATION RESULTS BY PROPOSED ESTIOMATION MODEL

Fig.3 shows the simulation model of bird's-eye view, and Table 1 shows the major simulation parameters. The first step is to design the proposed estimation model. The simulation environment consisted of six buildings, each 100 m high × 40 m long × 40 m wide. The intersection point of the black dotted lines (x- and y-axes in Fig.3) is defined as the reference point of (0,0). The reception point is changed in the y axis direction as its coordinate of (0, y). The

GPS satellite orbits are based on 24 hours from January 15, 2016 00:00:00 to January 16, 2016 00:00:00 [2].

Table 1 Major simulation parameters.

Parameter	Value
Number of GPS satellites	32
Positioning simulation time	24 hours
Positioning interval	10 minutes
Number of reflections n	1～4
Building size	40m× 40m× 100m
Building material	concrete

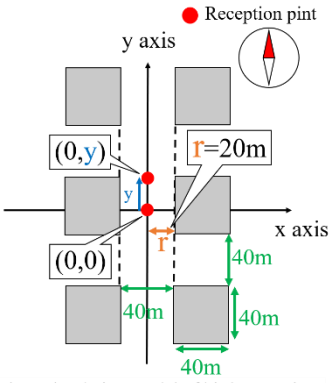

Fig.3 Simulation model of bird's-eye view.

In the proposed estimation models, n is estimated by using the pseudo range before the correction in addition to the received GPS signal power. In order to design the proposed model for n as follows.

1. Divide the pseudo range before the correction into ranges for each 1000 km in this paper
2. Determine the range of received GPS signal power by using the minimum received GPS signal power of direct signal
3. Determine the range of received GPS signal power by using the maximum received GPS signal power other than direct signal as a threshold

Fig.4 shows the proposed estimation model for the number of reflections n. In Fig.4. when the received GPS signal power is observed as -170 dBm and the pseudo range before the correction is calculated as 22500 km, the intersection of the received GPS signal power and the pseudo range before the correction is in the red range, so n can be estimated as 4.

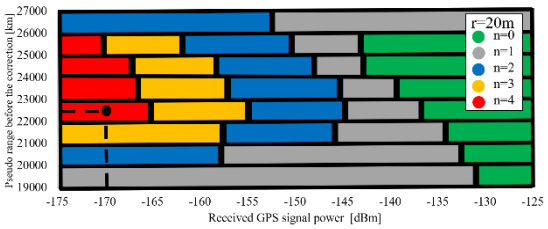

Fig.4 Proposed estimation model for the number of reflections n.

The proposed incident angle estimation model uses the pseudo range before the correction and the estimated number of reflections to estimate and designing the quadratic approximation for each number of reflections n.

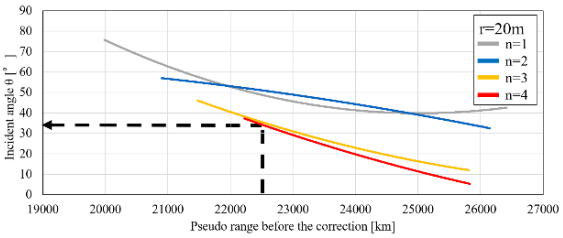

Fig.5 Proposed estimation model for θ.

Fig.5 shows the proposed estimation model for θ. When n is estimated to be 4 in Fig.4 and the pseudo range before the correction is calculated as 22500 km, the incident angle θ is estimated to be 35° by using the approximation curve for n of 4 in Fig.5.

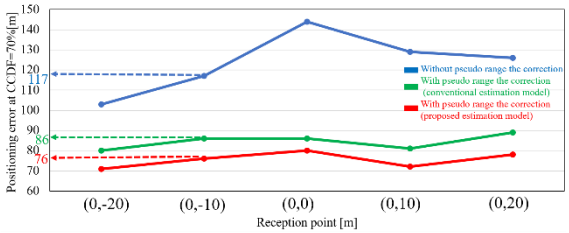

Fig.6 The positioning error at CCDF=70%

Finally, we evaluate the GPS computed distance error using the pseudo range correction method. Fig.6 shows the positioning error at CCDF (Complementary Cumulative Distribution Function) of 70%. The horizontal axis is the reception point and the vertical axis is the positioning error at CCDF of 70%.

This result is an example from January 15, 2016 00:00:00 to before January 16, 2016 00:00:00. In this figure, the blue line describes the performance of the normal GPS positioning without the pseudo range correction. Green line indicates the performance with the pseudo range correction applied by the conventional estimation. Red line shows the performance with the pseudo range correction applied by the proposed estimations. For example, when CCDF=70% at (0, 20), the pseudo range correction applied by the proposed estimations can obtain GPS calculated distance error of 78 m. This result is smaller than 129 m without pseudo range correction, 89 m with the pseudo range correction method applied by the conventional estimation model. It can be seen that the pseudo range correction method applied by the proposed estimation model can improve the GPS calculated distance errors by 48 m and 11 m, respectively.

CONCLUSION

In this paper, we have proposed and evaluate the pseudo range correction method applied by the new estimation models of the number of reflections and the incident angle of the GPS signals, using the received power and the pseudo range before the correction. For example, the GPS calculated distance errors at CCDF of 70 %, the pseudo range correction applied by the proposed estimations has obtained GPS calculated distance error of 78 m, smaller than 48 m without pseudo range correction, 11 m with the pseudo range correction method applied by the conventional estimations. The pseudo range correction with the proposed estimation models can improve the GPS positioning accuracies even in the condition of the various reception points.

References:

[1] Pratap Misra and Per Enge, “Global Positioning System: Signals, Measurements, and Performance,” Syoyo Bunko, 2004.

[2] Toshinari Hayakawa and Norifumi Murai and Takatoshi Sugiyama, “Pseudo Range Estimation Model Based on Received GPS Signal Power in Many Skyscrapers Environments,” ICTC2018,pp.329-331, Oct. 2018.

[3] https://apps.apple.com/jp/app/measure/id1280423470，”Mesure”，Shoichiro Takaki，App Store.

Extraction of useful products from specialty stores using clumpiness

Taro Numase[1, a], Yoshio Miki[1, b]

[1]Department of System Design, Graduate School of Engineering, Kogakuin University, Tokyo, Japan
E-mail: [a]gm21007@ns.kogakuin.ac.jp, [b]mikiyo@cc.kogakuin.ac.jp

Abstract

Marketing using ID-POS data plays a very important role in the CRM activities of retail companies. However, specialty stores, which have customers with fixed preferences and purchase bias toward popular products, are unable to extract useful information from purchase data using conventional analysis methods, and are still implementing measures based on intuition and experience. In this paper, we focused on the purchase interval and analyzed whether there was a difference in purchase content between customers with and without clumpiness by using the X-square test. As a result, it was found that product groups other than the popular product group may be driving consumer purchases.

INTRODUCTION: CRM (Customer Relationship Management) [1] is one of the important fields in the academic research of marketing science and has been actively researched for a long time. Currently, many retailers store individual purchase records called ID-POS data in each company's database. Many retailers analyze a large amount of accumulated ID-POS data and consider marketing measures based on the analysis results. However, specialty stores have not been able to utilize the large amount of ID-POS data that they have accumulated. In general, at specialty stores, narrowing down the type and genre of products to one type is the most effective way to increase sales. The reason is the characteristics of the customers of specialty stores. Most customers in specialty stores repeatedly purchase popular products, and have the characteristic that their tastes do not change over the long term. As a result, most of the sales of specialty stores are made up of popular products. Therefore, the owner of a specialty store should focus on one product and improve the quality. In recent years, the number of stores with a small number of products has been increasing in the specialty store industry. And, The RFM index is an index that many companies generally use as an application of ID-POS data. However, since there are many customers with similar tastes in specialty stores, it is difficult to classify them using only the RFM index. That is, ID-POS data is not used for marketing at specialty stores. Therefore, we consider the use of clumpiness index [2]. Clumpiness is the degree to which events do not follow even intervals. It is regarded as an important index in CRM in the future. The purpose of this paper is to define how each product influences the purchasing pattern of customers, and to logically show the products that play an important role in CRM to the management from the ID-POS data.

METHOD: We analyzed using the ID-POS data of one Western confectionery specialty store in Tokyo. The data used for the analysis is for the year 2018. First, determine the customers to be analyzed. When calculating the clumpiness index, most early withdrawal customers and new customers were determined to have clumpiness. This is because the period of enrollment is short. Here, the number of days obtained by subtracting the latest purchase date from the last purchase date is defined as the annual enrollment period P, and customers with an annual enrollment period of less than 30 days are excluded from the analysis. Therefore, we narrowed down the number of customers to be analyzed from 1651 to 1019. In addition, the customers to be analyzed are classified into two classes according to the presence or absence of clumpiness. The summary is shown in Table 1.

Table 1. Classification of customers to be analyzed.

	Clumpiness		
	0	**1**	**total**
P is less than 30	225	407	632
P is 30 or more	402	617	1019
total	627	1024	1651

Next, the purchase contents of the two classes of customers are compared by the X-square test. In this paper, we compared 19 product groups that were originally classified at the target stores. As shown in Table 2, the number of purchasers was counted in a cross table for each department, and it was investigated whether there was a difference in the number of purchasers with or without clumpiness.

Table 2. Example of created cross table (for cake).

	Purchase	
Clumpiness	**0**	**1**
0	112	290
1	184	433

RESULT: The result of our X-square test is shown in Tabel3. As shown in Table 3, the significance level below 5% was Fruit sorbet, 2018christmas, Summer fruit jelly, and chocolate in ascending order of p value. One thing these products have in common is that they are limited-time products. Next, Fig. 1 shows a comparison of the ratio of the number of

purchasers in each department to the number of people in the class. From Fig. 1, among the categories with p value of 5% or less, the purchase rate of Fruit sorbet and Summer fruit jelly is higher in the class without clumpiness. On the contrary, the purchase rate of 2018christmas and chocolate was higher in the class with clumpiness. Fruit sorbet and Summer fruit jelly are limited-time products sold only from spring to summer, and 2018christmas and chocolate are limited-time products sold in winter. The stores analyzed this time tend to have high sales due to the large number of visitors during the winter and the graduation season in March. Conversely, sales in summer tend not to increase even during the year. However, the purchase rate of fruit sorbet and summer fruit jelly, which are sold only during the summer, was higher among customers without clumpiness. There was also a significant difference in the purchase rate by class. The presence of these products may have created opportunities for customers to visit the store in the summer, which may have eliminated the bias in purchasing opportunities. In other words, these products may create opportunities for customers to visit stores during the summer when demand is low. At specialty stores, the mainstream movement is to improve the quality of products and increase sales by focusing on popular products. However, this analysis could logically show from the data that limited-time products may play an important role in customers' continued visits.

CONCLUSION: In this paper, we examined the use of the clumpiness index in consideration of the purchase interval in the CRM of specialty stores. From the analysis results, it was possible to show that product groups other than the popular product group play an important role. Currently, specialty stores are managed based on the intuition and experience of the manager. By utilizing ID-POS data, it is possible to propose theoretical measures based on the data to the management. In the future, it will be necessary to simulate how the product group judged to be important this time will affect sales.

Table 3. X-square test and p-value.

Product groups	X-squared	p-value
Fruit sorbet	15.3476086	8.94E-05
2018christmas	11.4684135	0.00070789
Summer fruit jelly	7.03124886	0.00800995
chocolate	4.04799598	0.04422381
Christmas goods	3.64350615	0.05628828
Baked confectionery assortment	2.81248034	0.09353366
Coupon	2.36290529	0.1242506
Gift	2.35636142	0.12477291
New Year	2.27682971	0.13132006
Donut	1.72383984	0.18919952
Halloween	1.65600679	0.19814334
Baked confectionery box	0.68995543	0.40617954
Cake	0.45417172	0.5003605
Baked confectionery separately	0.68995543	0.52406594
Baked confectionery bag	0.19548076	0.52406594
Mother's Day	0.18710002	0.66534128
Entremets	0.13032933	0.71809083
Cool & ice	0.08579186	0.76959669
Café	0.03424498	0.85318668

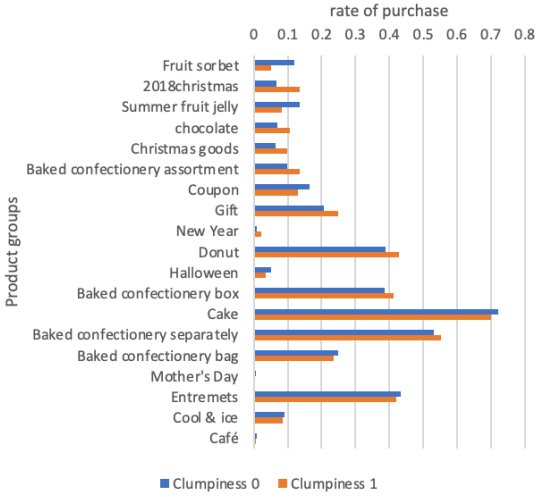

Fig. 1. Ratio of purchases in each department to class size.

Keywords:

CRM, ID-POS, Clumpiness, X-square test

References:

[1] Buttle, Francis. "Customer relationship management." Routledge, (2004)

[2] Zhang, Yao, Eric T. Bradlow, and Dylan S. Small. "Predicting customer value using clumpiness: From RFM to RFMC." *Marketing Science* 34.2 (2015): 195-208.

Examination of Measures to Encourage Unplanned Purchasing Using Social Norms at Specialty Stores

Ryou Miyokawa[1,a] and Yoshio Miki[1,b]

[1]Department of System Design, Graduate School of Engineering, Kogakuin University, Tokyo, Japan
E-mail: [a]gm21009@ns.kogakuin.ac.jp, [b]mikiyo@cc.kogakuin.ac.jp

Abstract

Specialty stores have customers who tend to make planned purchases, which cannot be applied in conventional research that targets customers who tend to make unplanned purchases. Therefore, this research used the concept of store-to-store movement as practiced in department stores to encourage people to visit the store from other stores by viewing the neighborhood area as if it were a department store. In addition, using the concept of Social Norms, which is one of the theories of behavioral economics, they examined measures to encourage unplanned purchases. The number of customers visiting the store before and after the measure was estimated by calculating the behavioral transition probabilistically. As a result, it was confirmed that the use of Social Norms increased the number of customers visiting the store.

INTRODUCTION: Nowadays, with the spread of ID-POS in selling various goods, it has become possible to acquire purchasing data as a matter of course. Along with this, various data analysis utilizing purchasing data has been actively carried out. Recent research has recommended similar products using co-filtering. These research target customers who purchase many products, such as e-commerce sites and supermarkets, and frequently make unplanned purchases. However, it is difficult to apply to customers who tend to make planned purchases, such as specialty stores, who decide what they want and come to the store. Therefore, in this research, measures to encourage non-planned purchases will be examined for specialty stores.

ADVANCE RESERCH: Department stores are a channel that has customers who tend to make planned purchases, such as specialty stores. In reference [1], INDSCAL is used to analyze the buying behavior and floor layout between departments in department stores. As a result, it has been clarified that in-store shopping behavior is carried out with combinations such as "men's clothing, men's goods, sports goods", "women's clothing, women's goods, and women's miscellaneous goods". As the name suggests, a specialty store specializes in one product. Therefore, it is difficult to analyze purchases between other departments in specialty stores. However, it is possible that there is a buying behavior with nearby shops, so it is necessary to consider it.

Behavioral economics is one of the fields of studying human behavior. Behavioral economics is "economics that does not make the assumptions of selfish and rational economics people" [2], and Professor Richard Thaler won the Nobel Memorial Prize in Economics in 2017 and is attracting attention. One of the theories of behavioral economics is the theory of Social Norms. "Social Norms are what many people in a society or group are doing and what to do or what is considered to be okay."[2] Using this Social Norm, research is being conducted on youth smoking prevention and reduction of electricity consumption. In reference [3], impulse purchases (unplanned purchases) are conducted from two aspects: a survey of undergraduate students in a virtual purchasing scenario and a survey of customers who are shopping at retail stores. The results show that normative evaluation influences impulse buying.

APPROACH: Conventionally, specialty stores have used ID-POS data to analyze in-store purchasing behavior. In this research, the concept of a department store is used, and by considering the neighborhood and the area where the store is located as if it were a department store, measures to encourage visits from outside the store are examined. In addition, using the concept of Social Norms, measures to promote unplanned purchases by mitigating the normative aspect are examined.

METHOD: The number of customers visiting the store is determined probabilistically, and a transition diagram is created. Estimate the number of customers using the service at the present and examine to what extent the number of users can be increased by using Social Norms from other researches.

VERIFICARION: In this research, ID-POS data of a confectionery specialty store is used for analysis. The data covers the period from 2003/8/8 to 2019/1/28, and includes not only what, when, and how many items were purchased by 3,500 members, but also optional member information such as birthday and gender. The percentage of age was calculated from the data of 763 members who correctly entered their birthdays. The majority of the customers were in their 30s to 60s, and the percentage of younger customers up to 29 years old was low. It was thought that the percentage of purchases by young people may be low because young people do not have the habit of purchasing at confectionery specialty stores and have a high threshold for visiting a store. Therefore, the research focused on young people (15-29 years old) and examined the extent of change before and after the measures.

For the sake of simplicity, it was assumed that the target confectionery store is visited only from within a 10-minute walking distance (1s=80m). According to the latest available National Census, there are 32,460 residents living within a 10-minute walking distance. Based on the ratio calculated above, the number of young people visiting a confectionery store can be estimated to be 102 if no measures are taken.

Reference [5] examines the difference in selection rates between fluorescent and LED using messages with Social Norms. Without the message, 65.1% chose LED. With the message using Social Norms, 73.0% chose LED. Therefore, the Social Norm increased the selection rate by about 1.1 times. If the same trend were to occur in specialty stores, the number would increase to 113.

DISCUSSION: It was speculated that the purchase rate would increase by presenting a message using the content of Social Norms. Therefore, it is presumed that the purchase rate will increase by giving the message that young people also purchase Western-style confectioneries at specialty stores and by relaxing the norms that young people may have. In this research, the messages used [5] include not only the content of Social Norms, but also the content related to electricity bills and financial aspects, so it is not clear whether they are more effective than Social Norms. Therefore, it is necessary to estimate using multiple researches or conduct field verification to examine the differences.

CONCLUTION: In this research, measures to encourage customers who tend to make planned purchases to make unplanned purchases from outside the store were examined using the theory of Social Norms. The results showed that the number of purchasers would increase if the results were comparable to those of other researches. However, this research is still in its infancy, and it is necessary to improve the accuracy from several previous researches, conduct field tests, and examine the differences from previous researches.

References:

[1] H. Tsurumi, A. Nakayama, An Analysis of Store-Touring Behavior in Department Store Using The Multidimensional Scaling Method for Individual Differenses(Japan), Applied Sociological Research, 47, 195-204(2005).
[2] M. Ogaki, S. Tanaka, Behavioral Economics: Toward a New Economics by Integrating with Traditional Economics(Japan), Yuhikaku(2014).
[3] Dennis W. Rook, Robert J. Fisher, Normative influences on impulsive buying behavior, Journal of consumer research, 22, 3, 305-313(1995).
[4] Agency for Natural Resources and Energy, Ministry of Economy, Trade and Industry, The much-talked-about "nudge method" is also verified! Disseminating information to expand the circle of energy conservation(Japan), 2020/07/14, https://www.enecho.meti.go.jp/about/special/johoteikyo/shoene_nudge.html, (reference date 2021/10/12)

Non-Invasive Concentration Variation Measurements of Chemical Solutions by Using a Birefringent Sensing Head in a Heterodyne Interferometer

Yi-Ren Sun and Ruey-Ching Twu*

Department of Electro-Optical Engineering, Southern Taiwan University of Science and Technology
Tainan, Taiwan
E-mail: rctwu@stust.edu.tw

Abstract

A prism-type beta-barium borate (BBO) sensing head was fabricated and evaluated for the measurements of fluidic concentration variations based on a non-intrusive technique. The sensing head can be coupled to a flow container with a water buffer layer. After measurements, the sensing head is easily cleaned for next usage.

Composition and concentration of liquid is an important parameter for quality control in the fields of pharmaceutical, food and chemical industry [1, 2]. The concentration variation of liquid can be monitored through the measurements on the density, conductive, dielectric constant, and refractive index. it is necessary to develop an easy, simple, accurate and real-time method of measuring liquid concentration. Usually, the toxic and high vaporization liquids are stored in a closed container. Moreover, some chemical reactions are safety concern for avoiding operator espoused in such harsh environment [3]. The inline measurement with a non-invasive technique is essential during the liquid transportation and chemical reaction periods.

To evaluate the flexibility of the proposed SH for the non-invaisve measurements. The different concentrations of hydrochloric acid (HCl) solutions were prepared by adjusting the weight ratios between the HCl and and pure water. The series of varied HCl concentration are 0%, 0.3125%, 0.625%, 1.25%, and 2.5% for the measurements.

Figure 1 shows a heterodyne interferometer measurement setup [4] and the coupling between the FC and the SH. The triangular shape FC was made with transparence acrylic sheet. The probe light is normally incident on the front side of FC. The refractive index of injection liquid (n_l) varies by the concentration change; this causes the probe light to deflect slightly through the hypotenuse of FC. Then it is passed through a tinny water layer and the packaged BBO-SH. Since the incident angle (θ_4) in the BBO interface is changed as well as the fluidic concentrations, the phase variation between two orthogonal polarizations is measured to comparing the phase difference in the sensing and reference signals.

Figure 2(a) gives the measured phase variations under the injection of pulse like fluidic HCl for different concentrations. The phase versus concentration is shown in Fig. 2(b). According to a linear fit for the measured data, the slope is represented for the measurement sensitivity. The measurement rsults show that the repeatability and stability. The achievable concentration resolution is 29 ppm.

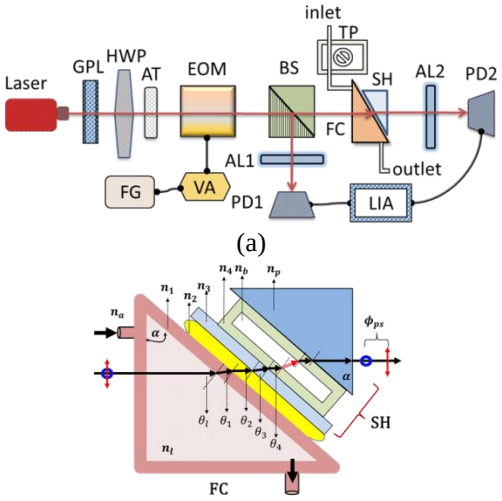

Fig. 1. (a) Measurement setup. (b) Sensing head (SH) coupling onto a flow container (FC) with a pure water layer.

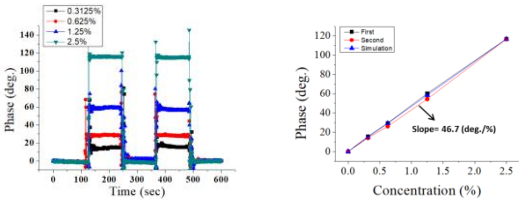

Fig. 2. Phase variations under the injection of pulse like fluidic HCl for different concentrations. (b) Phase versus concentration.

References:

[1] B. Schreiber, C. Wacinski, R. Chiarello, *Pharmaceutical Eng.*, **33**, 1-7 (2013).

[2] M. W. Johnson, K. Golden, G. Gilleskie, J. Pancorbo, R. R. Vilhena, *BioProcess International*, **13**, 60-67 (2015).

[3] Y. Choi; H. Jang, D. Byun; D.-H. Ko, *Thin Solid Films*, **709**, 138230 (2020).

[4] R. C. Twu, N. Y Yan, *Sensors and Actuators A: Physical*, **267,** 272–277 (2017).

A Computational Framework for Predicting the Surface Morphology of Laser Powder Bed Fusion Parts after Laser Polishing

Dac – Phuc Pham[1], Hong – Chuong Tran[1*]
[1]Department of Mechanical Engineering, Southern Taiwan University of Science and Technology, Tainan, Taiwan

[*] Email: tranhongchuong@stust.edu.tw

Abstract

Laser Powder Bed Fusion (LPBF) process can produce parts with complex structures by using the thermal energy of laser beam to melt specific area of metal powder layers in a layer-by-layer manner. The surface roughness of the as-built parts is one of the major requirements to determine the quality of final products. Laser Polishing employed laser radiation to melt a thin layer of metal to achieve a better surface quality. Accordingly, this technology has been demonstrated its strong potential in replacing mechanical polishing because of no additional cost for tooling is required. Accurately predicting the surface topology after applying laser polishing will create a foundation for optimizing the processing conditions for Laser Polishing. For solving this issues, in this work, an integrated computational framework including surface generation model, ray tracing model, heat transfer simulation and low pass filter was developed to predict the surface morphology of LPBF processed part after applying laser polishing. It is observed that by using the proposed simulation model, the predicted and measured results of mean roughness (R_a), mean roughness depth (R_z) and correlation length (cl) are in good agreement with error less than 10%.

Keywords: Additive Manufacturing, Laser Polishing, Surface Roughness, Stainless Steel 420, Laser Powder Bed Fusion

1. Introduction

Laser Powder Bed Fusion (LPBF) process use a high-energy-density laser beam to melt a specific area of metal powder to create a solidified layer with a particular thickness. Then, the solidified layer is lowered down a distance and a new metal powder layer is spread with a certain thickness, and a next layer is fused by the controlled laser beam. Owing to its working principles, L-PBF can produce intricate 3D parts with no tool and mold in a short amount of times. Thus, it has been received a considerable adoption from both industry and academia [1].

The physical phenomena associated with LPBF is highly complex. Additionally, there are numerous processing parameters that can affect the quality of the fabricated components. Due to the stochastic nature of LPBF process and numerous processing conditions, several kinds of defects can be induced during the process such as internal porosity [2], higher surface roughness parameters in comparison with traditional manufacturing process [3]. Authors in literature [4] reported that LPBF processed Stainless Steel 316L part have a surface roughness of Ra equaling to 16 μm.

Therefore, it is essential to find proper processing conditions for improving the surface finished of LPBF processed part. For instance, by optimizing the laser power, scanning speed and hatch distance, author in literature [5, 6] can observe a significant improvement on the surface roughness of LPBF processed part. Nevertheless, the roughness of LPBF-processed part still can't meet the industry standards [7]. Accordingly, several studies have employed laser polishing strategy to improve the surface quality of the top layer of fabricated parts. For instance, study in [8] used the same strategy to improve the density and surface roughness of LPBF AlSi10Mg parts.

The discussed literature indicates the importance of applying laser polishing for improving the surface finished of LPBF-processed parts. However, these studies find the parameters by using experimental trial and errors. Several studies used simulation tools for predicting the surface morphology of samples after applying laser polishing. However, in these studies, the influence of initial surface topology on the absorption of laser radiation is neglect.

The reviews of literatures provide many insights into the physical phenomena during laser polishing process. As the laser beam irradiates the metallic surface, part of the laser energy will be absorbed, while the rest is scattered back [9]. The absorption of laser beam is an important input parameter for the heat transfer simulation model. Additionally, the absorbed energy is influenced by the initial surface topology. These physical phenomena were neglected by the discussed studies. In an effort to addressed the discussed issues, this research focuses on building a computational framework which took into account the effect of initial surface morphology on the laser absorption for predicting the final topology

of surface induced by laser polishing. The proposed model is briefly described as follows.

Initially, the surface morphology produced by LPBF processed is measured and the parameters of mean roughness (R_a), mean roughness depth (R_z) and correlation length (cl) is then extracted from the measurement data. Then, a mathematical model proposed by literature [9] is employed to simulate one dimensional surface profiles based on the mentioned measurement results . Accordingly, the Bidirectional Reflectance Distribution Function (BRDF) mathematical model is employed to compute the laser absorption coefficient which is further transferred to the heat transfer simulation for computing the average melting period of the irradiated zones of the laser beam in the simulation domain. Finally, the average melting period were then used to calculate the critical attenuation frequency. Accordingly, the Fast Fourier Transform (FFT) algorithm is performed to convert the simulated LPBF processed surface profile to frequency domain. Then, low pass filter and critical attenuation frequency is then employed filtered out the initial frequency spectrum of the original surface. Finally, the inverse FFT were used to reconstruct the final topology of laser polished surface. The verification of the proposed framework is confirmed by comparing the calculated R_a , R_z and cl from simulated profile with those measured from laser polished surface.

2. Experimental procedure

2.1 Laser Powder Bed Fusion and Laser Polishing Process

In LPBF experiment, the powder size is the range of 20-60 µm and the powder material is Stainless Steel 420. The experiment is performed in a chamber filled with nitrogen and the oxygen concentration is less than 2000 ppm on a commercial Tong Tai LBPF machine AMP 160. In this research, the same processing settings are used to produce the entire sample to evaluate the impact of the location of the sample on surface roughness. Table 1 showed the parameters of the LPBF experiment. Once the LPBF process is finished, the samples were taken out and the surface roughness on the top surface of the samples were measured.

The details of measurement process will be described in the next sections. Then, the samples were put back to the LPBF machine for conducting laser polishing process. Figure 1 shows the layout of LPBF experiment and Laser Polishing experiment. Table 2 displayed the processing conditions for laser polishing experiment corresponding with the samples symbols indicated in Figure 1.

Table 1 Experimental Parameters for L-PBF process

Parameters	Value
Laser Power	270 (W)
Scanning Speed	600 (mm/s)
Hatching Space	140 (µm)
Layer Thickness	30 (µm)
Rotation angle between adjacent layers	67°
Laser Spot size	100 µm
Laser Type	Nd:Yag laser wavelength 1064 nm

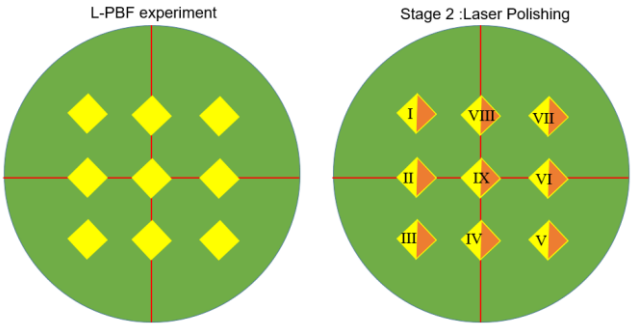

Fig. 1 Concept of L-PBF experiment and Laser Polishing experiment.

Table 2 Experimental Parameters for Laser Polishing Process

Case	Power (W)	Scanning Speed (mm/s)	Hatching Space (µm)
I	200	1000	100
II	200	800	100
III	220	550	100
IV	220	800	100
V	240	500	100
VI	240	750	100
VII	170	1100	100
VIII	170	600	100
IX	170	1300	100

2.2 Measurement of Surface Roughness

After the LPBF and Laser Polishing experiment, the surface morphology on the top surface of the samples were measured by means of confocal laser scanning microscope KEYENCE VK-X250. Figure 2a shows the typical measured surface topology and Figure 2b demonstrates the corresponding average surface profile. Then the basic three parameters that representing the surface topography R_a, R_z and cl were extracted.

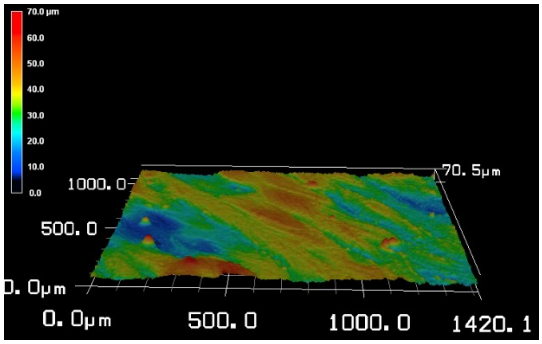

(a)

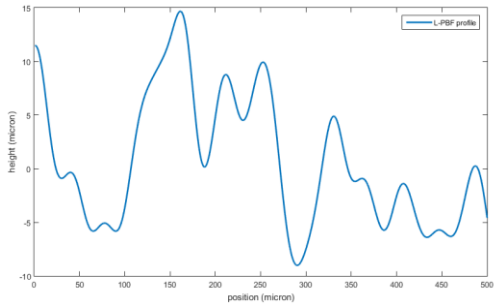

(b)

Fig. 2 (a) Measured surface topology; (b) Average surface profile.

3. Model Description

3.1 Surface generation and Ray-Tracing Model

The mathematical model proposed by Bergström et al. [9] is then used to construct a one-dimensional surface profile for each of the measured Ra, Rz, and *Cl* model. In general, this mathematical states that the one dimensional random roughness $y = \xi(x)$ can be statistically describes by using two distribution functions. The height probability distribution function $p = (\xi)$ and the auto-covariance function. The former function simulating the fluctuation of height from the mean reference ($\xi(x) = 0$), while the later function control the fluctuation of these height along the lateral direction. The Gaussian height function can be described as

$$p(\xi) = \frac{1}{\sigma\sqrt{2\pi}} e^{-\xi^2/2\sigma^2} \quad (1)$$

where σ is the mean roughness depth (Rz) of the simulated surface.

The auto-covariance function also conforms Gaussian distribution as

$$C(\tau) = \langle \xi(x_1)\, \xi(x_2) \rangle = \sigma^2 exp\left(-\frac{|x_1 - x_2|^2}{\tau^2}\right) \quad (2)$$

Where x_1 and x_2 are the coordinates of two distinct points located on the surface and τ is the correlation length. Figure 3 shows the as built average surface profile extracted from experiment and the corresponding one simulated by the current simulation model. It is seen that the Ra, Rz, and cl measured from experiment is 4.9±0.8, ,7.5±1.2, 24.16±1.3. While that attain from simulation profile are R_a , R_z , and *cl* is 5.01, 6.33, 24.11, respectively. Overall, it can be seen that the simulation model can simulate the general characteristics of the L-PBF processed profile.

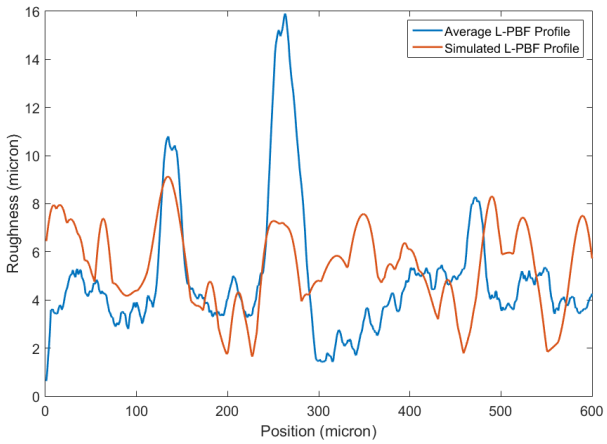

Fig. 3 Average profile from experiment and simulated surface profile.

During the laser re-melting process, the laser beam irradiates the surface of solidified metal part of the laser beam energy is absorbed by the metallic particles, while the remaining energy is scattered back. Bergström et al. [9] showed that the amount of absorbed laser energy is significantly dependent on the surface roughness of the powder bed and the optical properties of the metallic particles. In particular, for rough surfaces, the degree of interaction between the laser beam and the surface morphology increases dramatically, and hence the amount of laser energy absorbed by the powder bed increases. Accordingly, the present model employed the Bidirectional Distribution Reflection Function (BRDF) algorithm to take account of the effects of the surface morphology on the laser absorption. The BRDF algorithm has the form [9] as

$$\rho''_\lambda(\Omega_s, \Omega_i) = \frac{\pi}{cos(\theta_s)} \left(\frac{\frac{d\phi_s}{d\Omega_s}}{\frac{d\phi_i}{d\Omega_i}} \right), \quad (3)$$

where θ_s is the angle of the scattered light; ϕ_i and ϕ_s are the incident and scattered radiant powers, respectively; and Ω_i and Ω_s are the incident and solid angles, respectively.

Integrating Eq. (3) over the entire hemisphere leads to the following expression for the directional hemispherical reflectance:

$$\rho'_\lambda(\Omega_i) = \frac{1}{\pi} \int_{2\pi} \rho''_\lambda(\Omega_s, \Omega_i) cos(\theta_s) d\Omega_s \quad (4)$$

The absorption function of the metallic surface is then obtained as

$$A'_\lambda(\Omega_i) = 1 - \rho'_\lambda(\Omega_i). \quad (5)$$

3.2 Surface generation and Ray-Tracing Model

The calculated absorption in previous section were input to heat transfer simulation for calculating the melting period material irradiated by the laser beam.

Originally, the mathematical formulation for heat transfer simulation can be discussed as follows [10]

$$\rho c \frac{\partial T}{\partial t} = q(x,y,z,t) + \frac{\partial}{\partial x}\left(k_{xx}\frac{\partial T}{\partial x}\right) + \frac{\partial}{\partial y}\left(k_{yy}\frac{\partial T}{\partial y}\right) + \frac{\partial}{\partial z}\left(k_{zz}\frac{\partial T}{\partial z}\right), \quad (6)$$

where ρ is the material density (kg/m^3), c is the specific heat capacity (J/kgK), T is the temperature (K), t is the application time of the heat source (s), k is the thermal conductivity (W/(m.K)), and $q(x,y,z,t)$ is the heat generation per unit volume (W/m^3). According to the experimental settings, the initial condition was set as 293 K.

The laser heat flux applied on the top surface of the computational domain is described as follows [10]

$$q(x,y,t) = \frac{2AP}{\pi r_0^2} exp\left[-\frac{2((x-vt)^2+y^2)}{r_0^2}\right] \quad (7)$$

Where A is the absorption coefficient attained in the Section 3.2. P is the laser power , r_o is the laser beam radius, v is the scanning speed of the laser beam and x,y is the coordinates on the top surface of computation domain.

The heat loss due to convective cooling and radiative cooling is also taken into account in the present simulation model as [11,12]

$$Q_{rad} = -\sigma\epsilon(T^4 - T_a^4) \quad (8)$$

$$Q_{conv} = -h_c(T - T_a) \quad (9)$$

where T is the temperature of the workpiece T_a is the ambient temperature, σ is the Stefan constant ($5.669 \times 10^{-8}\ W/m^2K^4$), ϵ is the emissivity (0.4 for solid state and 0.1 for molten material), and h_c is the heat transfer coefficient ($h_c = 100\ W/m^2K$). Fig. 4 shows the initial, boundary conditions settings in the numerical model as well as the trajectory of laser beam during laser polishing process.

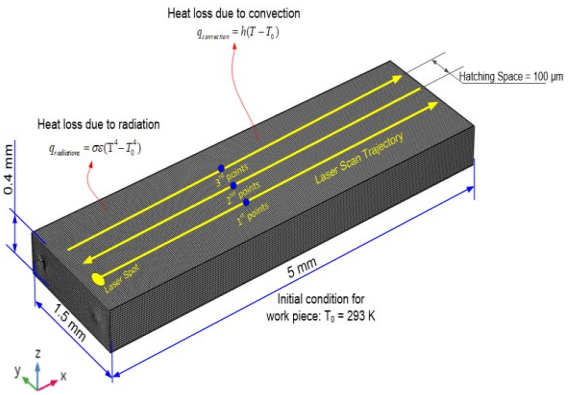

Fig. 4 Schematic diagram illustrating the initial and boundary conditions of the present simulation model

3.3 Simulated Polished Profile Using Low-Pass Filter

As the laser beam shines on the rough surface, the laser energy will be absorbed (see Section 3.2) by the metal surface. If the absorbed energy sufficient to melt the rough metal surface, the movement of molten metal will induce surface tension force which one of the major factor that lead to the smoothing effect of the initial surface profile. In other words, the polished surface topography can be simulated by assuming the attenuation of the highest frequency of the initial rough surfaces [13]. The critical frequency that can attenuate the higher frequency of the original surface can be written as proposed in literature [13]

$$f_{cr} = \left(\frac{\rho}{8\pi^2\mu t_m}\right)^{1/2} \quad (10)$$

in which f_{cr} (1/mm) represents the critical frequency , μ (Ns/m^2) is dynamic viscosity, ρ (kg/m^3) is density and t_m (s) is average melting period. It is noticed that average melting period is calculated by average all the melting period of the nodal points located on the center of the laser beam shown in Figure 4.

4. Results and discussion

For each case of surface morphology produced by LPBF processed described in section 3.1. The verified surface generation model was employed to reconstruct the surface morphology. Then, the simulated profile was then imported into the ray-tracing model for calculating the absorptivity of laser beam. The calculated absorption values corresponding to different cases of surface roughness were input to the verified heat transfer model described in section 3.2 for calculating the melting period. Figure 5 displayed the temperature history of 3 points indicated in Figure 4. For every nodal points on the center of laser scan tracks depicted in Figure 4, the corresponding melting period of each nodal points were computed and the average melting durations were averaged across the calculated values. Then Equation (10) is employed to determine the cut-off frequency for simulating the laser polished profile.

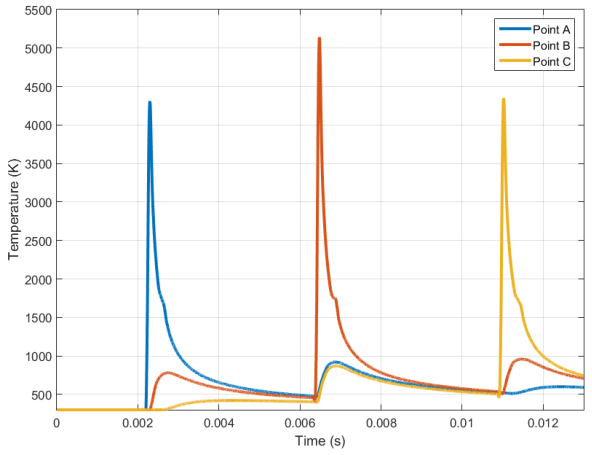

Fig. 5 Temperature profile of three points indicated in Fig. 4

For demonstrating the capability of the built-up model in predicting the surface morphology of samples after applying laser polishing, the comparison between the average polished profile and simulated polished

profile in Case VIII were shown in Figure 6. It is seen that the built up simulation model can capture the topology of polished surface attained from experiment. In particular, Ra, Rz and Cl of the laser polished profile from experiment is 4.01 µm,4.94 µm, 9.2 µm, respectively. While that attained from the simulated profile is Ra = 4.14 µm, R_z, =5.17 µm, cl =9.82 µm.

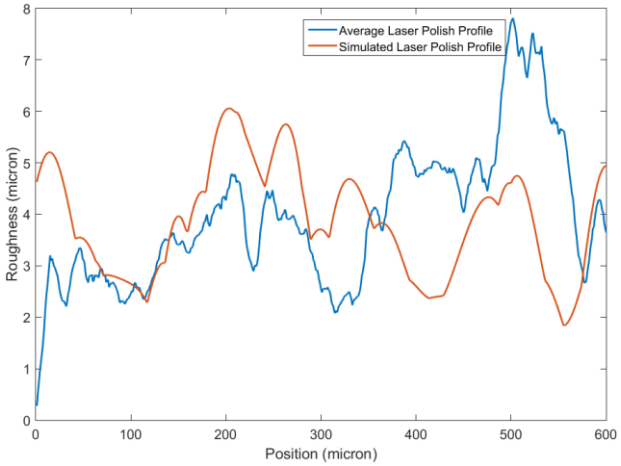

Fig. 6 Comparison between average measured profile and simulated profile from laser polishing

For further verifying the simulation model in

4. Conclusions

This work proposed a computational framework including surface generation algorithm, ray-tracing simulation, heat transfer and spatial frequency filtering algorithm for predicting the topology of LPBF processed surface after applying laser polishing. The major contribution of this work can be summarized as follows

- The surface roughness model can simulate the surface that have the same parameters of Ra, Rz and cl with those fabricated by the LPBF process.
- The ray tracing algorithm can be used to compute the absorptivity corresponding to different surface topology. It is found that rougher surface can absorbed more laser energy. Additionally, the calculated absorption has significant effect on the predicted surface morphology
- The two models above are integrated with heat transfer model and spatial frequency filtering algorithm for simulating the surface topology after applying laser polishing.

Overall, the built up model provides an effective tool for predicting the morphology of LPBF produced surface after applying laser polishing.

6. Acknowledgements

This work is funded by National Science Council under grant MOST 110-2222-E-218-002-MY2.

7. References

[1] L. Chen, B. Richter, X. Zhang, X. Ren, and F. E. Pfefferkorn, "Modification of surface characteristics and electrochemical corrosion behavior of laser powder bed fused stainless-steel 316L after laser polishing," *Additive Manufacturing,* vol. 32, p. 101013, 2020.

[2] Z. Snow, A. Nassar, and E. W. Reutzel, "Review of the Formation and Impact of Flaws in Powder Bed Fusion Additive Manufacturing," *Additive Manufacturing,* p. 101457, 2020.

[3] E. Yasa and J.-P. Kruth, "Application of laser re-melting on selective laser melting parts," *Advances in Production engineering and Management,* vol. 6, pp. 259-270, 2011.

[4] W. M. Tucho, V. H. Lysne, H. Austbø, A. Sjolyst-Kverneland, and V. Hansen, "Investigation of effects of process parameters on microstructure and hardness of SLM manufactured SS316L," *Journal of Alloys and Compounds,* vol. 740, pp. 910-925, 2018.

[5] J. C. Snyder and K. A. Thole, "Understanding laser powder bed fusion surface roughness," *Journal of Manufacturing Science and Engineering,* vol. 142, p. 071003, 2020.

[6] L. Cao, J. Li, J. Hu, H. Liu, Y. Wu, and Q. Zhou, "Optimization of surface roughness and dimensional accuracy in LPBF additive manufacturing," *Optics & Laser Technology,* vol. 142, p. 107246, 2021.

[7] T. Deng, J. Li, and Z. Zheng, "Fundamental aspects and recent developments in metal surface polishing with energy beam irradiation," *International Journal of Machine Tools and Manufacture,* vol. 148, p. 103472, 2020.

[8] W. Yu, S. L. Sing, C. K. Chua, and X. Tian, "Influence of re-melting on surface roughness and porosity of AlSi10Mg parts fabricated by selective laser melting," *Journal of Alloys and Compounds,* vol. 792, pp. 574-581, 2019.

[9] D. Bergström, J. Powell, and A. Kaplan, "A ray-tracing analysis of the absorption of light by smooth and rough metal surfaces," *Journal of applied physics,* vol. 101, p. 113504, 2007.

[10] H.-C. Tran and Y.-L. Lo, "Heat transfer simulations of selective laser melting process based on volumetric heat source with powder size consideration," *Journal of Materials Processing Technology,* vol. 255, pp. 411-425, 2018.

[11] H. Wang, Y. Kawahito, R. Yoshida, Y. Nakashima, and K. Shiokawa, "A model to calculate the laser absorption property of actual surface," *International Journal of Heat and Mass Transfer,* vol. 118, pp. 562-569, 2018.

[12] C. Multiphysics and C. M. H. T. Module, "COMSOL Multiphysics User's Guide," *Version: COMSOL Multiphysics*, vol. 3, 2014.

[13] E. Ukar, A. Lamikiz, S. Martínez, I. Tabernero, and L. L. De Lacalle, "Roughness prediction on laser polished surfaces," *Journal of Materials Processing Technology,* vol. 212, pp. 1305-1313, 2012.

Lightning Talk Session

Education and Human Studies & Energy and Transportation

November 23rd

Presentation No.	Title	Author	
EHSL1.	Effects of Skin and Water Conditions on Water Surface Perception	Kohei Kawamata, Miyuki G.Kamachi	287
EHSL2.	Influence of eating Meals on facial expressions	Mao Maekawa, Miyuki G. Kamachi	292
EHSL3.	A study of facilitation evaluation methods in group discussions for students	Takuya Hirayanagi, Daigo Misaki	296
ETL1.	Optimization of Service Frequency based on Short-term Passenger Forecasting on Scheduled Bus -Case Study on the Route for Kogakuin University-	Yuya Nagai, Yoshio Miki	297
ETL2.	Study on Driving Skill Analysis in Curve Sections using Adaboost Algorithm with Driving Simulator	Eisho Kanno, Masakazu Mukai	302
ETL3.	Development of Operando Raman Analysis at the Reaction Cross-Section of All-Solid-State Batteries	Takaaki Ono, Koji Hiraoka, Hibiki Miyauchi, Takeshi Kobayashi and Shiro Seki	304

Effects of Skin and Water Conditions on Water Surface Perception

Kohei Kawamata*, and Miyuki G. Kamachi**

*Informatics Program, Graduate School of Engineering, Kogakuin University, Tokyo, Japan
**Department of Information Design, Faculty of Informatics, Kogakuin University, Tokyo, Japan
E-mail: em21007@ns.kogakuin.ac.jp; miyuki@cc.kogakuin.ac.jp

Abstract

Prior research has revealed that the sensation of wetness is mainly related to temperature. Evaluation of the different conditions of the skin, such as glabrous or hairy, has revealed that body hair contributes to the perception of water surface. However, the effects of temperature on water surface perception remain uncertain, and previous studies have not involved objective evaluations. Therefore, this study aimed to subjectively and objectively evaluate water surface perception. The experimental conditions involved "covering part of the skin" and "water temperature" as parameters. As a result, participants subjectively perceived water surface clearly in a low temperature condition, while no significant or marginal effect was observed in the objective evaluation. In the "covering part of the skin" experiment, water surface was less clearly perceived compared to that with natural skin. Therefore, this study suggests that "low water temperature" and "condition of skin surface in direct contact to water" allows a clearer subjective water surface perception, and that skin condition (condition of skin surface in no direct contact to water) lowers the accuracy of objective water surface perception.

1. Introduction

Scuba diving is popular among people of all ages and genders, as a lifelong sport. However, it comes with a few challenges as compared to other sports. For example, transport to the seaside takes time, and this sport also depends on the sea condition. Additionally, one must be healthy and, in some cases, an individual may also require a doctor's certificate, as some people cannot dive if they have certain types of illnesses.

Yamashita et al. [1] were build underwater virtual reality (VR) environments. From their study, they found that it was difficult to track the head in underwater. They projected images on the floor and wall of the pool (cave). On the other hand, a simulator targeted for scuba diving (water was not used) was built by Jain et al [2]. Their system could reproduce visual, audio, tactile, and buoyancy sensations. In their experiments, they found that the sense of buoyancy due to breathing increased the sense of immersion. However, the user needed actual water diving in the former case, and water perception such as wetness was not reproducible in the latter case. Therefore, it is difficult to experience scuba diving on land, through a casual and virtual scenario.

In this study, we aimed to build an easy and immersive scuba diving simulator on land, which would reproduce the sensation of a person entering the water. Sato et al investigated the association between body hair and water surface perception[3]. In their study, the authors compared shaved and unshaved arms of participants. Additionally, a comparison was made between hairless and hairy skin, with one side covered by a liquid bandage. The results revealed that body hair contributed significantly to water surface perception.

Koshiba et al. further elucidated that wetness was affected by temperature, with the usage of wet filter paper in their study [4].

In this study, experiments were conducted to investigate the factors that caused the illusion of water surface in VR environments. Tactile accuracy of water surface perception was examined under various conditions in an environment where there were many uncertainties present.

2. Experimental Method

The common parts of all the experiments are explained as follows:

[Participants] The experiment included 10 participants (nine males and one female) in their 20s, who had no significant trauma on the finger surface. The same participants engaged in all experiments, and it took each of them two days to undergo all experiments. The order of the experiments was adjusted such that the liquid bandage in experiment 2 would not be affected (left behind). Therefore, experiment 2 was conducted at the end of the day.

[Procedure] The procedure was the same for all experiments. First, a mark was made at the midpoint between the first and second joints of the participants' index fingers. Figure 1 shows the image of the finger with an actual mark, dipped in the water. Next, the participants were required to put their index

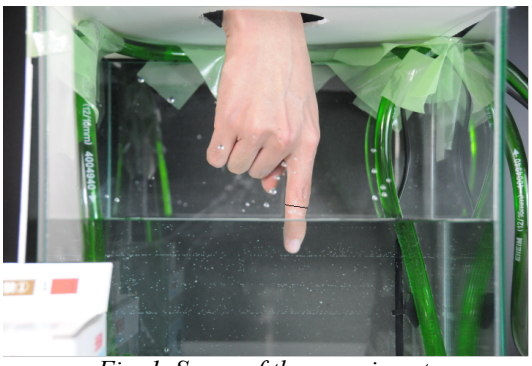

Fig. 1. Scene of the experiment (water surface and marks).

fingers into the water tank, and they were required to adjust the water level by tactile information only. The tank was covered and the participants were asked to answer only with tactile information. The positions of the water surface and fingers were recorded as images using a digital single-lens reflex camera (Nikon, D300). A cooler (Zensui, ZC-200α), heater (GEX, S220) and water pump (EHEIM, 1048) were used to maintain a constant water temperature. Two types of procedures were performed for aligning the water surface with the mark: entering of the finger into the water and leaving of the finger from the water. Figure 2 shows a diagram of the procedure. Entering water (↓) is a procedure to adjust the finger with water surface, when participants put their finger into the water and stop at the sign (line) on the finger. Leaving water (↑) is an opposite procedure to entering, when the entire finger is dipped into the water. Thereafter, participants adjust the finger so that the surface of the water and the mark are aligned when they remove their finger. One trial was conducted for each procedure. A total of 20 trials were conducted, with 10 performed for each procedure. The procedure was randomized, and the experiment was conducted accordingly in each stimulus condition. For the subjective evaluation, the participants were asked to rank the order in which they felt the water surface was clearer in each experiment.

2.1. Experiment 1: Water Temperature

In Experiment 1, we examined the effect of water temperature on water surface perception. Three different water temperatures were used as stimuli (Low Temp: 19°C, Middle Temp: skin temperature of each participant, High Temp: 40°C).

2.2. Experiment 2: Covering The Skin

We examined the effects of changes in skin condition on water surface perception. Two types of experiments were conducted, one with the area between the first and second joints covered with a liquid bandage, and one without the same condition.

2.3. Experiment 3: Fresh or Salt Water

In Experiment 3, we investigated whether changes in the salinity of water affected water surface perception. Scuba diving is mainly performed in the ocean; therefore, we examined the effect of the salinity of water on water surface perception. As a stimulus, we used salt water with the same salinity as that of seawater, and fresh water.

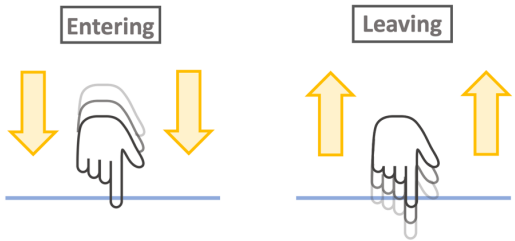

Fig. 2. Two types of procedures (Right: Entering water, Left: Leaving water)

3. Results

We initially planned to analyze the results by comparing the conditions within the experiments. However, it was observed that differences due to procedures appeared during the analysis of objective evaluation data. Therefore, we considered the procedure as one of the factors and conducted a two-way ANOVA for each experiment. The following were the two objective evaluation data that were analyzed—Mean data: Mean of measured values with misalignment orientation, and Absolute data: The average of the measured values (for each participant) converted to absolute values. From the absolute data, we concluded that it was possible to focus the analysis on the misalignment between the mark and the water surface.

3.1. Experiment 1: Water Temperature

Subjective evaluation of Experiment 1: We conducted a one-factor ANOVA for the three different temperatures. Consequently, temperature exhibited a significant effect. Multiple comparisons using the Bonferroni correction revealed a significant difference (p = .010) between Low Temp (M = 1.300, SD = 0.48305) and High Temp (M = 2.400, SD = 0.69921). Moreover, there was a marginally significant difference between Middle Temp (M = 2.300, SD = 0.82327) and Low Temp (M = 1.300, SD = 0.48305) (p = .069).

Objective evaluation: Figures 3 and 4 show the misalignment of the marks for each condition and procedure (+ direction: water surface is above the mark, - direction: water surface is below the mark). The mean data of the measurements (Figure 3)

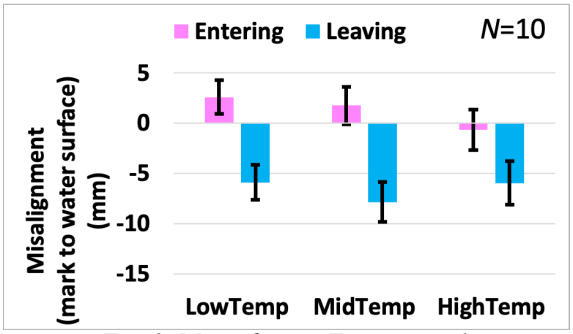

Fig. 3. Mean data in Experiment 1

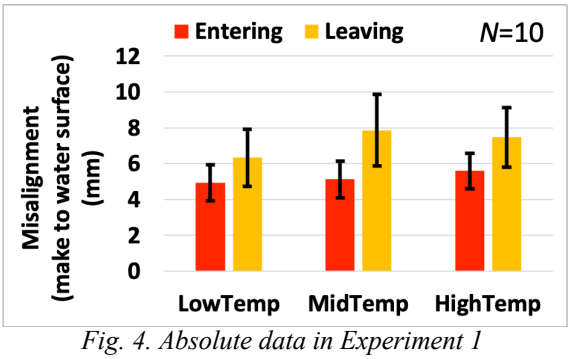

Fig. 4. Absolute data in Experiment 1

indicates a significant difference in the procedure (Entering, M = 1.202, SE = 1.844; Leaving, M = -6.586, SE = 1.799; p = .007). There was also a marginal significance noted in the interaction between temperature and procedure ($F_{2,18}$ = 3.056, p = .072). Therefore, a simple main effect test was conducted accordingly. The results revealed a marginal significance between low and high temperature at the time of water entry. (low temp M = 2.555, SE = 1.768; high temp, M =-0.677, SE = 2.132; p = .061) Also, a significant difference was noted between entering and leaving water at each temperature condition (entering water at low temp, M = 2.555, SE = 1.768; leaving water, M = -5.922, SE = 1.846; p = .004) (entering water at medium temp , M = 1.727, SE = 1.943; leaving water, M = -7.864, SE = 2.097; p = .013) (entering water at high temp, M = -0.677, SE = 2.132; leaving water, M = -5.972, SE = 2.300; p = .028). No significant differences were found in the other combinations or absolute data (Figure 4).

These results indicate that the water surface is clearly perceived when the water is cooler. However, the absolute data of the objective evaluation does not show any difference, suggesting that the effects on the accuracy of water surface perception are small.

3.2. Experiment 2: Covering The Skin

In the subjective evaluation, there was a marginal significance in the degree of perceived clarity of the water surface being higher in the side without the liquid bandage (uncovered, M = 1.2000, SD = 0.42164; covered, M = 1.8000, SD = 0.42164) (t = -2.250, d = 9, p = .051).

Figure 5 shows a graph of the average data of the measurements. From the mean data, a significant difference was observed within the conditions (uncovered, M = -2.746, SE = 1.173; covered, M = -3.256, SE = 1.179; p < .001). Significant differences were also noted within each procedure. (entering water, M = 5.142, SE = 0.969; leaving water, M = -4.633, SE = 1.706; p < .001) Furthermore, there was a marginal significance in interaction; therefore, a simple main effect test was conducted ($F_{1,9}$ = 3.395, p = .099). As a result, there was a significant difference between entering water (uncovered, M = 1.268, SE = 1.103; covered, M = 9.016, SE = 1.355; p = .001), leaving water (uncovered, M = -6.761, SE = 1.969; covered, M = 2.504, SE = 1.605; p = .004), covered (entering water, M = -9.016, SE = 1.355; leaving water M = -2.504, SE = 1.605; p < .001), and uncovered (entering water, M = 1.268, SE = 1.103; leaving water, M = -6.761, SE = 1.969; p = .005) without their respective conditions.

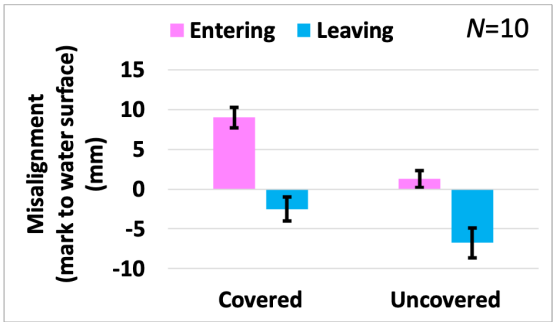

Fig. 5. Mean data in Experiment 2

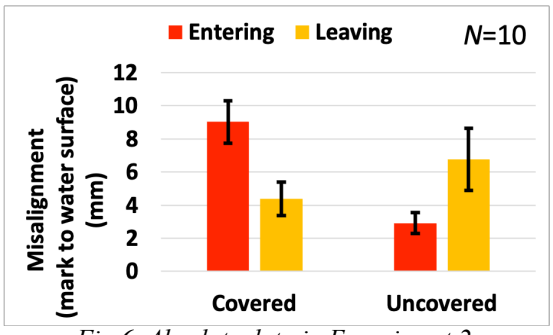

Fig.6. Absolute data in Experiment 2

The average of the measured values is presented as a graph of absolute data in Figure 6. The absolute data of the measurements show a significant difference in the interaction.

Therefore, we conducted a simple main effect test. ($F_{1,9}$ = 24.606, p = .001). As a result, there was a significant or marginal difference between covered （entering water, M = 9.016, SE = 1.355; leaving water, M = 4.376, SE = 1.070; p = .033), uncovered (entering water, M = 2.917, SE = 0.671; leaving water, M = 6.761, SE = 1.969; p = .082), entering water (uncovered, M = 2.917, SE = 0.671; covered, M = 9.016, SE = 1.355; p = .002), and leaving water (covered, M = 4.376, SE = 1.070; uncovered, M = 6.761, SE = 1.969; p = .073) without their respective conditions. These results suggest that the accuracy of water surface perception decreases when the state changes from direct to indirect contact of the skin with the water surface.

3.3. Experiment 3: Fresh or Salt Water

Figure 7 shows the average data of the measurements in Experiment 3, and Figure 8 shows the graph of the average of the measurements converted to absolute values. In Experiment 3, no significant or marginal differences were observed except in the procedure (entering water, M = 2.647, SE = 1.447; leaving water, M = -6.405, SE = 2.350; p = .005). Based on these results, there seems to be no difference between the effects of salt water and fresh water.

Fig. 7. Mean data in Experiment 3

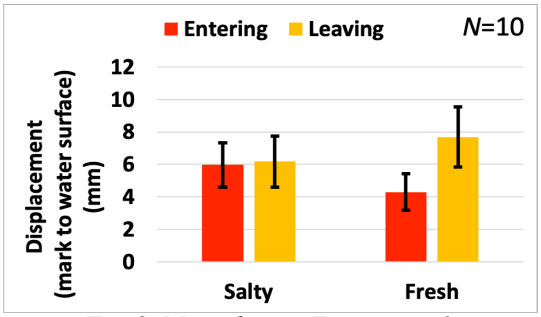

Fig. 8. Mean data in Experiment 3

4. Discussion

In Experiment 1 (water temperature), we used high, middle, and low temperature in order to investigate their effects on water surface perception. The results of the mean values of the measurements for the positional shift showed a significant tendency between the high and low temperatures when entering the water. Therefore, it is suggested that the location where the surface of the water and the mark are perceived to overlap is different. There was no significant or marginal difference in the magnitude of the shift. A significant feature of the subjective evaluation was that the water surface was more clearly perceived with a lower temperature.

In Experiment 2 (liquid bandage), we examined the effects of direct and indirect skin contact on the water surface perception, using a liquid bandage, by changing the condition from no decoration (but marked) to one in which the skin was partially covered. From the subjective evaluation, it was revealed that the level of clarity of the water surface perception decreased when the water surface did not touch the skin covered by the liquid bandage, compared to the condition without the liquid bandage.

Further, the objective evaluation revealed that the accuracy between the water surface and the mark was lower for the uncovered skin than that for the covered skin at the time of emergence. This may be due to the difference in accuracy between entering and leaving the water. From the results of the magnitude of deviations (absolute values of the measured values) between Experiments 1 and 3, the distance from the mark is farther in the "out of water" condition than in the "in water" condition, although there is no significant or marginal difference. Therefore, the accuracy tends to be low. These results indicate that the accuracy tends to be higher in entering than in leaving the water condition, and thus the accuracy decreases when a liquid adhesive bandage is applied. Conversely, when the water comes out, the accuracy tends to be lower than that when the water goes in. Therefore, even when the liquid bandage is applied, it does not have a significant effect on accuracy; hence, it is believed that the accuracy is relatively higher in the outflowing water.

In Experiment 3, we used salt water and fresh water to simulate seawater. Then, we examined the effects of the different types of water. However, there was no observed difference between the two types, although there was a difference between entering and leaving the water. Therefore, it is not necessary to change the stimuli between the sea and the lake in a VR environment to reproduce the water surface. Moreover, there are no issues associated with the use of fresh water.

These results suggest that an environment cooler than the skin temperature and a state in which the skin is covered are important to create the illusion of entering the water. Regarding the skin covering, the accuracy was lower when the finger was covered with a liquid bandage than when it was not, even when the finger was placed in the water and the direct skin contact was present.

One limitation of this experiment is the accuracy of the measurement, since the length of the finger in the water was measured based on its image. As the hole above the cover of the water tank was meant for the insertion of the hand, the positioning did not differ significantly from one participant to another. However, we cannot disregard the possibility that the measured positions of the fingers in the water might have differed depending on the size of the hand or the bend of the wrist. Therefore, the use of a motion capture device is considered to improve the measurement accuracy. However, the marker cannot be directly attached to the skin due to tactile sensation; hence, refraction of light when the finger enters the water may be a concern. We plan to conduct another investigation once we obtain a motion capture device that can avoid these limitations, and we believe that such investigation may lead to new discoveries.

To build a scuba diving simulator, it is also important to reproduce wetness sensation. It is known that this is related to temperature and tactile stimulation[5][6]. Furthermore, Shibahara et al. have developed a head-mounted display that can reproduce wetness sensation[6]. These studies suggest that temperature and tactile stimuli are important for reproducing wetness sensation; however, the authors did not reproduce wetness sensation for the whole body. Furthermore, in order to attach a device that presents temperature and tactile stimuli to the whole body, it is necessary to consider an appropriate layout. For example, it is unknown whether attaching stimulus-presenting devices to the hand at intervals of several centimeters can reproduce the sensation of wetting the entire hand or whether it is necessary to attach them at intervals of several millimeters. Therefore, we would like to investigate the subjective equivalent of wetting area to the skin. Subsequently, we would also like to research on the appropriate layout of the stimulus presentation device that makes it possible to reproduce the sensation of the whole body being wet.

5. Conclusion

In this study, we identified that the water surface

perception was clearer when the water temperature was low; however, no effects were observed in terms of accuracy. The accuracy of water surface perception decreased when the skin surface was covered with a liquid bandage. Further, the accuracy of water surface perception was considered to be higher when entering the water than when leaving.

Future experiments on wetting sensation are required in order to reproduce this sensation in water, which may consequently enhance our knowledge on water surface perception.

Acknowledgment

This study is supported by JSPS KAKENHI 17H01756 for M.G.K.

References:

[1] Shogo Yamashita, Xinlei Zhang, and Jun Rekimoto, AquaCAVE: Augmented Swimming Environment with Immersive Surround-Screen Virtual Reality. *UIST '16 Proceedings of the 29th annual symposium on User Interface Software and Technology*, pp.183-184. (2016)

[2] Dhruv Jain, Misha Sra, Jingru Gro, Rodrigo Marques, Raymond W, Immersive Scuba Diving Simulator Using Virtual Reality. *UIST '16 Proceedings of the 29th annual symposium on User Interface Software and Technology*, pp. 729-739. (2016)

[3] Michi Sato, Junya Miyake, Yuki Hashimoto, Hiroyuki Kajimoto, Tactile Perception of a Water Surface: Contributions of Surface Tension and Skin Hair. *Haptics: Generating and Perceiving Tangible Sensations, Part II: 7th International Conference*, pp. 58-64. (2010)

[4] Tomoko Koshiba, Teruko Tamura, Factors Governing the Wet Sensation of Human Skin. *Journal of the Japan Research Association for Textile End-Use*, Vol. 36, No. 1, pp. 119-124, (1995) (in Japanese)

[5] Mai Shibahara, Katsunari Sato, Illusion of Wetness by Dynamic Touch. *IEEE Transactions on Haptics*, Vol. 12, No. 4, 1 Oct.-Dec., pp. 533-541, (2019)

[6] Roshan Lalintha Peiris, Liwei Chan, Kouta Minamizawa, LiquidReality: Wetness Sensations on the Face for Virtual Reality. *Haptics: Science, Technology, and Applications*, pp. 366-378, (2018)

Influence of eating Meals on facial expressions

Mao Maekawa*, Miyuki G. Kamachi**

*Informatics Program, Graduate School of Engineering, Kogakuin University, Tokyo, Japan
**Department of Information Design, Faculty of Informatics, Kogakuin University, Tokyo, Japan
E-mail: em21023@ns.kogakuin.ac.jp; miyuki@cc.kogakuin.ac.jp

Abstract

Leftovers and extra cutting are considered the main cause of food wastage. Previous studies have indicated that the levels of sleepiness differ before and after meals. Furthermore, it is known that the forehead muscles contract and relax with the levels of sleepiness, and the cheek muscles relax after meals. Studies have also found that changes in the redness of the face are caused by five basic taste components. In this study, We aimed to clarify the differences by comparing facial expressions before and after meals. In the first experiments, participants identified facial expressions before and after meals. Two facial expression maps, before and after meals, were presented for 10 s on the display. Participants were instructed to select a facial expression image for "after" a meal. The results showed that it is possible to judge human facial expressions after meals by comparing the expressions before and after meals. The experiment was repeated 50 times at random. It was also found that the redness in the images may have a tiny effect on the level of discrimination. In the second experiment, the facial images before and after meals were analyzed using deep learning. Deep learning focused on the mouth and eye area when discriminating between facial images before and after a meal. It was concluded that there may be several differences between facial expressions before and after meals, especially in the areas around the eyes and mouth.

1. Introduction

Leftovers and extra cutting are considered the major causes of food wastage. In a survey of catering companies in order to determine the reasons for food wastage, leftover food in service bowls and those left by consumers were found to be the primary causes [1]. In response to this problem, measures such as takeaway bags that allowed people to take leftover food home, were taken; however, several people were reported to have felt embarrassed to take home leftovers [2].

Smartphones and tablets are now being used to order food at restaurants and for online food delivery services. When ordering food, the faces of people are usually in front of the display. Therefore, in this study, we focused on facial expressions of users since they should be useful to determine various types of their needs for foods. Previous studies have suggested that facial expressions change in response to food and taste stimuli. It is known that people feel sleepy after meals, and the frontal muscles relax or contract depending on the level of sleepiness. as compared to that before meals. Further, people relax their cheek muscles after taking meals, which is another characteristic indicative of sleepiness [3]. Facial expressions change as a result of such sleepiness after meals. There are five taste components of food, namely, sweet, umami, salty, sour, and bitter. Facial skin blood flow is affected by these components [4]. For example, blood flow in the eyelids increases in response to sweet and umami taste stimuli, and that in the eyelids and cheeks increase in response to sour and salty taste stimuli. In addition, the redness of the skin can be perceived by the changes in hemoglobin concentration. These facts indicate the possibility that taste can cause the redness of the face to vary. However, it is not clear whether the changes in the facial expressions before and after eating can be accurately identified, or whether there is a correlation between such changes that can be determined based on image statistics.

The current study aimed to reveal changes in facial expressions by comparing facial expressions before and after meals using Experiments 1 and 2. For this purpose, in Experiment 1, we investigated whether people could discriminate differences in facial expressions and what the various contributing factors could be, in this regard.

In Experiment 2, we used deep learning to investigate the differences in the feature values of facial images before and after a meal.

2. Experiment 1

The purpose of this experiment was to investigate whether participants could determine differences in facial expressions before and after meals.

2.1 Participants

A total of 20 participants (10 males, 10 females) of normal weight participated voluntarily.

2.2. Facial images

A total of 50 facial images (28 males and 22 females) were selected from among the collected facial images (males and females aged 10–70 years) before and after meals. The images were approximately 13.4 cm in width and 20.1 cm in height, on the display.

2.3. Method

The participants were instructed to compare the "before" and "after" facial images and to select the "after" facial image. The "before" and "after" facial images were presented horizontally on the display for 10 s. After 10 s, the images were removed from the screen, but the participants could still select the facial image for the "after" meal. The entire process, from

displaying the images to obtaining a response, was repeated 50 times, and the images were displayed randomly each time. After this, the participants were asked to rate their confidence level on a 5-point scale from 0% (not confident) to 100% (confident) in 25% increments. The participants were also asked to answer a questionnaire about the gender they found easy to identify and the part of the face they focused on when making the decision.

2.4 Result

A t-test was conducted on the correct response rate of the 20 participants to compare it with a chance level of 0.5 (50% correct response rate). The correct response rate for male and female participants was significant ($t(19)=3.834$, $p<.01$), indicating that the participants were able to partly judge between facial expressions for "before" and "after" the meals. Fig. 1 shows the correct response rates for the male and female participants. Error bars indicate the standard deviation. When a t-test was conducted on the correct response rate of male subjects only, it was not significant ($t(9)=2.616$, *n.s.*). However, when the same t-test was conducted on the correct response rate with only the female participants, the correct response rate was found to be significantly different ($t(9)=2.899$, $p<.05$). However, a two-group t-test without correspondence for the correct response rate between males and females showed that the gender difference in the correct response rate ($t(18)=0.609$, *n.s.*) was not significant. When we discriminated between facial expressions before and after meals, there were no differences in the correct response rate by gender, but the results indicated that females may be able to discriminate facial expressions better than males.

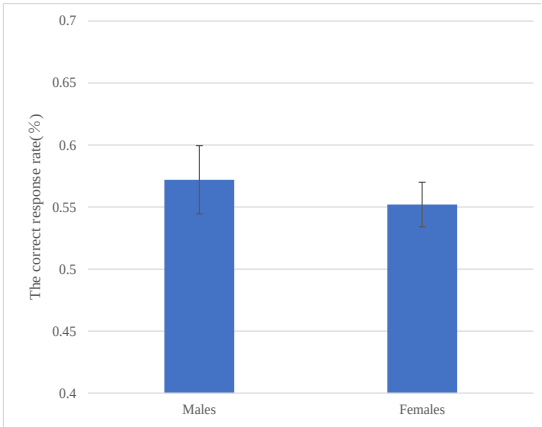

Fig. 1. Correct response rate for male and female participants.

Furthermore, in Experiment 1, a multiple regression analysis was conducted using the response rate of facial expressions for "after meals" for all the facial images used in the experiment as the criterion variable, and the facial image features (luminance value, contrast, and RGB values of lips, around the eyes, cheeks, nose, and chin) as the explanatory variables. The multiple coefficients of determination of the "R" value, 0.032, were relatively larger than those of the other variables. When participants discriminated between facial expressions of "before" and "after" the meal, the redness information (indicating "R" value on the skin affected the discrimination. In order to check whether this tendency appears strongly on visible changes on faces, an additional multiple regression analysis was conformed on the facial images (images of 16 people) —for which the response rate of facial expressions for "after" the meal was 75% or higher. The results showed that the multiple coefficients of determination of the "R" value (0.127) were relatively large. The pixel information of "R" (redness) may affect the response when participants determined facial expressions for "after" the meal. Table 1 shows the coefficients of the R-values for all the images and those with a response rate of 75% or higher. Among the explanatory variables for the R-values of all the facial images, changes in redness around the eyes and nose were shown to influence the discrimination. In the images with a high response rate of facial expressions for "after" meal, the changes in the redness of the lips, around the eyes, and nose were also found to influence the discrimination.

Table 1. Coefficients of R-values for all images and images with a response rate of 75% or higher.

Parts of face	All	75% or more
Lip	-0.000175	-0.00786
Around eyes	-0.00115	0.003543
nose	0.001268	0.004305
Chin	0.000037	0.002264
Cheek	-0.000357	-0.000599

3. Experiment 2

The purpose of this experiment was to investigate the differences in the physical features of the face before and after meals. A convolutional neural network (CNN) was used for the investigation using deep learning.

3.1 Facial images

Facial images were taken by the collaborators showing the front of their faces 1 min before and after taking the meal. For deep learning, we cropped the width of the face to include only the cheeks and edited the each of the images to be 400 px wide and 400 px high to avoid personal identification due to differences in the presence or absence of bangs on the forehead or the density of the eyebrows. The background was also cropped.

3.2 Method

This study used facial images from 61 participants for Experiment 2. These set of facial images were divided for training and testing in the 7:3 ratio, and the images were labeled as before or after a meal. The number of facial images was also increased by rotating, blurring, and thresholding the images. A 16-layer

trained model (Visual Geometry Group: VGG16), trained on color images of common objects, was used to train the model with fewer images; the trained model was used to perform transfer learning. In addition, Grad-CAM was used to visualize the important parts of the discrimination using a heat map.

3.3 Results

Fig. 2 shows a portion of the output heat map.

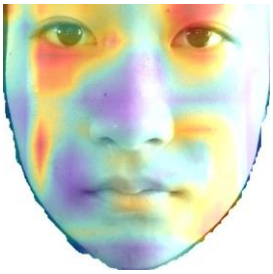

Fig.2. Portion of the output heat map

The heat map shows the areas of the image that are important when classifying an image. More importance is given to the discrimination if the color is closer to red, whereas less importance is given when it is closer to blue. As shown in Fig. 2, the main emphasis was placed on the area between the eyes, eyelids, under the nose, and chin when they were discriminated. This indicates that there may have been a difference in facial expression before and after the meal around the eyes and mouth. There were also several images in which the contour of the face was emphasized, although the levels of emphasis placed on it were low when classifying the images.

4. Discussion

The results of Experiment 1 indicated that the images that were considered to be "after meal" facial expressions were influenced by changes in the redness around the nose and eyes. Since the sense of taste affects the blood flow around the eyes, it is thought that the change in blood flow due to taste affects the correct answer rate [4]. However, since blood flow in the chin does not change in response to taste, the redness value in the chin image was not specifically related to the percentage of correct answers. In Experiment 2, deep learning was applied to focus on the areas around the eyes and mouth when making the discrimination. It was assumed that the relaxation of the muscles due to drowsiness that was present before the meal disappeared immediately after the meal; this is because the frontalis and the levator palpebrae superioris muscle and the musculus orbicularis around the mouth relax during sleepiness [3]. Our result suggests that there was a slight difference with regard to the areas around eyes and mouth.

The experimental results suggested that facial expressions do in fact change in response to taste and sleepiness. However, people have shown responses to factors other than taste. When people continue to eat the same food or food with similar tastes, they feel bored; this feeling is called sensory-specific satiety. It has been shown that sensory-specific satiety induces facial expressions of anger and sadness [5]. In a previous study, the authors proposed a model to predict hedonic ratings of gustatory stimuli based on hedonic ratings and facial expressions [6]. That model is an equation to predict hedonic ratings from subjects' facial expressions to gustatory stimuli, and was created from eight facial expressions (happy, angry, disgusted, surprised, scared, neutral, and embarrassed) and subjects' hedonic rating scores using artificial intelligence and multiple regression analysis. In these studies, novel approaches were proposed to predict consumers' evaluations of food intake based on their facial expressions and their evaluations of satiety and boredom. In the future, collection of data on facial expressions related to hunger and satiety, food intake, and consumers' evaluations of meals is necessary. The final goal of our study is to predict consumers' food intake based on their facial expressions by analyzing such data.

5. Conclusion

This study focused on investigating the differences between a person's face before and after meals. It was found that facial expressions before and after meals can be distinguished to some extent, although some differences between men and women were noted. The redness of the feature values around the eyes and nose was found to be a factor in the discrimination. In addition, deep learning showed that the eyes and mouth were important areas when discriminating between facial expressions before and after meals, suggesting that significant differences existed between them.

In the future, when facial expressions during hunger and satiety will be collected, four levels of evaluation (e.g., satiety and hunger), information on food intake, and calorie intake will also be simultaneously collected. Based on these data, deep learning analysis will be performed to obtain satiety and intake estimates based on the analyzed facial expressions.

Acknowledgements

We wish to thank all the participants, our collaborator, Mr. Kosuke Shida, and Mr. Motonori Kurosumi for their helpful comments on the research topics. This study was supported by research funds from POLA Chemical Industries, Inc. to M. G. K.

References

[1] Betz, A., Buchli, J., Göbel, C., Müller, C., "Food waste in the Swiss food service industry-Magnitude and potential for reduction," *Waste Management*, Vol. 35, pp. 218-226, 2015.

[2] Renata, D., Aira, M, "Food waste generation: restaurant data and consumer attitudes," *Environmental Research*, Vol. 75, No. 2, pp. 7-14, 2019.

[3] Ishida, K., Ichimura, A., Kamijo, M., "A study of facial muscular activities in drowsy expression," *Kansei Engineering International Journal*, Vol. 9, No. 2, pp. 57-66, 2010.

[4] Kashima, H., Hayashi, N., “Basic taste stimuli elicit unique responses in facial skin blood flow,” *PLOS ONE*, Vol. 6, No. 12, e28236, 2011.
[5] He, W., Boesveldt, S., Delplanque, S., de Graaf, C., de Wijk, R. A., “Sensory-specific satiety: Added insights from autonomic nervous system responses and facial expressions,” *Physiology & Behavior*, Vol. 170, pp. 12-18, 2017.
[6] Yamamoto, T., Mizuta, H., Ueji, K., “Analysis of facial expressions in response to basic taste stimuli using artificial intelligence to predict perceived hedonic ratings,” *PLOS ONE*, Vol. 16, No. 5, e0250928, 2021.

A study of facilitation evaluation methods in group discussions for students

Takuya Hirayanagi [1, a], and Daigo Misaki [1, b]

[1] Department of Mechanical Engineering, Graduate School of Engineering, Kogakuin University, Tokyo, Japan
[a] am21048@ns.kogakuin.ac.jp, [b] misaki@cc.kogakuin.ac.jp

Abstract

An empirical study on the effectiveness of facilitators in group discussions among students was conducted through a questionnaire survey. The results in this study showed that the facilitated groups had higher evaluations of the questions in the questionnaire.

Introduction

In recent years, with the progress of globalization and the development of AI technology, opportunities to communicate with people of diverse values have increased. In light of this, active learning (AL) is being promoted in the field of education with the aim of developing proactive and more interactive human resources [1].

The presence of a facilitator is important in the implementation of AL. A facilitator is a person who is in charge of activating the discussion from a neutral position, and educators who implement AL are required to have facilitation skills [2]. In addition, due to the impact of COVID-19, AL, which was originally designed for face-to-face group learning, is now difficult to implement, and online group learning is increasing. However, until now, there have not been sufficient examples of the effectiveness of online facilitators. In this paper, we conducted an online problem-solving discussion to verify the effectiveness of facilitators through a questionnaire.

Conversation Activation Techniques

In this study, open-ended questions (OQ) are used to stimulate conversations. OQs are questions that use what, how, etc., as represented by 5W1H. If OQ is found to be an activator of conversation, the facilitator can use it in appropriate situations to activate the conversation. Therefore, in this study, I hypothesized that the OQ asked by the facilitator would be effective in generating ideas among the participants.

Basic Experiment

Using Zoom, a video web conferencing tool, a facilitator (the author) facilitated a discussion among three university students. The facilitator used OQ to conduct the discussion in three groups, one group to activate the conversation and one group not to. After the discussion, the participants were asked to rate the following seven questions on a 5-point scale from 1 (bad) to 5 (good).

(1) Did you enjoy the group discussion?
(2) Were the topics of the conversations interesting to you?
(3) Were you able to speak positively?
(4) Please self-evaluate the content of your remarks.
(5) Did you feel safe to speak?
(6) Did you feel that you could trust the other participants?
(7) Do you think the group discussion was active?

Figure 1 shows the results of the discussion evaluation (mean and standard deviation).

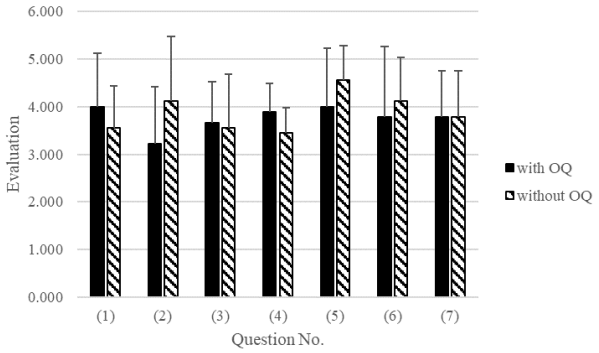

Fig.1. Results of the discussion evaluation.

Consideration and Conclusion

From the results of the questionnaire, the mean values of (1) and (7), which indicate the atmosphere of the dialogue, and (3) and (4), which are questions about idea generation, were high, suggesting that the facilitators were effective in the discussions.

It was found that the facilitator's use of OQ can be expected to have the effect of generating ideas from the participants and enhancing the atmosphere of the place. And, the subject of further research is to collect data that can objectively evaluate discussions based on the conversational voice and facial expressions of participants, and to verify the effectiveness of facilitation with more reliability.

References:

[1] Prince, Michael. "Does active learning work? A review of the research." Journal of engineering education 93.3 223-231 (2004).
[2] Haythornthwaite, C. "Facilitating collaboration in online learning." Journal of Asynchronous Learning Networks 10.1 7-24 (2006).

Optimization of Service Frequency based on Short-term Passenger Forecasting on Scheduled Bus
-Case Study on the Route for Kogakuin University-

Yuya Nagai, Yoshio Miki

Department of System Design, Master Degree of Engineering, Kogakuin University, Tokyo, Japan
E-mail: gm20003@g.kogakuin.jp

Abstract
With the development of information technology, data-driven operation of regular sightseeing buses has been attempted. In the same way, we are also investigating the operation optimization of specific operation routes as a case study of operation optimization based on short-term demand forecasting, on a route for Kogakuin University. In this paper, we confirmed the amount of effect of operation efficiency improvement by optimizing the operation frequency of the relevant route. As a result, it was confirmed that there is room to reduce the operation time by several thousand hours per year. However, this is a theoretical prediction, and the actual amount of reduction depends on the performance of the user prediction. We are currently working on a prediction model to get closer to the theoretical value. We are trying to create a prediction model that takes uncertainty into account, rather than a point estimate. If anyone has any knowledge about this, I would be very interested in learning more about it.

Introduction
With the development of information technology, attempts to achieve data-driven operations have begun even in scheduled bus.

Therefore, in order to realize data-driven operation in scheduled bus, we are also studying dynamic frequency optimization of specific transportation routes for Kogakuin University as a case study of dynamic frequency optimization based on short-term demand forecasting.

This paper confirms the amount of operational efficiency improvement of optimization on the relevant routes.

As a result, depending on the maximum allowable number of passengers per vehicle on the main and auxiliary routes, we were able to confirm the possibility of improving operational efficiency by several thousand hours per year.

Method Overview
The frequency setting method we are considering optimizes the frequency of the sub route by considering the situation of the main route on a weekly to monthly basis based on the number of people predicted by the demand for each time period, as shown in the flow in Figure 1.

- Our frequency setting method assumes that the frequency of the main route is fixed, and determines the frequency of the sub route.
- Since the magnitude and variability of demand varies from time to time, and we want to handle uncertainty on an hourly basis, we prepare a forecasting model for each arbitrary time period.
- The frequency of changes is expected to be on a weekly to monthly basis due to the performance of the current weather forecast.

Optimization Method
The optimization method we considered this time is to minimize the number of unloads as the first priority, and then to optimize the frequency of sub-routes so that the fleet size is minimized.

- The frequency of the main route is assumed to be predetermined.
- Since this method is only used to determine the frequency of operation of sub-routes, the possibility of operation is not included in the constraints at this stage.
- Equation 3 expresses that if a limit for the frequency of operation of a sub-route is specified as a parameter, it will be used, but if not, the frequency of the physical limit will be set as the limit.

Table 1. Parameters, constant and variables for optimization

Parameters	**Description**
PM_t	Passengers on main route
PS_t	Passengers on sub route
CM_t	Capacity on main route
CS_t	Capacity on sub route
FM_t	Frequency on main route
LFS_t	Limit frequency on sub route
TI_t	Time interval on minute
$PLDI$	Physical limit departure interval on minute
Constant	**Description**
FPS_t	Fleet size for passengers using sub route
LFP_t	Limit unfulfill passenger
Variables	**Description**
fs_t	Frequency on sub route

$$FPS_t = fs_t CS_t + (FM_t CM_t - PM_t) \tag{1}$$

$$LFP_t = \begin{cases} 0 & (PS_t - EF_t <= 0) \\ PS_t - EF_t & (PS_t - EF_t > 0) \end{cases} \tag{2}$$

$$LFS_t = \begin{cases} LFS_t & (LFS_t >= 0) \\ \lfloor TI_t / PLDI \rfloor & (LFS_t < 0) \end{cases} \tag{3}$$

$$\text{minimize} \quad \sum_{t=0}^{n} fs_t \tag{4}$$

subject to

$$PS_t - FPS_t \leq LFP_t \tag{5}$$

$$fs_t = \{n | 0 \leq n \leq LFS_t, n \in \mathbb{Z}\} \tag{6}$$

$$FM_t = \{n | n \geq 0, n \in \mathbb{Z}\} \tag{7}$$

$$LFS_t = \{n | n \geq 0, n \in \mathbb{Z}\} \tag{8}$$

$$CS_t = \{n | n \geq 0, n \in \mathbb{Z}\} \tag{9}$$

$$CM_t = \{n | n \geq 0, n \in \mathbb{Z}\} \tag{10}$$

$$PS_t = \{n | n \geq 0, n \in \mathbb{Z}\} \tag{11}$$

$$PM_t = \{n | n \geq 0, n \in \mathbb{Z}\} \tag{12}$$

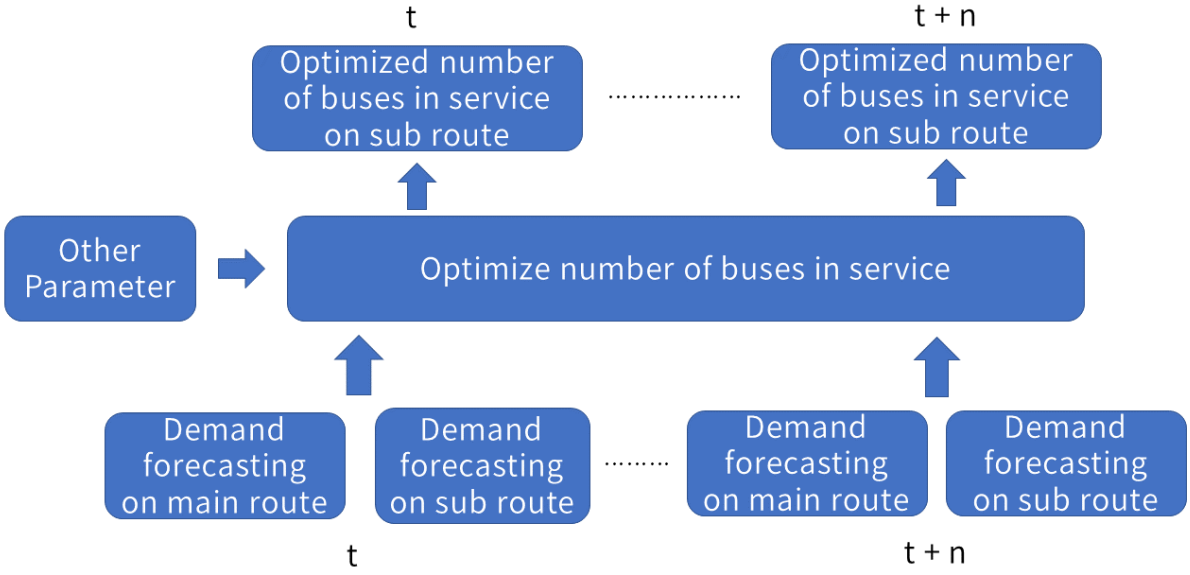

Fig. 1. The flow of frequency settings for sub route

Evaluation

Method and Situation

- The main route is the route that includes Kogakuin University as a stop from Keio-Hachioji Station operated by Nishi-Tokyo Bus, and the sub-route is the route that connects the north exit of Hachioji Station and Kogakuin University between two points.
- Since the first departure from the station toward the university differs between the main and sub-routes, the data was compiled according to the starting point of the sub-route.
- The data source is a smart card provided by Nishi-Tokyo Bus.
- Since the main routes are operated regardless of the university, the number of trains and the number of passengers were counted in 20-minute increments according to the minimum frequency of the main routes.
- In order to confirm the expected efficiency of the operation and to explore the sensitivity of the allowable upper user limit parameter, we calculated the reduced number of operations and the reduced operating hours when one of the upper user limit parameters was fixed at about 60, which is the upper limit for large buses, and the other upper user limit was varied from 30 to 60.
- Optimization was applied both in the direction of the university from the railroad station and in the direction of the railroad station from the university.

Result

Although it depends on the maximum allowable number of users per vehicle on the main and sub-routes, we were able to confirm the possibility of reducing operating hours by several thousand hours per year. Table 2 shows the effect size when the maximum permissible user limit for the sub-route is fixed and the maximum permissible user limit for the main route is varied by 10 between 30 large bus seats and 60 physical limit passengers. Similarly, Table 3 shows the effect size when the main route is fixed and the sub route is changed. Depending on the maximum allowable users, we can see the potential for several thousand hours of efficiency gains per year.

It was confirmed that keeping the allowable user limit of the main route higher than the allowable user limit of the sub-route was more effective in improving operational efficiency. Figures 2 and 3 show the rate of change in the amount of reduction when increasing the allowable user limit in Tables 2 and 3. Comparing the two figures, it can be seen that even when the upper limit of the sub-route was increased, the increase was only about 1 %, while for the main route, when the limit was increased from 30 to 40, the increase was at least twice as large. It was found that the maximum permissible number of users on the main route was effective in improving the efficiency of the operation.

Conclusion

In this study, as one of the ways to improve operational efficiency in order to maintain the scheduled bus in Japan, we assumed that the frequency optimization based on the short-term passenger forecasting would be realized on the routes for Kogakuin University, and studied the method of frequency optimization.

Depending on the maximum allowable number of passengers per vehicle on the main and auxiliary routes, we were able to confirm the possibility of improving operational efficiency by several thousand hours per year.

The amount of improvement in this evaluation is only a theoretical value of the expected value, and the actual amount of improvement in operational efficiency depends on the performance of the passenger forecasting model. The amount of improvement in operational efficiency depends on the performance of the passenger forecasting model. This evaluation was conducted on the assumption that the number of users can be predicted with 100 % accuracy in order to examine the expected value of improvement in operational efficiency. Since it is no realistic to create the passenger forecasting model with 100% accuracy, the assumption in this evaluation deviates from reality. Therefore, the degree to which operational efficiency can be improved depends on the ability of the passenger forecasting model.

We are researching on the passenger prediction to get closer to the theoretical value. We are trying to create a prediction model that takes uncertainty into account, rather than a point estimate. If you have any knowledge, we would appreciate it if you could share it with me.

Table. 2. Effect size when the capacity of the sub route is fixed and the capacity of the main route is varied

Parameter	**Evaluation index**	2016	2017	2018	2019	2020
30 – 60	Reduced frequency	13176	12761	13512	10440	4678
	Reduced operating time (hour)	4392	4253	4504	3480	1559
40 – 60	Reduced frequency	14539	14756	14756	11891	4686
	Reduced operating time	4846	4720	4918	3963	1562
50 – 60	Reduced frequency	15499	15148	14756	12931	4690
	Reduced operating time	5166	5049	5199	4310	1563
60 - 60	Reduced frequency	16212	15834	16226	13623	4695
	Reduced operating time	5404	5278	5408	4541	1565

Table. 3. Effect size when the capacity of the main route is fixed and the capacity of the sub route is varied

Parameter	**Evaluation index**	2016	2017	2018	2019	2020
60- 30	Reduced frequency	4924	4424	5779	2784	793
	Reduced operating time (hour)	1641	1474	1926	928	264
60 – 40	Reduced frequency	11513	10885	12030	8944	3390
	Reduced operating time	3837	3638	4010	2981	1130
60 – 50	Reduced frequency	14510	14062	14710	11994	4362
	Reduced operating time	4836	4687	4903	3998	1454
60 - 60	Reduced frequency	16212	15834	16226	13623	4695
	Reduced operating time	5405	5278	5408	4541	1565

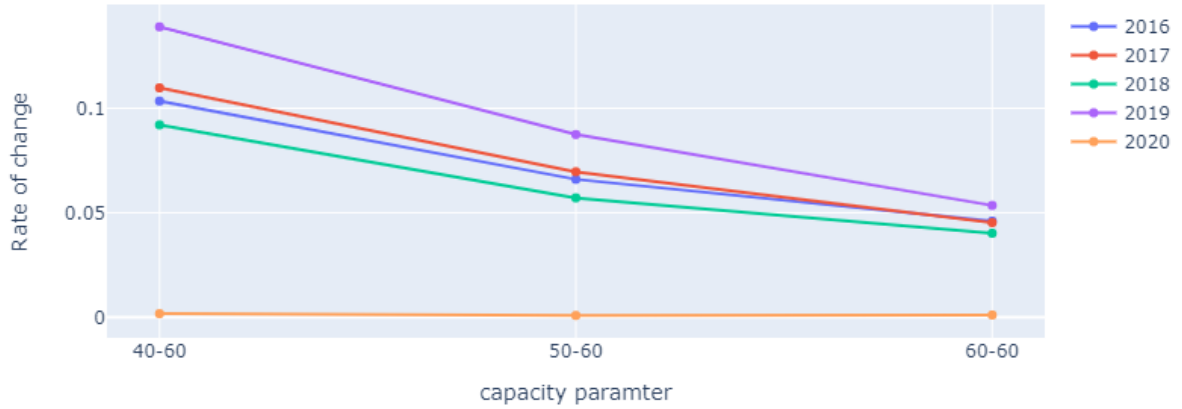

Fig. 2. The rate of change when the parameters of the sub route are fixed and the parameters of the main route are changed

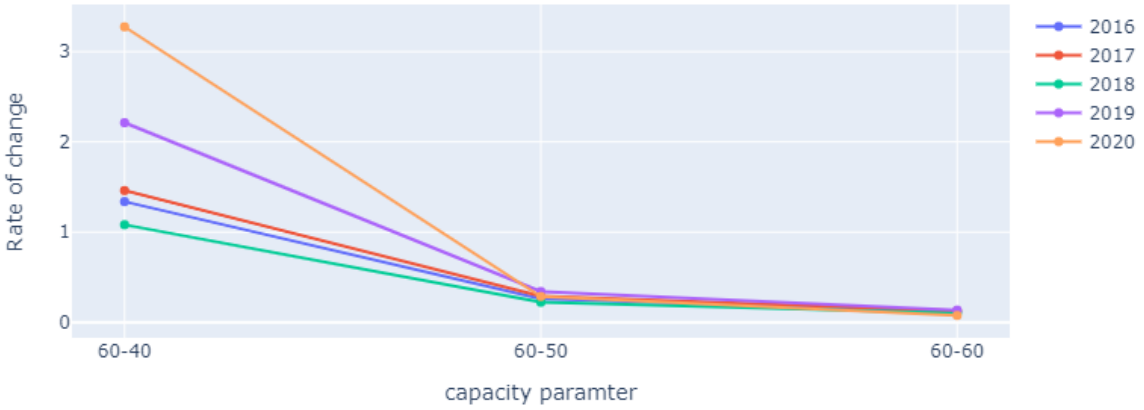

Fig. 3. The rate of change when the parameters of the sub route are fixed and the parameters of the main route are changed

Study on Driving Skill Analysis in Curve Sections using Adaboost Algorithm with Driving Simulator

Eisho Kanno*[1] and Masakazu Mukai[2]

[1]Electrical Engineering and Electronics Program, Kogakuin University, Tokyo, Japan
[2]Department of Electrical and Electronic Engineering, Kogakuin University, Tokyo, Japan
E-mail: mukai@cc.kogakuin.ac.jp

Abstract

This study considers a driving skill analysis method to understand the driver for comfortable automatic driving system. In this paper driving data is obtained from a driving simulator experiment. An AdaBoost algorithm is used to extract driving features from the driving data.

1. Introduction

Driving skills of drivers have a great influence on safety and driving comfort. To supply effective advice to low-skilled drivers some extraction methods for driving feature is studied [1][2]. For automatic driving control system, analysis of the driving skills of drivers is important. In this study, the driving data is prepared by using the driving simulator. For the driving data AdaBoost algorithm is used to distinguish high-skilled drivers and low-skilled drivers.

2. Methods

2.1. Driving Simulator Experiment

A driving simulator is used to obtain driving data. In the driving simulator a course shown in Fig. 1 with 6 curves is used. The driving data includes driver's steer position, accelerator pedal position, brake pedal position, steering speed, accelerator operating speeds, brake operating speeds, velocity, distance from centerline, longitude jerk, and lateral jerk.

2.2. Training Data for AdaBoost Algorithm

The AdaBoost algorithm is a machine learning algorithm. Its training data must be defined in the data pre-processing. In this study, the driving data is separated into two groups: high-skilled and low-skilled by using summation of jerk and average speed.

2.3. Prepare Driving Data

To compare the driving data, driving data is decomposed into frequency components by wavelet transform. Then the transformed data is normalized by distance so that it can be compared at the same location. The driving data for AdaBoost algorithm is produced by adding a sub-windows function. For the data the trained AdaBoost algorithm is applied. Finally, driving features that represent the difference between the high-skilled drivers and low-skilled drivers are automatically extracted.

3. Results

The results of using the AdaBoost algorithm, the places where features appeared, were listed in Fig. 1. The driving features appeared on each curve, the features of steering speed were appeared on curve 1, curve 3, and curve 6. The features of steering position appeared on curve 5. This showed that the steering operation of the low-skilled drivers was unstable. Furthermore, the features of the brake operation speed appeared on curve 4. It shows that the low-skilled drivers tended to operate the brake pedal even on gentle curves. Finally, the features of the accelerator operation speed appeared on curve 2. It turned out that the high-skilled drivers rely on the operation of the accelerator pedal when entering a curve.

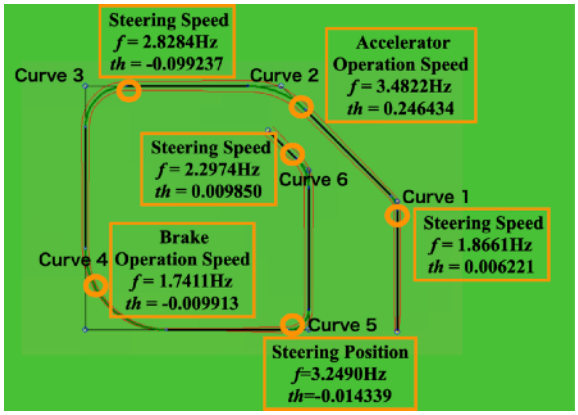

Fig. 1. Places where features appeared.

4. Conclusion

This study considers a driving skill analysis method using AdaBoost algorithm to understand the driver for comfortable automatic driving system.

References:

[1] S. Li, D. Yamaguch, T. Hirasawa, Y. Sato, Y. Suda, S. Takeuchi, S. Yoshioka, Driving Feature Extraction between Skilled and Unskilled Drivsrs'Groups, *Seisan-kenkyu,* Vol. 24, No. 2 (2012).

[2] S. Li, S. Yamabe, Y. Sato, T. Hirasawa, Y. Suda, N. P. Chandrasiri, K. Nawa, Driving Feature Extraction from High and Low Skilled Drivers in Curve Sections Based on Machine Learning, *Journal of Mechanical Systems for Transportation and Logistics*, Vol. 6, No. 2 (2013).

[3] M. Miyake, T. Ikegami, *A*n Investigation of Boosting Algorithm as Complex Adaptive System, *The 30th Annual Conference of the Japanese Society for Artificial Intelligence* (2016).

Development of *Operando* Raman Analysis at the Reaction Cross-Section of All-Solid-State Batteries

Takaaki Ono[1)], Koji Hiraoka[1)], Hibiki Miyauchi[1)], Takeshi Kobayashi[2)] and Shiro Seki[1)]

1)Graduate school of applied chemistry and chemical engineering, Kogakuin University, Tokyo, Japan
E-mail: bm21011@ns.kogakuin.ac.jp
2)Central Research Institute of Electric Power Industry, Kanagawa, Japan

Abstract

Currently, Li-ion batteries (LIBs) are attracting attention as power storage device for electric load-leveling by using renewable energy. However, conventional LIBs have relatively low safety owing to their flammability of organic liquid electrolyte. All-solid-state batteries (ASSBs) using solid electrolyte are strongly desired for high safety systems. Especially, oxide-type ASSBs, which are consisted of oxide electrodes and electrolytes are under intense investigated because of their high chemical and moisture stability. However, ASSBs using oxides has relatively high internal resistance including electrode/electrolyte interfacial resistance. Recently, multi-step sintering method [1] was proposed for fabrication process of oxide-type ASSBs. The obtained cell is composed of pre–sintered positive electrode (PE) /electrolyte pellet and negative electrode (NE)/electrolyte pellet, and finally formed PE/solid electrolyte, NE/solid electrolyte, and solid electrolyte/solid electrolyte interfaces by addition of adhesion reagent. In this study, we focused on the reaction mechanism and degradation behavior at these interfaces, *operando* Raman measurement at might be the cross-sectional of [$Na_3V_2(PO_4)_3$(NVP) | $Na_3Zr_2(SiO_4)_2PO_4$(NZSP) | $Na_3V_2(PO_4)_3$] cells were investigated using confocal Raman spectrometry.

Experimental

[$Na_3V_2(PO_4)_3$(NVP) | $Na_3Zr_2(SiO_4)_2PO_4$(NZSP) | $Na_3V_2(PO_4)_3$] cells were fabricated by the multi-step sintering method using Spark-Plasma-Sintering (SPS). Cross-section of fabricated ASSB was polished with sandpaper and introduced into *operando* cell. Firstly, constant current charge discharge measurements were performed at 60 ℃, 12.7 μA cm^{-2} and cut off voltage of 0.5 to 2.5V, as pre-cycling. After that, *operando* Raman measurements at charge process were carried out at room temperature and 39.2 μA cm^{-2}. Raman measurements of PE, electrolyte and NE were carried out each 1h.

Results and Discussion

Fig.1 shows charge profile of the ASSB during *operando* Raman measurements. Charge capacity was approximately 60 % of theoretical capacity of NVP (117 mAh g^{-1}) at room temperature. Fig. 2 shows Raman spectra of ASSB each state of charge (SOC) : 0, 57, and 100 %, respectively. In electrolyte, major peaks were observed at 925 cm^{-1} and 1030 cm^{-1} attributed P-O and Si-O bonds, respectively. These peaks exhibited no SOC dependences. Therefore, changes for crystal structure and vibration mode of NZSP electrolyte were not confirmed, and stable structure of NZSP should be maintained under charge process. In PE and NE, Clear peaks of D-band and G-band resulting from carbon as conductive additive were observed at 1350 cm^{-1} and 1590 cm^{-1}, respectively. The peaks of D and G bands were not changed for charge process owing to their stability against SOC. Raman spectra of NVP were reported to appear under 1200 cm^{-1} [2], and observed broad peaks region of 550-1200 cm^{-1} assigned to vibration of NVP. Intensity of several peaks increased with SOC. Especially, in Raman spectra of NE, weak and sharp peaks were appeared about 1070 cm^{-1}, 940 cm^{-1} and 835 cm^{-1}, respectively, over SOC 0 %. These peaks reflected with phase transition of NVP according to Na ion doping. Additionally, Raman spectra of NVP region of 500 - 1200 cm^{-1} are reported to related to PO_4 vibration modes [3]. Therefore, PO_4 bonds are suggested to sensitively correspond with change of atomic number of Na during charge process. From *Operando* Raman analysis for ASSB, NVP peaks were confirmed to reflect charge state, and proposed analysis methods can be applied to directly observation of electrochemical reaction.

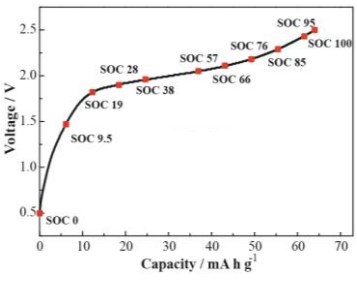

Fig.1 Charge profile of ASSB.

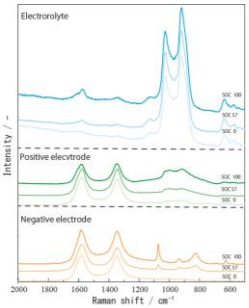

Fig.2 SOC dependencies of Raman spectra in the ASSB.

References:

[1] T. Kobayashi, *et.al.*, *J. Power. Sources.* **450** 227597 (2020).
[2] P. K. Jha1, *et.al.*, *Silicon*, **9** 411-419 (2017).
[3] Z. Jian, *et. al.*, *Adv. Energy Mater*, **3** 156-160 (2013).

Acknowledgements:

This work was supported by the Feasibility study Program on Energy and New Environment Technology, and New Energy and Industrial Technology Development Organization (NEDO).

Lightning Talk Session

Mechanical Engineering

November 23rd

Presentation No.	Title	Author	
MEL1.	Research on Motion Analysis of Pedestrians Using OpenPose	Genki Bamba, Kazuki Weerakoon Miyakawa,Takashi Kato, and Daigo Misaki	306
MEL2.	Audio glasses for confining acoustic field in near field	Shuzo Terauchi, Tsutomu Kaizuka	307
MEL3.	Jet formation after droplet impact into water pool	Futa Minami, K. Hasegawa	308
MEL4.	Visualization of vibration behavior of multiple samples levitated in an acoustic field	Manami Murata, K. Hasegawa	309
MEL5.	Study on the presentation method of the automated driving experience simulator by wizard of oz prototyping	Kazuki Miyakawa Weerakoon, Genki Bamba, Takashi Kato, and Daigo Misaki	310
MEL6.	Development of a robot to assist in optimal parts supply at cell production sites	Shutaro Ito, Daigo Misaki	311
MEL7.	Development of Self-Lubricating Slide Bearings with Sintered Porous Metals	Taiga Itoi, S. Kawajiri, Y. Sasaki, E. Takami, Y. Fujita, and M. Shiomi	312

Research on Motion Analysis of Pedestrians Using OpenPose

Genki Bamba[1,a], and Kazuki Weerakoon Miyakawa[1,b],Takashi Kato[1.c] and Daigo Misaki[1.d]

[1]Graduate School of Engineering, Kogakuin University, Tokyo, Japan
[a]am21047@ns.kogakuin.ac.jp,[b]am21007@ns.kogakuin.ac.jp,[c]am20020@ns.kogakuin.ac.jp,[d]misaki@cc.kogakuin.ac.jp

Abstract

As the research on automatic driving progresses, it is essential to discuss the prediction of pedestrian movements. In this paper, we proposed a method of motion analysis from the skeletal estimation of an actual pedestrian using OpenPose. And, we were able to verify sufficient accuracy for motion analysis from the skeletal analysis.

In recent years, it is important to discuss the prediction of pedestrian behavior in the context of research on automated driving. The mainstream methods currently being considered for pedestrian recognition in automated vehicles are high-resolution LIDAR-based recognition[1] and object shape recognition[2]. On the other hand, these kinds of algorithms are not only expensive but also time-consuming to introduce and implement. In this study, we propose a method to analyze pedestrian motion from actual skeletal estimation using OpenPose.

METHODOLOGY

As a method for skeletal estimation, we used the OpenPose [3] proposed by Cao et al. at CMU. the reason for adopting OpenPose is that it has no restriction on sensing distance and can be used regardless of outdoor sunlight.

We proposed a method to identify the posture and motion of a walker by obtaining six points of information from OpenPose: head, neck, both hands, and feet. Furthermore, to obtain more accurate joint information from the analysis results, we excluded joint points with a confidence level of less than 70%.

In addition, the positional correction was made so that the subject's neck position was the origin. By the neck position was the origin, the coordinates of the neck were calculated as $X_{neck}(x_{neck}, y_{neck})$ the attitude information is $X_i(x_i , y_i)$ and the position correction is performed. The attitude information X(x , y) is shown in equation (1) below.

$$X(x , y)=X_i - X_{neck} =(x_i - x_{neck} , y_i - y_{neck}) \quad (1)$$

As a basic experiment, we used video data captured at an actual crosswalk, from which we used a video of pedestrians trying to use the crossing. Figure 1 shows the experimental scene and skeletal analysis.

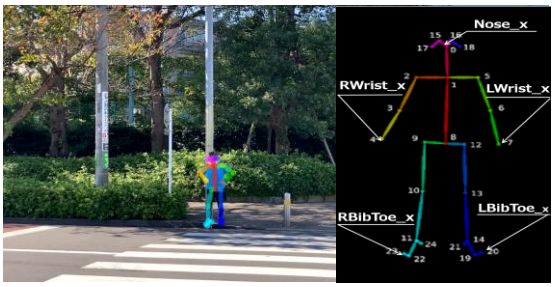

Fig.1. Experimental scene and posture analysis

RESULTS AND DISCUSSION

Figure 2 shows the results of the motion analysis of the pedestrian. The joint points of OpenPose were extracted using the subject's neck position as the origin. As for the accuracy of the skeletal analysis, when Nose_x (Redline in Fig.2.), which has the smallest range of motion among all the joint points, was shaken left and right, the movement of about 20 pixels was clearly shown four times in the graph. In addition, the slight movement of the limbs by the pedestrian before crossing the street could be confirmed from the skeletal analysis.

From these results, we were able to verify sufficient accuracy for motion analysis from the skeletal analysis. We also believe that our proposed method can be applied to pedestrian motion prediction in the future.

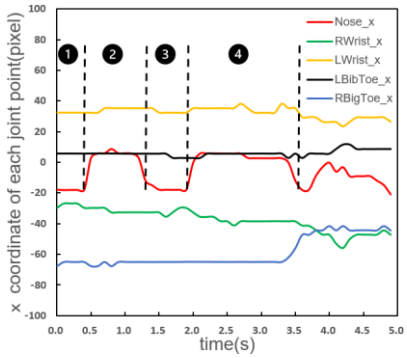

Fig.2. X coordinates of each joint point in OpenPose

Analysis of pedestrian-vehicle interaction and research on regional differences in pedestrian behavior are subjects of further study.

References:

[1]Kidono, Kiyosumi, et al. "Pedestrian recognition using high-definition LIDAR." 2011 IEEE Intelligent Vehicles Symposium (IV). IEEE, 2011.

[2] Schwarting, Wilko, Javier Alonso-Mora, and Daniela Rus. "Planning and decision-making for autonomous vehicles." *Annual Review of Control, Robotics, and Autonomous Systems* 1 (2018): 187-210.

[3] Cao, Zhe, et al. "OpenPose: realtime multi-person 2D pose estimation using Part Affinity Fields." *IEEE transactions on pattern analysis and machine intelligence* 43.1 (2019): 172-186.

Audio glasses for confining acoustic field in near field

Shuzo TERAUCHI[1], Tsutomu KAIZUKA[2]

Department of Mechanical Science and Engineering, School of Advanced Engineering,
Kogakuin University, Tokyo, Japan
s518042@ns.kogakuin.ac.jp[1], tkaizuka@cc.kogakuin.ac.jp[2]

Abstract

Headphones and earphones provide personal audio in which sound leakages to surroundings are avoidable. However, wearing such devices causes uncomfortableness and prevents from listening to other people. Recently, new types of wearable audio devices, e.g., shoulder-mounted, ear-mounted (open-ear), and glass-type loudspeakers, became prevalent. However, the new devices cannot avoid sound leakages to surroundings, because the loudspeakers are not contained in housings. In our earlier works[1][2], loudspeaker arrays for enhancing the near fields were proposed. The technique enables to avoid sound leakages without containing loudspeakers in housings. In the proposed method, the listening point must be located in the near field of the loudspeaker arrays. According to the literature [2], shoulder-mounted loudspeakers are not suitable for this application, because the distance between a loudspeaker array and listening point is too large especially at high frequencies. Ear-mounted loudspeakers are promising, because the distance between a loudspeaker array and listening point is small enough in the speech frequency range [2]. In this study, glass-type loudspeakers are investigated as an application example of the proposed method.

Figure 1 shows an audio glasses numerically simulated in this study. The frame and lenses were modeled as a rigid body. Three point acoustic sources are deployed on each of the right and left sides of the frame. By reffering to the literatures [1][2], acoustic transfer functions on the surface of the loudspeaker array was calculated, and a generalized eigenvalue problem based on the acoustic transfer functions was solved. The three point acoustic sources on each side were considered in the generalized eigenvalue problem. The real eigenvectors indicates amplitudes and polarities of the individual loudspekears, and the real eigenvalues represents the ratio of the reactive acoustic power to the active acoustic power. Hence, the loudspeaker array was driven according to the eigenvector with the maximum eigenvalue. This eigenvector resulted in a longitudinal quadrapole source, which means that the two neighboring sources were driven with a half amplitude and opposite phase in comparison to the center source. For comparison, a conventional audio glasses was also examined. Only the center source on each side of the frame was driven in this case. The distance between the listening point and center source is 0.02 m.

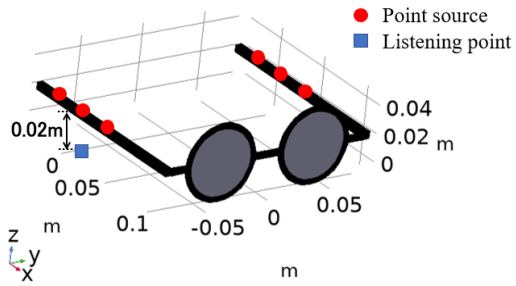

Fig. 1. Geometry of audio glasses.

Figure 2 shows the sound pressure levels generated by the conventional and proposed methods. The reference value of the sound pressure levels is the amplitude of the sound pressure at the listening point. The acoustic field was successfully confined near the audio glasses by the proposed method.

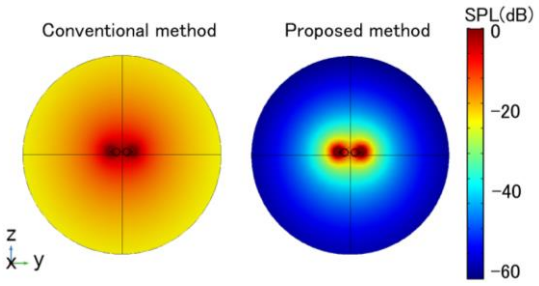

Fig. 2. Sound pressure levels generated by audio glasses at 300 Hz.

References

[1] T. Kaizuka, K. Nakano, *Radiation modes and acoustic field confined near acoustic sources*, J. Acoust. Soc. Am. 146, EL299 − EL305 (2019).

[2] S. Terauchi, T. Kaizuka, *Near-field loudspeaker array: Layout of loudspeakers*, in Dynamics and Design Conference (2021).

Jet formation after droplet impact into water pool

F. Minami[1], K. Hasegawa[2]

1. Department of Mechanical Engineering, Graduate School of Engineering, Kogakuin University, Tokyo, Japan,
2. Department of Mechanical Engineering, Kogakuin University, Tokyo, Japan
E-mail: am20064@ns.kogakuin.ac.jp

Abstract

The impact behavior of a droplet on a liquid pool is very important as a fundamental phenomenon for the falling impact of raindrops and the splashing of waves on the sea surface. Here we present an experimental study on the effect of droplet ch1aracteristics on the impact of a droplet on a liquid pool. In this study, we used different droplets with varying surface tension, viscosity, density, and miscibility with water to visualize the impact behavior of a single droplet on a water pool using a high-speed camera. In order to clarify the effect of droplet characteristics on the impact behavior, image processing was performed on the obtained high-speed images to quantify the shape of the cavity and the liquid jet formed after the droplet impacted the water pool. These experimental results provide physical insight into the process of droplet impact on a water pool and pave the way for applications.

Liquid droplet impact phenomena are important as the basis for raindrop impact and wave splash on the sea surface. In particular, it has been suggested that the sea level fluctuation that occurs during the generation of wave spray affects cloud formation, and it is expected that the clarification of this phenomenon can be applied to improve the accuracy of cloud development prediction[1][2]. In this study, we aim to clarify the effect of fluid properties of impacting droplets on their impact behavior. In order to investigate the effect of fluid properties, we conducted experiments with pure water, ethanol, and silicone oil as the droplets and pure water as the liquid pool Droplet diameters ranged from 1.6 to 3.4 mm. The depth of the droplet pool was fixed at 30 mm. Here, the impact velocity was fixed at 2.4 m/s and Fr number was set to $250 < Fr < 300$.

Figure 1 shows the impact process of each droplet on the water pool In the case of the ethanol droplet, it is observed that the droplet jet was enlarged due to the effect of fine droplets dispersing from the tip of the crown and mixing with the water pool. In the case of silicone oil droplets, it was confirmed that the cavity shape was different with other two droplets. After the droplet sank under the pool and the formation and contraction of the tapered cavity, the ejection and pinch-off of the sharpened jet were observed.

Figure 2 shows the estimated energy balance before and after the droplet impact. The impact energy was expressed by the kinetic energy and surface energy of the impact droplet. The cavity energy assumed with the cavity energy, wave-swell energy, and surface energy. It is suggested that approximately 70% of the impact energy was converted into the cavity energy for all cases. On the other hand, the rest of 30% of the lost energy were unclear so that it is important to visualize the flow field inside the pool to understand the phenomenon.

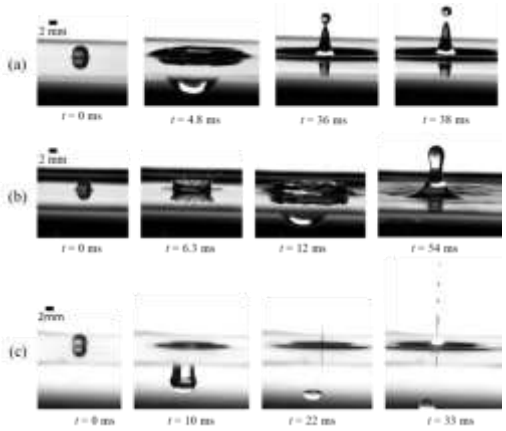

Fig. 1. Effect of droplet properties on droplet impact onto water pool.
(a) water: σ = 72.7 mN/m, miscible,
(b) ethanol: σ = 22.3 mN/m, miscible,
(c) silicone oil: σ = 21.1 mN/m, immiscible.

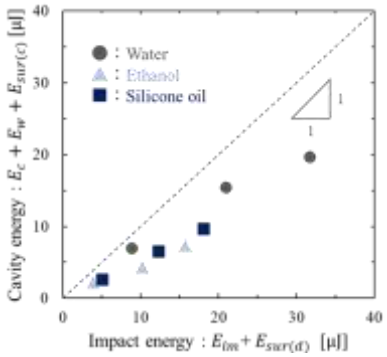

Fig. 2. Energy balance before and after the droplet impact on water pool.

References:

[1] M. E. Salter et al., Geophysical Research Letters, **43**, 8277-8285 (2016).

[2] Guy-Jean Michon et al., Phys. Rev. Fluids. **2**, 023601 (2017).

Visualization of vibration behavior of multiple samples levitated in an acoustic field

M. Murata[1], K. Hasegawa[2]

1. Graduate School of Engineering, Kogakuin University, Tokyo, Japan,
2. Department of Mechanical Engineering, Kogakuin University, Tokyo, Japan
E-mail: am20067@ns.kogakuin.ac.jp

Abstract

In recent years, contactless sample manipulation technology in midair has been attracting great attention in the fields of biochemistry and pharmaceutical science. Although one of the promising methods is acoustic levitation, most studies focused on a single sample. Therefore, it is important to elucidate the stability of multiple samples in acoustic levitation. Here, we aim to understand the droplet-droplet interaction in acoustic levitation and improve the levitation stability of droplets. In this paper, the effect of multiple samples levitation in an acoustic field on the stability of levitation is discussed.

The contactless sample manipulation technology is expected to be used in analytical chemistry, biology, physical properties measurement, and materials development for processing any sample (liquid and solid) in midair. The acoustic levitation method [1] is one of the most promising contactless sample manipulation methods because it enables the levitation of a sample based on the use of acoustic radiation pressure without the adsorption, contamination, and heterogeneous nucleation caused by the vessel wall surface. The present study describes the levitation stability of multiple droplets in acoustic levitation. To characterize the droplet dynamics, droplets motion in resonant acoustic fields were visualized and quantified. Based on the experimental data, we modeled the droplet oscillation by spring-mass system [2].

A sample can be levitated near the nodes of the acoustic standing wave. The frequency is 19.3 kHz and the wavelength λ is 18 mm. The width of the horn and reflector is 36 mm (≈ 2λ). The distance between the horn and reflector is 49 mm (≈ 5λ/2). The test droplets were water of approximately 2.0 mm (≈ λ/10) in equivalent diameter. To study the levitation stability, we analyzed the horizontal translational motion of the levitating droplet [4]. The center of gravity of the droplet was quantified by image analysis.

Fig. 1 shows the translational motion in the horizontal direction of a single droplet levitated at the 3rd node. The result indicates the translational motion of droplet with the displacement of ±0.2 mm. Fig. 2 shows the horizontal translational motion of two droplets. The displacement of the droplet at the third node was smaller than that at the 2nd node. This is probably since the droplet at the 2nd node was more affected by the horn than the droplet at the 3rd node. Fig. 3 shows the horizontal translational motion of the three droplets. The droplet at the 3rd node demonstrated a smallest displacement, while the those at the 2nd and 4th node were larger and droplets unsteadily vibrated. These results suggest that the horizontal translational motion of the droplet at the 3rd node was suppressed even when two or three droplets are levitated. We assumed that the horizontal translational motion of droplet presented the droplet-droplet interaction in the resonant acoustic fields.

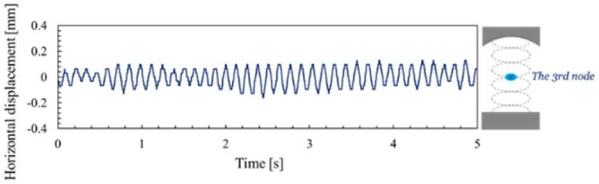

Fig. 1. Horizontal displacement when a single droplet was levitated at the 3rd node.

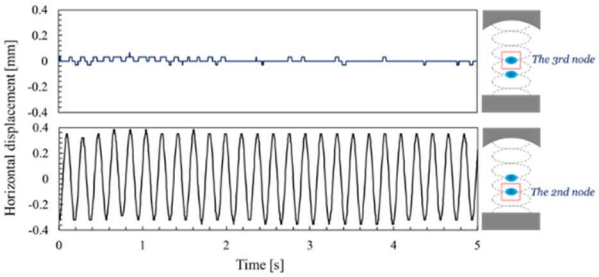

Fig. 2. Horizontal displacement of the droplet when two droplets were levitated at the 2nd node and the 3rd node.

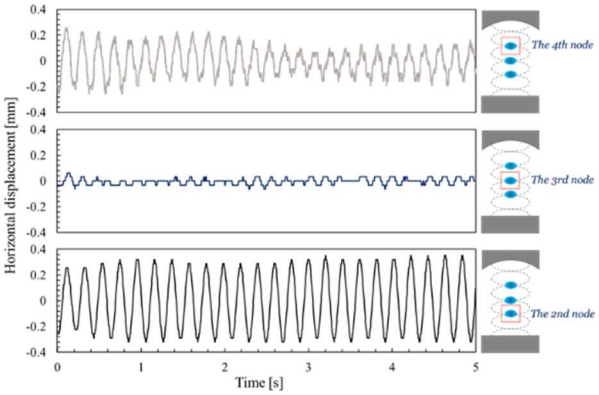

Fig. 3. Horizontal displacement of three droplets were levitated at the 2nd node, the 3rd node, and the 4th node.

References:

[1] D. Foresti, M. Nabavi, M. Klingauf, A. Ferrari and D. Poulikakos, *Proc. Natl. Acad. Sci. USA.*, **110**, 12549-12554, (2013).

[2] K. Hasegawa, K. Kono, *AIP Adv.*, **9**, 5-035313, (2019).

Study on the presentation method of the automated driving experience simulator by wizard of oz prototyping

Kazuki Miyakawa Weerakoon[1.a], Genki Bamba[1.b], Takashi Kato[1.c] and Daigo Misaki[1.d]

[1]Graduate School of Engineering, Kogakuin University, Tokyo, Japan
[a]am21007@ns.kogakuin.ac.jp, [b]am21047@ns.kogakuin.ac.jp, am20020@ns.kogakuin.ac.jp,
[d]misaki@cc.kogakuin.ac.jp,

Abstract

To design safe and convenient autonomous vehicles it is essential to understand the needs and behaviors of users. In this study, we studied how to represent the wizard of OZ prototyping for a realistic autonomous driving experience using the low-cost system.

Autonomous vehicles are spreading rapidly, and it will become popular that Level 3 autonomous vehicles, in which the driver is responsible, will become more popular in the future. As a result, research on autonomous vehicles will become more active. For the subject to experience the state of autonomous driving, it is necessary to reproduce the situation of autonomous driving. However, the system of autonomous driving itself is complex and very difficult to reproduce. Therefore, in this research, we decided to reproduce autonomous driving using Wizard of Oz prototyping.[1] Wizard of Oz prototyping is an experiment in which a human pretends to be a machine. That makes it relatively easy to reproduce autonomous driving.

In recent years, HMD and the triple display with 4K have become inexpensive to build and can be used to reproduce the view in all directions, which gives a more realistic feeling.[2] However, HMD has the disadvantage of not being able to see your own body or the interface, making it difficult to perform complex operations. On the other hand, the triple display does not reproduce the same level of vision as HMD, but it does allow you to see what is at hand, which has the advantage of allowing you to perform complex operations. From this point of view, the triple display is suitable for experiments that require a sense of presence and complex operations by the subject. The features of the three HMD presentation methods are shown in Table 1. Figure1 shows the basic setup of the presentation.

Table 1. specification of display

	Single	Head monted	Triple
Image resolution	3840 × 2160	2160×1200	(3840 × 2160) × 3
Outside visibility	visible	invisible	visible
VR sicness	Not occur	Occur	Not occur
Price	$200	$400	$200 × 3

Fig.1. Three types of presentation methods

We conducted experiments under three conditions: single display, triple display with three screens, and HMD, and compared each of them. Figure 2 shows the system diagram of our experiment. Since we will be using wizard of oz prototyping, one person will control the car on the other display, and the subject will watch the car move on the HMD or triple-display or single display.

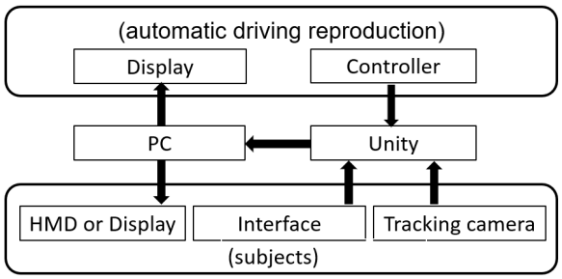

Fig.2. Wizard of OZ Prototype System diagram

In this study, subjects were asked to experience autonomous driving conditions with a single display, HMD, and Triple displays. By using the triple displays, the field of view became wider. This makes it possible to simulate accidents such as pedestrian ejections. The triple-display also allows us to see the outside, so we could experiment with interfaces. Furthermore, since VR sickness does not occur, it is easy to conduct experiments for a long time.

In the future, we will use these experimental devices to conduct interface experiments and explore suitable interfaces for autonomous vehicles.

References:

[1]Brian Mok, David Sirkin, Srinath Sibi, David Miller, Wendy Ju. Understanding Driver-Automated Vehicle Interactions through Wizard of Oz Design Improvisation. Proceedings of Driving Assessment'15 June 22-25, 2015. Salt Lake City, UT. 386-392.

[2]Kato Takashi, Daigo Misaki, Proposal of a system using a driving simulator to demonstrate human–machine interaction during an emergency. Journal of Research and Applications in Mechanical Engineering, 2021, 9.1.

Development of a robot to assist in optimal parts supply at cell production sites

Shutaro Ito[1,a] , Daigo Misaki[1,b]

[1]Graduate School of Engineering, Kogakuin University, Tokyo, Japan
[a]am20010@g.kogakuin.jp, [b]misaki@cc.kogakuin.ac.jp,

Abstract

At cell production sites, automated assembly is not possible due to the high-mix low-volume production, and parts must be supplied. Therefore, in this study, we developed a robot that combines AGV and personal mobility, and verified the optimization of parts supply work at cell production sites.

Introduction

In recent years, the shortage of manpower has become an issue at production sites, and there is a need to improve efficiency through automation. In such a situation, at cell production sites, it is easier to automate the parts k supply process, which is the preparation for assembly, than to automate the assembly process. In this research, we are developing and evaluating a parts supply support robot that can perform the optimal moving method in cell production sites. We will also study the optimization of work-sharing between humans and robots by making the robot have both AGV and personal mobility functions.

Development of parts supply robots

As a result of meeting with people on the production floor and conducting a needs survey, the specifications required to support parts supply operations are as follows.

[1] The ability to move through a complex and narrow factory, such as between shelves, with a route width of less than one person.

[2] Ability to load and transport cargo (machine + man + cargo)

[3] Ability to pass close to a person at a safe speed (below the speed limit for electric wheelchairs).

Figure 1 shows a prototype of the robot I built. Based on the required specifications, this robot has a compact body design and a high-power motor. The features of this robot are that it can move left and right by using 4-wheeled omni-wheels, and that it can make pivot turns. This allows the robot to move efficiently in a narrow work area. Table 1 shows the design specifications of the robot, and the design meets the required specifications.

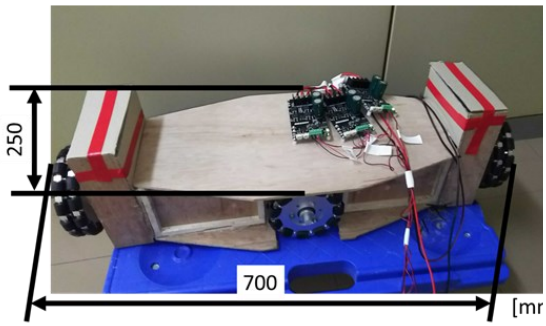

Figure 1. Prototype robot.

Table 1. Design concept of the robot.

	Requirement	Prototype
Weight[kg]	none	20
X,Y,Z[mm]	<750, <300, <750	700, 250, 220
Moving	forward/backward /turn	forward/backward /left-right/turn
Payload[kg]	>100	223
Speed[km/h]	<6.0	4.93

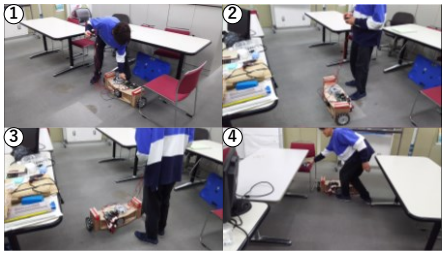

Figure 2. AGV simulation.

Robot operation test and evaluation

The width of the road was set at 1000[mm] for two people, and a load of 4[kg] was loaded as an experiment to carry light parts to the destination. Figure 2 shows the experiment in the order of images 1 to 4. The robot was able to carry the load and repeat straight and turning movements to reach the destination. However, the left and right movements were moving at a speed higher than the required specifications. In addition, when carrying heavy loads, the load on the shaft of the gearbox became too great and it could not operate properly. Thus, among the required specifications, the size, speed, and moving capacity met the requirements, but the left-right movement and loading capacity could not be realized. This was due to the emphasis on compact body design. As a result, a gearbox for left-right movement could not be installed, and the gearbox that was installed had a weak structure. In order to improve this situation, we decided that it was necessary to use a dolly to tow heavy objects and that the body design needed to be reviewed.

References:

[1] SHEN, Yu, et al. Omni-directional AGV motion trajectory planning under the polar coordinate system. In: 2016 IEEE International Conference on Consumer Electronics-China (ICCE-China). IEEE, 2016. p. 1-5.

[2] THEUNISSEN, Jacobus, et al. Smart AGV System for Manufacturing Shopfloor in the Context of Industry 4.0. In: 2018 25th International onference on Mechatronics and Machine Vision in Practice (M2VIP). IEEE, 2018. p. 1-6.

Development of Self-Lubricating Slide Bearings with Sintered Porous Metals

T. Itoi*, S. Kawajiri, Y. Sasaki, E. Takami, Y. Fujita and M. Shiomi

Department of Mechanical Science and Engineering, School of Advanced Engineering, Kogakuin University, Tokyo, Japan
E-mail: s518009@ns.kogakuin.ac.jp

Abstract

Miniature maintenance-free bearings are required as small-sized motors are widely used. Slide or plain bearings are reasonable for downsizing of bearings because the size of rolling-element bearings is limited due to the size of rolling-element. Since a bush or a sleeve with openings of the slide bearing is drawback in downsizing, porous metals are examined for application of miniature maintenance-free slide bearings in the paper.

Sintered porous metals are fabricated by space holder technique[1]. The base material was stainless steel powder (SUS316L from Toko Tshusho Corp.) and NaCl power (size: 150–600μm) was used as a space holder. The mixture of stainless steel and NaCl powders was compacted with dies and sintered in a vacuum furnace. In sintering process, NaCl powder heated at around 800°C was melted and vaporized, then disappeared from the powder compact. The stainless-steel compact with small space made from NaCl powder was sintered at 1350°C, and finally the sintered porous metal was made.

Fig. 1 shows the cross section of the sintered porous metal. The pore shapes are similar to the shape of NaCl powder. The areas of the pores are measured and the equivalent circular diameters of pores are calculated, in which the area of the pore is considered to be that of circle.

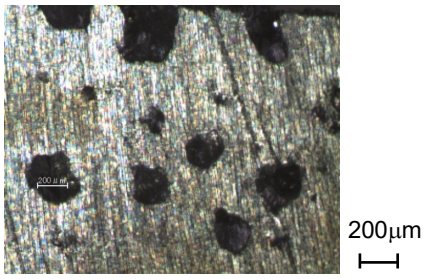

Fig. 1. Cross section of sintered porous metal.

Fig. 2 shows the distribution of the pore size in the sintered porous metal. The pores sized in the range of 0.1–0.15mm are dominant, and the average of the pore size is 0.181mm.

To examine the sintered porous metals as self-lubricating bearings, lubricant oil is infiltrated into the pores and friction test is conducted. The lubricant oil used in the experiment is ISO VG42, the viscosity of which is 0.04 Pa·s.

Fig. 3 shows the relationship between the weight of infiltrated oil and porosity of the sintered porous metal. Simple immersion and vacuum infiltration are carried out. It is clear that vacuum infiltration makes lubricant oil infiltrate into the sintered porous metal.

Friction coefficient of the sintered porous metal is measured by drawing from flat tools under a load. It is confirmed that the friction coefficient of the sintered porous metal decreases with infiltration of lubricant oil into the pores and lubrication between the sintered porous metal and tool is improved.

This study is supported by Toko Tsusho Corporation.

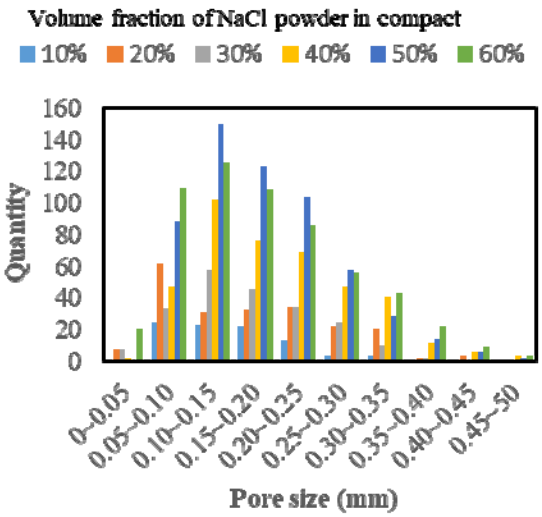

Fig. 2. Distribution of pore size in sintered porous metal.

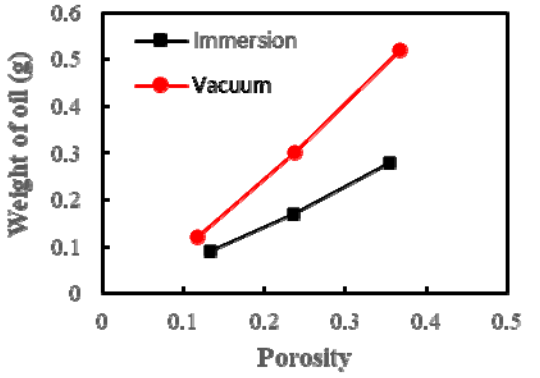

Fig. 3. Relationship between weight of infiltrated oil and porosity of sintered porous metal.

References

[1] Y.Y. Zhao, D.X. Sun, *Scr. Mater.*, **44**, 105–110 (2001).

Lightning Talk Session

Architectural and Civil Engineering

November 23rd

Presentation No.	Title	Author	
ACEL1.	Evaluation of Plaster Layer of Wood lath and Plaster Ceiling in Non-Destructive Testing	Sakura Yoshida, Kentaro Oka, Masaki Tamura	314
ACEL2.	Quantitative evaluation of the deterioration state of the modified wood shingle exposed outdoors and construction of an index to judge the deterioration	Hideto Takeuchi, Masaki Tamura	316
ACEL3.	Examination of resin repair method for wood damaged by termites	Yusuke Harada, Masaki Tamura	318
ACEL4.	Study on transportation power in DHC area for the AEM	Ryuhei Tanaka, Yusuke Nakajima	322
ACEL5.	History and development of wood lath and plaster techniques in Japan	Kentaro Oka, Masaki Tamura	326
ACEL6.	GIS-Based Assessment of Emergency Referral Systems and Ideal Locations for Ambulance Stations in the Province of Cavite, Philippines	Kathleen Ann E. Villapol, Jedidiah Joel C. Aguirre, Judie Ann A. Ramos, and Harvey S. Maunahan	329

The 20th International Symposium on Advanced Technology (ISAT-20)

Evaluation of Plaster Layer of Wood lath and Plaster Ceiling in Non-Destructive Testing

Sakura Yoshida[1,a*] Kentaro Oka[2] Masaki Tamura[3]

[1] Department of Architecture, School of Architecture, Kogakuin University, undergraduate, Tokyo, Japan
[2] Department of Architecture, Senior researcher, Kogakuin University, Tokyo, Japan, M. Eng.
[3] Department of Architecture, Kogakuin University, Tokyo, Japan, Dr. Eng
[a*] db18335@ns.kogakuin.ac.jp

Abstract

In this study, we describe methods of "health check" of historical buildings, which is nondestructive testing. The subject of this study is a wood lath and plaster ceiling. we were able to investigate the hardness and deterioration of the plaster on the wood lath and plaster ceiling. We were also able to confirm the change in values with the number of tests.

1. Introduction

In Japan, there are many disasters such as earthquakes. As a result, concerns about the preservation of historical buildings have been increasing. The safety of buildings may be decided not only by its structure but also by its surface finish. It is desirable that historical buildings have been properly repaired and used for a long time. On the other hand, it is necessary to investigate the condition of materials in advance for building repair.

In this study, we describe methods of "health check" of historical buildings, which is nondestructive testing. The subject of this study is a wood lath and plaster ceiling.in advance for building repairment. [1,2]

2. About Wood-Plastered Plaster for Ceiling

In Japan, European building techniques became widespread around the 19th century, and the wood lath and plaster technique was introduced along with them. Plastering techniques have existed in Japan since ancient times. On the other hand, there was not much experience in the construction of walls and ceilings adopted wood lath and plaster.

Plasters are applied into slits in the wood laths. Photo 1 shows examples of a wood lath and plaster ceiling. Figure 1 shows a conceptual diagram of wood lath and plaster. However, there is a possibility that the plaster may fall off due to long-term use or external forces such as earthquakes.

Photo 1: An example of a wood lath and plaster ceiling

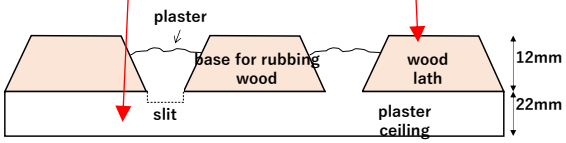

Fig 1: Conceptual diagram of wood plastering

Table 1: Equotip hardness nondestructive tester for plaster board

Hardness	— v：Impactor repulsion velocity(m/s) v_0：Impactor blow speed (m/s) ex) Hard solid building material (stone, concrete)(800~1000) Medium solid building material (500~800) Soft solid building material (~500)
Testing	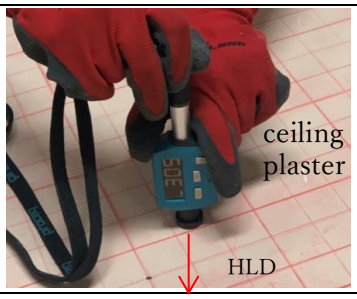

3. Evaluation of the plaster layer in a non-destructive test

In this test, the hardness of the plaster was quantified by the non-destructive test. The condition of the plaster is assessed by non-destructive test measurements. We used an equotip hardness tester for the non-destructive test. This is because plaster is brittle and needs to be tested with weak force. Therefore, the equotip hardness tester, which can quantify the hardness with weak force, was used to test the plaster. Table 1 shows the equotip hardness tester. Test specimens 1 and 2 were tested once each. Another test specimen was tested 15 times in succession against the same surface. Table 2 shows the information of the test specimens. Figures 2 and 3 show the test results.

In one test, it was possible to check the hardness and deterioration of the plaster close to the surface. In this test, we were able to see individual differences in the plaster surface. From Figure 2, it can be seen that when the same surface is struck repeatedly, the value gradually increases. This may reflect the internal condition of the plaster as the surface is compressed. In addition, in this test, we found that the values varied depending on the deterioration of the plaster and the thickness of the plaster layer.

4. Conclusion

Through this non-destructive test, we were able to investigate the hardness and deterioration of the plaster on the wood lath and plaster ceiling. We were also able to confirm the change in values with the number of tests.

Table 2 Information on the test specimen

	Test specimen 1	Test specimen 2	Test specimen 3
Thickness of plaster layer (mm)	10～12	18～22	21.9
Number of tests (times)	1	1	15
Results of HLD value	Average 220	Average 261	Start 344 Last 588 Average 511

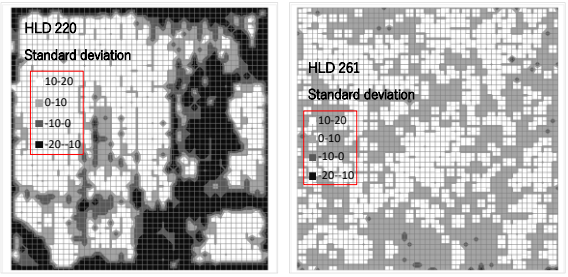

a) specimen 1 b) specimen 2

Fig 2: Example of nondestructive testing results for plaster ceiling (1m × 1m)

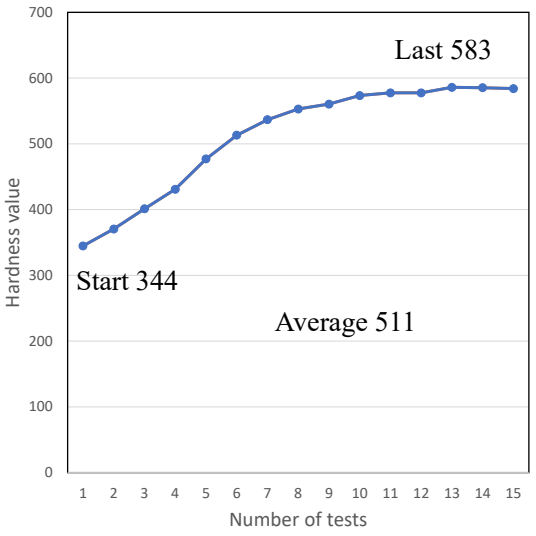

Figure 3: Tendency of hardness value property in case of strucking several times for plaster ceiling (1~15 times)

References

[1] Kentaro Oka, M. Tamura, Osamu Gotot, Hiroaki Maruyama and Junichi Yokoshima, Experimental Study on Conservation and Preservation for historical Architecture using Plaster Finishing Material,SCMT4The Fourth International Conference on Sustainable Construction Materials and Technologies ,Las Vegas, USA,2016

[2] Misako Hanza, M.Tamura, Kentaro Oka, and Osamu Goto,Deterioration Evaluation of the StuccoLath Ceilings in the Historic Building in Japan, 17th International Symposium on Advanced Technology(ISAT-17) Engineering Innovation for Sustainable Future November 13 – 15, 2018Danang, Vietnam

2022 International Symposium on Advanced Technology (ISAT-20)
Extended Abstract

Quantitative evaluation of the deterioration state of the modified wood shingle exposed outdoors and construction of an index to judge the deterioration

Hideto Takeuchi [1, a *] Masaki Tamura [2]

[1] Bachelor Course student, Dept.of Arch.,Graduate School of Engineering,Kogakuin Univ.,Tokyo,Japan

[2] Kogakuin University, Dr.Eng, School of Architecture Department of Architecture,Tokyo, Japan

[a *] db18183@g.kogakuin. jp

ABSTRACT

The service life of wood shingle roof is about 25 to 30 years, and there are problems such as repair costs and a decrease in craftsmen. In order to preserve tradition, it is necessary to improve the durability of the shingle roof and reduce costs. This study has two objectives. The first is to investigate each item of test specimens that have been exposed to the outdoors for a long period of time, with the aim of prolonging the length of the wood shingle roof. Then, I will clarify what kind of wood and what kind of reforming treatment is effective. The second is to create an index that quantitatively evaluates the deterioration of wood based on the measured data. As a result of the research, it was clarified that the surface treatment was almost peeled off, but the deterioration was relatively suppressed in the place where the white paint was applied. It was also found that long-aged wood has high durability.

1. Introduction

In recent years, while environmental problems such as global warming have been attracting attention, the realization of a low-carbon society has been advocated. Wood has the effect of storing carbon and reducing carbon dioxide emissions, and contributes to low carbonization. Therefore, the utilization of wood is expected more and more. The wood shingle roofing is used in traditional wooden construction and is a type of roofing method. It is also used for traditional architecture such as ”Kaenji Shariden” and “Jishoji Kannonden”, which are made by stacking thin and short boards. However, the service life of wood shingle roof is about 25 to 30 years, and there are problems in terms of the decrease in the number of craftsmen with traditional techniques and the cost. Therefore, I will investigate the deterioration status of the modified wood roofing, verify the difference in the deterioration status for each reforming process, and aim for a longer period of re-roofing. The test piece uses the material shown in Table1. This table shows the classification of the materials used by kinds of trees, habitats, age, etc. Table2 shows the reforming treatment applied to each wood. The photograph and model of the specimen are shown in Fig.1.

Table1.Type of wood and symbol number

Symbol number	Wood type
Aas45	Akita cedar planted 46 years old
Aas90	Akita cedar planted 88 years old
Ans170	Akita cedar natural 170 years old
Ank50	Akita chestnut tree natural 50 years
Mas35	Miyazaki cedar planted 35 years old
Mas80	Miyazaki cedar planted 80 years
Sa	Chichibu Spanish mackerel tree

Table2.Types of reforming treatment and Color

No.	Types of reforming treatment	Color
①	Highly durable silicone paint	Clear
②	Highly durable acrylic silicone paint	White
③	Stain paint	Black
④	Stain paint	White
⑤	Persimmon astringent liquid	Brown
⑥	Pyroligneous acid	Brown
⑦	None (Draining copper plate)	—
⑧	None	—

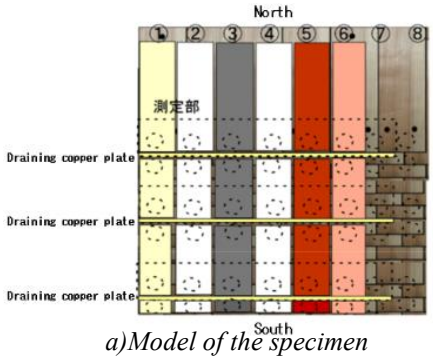

a)Model of the specimen

b)Photograph of the specimen

Fig1.Photograph and model of the specimen

2. Fading of the surface of the wood shingle, judged by the L*a*b* value

Based on the data measured continuously from 2009, it was evaluated using the L * a * b * color system of JIS Z 8721. The results are shown in Fig.2. Paints other than the highly durable acrylic silicone paint, which is numbered 2, have peeled off, and L * a * b * is approaching the same value. Looking at the variation between the time of construction and the latest data for each reforming process, the L * value decreased from 14.9 to 4.1, the a * value decreased from 5.0 to 0.4, and the b * value decreased from 9.2 to 2.7.

3. Measurement of elution / defect of wood shingle deteriorated by ultraviolet rays

As the deterioration of wood progresses, the components of wood elute after the surface fading. This summary describes the measurement results of the eluted region for the seven specimens undergoing exposure testing. Of the areas surrounded by yellow line shown in Fig.3, the parts that are missing (gray) and the parts that are not in the missing state (red) are determined by image analysis by the ratio of the number of pixels. In this experiment, the gray area is the “Defective part” and the red area is the “Healthy part”. Fig.4 (a) is the average value of the measurement results for each modified treatment, and Fig.4(b) is the average value of the measurement results for each wood used. It was found that the defective area was relatively small in the part coated with the white paint, and the defective area was smaller in the test piece using the older wood.

4. Conclusion

This study found a correlation between wood age and durability. In addition, although the paint used for the reforming treatment was peeled off as a whole, it was confirmed that the deterioration was relatively suppressed where the white paint was applied. In order to quantitatively evaluate the function of the wood shingle as a building material, I will study the measurement of moisture content and fire resistance in the future.

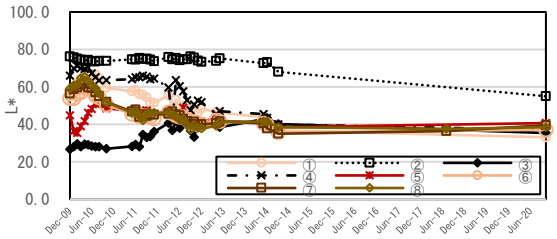

*a) L * value of Aas45*

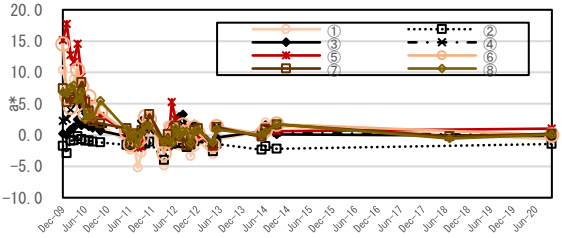

*b) a * value of Aas45*

Fig2 Aging of color values(Aas45)

Fig3 Aging of color values(Aas45)

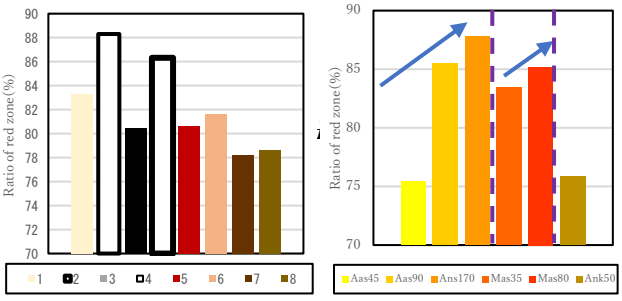

a) By modified treatment *b) By type of tree*

Examination of resin repair method for wood damaged by termites

A)Yusuke Harada *, B)Masaki Tamura
A) Master Course student, Dept.of Arch.,Graduate School of Engineering,Kogakuin Univ.,Tokyo,Japan
B) Kogakuin University, Dr.Eng, School of Architecture Department of Architecture,Tokyo, Japan
A)* dm20044@ns.kogakuin.ac.jp

Abstract

Many of Japan's important cultural architectures are made of wood materials, and in order to extend the life of the building, it is necessary to repair the damage caused by termites. The purpose of this study is to investigate the passage and progress rate of the resin when injecting the repair agent in order to investigate the efficient injection method of the repair agent. As a result of the research, it was found that the increased viscosity and hole angle of the simulated repair agent increase the amount required for the simulated repair agent to reach the lower part.

1. Introduction

Wooden materials have been used in buildings for a long time in Japan, and many wooden buildings have been achieved historical values. In recent years, there has been a movement to evaluate the traditional technologies and techniques, and in 2020, "Traditional technique for inheriting traditional architectural craftsmanship and wooden structures" was registered as an intangible cultural heritage by UNESCO. However, the number of skilled craftsmen have continued to decline, and it is difficult for craftsmen alone to repair and maintain the buildings and the historical values. In particular, eating damages by termites reduces the strength of wooden buildings, so it is important to take measures to extend the life of the building. The purpose of this study is to investigate the passage and progress rate of the resin when injecting the repair agent in order to investigate the efficient injection method of the repair agent. The surface of the wood is shaved into a semicircle to create a specimen that can visualize the inside. After that, a simulated repair agent is injected into the specimen, and the amount required for the simulated repair agent to reach the lower part is examined.

2. Research outline

Table 1 shows the contents of the experiment, Table 2 shows the materials used, and Table 3 shows the experimental factors and levels. This time, we used Cedar, which is generally used, as a specimen and prepared two types, type1 that is long in the direction of the flat grain of the wood and type2 that is long in the direction of the butt end. Then, holes with diameters of 4 mm and 8 mm were made on four surfaces other than the edge surface of the specimen, and a simulated repair agent was injected. We prepared two types of simulated repair agents, water and 1% methylcellulose, and set the hole angles to four types: 30 °, 45 °, 60 °, and 90 °, considering the complexity of termite damage.

Table1 materials used

Tree species	type	feature	Injection surface
Cedar	Type1 (Beam vertical timber Pillar horizontal timber) (54mm×54mm×100mm)	long in the flat grain	butt end surface/ straight surface
	Type2 (Beam horizontal timber Pillar vertical timber) (54mm×54mm×100mm)	long in the butt end	flat grain surface/ straight surface

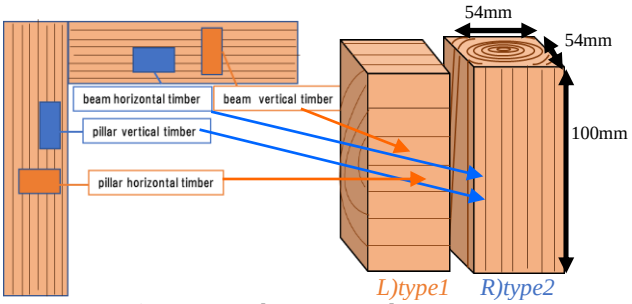

a) How to take type1 and type2

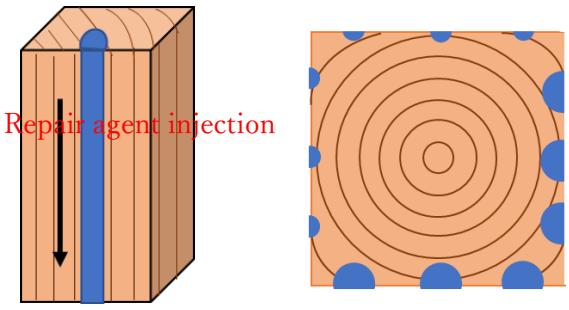

L) side *R) Top*

c) Image of specimen
Fig. 1 Specimen

3. How to repair termite damage

Regarding the repair agent injection method assumed in Fig. 2, Photo 1 shows the building damaged by termites. In this study, we are studying on-site repair methods by separating horizontal members such as beams and vertical members such as pillars. It is difficult to utilize the own weight of the repair agent for injecting the repair agent in the longitudinal direction of the horizontal members. Therefore, prepare a plurality of injection ports so that the flow flows from a high place to a low place. The vertical member can be injected to the lower part by using the weight of the repair agent. However, since it is difficult to completely inject in the L direction, it is assumed that the injection port must be slanted and its own weight must be used. In this experiment, in order to confirm whether the repair agent flows by its own weight, it was injected drop by drop, and the injection amount required to reach the lower part was measured.

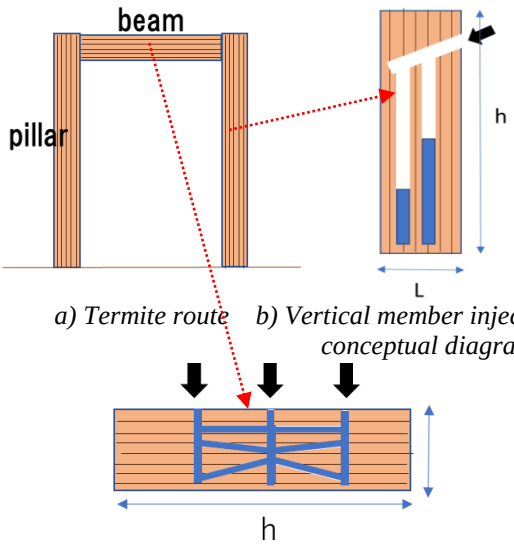

a) Termite route *b) Vertical member injection conceptual diagram*

c) Horizontal member injection conceptual diagram

Fig. 2 Repair agent injection method

4. Injection of simulated repair agent

4.1 Comparison of the injection amount required for the repair agent to reach the lower part due to the difference in the injection surface

4.1.1 Overview

Photo 2 shows specimen photograph, and Photo 3 shows the test photograph. The purpose of this experiment is to investigate how the injection amount until the repair agent reaches the lower part changes depending on the surface on which the repair agent is injected. For type1, holes with diameters of 4 mm and 8 mm were drilled on the butt end surface and straight surface, and for type2, holes with diameters of 4 mm and 8 mm were drilled on the flat grain surface and straight surface. After that, a simulated repair agent was injected, and the injection amount until reaching the bottom was measured. At that time, the simulated repair agent was injected drop by drop without applying pressure because the simulated repair agent proceeded by its own weight. In addition, since the holes made by termites are expected to have various angles, injection was performed at four angles of 30 °, 45 °, 60 °, and 90 °.

4.1.2 Exam results

Figure 3 shows a comparison of the amount of simulated repair agent required to reach the bottom on the butt end surface and the straight surface. Figure 4 shows a comparison of the amount of simulated repair agent required to reach the bottom on the flat grain surface and the straight surface. Comparing the butt end surface and the straight surface in Fig. 3, there was a large difference in the required injection amount to reach the lower part. In particular, the largest difference was seen at 30 °, and the difference between the two surfaces tended to decrease as it approached 90 °.–In the comparison between the flat grain surface and the straight surface in Fig. 4, there was almost no difference in the required injection amount to reach the lower part, and

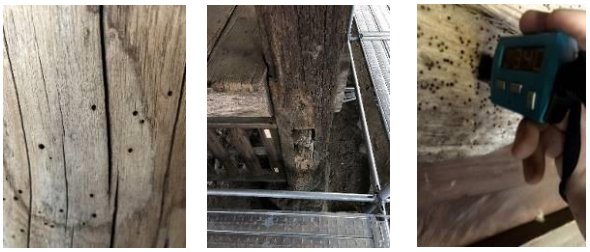

Photo1 Damage to termites on wooden cultural properties

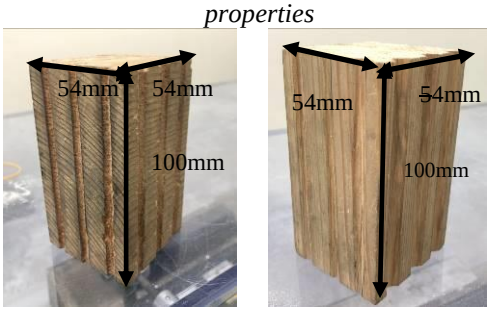

a)type1 b)type2

Photo2 specimen

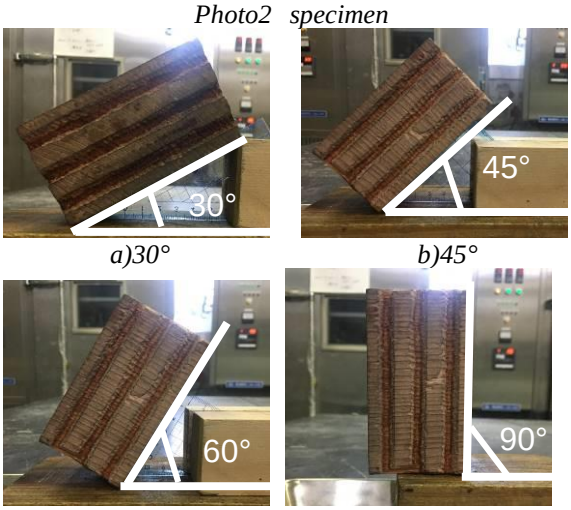

a)30° *b)45°*

c)60° *d)90°*

Photo3 Injection angle

the required injection amount to reach the lower part tended to decrease as the angle increased. Comparing the results of Fig. 3 and Fig. 4, the butt end surface was the largest at any diameter and at any angle. From this, it is considered that it is more difficult to pour the repair agent into the butt end surface than the other surfaces.

4.2 Comparison of injection volume required for the repair agent to reach the bottom according to the size of the hole

4.2.1 Overview

The purpose of this experiment is to investigate the difference in the injection amount until the repair agent reaches the lower part depending on the diameter of the hole when injecting the repair agent. This time, the results of 4.1 were compared on the same surface and with different hole diameters, and each was considered.

4.2.2 Exam results

Figures 5 and 6 show a comparison of the amount of simulated restoration required to reach by the size of the hole diameter. There was a difference in the amount of simulated restorative required to reach the bottom at 30 ° for both the 4 mm and 8 mm diameter holes on the butt end surface and the straight surface of Figure 5.―However, as the injection angle approached 90 °, the difference became smaller, and there was no difference between the 4 mm and 8 mm diameter holes between 60 ° and 90 °.-There was no significant difference between the diameters of 4 mm and 8 mm between the flat grain surface and the straight surface in Fig. 6, and they tended to decrease as the angle approached 90 °.

4.3 Comparison of injection volume required to reach the bottom due to the viscosity of the repair agent

4.3.1 Overview

The purpose of this experiment is to investigate the difference in the injection amount until the repair agent reaches the lower part depending on the viscosity of the repair agent to be injected. In the data of 4.1 and 4.2, water (0.001 Pa · s) was used as a simulated repair agent, but this time, a 1% aqueous solution of methyl cellulose (0.25 Pa · s) was used, and the effect of viscosity was investigated.

4.3.2 Exam results

Figure 7 shows a comparison of the amount of simulated restorative required to reach the bottom of the butt end surface and the straight surface. Figure 8 shows a comparison of the amount of simulated repair agent required to reach the bottom on the flat grain surface and the straight surface. Figures 9 and 10 show a comparison of the amount of simulated restoration required to reach by the size of the hole diameter. Figures 9 and 10 show a comparison of the viscosity of the simulated repair agent and the amount required to reach the bottom.-Basically, even with a viscosity of 0.25 Pa · s, a decreasing tendency

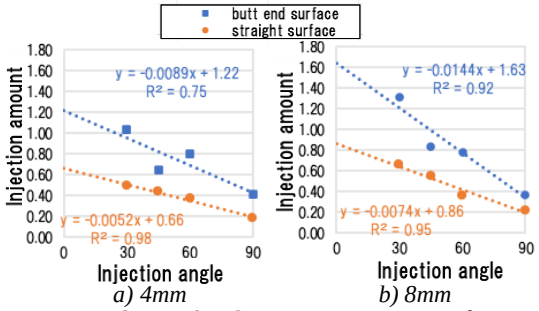

a) 4mm *b) 8mm*

Fig.3 Relationship between injection surface and injection angle (0.001Pa・s)(type1)

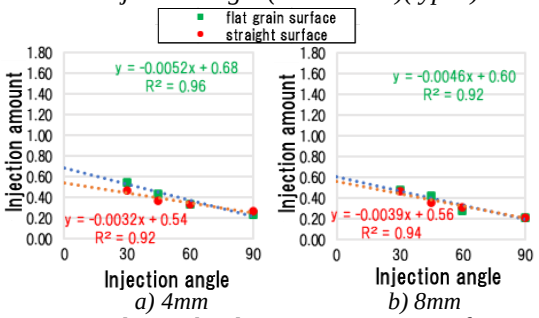

a) 4mm *b) 8mm*

Fig.4 Relationship between injection surface and injection angle (0.001Pa・s) (type2)

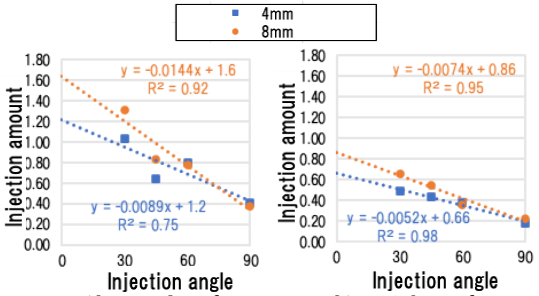

a)butt end surface *b)straight surface*

Fig.5 Relationship between hole diameter and injection angle(0.001Pa・s) (type1)

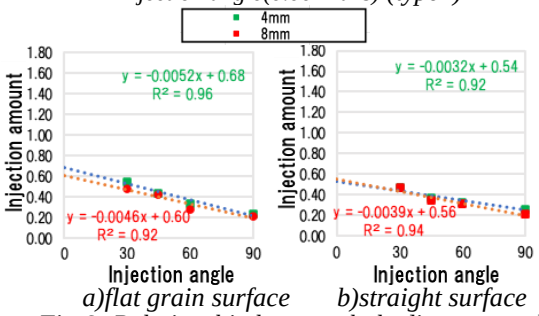

a)flat grain surface *b)straight surface*

Fig.6 Relationship between hole diameter and injection angle(0.001Pa・s) (type2)

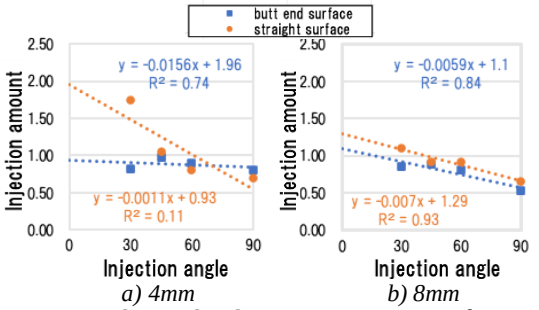

a) 4mm *b) 8mm*

Fig.7 Relationship between injection surface and injection angle (0.25Pa・s) (type1)

similar to that with a viscosity of 0.001 Pa · s was shown. However, looking at the figure11 and 12, there was a large difference between the viscosity of 0.001 pa · s and the viscosity of 0.25 Pa · s.-From this, it is considered that it is difficult to fill as deeply as the repair agent has a viscosity.

5. Conclusion

1) When injecting the repair agent, it is considered that the butt end surface is more difficult to inject than the other surfaces. The reason may be that the annual rings, which are the hard parts of the wood, are causing friction. Therefore, it can be inferred that the denser the annual rings of wood, the more difficult it is to inject the repair agent.
2) The closer the injection angle is to 90 °, the easier it is to inject the repair agent.
3) Basically, the higher the viscosity of the repair agent, the more difficult it is to inject it deep into the hole.

REFERENCES

[1] Kazuo Sumiya ,1965, Relations between defects in wood and velocity of ultrasonic wave, Wood Research: Report of Wood Research Institute, Kyoto University, 34: 22-36
[2] Cultural Property Building Preservation Technology Association, 1979, Hakogi House (thousand years the house) Preservation and Repair Work Report, Important Cultural Property Hakogi House Repair Committee

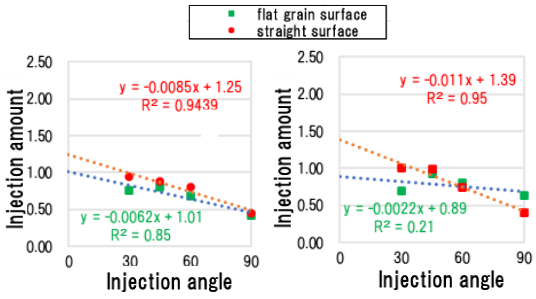

a) 4mm *b) 8mm*

Fig.8 Relationship between injection surface and injection angle (0.25Pa･s)(type2)

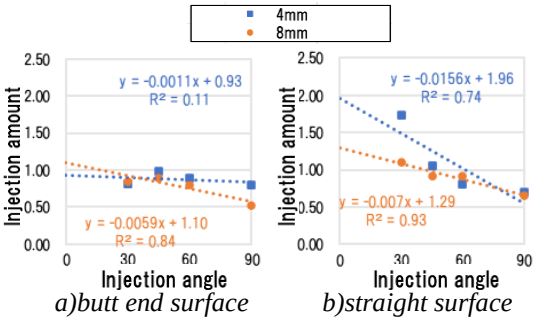

a)butt end surface *b)straight surface*

Fig.9 Relationship between hole diameter and injection angle(0.25Pa･s)(type1)

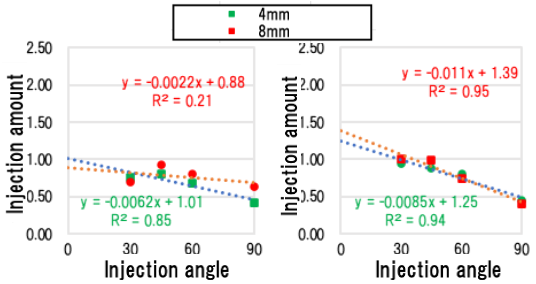

a)flat grain surface *b)straight surface*

Fig.10 Relationship between hole diameter and injection angle(0.25Pa･s) (type2)

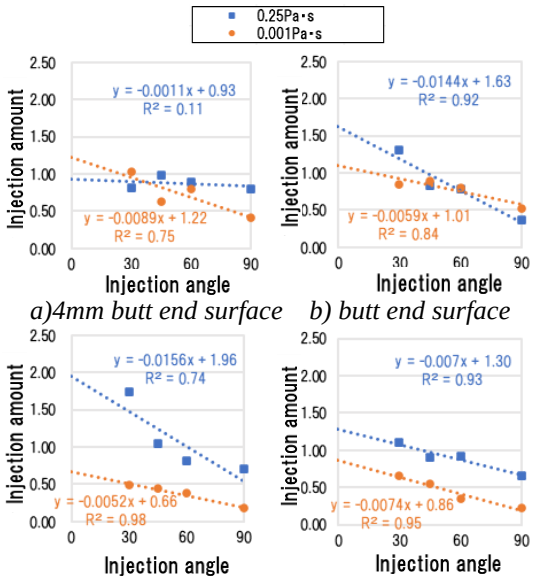

a)4mm butt end surface *b) butt end surface*

c) 4mm straight surface *d) 8mm straight surface*

Fig11 Relationship between viscosity and injection angle(type1)

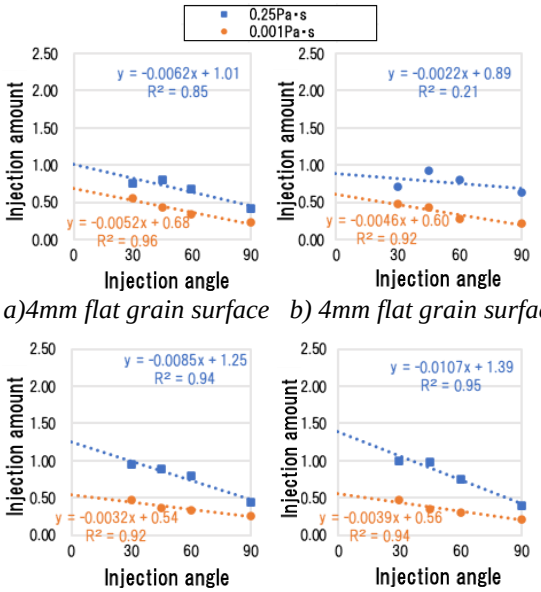

a)4mm flat grain surface *b) 4mm flat grain surface*

c)4mm straight surface *d) 8mm straight surface*

Fig11 Relationship between viscosity and injection angle(type2)

Study on transportation power in DHC area for the AEM

Ryuhei Tanaka*1, Yusuke Nakajima*2

Graduate student, Kogakuin Univ.*1 Prof., School of Architecture, Kogakuin Univ., Dr. Eng.*2
da21041@ns.kogakuin.ac.jp*1 yusuke@cc.kogakuin.ac.jp*2

Abstract

In these years, Information Technology is surprisingly developing and it is not exception in buildings. Tamachi DHC is one of advanced DHC areas. In this area, the plant analyzes BEMS and changes energy supply method. However, these systems are expensive and difficult to build on existing DHC. The purpose of this study is to clarify the factors of increase of transportation power on DHC and difference of transportation power on buildings by receiving system. In addition, analyzing BEMS which buildings on the area have, we will suggest the way of AEM which plant and buildings work together for energy conservation on whole the area. As a result, transportation power of chilled water on DHC is influenced by return temperature in summer and supply pressure in winter. Direct receiving system is more difficult to get temperature gap on low cold heat demand in winter and midnight in summer than indirect receiving system (heat exchanger system). In addition, direct receiving system needs more transportation power to carry chilled water. In conclusion, receiving equipment is influenced to transportation power in DHC and its buildings.

1. Preparation Procedures

1. In the beginning

District Heating and Cooling (DHC) is the system which create heat and chilled water on plant and supply some buildings. It is the efficient way to supply cold and hot heat source and electric power on high energy demand area. However, it has unique transportation power and it has some problems, for example, energy loss from chilled water pump and difficulty with getting temperature gap on low cold heat demand and increasing transportation power per cold heat demand. It is important to improve transportation power. In addition, there are some type of receive equipment, for example, direct supply system and heat exchanger system. There are few studies about difference of these systems and effect to plant.

The purpose of this study is to clarify the factors of increase of transportation power on DHC and difference of transportation power on buildings by receiving system. In addition, analyzing BEMS which buildings on the area have, we will suggest the way of AEM which plant and buildings work together for energy conservation on whole the area.

2. Analyzing of transportation pawer on DHC

2.1. Overview of target area

We get day report from 12 plants and we can figure out transportation power from 10 plants. We select these 10 plants to target area.

On plants which not measure power consumption per pump, we make approximation among flow of chilled water and power consumption from patrol day report which administrator fills in to inspect plant equipment.

We show overview of target area on table.1 and 2. Only area-G changes past pressure in accordance with terminal bypass pressure.

Table.1. Overview of target area

Area	Refrigeration capacity	Terminal building distance	Heat exchanger system
	(RT)	(m)	(%)
A	6320	239	12
B	3450	59	10
C	3800	158	95
D	15390	1457	78
E-1	6600	311	2
E-2	4600	31	0
F	61000	1260	18
G	11000	367	100
H	3600	82	3
I	4100	300	49

Table.2. Overview of target area

Area	Past pressure	Return pressure	Past temp.	Return temp.
	(MPa)	(MPa)	(℃)	(℃)
A	0.69	0.41	7.0	13.0
B	0.77	0.55	6.5	13.5
C	0.77	0.48	7.0	13.0
D	0.76	0.45	7.0	15.0
E-1	0.88	0.62	7.0	14.0
E-2	0.99	0.65	6.5	13.5
F	1.29	0.89	4.0	12.0
G	0.79/0.59	0.55	7.0	14.0
H	1.28	1.03	7.0	13.0
I	0.90	0.56	7.0	13.0

2.2. Analyzing by Multiple regression analysis

We use Multiple regression analysis to analyze the factors of increasing on transportation power. We show parameters on Table.3. We establish summer (Jun. ~ Sept.), intermedial stage (Apr., May, Oct., Nov.), winter (Dec. ~ Mar.).

Table.3. Parameter

Parameter	Unit	Explanation
Transportation power	kWh/GJ	Power consumption of pump
Pressure	MPa	"Past pressure" – "Return pressure"
Flow	m^3/GJ	Flow of chilled water per heat demand
Heat loss	GJ	"Created energy" – "Sold energy"
Temperature gap	℃	"Return temp." – "Past temp."
Distance	m	Distance for the terminal building
Equipment	%	Percentage of total floor area on heat exchanger building

(a) Year-round analysis

At first, we analyze the factor of increasing on transportation power per heat demand. We show the result that transportation power is defined as response variable on Table.4. Transportation power is increased by flow of chilled water per heat demand and pressure.

Second, we analyze the factor of increasing on flow of chilled water per heat demand and pressure. Flow is increased by temperature gap. Pressure is increased by past pressure.

Table.4. Analysis on transportation power (year-round)

Variable	Unit	Standard partial regression coefficient
Pressure	MPa	0.7890
Temperature gap	℃	-0.5127
Heat loss	GJ	0.0179
Flow	m^3/GJ	0.4517
Distance	m	-0.0303
Equipment	%	-0.0389

(b) Seasonal analysis

According to the year-round analysis, transportation power is increased by flow of chilled water per heat demand and past pressure. Then, we analyze difference of impact duo to season.

We show the result that transportation power is defined as response variable in summer on Table.5. Transportation power is increased by flow of chilled water per heat demand rather than pressure in summer.

We show the result that transportation power is defined as response variable in winter on Table.6. Transportation power depends on pressure. Flow of chilled water per heat demand has a little effect in winter.

Table.5. Analysis on transportation power (summer)

Variable	Unit	Standard partial regression coefficient
Pressure	MPa	0.4811
Temperature gap	℃	-0.1588
Heat loss	GJ	0.0220
Flow	m^3/GJ	0.6255
Distance	m	-0.1213
Equipment	%	-0.1450

Table.6. Analysis on transportation power (winter)

Variable	Unit	Standard partial regression coefficient
Pressure	MPa	0.9735
Temperature gap	℃	-0.6429
Heat loss	GJ	-0.0401
Flow	m^3/GJ	0.3393
Distance	m	0.0281
Equipment	%	0.0391

2.3. Feature of efficient way of operation on transportation power on DHC

Transportation power is influenced by temperature gap in summer and pressure in winter. We show transportation power and value of other factors on Fig.1. Area-G changes pressure and is controled staying low pressure in winter. It is the reason of low transportation power. In area-F, it can get high temperature gap but pressure is also high. It is the reason of inefficiency in area-F.

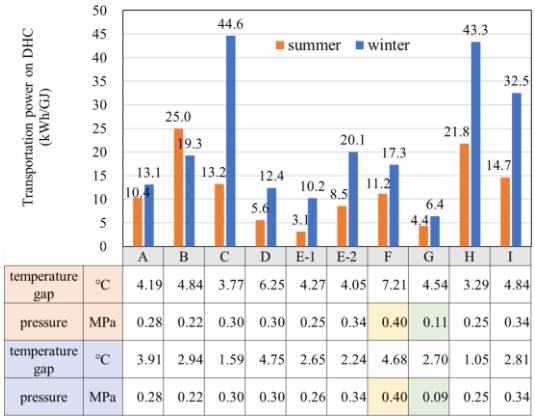

		A	B	C	D	E-1	E-2	F	G	H	I
temperature gap	℃	4.19	4.84	3.77	6.25	4.27	4.05	7.21	4.54	3.29	4.84
pressure	MPa	0.28	0.22	0.30	0.30	0.25	0.34	0.40	0.11	0.25	0.34
temperature gap	℃	3.91	2.94	1.59	4.75	2.65	2.24	4.68	2.70	1.05	2.81
pressure	MPa	0.28	0.22	0.30	0.30	0.26	0.34	0.40	0.09	0.25	0.34

Fig.1. Transportation power and value of other factors

3. Analyzing of transportation pawer on buildings

3.1. Overview of target building

We analyze BEMS on two buildings to clarify the difference of transportation power on buildings due to the difference of receiving system. These buildings are on same DHC area and controlled by same administer. Both building have two routes of piping. One of it circulates lower floor and the other circulates upper floor. We analyze date measured in 2010, because building-B's flowmeter had been broken since 2013 until 2020 and we consider the influence in 2011and 2012 due to the Great East Japan earthquake. We show overview of target building on table.7.

Table.7. Overview of target building

Name	Building-A	Building-B
Total floor area (m^2)	51,319	37,677
Building use	Shop・Office	University
Receive equipment	Heat exchanger system	Direct supply system
Floors	28	28

3.2. Analyzing on temperature gap

We show temperature gap in summer and winter on Fig.2 and 3. Direct supply system can high temperature gap on the daytime in summer. However, it couldn't get temperature gap in winter and night in summer. It is the reason that much chilled water flow to bypass in low heat demand.

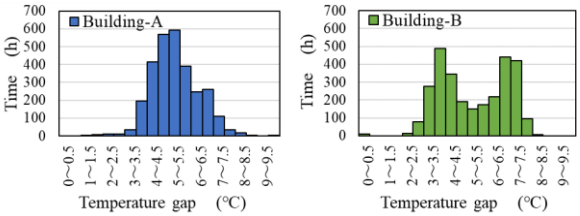

Fig.2. Temperature gap (summer)

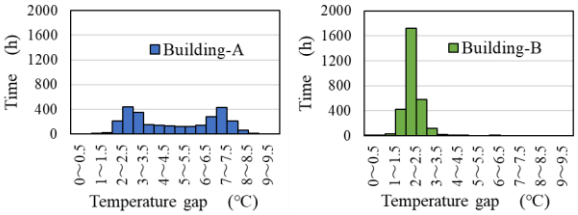

Fig.3. Temperature gap (winter)

3.3. Analyzing on transportation power on building per energy

We show transportation power per energy in summer and winter on Fig.4 ~ 7. In winter, heat pump air conditioning system is used in upper floor of building-B. Therefore, there is few days using chilled water. Heat exchanger system is efficiently on both routes and in both seasons. Direct supply system is also efficiently on lower floor in summer. However, it is more inefficiently on upper floor than lower floor. Energy per flow of two routes is almost same value, about 25 MJ/ ㎥ , but upper floor needs more transportation power like Fig.9. In winter, direct supply system is extremely inefficiently due to low temperature gap.

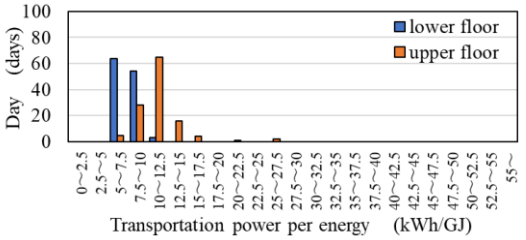

Fig.4. Transportation power per energy (Building-A, summer)

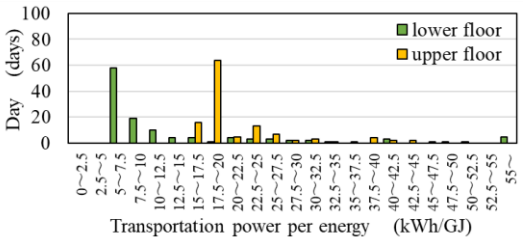

Fig.5. Transportation power per energy (Building-B, summer)

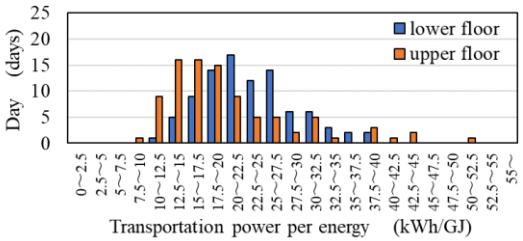

Fig.6. Transportation power per energy (Building-A, winter)

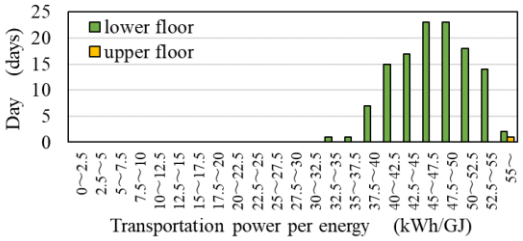

Fig.7. Transportation power per energy (Building-B, winter)

3.4. Analyzing on transportation power on building per flow of a chilled water

We show transportation power on building per chilled water on Fig.8 and 9. There is only pressure loss in piping in building using heat exchanger system. However, it is necessary to bring chilled water to top of building using direct supply system. In this reason, transportation power needs more energy on upper floor in direct supply system.

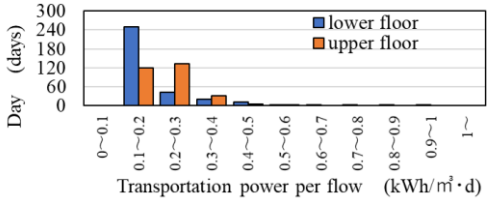

Fig.8. Transportation power per flow (Building-A)

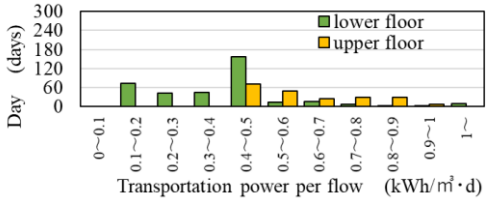

Fig.9. Transportation power per flow (Building-B)

3.5. Comparison of temperature gap with other area

In this section, we study whether it is standard feature that we can see on building-A and B. We couldn't get transportation power on building from plant day report, so we analyze only temperature gap.

We show temperature gap on building in area-F, G and I on Fig.10 ~ 15. In area-F, on building-h, I, j, k and l, it can get high temperature gap both summer and winter. However, on building-d, e and f, it couldn't get temperature gap in winter. All buildings in area-G use heat exchanger system and get high temperature gap both summer and winter. In area-I,

on building-h, and i, it couldn't get temperature gap in winter. The reason why building-b also couldn't get temperature gap is that it is a station and there is no demand of chilled water.

From these study, direct supply system is influenced by heat demand and way of control.

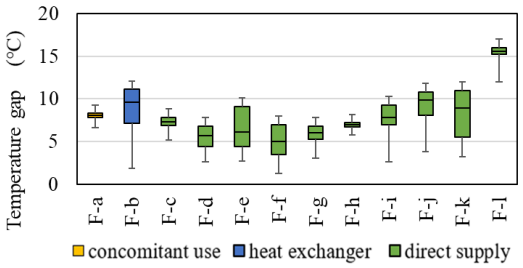

Fig.10. Temperature gap on area-F (summer)

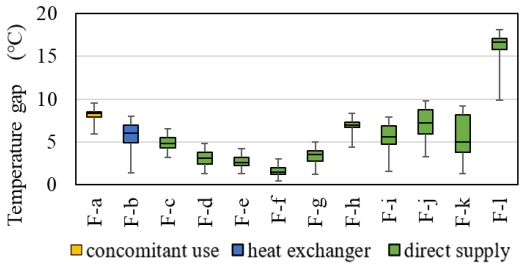

Fig.11. Temperature gap on area-F (winter)

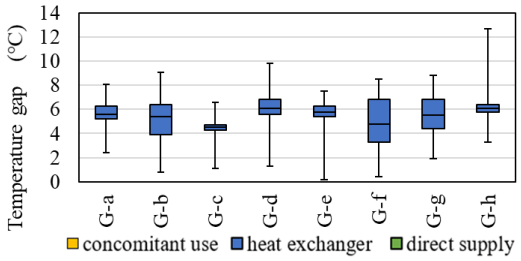

Fig.12. Temperature gap on area-G (summer)

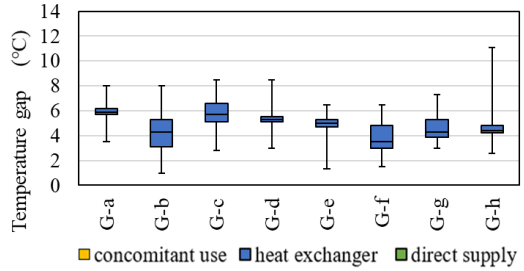

Fig.13. Temperature gap on area-G (winter)

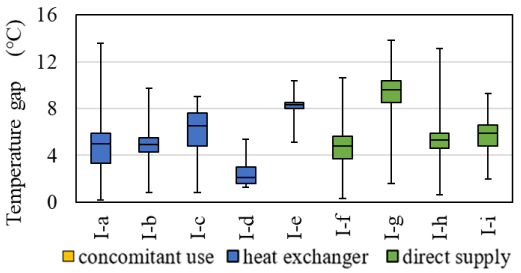

Fig.14.Temperature gap area-I (summer)

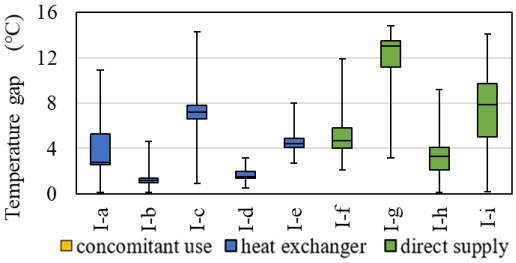

Fig.15. Temperature gap on area-I (winter)

4. Conclusions

In this study, we analyze transportation power on both plant and building and can get some feature on whole the area.

1. Transportation power on plant is influenced by chilled water per heat demand and pressure. In order to decreasing transportation power, it is necessary to get high temperature gap and control in lower pressure.
2. In summer, transportation power is more influenced by chilled water per heat demand and in winter, it is more influenced by pressure.
3. It is difficult for direct supply system to get temperature gap and there is a tendency that transportation power become higher.
4. There is only pressure loss in piping on heat exchanger system. However, direct supply system needs to bring chilled water to top of the building and needs more energy. In addition, it couldn't use pressure from DHC on building-B.
5. Building introducing heat exchanger system doesn't get great gap in temperature gap between summer and winter. However, some of the building introducing direct supply system couldn't get temperature gap. Direct supply system is influenced by heat demand and way of control.

We will simulate some energy conservation method like demand response, lowering past presser, using thermal storage tank and charging on electric vehicle.

5. References

[1] K Koyama. Research on transportation power and heat loss of District Heating and Cooling. The Society of Heating, Air-Conditioning Sanitary Engineers of Japan Vol.2014.9.3~5 (Akita), pp.157-160

[2] T Hagiwara. Saving Energy of Supply Chilled water Pump that uses Inverter for District Heating and Cooling. The Society of Heating, Air-Conditioning Sanitary Engineers of Japan Vol.2004.9.8~10 (Nagoya), pp.189-192

[3] O Kunitomo. CO_2-Reducing City Planning by Smart Energy Network Part11. The Performance Evaluation of Conveying Power Decreases, Renewable (Unused) Energy and CGS. The Society of Heating, Air-Conditioning Sanitary Engineers of Japan Vol.2016.9.14~16 (Kagoshima), pp.17-20

History and development of wood lath and plaster techniques in Japan

Kentaro Oka[1,a] and Masaki Tamura[2,b]

[1] Department of Architecture, Senior researcher, Kogakuin University, Tokyo, Japan, M. Eng.
[2] Department of Architecture, Kogakuin University, Tokyo, Japan, Dr. Eng.
[a] du41633@ns.kogakuin.ac.jp, [b] masaki-t@cc.kogakuin.ac.jp

Abstracts

INTRODUCTION In Japan, more and more buildings are being damaged by disasters such as earthquakes and floods[1]. Therefore, there is an increasing concern about the preservation of traditional architecture. Plastering is one of traditional construction methods, and its quality is easily affected by skills of plasterers and characteristics of materials, and thus the difference in quality is huge.

In Japan, plastering techniques have existed since ancient times, but around the 19th century, plastering techniques of European origin began to be introduced. As an example, there is wood lath and plaster technique, which until then were almost unheard of in Japan at that time. This is because the main plastering technique in Japan until then was a combination of bamboo lath, clay, straw and plaster.

Wood lath and plaster became popular along with the "European style architecture" in Japan, and evolved, being combined with ancient Japanese techniques as they were used for walls and ceilings. Fig.1 shows the cases of Japanese plastering. While many of these walls and ceilings still remain today, they may have been damaged over the years. These preservation methods attempt to reinforce components from the surface or the back side, and reconstruction of the members should be avoided as far as possible[2-4]. In addition, prior to the preservation of buildings, it is necessary to understand their health by observing them and surveying documents.

In this paper, we investigate a construction manual from 1930s to analyze details of wood lath and plaster ceilings. In addition to this, other documents on wood lath and plaster at that time will also be investigated and the characteristics of technique will be discussed.

SURVEY AND EVALUATION The survey target is one historical building completed in the 1930s. For the specification of the ceiling, we interviewed the people in charge of management about the contents related to the specification of construction at that time, and collected information such as construction manuals. (herinafter referred to as "1930s document") On the basis of 1930s document, we compared them with reports by Matsumoto et al., documents from the same period as the subject building construction, and standards of later years. Then, the specification of the wood lath and plaster ceilings of the subject building, including material dimensions and formulations, were evaluated relatively.

a)Traditional Japanese plastering (bamboo lath)

b)Plastering of wood laths

c) Above the wood laths and plaster ceiling

d)A case of plaster ceiling (wood lath, in 1911)

Fig.1. The cases of Japanese plastering

Table 1. Materials used for the building components of the historical building

Parts	Materials	Main roles
Laths	Cedar bord	Foundation
Plasters	Slaked lime	Binder (Hard)
	Shell lime	Binder (Improve workability, Anticrack)
	River sand	Hardner, Anticrack
	Seaweed extract	Water retention, Improve workability
	Hemp fiber	Reinforcing binder
	Palm bark	
	Palm fiber	

MATERIALS USED IN JAPANESE PLASTERING Table 1 shows materials used for building components of the historical building. The materials used for wood lath and plaster were similar to those described in the general document at the time of construction. Their features are blended two different binders, one made from limestone and the other from shells. Both have different advantages, the former has strength, the latter has workability and anti-crack. As a similar technique, plasterers mix seaweed extract into the plaster in Japan. Seaweed helps plaster to retain water and improve work efficiency. All of the above are examples of characteristics of Japanese plastering techniques.

COMPOSITIONS OF WOOD LATHS Table 2 shows comparison of the wood laths substrate specifications under investigation with other document sources. The units of measurement in each document were converted to SI units because they were expressed in old standards. In each document,

Table 2. Comparison of the wood lath substrate specifications under investigation with other document sources

Documents	Period	Width (mm)	Thickness (mm)	Cross-section	Slit width (mm)	Joints	Nailing
Reports by Matsumoto et al.[5]	1869～1911	20～100 (avg.57.6)	2～24 (avg.12)	Not described	0～18 (avg.8.6)	Not described	1～2 nails
1923 document [6]	1923	28.5～36	7.5		12	Alternately	2 nails
AIJ Pamphlets [7]	1930	30～36	7.5(Use thick for ceilings)		6～9	Butt joint Alternately (every 8 lines)	2 nails (Galvanized)
1930s document (Interview)	1930s	36	12	For the ceiling, cut it into a trapezoidal shape	9	Slit of 3mm Alternately(every line)	2 nails (Galvanized)
Nippon-kabe no Kenkyu [9]	1954	39	7	Not described	6～10	Butt joint Alternately (every 10 lines)	2 nails
JASS*15 Plastering 1st ed.	1957	33			7	Butt joint Alternately (every 6 lines)	
JASS11 Carpentry 1st ed.	1959	36				Slit of 3mm Alternately(every 6 lines or less)	
JASS11 Carpentry 1st additional. ed.	1961	40			Not described		
JASS15 Plastering 2nd ed.	1975				7 (Walls) 10 (Ceilings)		

*JASS: Japanese Architectural Standard Specification

unless there are special notes, no distinction between walls and ceilings in the substrate dimensions is regarded. As previously stated, except for a few special cases, the wood lath and plaster is said to have been popularized as a technique used for building components only after 19th century. Matsumoto et al. reported the results of a field survey of wood lath bases specifications from the dawn of the wood lath and plaster method to the late Meiji era (Meiji: Japanese era name: 1868-1912).

According to the results, the average of the cross-sectional dimensions of wood laths is larger than those described in Japanese Architectural Standard Specification (JASS), etc., and the variation tends to be large. The variation in the slit width is also large, and it is stated that there are some members with 0 mm[5]. The reason for this is that the mechanism of the wood lath and plaster method was not sufficiently understood before the wood lath and plaster method was standardized under the building specifications by the Architectural Institute in 1923 (hereinafter referred to as “1923 document”, it is earliest JASS) [6].

Since the publication of the 1923 document, the cross-sectional dimensions of the wood laths described in the various documents are similar to those in 1923. This means that the 1923 document may have been the standard for many of other documents at the time. On the other hand, there are traces of ingenuity to improve the strength of wood laths in some of the documents. (e.g., thickness of lath, construction of joints, nailing of lath) [7]

It is worth noting that the 1930s document is the only one that mentions the cross-sectional shape of wood laths, and it says, "The one used for the ceiling is cut into a dovetail shape (reverse taper)...". It is presumed that the intention was to prevent plaster from falling off at slits by using a trapezoidal cross-section for the wood lath.

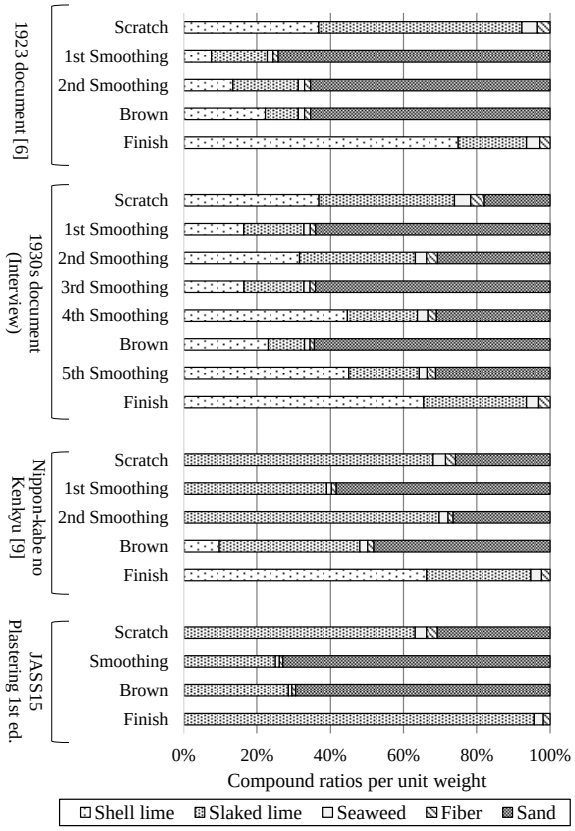

Fig. 2. Each coat of plaster compounding ratio described in each document

COMPOSITIONS OF PLASTERS Fig. 2 shows each coat of plaster compounding ratio described in each document[8,9]. All compounding ratios in documents were converted to kg and graphed as ratios per unit weight.

It is generally recommended for compounding ratio of plastering materials to be lean mixed (low binder ratio) toward the finish coat, and the various documents shows the same tendency. Additionally, the compounding ratio of each layer in the 1930s document is similar not only to that in the 1923 document but also to that in later documents. Therefore, we think that the ratio of plaster in the 1930s document was already developed by the time the 1923 document was published. However, the ratio of a scratch coat in the 1930s document has a larger compounding ratio of sand than in the 1923 document, and this part of the specification is close to the content of later documents. Since drying shrinkage of plaster is inhibited by increasing the ratio of sand, that is assumed to be the intension. However, it is important to balance the compounding ratios of sand and plaster strength.

Table 4 shows example of methods to prevent plaster from peeling off, and Fig. 3 shows ceiling cross section referring to the 1930s document. It shows that plastering ceilings of the historical building had high quality considering the size and cross-sectional shape of wood laths, the construction of joints, and the number of coats. This means that the techniques introduced in the 19th century had been improved by the 1930s, which is unique to Japan. However, not all buildings have such specification, so it is likely that different techniques were used depending on purposes such as durability and strength of the building.

CONCLUSION Japanese plastering techniques were combined with techniques of European origin around the 19th century. One of the examples is wood lath and plaster, which was an inexperienced technique for plasterers in Japan. However, those techniques were developed independently in Japan by the 1920s and were included in the specification documents. The documents were considered to prevent of plaster from falling off. (e.g., cross-sectional dimensions of wood laths, slit width, construction of joints, nailing of lath, compound ratio of plaster)

Based on that, we interviewed and researched the specifications of historic buildings built in the 1930s. As it turned out, the specifications were similar to other documents of the time, and furthermore, the cross-section of the lath was cut into a trapezoidal shape. This cutting method was not mentioned in any of the documents, and it was determined that the method was managed for different purposes of buildings.

Table 4. Example of methods to prevent plaster from peeling off

Elements	Methods
Wood lath	Cut into a reverse taper.
Scratch coat	Remove dirt from lath surfaces and fill the slit with plaster.
Palm bark	After carefully loose the bark, integrate it with the plaster.
Palm fiber	Tie to a nail, and hang it on wood laths at regular intervals. Integrate the fiber hanging down with the plaster.

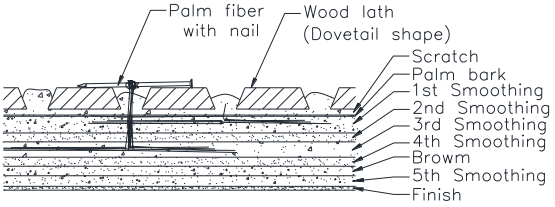

Fig. 3. Ceiling cross section referring to the 1930s document

References

[1] Architectural Institute of Japan. *Preliminary Reconnaissance Report of the 2011 Tohoku-Chiho Taiheiyo-Oki Earthquake*. Maruzen Publishing. 2011. (in Japanese)

[2] Sawano, K. et al.. *Development of Maintenance and Conservation Methods for historical Architecture using plaster wall materials (Part2) Repairmending Method of Wood SIiding and Plaster in Existing Architecture*. Journal of Japan Society for Finishings Technology. pp.207-210. 2015. (in Japanese)

[3] Oka, K. et al.. *Development of Maintenance and Conservation Methods for historical Architecture using plaster wall materials (Part3) Performance Evaluation of Destruction Mechanism and Repair Effect in Lath and Piaster Ceiling*. Journal of Japan Society for Finishings Technology. pp.211-214. 2015. (in Japanese)

[4] Oka, K. et al.. *Development of Maintenance and Conservation Methods for historical Architecture using plaster wall materials (Part6) Repair of wooden lath and plaster ceiling in Iwate bank*. Journal of Japan Society for Finishings Technology. 2016. (in Japanese)

[5] Matsumoto, N. *A Study on External Wall of Modern Timber Architecture in Japan (part5) A Bibliographic Survey on Dimensions and Details of Wooden Lath*. Summaries of technical papers of annual meeting. Architectural Institute of Japan. pp.441-442. 2015. (in Japanese)

[6] Architectural Institute of Japan. *Japanese Architectural Standard Specifications*. Journal of architecture in Japan. 1923. (in Japanese)

[7] Yoshida, K. *Shikkui-kabe no Chishiki (Knowledge of Plaster walls)*. AIJ Pamphlets. Architectural Institute of Japan. 1930. (in Japanese)

[8] Yamada, K. *Nippon no Kabe (Japanese Walls)*. Shinshindo Publishing. 1982. (in Japanese)

[9] Nakamura, S. *Nippon-kabe no Kenkyu (Study of Japanese wall)*. Sagami Syobo Publishing. 1954. (in Japanese)

GIS-Based Assessment of Emergency Referral Systems and Ideal Locations for Ambulance Stations in the Province of Cavite, Philippines

Kathleen Ann E. Villapol*, Jedidiah Joel C. Aguirre, Judie Ann A. Ramos, and Harvey S. Maunahan

Department of Civil Engineering, College of Engineering and Agro-Industrial Technology, University of the Philippines Los Baños, Laguna, Philippines
E-mail: kevillapol@up.edu.ph

Abstract

In this paper, the Emergency Referral System (ERS) of Cavite Province was assessed through ArcGIS Pro Network Analyst, with the Service Area Reach and Location-Allocation Extensions. The response time, the time it takes the ambulance to be dispatched to the destination of interest, was classified into four major levels: Good, adequate, substandard, and poor. A list of hospitals, Rural Health Units (RHUs) and Barangay Health Units (BHUs) in Cavite Province was obtained the Department of Health (DOH)[3]. Using the Network Analyst-Service Area Reach Analysis of ArcGIS Pro, it was found that only 20.66% of the population in Cavite Province had access to Ambulance services that provide good response time. Using the Location-Allocation feature of ArcGIS Pro, health facilities that offer emergency room (ER) without ambulance services were chosen as candidate facilities, hospitals that have ER services were designated as required facilities, and the BHUs as Demand Points. 23 of the candidate facilities identified in this study were chosen to maximize the good response time service to the remaining BHUs while minimizing the number of candidate facilities chosen. Even with the additional chosen facilities, only 61.35% of the population in Cavite Province has access to ambulance services with good response time.

Key Words: Geographic Information System (GIS), ArcGIS Pro, Network Analyst, emergency referral system, ambulance response time, ambulance stations, emergency services

Introduction

Cavite is one of the fastest growing provinces, and being situated close to the West Valley fault and Taal volcano make it highly susceptible to calamities[5]. The lower areas of Cavite such as Maragondon, Naic, Dasmarinas, etc. are prone to flash floods[6]. Moreover, prime locations such as Tagaytay city imposes heavy traffic conditions that often overflows towards Amadeo, Mendez, and Silang. Furthermore, the preparedness of health centers in the Philippines given major calamities such as earthquakes, flash floods, typhoons, volcanic eruptions, etc. regarding ambulance response time does not meet the global standard of 8 minutes[1].

One of the common issues involved in Emergency Referral Systems (ERS) is the lack of operating expenses, decaying infrastructure, and distinction between levels of service such as not all Rural Health Units (RHUs) providing ambulance services[4].

BHUs provide primary services and determine whether a patient requires secondary services from RHUs and Hospitals with ER. There have been cases wherein primary and secondary health units are situated close to one another limiting the ambulance service area reach to certain locales[2]. Due to all of this, the Province of Cavite lacks proper ERS services.

Methodology

The geocoded table of health facilities with permanent ambulance stations was inputted into the Service Area Reach extension as the facilities whose reach is to be observed. The service area was set to driving time. The driving times from the location were segregated into three: 0-8 minutes, 8-12 minutes, and 12 to 16 minutes. The direction was set away from facilities.

The geocoded table of the health facilities, both those that provide ambulance services and those that only provide Emergency Room service for the province of Cavite, and the locations of the BHUs and their respective population weights were segregated into three groups and inputted into ArcGIS Pro Network Analyst: Location-Allocation Extension: Maximize Coverage-Minimize Facilities Type. The health facilities were segregated as follows:

1. Required Facilities – Hospitals with Emergency Room and Ambulance Services
2. Chosen Facilities – Hospitals and RHUs without permanent ambulance departure stations.
3. Demand Points – Population weighed BHUs

Results and Discussion

Using ArcGIS Pro, the base map was georeferenced to the 1992 Philippine Reference System. The Network Analyses layers, specifically the Service Area Reach Extension and the Location-Allocation Extension, were georeferenced to 1984 World Geodetic System.

Service Area Reach Extension

The results of the Service Area Reach extension indicates that 56.51% of Cavite province has Poor Response Time, that being a response time of 16 minutes and over. Moreover, 9.86% have Substandard, 12.97% have Adequate, and only 20.66% have access to Good Response Time. The summary of the results, including total areas in terms of Hectares (Ha) of Good, Adequate, Substandard, and Poor Response Times can be seen in Table 1.

Table 1. Area of Cavite with varying Response Times.

RESPONSE TIME	CUTOFF RANGE (min)	TOTAL AREA (Ha)	AREA%
Good	0-8	29,491.31	20.66
Adequate	8-12	18,160.39	12.97
Substandard	12-16	14,069.15	9.86
Poor	>16	80,640.59	56.51

Figure 1 shows that most of the northeast portion of Cavite has, on average, Adequate to Good Response Time. The cities of Bacoor, Cavite, Dasmarinas, the Municipality of Imus, and the Municipality of Noveleta are the only five municipalities and cities that have facilities which provide the area with Good Response Time. The Municipalities of Carmona, Naic, Tanza, Kawit, Silang, General Trias City, and Trece Martirez City have facilities which provide an Adequate to Good Response Time.

However, majority of the southwest portion of Cavite has Substandard to Poor Response Time, with Tagaytay City being the only exception wherein it contains facilities with a Substandard to Adequate Response Time. The Municipality of Amadeo has a Substandard to Adequate response, while the Municipalities of Alfonso, Maragondon, Mendez, and Ternate have facilities which provide Substandard to Adequate Response Time, while the Magallanes, General Emilio Aguinaldo, and Indang have Poor Response Time. Figure 1 includes the reach of the facilities even outside the province to showcase that some facilities provide service outside Cavite.

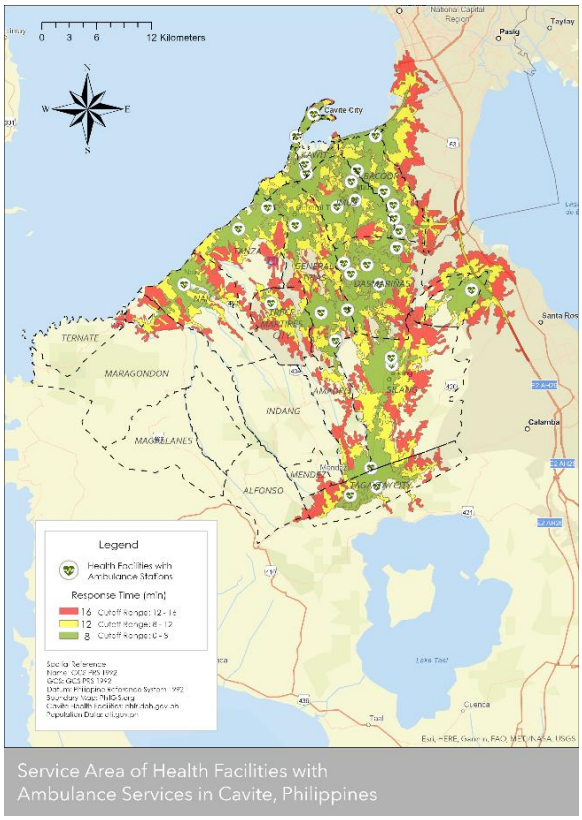

Fig. 1. Service Area of Health Facilities with Ambulance Service in Cavite, Philippines.

Location-Allocation Extension

Network Analyst: Location-Allocation Extension was set to the "Maximize Service Area – Minimize Facilities" to find the maximum number of BHUs that can be serviced by the minimum number of facilities chosen. The geocoded table featuring the list of Health Facilities with permanent Ambulance Stations were set as the Required Facilities to cater to Demand Points, amounting at a total of 666 BHUs. Figure 2 shows the locations of the Chosen Facilities for Ambulance Stations.

Some Candidate Facilities that were not chosen due to many possible reasons: Either they are located too far from the BHUs in question; the traffic conditions in the given locations do not permit for the Ambulances to arrive within the eight-minute mark, the road condition (e.g., one-way traffic) which do not permit Ambulances to pass that route, the BHUs have already been addressed by the Health Facilities with permanent Ambulance Stations; or that BHUs can be addressed by another Candidate Facility with a more prime location.

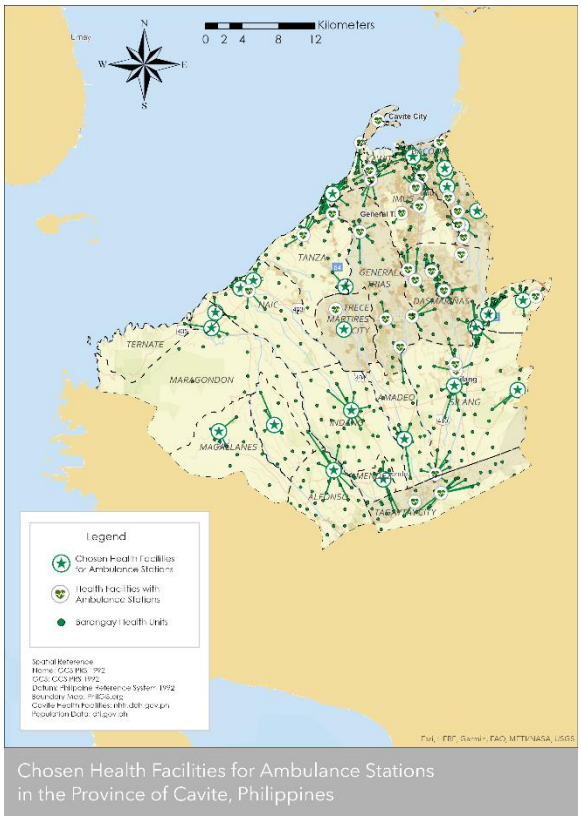

Fig. 2. Chosen Health Facilities for Ambulance Stations in the Province of Cavite, Philippines

Table 2 lists the Chosen Facilities and the number of BHUs they address. These should be the facilities prioritized when establishing Ambulance Stations, or when deciding where to allocate existing Ambulance Services.

Table 2. Chosen Health Facilities and the Number of BHUs addressed.

HEALTH FACILITY NAME	BHUs
Alfonso Rural Health Unit	18
Amadeo Rural Health Unit	2
Strike sa Serbisyo City Health Unit II (Floraville)	5
Strike sa Serbisyo City Health Unit III (Salinas)	24
Strike sa Serbisyo Lying-in & City Health Unit IV	5
Strike sa Serbisyo City Health Unit V (Molino III)	1
Strike sa Serbisyo City Health Unit VI (Queens Row)	1
Carmona Rural Health Unit	12
General Emilio Aguinaldo Rural Health Unit	4
General Mariano Alvarez Rural Health Unit I	17
Indang Rural Health Unit	11
Our lady of the way medical & pediatric clinic	4
Maragondon Rural Health Unit	3
Mendez-Nunez Rural Health Unit	13
Naic Medicare Hospital	4
Naic Rural Health Unit	8
Rosario Rural Health Unit II	20
Adventist University of the Ph Health Service	3
Bulihan Rural Health Unit	21
Silang Rural Health Unit	16
Arsecom Infirmary	4
Ternarte Rural Health Unit	2
Trece Martirez City Health Office	2
TOTAL	200

It was observed that with the additional Chosen Facilities the municipalities of Bacoor, Carmona, and Rosario now have 100% of their population having access to Good Response Time with the additional Ambulance Stations to be set in the Chosen Facilities. The Cities and Municipalities with 50% or less of their population having access to Good Response Time, even with the additional Chosen Facilities, are the Municipalities of Alfonso, Amadeo, General Emilio Aguinaldo, Indang, Magallanes, Maragondon, Ternate, Trece Martires, and the city of Imus. These municipalities and city should be prioritized by the Local Government Units (LGUs) when establishing new independent Ambulance Stations.

Table 3. Health Facilities Impact on BHUs and Population in Cavite Province.

FACILITY TYPE	NO. OF FACILITIES	BHUs	POPULATION %
Required	34	208	31.89
Chosen	23	200	29.46
TOTAL	57	408	61.35

The summary of the impact of the chosen facilities seen in Table 3, found that the 34 Required Facilities, otherwise known as the health facilities with ER services and permanent ambulance stations, only service 208 BHUs and 31.89% of the population of Cavite Province. It was also found that a maximum of 200 BHUs can be serviced by a minimum of 23 Candidate Facilities. If the 23 Chosen Facilities were to have permanent Ambulance Stations, an additional 29.46% of the population of Cavite will have access to Ambulance Services with Good Response Time, effectively increasing the total percentage of the population with Good Response Time within Cavite Province to 61.35%. The Chosen Facilities listed in Table 2 and summarized in Table 3 shows that there is still 38.65% of the population of Cavite Province that does not have access to Ambulance Services that meet the global standard Response Time of eight minutes; Therefore, there is a need for the establishment of additional facilities for Ambulance Stations in Cavite Province

References:

[1] Estember, R. D., Isip, I. G. A., & Misal, M. C. C. (2019). *An Optimization-based Approach Model for the Improvement of the Performance of Emergency Medical Service Ambulances*. 1163–1171.

[2] Dayrit, M., Lagrada, L., Picazo, O., Pons, M.,& Villaverde, M. (2018). Philippines Health System Review 2018. *Health Systems in Transition, 8*(2),1164.http://apps.searo.who.int/PDS_DOCS/B5438.pdf

[3] Department of Health. (2019). *National Healthy Facility Registry v2.0*. www.nhfr.doh.gov.ph *GIS - Maps | City of Delta Colorado*. (2020). Retrieved November 16, 2020, from https://cityofdelta.net/planning/page/gis-maps

[4] Grundy, J., Healy, V., Gorgolon, L., & Sandig, E. (2003). Overview of devolution of health services in the Philippines. *Rural and Remote Health, 3*(2), 220. http://www.ncbi.nlm.nih.gov/pubmed/15877513

[5] Notorio, P. A. C., Mandigma, E. C., Desingano, B. R., Buenviaje, J. S., & Mejia, G. C. R. (2016). Sustainable tourism development needs in the province of Cavite, Philippines. *Social Sciences (Pakistan), 11*(20), 4871–4874. https://doi.org/10.3923/science.2016.4871.4874

[6] Philippine Statistics Authority. (2015). *Provincial Government of Cavite Local Government Report*. https://psa.gov.ph/sites/default/files/CAVITE.pdf

Lightning Talk Session

Environmental Chemistry and Chemical Engineering

November 23rd

Presentation No.	Title	Author	
ECCL1.	Exfoliation Behavior of Graphite in Sulfuric Acid Electrolyte	Ryuichi Maekawa, Yusuke Muramatsu, Takumi Hisadome, and Hideki Hashimoto	333
ECCL2.	Metylation Benzene with Methane Catalyzed by Co/MFI Zeolite	Kai Tanaka, K.Okumura	334
ECCL3.	Preparation a Series of Polybenzimidazole Random Copolymer Membranes based on a Polyphosphoric Acid Process	Hsiao-Wu Lai, Zhi-You Lin, and Cheng-Chien Wang	335
ECCL4.	Application of single-particle electrochemical measurement for various positive electrode materials	Tamotsu Sawahashi, Kasane Takai, Kei Nishikawa, Takeshi Kobayashi, and Shiro Seki	336

Exfoliation Behavior of Graphite in Sulfuric Acid Electrolyte

Ryuichi Maekawa, Yusuke Muramatsu, Takumi Hisadome, Hideki Hashimoto

Department of Applied Chemistry, School of Advanced Engineering, Kogakuin University, Tokyo, Japan
E-mail: hideki-h@cc.kogakuin.ac.jp

Abstract

Because graphite is composed of graphene layers weakly bonded via van der Waals forces, it is easy to obtain graphene-like two-dimensional materials from graphite through various exfoliation techniques. The chemical oxidation and exfoliation of graphite is the most promising industrial method, but it requires large amounts of oxidants, strong acids, and pure water. The electrochemical exfoliation method, which uses electrochemical oxidation and ion intercalation to exfoliate graphite, has attracted much attention as a clean process that does not require oxidants[1]. In the anodic electrochemical exfoliation using a sulfuric acid electrolyte, radical species generated from water splitting reaction functionalize the edges of graphite. Sulfate ions are subsequently intercalated between the expanded graphene layers, and the exfoliation was induced by the pressure of the generated gaseous products[2,3]. However, the effect of the electrolytic factor on the structure of the exfoliated products has not been clarified. In this study, we focused on the anodic reaction to clarify the effect of electrolytic factors on the exfoliation behavior of graphite using sulfuric acid electrolyte.

Constant voltage electrolysis at 5-20 V or constant current electrolysis at 5 A in 0.1-5 mol dm^{-3} sulfuric acid were conducted using graphite foil as an anode. After electrolysis, the sample dispersed in the electrolyte was filtered, washed, and stored in N,N-dimethylformamide (DMF) to evaluate the dispersibility. The morphology of the prepared samples was characterized by optical microscopy and scanning electron microscopy (SEM), and the crystal structure of the samples were characterized by X-ray diffractometry (XRD).

As a result of constant voltage electrolysis of graphite foil using various concentration sulfuric acids, the initial current value increased with increasing voltage, and the time for the completion of exfoliation of the immersed area in the electrolyte became shorter. These results suggest that highly concentrated electrolyte yielding high current value is preferable for short time exfoliation. We kept the current constant and varied the concentration of the electrolyte and found that the exfoliation process was completed within a few minutes when using sulfuric acid with concentrations of $\geq$1 mol dm^{-3}. However, there was no linear relationship between the amount of electricity and the time required to complete exfoliation, suggesting that a part of unreacted graphite anode fell off in the electrolyte under the conditions where exfoliation was completed in a short time.

References

[1] H. Chen, C. Li, L. Qu, *Carbon* **140**, 41-56 (2018).

[2] K. W. Hathcock et al, *Anal. Chem.*, **67**, 2201-2206 (1995).

[3] S. Pei et al, *Nat. Commun.*, **9** (1), (2018).

Metylation Benzene with Methane Catalyzed by Co/MFI Zeolite

K.Tanaka and Pf. K.Okumura

Department of Chemistry Graduate School of Engineering, Kogakuin University, Tokyo, Japan
E-mail: bm21032@ns.kogakuin.ac.jp

Abstract There is a need to derive methane into high value-added organic compounds, but it is difficult to derive methane into other organic compounds due to the high binding energy of the C-H bond. The methylation of benzene has been studied because it can be used to obtain high value-added compounds such as p-xylene. We found that cobalt acetate was used as a cobalt precursor and the catalyst was supported on MFI by ion-exchange method to obtain toluene in 5% yield. The yield of toluene was investigated by varying the concentration of cobalt acetate solution and the Si/Al_2 ratio of MFI. In the ion-exchange method, it was found that the higher the concentration, the higher the cobalt loading, Co/Al = 0.5 or higher. Si/Al_2 ratio comparison showed that small Si/Al_2 deactivation and large Si/Al_2 ratio deactivation.

1.Introduction Methane, the main component of natural gas, is abundant on earth and is currently expected to be used as a carbon resource to replace petroleum as a raw material for chemical products. In particularly conversion of methane into value-added organic compounds,i.e. alkenes efforts have been made in strongly required. Methylation of benzene ring with methane can be an option of effective use of methane, because it can produce such a valued compound as pala-xylene.For example, combinding the methylation of benzene into toluene (Reation (1)). However it is difficult to selectively direct methane to other compounds because of the large binding energy of the C-H bond. In our previous study, we found that the catalyst supported on NH-MFI by ion-exchange method using cobalt acetate gave 5 % yield in this reaction. The concentration of the aqueous cobalt acetate solution and the Si/Al_2 ratio of NH-MFI were newly investigated.

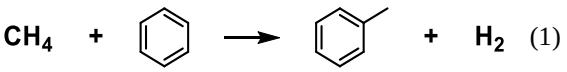

(1)

2.Experiment Cobalt was supported on NH-MFI (Si/Al_2=52) by the ion-exchange method using different concentrations of cobalt acetate as a raw material, resulting in NH-MFI-supported cobalt catalyst. The reaction were carried out in a fixed bed circulating reactor at 813 K for 1 h in a nitrogen atmosphere with 0.3 g of catalyst, methane/benzene = 29, W/F = 4 g s mol^{-1} after pretreatment. The analysis was carried out directly in gas form with MGS using FID-GC. The cobalt loading of the catalysts was determined with an atomic absorption spectrophotometer. XAFS was used to analyze the catalysts.

3.Results and Discussion The cobalt loading of the catalysts prepared by ion exchange increased with increasing cobalt acetate concentration during preparation. Fig.1 shows the yield of the target product, toluene, and its change with time. The MFI with a large Si/Al_2 ratio became active gradually and did not deactivate, while the MFI with Si/Al_2=23 showed high yield from the beginning of the reaction, but the yield decreased with time. The radial distribution function by XAFS is also shown in Fig.2. Despite being prepared by the ion-exchange method, when cobalt acetate was used as the Co precursor during preparation, aggregates of cobalt not supported on the ion exchange sites of the Co-O-Co bond were observed. This spectrum was similar to the spectrum of cobalt hydroxide. This was thought to be because the pH of the cobalt acetate solution was close to basic and cobalt hydroxide was formed during preparation.–Based on this and the change in toluene yield over time, it was considered that cobalt species supported by ion exchange were highly active and less selective, while cobalt species supported without ion exchange were highly active and selective.

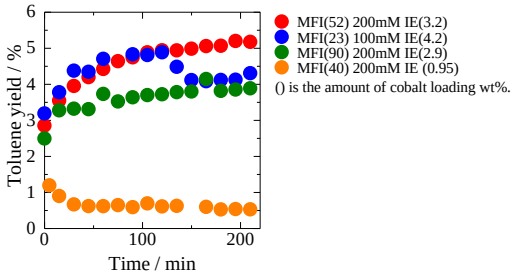

Fig.1 Changes in toluene yield over time for catalysts prepared using MFIs with different Si/Al_2 ratios.

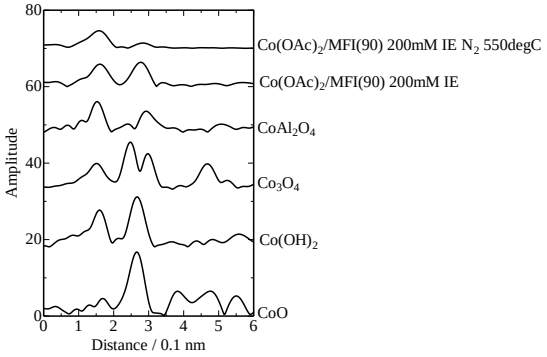

Fig.2 EXAFS radial distribution functions for cobalt in various states.

Preparation a Series of Polybenzimidazole Random Copolymer Membranes based on a Polyphosphoric Acid Process

Hsiao-Wu Lai*, Zhi-You Lin, Cheng-Chien Wang,

Department of Chemical and Materials Engineering, Southern Taiwan University of Science and Technology, Tainan, Taiwan
E-mail: swlai@stust.edu.tw

Abstract

In this work, the random copolymer of meta/para-polybenzimidazole (PBI) membranes were synthesized and fabricated as a candidate for hydrogen pump using polyphosphoric acid (PPA) process. Amounts of diacid monomers, IPA/TPA, were used and polymerized with 3,3,4,4-Tetraaminobiphenyl (TAB) to prepare a polymer that was composed of random copolymer (m/p-) polybenzimidazole unit. The membrane properties, such as structure, thermal and chemical stability, proton conductivity, mechanical properties, and ability to be manufactured into a membrane and electrode assembly (MEA), are discussed in detail by Fourier transform infrared (FTIR), thermogravimetric analysis (TGA), Fenton tests, Four Point Probe and Tensile testing. Membranes formed from the (m/p-) polybenzimidazole were found to be possessed higher acid doping levels, and showed improved proton conductivity, when compared to the commercial m-PBI.

Keywords:

Polybenzimidazole; m/p-PBI; hydrogen pump

Acknowledgments:

The corresponding author would like to thank Southern Taiwan University of Science and Technology (STUST) and Industrial Technology Research Institute (ITRI) for providing financial support for this research work.

References:

[1] Huang, F.; Pingitore, A.T.; Benicewicz, B.C. Electrochemical Hydrogen Separation from Reformate Using High-Temperature Polybenzimidazole (PBI) Membranes: The Role of Chemistry. ACS Sustain. Chem. Eng. 2020, pp. 6234–6242.

[2] Pingitore, A. T.; Huang, F.; Qian, G.; Benicewicz, B. C. Durable High Polymer Content m/p-Polybenzimidazole Membranes for Extended Lifetime Electrochemical Devices. ACS Appl. Energy Mater. 2019, pp. 1720−1726.

[3] Borjigin, H.; Stevens, K. A.; Liu, R.; Moon, J. D.; Shaver, A. T.; Swinnea, S.; Freeman, B. D.; Riffle, J.; McGrath, J. E. Synthesis and characterization of polybenzimidazoles derived from tetraaminodiphenylsulfone for high temperature gas separation membranes. Polymer 2015, pp. 135−142.

Application of single-particle electrochemical measurement for various positive electrode materials

Tamotsu Sawahashi[1)], Kasane Takai[1)], Kei Nishikawa[2)], Takeshi Kobayashi[3)], Shiro Seki[1)]

1) Graduate school of applied chemistry and engineering, Kogakuin University, Tokyo, Japan
E-mail: bm21025@ns.kogakuin.ac.jp
2) National Institute for Materials Science, Ibaraki, Japan
3) Central Research Institute of Electric Power Industry, Kanagawa, Japan

Abstract

Electrode active materials of electrode play an important role for battery performances. To further performance of lithium-ion batteries, essential understanding of active material is important for practical application. However, performance evaluation of active material individually is difficult owing to their complexity of applied sheet consisted of active material, binder and conductive additive. Therefore, in this study, single-particle electrochemical measurements (SPEMs) were examined for active materials. Additionally, electrochemical properties were compared with single particle and applied-type electrode.

Experimental

All SPEMs were carried out in the argon-filled glovebox (-80℃ dew point). Very thin Pt wires of 10μm or 20μm were inserted into glass capillary to obtain microprobe. Prepared microprobes could be contacted for SPEMs of various single active material particles. Li or Na foil were attached to a stainless steel cup as the counter and reference electrode. After particles of active materials were dispersed onto a glass filter, the electrolyte of 1M-LiFSA or NaFSA / ethylene carbonate (EC) were added into SPEMs cell. A example of single particle of positive electrode material (LMNO) is shown in Fig.1 as SEM image. Confirmation of electrical connection between microprobe and single particle by digital microscope, electrochemical measurements were carried out. Also, to evaluate properties of conventional coin-type cell, the applied-type positive electrodes were prepared using LMNO as an active material, PVDF as binder and acetylene black as a conductive additive by weight ratio 86:7:7, respectively. Prepared electrodes were assembled with metallic Li negative electrode and 1M-LiFSA/EC electrolyte using 2032-type coin cells. The assembled coin cells were evaluated by charge-discharge measurement to compare single particle properties.

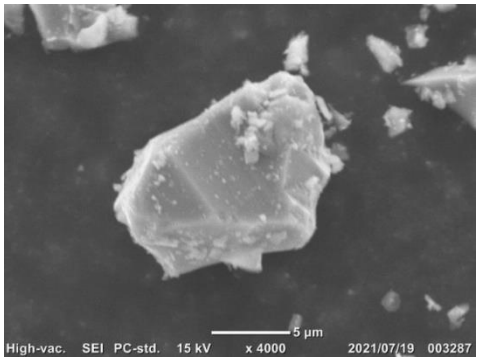

Fig. 1 SEM image of $LiMn_{1.5}Ni_{0.5}O_4$ (LMNO) single particle.

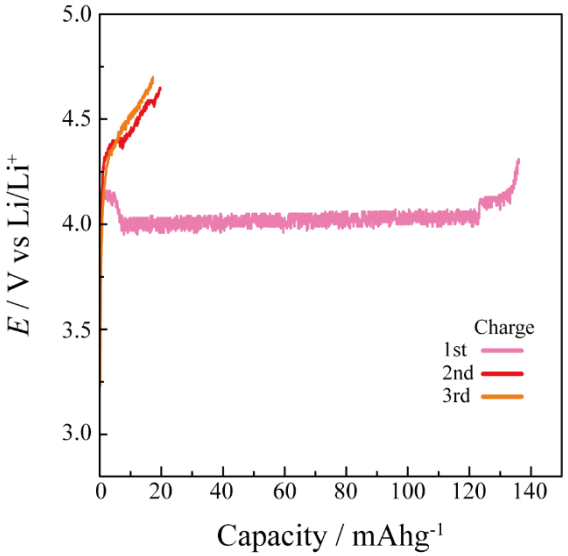

Fig. 2 Charge profiles of LMNO single particle for 1st~3rd cycles.

Results and Discussion

Fig. 2 shows the voltage profiles of the charge-discharge measurements of SPEMs cell using LMNO active material. The weight and capacity of single particle (ng order) were calculated from the apparent particle diameter and theoretical density of LMNO. Although charge capacity closed to theoretical value, sufficient reversible capacity couldn't be observed owing to their remarkable low reactivity of electrode should be happened cell degradation such as electrolyte decomposition. In this presentation, we will report about comparison between single particle and coin-cell properties using LMNO and NCO active materials.

References:

[1] T. Konya *et al.*, *Powder Diffraction*, 34 (2019).
[2] K. Nishikawa *et al.*, *Electrochemistry*, **85**, 72-76, (2017).
[3] T. Saito *et al.*, *J. Phys. Chem.*, **124**, 16758-16762, (2020).

Edited by
The 20th International Symposium on Advanced Technology (ISAT-20)

Published by
Kogakuin University of Technology & Engineering, Japan
1-24-2 Nishi-Shinjuku, Shinjuku, Tokyo, Japan
ISSN 2434-4273

Organized by
Kogakuin University of Technology & Engineering, Japan
Co-Organized by
Southern Taiwan University of Science and Technology, Taiwan
Kogakuin University of Technology and Engineering, Japan
The University of Danang - University of Science and Technology, Vietnam
University of Philippines Los Baños, Philippines